

**Development and Implementation of New DFT/MRCI
Hamiltonians for Odd and Even Numbers of Electrons**

INAUGURAL-DISSERTATION

zur

Erlangung des Doktorgrades der
Mathematisch-Naturwissenschaftlichen Fakultät
der Heinrich-Heine-Universität Düsseldorf

vorgelegt von

ADRIAN HEIL

aus Düsseldorf

Düsseldorf, September 2019

Aus dem Institut für Theoretische Chemie und Computerchemie
der Heinrich-Heine-Universität Düsseldorf

Gedruckt mit Genehmigung der
Mathematisch-Naturwissenschaftlichen Fakultät der
Heinrich-Heine-Universität Düsseldorf

Berichtersteller:

1. Univ.-Prof. Dr. Christel M. Marian
2. PD Dr. Oliver Weingart

Tag der mündlichen Prüfung: 8.11.2019

"Things are only impossible until they are not."

– Jean-Luc Picard

Eidesstattliche Erklärung

Ich versichere an Eides statt, dass die Dissertation von mir selbst verfasst und ohne unzulässige fremde Hilfe unter Beachtung der Grundsätze zur Sicherung der guten wissenschaftlichen Praxis an der Heinrich-Heine-Universität Düsseldorf erstellt worden ist. Die aus fremden Quellen direkt oder indirekt übernommenen Gedanken sind als solche kenntlich gemacht. Die Dissertation wurde in der vorgelegten oder in ähnlicher Form noch bei keiner anderen Prüfungsbehörde eingereicht. Es wurden keine früheren erfolglosen Promotionsversuche unternommen.

Düsseldorf, den 18.9.2019

Danksagung

Zu allererst möchte ich mich bei meiner Doktormutter Prof. Dr. Christel M. Marian für das interessante und neuartige Thema sowie die hilfreichen Diskussionen und die gute Betreuung bedanken. Auch weiß ich die Gelegenheiten und Möglichkeiten im Rahmen dieser Promotion sowie die Freiheiten und das damit verbundene in mich gesetzte Vertrauen sehr zu schätzen. Ebenfalls möchte ich mich bei PD Dr. Oliver Weingart für die Übernahme des Korreferats, insbesondere auch für die Kurzfristigkeit, sowie für hilfreiche Diskussionen zu Lösungsmittelleffekten bedanken.

Darüber hinaus gilt mein Dank Dr. Martin Kleinschmidt für hilfreiche Diskussionen, insbesondere zu technischen Fragestellungen.

Bedanken möchte ich mich auch bei Dr. J. Dominik Spiegel und Dr. Igor Lyskov für interessante und angenehme Gespräche und Diskussionen im fachlichen und fachfremden Kontext, sowie bei allen aktuellen und (inzwischen) ehemaligen Mitgliedern des Instituts für Theoretische Chemie und Computerchemie für die schöne gemeinsame Zeit.

Mein besonderer Dank gilt meiner Verlobten Paulina Trusova für die Unterstützung während der Promotion und auch für die Geduld, wenn ich am Wochenende 'kurz mal einen Job abschicken' wollte und es dann doch etwas länger wurde. Ebenfalls danke ich Paulina Trusova sowie Fabian Zillgens für das Korrekturlesen dieser Arbeit.

Der Deutschen Forschungsgesellschaft (DFG) danke ich für die finanzielle Unterstützung dieser Promotion mit der Projektnummer MA-1051/14-2.

Contents

Abbreviations	II
List of Publications	V
1 Introduction	1
2 Theory	5
2.1 Vertical Transitions and Excited States Processes	5
2.2 Density Functional Theory	6
2.3 Open Shells in Density Functional Theory	9
2.4 DFT Functionals	14
2.5 Configuration Interaction and Electron Correlation	15
2.6 The Combination of DFT and MRCI	19
3 The Datasets for Training and Testing	24
3.1 Dataset for Training	24
3.2 Dataset for Testing	25
3.3 Photoelectron Spectroscopy	26
4 Interface Development	31
4.1 Interface to Dalton	31
4.2 Interface to ORCA 4.0	34
5 DFT/MRCI Hamiltonian Development	39
5.1 The R2017 Hamiltonian (Paper 1)	39
5.2 The R2018 Hamiltonian (Paper 2 and 3)	42
6 Application of the New Hamiltonians	49
6.1 C [∧] N-Platinum Complexes (Paper 4)	49
6.2 Zinc(II) Tripyrrindione Radical (Paper 5)	51
6.3 Blatter Radical (Paper 3)	54
6.4 Triarylamine-Perchlorotriphenylmethyl Radicals	59
6.5 TTM-1Cz Radical	63
6.6 PAH-DTDA Radicals	65
7 Conclusion	69
References	72
Included Papers	82

List of Abbreviations

2-MeTHF	2-Methyltetrahydrofuran
acac	Acetylacetonate
ADC(2)	Algebraic-Diagrammatic Construction
bzq	Benzo[h]quinolinyl
CASSCF	Complete Active Space Self-Consistent Field
CC	Coupled Cluster
CC2	Approximate Coupled-Cluster Singles and Doubles
CC3	Approximate Coupled-Cluster Singles, Doubles and Triples
CCSD	Coupled-Cluster Singles and Doubles
CI	Configuration Interaction
CIS	Configuration Interaction Singles
dbq	Dibenzo[f,h]quinolinyl
DCM	dichloromethane
DFT	Density Functional Theory
DFT/MRCI	Combined DFT and MRCI
DFT/MRSOCI	Combined DFT and MRSOCI
dpm	Dipivolylmethanoate
DTDA	1,2,3,5-Dithiadiazolyl
ES	Excited State
eV	Electronvolt
FC	Franck-Condon
FCA	Frozen Core Approximation
GS	Ground State
HDOMO	Highest Doubly Occupied Molecular Orbital
HEG	Homogenous Electron Gas
HF	Hartree-Fock

HOMO	Highest Occupied Molecular Orbital
IC	Internal Conversion
IQE	Internal Quantum Efficiency
ISC	Intersystem Crossing
K	Kelvin
KS	Kohn-Sham
LC	Ligand Centred
LCD	Liquid Crystal Display
LED	Light Emitting Diode
LSDA	Local Spin Density Approximation
LUMO	Lowest Unoccupied Molecular Orbital
LYP	Lee, Yang, Parr
MAE	Mean Absolute Error
MaxAE	Maximum Absolute Error
MC-PDFT	Multiconfiguration Pair-Density Functional Theory
MCTDH	Multiconfigurational Time-Dependent Hartree
MeCN	Acetonitrile
MRCI	Multireference Configuration Interaction
MRSOCI	Multireference Spin-Orbit Configuration Interaction
MRMP2	Multireference PT2
NGA	Non-Separable Gradient Approximation
nm	Nanometre
OLED	Organic Light Emitting Diode
PAH	polycyclic aromatic hydrocarbons
PBE	Perdew, Burke and Enzerhof pure functional
PCTM	Perchlorotriphenylmethyl
PES	Potential energy surface
pm	Picometre

ppy	2-Phenylpyridyl
QM/MM	Quantum mechanics/ molecular mechanics
RASSCF	Restricted Active Space Self-Consistent Field
rISC	Reverse Intersystem Crossing
RMSE	Root-Mean-Square Error
RODFT	Restricted Open-Shell DFT
RT	Room Temperature - 298 K
SOMO	Singly Occupied Molecular Orbital
TARA	Triarylamine
TDHF	Time-Dependent Hartree-Fock
THF	Tetrahydrofuran
TTM	Tris(2,4,6-trichloro)methyl
UKS	Unrestricted Kohn-Sham
VWN	Vosko, Wilk, Nusair
WFT	Wave Function Theory
ZPE	Zero-Point Energy

List of Publications

Included as part of this thesis:

1. *DFT/MRCI Hamiltonian for odd and even numbers of electrons.*

Adrian Heil and Christel M. Marian, *J. Chem. Phys.*, 147, 194104 (2017)

Own contribution: Development and implementation of the R2017 Hamiltonian; collection of experimental vertical excitation energies of open-shell molecules for training and testing; quantum chemical calculations; statistical evaluation; creation of figures; first draft of manuscript

2. *On the performance of DFT/MRCI Hamiltonians for electronic excitations in transition metal complexes: The role of the damping function.*

Adrian Heil, Martin Kleinschmidt and Christel M. Marian, *J. Chem. Phys.*, 149, 164106 (2018)

Own contribution: Development and implementation of the R2018 Hamiltonian; collection of some of the experimental vertical excitation energies of transition metal complexes for testing; quantum chemical calculations; creation of figures; statistical evaluation; first draft of manuscript

3. *The DFT/MRCI method.*

Christel M. Marian, Adrian Heil and Martin Kleinschmidt. *WIREs Comput. Mol. Sci.*, 9, e1394 (2019)

Own contribution: Section on the benchmark of transition metal complexes; section on radicals; quantum chemical calculation of the Blatter radical; creation of figures; statistical evaluation

4. *Structure-Emission Property Relationships in Cyclometalated Pt(II) β -Diketonate Complexes.*

Adrian Heil and Christel M. Marian, *Inorg. Chem.*, 58, 6123 (2019)

Own contribution: Section on (C \wedge N) Pt Complexes; Quantum chemical calculations of (C \wedge N) Pt Complexes; supplemental material; creation of figures

5. *DFT/MRCI-R2018 Study of the Photophysics of the Zinc(II) Tripyrrindione Radical: Non-Kasha Emission?*

Adrian Heil and Christel M. Marian, *Phys. Chem. Chem. Phys.*, accepted (2019)
DOI:10.1039/C9CP04244J

Own contribution: Quantum chemical calculations; creation of figures; first draft of manuscript

Not included as part of this thesis:

1. *On the photophysics of four heteroleptic iridium(III)phenylpyridyl complexes investigated by relativistic multi-configuration methods.*

Adrian Heil, Kathleen Gollnisch, Martin Kleinschmidt and Christel M. Marian, *Mol. Phys.*, 114, 407–422 (2016)

Own contribution: Quantum chemical calculations on the cis Ir-complexes; creation of figures

2. *Simulation of X-ray absorption spectra using core-valence separated DFT/MRCI.*

Issaka Seidu, Simon P. Neville, Martin Kleinschmidt, Adrian Heil, Christel M. Marian, and Michael S. Schuurman, *J. Chem. Phys.*, accepted (2019)

Own contribution: Supply of and instructions to the Dalton interface for open-shell calculations with the DFT/MRCI program; corrections in the draft

Abstract

DFT/MRCI is a well-established semi-empirical quantum chemical method originally developed by Grimme and Waletzke [J. Chem. Phys., 111, 5645 (1999)]. Recently, a redesigned DFT/MRCI Hamiltonian, named R2016, was developed by Lyskov et al. [J. Chem. Phys., 144, 034104 (2016)] to improve the treatment of bi-chromophores.

Up until now the DFT/MRCI method was limited to closed-shell systems. In this thesis, the R2016 Hamiltonian of Lyskov et al. was successfully extended to open-shell systems based on restricted open-shell Kohn-Sham orbitals as the anchor configuration. The necessary orbitals are calculated with the Dalton program, for which an interface to the DFT/MRCI program was developed. Experimental electronic excitation energies of doublet states have been gathered from literature, since a collection of these states suitable for testing and training a parameter set does not exist. The new Hamiltonian, named R2017, is able to match the accuracy and computational performance on closed-shell and open-shell organic molecules that was achieved by the previous Hamiltonians on closed-shell molecules. The resulting accuracy, expressed as the root-mean-square error (RMSE), is below 0.2 eV.

While all DFT/MRCI Hamiltonians provide good results on organic molecules, a benchmark of transition metal complexes found an underestimation of vertical excitation energies, especially with the R2016 and R2017 Hamiltonians. The cause could be traced back to the off-diagonal damping function employed in both redesigned Hamiltonians. These findings instigated the development of a new Hamiltonian based on the R2017 Hamiltonian with improved vertical excitation energies for transition metal complexes, dubbed R2018 Hamiltonian. The RMSE of organic transition metal complexes is improved to 0.15 eV from the previously achieved accuracy of 0.20 and 0.25 eV of the original and R2016 Hamiltonians, respectively. The R2018 Hamiltonian provides the highest accuracy on organic transition metal complexes among the four Hamiltonians and matches the accuracy of the original Hamiltonian on inorganic transition metal complexes with considerable improvements over the R2016 and R2017 Hamiltonians. The previously achieved good results on organic molecules are retained, making the new Hamiltonian suitable for a broad range of applications.

The two new Hamiltonians, R2017 and R2018, are applied to a range of molecules and transition metal complexes with odd and even numbers of electrons. In general, a good agreement with the experimentally observed photophysical properties is achieved. The results of the computations can be used to assign electronically excited states and interpret and elucidate relaxation pathways following electronic excitation.

Apart from the successful applications, the new Hamiltonians show an overestimation of transition energies in all calculated polychlorinated triphenylmethyl radicals. The results and potential origin of the errors are discussed.

Zusammenfassung

DFT/MRCI ist eine etablierte semiempirische quantenchemische Methode, die ursprünglich von Grimme und Waletzke [J. Chem. Phys., 111, 5645 (1999)] entwickelt wurde. Kürzlich wurde ein überarbeiteter DFT/MRCI Hamiltonoperator (R2016) von Lyskov et al. [J. Chem. Phys., 144, 034104 (2016)] entwickelt, um die Beschreibung von Bichromophoren zu verbessern.

Die Anwendung der DFT/MRCI-Methode war bisher auf geschlossenschalige Systeme limitiert. In dieser Doktorarbeit wurde der R2016 Hamiltonoperator von Lyskov et al. erfolgreich um offenschalige Systeme erweitert, deren Ankerkonfiguration auf *restricted open-shell* Kohn-Sham-Orbitalen basiert. Die dafür notwendigen Orbitale werden mit dem Programm Dalton berechnet, für das eine Schnittstelle zum DFT/MRCI-Programm entwickelt wurde. Experimentelle elektronische Anregungsenergien von Dublettzuständen wurden aus der Literatur zusammengestellt, da ein Datensatz dieser Zustände, der zum Anpassen und Testen eines Parametersatzes geeignet wäre, nicht existiert. Mit dem neuen Hamiltonoperator (R2017) wird dieselbe Genauigkeit und rechnerische Geschwindigkeit bei geschlossen- und offenschaligen organischen Molekülen erreicht, die von den vorherigen Hamiltonoperatoren für geschlossenschalige Moleküle erreicht wurde. Die Genauigkeit wird durch die Wurzel aus den gemittelten Fehlerquadraten (*root-mean-square error*, *RMSE*) angegeben und liegt unterhalb von 0.2 eV.

Während mit allen DFT/MRCI-Hamiltonoperatoren gute Ergebnisse für organische Moleküle erzielt werden können, wurde in einem Benchmark von Übergangsmetallkomplexen festgestellt, dass die vertikalen Übergangsenergien dieser Systeme unterschätzt werden, insbesondere im Fall der R2016 und R2017 Hamiltonoperatoren. Die Ursache konnte auf die Dämpfungsfunktion der Außerdiagonalelemente zurückgeführt werden, die in den beiden überarbeiteten Hamiltonoperatoren eingesetzt wird. Auf Grundlage dieser Erkenntnisse wurde ein neuer Hamiltonoperator (R2018) entwickelt, der auf dem R2017 basiert und durch eine ausgewogenere Dämpfung die vertikalen Anregungsenergien von Übergangsmetallkomplexen besser beschreibt. Der RMSE reduziert sich für organische Übergangsmetallkomplexe auf 0.15 eV, was eine Verbesserung im Vergleich zum originalen und R2016 Hamiltonoperator darstellt, die bei 0.20 bzw. 0.25 eV liegen. Mit dem neuen R2018 Hamiltonoperator wird die höchste Genauigkeit für organische Übergangsmetallkomplexe unter den vier Hamiltonoperatoren erreicht. Zusammen mit dem originalen Hamiltonoperator stellt dies die beste Beschreibung anorganischer Übergangsmetallkomplexe dar, was einer deutlichen Verbesserung der Ergebnisse von R2016 und R2017 entspricht. Die bereits guten Ergebnisse für organische Moleküle werden auch im neuen Hamiltonoperator beibehalten, was eine große Bandbreite an Anwendungsmöglichkeiten eröffnet.

Bei der Anwendung der neuen Hamiltonoperatoren R2017 und R2018 auf eine Reihe von Molekülen und Übergangsmetallkomplexen mit gerader und ungerader Anzahl von Elektronen wird im Allgemeinen eine gute Übereinstimmung mit experimentell beobachteten photophysikalischen Eigenschaften erreicht. Folglich können die Ergebnisse der Berechnungen dazu verwendet werden, elektronisch angeregte Zustände zuzuordnen sowie Relaxationspfade zu interpretieren und aufzuklären.

Überschätzungen der Übergangsenergien zeigen sich hingegen in allen berechneten polychlorierten Triphenylmethylradikalen. Die Ergebnisse und die mögliche Ursache der Fehler werden diskutiert.

1 Introduction

In electronic devices and displays, light sources with a good colour profile and a high efficiency and longevity are of great importance. For a long time, light emitting diodes (LEDs) based on semiconductors have been used. By altering their crystal structure, changes in the band gap are introduced, which leads to colour variations. In recent years, alternative lighting devices with advantages over LEDs including microLEDs [1, 2], perovskite-based LEDs [3–5] and organic LEDs [6, 7] (OLEDs) have been developed. OLED displays have several advantages over regular LEDs by providing a higher contrast, a higher colour purity, wider viewing angles, faster response times, better power efficiency and true blacks [8]. Displays based on LEDs on the other hand employ a liquid crystal display (LCD) to cover certain colours of each pixel of the white backlighting that is provided by a white LED. In order to provide a practical advantage over LEDs, a high quantum efficiency and stability of the OLED dye is mandatory.

An OLED is composed of an organic material with the ability to emit light under certain circumstances. This material is situated between an anode and a cathode. When a voltage is applied, the organic material is charged. The created electrons and electron-holes recombine in the emission layer of the OLED, where they create an exciton. This exciton decays under emission of electromagnetic radiation.

A very important property to consider in any luminescent exciton is the spin statistics. In the recombination process of an electron-hole pair the resulting state is a singlet with a chance of 25% and a triplet with a chance of 75%, when considering closed-shell species [9]. Since the transition from the excited triplet state to the singlet ground state is a spin-forbidden process, only the 25% singlet population can function as an emitting state. This limits the internal quantum efficiency (IQE) to 25%. Several approaches exist to circumvent this limitation. One possibility is to employ heavy atoms within the dye which allows the transition from a triplet to the singlet ground state through spin-orbit coupling. Through this mechanism an IQE of up to 100% is possible [10–12]. An alternative to this triplet harvesting is by repopulating the lowest excited singlet state through reverse intersystem crossing (rISC) from the excited triplet state [13–15].

While all previously discussed possibilities involve closed-shell species, a different way was recently introduced by Peng et al. [16]. By using open-shell species as a dye, the resulting singlet-doublet or triplet-doublet coupled electron-hole pair will – depending on the energy – result in an excited state with one unpaired electron, which can only be a doublet state. A quartet state, on the other hand, requires three open shells with unpaired spins. The first quartet state is energetically unfavoured compared to doublet states and typically lies energetically above the lowest excited doublet state(s). Therefore, both singlet and triplet excitons can be utilised as the resulting doublet state is energetically favoured. A formation ratio of 100% for a doublet excited state [17] and an external quantum efficiency of 27% [18] have recently been reported for open-shell emitters.

While open-shell systems are prone to dimerisation, disproportionation and interaction with atmospheric oxygen, several stable structures have emerged in recent years [19], of

which some are fluorescent. Tris(2,4,6-trichlorophenyl)methyl radicals with varying substituents – or with one phenyl replaced by a pyridine – are often used in open-shell emitters [16–18, 20–24]. By substituting chlorine with other halogens, the photophysical properties of these radicals can be tuned even further [25]. Other stable fluorescent radicals are based on the Blatter radical [26, 27], 1,2,3,5-dithiadiazolyl (DTDA) radicals that have been linked to aromatic molecules like anthracene and pyrene [28, 29] and the zinc(II) tripyrrindione radical [30]. Nitroxide radicals [31, 32] or lanthanide complexes with chelating nitronyl nitroxide radicals [33] also belong to the group of stable fluorescent radicals.

The calculation and description of excited states are a requirement for the prediction of photophysical properties of (potential) OLED dyes. The reliable description of excited states with good accuracy, however, is a challenging task. Many of the methods used for describing these states start from a converged Hartree-Fock [34–37] (HF) calculation and thus form the group of so-called post-HF methods. Among those are coupled-cluster [38, 39] (CC) methods like CC singles and doubles (CCSD) or approximate singles and doubles [40] (CC2) and approximate CC singles, doubles and triples [41] (CC3). Configuration Interaction (CI) in its computationally least-demanding approach as CI singles (CIS) was extended by perturbative doubles to CIS(D) [42]. Other successful methods are the algebraic-diagrammatic construction [43] (ADC(2)), complete active space self-consistent field [44] (CASSCF) and restricted active space self-consistent field [45, 46] (RASSCF). Starting from the latter two, Møller-Plesset perturbation theory in second order [47] (MP2) can be extended to multireference MP2 [48] (MRMP2) or complete active space perturbation theory in second order [49, 50] (CASPT2) for the description of excited states. Hartree-Fock can also be used for excited state calculations as time-dependent Hartree-Fock (TDHF). A different approach, related to TDHF, is the time-dependent density functional theory [51–54] (TDDFT). TDDFT combines a good accuracy for many applications with a low computational demand, allowing excited-state calculations on systems with 50-500 atoms. However, it is limited to single excitations, as is TDHF, making both methods unable to treat states with doubly excited characters.

A different kind of approach seeks a combination of various methods, either to increase the accuracy of a fast method or to lower the computational cost of an accurate method. These combinations make it possible to calculate larger system with good accuracy. One of these approaches combines the semi-empirical orthogonalisation-corrected methods OM1 [55, 56], OM2 [57, 58] and OM3 [59, 60] with MRCI as OMx/MRCI [61, 62]. Other recently developed methods include multiconfiguration pair-density functional theory [63] (MC-PDFT) and the combination of DFT and restricted open shell CI singles (ROCIS) which is called DFT/ROCIS [64, 65]. Among these is also the method that is the focus of this thesis, the combined DFT and MRCI method (DFT/MRCI).

The DFT/MRCI method [66, 67] is a semi-empirical method for computing excited states of closed-shell molecules, depending on a closed-shell determinant. It combines Kohn-Sham (KS) orbitals from DFT with multireference configuration interaction (MRCI). In this approach, the dynamic correlation is computed on DFT level while static correlation is provided by MRCI. Since calculating the dynamic correlation requires a long CI expansion, the configuration interaction expansion can be shortened if the dynamic correlation

is already accounted for. To avoid double counting of electron correlation, the integrals are scaled by empirically determined parameters. The advantages of the DFT/MRCI method are a high computational speed with an error less than 0.2 eV, making it possible to calculate photophysical properties of large molecules with a good accuracy [66]. The method was originally developed by Grimme and Waletzke [66]. It represents a generalisation as well as an extension of the previously developed DFT/SCI [68] method, that combines DFT with CI limited to single excitations. From its original release in 1999, the DFT/MRCI method was steadily improved and extended. The parallelisation of the code by Kleinschmidt et al. [69] made it possible to calculate even larger systems in the same amount of time. An extension to include spin-orbit coupling based on the DFT/MRCI wave function was released as a separate program called *SpockCI* [70–72] to include properties that are missing in DFT/MRCI due to a spin-free Hamiltonian.

The DFT/MRCI Hamiltonian was redesigned in 2016 by Lyskov et al. [73] to address shortcomings of the original Hamiltonian regarding bi-chromophoric systems that are involved in processes like singlet fission or triplet-triplet up-conversion. This Hamiltonian was later named R2016 [67]. By developing a new correction for the matrix elements, a set of four parameters used for all multiplicities represented by an even number of electrons (singlets, triplets, quintets, ...) was introduced. In the original approach by Grimme and Waletzke, only singlet and triplet multiplicities were possible, using different parameter sets for each multiplicity.

The DFT/MRCI method has been successfully applied in excited states calculations of organic molecules [74–80] and transition metal complexes [81, 82], in excitation energy transfer processes [83, 84], in singlet fission [85] and in benchmark calculations [86–90]. In calculations combining quantum mechanics and molecular mechanics [91] (QM/MM), DFT/MRCI has been successfully employed in the quantum-mechanics region of large biomolecules for calculating vertical excitation energies [92–94]. While these examples demonstrate the broad range of applications, DFT/MRCI lacks the ability to compute vertical excitation energies needed for the emerging field of doublet emitters.

The aim of this thesis is the development of a new DFT/MRCI Hamiltonian capable of treating open-shell as well as closed-shell systems with an error comparable to the original and R2016 Hamiltonian. In order to treat open-shell systems, an anchor configuration based on restricted open-shell Kohn-Sham (ROKS) is required. The ROKS orbitals are calculated with the Dalton program [95]. A new interface between Dalton and DFT/MRCI was needed for the usage of the Dalton program in combination with DFT/MRCI. Due to the advantages of the R2016 Hamiltonian over the original one, the new open-shell Hamiltonian should be based on the R2016 Hamiltonian. A broad and diverse set of experimental excitation energies had to be assembled for developing and testing a new parameter set. The new Hamiltonian is then applied to systems of broader interest to investigate their photophysical properties. All steps outlined above were carried out and are included in this thesis, resulting in the development, implementation and application of a new all-multiplicity Hamiltonian, the R2017 Hamiltonian.

Additionally, it was found that the R2016 and R2017 Hamiltonians and to a smaller degree

also the original Hamiltonian underestimate the vertical excitation energies in transition metal complexes. A new damping function for off-diagonal matrix elements greatly improved these excitation energies. Together with a newly optimised parameter set, the all-multiplicity R2018 Hamiltonian was developed and implemented.

This thesis is divided into five sections:

1. The first part introduces the theoretical framework on which the DFT/MRCI method and the development of a new Hamiltonian are based. This includes DFT in general and for open-shell systems, MRCI and CI matrix elements and the previous developments of DFT/MRCI, namely the original development of Grimme and Waletzke and the redesign by Lyskov et al.
2. The second part introduces the datasets that play an important role in the training (parametrisation) and testing of the DFT/MRCI Hamiltonians. The sets are composed of organic molecules and transition metal complexes.
3. The third part introduces the two interfaces to the DFT/MRCI program developed over the course of this thesis. The first interface is needed for transforming the ROKS orbitals calculated with the Dalton program to Turbomole format. Turbomole lacks the ability to compute ROKS orbitals and the DFT/MRCI program is interfaced against Turbomole. This interface is named *d2tm*. The second interface is implemented in the DFT/MRCI program and makes it possible to read the integrals and molecular data following a ORCA 4.0 [96, 97] DFT single-point calculation. The ORCA program provides RI-integrals and orbitals for closed-shell molecules, thus making the DFT/MRCI program available to a broader audience within the scientific community.
4. The fourth part describes the development and parametrisation of the new Hamiltonians, dubbed R2017 and R2018, and the assessment of the accuracy. In this section the effect of the off-diagonal damping on the correlation energy is discussed.
5. In the last part, the R2017 and R2018 Hamiltonians are applied to various systems, including closed-shell transition metal platinum complexes and open-shell doublet emitters. The doublet emitters include the zinc tripyrrindione complex, the Blatter radical, PAH-DTDA radicals and molecules based on the triphenylmethyl radical.

2 Theory

2.1 Vertical Transitions and Excited States Processes

Vertical transitions are based on the Franck-Condon principle [98–100] that states that the geometry relaxation is much slower than the change in the electronic structure following a (de)excitation process. While the electronic structure undergoes a change during the process, the relaxation of the geometry is delayed. Since there is no change in geometry, the (de)excitation transition is assumed to be a vertical transition. The Franck-Condon principle is employed within the DFT/MRCI calculations, where absorption from the ground state is based on the ground-state geometry and emission from an excited state is calculated at the minimum of the corresponding excited state. Besides vertical transitions, important measures are adiabatic transitions that describe the energy between two states at their corresponding relaxed geometry and 0-0 transitions that are based on the adiabatic energy and include the zero-point energy of each state. All these transitions are considered to absorb or emit energy in form of electromagnetic radiation. Besides photo-excitation, other possibilities to access the excited state include photoelectron emission (see Sec. 3.3) and electroluminescence.

The processes involving excited states are represented schematically as a Jablonski diagram in Fig. 1. After excitation, the geometry relaxes vibronically (brown arrow). From here, several radiative and non-radiative processes compete. These include non-radiative processes such as internal conversion (IC) and intersystem crossing (ISC). IC describes an iso-energetic transition from one excited state to a higher vibrational level of a different electronic state without change in multiplicity. The same process but with a change in multiplicity is the ISC. Kasha’s rule [101] states that emission stems from the lowest

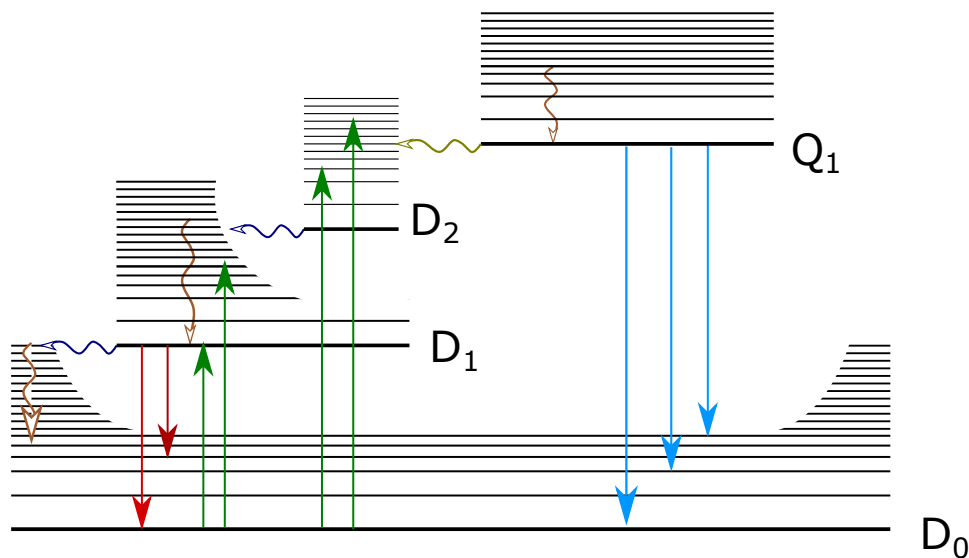


Figure 1: Jablonski diagram showing the radiative and non-radiative processes in an open-shell system. The horizontal dark-blue arrows represent the internal conversion (IC) and the olive arrows the intersystem crossing (ISC). The brown arrows indicate the vibrational relaxation within an excited state. The red arrows represent fluorescence and the blue phosphorescence. The green arrows mark the absorption from the ground state to various excited states.

Table 1: Typical time scales of excited state processes [102]. The two rates for internal conversion refer to a fast and a slow rate. The fast rate takes place between excited states (ES), for example $D_2 \rightarrow D_1$ whereas the slow rate describes the depopulation to the ground state (GS), for example $D_1 \rightarrow D_0$. All transitions given below are examples referring to doublet (and quartet) states but can occur with the same rates in any analogue case like singlet (and triplet) states.

Process	Transition	Rate [s^{-1}]
Absorption	$D_0 \rightarrow D_n$	10^{15}
Solvent reorganisation		$10^{12}-10^{13}$
Internal conversion (ES)	$D_n \rightarrow D_1$	$10^{10}-10^{14}$
Vibrational relaxation	$D_{n,\nu=n} \rightarrow D_{n,\nu=0}$	$10^{10}-10^{12}$
Fluorescence	$D_1 \rightarrow D_0$	10^7-10^9
Internal conversion to GS	$D_1 \rightarrow D_0$	10^6-10^7
Intersystem crossing	$Q_n \rightarrow D_n$	10^5-10^8
Phosphorescence	$Q_1 \rightarrow D_0$	$10^{-2}-10^3$

excited state of each multiplicity, which is shown in Fig. 1 in red (fluorescence) and blue (phosphorescence). While Kasha’s rule predicts emission from the lowest excited state, this does not necessarily mean that there is an emission measurable, as non-radiative decay to the ground state via IC or ISC is also possible. The Jablonski diagram depicts a high-lying Q_1 excited state above several excited doublet states, which is usually the case in open-shell species. Quartet states require at least three open shells with same-spin electrons while a doublet state requires only one unpaired electron. This is different from closed-shell systems, where excited singlet and triplet states both require two open-shell electrons, with the opposite spins for a singlet and with same spins for a triplet. Due to the exchange energy, the first excited triplet state is typically energetically below the first excited singlet state. In the recombination process of an electron-hole pair, the lowest singlet and triplet state are therefore energetically accessible. In an open-shell species on the other hand, a energetically low-lying doublet state is favoured compared to the first quartet state at a higher energy. This leads to the advantages of doublet emitters for OLEDs as the formation ratio of the doublet exciton can reach up to 100%. Typical time scales of these processes can be found in Tab. 1.

2.2 Density Functional Theory

Since the DFT/MRCI method uses Kohn-Sham orbitals as a basis, density functional theory plays an important role within the methodological framework.

The origins of DFT reach back to the 1920s. Thomas [103] and Fermi [104] showed that the kinetic energy of atoms and molecules can be approximated via the electron density as a functional of the homogenous electron gas (HEG) instead of using a wave function based approach. This was extended by Dirac [105], who expressed the exchange energy as a functional of the density. This led to the Thomas-Fermi-Dirac model, where the attraction between the nuclei and the electrons as well as the Coulomb repulsion are

described as functionals of the density [106]. Years later, in the 1950s, Slater [107] proposed mixing WFT with DFT by taking the exchange interaction from Hartree-Fock instead of the functional that was introduced by Dirac. The basis for DFT was founded theoretically by Hohenberg and Kohn in the mid-1960s [108]. The Hohenberg-Kohn theory is exact for systems where the density is nearly constant or slowly varying.

In the simplest form, the DFT Hamiltonian for N non-relativistic, interacting electrons in an arbitrary external potential in atomic units is [108]

$$\hat{\mathcal{H}} = -\frac{1}{2}\sum_{i=1}^N \nabla_i^2 + \frac{1}{2}\sum_{i \neq j}^N \frac{1}{|\vec{r}_i - \vec{r}_j|} + \sum_{i=1}^N \nu(\vec{r}_i) \quad (1)$$

where the first summand of Eq. (1) represents the kinetic energy operator T , the second term the electron-electron interaction V_{ee} and $\nu(\vec{r})$ the one-particle external potential.

The ground-state density $\rho(r)$ leads to the number of electrons by integration

$$N = \int \rho(\vec{r}) d\vec{r} \quad (2)$$

and therefore determines the full Hamiltonian $\hat{\mathcal{H}}$ and all properties determined by $\hat{\mathcal{H}}$. These include the ground-state wave function $\Psi(r_1 \dots r_N)$, excitation energies and potential energy surfaces [109]. The potential $\nu(\vec{r})$ is a unique functional of $\rho(\vec{r})$ up to an additive constant. The proof is carried out by reductio ad absurdum. If another potential $\nu'(\vec{r})$ with ground state Ψ' results in the same density $\rho(\vec{r})$, the ground states Ψ and Ψ' lead to different Schrödinger equations. They can therefore not be equal when $\nu(r) \neq \nu'(r) + \text{const}$. The ground-state energies and Hamiltonians of Ψ and Ψ' are indicated by E and E' as well as $\hat{\mathcal{H}}$ and $\hat{\mathcal{H}}'$. The energy E of the ground state can be expressed within the Rayleigh-Ritz principle as

$$\begin{aligned} E &= \langle \Psi | \hat{\mathcal{H}} | \Psi \rangle < \langle \Psi' | \hat{\mathcal{H}} | \Psi' \rangle = \langle \Psi' | \hat{\mathcal{H}}' | \Psi' \rangle - \langle \Psi' | \hat{\mathcal{H}} - \hat{\mathcal{H}}' | \Psi' \rangle \\ &= E' + \int \rho(\vec{r}) (\nu(\vec{r}) - \nu'(\vec{r})) dr. \end{aligned} \quad (3)$$

Analogous to Eq. (3), the energy E' of the ground state is

$$\begin{aligned} E' &= \langle \Psi' | \hat{\mathcal{H}}' | \Psi' \rangle < \langle \Psi | \hat{\mathcal{H}}' | \Psi \rangle = \langle \Psi | \hat{\mathcal{H}} | \Psi \rangle - \langle \Psi | \hat{\mathcal{H}}' - \hat{\mathcal{H}} | \Psi \rangle \\ &= E + \int \rho(\vec{r}) (\nu'(\vec{r}) - \nu(\vec{r})) dr. \end{aligned} \quad (4)$$

The energies in Eq. (3) and (4) contradict each other. It follows that the density $\rho(\vec{r})$ determines the potential $\nu(\vec{r})$ to within a constant. The energy can therefore be written as a functional of the density as

$$E_{\nu(r)}[\rho] = \int \nu(\vec{r})\rho(\vec{r})d\vec{r} + F[\rho] \quad (5)$$

where the functional $F[\rho]$ is defined as the sum of kinetic energy $T[\rho]$ and electron-electron interaction $V_{ee}[\rho]$,

$$F[\rho(r)] = \left\langle \Psi \left| -\frac{1}{2} \sum_{i=1}^N \nabla_i^2 + \frac{1}{2} \sum_{i \neq j}^N \frac{1}{|\vec{r}_i - \vec{r}_j|} \right| \Psi \right\rangle. \quad (6)$$

When the correct density $\rho(\vec{r})$ of a system is known, $E_{\nu(r)}[\rho]$ is the ground-state E [108].

The density that minimises the energy in Eq. (5) corresponds to the ground-state density and leads to the Euler equation

$$\mu = \nu(\vec{r}) + \frac{\delta F[\rho]}{\delta \rho(\vec{r})} \quad (7)$$

with the constraint that the density determines the number of electrons by integration.

Kohn and Sham [110] developed a simplification for the kinetic energy by introducing

$$T_s[\rho] = \left\langle \Psi_s \left| \sum_{i=1}^N \left(-\frac{1}{2} \nabla_i^2 \right) \right| \Psi_s \right\rangle = \sum_{i=1}^N \left\langle \psi_i \left| -\frac{1}{2} \nabla_i^2 \right| \psi_i \right\rangle. \quad (8)$$

The new kinetic energy $T_s[\rho]$ restricts the density to be noninteracting ν -representable, i.e. for a given density $\rho(\vec{r})$ there must exist a noninteracting ground state.

By separating the contributions, the functional $F[\rho]$ in Eq. (6) can be rewritten as

$$F[\rho] = T_s[\rho] + J[\rho] + E_{xc}[\rho] \quad (9)$$

with

$$J[\rho] = \frac{1}{2} \int \int \frac{\rho(\vec{r})\rho(\vec{r}')}{|\vec{r} - \vec{r}'|} d\vec{r} d\vec{r}' \quad (10)$$

as the interaction energy. $T_s[\rho]$ represents the kinetic energy of a noninteracting system as above. The third term in Eq. (9) represents the exchange-correlation energy and is defined as

$$E_{xc}[\rho] = T[\rho] - T_s[\rho] + V_{ee}[\rho] - J[\rho]. \quad (11)$$

The Euler equation in Eq. (7) is now

$$\mu = \nu_{eff}(\vec{r}) + \frac{\delta T_s[\rho]}{\delta \rho(\vec{r})}. \quad (12)$$

The Kohn-Sham effective potential can be expressed as

$$\nu_{eff}(\vec{r}) = \nu(\vec{r}) + \frac{\delta J[\rho]}{\delta \rho(\vec{r})} = \nu(\vec{r}) + \int \frac{\rho(\vec{r}')}{|\vec{r} - \vec{r}'|} d\vec{r}' + \nu_{xc}(\vec{r}) \quad (13)$$

with the exchange-correlation potential

$$\nu_{xc}(\vec{r}) = \frac{\delta E_{xc}[\rho]}{\delta \rho(\vec{r})}. \quad (14)$$

Eq. (12) with the constraint Eq. (2) yields the same equation as non-KS DFT for a system of noninteracting electrons in an external potential $\nu_s(\vec{r}) = \nu_{eff}(\vec{r})$. Hence, the density for a given $\nu_{eff}(\vec{r})$ is procured by solving [111]

$$\left(-\frac{1}{2}\nabla^2 + \nu_{eff}(\vec{r}) \right) \psi_i = \varepsilon_i \psi_i \quad (15)$$

with

$$\rho(\vec{r}) = \sum_{i=1}^N |\psi_i(\vec{r})|^2. \quad (16)$$

Eq. (13)–(16) are the Kohn-Sham equations. Eq. (15) shows that the moving electrons can be considered in the same manner as a system of noninteracting electrons [112]. The electrons are treated as moving in the potential $\nu_{eff}(\vec{r})$, which contains all interactions between the electrons [112].

The energy then is

$$E = \sum_{i=1}^N \varepsilon_i - \frac{1}{2} \int \int \frac{\rho(\vec{r}) \rho(\vec{r}')}{|\vec{r} - \vec{r}'|} d\vec{r} d\vec{r}' + E_{xc}[\rho] - \int \nu_{xc}(\vec{r}) \rho(\vec{r}) d\vec{r}. \quad (17)$$

DFT is widely used for electronic structure calculations due to its practicality and universality [113]. Kohn-Sham DFT is covering the dynamic electron correlation, but the static Coulomb correlation is neglected. Static correlation arises from a strong interaction of electronic states that are degenerate or near-degenerate [106].

2.3 Open Shells in Density Functional Theory

The DFT method as outlined in Sec. 2.2 is applicable to restricted orbitals, i.e. orbitals that are either doubly occupied or vacant, with the same orbital for α and β spin. In order to construct an anchor configuration for the DFT/MRCI method for doublet and quartet

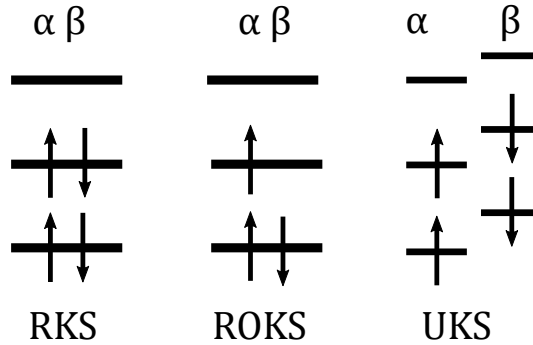


Figure 2: Differences between closed-shell (RKS), restricted open-shell (ROKS) and unrestricted (UKS) Kohn-Sham orbitals. While the spin of the open shells in ROKS and UKS is arbitrary, an α -spin is conventionally used.

states, or more generally for states with an odd number of electrons, a different orbital basis is required. Several ways of constructing the open-shell determinant come to mind. The most common variant is to take an unrestricted approach with two unique sets of spin orbitals for α and β electrons. This ansatz requires any post-HF method to employ unrestricted orbitals as well. In this case, unrestricted configuration interaction (UCI) is not built on a good theoretical foundation [114, 115] and the results are unreliable. A different way is to start from a closed-shell determinant and removing or adding one electron. This will lead to unphysical orbital energies and is not suitable for a method that is directly based on the orbital energy like DFT/MRCI. The third way is a different type of DFT, namely restricted open-shell Kohn-Sham. Here, all doubly occupied orbitals are restricted orbitals in addition to fractionally occupied open shells. The ROKS approach is suited best for the DFT/MRCI method. The UKS approach, while not directly employed within the DFT/MRCI framework, still plays an important role for geometry optimisations and TDDFT calculations in this thesis.

Both UKS and ROKS use a noninteracting reference with two independent subsystems. In the UKS approach, these are the spins α and β . In the ROKS approach, on the other hand, these are closed and open shells, which are marked with the indices c and o in the following. The shells of α and β electrons are restricted to be identical. The scheme of the differences between restricted and restricted open-shell Kohn-Sham and unrestricted Kohn-Sham is shown in Fig. 2.

2.3.1 Restricted Open-Shell Kohn-Sham Density Functional Theory

The restricted orbital Kohn-Sham method was developed by Filatov and Shaik [116, 117] in the late 90s. It is based on the work of Roothan [118], who extended the Hartree-Fock method to restricted open shells. The multiplet states are built from linear combinations of determinants Φ_L since $[\hat{\mathcal{H}}, \hat{S}^2] = 0$ [119]. These have the form

$$\Psi(r) = \sum_L a_L \Phi_L \quad (18)$$

In its general form, the multiplet energy is determined as the sum of the energies of

different microstates Φ_L , with weights c_L that are fixed by symmetry as

$$E = \sum_L c_L E(\Phi_L), \quad \sum_L c_L = 1. \quad (19)$$

The microstates are considered as states of mixed symmetries. In the noninteracting case they can be represented by a single determinant [120]. Restricted open-shell Kohn-Sham shows strong similarities to the restricted open-shell Hartree-Fock method [118], but differs in the construction of the microstates. In the ROHF case, the wave function is averaged over the microstates, whereas in the ROKS case the energy and density are averaged [120].

The determinants Φ_L are constructed from the same set of N_c closed-shell orbitals ψ_k and N_o open-shell orbitals ψ_m . In the following, k, l refer to closed shells, m, n to open shells and i, j to a general set of orbitals.

The density of the microstates is analogous to the closed-shell case in Eq. (16) and includes the open shells as

$$\rho_L^\sigma(\vec{r}) = \sum_{k=1}^{N_c} |\psi_k(\vec{r})|^2 + \sum_{m=N_c+1}^{N_c+N_o} n_{m,L}^\sigma |\psi_m(\vec{r})|^2, \quad \sigma = \alpha, \beta \quad (20)$$

with $n_{m,L}^\sigma$ as the integer orbital occupation number.

Similar to the closed-shell RKS case in Eq. (17), the energy can be expressed by summing over orbitals instead of electrons as

$$E = \sum_k 2h_k + \sum_{k,l} 2J_{kl} + \sum_m f_m \left[2h_m + 2 \sum_k 2J_{km} + \sum_n 2f_n a_{mn} J_{mn} \right] + \sum_L c_L E_{xc,L} \quad (21)$$

which includes an interaction term J_{km} between closed shells k and open shells m . The one-electron integrals include the kinetic energy and the interaction with the external potential, corresponding to the first and third terms of Eq. (1). The two-electron integrals J_{kl} are the Coulomb integrals $J_{kl} = \langle kl|kl \rangle$. The occupation of the m th orbital is given by

$$f_m = \frac{1}{2} \sum_L c_L (n_{m,L}^\alpha + n_{m,L}^\beta) \quad (22)$$

and the coupling coefficient is

$$a_{mn} = \frac{1}{4f_m f_n} \sum_L c_L (n_{m,L}^\alpha + n_{m,L}^\beta) (n_{n,L}^\alpha + n_{n,L}^\beta). \quad (23)$$

The exchange-correlation potential from Eq. (14) becomes

$$\nu_{xc}(r) = \frac{\delta E_{xc,L}[\rho]}{\delta \rho_L(\vec{r})} \quad (24)$$

by taking the microstates into account. By summing over the microstates, the exchange-correlation potentials for the sets of closed and open shells are

$$V_{xc}^c = \frac{1}{2} \sum_L c_L \left(\nu_{xc,L}^\alpha + \nu_{xc,L}^\beta \right) \quad (25)$$

and

$$V_{xc}^o = \frac{1}{2f} \sum_L c_L \left(\nu_{xc,L}^\alpha n_{m,L}^\alpha + \nu_{xc,L}^\beta n_{m,L}^\beta \right) \quad (26)$$

which includes the occupation of the m th open shell.

In order to apply the variational principle to obtain the orbital equations, a new operator for the Coulomb interaction has to be introduced for open shells, as these shells depend on the fractional occupation. The resulting operator describing the total Coulomb interaction of closed-shell and open-shell orbitals is

$$\hat{J}_T = \sum_k \hat{J}_k + f \sum_m \hat{J}_m. \quad (27)$$

For any orbital ψ_i , closed-shell, open-shell or virtual, the following eigenvalue equation [116] is obtained

$$\begin{aligned} \left(-\frac{1}{2} \nabla^2 + \nu(\vec{r}) + 2\hat{J}_T + V_{xc}^c + \sum_m \left\{ \hat{\gamma} \left[2\hat{J}_o^m + \beta \left(V_{xc}^c - V_{xc,m}^o \right) \right] |\psi_m\rangle \langle \psi_m| \right. \right. \\ \left. \left. + |\psi_m\rangle \langle \psi_m| \left[2\hat{J}_o^m + \beta \left(V_{xc}^c - V_{xc,m}^o \right) \right] \hat{\gamma} \right\} \right) |\psi_i\rangle = \varepsilon_i |\psi_i\rangle \end{aligned} \quad (28)$$

with the density operators

$$\hat{\rho}_o = \sum_m |\psi_m\rangle \langle \psi_m| \quad (29)$$

and

$$\hat{\gamma} = \hat{\rho}_c - (1-f) + \frac{1-f}{2} \hat{\rho}_o. \quad (30)$$

In the case that is relevant for DFT/MRCI, only one half-closed shell, i.e. a singly occupied orbital, is considered. For a singly occupied shell the coupling coefficient is $f = 1/2$, with

$\alpha_{mn} = 0$ and $\beta = 2$ and the exchange-correlation potential is $V_{xc,m}^o = V_{xc,n}^o = V_{xc}^o$. This simplifies Eq. (28) to

$$\left(-\frac{1}{2}\nabla^2 + \nu(\vec{r}) + 2\hat{J}_T + V_{xc}^c + 2\hat{\gamma}(V_{xc}^c - V_{xc}^o)\hat{\rho}_o + 2\hat{\rho}_o(V_{xc}^c - V_{xc}^o)\hat{\gamma} \right) |\psi_i\rangle = \varepsilon_i |\psi_i\rangle. \quad (31)$$

Within the ROKS theory, the conventional naming of the highest occupied molecular orbital (HOMO) of closed-shell orbitals is ambiguous, since both the doubly and singly occupied orbitals are occupied and HOMO might refer to both. For this reason the highest doubly occupied molecular orbital is called HDOMO while the singly occupied molecular orbital of a system with a doublet ground state is called SOMO.

2.3.2 Unrestricted Kohn-Sham

The unrestricted Kohn-Sham [121–123] (UKS) orbitals (just as unrestricted Hartree-Fock orbitals) are disadvantageous within the configuration interaction method. The wave function is not an eigenfunction of the \hat{S}^2 operator and – due to this property – spin contamination can occur in unrestricted wave functions, caused by differences in the spatial parts of the α and β orbitals [114]. However, UKS still plays an important role in the framework of DFT/MRCI as the DFT/MRCI method depends on optimised geometries of the ground state and/ or excited states. UKS is widely available in quantum chemical programs, including analytical gradients and Hessians for excited states. For optimising the structure of an excited doublet state, UKS is currently the only available option within the time-dependent density functional theory.

The wave function is constructed as a Slater determinant of spin-orbitals. In the unrestricted formalism, the potential in Eq. (9) has to be rewritten to take the α and β spin densities into account

$$F[\rho^\alpha, \rho^\beta] = T_s[\rho^\alpha, \rho^\beta] + J[\rho^\alpha + \rho^\beta] + E_{xc}[\rho^\alpha, \rho^\beta]. \quad (32)$$

Analogous to the restricted Kohn-Sham orbitals in Eq. (16) and the restricted open-shell orbitals in Eq. (20), the density is

$$\rho(\vec{r}) = \sum_{i=1}^{N^\alpha} |\psi_i^\alpha(\vec{r})|^2 + \sum_{i=1}^{N^\beta} |\psi_i^\beta(\vec{r})|^2. \quad (33)$$

The Kohn-Sham potential, analogous to Eq. (13) of the RKS equations, is given by

$$\nu_{eff}^\sigma(\vec{r}) = \nu(\vec{r}) + \int \frac{\rho^\alpha(\vec{r}') + \rho^\beta(\vec{r}')}{|\vec{r} - \vec{r}'|} d\vec{r}' + \nu_{xc}^\sigma(\vec{r}), \sigma = \alpha, \beta \quad (34)$$

with the exchange-correlation potential similar to Eq. (14) of the restricted and Eq. (24)

of the restricted open-shell orbitals as

$$\nu_{xc}^{\sigma} = \frac{\delta E_{xc} [\rho^{\alpha}(r)\rho^{\beta}(r)]}{\delta \rho^{\sigma}(r)}, \sigma = \alpha, \beta. \quad (35)$$

Thus, the eigenvalue equation (15) becomes [124]

$$\left(-\frac{1}{2}\nabla^2 + \nu_{eff}^{\sigma}(\vec{r})\right)\psi_i^{\sigma} = \varepsilon_i^{\sigma}\psi_i^{\sigma}, \sigma = \alpha, \beta. \quad (36)$$

2.4 DFT Functionals

In order to apply the DFT method, knowledge of the exchange-correlation energy (see Eq. (9), (21) and (32)) is necessary. But as the exact exchange-correlation energy functional is not known, approximate functionals are used. The amount of available exchange-correlation functionals is so large that some authors call it a ‘zoo’ [125]. In the following, the functionals that play a key role in this thesis are introduced. The most important of them is the BHandHLYP functional due to its role within the DFT/MRCI method. Other functionals were used for geometry optimisations and excited state TDDFT reference energies in the context of validating and comparing the performance of DFT/MRCI.

2.4.1 BHandHLYP

The BHandHLYP [126, 127] functional employs a 1:1 mix of Hartree-Fock and the local spin density approximation [108, 110] (LSDA) with the Becke88 [128] correction. The class of functionals that mix exact and DFT exchange is called hybrid functionals. For describing the correlation energy, the LYP correlation by Lee, Yang and Parr [127] is used. The correlation functional was derived by fitting the density of helium. The exchange-correlation energy in BHandHLYP is

$$E_{xc} = 0.5E_x^{HF} + 0.5E_x^{LSDA} + 0.5\Delta E_x^{B88} + E_c^{LYP} \quad (37)$$

The Becke88 [128] exchange is a correction to the LSDA exchange.

2.4.2 B3LYP

The B3LYP functional is used for geometry optimisations in the purely organic vertical excitation training (fitting) and testing sets of the R2017 parameter set (Paper 1). This set is also employed for the R2018 Hamiltonian (Paper 2). The set of molecules can be found in Sec. 3.

The B3LYP functional employs exchange interaction from Hartree-Fock and LSDA with the Becke88 correction in combination with LYP and Vosko, Wilk, and Nusair [129] (VWN) correlation. The exchange-correlation energy is obtained by

$$E_{xc} = 0.2E_x^{HF} + 0.8E_x^{LSDA} + 0.72\Delta E_x^{B88} + 0.81E_c^{LYP} + 0.19E_c^{VWN} \quad (38)$$

2.4.3 PBE0

The PBE0 [130] functional, also known as PBE1PBE or PBE hybrid, is the hybrid version of the pure Perdew, Burke, and Ernzerhof (PBE) [131, 132] functional. The exchange is described by a 1:3 mix of exact to PBE exchange. The PBE0 functional is used for geometry optimisations of transition metal complexes in Paper 2 [133] and Paper 4 [134], for the optimisation of the Blatter radical in Paper 3 [67] and for the PAH-DTDA, TARA-PCTM and TTM-1Cz radicals in Sec. 6. The functional is based on the PBE exchange correlation. The exact exchange is introduced by substituting 25% of the the PBE exchange with exact exchange as

$$E_{xc} = E_{xc}^{PBE} + \frac{1}{4} \left(E_x^{HF} - E_x^{PBE} \right) \quad (39)$$

2.4.4 MN15

The MN15 [135, 136] functional is a new functional developed for a broader range of applications [135]. The functional is based on a non-separable gradient approximation (NGA) of type global-hybrid meta-NGA and improves the accuracy of systems with multiconfigurational character. For this reason, it was employed in Paper 5 [137] for optimising the ground state and the multiconfigurational excited states D_1 and D_3 . The exchange-correlation energy is

$$E_{xc} = 0.44E_x^{HF} + E_{nxc}^{MN15} + E_c^{MN15} \quad (40)$$

with E_{nxc} as the non-separable local exchange-correlation energy [135].

2.5 Configuration Interaction and Electron Correlation

Multireference configuration interaction (MRCI) is – next to density functional theory – the second part of the DFT/MRCI method. The anchor configuration is constructed from a DFT basis and the calculation of matrix elements is carried out in a truncated CI scheme.

Configuration interaction is a post-Hartree-Fock method that dates back to the late 1920s [138]. It introduces the electron correlation missing in the mean-field approach of Hartree and Fock [139]. Correlation energy is defined as the difference between the exact energy and the energy obtained within the Hartree-Fock theory in a complete basis set, the HF limit [140]. The correlation energy describes only a small part of the total energy, e.g. 0.5% in case of H_2O . But the bond energy is about the same amount and thus small energy contributions can lead to large effects [141]. Correlation can be divided

into two categories: dynamic [142] and static (or non-dynamic) [143, 144] correlation. Dynamic correlation is caused by correlation of electron movement, i.e. the movement of one electron influences the movement of other electrons. Static correlation is brought on by rearrangements of electrons in non-closed shells and near-degenerate states. Examples for systems with non-closed shells include excited states in general as well as doublet and triplet states [143]. While static correlation and dynamic correlation have different origins, it is impossible to differentiate between them quantitatively [145]. Despite the definition of electron correlation, a different kind of correlation is included in Hartree-Fock (and all post-HF methods), the Fermi correlation between parallel spins found in the exchange term of Hartree-Fock [144].

Configuration interaction is conceptually simple, but computationally very demanding. This is caused by an exceptionally large number of CSFs that have to be considered, even in small systems. For a system of m orbitals occupied by N electrons with the total spin S , the number of CSFs n can be calculated by Weyl's formula [146–148] when neglecting symmetry considerations as

$$n = \frac{2S+1}{m+1} \binom{m+1}{\frac{1}{2}N-S} \binom{m+1}{\frac{1}{2}N+S+1} \quad (41)$$

when all possible excitations are considered, i.e. the full CI case. The total spin has an effect on the spin coupling which in turn leads to a different number of CSFs. A configuration with one open shell only generates one doublet CSF, whereas a configuration with three open shells leads to two doublet and one quartet CSF.

The time-independent non-relativistic Hamiltonian with clamped nuclei is

$$\hat{H} = \sum_{A<B} \frac{Z_A Z_B}{r_{AB}} - \sum_i \frac{1}{2} \nabla_i^2 - \sum_i \sum_A \frac{Z_A}{r_{Ai}} + \sum_{i<j} \frac{1}{r_{ij}} \quad (42)$$

with i, j as electrons and A, B as nuclei.

The CI wave function can be expressed as the reference determinant $|\Psi_0\rangle$ with excitations. In the simplest case, only single excitations are considered, leading to the CI singles (CIS) approach

$$|\Psi^{CIS}\rangle = c_0 |\Psi_0\rangle + \sum_{ar} c_a^r |\Psi_a^r\rangle \quad (43)$$

summing over all possible single excitations from the occupied orbital a into the vacant (or singly occupied) orbital r . The coefficients c_a^r are determined variationally [139]. While this approach is computationally not very demanding, it cannot handle double excitations from the ground-state determinant. These shortcomings can be corrected by introducing double excitations and thus extending Eq. (43) to

$$|\Psi^{CISD}\rangle = c_0 |\Psi_0\rangle + \sum_{ar} c_a^r |\Psi_a^r\rangle + \sum_{abrs} c_{ab}^{rs} |\Psi_{ab}^{rs}\rangle. \quad (44)$$

Expanding Eq. (44) even further to include all possible n-tuple excitation leads to the full CI treatment. Usually, only single and double excitations are considered [149].

Wetmore and Segal [150, 151] developed a technique for a more efficient CI treatment, which is implemented in the DFT/MRCI program. In second quantisation, $\hat{a}_{i\sigma}^\dagger$ is the creation and $\hat{a}_{j\sigma}$ is the annihilation operator, where i, j, k, l describe the spatial orbitals and σ, τ, μ, ν the spin (α or β). These operators follow the anti-commutation rules of fermions (e.g. electrons) to preserve the anti-symmetry principle [150]

$$[\hat{a}_{i\sigma}^\dagger, \hat{a}_{j\sigma}]_+ = \delta_{ij} \delta_{\sigma\tau} \quad (45)$$

and

$$[\hat{a}_{i\sigma}^\dagger \hat{a}_{j\tau}^\dagger]_+ = [\hat{a}_{i\sigma} \hat{a}_{j\tau}]_+ = 0. \quad (46)$$

The spin-independent Hamiltonian in second quantisation is

$$\hat{H} = \sum_{ij} h_{ij} \sum_{\sigma} \hat{a}_{i\sigma}^\dagger \hat{a}_{j\sigma} + \frac{1}{2} \sum_{ijkl} V_{ijkl} \sum_{\sigma\tau} \hat{a}_{i\sigma}^\dagger \hat{a}_{k\tau}^\dagger \hat{a}_{l\tau} \hat{a}_{j\sigma} \quad (47)$$

with h_{ij} as one-electron integrals and $V_{ijkl} = \langle ik|jl\rangle$ as two-electron four-index integrals in Dirac notation. $\hat{E}_i^j = \hat{a}_{i\alpha}^\dagger \hat{a}_{j\alpha} + \hat{a}_{i\beta}^\dagger \hat{a}_{j\beta}$ is the one-electron excitation operator in spatial coordinates and $\hat{\varepsilon}_\sigma^\tau = \sum_i \hat{a}_{i\sigma}^\dagger \hat{a}_{i\tau}$ in spin coordinates. These one-electron excitation operators follow the commutator rules

$$[\hat{E}_i^j, \hat{E}_k^l] = \delta_{jk} \hat{E}_i^l - \delta_{il} \hat{E}_k^j, \quad [\hat{\varepsilon}_\sigma^\tau, \hat{\varepsilon}_\mu^\nu] = \delta_{\mu\tau} \hat{\varepsilon}_\sigma^\nu - \delta_{\sigma\nu} \hat{\varepsilon}_\mu^\tau. \quad (48)$$

The spin and spatial coordinates commute as

$$[\hat{E}_i^j, \hat{\varepsilon}_\sigma^\tau] = 0. \quad (49)$$

The Hamiltonian in Eq. (47) can then be rewritten as

$$\hat{H} = \sum_{ij} h_{ij} \hat{E}_i^j + \frac{1}{2} \sum_{ijkl} V_{ijkl} (\hat{E}_i^j \hat{E}_k^l - \delta_{jk} \hat{E}_i^l). \quad (50)$$

The Hamiltonian in Eq. (50) on the other hand can be expressed by means of the Fock matrix elements

$$F_{ij} = h_{ij} + \sum_k \left(V_{ijkk} - \frac{1}{2} V_{ikkj} \right) \bar{w}_k \quad (51)$$

and the Hartree-Fock energy

$$E^{HF} = \sum_i \bar{w}_i F_{ii}^{HF} - \frac{1}{2} \sum_{ik} \bar{w}_i \bar{w}_j \left(V_{ijij} - \frac{1}{2} V_{ijji} \right) \quad (52)$$

of an anchor configuration with occupation \bar{w}_i of the i th MO as

$$\begin{aligned} \hat{\mathcal{H}} = & E_{SCF} - \sum_i F_{ii} \bar{w}_i + \frac{1}{2} \sum_{ij} \left(V_{ijij} - \frac{1}{2} V_{ijji} \right) \bar{w}_i \bar{w}_j + \sum_{ij} F_{ij} \hat{E}_i^j \\ & - \sum_{ijk} \left(V_{ikjk} - \frac{1}{2} V_{ikkj} \right) \bar{w}_k \hat{E}_i^j + \frac{1}{2} \sum_{ijkl} V_{ijkl} \left(\hat{E}_i^j \hat{E}_k^l - \delta_{jk} \hat{E}_i^l \right). \end{aligned} \quad (53)$$

Matrix elements can be expressed as a modification of the SCF result. Because there are only one- and two-electron operators in Eq. (53), matrix elements between two configurations differing in more than two occupations are zero. Therefore, it is possible to group the matrix elements in three cases [150, 151]: diagonal elements H_{nn} , one-electron occupation difference $H_{nn'}$ and two-electron occupation difference $H_{nn''}$. Hence, the diagonal CI matrix elements are

$$\begin{aligned} H_{nn} = & E^{SCF} + \sum_i F_{ii} \Delta w_i + \frac{1}{2} \sum_{i \neq j} V_{ijij} \Delta w_i \Delta w_j \\ & + \frac{1}{2} \sum_{i \neq j} V_{ijji} \left(-\frac{1}{2} \Delta w_i \Delta w_j + \frac{1}{2} w_i w_j - w_i + \eta_{ij}^{ji} \right) \\ & + \frac{1}{2} \sum_i V_{iiii} \left(\frac{1}{2} \Delta w_i \Delta w_j + \frac{1}{2} w_i w_j - w_i \right) \end{aligned} \quad (54)$$

with the spin coupling $\eta_{ij}^{ji} = \langle \omega w | E_i^j E_j^i | \omega' w' \rangle = (E_j^i | \omega w \rangle)^\dagger \cdot E_j^i | \omega' w' \rangle$ and the occupation difference $\Delta w_i = w_i - \bar{w}_i$ between the configuration and the ground-state anchor configuration. The matrix element coupling two configurations with an occupation difference of one electron is

$$\begin{aligned} H_{nn'} = & F_{ij} \eta_i^j + \sum_{k \neq i, j} V_{ikjk} \Delta w'_k \eta_i^j + \sum_{k \neq i, j} V_{ikkj} \left(-\frac{1}{2} \Delta w'_k \eta_i^j + \frac{1}{2} w'_k \eta_i^j - \eta_i^j + \eta_{ik}^{kj} \right) \\ & + V_{iii} \left(\frac{1}{2} \Delta w'_i + \frac{1}{2} w'_i \right) \eta_i^j - V_{ijjj} \left(\frac{1}{2} \Delta w'_j + \frac{1}{2} w'_j - 1 \right) \eta_i^j \end{aligned} \quad (55)$$

and for a two-electron difference

$$H_{nn''} = \left(V_{ikjl} \eta_{ik}^{jl} + V_{iklj} \eta_{ik}^{lj} \right) [(1 + \delta_{ik})(1 + \delta_{jl})]^{-1}. \quad (56)$$

Following the commutator relations in Eq. (48) and (49), the operators \hat{S}^2 and \hat{S}_z can be expressed in second quantisation as

$$\hat{S}^2 = \frac{1}{2} \sum_{\sigma\tau} \left(\hat{\varepsilon}_{\sigma}^{\tau} \hat{\varepsilon}_{\sigma}^{\tau} - \frac{1}{2} \hat{\varepsilon}_{\sigma}^{\sigma} \hat{\varepsilon}_{\tau}^{\tau} \right), \quad \hat{S}_z = \frac{1}{2} \left(\hat{\varepsilon}_{\alpha}^{\alpha} - \hat{\varepsilon}_{\beta}^{\beta} \right). \quad (57)$$

In order to extend the CI method towards a multireference picture [152], reference configurations have to be created. This can be done via an active space by defining the number of active electrons and active frontier orbitals in an n-tuple excitation, manually by selecting the orbitals or iteratively. In the DFT/MRCI program [67], starting from either an active space or a manual selection that usually includes single and double excitations, the reference space is then determined iteratively. The iterative approach selects the most strongly interacting references so that the number of references remains limited [152].

2.6 The Combination of DFT and MRCI

The DFT/MRCI method, originally developed by Grimme and Waletzke [66], is a well-established method for calculating vertical transition energies. The advantages include a good accuracy with an error of below 0.2 eV [66] with a relatively high computational speed. This is accomplished by taking dynamic electron correlation from DFT and static correlation from MRCI. This makes it possible to limit the calculation size, ranging from a few thousand CSFs in small molecules to a few million CSFs in larger organometallic complexes. The process speeds up the calculation dramatically. As an example, the transition metal complex $\text{Rh}(\text{phen})_3^{3+}$ in the basis SVP [153] for the ligand atoms and ecp-28-mwb-TZVP [154] Wood-Boring effective core potential (ECP) with the corresponding valence basis for Rh is given. In frozen-core approximation, 210 electrons in 554 orbitals in singlet multiplicity are included. The calculation with the R2018 Hamiltonian leads to ≈ 45 mil CSFs with a selection threshold of one Hartree [133]. In comparison, using Weyl's formula in Eq. (41), the same complex results in $\approx 3.97 \times 10^{220}$ CSFs in a full CI calculation. Without frozen-core approximation, 296 electrons in 665 orbitals are to be considered, resulting in $\approx 1.03 \times 10^{310}$ CSFs. It is clear by these numbers alone that the full CI calculation is impossible to carry out on larger systems in the foreseeable future, if ever.

The DFT/MRCI calculation, on the other hand, only takes about five days on nine Intel(R) Xeon(R) E5-2660 CPUs for the lowest 50 roots. By combining DFT and MRCI, the CI expansion can be shortened, since the static correlation converges fast and the dynamic correlation converges slowly in MRCI. Still, some dynamic correlation is provided by MRCI. To avoid double counting, a correctional Hamiltonian is needed.

The three types of CI matrix elements in Eq. (54) – (56) can be parted into three (partly different) categories within the DFT/MRCI approach. The first is the diagonal correction

for genuinely diagonal matrix element, which have the same space part and spin part. The second is an off-diagonal matrix element with the same space part but different spin parts. The third is a correction for purely off-diagonal matrix elements between configurations that differ by one or two electrons. These purely off-diagonal elements are damped depending on the energy difference of the interacting configurations.

The corrections of the diagonal elements are introduced by replacing the HF-like orbital energies F_{ii}^{HF} of Eq. (51) that are constructed from the given KS basis as an effective one-electron matrix element with the Kohn-Sham orbital energies F_{ii}^{KS} . Additional shifts are instigated by $\Delta E_{\text{coul}} - \Delta E_{\text{exch}}$, which depend on a scaling of Coulomb- and exchange-like integrals V_{ijij} and V_{ijji} . The scaling of those integrals depends on the specific DFT/MRCI Hamiltonian. The general expression for the correction of diagonal matrix elements is

$$\begin{aligned} \langle \omega w | \hat{\mathcal{H}}^{DFT} - E^{DFT} | \omega w \rangle &= \langle \omega w | \hat{\mathcal{H}} - E^{HF} | \omega w \rangle \\ &\quad - \sum_{i \in c}^{n_{exc}} (F_{ii}^{HF} - F_{ii}^{KS}) + \sum_{i \in a}^{n_{exc}} (F_{ii}^{HF} - F_{ii}^{KS}) + \Delta E_{\text{coul}} - \Delta E_{\text{exch}} \end{aligned} \quad (58)$$

with n_{exc} as the number of excitations relative to the anchor configuration. The indices a and c represent annihilated and created electrons and the energy E^{HF} is defined as in Eq. (52). The second correction, i.e. the correction of matrix elements between configurations with the same space part, is discussed in later sections. The third correction concerns the off-diagonal elements between CSFs with one- or two-electron differences in Eq. (55) and (56), which are required for the correct description of static and dynamic correlation. Static correlation is taken into account by a small number of energetically low-lying configurations, while on the other hand dynamic correlation requires a large number of energetically high-lying configurations. Since dynamic correlation is already contained in the DFT part, a damping function that depends on the energy difference is required. In this manner, the interaction between energetically high-lying configurations is avoided. Additionally, a scaling of all off-diagonal elements is required to avoid double counting the correlation energy already included in the diagonal elements. These corrections of off-diagonal elements are discussed in the subsections of the DFT/MRCI Hamiltonians and in greater detail in the context of the newly developed R2018 Hamiltonian in Sec. 5.2. A general scheme of the corrections included in the DFT/MRCI method is shown in Fig. 3.

Two previous versions of the DFT/MRCI Hamiltonian exist. The first one is the Hamiltonian developed by Grimme and Waletzke [66], which is therefore called original Hamiltonian. This Hamiltonian is discussed in Sec. 2.6.1. The other Hamiltonian is the redesigned Hamiltonian developed by Lyskov et al. [73] in order to remedy some shortcomings of the original Hamiltonian. It employs just one parameter set for all multiplicities. This Hamiltonian was later renamed to R2016 and is discussed in Sec. 2.6.2. The newly developed Hamiltonians R2017 and R2018, which are based on the redesigned approach, can be found in Sec. 5.1 and 5.2, respectively.

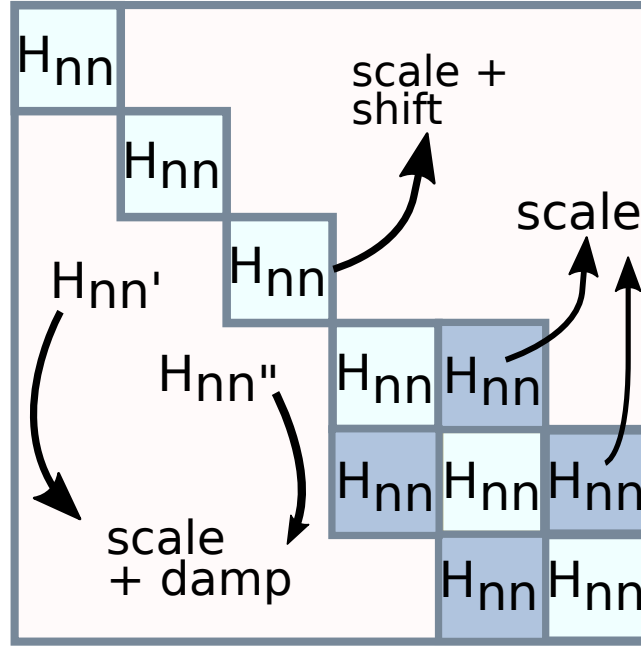


Figure 3: Schematic representation of the corrections to the DFT/MRCI matrix elements

2.6.1 Original Hamiltonian

Grimme and Waletzke developed a Hamiltonian for singlet and triplet states [66]. The Hamiltonian depends on five parameters and is parametrised against experimental vertical excitation energies of ten organic molecules, with a different parameter set for singlets and triplets. This Hamiltonian and parameter set is called Original from now on. The correction of Coulomb and exchange interactions is

$$\Delta E_{coul} - \Delta E_{exch} = \frac{1}{n_{exc}} \sum_{i \in c}^{n_{exc}} \sum_{i \in a}^{n_{exc}} (p_J V_{ijij} - {}^m p [N_o] V_{ijji}) \quad (59)$$

with n_{exc} as the number of excitations, N_o the number of open shells in a configuration, c and a the annihilated and created electrons, p_J the parameter for scaling Coulomb integrals and ${}^m p [N_o]$ for exchange integrals with multiplicity m . For a singlet state with $m = 1$, the corresponding coefficient is

$${}^1 p [N_o] = {}^1 p [0] + N_o {}^1 \alpha \quad (60)$$

and for a triplet state with $m = 3$ it is

$${}^3 p [N_o] = N_o {}^3 \alpha . \quad (61)$$

The off-diagonal matrix element between CSFs with the same space part and different spin part is unchanged as

$$\langle \omega w | \hat{\mathcal{H}}^{DFT} | \omega' w \rangle = \langle \omega w | \hat{\mathcal{H}} | \omega' w \rangle \quad (62)$$

and therefore calculated exactly.

The correction term for the off-diagonal elements between CSFs with a one- or two-electron difference

$$\langle \omega w | \hat{\mathcal{H}}^{DFT} | \omega' w' \rangle = \langle \omega w | \hat{\mathcal{H}} | \omega' w' \rangle p_1 \cdot e^{-p_2 \cdot \Delta E_{\omega w'}^4} \quad (63)$$

contains a scaling parameter p_1 and a damping function that depends on a parameter p_2 . The scaling parameter p_1 is needed to avoid double counting of some correlation that is already included in the diagonal matrix elements and their respective scaling. Therefore, the scaling parameter depends mainly on the diagonal matrix elements. The exponential function damps the interaction between two CSFs. In this manner CSFs interact only if they are energetically close to account for static correlation.

2.6.2 R2016 Hamiltonian

While the original Hamiltonian generally yields good results, it has a few shortcomings that include bi-chromophores and artificially low-lying doubly excited states [73]. This motivated Lyskov et al. to develop a redesigned Hamiltonian [73], capable of addressing these issues. The new Hamiltonian – later renamed to R2016 – features a unified parameter set for all multiplicities with an even number of electrons. Two parameters are introduced, the p_J parameter for scaling Coulomb-type integrals and the p_X parameter for scaling exchange-like integrals.

For the diagonal matrix element Eq. (58), the corrections for Coulomb and exchange interactions are

$$\begin{aligned} \Delta E_{coul} - \Delta E_{exch} = & p_J \left(- \sum_{\substack{i,j \in c \\ i > j}}^{n_{exc}} V_{ijij} - \sum_{\substack{i,j \in a \\ i > j}}^{n_{exc}} V_{ijij} + \sum_{i \in c}^{n_{exc}} \sum_{j \in a}^{n_{exc}} V_{ijij} \right) \\ & - p_X \left(\frac{1}{2} \sum_{i \in c}^{n_{exc}} \sum_{j \in a}^{n_{exc}} V_{ijji} + \sum_{\substack{i,j \in o \\ i > j}}^{N_o} V_{ijji} \eta_{ij}^{ji} \right). \end{aligned} \quad (64)$$

In case of an off-diagonal element with the same space part but a different spin part, the matrix element is scaled as

$$\langle \omega w | \hat{\mathcal{H}}^{DFT} | \omega' w \rangle = \langle \omega w | \hat{\mathcal{H}} | \omega' w \rangle (1 - p_X). \quad (65)$$

The matrix element in Eq. (65) is therefore scaled by a factor of approx. $2/3$, contrary to the original ansatz, which employs the exact matrix element in Eq. (62).

The damping and scaling term for off-diagonal matrix elements differing in one- or two-electron occupations that was found to perform best is given by

$$\langle \omega w | \hat{\mathcal{H}}^{DFT} | \omega' w' \rangle = \langle \omega w | \hat{\mathcal{H}} | \omega' w' \rangle \frac{p_1}{1 + (p_2 \cdot \delta \epsilon^5) \cdot \arctan(p_2 \cdot \delta \epsilon^5)} \quad (66)$$

with p_1 as a scaling and p_2 as a damping parameter. The R2016 Hamiltonian has been fitted to a set of various organic molecules with a broad range of orbital types, including π , n and Rydberg orbitals. The resulting root-mean-square error is below 0.2 eV for the testing set of closed-shell organic molecules shown in Sec. 3.

3 The Datasets for Training and Testing

Two separate datasets for training and testing have been obtained. Since the new Hamiltonians R2017 and R2018 are all-multiplicity Hamiltonians, both closed-shell and open-shell molecules have to be included. The experimental excitation energies of closed-shell organic molecules for the training and testing sets have been taken from [73]. The data on open-shell molecules has been collected from literature to create the training and testing sets, since a collection of these states did not exist previously [155]. Additionally, a dataset on the electronic excitation energies of organic and inorganic transition metal complexes was collected for testing the accuracy of the Hamiltonians. These sets are introduced in the following two subsections.

Since molecules with a radical ground state are generally not very stable, experimental electronic absorption spectra and state assignments are rare. Photoelectron spectra on the other hand are more abundant in literature. Due to the nature of this spectroscopic method, the states obtained in this manner correspond to an excitation from a doubly occupied to the singly occupied orbital. The states of open-shell molecules in the training and testing sets are therefore moderately skewed towards this type of excitation due to the availability of experimental data. An overview of this method is given in Sec. 3.3.

3.1 Dataset for Training

The training set of the R2017 Hamiltonian consists of 117 excited states in total. Among these are the excited states of closed-shell molecules of the R2016 fitting set [73], which consists of 39 singlet and 26 triplet states. Additionally, 52 doublet states have been gathered from literature. The number of states of each excitation type can be found in Tab. 2.

For the R2018 Hamiltonian, the four lowest singlet and four lowest triplet states of Cu^+ , the two lowest doublet states of Cu and the lowest singlet and lowest triplet state of ruthenocene have been added to the list of states used in the R2017 parameter optimisation. The new additions include transitions involving d-orbitals for a more balanced description of excited state energies in transition metal complexes. By extending the list of experimental reference data, a total of 131 excited state energies are included in the training set of the R2018 Hamiltonian. A discussion on the effect of the additional states can be found in Sec. 5.2.

An overview of all organic molecules involved in the R2017 and R2018 parameter optimisations can be found in Fig. 4. The figure includes ruthenocene, which is only used in the R2018 parametrisation.

Table 2: Excitation types in the organic training set used for parametrising the R2017 Hamiltonian. The total number of closed-shell singlet and triplet states is 65 and the total number of open-shell states amounts to 52. For the R2018 Hamiltonian, additional states involving the d-orbitals have been included, resulting in a total of 131 states.

Type	Closed-Shell States	Open-Shell States	Total
$\pi \rightarrow \pi^*$	31	25	56
$n \rightarrow \pi^*$	28	9	37
$\sigma \rightarrow \pi^*$	-	12	12
$\pi \rightarrow Ryd$	2	2	4
$n \rightarrow Ryd$	4	-	4
$n \rightarrow n^*$	-	3	3
$\sigma \rightarrow n^*$	-	1	1

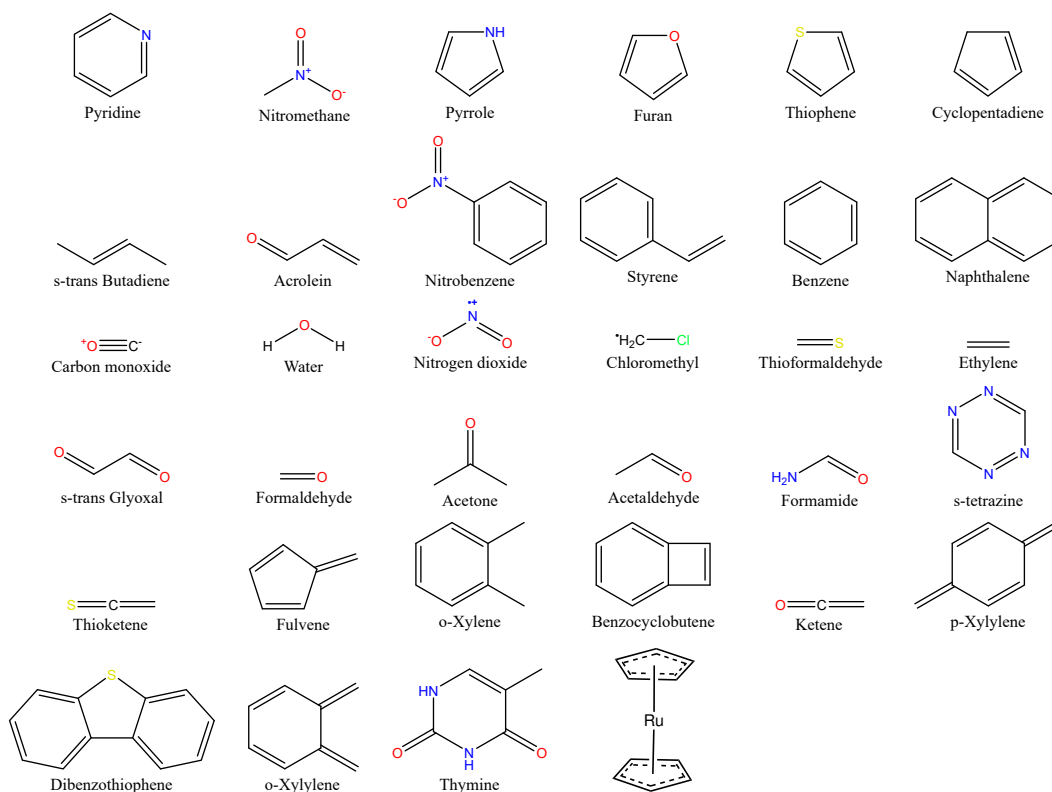


Figure 4: Molecules used in the training set. All organic molecules were employed in the parametrisation of the R2017 and R2018 Hamiltonian. Ruthenocene was only used for the R2018 Hamiltonian together with Cu and Cu^+ .

3.2 Dataset for Testing

3.2.1 Organic Molecules

The testing set for assessing the accuracy of electronic excitation energies consists of 310 states in total. The set contains the 160 states of [73], composed of 93 singlet and 67 triplet states in addition to 150 doublet states collected from literature. An overview of all excitation types in the set can be found in Tab. 3. The chemical structures of the open-shell and closed-shell organic molecules are shown in Fig. 6 and 7, respectively.

Table 3: Most common excitation types in the organic testing set used for assessing the R2017 and R2018 Hamiltonians. The total number of closed-shell singlet and triplet states is 160 and the total number of open-shell states is 150.

Type	Closed-Shell States	Open-Shell States	Total
$\pi \rightarrow \pi^*$	108	106	214
$n \rightarrow \pi^*$	20	25	45
$\pi \rightarrow Ryd$	26	3	29
$n \rightarrow Ryd$	2	5	7
$\sigma \rightarrow \pi^*$	4	2	6
$n \rightarrow n^*$	-	3	3
$\sigma \rightarrow n^*$	-	2	2
$\sigma \rightarrow Ryd$	-	2	2
$\pi \rightarrow n^*$	-	1	1
$\sigma \rightarrow Ryd$	-	1	1

3.2.2 Closed-Shell Transition Metal Complexes

The testing set for transition metal complexes consists of in total 67 electronic excitation energies. 40 energies are from organic and 27 from inorganic transition metal complexes. In case of all redesigned Hamiltonians, two states of MnO_4^- could not be reproduced in the calculations, thus lowering the number from 27 to 25. For a more detailed discussion on the states and the two missing states of permanganate see [133]. The set includes a variety of excitation types, most of them being of MLCT and LC type or mixtures thereof. A few MC and LMCT transitions are also included. The chemical structures of all inorganic and organic transition metal complexes can be found in Fig. 8.

3.3 Photoelectron Spectroscopy

Molecules with a doublet ground state are unstable in solution at room temperature in many cases. For this reason, many of the experimental reference data used in Paper 1 and Paper 2 for vertical excitation energies stem from photoelectron spectroscopy (PES) [156]. This method is based on the photoelectric effect [157]. For the purpose of measuring the lowest excited states of a probe, radiation in the ultraviolet range is used for ionisation [158, 159], while X-ray radiation is used for core electrons [160]. A common sources of UV light is Helium(I) at 21.22 eV [161]. The ionisation energy E_I is given by

$$E_I = E_{phot} - E_k \quad (67)$$

with E_{phot} as the energy of the radiation

$$E_{phot} = h\nu \quad (68)$$

where h is Planck's constant and ν is the frequency of the photon. The kinetic energy E_k of the ejected electron is measured in a spectrometer. Because PES ejects an electron, the

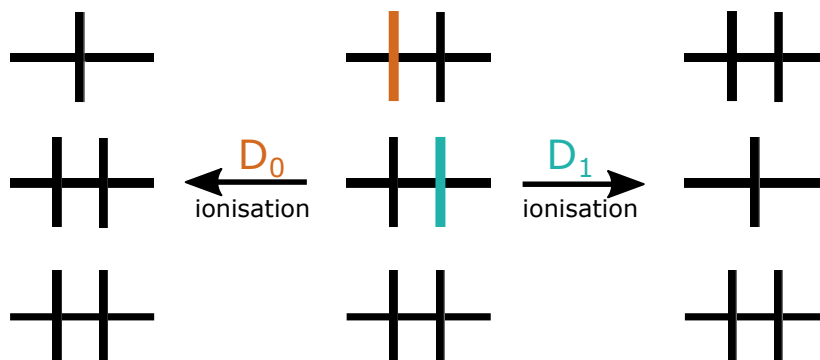


Figure 5: Ionisation of a closed-shell ground state to an open-shell doublet species in the ground state (left) and an excited state (right). The excited state in this example is characterised by a DOMO \rightarrow SOMO transition.

molecule that is measured is not the same molecule that is used as a probe. A closed-shell molecule with n electrons is ionised leading to an open-shell molecule with $n-1$ electrons and a doublet multiplicity. Therefore, PES is well suited to measure radical cations of neutral closed-shell molecules. In order to measure the electronic states of a neutral molecule, the corresponding $n+1$ electron anion must be used as a probe. Photoelectron spectroscopy can also be used in femtosecond time-resolved measurements for studying dissociation dynamics [162] and wave-packet motion [163].

The first peak in the photoelectron spectrum corresponds to the ground state of the ionised species. The transition energies of the excited states are received by subtracting the energy of the first peak from the following peaks [164]. This corresponds to the vertical ionisation energy. In case of the adiabatic energy, the minimum energy, i.e. the beginning of a band, is considered [165]. A scheme of the ionisation process starting from a closed-shell ground state can be found in Fig. 5. In the middle, a closed-shell species is shown, which is then ionised. When the HDOMO is ionised, the orbital becomes singly occupied and the resulting species corresponds to the doublet ground state (left). If an energetically lower orbital is ionised, the resulting state corresponds to a transition from this orbital to the SOMO, which is shown on the right. This example state is characterised by a HDOMO \rightarrow SOMO transition relative to the doublet ground state on the left. If, for example, the vertical ionisation potentials of the closed-shell species in the middle of Fig. 5 are 10 eV for the highest orbital (ionisation of the orange electron) and 12.2 eV for the second highest orbital (ionisation of the cyan electron), the vertical transition energy to the D_1 state is 2.2 eV.

The advantages of PES include the measurement of spectra of radical cations that might not be stable otherwise and accessibility to states that are forbidden by selection rules in an electronic absorption spectrum. The disadvantage follows from the occupation. The highest orbital that can be ionised becomes the SOMO in the ionised species, thus only transitions to the SOMO can be measured via PES. States that are characterised by a transition from an occupied orbital (SOMO/DOMOs) to a vacant orbital are therefore not included in a photoelectron spectrum.

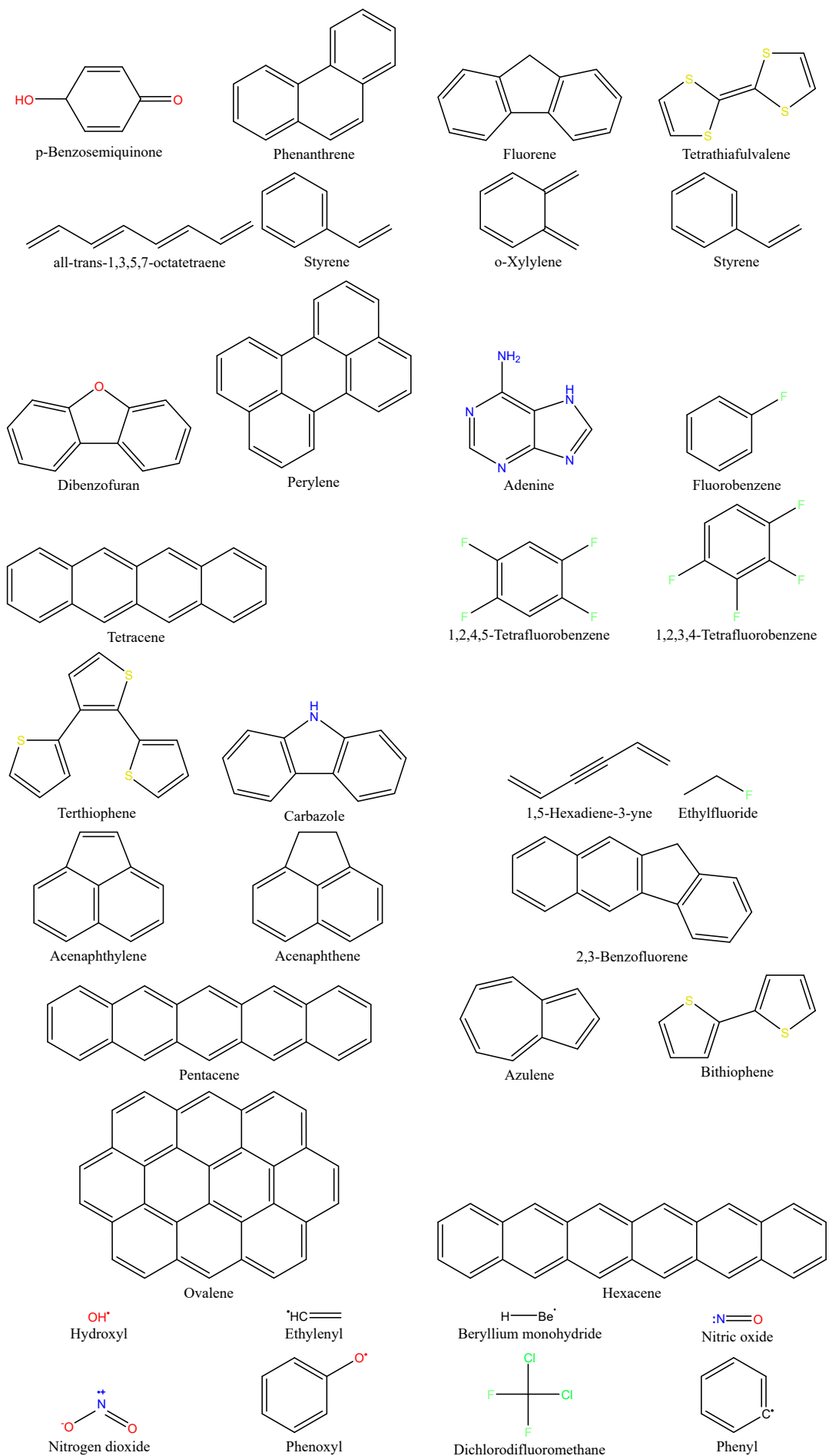


Figure 6: Molecules with doublet states used for testing

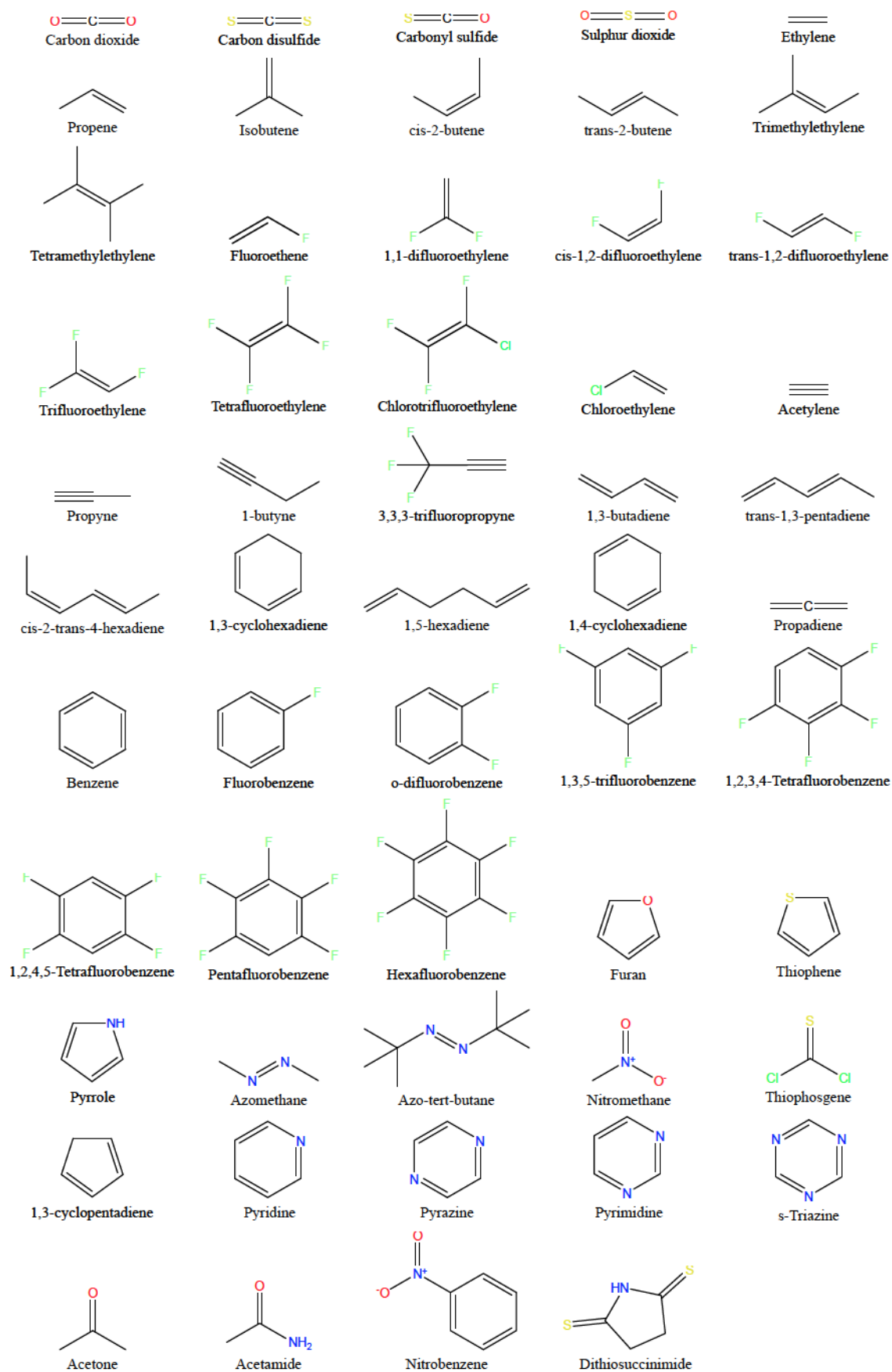


Figure 7: Molecules with singlet and/ or triplet states used for testing

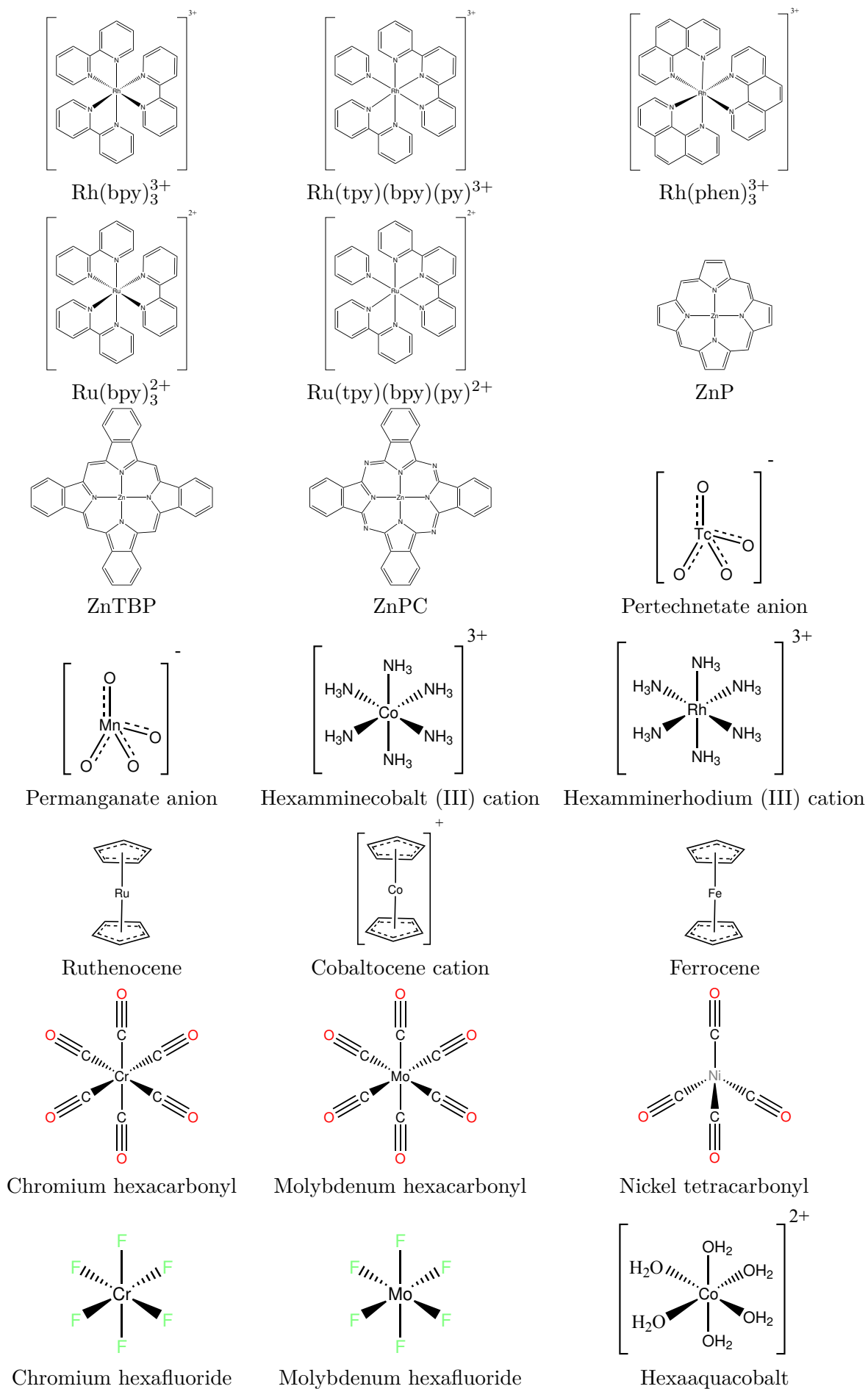


Figure 8: Transition metal complexes used as benchmark molecules

4 Interface Development

4.1 Interface to Dalton

The default interface for the DFT/MRCI program is Turbomole. For open-shell systems, however, Turbomole does not provide the functionality to compute ROKS orbitals as of version 7.1. The free and open-source program Dalton [95] is able to perform those calculations. The interface to Dalton – called *d2tm* – makes it possible to compute ROKS orbitals for open-shell systems and use them in a DFT/MRCI calculation. The program is written in the C programming language standard ISO/IEC 9899:1999 (colloquially called C99). RKS orbitals as well as implicit solvents via PCM are also possible. The interface was originally developed for Dalton 2015.0 [166], but is fully compatible to the later releases Dalton 2016 [167] and Dalton 2018 [168].

The program works both ways, being able to generate a Dalton input starting from an optimised geometry in Turbomole format and to generate files from a finished Dalton single-point calculation back to Turbomole format.

4.1.1 Dalton Run from an Optimised Geometry

Starting from Cartesian coordinates and a basis set file in Turbomole format, the interface provides the input options listed in Table 4. For the import of Turbomole files, the files *coord* and *basis* in Turbomole-format have to be present. A flow chart describing the program flow in import mode is shown in Fig. 9.

4.1.2 Symmetry Aspects in Dalton

A special requirement for generating the input for the Dalton run affects symmetry. Dalton is capable of using symmetry for D_{2h} and subgroups (same as the *mrci* program) and it is able to autodetect the symmetry of a molecule, but doing so modifies the geometry. This modified geometry is not accepted by Turbomole-based programs like *ritraf* for generating RI-integrals for the DFT/MRCI run. The solution to this problem is the use of predefined

Table 4: Import arguments for the Dalton interface *d2tm*

Argument	Description
-i	Invokes the import mode (mandatory)
-c <charge>	Specifies the charge of the system
-f <functional>	Specifies the DFT functional (default functional: BHandHLYP)
-p	Specifies a solvent calculation with PCM (default solvent: Acetonitrile)
-s <point group>	Specifies the symmetry of the system, limited to D_{2h} and subgroups. Symmetry generators are used to provide the same order of irreducible representations as Turbomole

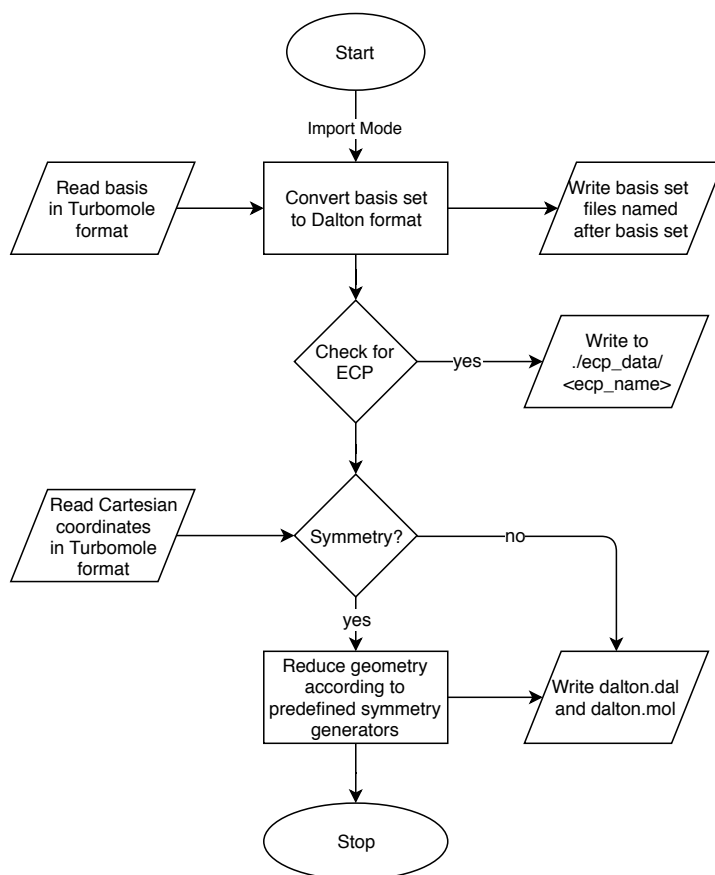


Figure 9: Flow chart of the import mode of *d2tm* for generating a Dalton input starting from an optimised geometry and a basis set in Turbomole format.

symmetry generators in Dalton, which generate a molecule with a specific symmetry during the calculation from a starting structure of unique centres. This means that any atom that can be transformed to another atom in the input file by symmetry operations specified in the input, like rotations about an axis, has to be removed from the input file. In order for symmetry generators to work in the *d2tm* interface, the molecule has to be placed in its centre of mass at (0,0,0). When using Turbomole for geometry optimisations, this is always the case.

The *d2tm* interface employs all symmetry operation in a specific point group and checks for atoms that are redundant in respect to that operation. All redundant atoms are removed. The structure for the Dalton input consists only of unique atoms from which the desired molecule can be rebuilt in the Dalton calculation by means of the symmetry generators. A list of the symmetry generators used in the *d2tm* program which lead to an output (geometry and orbitals) that is accepted by Turbomole is found in Tab. 5. The order of the generators is invariable, as it determines the way the symmetry of the orbitals is determined in Dalton. The number of generators is $\log_2 g$, with g as the order of the point group.

The following example (Fig. 10) takes the molecule ethene, which has D_{2h} symmetry and is planar. At “start” (as in the Dalton input) the molecule is reduced to its unique atoms with regard to symmetry operations. Then the generator Z is employed. Since the molecule is planar within the XY -plane, there is no change. Next, the generator Y is employed,

Table 5: List of symmetry generators of all supported point groups of Dalton (D_{2h} and subgroups). Note that the generator always describes the parameter that is changing when employing that generator. Generator X refers to a reflection in the YZ-plane, while generator XY refers to a rotation about the Z-axis. Generator XYZ refers to an inversion.

Point group	Generators
C_1	-
C_s	Z
C_2	XY
C_i	XYZ
C_{2v}	X, Y
C_{2h}	Z, XY
D_2	XZ, YZ
D_{2h}	X, Y, Z

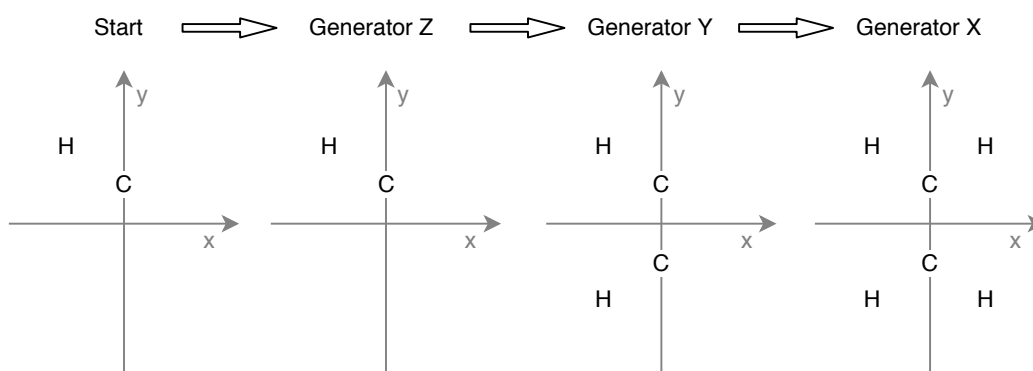


Figure 10: Visualisation of the Dalton input for ethene in D_{2h} symmetry, with the Z-axis pointing towards the observer. Start refers to the structure in the input file dalton.mol.

leading to a reflection in the XZ-plane. Finally, the X generator with a reflection in the YZ-plane is employed, resulting in the final structure of the ethene molecule. The *d2tm* interface reduces the structure in reverse direction.

4.1.3 Generate Input Files from Dalton Run

The calculations has to be started using the following arguments:

```
dalton -get "DALTON.CM AMFI_SYMINFO.TXT DALTON.MOPUN midasifc.cartrot"
dalton
```

with the latter dalton as the name of the input (dalton.dal and dalton.mol).

This ensures that all files are present for the export of the Dalton output to Turbomole format.

After a successful Dalton run the output can be converted to Turbomole format. This is done by simply calling *d2tm -e*. This works for all previous input settings as well as for RKS and ROKS calculations. A flow chart describing the flow of the program in export

mode is shown in Fig. 11.

The conversion back to Turbomole format is necessary to compute four-index integrals within the RI approximation, as Dalton is not capable of providing these integrals as of version 2018. Afterwards, the Turbomole-specific programs *rimp2prep*, *oneint* and *ritraf* can be executed. The input for the *mrci* program is identical between a Turbomole and Dalton single point calculation.

4.2 Interface to Orca 4.0

In Orca Version 4.0 [96, 97] and later, an interface from ORCA to the *mrci* program has been implemented by Frank Neese and his team. Unlike Dalton, ORCA is a standalone program with respect to *mrci*, meaning that all necessary integrals and molecular information are provided by ORCA without the need of any other program.

Starting from an optimised geometry, a single-point calculation for generating Kohn-Sham orbitals and RI integrals by using the DFTMRCI keyword is shown below for the H₂O molecule.

```
! def2-TZVP def2-TZVP/C def2-JK RI-JK BHLYP
! DFTMRCI SCFCONV7 Grid3 UseSym
* xyz 0 1
o 0 0 -0.3909593631884944
h -0.7614630581482476 0 0.1954796815942499
h 0.7614630581482476 0 0.1954796815942499
*
```

The flow chart of the ORCA interface, which is integrated into the *mrci* program and accessed via the *\$orca* keyword in the *mrci* input, is shown in Fig. 12.

The interface option in ORCA generates two files, namely *orca.bkji* and *orca.DFTMRCI.inp*, which contain everything that is needed for a DFT/MRCI or ab-initio MRCI run. In order to read those files, an ORCA interface was implemented within the *mrci* program. The interface is written in fixed form Fortran, as is the rest of the *mrci* program.

The *mrci* program requires information about orbital energies, symmetry of the molecule and each orbital, occupied and vacant orbitals and in case of a ab-initio MRCI or MRMP2 run, the one-electron integrals (which are not required for DFT/MRCI) from *orca.DFTMRCI.inp*, the RI integrals from *orca.bkji* and a user-selected frozen core from the input file of the *mrci* program.

It is possible to do either a complete calculation with the ORCA files or just generating the files *bkji*, *control*, *energy*, *mos.bin* and *oneint* by using the *\$interface* keyword in addition to the *\$orca* keyword. If the *\$interface* keyword is specified, the program stops after writing all files in Turbomole format to disc. Otherwise, the files in Turbomole format are generated automatically in the course of a calculation as they are needed by programs that are based on the DFT/MRCI results. These programs include *proper* for transition

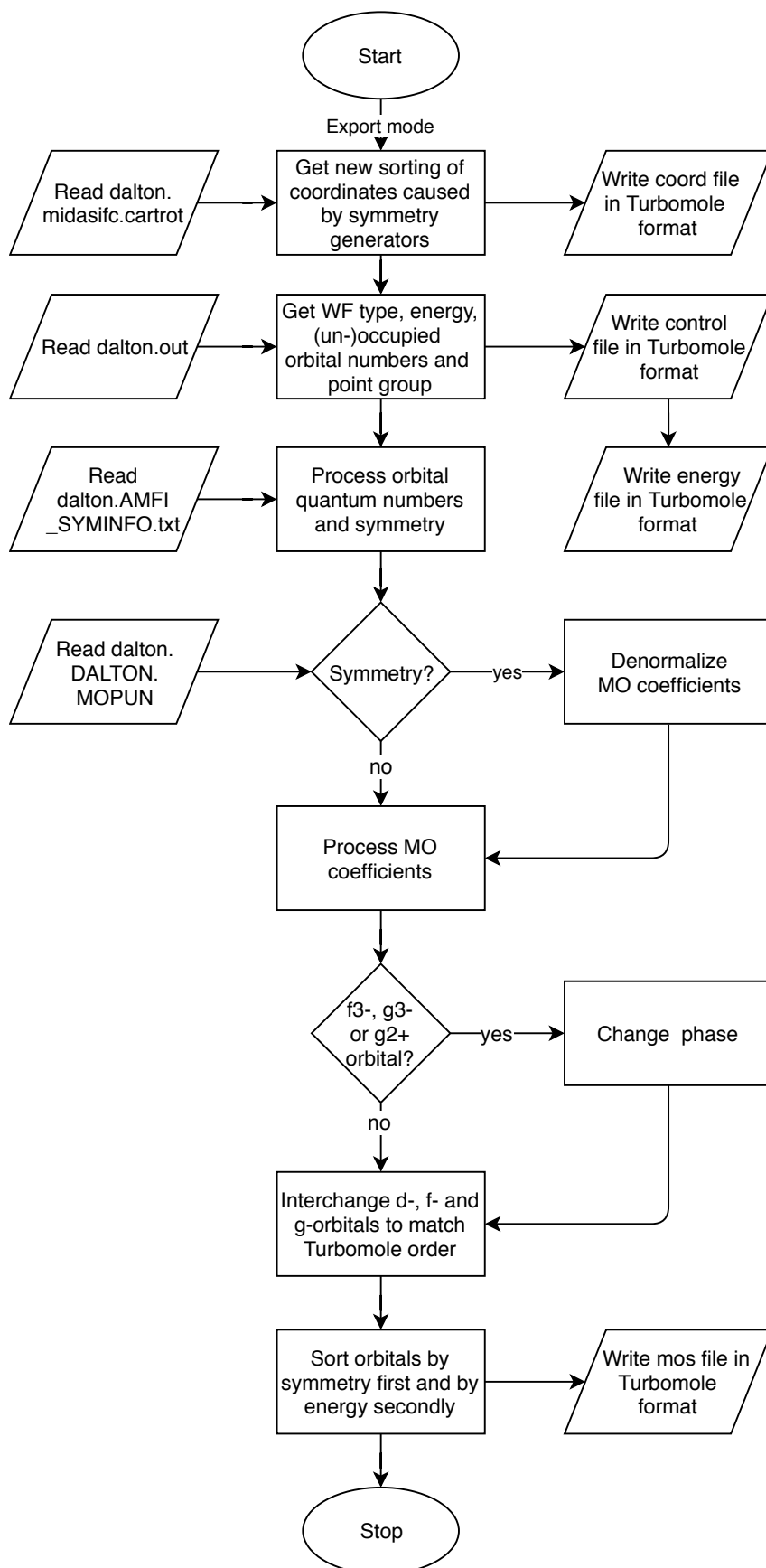


Figure 11: Flow chart of the export mode of *d2tm*, from Dalton output to Turbomole format files for DFT/MRCI

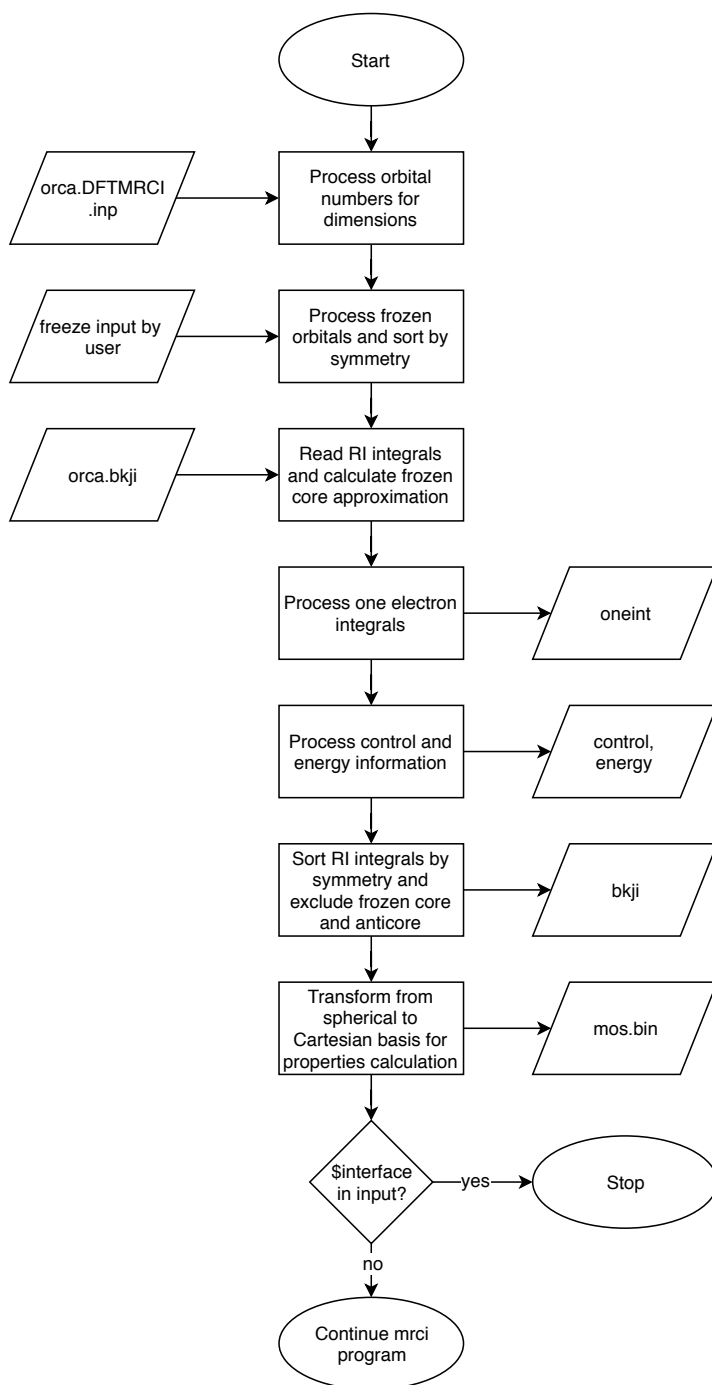


Figure 12: Flow chart for the ORCA interface within the *mrci* program.

properties and *spockCI* for spin-orbit coupling. In order to freeze orbitals, two keywords can be used, *\$freeze* and *\$efreeze*.

The keyword *\$freeze* freezes orbitals automatically via an energy threshold. When no threshold is specified, the default values are taken, which freeze all orbitals below $-3.0 E_h$ and above $2.0 E_h$. The other keyword *\$efreeze* is used to manually specify orbitals that are frozen.

In order to reduce the computational demand in case of an ab-initio MRCI or MRMP2 calculation, the frozen-core approximation (FCA) is applied when frozen orbitals are specified. These user-specified frozen-core orbitals are discarded, but their energy is retained

and added to the nuclear repulsion energy E_{nuc} as

$$E_{nuc}^{FCA} = E_{nuc} + \sum_i^{n_{frozen}} h_{ii} + \sum_{ij}^{n_{frozen}} (2V_{ijij} - V_{ijji}). \quad (69)$$

The one-electron integrals of the remaining (non-frozen) set of orbitals are altered to include the interaction with the set of frozen-core orbitals as

$$h_{ij}^{FCA} = h_{ij} + \sum_{kl}^{n_{frozen}} (2V_{ijkl} - V_{ilkj}). \quad (70)$$

Additionally, for running the properties program *proper* after the mrci run for calculating molecular properties like dipole and transition dipole moments, a binary file named *mos.bin* is created. *mos.bin* contains the coordinates, basis set, molecular orbitals and nuclear repulsion energy, which are also read from *orca.DFTMRCI.inp*. The *mos.bin* file contains the Cartesian orbitals in the 6d/10f/15g notation, while ORCA provides orbitals in the 5d/7f/9g notation. The transformation as implemented in the subroutine `write_mosbin()` is shown for d-orbitals in Tab. 6, for f-orbitals in Tab. 7 and for g-orbitals in Tab. 8. The order of the Cartesian orbitals corresponds to the order in the *proper* program. The transformation follows the definition of the spherical orbitals within the respective program, here ORCA. For example, orbital d_1 is defined as a linear combination of Cartesian functions in the xx, yy and zz component. In the transformations of these orbitals from spherical back to Cartesian functions all three Cartesian components are dependent on the orbital d_1 . The Cartesian components itself rely on the definition in the basis.

Table 6: Transformation from 5d to 6d orbitals.

Cartesian function	Spherical function
d_{xx}	$-\frac{1}{\sqrt{12}}d_1 + \frac{1}{2}d_4$
d_{yy}	$-\frac{1}{\sqrt{12}}d_1 - \frac{1}{2}d_4$
d_{zz}	$\frac{2}{\sqrt{12}}d_1$
d_{xy}	d_5
d_{xz}	d_2
d_{yz}	d_3

Table 7: Transformation from 7f to 10f orbitals

Cartesian function	Spherical function
f_{xxx}	$-\frac{1}{\sqrt{40}}f_2 + \frac{1}{\sqrt{24}}f_6$
f_{yyy}	$-\frac{1}{\sqrt{40}}f_3 + \frac{1}{\sqrt{24}}f_7$
f_{zzz}	$\frac{2f_1}{\sqrt{60}}$
f_{xxy}	$-\frac{1}{\sqrt{40}}f_3 - \frac{3}{\sqrt{24}}f_7$
f_{xxz}	$\frac{1}{\sqrt{60}}f_1 - \frac{1}{2}f_4$
f_{xyy}	$-\frac{1}{\sqrt{40}}f_2 - \frac{3}{\sqrt{24}}f_6$
f_{yyz}	$-\frac{3}{\sqrt{60}}f_1 - \frac{1}{2}f_4$
f_{xzz}	$\sqrt{\frac{2}{5}}f_2$
f_{yzz}	$\sqrt{\frac{2}{5}}f_3$
f_{xyz}	f_5

Table 8: Transformation from 10g to 15g orbitals

Cartesian function	Spherical function
g_{xxxx}	$\frac{3}{\sqrt{6720}}g_1 + \frac{1}{\sqrt{336}}g_4 + \frac{1}{\sqrt{192}}g_8$
g_{yyyy}	$\frac{3}{\sqrt{6720}}g_1 - \frac{1}{\sqrt{336}}g_4 + \frac{1}{\sqrt{192}}g_8$
g_{zzzz}	$\frac{8}{\sqrt{6720}}g_1$
g_{xxyy}	$-\frac{1}{\sqrt{84}}g_5 + \frac{1}{\sqrt{12}}g_9$
g_{xxzz}	$-\frac{3}{\sqrt{168}}g_2 + \frac{1}{\sqrt{24}}g_6$
g_{xyyy}	$-\frac{1}{\sqrt{84}}g_5 - \frac{1}{\sqrt{12}}g_9$
g_{yyyz}	$-\frac{3}{\sqrt{168}}g_3 + \frac{1}{\sqrt{24}}g_7$
g_{xzzz}	$\frac{4}{\sqrt{168}}g_2$
g_{yzzz}	$\frac{4}{\sqrt{168}}g_3$
g_{xxyy}	$\frac{6}{\sqrt{6720}}g_1 - \frac{6}{\sqrt{192}}g_8$
g_{xxzz}	$-\frac{24}{\sqrt{6720}}g_1 - \frac{6}{\sqrt{336}}g_4$
g_{yyzz}	$-\frac{24}{\sqrt{6720}}g_1 + \frac{6}{\sqrt{336}}g_4$
g_{xxyz}	$-\frac{3}{\sqrt{168}}g_3 - \frac{3}{\sqrt{24}}g_7$
g_{xyyz}	$-\frac{3}{\sqrt{168}}g_2 - \frac{3}{\sqrt{24}}g_6$
g_{xyzz}	$\frac{6}{\sqrt{84}}g_5$

5 DFT/MRCI Hamiltonian Development

5.1 The R2017 Hamiltonian (Paper 1)

The following results have been published in Paper 1 [169].

The R2016 Hamiltonian (Sec. 2.6.2), while providing a multiplicity-independent parameter set, is still dependent on a closed-shell parent determinant and has no correction terms for open shells. The Hamiltonian is therefore limited to multiplicities based on an even number of electrons. In order to calculate vertical transition energies of doublet or quartet systems as well as ionisation potentials and electron affinities, a new Hamiltonian that can handle both open-shell and closed-shell parent determinants is needed. This led to the development of a new Hamiltonian called R2017 that is discussed in this section.

Starting from this restricted open-shell parent determinant, additional corrections have to be included in the Hamiltonian. With the diagonal correction of R2016 as a the foundation, the new correction for Coulomb and exchange-like integrals becomes

$$\begin{aligned} \Delta E_{coul} - \Delta E_{exch} = & p_J \left(- \sum_{\substack{i,j \in c \\ i > j}}^{n_{exc}} V_{ijij} - \sum_{\substack{i,j \in a \\ i > j}}^{n_{exc}} V_{ijij} + \sum_{i \in c}^{n_{exc}} \sum_{j \in a}^{n_{exc}} V_{ijij} + \sum_{i \in s}^{n_{single}} \frac{1}{2} V_{iii} |\Delta w_i| \right) \\ & - p_X \left(\frac{1}{2} \sum_{i \in c}^{n_{exc}} \sum_{j \in a}^{n_{exc}} V_{ijji} - \frac{1}{2} \sum_{\substack{i \in c \\ j \in c,s}}^{n_{exc}} V_{ijji} - \frac{1}{2} \sum_{\substack{i \in a \\ j \in a,s}}^{n_{exc}} V_{ijji} + \sum_{\substack{i,j \in o \\ i > j}}^{N_o} V_{ijji} \eta_{ij}^{ji} \right) \end{aligned} \quad (71)$$

with the parameters p_J for the Coulomb-like and p_X for the exchange-like integrals.

The R2017 is similar to Lyskov's R2016 Hamiltonian. In case of a closed-shell anchor configuration the R2017 is identical to the R2016 Hamiltonian in all aspects but the parameter set, as the set of open shells s is zero and the terms summing over these shells vanish.

The new corrections treat the interaction between two created or two annihilated electrons of which one is in a singly occupied orbital in the parent determinant. Additionally, the diagonal integrals V_{iii} play an important role whenever a doubly occupied or vacant orbital is changed to vacant or doubly occupied, respectively. For closed-shell anchor configurations, this is already handled in the first and second terms of the Coulomb correction, when i and j refer to the same orbital. However, the SOMO of the anchor configuration only needs a single excitation to be doubly occupied or vacant, which necessitates the fourth term in the Coulomb correction.

A completely different correction on the CI level is necessary due to an error in Eq. (54) involving the diagonal integral of the SOMO s which introduces an artificial shift of $-\frac{1}{4}V_{sss}$ to all configurations when an odd number of electrons is considered. Since the integ-

ral is subtracted from all configurations, this error simply shifts the total energies of all states by the same amount and can be added again during or after the calculation. The error is therefore only noticeable when the total energies of two systems are compared, i.e. the calculation of ionisation potentials, electron affinities and adiabatic energies. The error is most noticeable in IP and EA, because in these types of calculations, one system has an odd number of electrons and is affected by the error and the other system has an even number of electrons and is unaffected. Therefore, all IP and EA are shifted by $-\frac{1}{4}V_{ssss}$, resulting in an error of approx. 1.5–3 eV. The calculations of adiabatic energies of open-shell systems are also affected, but less pronounced. Since the adiabatic energy corresponds to the difference of the total energies at two different geometries of the same molecule, e.g. of the ground state and an excited state, the orbitals at both geometries are not identical. The integral V_{ssss} is (slightly) different at each geometry, which introduces an error in these energies that corresponds to the difference of the two shifts at each geometry. Since the previously developed original and R2016 Hamiltonians are not capable of IP and EA and open-shell calculations in general, all results previously obtained with these Hamiltonians are unaffected. This correction was implemented within the code for MRCI matrix elements in the *mrci* program as it affects both DFT/MRCI and ab-initio MRCI.

The functional forms of the off-diagonal corrections are identical to Eq. (65) and (66) of the R2016 Hamiltonian, differing only in the applied parameter sets. The correction for matrix elements with the same space and different spin part therefore is

$$\langle \omega w | \hat{\mathcal{H}}^{DFT} | \omega' w' \rangle = \langle \omega w | \hat{\mathcal{H}} | \omega' w' \rangle (1 - p_X) \quad (72)$$

and the correction for one- and two-electron differences is

$$\langle \omega w | \hat{\mathcal{H}}^{DFT} | \omega' w' \rangle = \langle \omega w | \hat{\mathcal{H}} | \omega' w' \rangle \frac{p_1}{1 + (p_2 \cdot \delta\epsilon^5) \cdot \arctan(p_2 \cdot \delta\epsilon^5)}. \quad (73)$$

The new Hamiltonian is parametrised with the training dataset described in Sec. 3.1. The Nelder-Mead simplex algorithm [170] was used to find the parameters that result in the lowest RMSE. The algorithm executes a Python script for each parameter set. The Python script controls the corresponding DFT/MRCI runs for every parameter set determined by the Nelder-Mead simplex algorithm. After the DFT/MRCI run, the new state is assigned to an experimental energy by comparing it to a reference state. This reference state was calculated with the original Hamiltonian for closed-shell molecules and with the ab-initio MRCI of the *mrci* program for open-shell molecules using the same functional and basis sets. After the DFT/MRCI run is finished, all states in the output are evaluated since they change their energy and, to some degree, their character. The inner product between all states and the reference state is calculated by the Python script. If an inner product larger than 0.7 is found, it is assumed that the state corresponds to the reference state. The energy of this state is printed to a list. After all DFT/MRCI calculations for all molecules using one parameter set are complete, the RMSE between the energies of the new states and the experimental energies is calculated. This RMSE value is returned to the Nelder-

Table 9: The optimised parameters for the R2017 Hamiltonian. MAE refers to the mean absolute error and MaxAE to the maximum absolute error of the training (fitting) set. Energies of RMSE, MAE and MaxAE are given in eV.

$\delta E_{\text{sel}}(E_h)$	p_J	p_X	p_1	p_2	RMSE	MAE	MaxAE
1.0	0.5030	0.3587	0.5639	22.0912	0.182	0.144	0.578
0.8	0.5008	0.3570	0.5735	26.5414	0.186	0.149	0.578

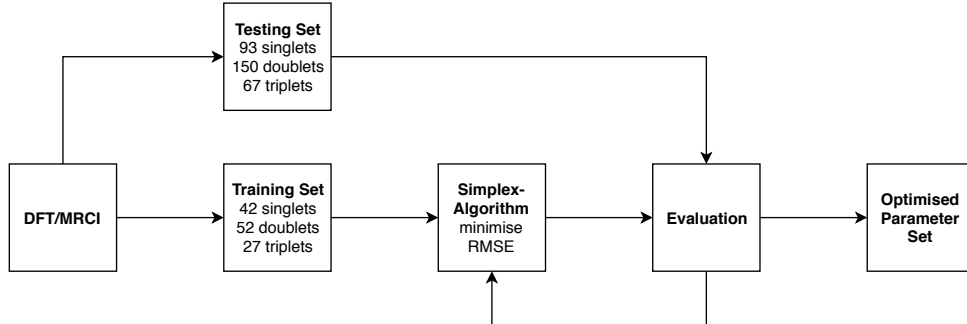


Figure 13: Scheme of the parametrisation process of the R2017 parameters p_1 , p_2 , p_J and p_X . Testing and training set are made up of different excited states. The testing set evaluation determines the final error of the parameter set, expressed by means of the RMSE.

Mead simplex algorithm. The simplex algorithm evaluates the new RMSE with regard to the parameters and alters one parameter. Subsequently, a new cycle begins. After usually 125-150 iterations, a minimum is found within the convergence criteria of 10^{-7} eV. The final parameters can be found in Tab. 9. The steps involved in the parametrisation are shown in Fig. 13. All experimental data and the results of the final parametrisation step can be found in the supplemental material of [169].

After successfully obtaining a parameter set that is minimised with regard to the RMSE, the parameter set is tested against a different set of excitation energies not included in the testing set. This testing dataset is described in detail in Sec. 3.2. The statistical evaluation of this assessment can be found in Tab. 10. The RMSE obtained with this set is 0.16 eV, retaining the good accuracy of the previous Hamiltonians.

The correlation diagram and histogram for the 310 excited states in the testing set are shown in Fig. 14. From the histogram it can be seen that the deviations of the results from experiment follow a normal distribution.

A detailed evaluation, calculated ionisation potentials and a list of the energies of the testing and training set can be found in Paper 1 [169] and its supplementary material.

Table 10: Statistical evaluation of the results obtained for the 310 excited states in the testing set using the R2017 Hamiltonian with different selection thresholds and the corresponding parameters in Tab. 9. All errors are in eV.

$\delta E_{\text{sel}}(E_h)$	RMSE	MAE	Mean	Min	Max
1.0	0.16	0.12	0.02	-0.44	0.42
0.8	0.16	0.13	0.03	-0.45	0.45

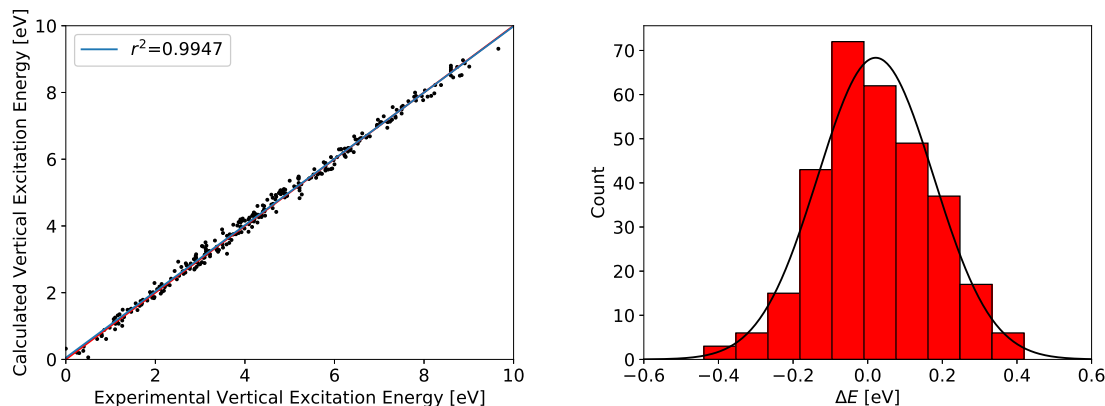


Figure 14: On the left, the correlation diagram between calculated and experimental data of the testing set consisting of 93 singlet, 150 doublet and 67 triplet states is shown. The red line corresponds to the bisector and the blue line to the linear regression. Both lines cover each other partially due to the high correlation. On the right, the histogram of the error ($E_{\text{calc}} - E_{\text{exp}}$) is shown. The distribution is almost normal. Both calculations were carried out using a selection threshold of $1.0 E_h$. (Reprinted with permission from Ref. [169]. Copyright 2017 AIP Publishing)

5.2 The R2018 Hamiltonian (Paper 2 and 3)

The results of this section have been published in Paper 2 [133] and Paper 3 [67]. Some unpublished in-depth information on the damping function and correlation energy is presented.

5.2.1 The Search for the Best Damping Function

In a test set of 67 excited states of transition metal complexes (40 organic and 27 inorganic), it was found [67] that the two redesigned Hamiltonians considerably underestimate the excitation energies of these complexes. This was noticeable to a stronger degree in case of the inorganic transition metal complexes. Similar results were also found in an earlier study [171]. In order to provide a better description of the vertical excitation energies in transition metal complexes, the damping function for the off-diagonal matrix elements needs to provide less damping in an energy range starting at $0.4 E_h$ (Fig. 15). The function of the R2016 and R2017 Hamiltonians declines too fast at a low energy difference and is thus, in its current form, not suitable, as can be seen from the underestimation of the excitation energies. The next possibility that comes to mind is the damping function of the original Hamiltonian Eq. (63), which provides a better agreement with experimental data. However, the scaling parameter p_1 is lower in the redesigned Hamiltonians than it is in the original one, because the correlation energy already included in the diagonal term is different. This leads to a stronger damping at any energy difference. Not all functions are suitable to fulfil the requirements. Depending on the function, it is too rigid as the scaling parameter p_1 also scales degenerate and near-degenerate configurations. A better suited function is therefore needed, one that does not decline over a larger energy difference. Additionally, the function should reach a value of approximately zero at the specified selection threshold, which is $1.0 E_h$ in case of a standard selection and $0.8 E_h$ in case of a short selection.

Table 11: Parameters and RMSE for possible damping functions. The last line of the table shows the damping functions and final parameter set employed in the R2018 Hamiltonian. The parametrisation was carried out with a selection threshold of $1.0 E_h$.

Function	p_J	p_X	p_1	p_2	RMSE/ eV
$\frac{p_1}{1+(p_2 \cdot \delta\epsilon^5) \cdot \arctan(p_2 \cdot \delta\epsilon^5)}$	0.5109	0.3503	0.5768	16.3471	0.190
$p_1 \cdot \exp(p_2 \cdot \delta\epsilon^4)$	0.5089	0.3648	0.5805	3.976	0.189
$p_1 \cdot \exp(p_2 \cdot \delta\epsilon^5)$	0.5066	0.3593	0.5611	3.6738	0.191
$p_1 \cdot \exp(p_2 \cdot \delta\epsilon^6)$	0.5089	0.3624	0.5584	4.4717	0.193

The p_1 parameter can be considered as nearly constant and the damping function should reach zero at the energy of the selection threshold, which limits the possible values of the p_2 parameter. With the two approximate parameter values, new functions can be plotted to evaluate their damping profile. The first functions that come to mind are the ones that are already in use, but they are limited in their profile for transition metal complexes. Other possibilities include exponential functions with a different energy dependency, e.g. $p_1 \cdot \exp(p_2 \cdot \delta E^n)$. Only exponential functions with $3 < n < 7$ match the criteria as all others lead to damping in the wrong energy range, either too strong or too weak.

To optimise the Hamiltonian with the damping functions, the fitting set from Ref. [169] has been expanded. The lowest four singlet and four triplet states of the Cu^+ ion, the two lowest doublet states of the Cu atom in addition to one singlet and the lowest triplet state of ruthenocene were amended. All new systems are small enough to be used in an iterative parametrisation scheme outlined in Sec. 5.1. A description of the dataset employed in the parametrisation can be found in Sec. 3.1. The results of the parametrisations are shown in Fig. 15 and Tab. 11.

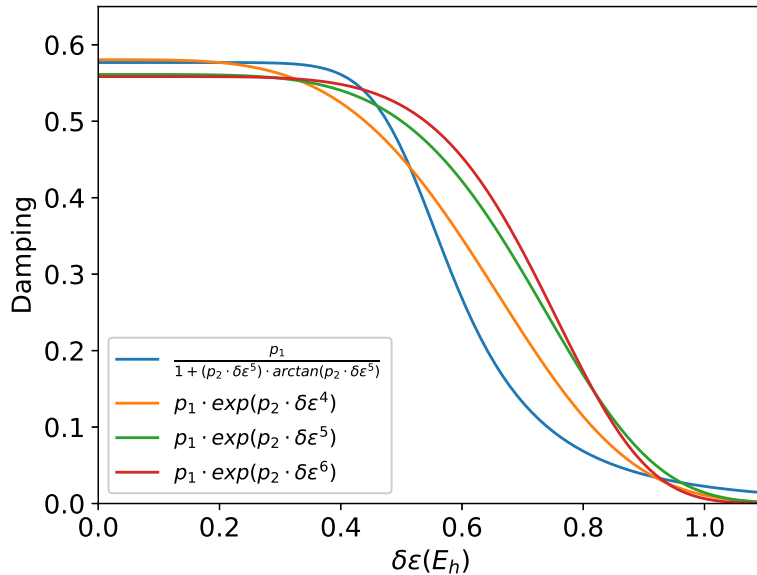


Figure 15: Parametrisation of possible damping functions for a selection threshold of $1.0 E_h$ using the fitting set from Ref. [133].

It can be seen that within this fitting set all four damping functions result in almost identical parameters for p_1 , p_J and p_X and the resulting RMSE differs by less than 5 meV. However, the exponential function with $n=4$ yields the lowest RMSE and the one with $n=6$ yields the highest one. It is therefore obvious, even when including 12 additional states of Cu/Cu⁺ and ruthenocene, why those damping functions were originally chosen for the Original, R2016 and R2017 Hamiltonian. A more pronounced difference can be seen in case of the p_1 parameter, which scales two coupled configurations. The values of p_2 deviate as well, but since it refers to different functions, a comparison of the parameter values is not appropriate. The difference becomes more evident, when comparing the function profiles in Fig. 15. The functions with the best RMSE in the mostly organic test set are showing the strongest damping in the energy range between 0.4 and 0.8 E_h. This will result in too little correlation energy in the ground state relative to the excited states in transition metal complexes and thus artificially lower the excitation energy in those complexes. The exponential functions with $n=5$ and $n=6$ on the other hand show the most promising function profile.

The $n=5$ exponential term still underestimates the excitation energies of transition metal complexes, while the $n=6$ term is a good match. This new damping function in Eq. (74) combined with the on-diagonal expressions of the R2017 Hamiltonian in Eq. (71) and the expression of the R2016 and R2017 Hamiltonian for scaling configurations with the same space and different spin part in Eq. (72) results in a new Hamiltonian. This Hamiltonian is called R2018.

$$\langle \omega w | \hat{\mathcal{H}}^{DFT} | \omega' w' \rangle = \langle \omega w | \hat{\mathcal{H}} | \omega' w' \rangle p_1 \cdot e^{-p_2 \cdot \Delta E_{\omega w'}^6} \quad (74)$$

It can be seen from the RMSE in Tab. 12 and Fig. 16 (left), and from the MAE in Fig. 16 (right) that the new R2018 Hamiltonian improves the accuracy on transition metal complexes considerably compared to the other redesigned Hamiltonians. For inorganic complexes the error is lowered to that of the original Hamiltonian, in case of organic complexes, the accuracy is best among all Hamiltonians. For organic molecules of both closed-shell and open-shell type, the accuracy is almost identical to the older three Hamiltonians.

Table 12: RMSE of the four Hamiltonians on different sets of excited states. The number in parentheses refers to the number of excited states in this set. In case of 27 inorganic transition metal complex excited states, only 25 could be assigned in case of the three redesigned Hamiltonians. The sets of transition metal complexes comprise singlet and triplet states. All calculations were carried out with a selection threshold of 1.0 E_h and the corresponding parameter sets. All values are in eV.

	Original	R2016	R2017	R2018
Organic Closed-Shell (160)	0.16	0.15	0.15	0.17
Organic Open-Shell (150)	-	-	0.16	0.17
Organic TM Complex (40)	0.20	0.25	0.30	0.15
Inorganic TM Complex (27)	0.50	0.83	0.89	0.50

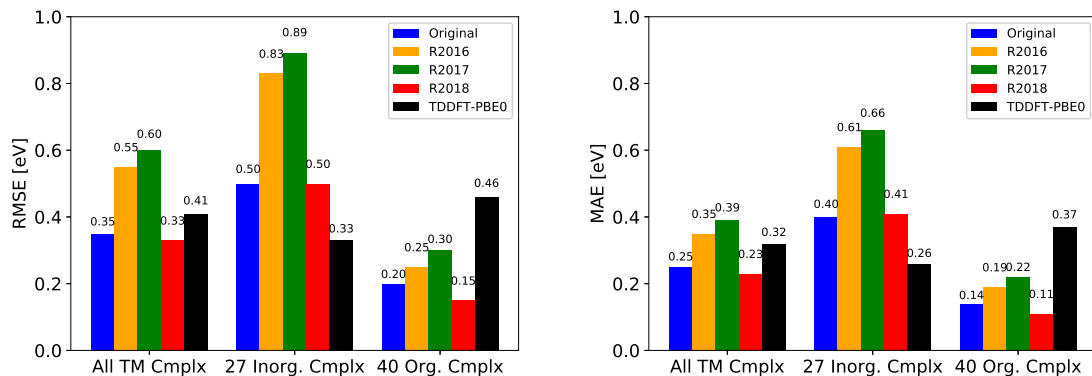


Figure 16: Bar charts comparing the result of the testing set of transition metal complexes of the four DFT/MRCI Hamiltonians and TDDFT-PBE0. The results are shown in total of all 67 (65) excited states and divided into 27 (25) inorganic and 40 organic transition metal complexes. In case of the organic transition metal complexes, only 25 states could be assigned in case of the three redesigned Hamiltonians, lowering the total amount of states to 65. On the left-hand side, the RMSE and on the right-hand side, the MAE is shown. All calculations were carried out using the standard parameter set and selection threshold. The figures are reproduced from [133], with the permission of AIP Publishing.

A more detailed statistical evaluation of the R2018 Hamiltonian and the other three Hamiltonians as well as an overview of the computational results of the transition metal complexes can be found in Paper 2 [133].

5.2.2 The New Damping

In order to investigate the magnitude of the influence of the changed fitting set and the changed function, both have to be checked independently. This is accomplished by using two different damping functions, the former one is $\frac{p_1}{1+(p_2 \cdot \delta \epsilon^5) \cdot \arctan(p_2 \cdot \delta \epsilon^5)}$ (of the R2017 Hamiltonian) and the new one is $p_1 \cdot \exp(p_2 \cdot \delta \epsilon^6)$ (of the R2018 Hamiltonian). Since all other terms are identical, those are simply the direct comparison between the R2017 and R2018 Hamiltonian. The fitting sets are taken from [169] (the purely organic R2017 fitting set) and from [133] (the R2018 fitting set) and can be found in Sec. 3.1. The resulting parameters and their RMSE are shown in Tab. 13.

It can be seen that the variation of each parameter with respect to the different fitting set is mostly negligible with the exception of the p_2 parameter. This difference becomes

Table 13: Parameters and resulting RMSE for the two Hamiltonians R2017 and R2018 optimised with both the R2017 and R2018 fitting sets. The parameters of the R2017 set of the R2017 Hamiltonian correspond to those in Tab. 9.

Hamiltonian (Fitting Set)	p_J	p_X	p_1	p_2	RMSE/ eV
R2017 (R2017 set)	0.5030	0.3587	0.5639	22.0912	0.182
R2017 (R2018 set)	0.5109	0.3503	0.5768	16.3471	0.190
R2018 (R2017 set)	0.5086	0.3584	0.5634	5.7279	0.192
R2018 (R2018 set)	0.5089	0.3624	0.5584	4.4717	0.193

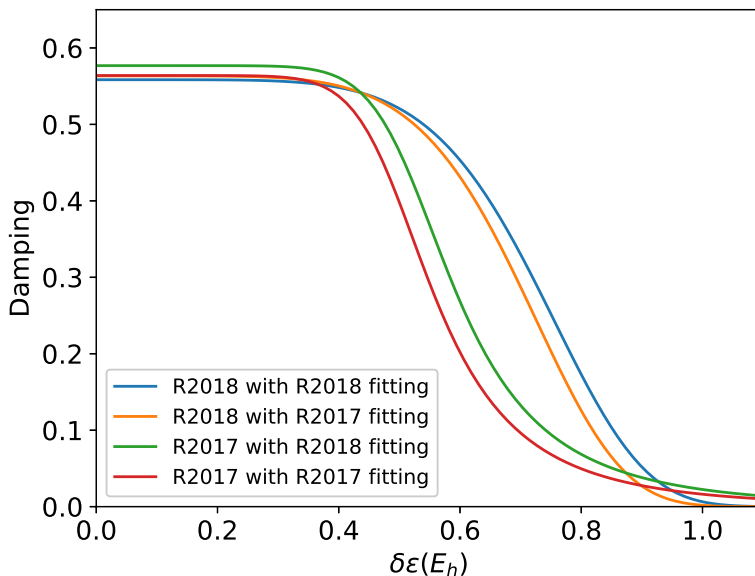


Figure 17: Damping of the R2017 and R2018 Hamiltonians employing parameter sets optimised with the R2017 and R2018 fitting set with a selection threshold of $1.0 E_h$. Parameters are shown in Tab. 13.

more visible when looking at the resulting damping profile in Fig. 17. It is noticeable that the added states of transition metals lower the damping of both the R2017 and R2018 Hamiltonian, but the difference in damping is mostly brought on by the function itself rather than by the addition of new states to the fitting set. The influence of the off-diagonal damping becomes even clearer in the next section when looking at an example that is very sensitive towards the off-diagonal damping.

5.2.3 Off-Diagonal Damping and Correlation

The 2^1T_2 state of the second-row transition metal complex TcO_4^- is characterised by a $d/\pi \rightarrow d^*/\pi^*$ transition, from the $1t_2$ and $2t_2$ to the $2e$ orbital. The energy of this state as well as other states in this complex strongly depend on the damping function, as was first noticed in a benchmark calculation of various transition metal complexes in Ref. [133]. R2016 and R2017, which have the strongest damping, vastly underestimate the transition energies in TcO_4^- , while the original Hamiltonian provides results closer to the experiment. The R2018 comes closest.

It can be seen in Tab. 14 that the energies of the 2^1T_2 state are dependent on the damping seen in Fig. 17. The R2016 Hamiltonian, which employs a parameter set with a p_2 value of 18.2960 and similar parameters otherwise, results in a transition energy of 4.45 eV. Although the difference in correlation energy does not reproduce the total variation of the energy of the state for each Hamiltonian and fitting set combination, the trend is clearly visible. The ground state correlation change is stronger (more negative) with a lower damping, i.e. the R2018 Hamiltonian with its corresponding parameter set, than it is for the excited state. As a result, the excited states are artificially lowered in the case of a stronger damping function as employed in R2016 and R2017.

5.2.4 Effect of the Selection Threshold on Correlation

The dynamic correlation is treated by the interaction between configurations with a large energy difference. A shorter CI expansion therefore is expected to influence the correlation energy. Since reducing the selection threshold from $1.0 E_h$ to $0.8 E_h$ reduces the computational demand, i.e. number of CSF and the resulting memory and CPU time impacts, by a factor of ≈ 10 [133], a deeper understanding of the impact on the correlation energy is desirable. This is achieved by employing the same case as in Sec. 5.2.3. In combination with the short selection threshold ($0.8 E_h$), four parameter sets are optimised for the short selection. These are compared to the standard parameter set ($1.0 E_h$) of the R2018 Hamiltonian and the short parameter set of the R2016 Hamiltonian. The standard set of R2018 has the lowest damping of all sets in this comparison and the short set of R2016 the strongest. *Fitting* refers to a new set of parameters that was optimised using the fitting (or training) set of one specific Hamiltonian. *Set* refers to the set of already optimised parameters of a specific Hamiltonian. The R2016 and R2017 sets can be interchanged because in a closed-shell species both Hamiltonians share the same functions and can in principle employ the same parameter sets.

It can be seen from Tab. 15 that – just as in the $1.0 E_h$ selection in Tab. 14 – the damping directly and strongly influences the electron correlation. The excited state correlation is changed to a smaller degree than the correlation of the ground state when varying the strength of the damping. A strong damping function, e.g. the one employed in the short set of the R2016 Hamiltonian, leads to a stronger correlation difference between excited state and ground state and thus lowers the energy of the excited state relative to the ground state. A weaker damping, e.g. the standard set of the R2018 Hamiltonian, leads to a lower difference and thus a higher relative energy of the excited states. When the damping is too weak for the chosen selection threshold the energy of the excited state is overestimated, as can be seen in case of the R2018 standard set. It is worth noting that employing the standard R2018 set in a calculation with a threshold of $0.8 E_h$ is not recommended due to the slow decline of the damping function.

In contrast to the standard selection in Sec. 5.2.3, it can be seen that the shorter selection

Table 14: Depiction of the influence of the off-diagonal damping on the correlation energies and their effect on the vertical transition energies in different DFT/MRCI Hamiltonians and parameter sets in the T_2 state of TeO_4^- . Due to symmetry limitations of the DFT/MRCI program, the state splits into a_1, b_1, b_2 . The three resulting states are averaged in order to obtain the calculated energy and the correlation energy of the excited state. The correlation energy is defined as the difference in total energy between DFT/MRCI result and the reference space diagonalisation. All energies including correlation are in eV. All calculations are carried out using a selection of $1.0 E_h$.

	Energy	Correlation GS	Correlation 2^1T_2 state	ΔE (2^1T_2 -GS)
R2017 (R2017 set)	4.36	-0.4433	-1.3617	-0.9184
R2017 (R2018 fitting)	4.48	-0.6060	-1.5138	-0.9078
R2018 (R2017 fitting)	4.87	-1.1540	-1.7527	-0.5987
R2018 (R2018 set)	4.98	-1.4335	-1.9608	-0.5273
Experiment [172]	5.1			

Table 15: Depiction of the influence of the off-diagonal damping on the correlation energies and their effect on the vertical transition energies in different DFT/MRCI Hamiltonians and parameter sets in the T_2 state of TcO_4^- . Due to symmetry limitations of the DFT/MRCI program, the state splits into a_1, b_1, b_2 . The three resulting states are averaged in order to obtain the calculated energy and the correlation energy of the excited state. The correlation energy is defined as the difference in total energy between DFT/MRCI result and the reference space diagonalisation. All energies including correlation are in eV. All calculations are carried out using the short selection threshold, i.e. $0.8 E_h$.

	Energy	Correlation GS	Cor. 2^1T_2 state	ΔE (2^1T_2 -GS)
R2017 (R2016 short set)	4.27	-0.1252	-0.8463	-0.7211
R2017 (R2017 short set)	4.46	-0.3075	-1.0204	-0.7129
R2017 (R2017 standard set)	4.57	-0.3761	-1.0839	-0.7078
R2017 (R2018 short fitting)	4.57	-0.4290	-1.1315	-0.7025
R2018 (R2017 short fitting)	4.83	-0.6919	-1.2349	-0.5430
R2018 (R2018 short set)	4.82	-0.6884	-1.2517	-0.5633
R2018 (R2018 standard set)	5.36	-1.311	-1.4034	-0.0924
Experiment [172]	5.1			

reduces the total correlation, with the excited state being more strongly affected than the ground state. For this reason, the shorter selection yields higher excited state energies than the standard selection when employing the same parameter set. The damping functions that are utilised in Tab. 15 are shown in Fig. 18.

At least in case of a species that is very sensitive regarding the profile of the damping function the effect on the correlation contributions is evident from Fig. 18.

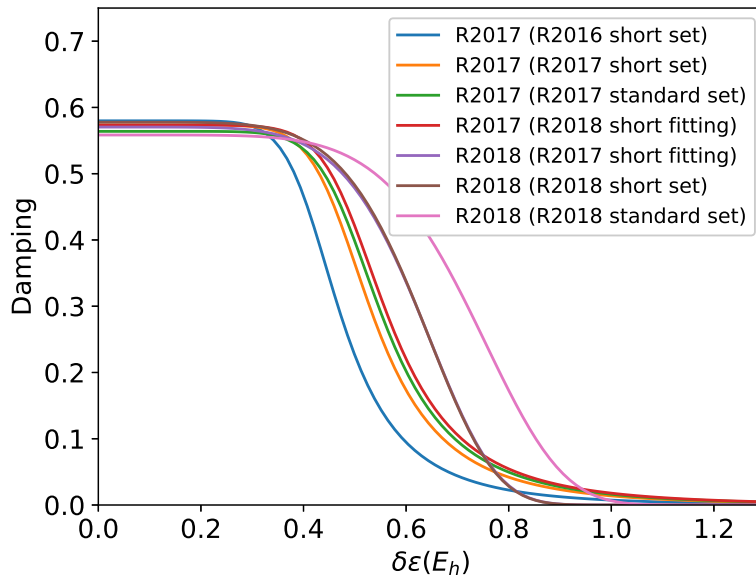


Figure 18: Different damping parameters employed in the off-diagonal damping of the R2017 and R2018 Hamiltonians. Short refers to an fitting for a short selection and standard to that of the standard selection.

6 Application of the New Hamiltonians

6.1 C \wedge N-Platinum Complexes (Paper 4)

The following results have already been published in Paper 4 [134].

A group of three structurally similar cyclometalated (C \wedge N)Pt(O \wedge O) complexes was measured by Bossi et al. [173]. These complexes are a set of phosphorescent triplet emitters with a possible application for OLEDs. 2-phenylpyridyl (ppy), benzo[h]quinoliny (bzq) and dibenzo[f,h]quinoliny (dbq) were employed as C \wedge N ligands with an increasing π system for tuning the emission properties. Acetylacetonate (acac) and dipivolylmethanoate (dpm) were used as auxiliary O \wedge O ligands.

The spectroscopic measurements of Bossi et al. [173] showed a counter-intuitive shift of the emission maximum. While the π system increases from ppy to bzq to dbq, the emission wavelength does not follow the same trend. From ppy to bzq, the 0-0 emission wavelength increases from 479 nm (2.59 eV) to 495 nm (2.50 eV) as expected when enlarging the π system. However, when increasing the π system further, from bzq to dbq, the emission wavelength decreases to 470 nm (2.64 eV). The emission wavelength of (dbq)Pt(acac) is not only shorter than that of (bzq)Pt(acac) but even shorter than that of (ppy)Pt(acac) [173].

In order to explain this counter-intuitive trend, the three complexes were investigated by means of the newly developed R2018 Hamiltonian. The R2018 Hamiltonian was developed to improve the vertical transition energies of transition metal complexes, making it well suited for calculating platinum complexes.

Experimental observations [173, 174] and a test calculation have shown that the dpm auxiliary ligand can be replaced by acac without change in spectroscopic or structural properties in order so reduce the computational demand. The complexes with the acac auxiliary ligand (ppy)Pt(acac), (bzq)Pt(acac) and (dbq)Pt(acac) are shown in Fig. 19.

On top of the R2018 wave function, a DFT/MRSOCI run using the *spockCI* program [70–72] was carried out to include the spin-orbit effects in these heavy transition-metal compounds. The 0-0 emission energies were calculated by adding the difference of the zero-point energy (ZPE) to the adiabatic energy difference between the T₁ and the S₀ state. The resulting 0-0 emission energies are in good agreement with the experiment [173].

The emission spectrum of (ppy)Pt(acac) is shown in Fig. 20. The experimental 0-0 emission energy at 2.59 eV (479 nm) is well reproduced in the DFT/MRSOCI calculation at

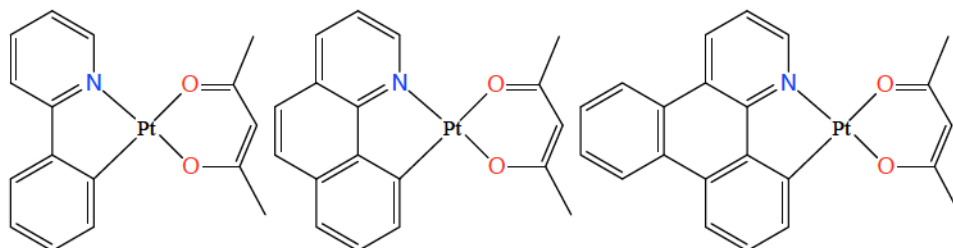


Figure 19: Chemical structures of (ppy)Pt(acac), (bzq)Pt(acac) and (dbq)Pt(acac).

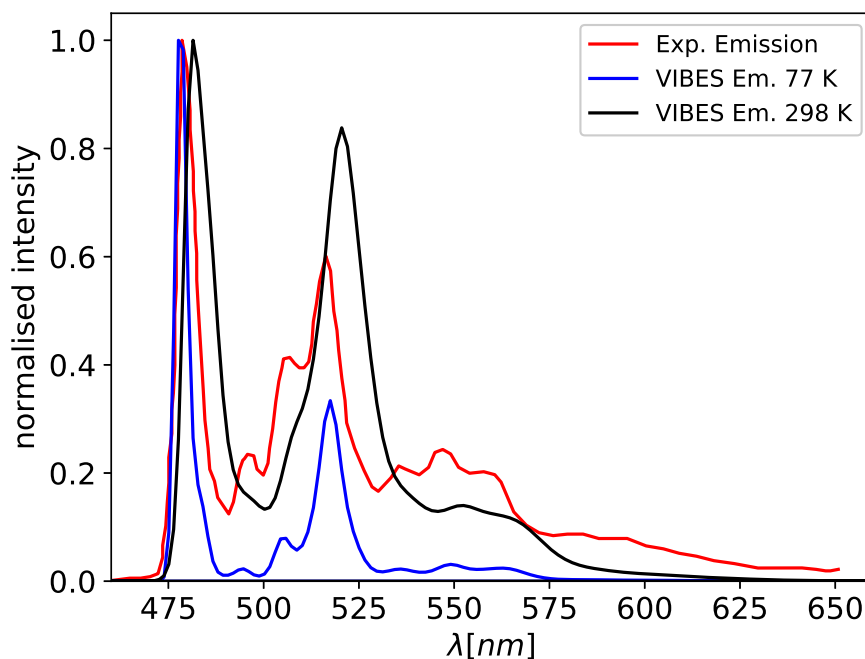


Figure 20: Calculated vibes emission spectra of (ppy)Pt(acac) at 77 K and 298 K compared to experimental [173] spectrum. The calculations were carried out in vacuum and the experimental spectrum was measured at 77 K in 2-MeTHF.

2.60 eV. Without spin-orbit coupling, the DFT/MRCI energy is 2.51 eV. The averaged phosphorescence lifetime is 12 μ s in the DFT/MRSOCI calculation, which is slightly larger than the experimental lifetime of 9 μ s at 77 K in 2-methyltetrahydrofuran (2-MeTHF).

In case of the (bzq)Pt(acac) complex, the experimental 0-0 emission is red-shifted in comparison to the (ppy)Pt(acac) complex to 2.32 eV. The corresponding calculated energies are also red-shifted. The DFT/MRSOCI energy lies at 2.46 eV and the DFT/MRCI energy at 2.35 eV. The averaged phosphorescence lifetime is approximately one order of magnitude larger than in the smaller (ppy)Pt(acac) complex at 109 μ s in the DFT/MRSOCI calculation. The measured lifetime is 125 μ s. The VIBES spectra at 77 K and 298 K can be

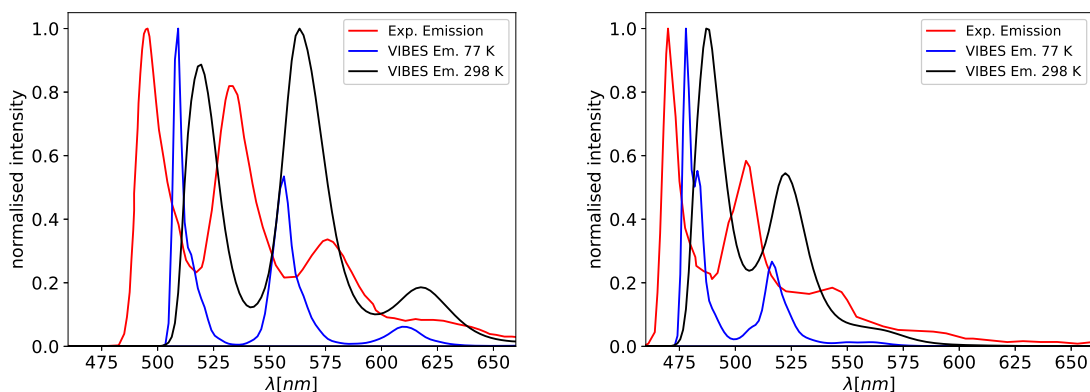


Figure 21: Calculated vibes emission spectra of (bzq)Pt(acac) (left) and (dbq)Pt(acac) (right) at 77 K and 298 K compared to experimental [173] spectrum. The calculations were carried out in vacuum and the experimental spectrum was measured at 77 K in 2-MeTHF.

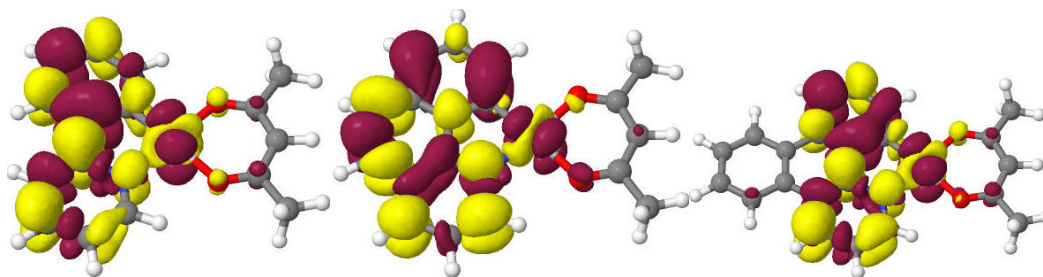


Figure 22: Difference densities of the T_1 states of the complexes $(ppy)Pt(acac)$, $(bzq)Pt(acac)$ and $(dbq)Pt(acac)$ with an $|\text{isovalue}|$ of 0.001. A loss of electron density with respect to the S_0 ground state is shown in red and a gain in blue.

found in Fig. 21 (left) in comparison to the experiment.

The blue-shifted $(dbq)Pt(acac)$ complex lies at 2.64 eV in the experiment and at 2.61 eV and 2.53 eV in the DFT/MRSOCI and DFT/MRCI calculations, respectively. The phosphorescence lifetimes are similar to the smallest complex $(ppy)Pt(acac)$ at 10 μs in the DFT/MRSOCI calculation and 7 μs in the experiment. The corresponding VIBES calculation can be found in Fig. 21 (right).

The DFT/MRSOCI calculations reproduce the trends of the experiment very well regarding phosphorescence lifetime and energy for all three complexes. Due to the limitations of the spin-free Hamiltonian, DFT/MRCI can only provide emission energies. These are also in good agreement to the experiment, but red-shifted by ≈ 0.1 eV.

It is evident that the smallest and largest complexes $(ppy)Pt(acac)$ and $(dbq)Pt(acac)$ are more similar regarding their photophysical properties in both the calculations and measurements while the $(bzq)Pt(acac)$ complex is different. The reason for this behaviour can be explained by comparing the difference densities between the T_1 and the S_0 states in Fig. 22. While $(dbq)Pt(acac)$ is the largest of the three complex, the difference density is very similar to that of the $(ppy)Pt(acac)$ complex. The extension of the π system in the dbq ligand therefore does not affect the T_1 emission properties. In contrast, the $(bzq)Pt(acac)$ shows an alteration in the density across the bzq ligand, leading to the expected red-shifted emission. This also explains the long phosphorescence lifetime of $(bzq)Pt(acac)$ since it has a higher percentage of ligand-centred (LC) contribution in comparison to the other two complexes.

A more detailed discussion including computational details, the S_1 and T_{MC} states, zero-field splittings and the calculations on the $(C\wedge C^*)Pt(O\wedge O)$ complexes can be found in the corresponding publication [134].

6.2 Zinc(II) Tripyrrindione Radical (Paper 5)

The following results have been published in Paper 5 [137].

The zinc tripyrrindione radical ($[Zn(TD1^\bullet)(H_2O)]$) (Fig. 23) together with the free ligand tripyrrin-1,14-dione (H_3TD1) have been investigated regarding their geometrical and photophysical properties. Upon excitation, the complex shows a strong absorption band at

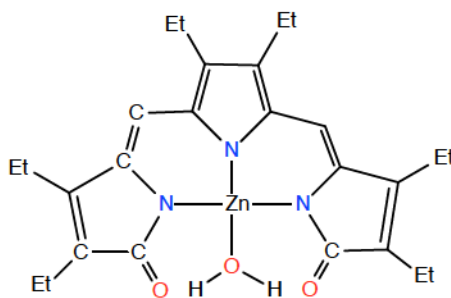


Figure 23: Chemical structure of the zinc tripyrrindione radical.

599 nm with three small bands with low oscillator strength in the long wavelength region at 927 nm (1.34 eV), 823 nm (1.51 eV) and 726 nm (1.71 eV). Following the excitation, fluorescence at 644 nm has been observed. The fluorescence lies energetically below the strong 599 nm absorption but energetically above the three small bands at 726 – 927 nm [30]. The fluorescence can therefore not stem from the lowest excited state but from either a higher excited state or via an alternative mechanism like the free ligand or an anion-cation ion-pair.

In order to get a better understanding of the emission of the $[\text{Zn}(\text{TD1}^\bullet)(\text{H}_2\text{O})]$ radical, the complex has been theoretically investigated by employing the newly developed DFT/MRCI-R2018 Hamiltonian [133]. The calculated absorption spectrum is in good agreement with the experiment and can be found in Fig. 24.

Of the three small bands in the low-energy section of the spectrum, the ones at 927 nm and

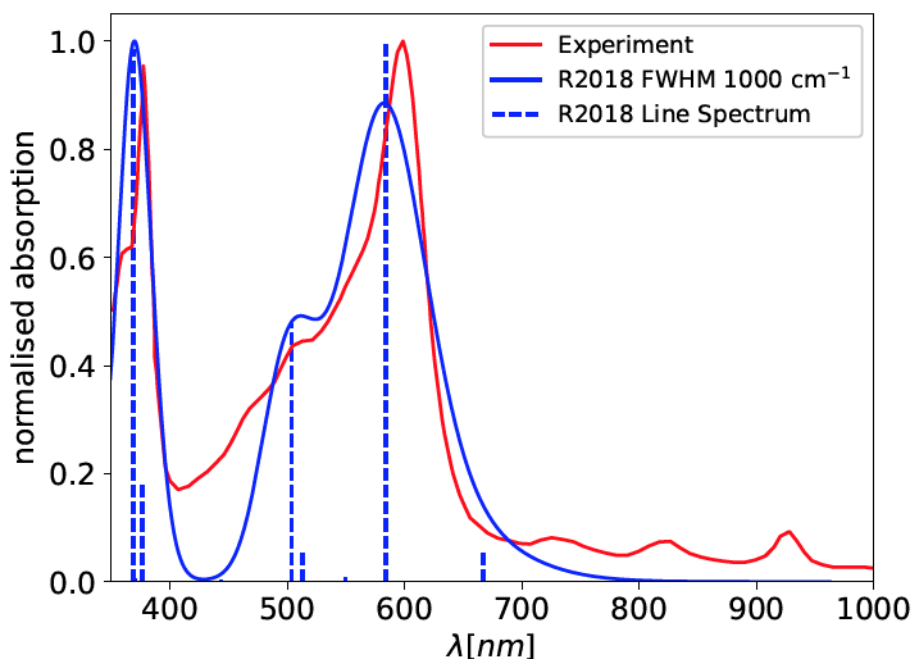


Figure 24: Calculated absorption spectrum of $[\text{Zn}(\text{TD1}^\bullet)(\text{H}_2\text{O})]$ in comparison with the experimental [30] spectrum. The line spectrum has been calculated using the R2018 Hamiltonian and broadened by 1000 cm^{-1} FWHM. The experimental spectrum was measured in tetrahydrofuran (THF) and the calculation was carried out in vacuum.

823 nm are vibronic transitions to the D_1 state. The third band at 726 nm corresponds to the D_2 state at 667 nm in the calculation. The bright transition at 599 nm (2.07 eV) in the experiment was found to be a D_3 transition at 586 nm (2.12 eV) in the R2018 calculation. The shoulder at approx. 500 nm in the experiments corresponds to the D_6 state at 504 nm (2.46 eV). The bright transition measured at 375 nm was found to be a transition to the D_{11} state with a calculated energy of 369 nm (3.36 eV).

The emission is measured at 644 nm after excitation at 599 nm. Since the D_1 and D_2 state were measured to be below this energy, the emission is either in violation of Kasha's rule [101] by stemming from the D_3 state or is done via an alternative route. The tested possibilities and their results are as follows:

1. A reduced species $[\text{Zn}(\text{TD1})(\text{H})]$ was investigated. This closed-shell species absorbs at 881 nm, similar to the D_1 state of the zinc tripyrrindione radical. This excludes an S_1 emission at 644 nm of this complex.
2. The free ligand $\text{H}_3\text{TD1}$ is a possibility as it is detectable in solution after demetalation. The absorption spectrum shows a strong conformer-dependency due to the flexible structure. The $S_0 \rightarrow S_1$ transitions of the most stable conformers lie at approx. 470–480 nm and the emission follows at about 550 nm in both experiment [175] and calculation. This excludes the free ligand as a possible source of emission at 644 nm.
3. An exciplex with a THF solvent molecule coordinating at the zinc atom shows an absorption spectrum very similar to $[\text{Zn}(\text{TD1}^\bullet)(\text{H}_2\text{O})]$ but slightly red-shifted. The vertical transition energies deviate by up to -0.05 eV. Due to the high similarity between both species the exciplex-formation does not lead to a D_1 emission at 644 nm.
4. The possibility of an ion-pair formation caused by the disproportionation into a $[\text{Zn}(\text{TD1})]^+$ cation and a $[\text{Zn}(\text{TD1})]^-$ anion was investigated. A similar observation [176] was made by Gautam et al. in the structurally similar $[\text{Pd}(\text{TD1}^\bullet)(\text{H}_2\text{O})]$ radical. The vertical S_1 emission energies of both species match the experimental emission energy very well at 619 nm for the anion and 715 nm for the cation with oscillator strengths of 0.62 and 0.34, respectively. However, the disproportionation is unlikely as the ionisation potential and electron affinity of $[\text{Zn}(\text{TD1}^\bullet)(\text{H}_2\text{O})]$ lie at 6.02 eV and -2.18 eV, respectively. The distance between the anion-cation pair needs to be at the van der Waals radius to allow the Coulomb attraction to compensate the energy difference between ionisation potential and electron affinity.
5. Non-Kasha emission from the D_3 state of the $[\text{Zn}(\text{TD1}^\bullet)(\text{H}_2\text{O})]$ radical. The vertical emission energy lies at 622 nm (1.99 eV) with an oscillator strength of 0.29. This corresponds to a fluorescence lifetime of 19.9 ns.

Of the five possibilities, the non-Kasha seems to be the only viable option due to the energy difference of the ion-pair. In-depth discussions on the emission, the geometry and the absorption of the $[\text{Zn}(\text{TD1}^\bullet)(\text{H}_2\text{O})]$ radical and the structure, absorption and emission of the free $\text{H}_3\text{TD1}$ ligand are published in Paper 5 [137].

6.3 Blatter Radical (Paper 3)

The absorption has been theoretically investigated in Paper 3 [67] using the R2017 Hamiltonian. In the following, some additional discussions are added to the previously published results in order to get a deeper understanding of the photophysical processes, especially of the emission process.

The 1,3-diphenyl-1,4-dihydro-1,2,4-benzotriazin-4-yl (Blatter) radical [26] and several derivatives of the Blatter radical are known in literature [177–181]. The group of these radicals is used in a broad range of applications, including pressure-sensitive semiconductors [182], polymer initiators [183, 184], metal-free magnets [177] and organic spintronic devices [181]. The Blatter radical as the parent radical has recently been investigated by Karecla et al. [27]. The radical (Fig. 25) was found to be stable at room temperature and insensitive to air and moisture.

6.3.1 Computational Details

All geometry optimisations and vibrational analyses were performed with Gaussian 16 [185] program. The ground state was optimised with UDFT and the excited states with UT-DDFT. For all states the PBE0 [130, 131] functional has been used. For carbon and hydrogen the def-SV(P) basis sets [153] and for nitrogen the def2-SVPD basis sets [186] were utilised. For the four-index V_{ijkl} integrals, the resolution-of-the-identity (RI) approximation [66, 187, 188] was employed with SVP [189] as the auxiliary basis for carbon and hydrogen, def2-SVPD [190] for nitrogen.

All U(TD)DFT-PBE0 calculations were carried out in a polarisable continuum model [191] (PCM) with DCM as the solvent.

The BHandHLYP [126, 127] orbitals have been optimised using Dalton 2016.1 [95, 167]. The orbitals have been converted from Dalton to Turbomole format using the *d2tm* inter-

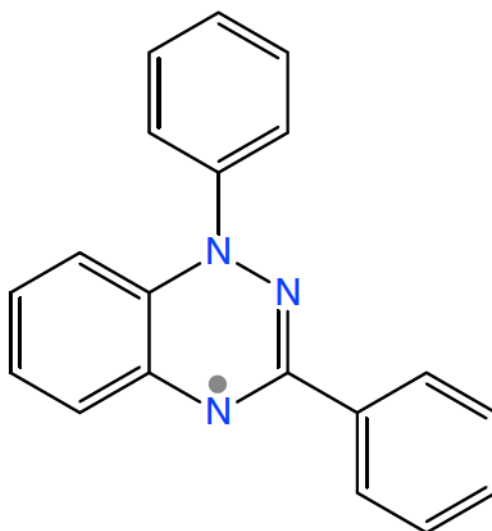


Figure 25: Structure of the Blatter radical.

face [169]. The DFT/MRCI calculations were carried out with the DFT/MRCI program [66, 69] using the R2017 Hamiltonian [169]. 60 roots with a selection threshold of $1.0 E_h$ have been calculated using a purpose-built *mrci* version to circumvent the default limitation to 50 roots.

Franck-Condon profiles of the absorption to and emission from the D_1 and D_2 states were calculated with the VIBES program [192, 193], employing a Fourier transform approach and including temperature and Duschinsky effects [194]. A damping of 10 cm^{-1} full width at half maximum (FWHM) was used. The temperature was set to 298 K and the time interval to 300 fs. The grid was expanded over 16 384 points.

6.3.2 Geometry

The D_0 ground state and the first two excited states D_1 and D_2 were optimised. Experimental structure data is not available. Relevant bond lengths and dihedral angles are shown in Tab. 16.

The structure varies substantially among the three states, especially with regard to the bonds involving the nitrogen centres. The frontier orbitals HOMO, SOMO and LUMO are shown in Fig. 26.

6.3.3 Absorption

The radical absorbs light in a broad spectral range, with small absorption bands at 554 nm, 492 nm, 428 nm, 371 nm and 323 nm and a strong absorption band with a maximum at 272 nm and a shoulder at 286 nm in dichloromethane (DCM).

The resulting absorption spectrum compared to the experimental spectrum is shown in

Table 16: Bond lengths and dihedral angles comparing the ground state and the energetically lowest two excited states of the Blatter radical. See Fig. 25 for atom labels. All bond lengths are in pm, all dihedral angles in degrees.

	D_0	D_1	D_2
N_1-N_2	134	129	136
N_2-C_1	133	139	133
C_1-C_2	149	144	147
C_2-C_3	140	142	141
C_1-N_3	133	134	135
N_3-C_8	136	131	134
N_1-C_{14}	142	144	140
$C_{12}-C_{13}$	139	137	140
$C_{14}-C_{15}$	140	139	141
$N_2-C_1-C_2-C_3$	-2	1	-7
$N_2-N_1-C_{14}-C_{15}$	-50	-62	-31

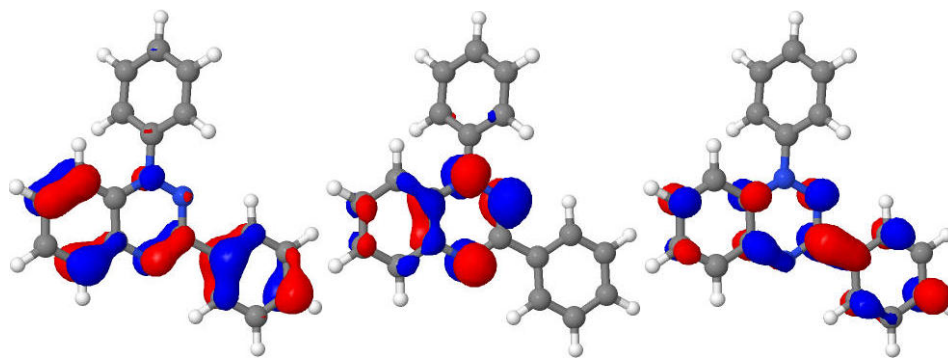


Figure 26: Frontier ROKS orbitals of the Blatter radical showing the HDOMO (left), the SOMO (middle) and the LUMO (right) calculated with BHandHLYP.

Fig. 27. The calculated spectrum is in good agreement to the experiment. The short wavelength region of the spectrum below 300 nm matches the experimental transitions very well. These transitions involve excitations from a doubly occupied into an unoccupied orbital and have a multiconfigurational character. The long wavelength region above 300 nm is blue-shifted by approx. 0.15 eV with respect to the experiment, with the exception of the D_1 state. These transitions involve the SOMO (Fig. 26). The characters of most of the low-lying states of the Blatter radical are highly multiconfigurational.

The D_1 band peaks at 554 nm (2.24 eV) in the experiment with a very low intensity. In the R2017 calculation, the vertical absorption is red-shifted to 593 nm (2.09 eV). The state is mainly (73%) composed of a SOMO \rightarrow LUMO transition and is dark with an oscillator strength of 0.0002. The difference density of the state is shown in Fig. 28.

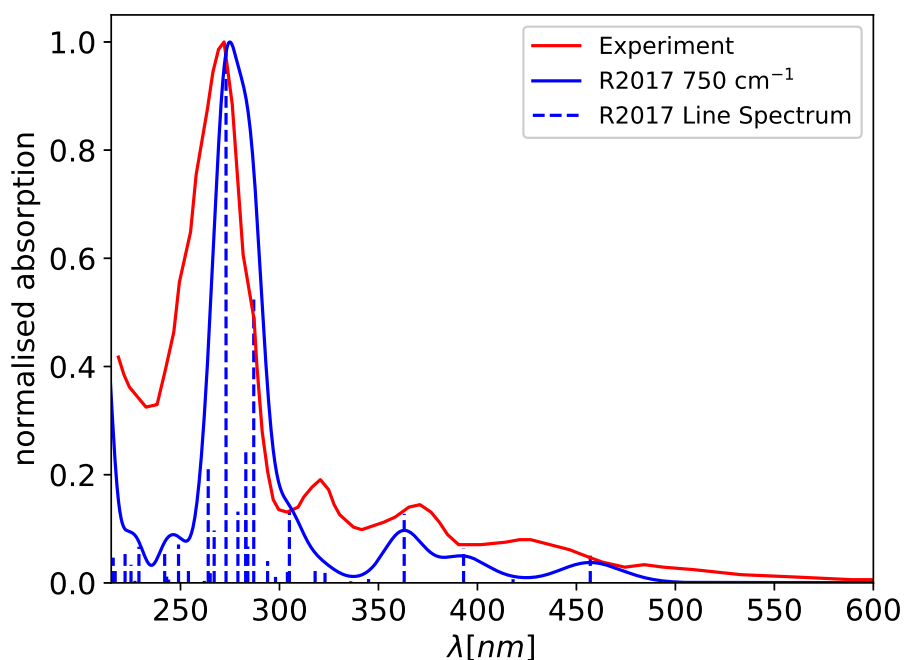


Figure 27: DFT/MRCI-R2017 calculated absorption of the Blatter radical with a polarisable continuum model (PCM) compared to the experiment [27], both with DCM as a solvent. The calculated line spectrum has been broadened by 750 cm^{-1} .

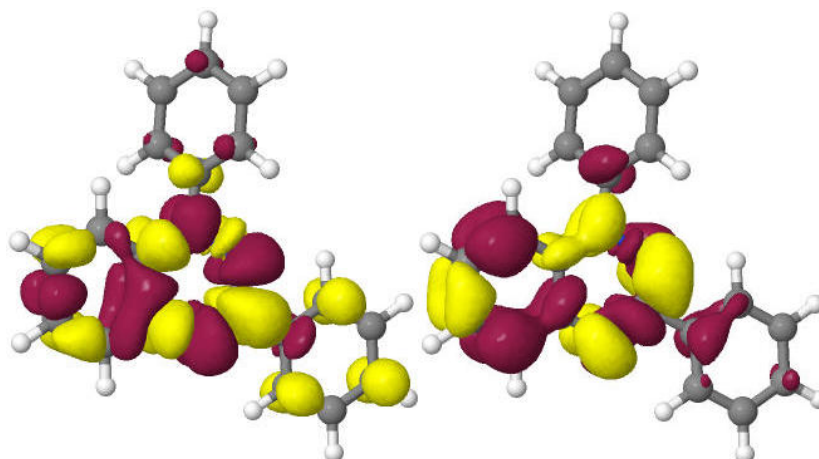


Figure 28: Difference densities with an $|\text{isovalue}|$ of 0.001 of the D_1 state (left) and the D_2 state (right) at the D_0 geometry. A loss of electron density with respect to the D_0 state is shown in red and a gain in yellow.

The D_2 state was found to be at 492 nm (2.52 eV) in the experiment. The R2017 in comparison is blue-shifted to 455 nm (2.72 eV). The state is mainly (57%) composed of a HDOMO \rightarrow SOMO transition. The oscillator strength is 0.024, corresponding to a small peak in Fig. 27. The difference density of this state can be found in Fig. 28. The change in density of the D_2 state as well as that of the D_1 state is mainly located on the benzotriazine structure with some involvement of the C_2 and C_{14} atoms.

The next smaller peaks in the measured spectrum correspond to the D_4 , D_5 and D_8 states. While the D_4 state consists of transitions from the SOMO, the D_5 and D_{10} states consist of transitions into the SOMO. The states lie at 428, 371 and 322 nm in the experiment and at 393, 362 and 305 nm in the R2017 calculation, respectively.

6.3.4 Emission

In the experiment, emission at 595 nm (2.08 eV) in DCM at room temperature is measured following an excitation at 490 nm. In other solvents like n-hexane or tetrahydrofuran, the emission is red-shifted to about 611 nm (2.02 eV).

In the TDDFT-PBE0 optimisation of the D_1 state, the vertical emission wavelength is 954 nm (1.30 eV). The DFT/MRCI-R2017 calculation at that geometry arrives at a very similar vertical emission energy of 945 nm (1.31 eV), resulting in a large Stokes shift of 0.78 eV. The character of this state is to over 90% composed of a SOMO \rightarrow LUMO transition.

The Franck-Condon spectrum in Fig. 29 shows the $D_1 \leftarrow D_0$ absorption and the $D_1 \rightarrow D_0$ emission. The spectrum shows that a large Stokes shift and a strong vibrational progression dominate the spectrum. It is also noticeable that the experimentally observed emission with a maximum at 595 nm cannot stem from the D_1 minimum as the 0-0 overlap is at 733 nm. The adiabatic energy difference between the D_0 and D_1 state is 1.76 eV. The Franck-Condon spectrum confirms that the D_1 is not the emitting state.

The vertical emission energy of the optimised D_2 state lies at 536 nm (2.31 eV) in the

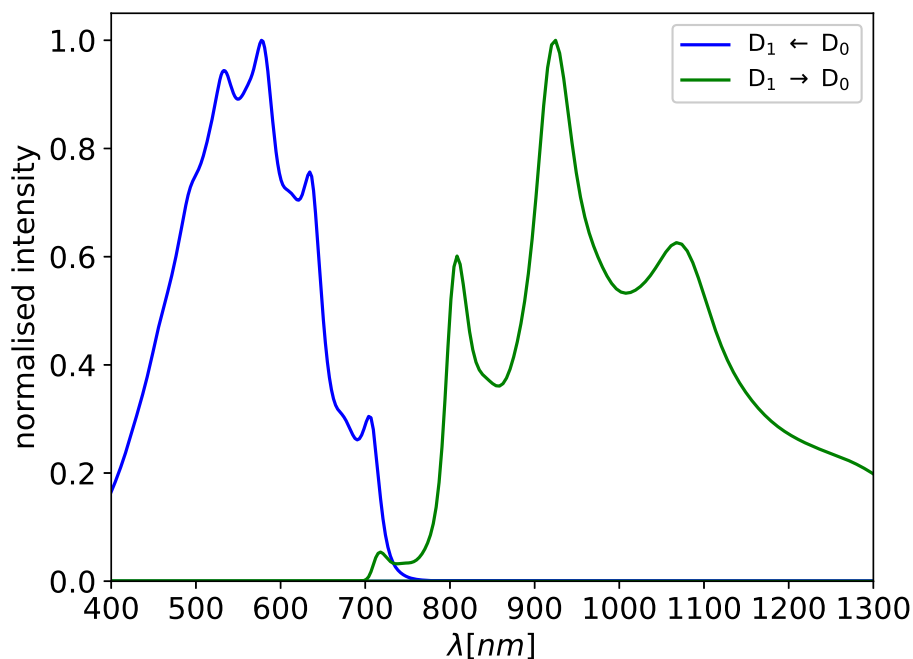


Figure 29: Franck-Condon D_1 emission and absorption spectrum calculated at a temperature of 298 K with DCM as solvent.

DFT/MRCI-R2017 calculation. The state is multiconfigurational and mainly composed of a HOMO \rightarrow SOMO, SOMO \rightarrow LUMO and HOMO-1 \rightarrow SOMO transition, with coefficients -0.7, 0.35 and -0.31, respectively. The oscillator strength is 0.033, resulting in a fluorescence lifetime of 129.4 ns. At the geometry of the D_2 state, the vertical transition energy of the D_1 is strongly blue-shifted to 606 nm (2.05 eV). The energy difference between the D_1 and D_2 state is 0.74 eV.

The Franck-Condon spectrum of the D_2 - D_0 transition is shown in Fig. 30 (left). The maximum of the calculated emission is found to be at 627 nm (1.98 eV), thus underestimating the experimental maximum by 0.10 eV at RT. The spectrum of the calculated

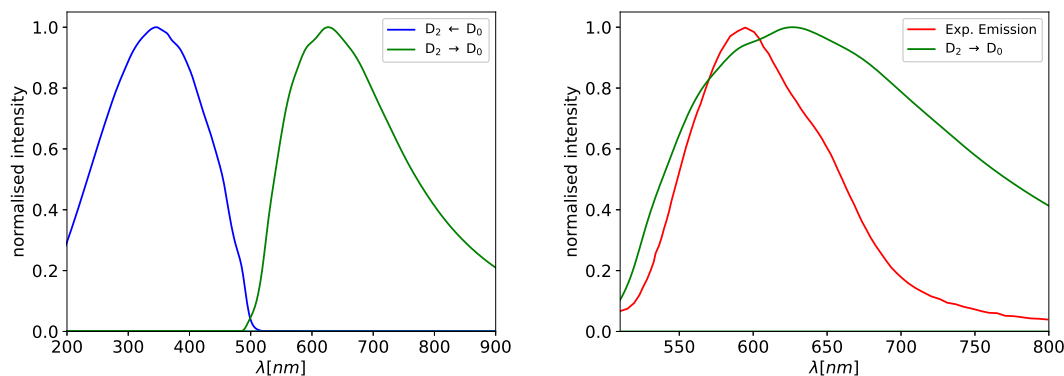


Figure 30: On the left, the Franck-Condon D_2 emission and absorption spectra calculated at a temperature of 298 K with DCM as solvent are shown. On the right-hand side, the calculated Franck-Condon spectrum of the $D_2 \rightarrow D_0$ emission at RT compared to the experimental spectrum[27] is shown.

Franck-Condon D_2 emission compared to the experimental emission spectrum measured in DCM can be found in Fig. 30 (right). The adiabatic difference between the D_0 and D_2 states is 2.49 eV.

The 0-0 overlap varies drastically between different states of the Blatter radical. The largest overlap is between the D_1 state and the ground state with a value of 0.09. The overlap between the D_2 state and the ground state on the other hand is almost two orders of magnitude smaller at 0.001. The 0-0 overlap between the two excited states D_1 and D_2 is virtually nonexistent with a value of 3×10^{-6} .

6.3.5 Conclusion

The calculated absorption spectrum is in good agreement with the experiment. The D_1 state is energetically underestimated while the D_2 , D_4 , D_5 and D_{10} states are overestimated. The bright transition at 272.4 nm and the shoulder at 286 nm are very well matched in the experiment with a deviation of 0.01 eV or below.

The experimental emission was measured at 595 nm. While the absorption to the D_1 state would fit energetically when assuming a small Stokes shift, the emission energy is strongly lowered at the relaxed D_1 geometry. The comparison of the Franck-Condon spectra of the $D_1 \leftarrow D_0$ and $D_2 \leftarrow D_0$ transitions indicates emission from the D_2 state at a wavelength of 627 nm. The emission shows some similarities to that of the zinc tripyrindione radical in Sec. 6.2.

6.4 Triarylamine-Perchlorotriphenylmethyl Radicals

Triarylamine-perchlorotriphenylmethyl radicals, consisting of triarylamine (TARA) as an electron donor and perchlorotriphenylmethyl (PCTM) as an electron acceptor, have shown high fluorescence at RT [195]. Heckmann et al. experimentally investigated a series of TARA-PCTM radicals with different substituents which alter the donor strength of the TARA moiety. Those compounds have been named **1–7** (Fig. 31).

The substituents influence the redox potentials of the TARA greatly. Dapperheld et al. measured a variation of more than 1 V between MeO (**1**) and NO_2 (**7**) [196]. It is therefore possible to change the energy of the CT state and the photophysical properties of the TARA-PCTM radical by introducing small electron donating or withdrawing substituents on the TARA moiety.

The TARA-PCTM molecule is well suited as a potential OLED emitter as it is fluorescent at room temperature in solution. Due to its size, not many methods are suitable for providing a deeper understanding of the electronic structure of TARA-PCTM and its photophysical properties. TARA-PCTM is a large molecule, containing up to 525 electrons (compound **7**, NO_2). Even when replacing the 10 core electrons of chlorine with an effective core potential (ECP), the number of electrons is only reduced by 140. In order to gain a deeper understanding of the molecule and its photophysical properties, the DFT/MRCI

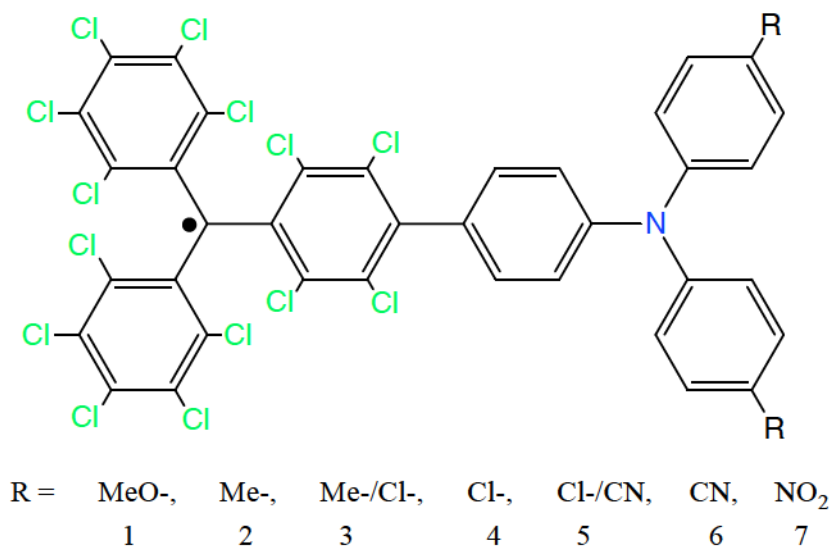


Figure 31: TARA-PCTM with various substituents as compound 1-7.

method is well suited as it is capable of both handling large systems and calculating systems with an open-shell character.

6.4.1 Computational Details

The geometries of all compounds have been optimised with Turbomole V7.1 [197]. The ground state has been optimised with UDF-T and the D_1 excited state with TDDFT [198], both employing the PBE0 [130, 131] functional. Vibrational analyses were carried out with the SNF program [199]. For carbon, oxygen, nitrogen and hydrogen the def-SV(P) basis set [153] and for chlorine the ecp-10-sdf basis and ECP [200] have been used. The ECP replaces the 10 core electrons of chlorine. The BHandHLYP [126, 127] ROKS orbitals for the DFT/MRCI run have been calculated with Dalton 2018.0 [95, 168] and converted from Dalton to Turbomole format using the *d2tm* interface [169]. Vertical excitation and emission energies were calculated with the DFT/MRCI method [66, 67] using the R2018 Hamiltonian [133]. The DFT/MRCI run was carried out with a selection threshold of $0.8 E_h$ with 31 roots for the absorption and 10 roots for the emission, each in doublet multiplicity. The resolution-of-identity (RI) approximation [66, 187, 188] was employed for the four-index V_{ijkl} integrals with SVP [189] as the auxiliary basis for carbon, nitrogen, oxygen and hydrogen and TZVP [189] for chlorine.

6.4.2 Results

The calculation of the set of TARA-PCTM radicals with various substituents in Fig. 31 yields absorption and emission energies to and from the lowest excited state which are in good agreement with the experiment. The calculated absorption of the CT band, which is the lowest excited state (D_1) in all seven TARA-PCTM molecules, is shown in Fig. 32 (left). For compound 7, no experimental energy could be obtained by Heckmann et al., because the CT band was blue-shifted into the next absorption band.

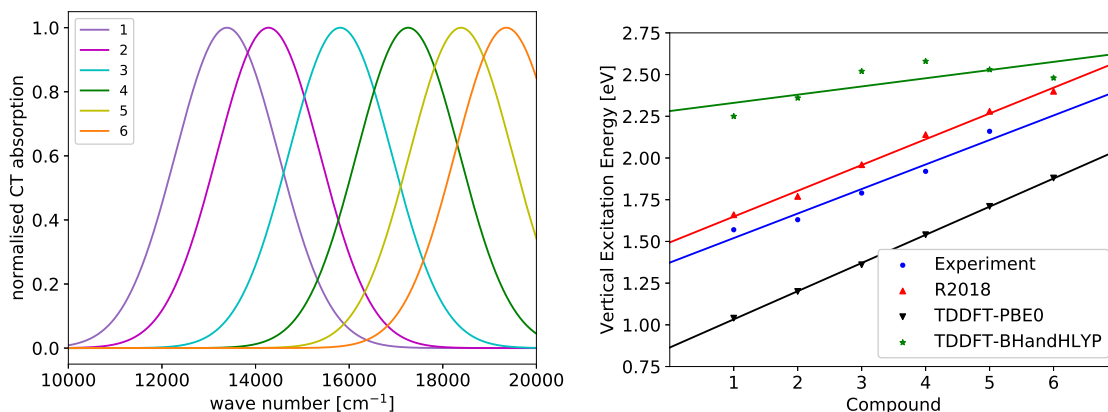


Figure 32: Calculated vertical absorption energies of the CT-band of compounds **1-6**. The absorption has been broadened by a Gaussian function with a FWHM of 2500 cm^{-1} (left-hand side). Correlation diagram of the CT excitation energies and linear regression of compounds **1-6** for R2018-DFT/MRCI, TDDFT-PBE0 and TDDFT-BHandHLYP and of compounds **1-5** for experimental[195] data (right-hand side).

A comparison of the R2018 energies to experimental [195] and calculated TDDFT energies with the PBE0 and BHandHLYP functional is shown as a correlation diagram in Fig. 32 (right). It can be seen that the DFT/MRCI-R2018 results are in good agreement to the experiment throughout the various substituents with a slight overestimation of approx. 0.15 eV . The TDDFT-PBE0 results also show an increasing vertical excitation energy from compound **1** to **6**, similar to the DFT/MRCI and experimental results. However, the results are underestimating the energies by $\approx 0.5\text{ eV}$. TDDFT-BHandHLYP, on the other hand, does not reproduce the energy variation of the CT band at all. The deviation from the experiment ranges from 0.32 eV in compound **5** to 0.73 eV in compound **2** and **3**.

A similar trend is noticeable in the emission from the CT state, affecting both the variation of the energy among the compounds, which can be seen in Fig. 33 (left) and the deviation to the experiment in Fig. 33 (right). For compound **1**, no emission was measured [195].

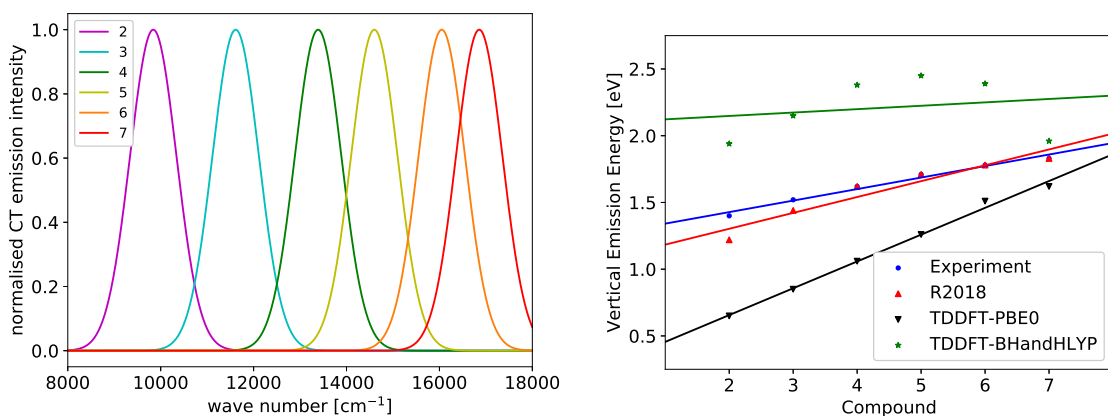


Figure 33: Calculated vertical emission energies at the D_1 structure of compounds **2-7**. The emission has been broadened by a Gaussian function with an FWHM of 1250 cm^{-1} (left-hand side). Correlation diagram of the CT emission energies and linear regression of compounds **2-7** for R2018-DFT/MRCI, TDDFT-PBE0, TDDFT-BHandHLYP and for experimental [195] data (right-hand side).

In the emission, the deviation of the DFT/MRCI-R2018 energies to the experimental values is lower than in the absorption in Fig.32 (right), ranging from an underestimation by 0.182 eV for compound **2** to an exact match of the energies in compound **4–7**. The TDDFT results are similar to the trends of the CT absorption. PBE0 underestimates the vertical emission energies in all compounds, while BHandHLYP shows an overestimation.

When comparing the absorption of energetically higher states, a strong difference to experimental energies is noticeable. A dominant band in the experiment [195] at 26000 cm^{-1} is measured in all radicals, which originates from a local excitation on the PCTM moiety. This band is missing in the DFT/MRCI calculations of all compounds. A comparison between TDDFT employing the PBE0 functional of the geometry optimisation and the BHandHLYP functional of the DFT/MRCI run in comparison to DFT/MRCI-R2018 is shown in Fig. 34. A strong absorption can be seen at about 27000 cm^{-1} in the TDDFT-PBE0 spectrum. This band corresponds to the R2018 band at approx. 32000 cm^{-1} . The smaller band in the TDDFT-PBE0 spectrum at 31000 cm^{-1} corresponds to the shoulder in the R2018 spectrum at approx. 35000 cm^{-1} . Additionally, the TDDFT-PBE0 band at 22000 cm^{-1} corresponds to the R2018 band at 25000 cm^{-1} . The same assignment can be made for the TDDFT-BHandHLYP spectrum. It can be seen that the bands of the R2018 and TDDFT-PBE0 spectral bands are similar and the characters of the excited states are dominated by the same transitions. The transition energies, however, are blue-shifted in the R2018 calculation by approx. $3000\text{--}4000\text{ cm}^{-1}$.

On the one hand, there is a difference of the transition energies between TDDFT calculations employing the BHandHLYP and PBE0 functionals. On the other hand, similar transition energies between TDDFT-BHandHLYP and DFT/MRCI are obtained. The deviations might therefore be based on an improper description of the electronic structure by the BHandHLYP functional and require a closer look. An inspection of the density distribution between the PBE0 and BHandHLYP orbitals, however, show no visually dis-

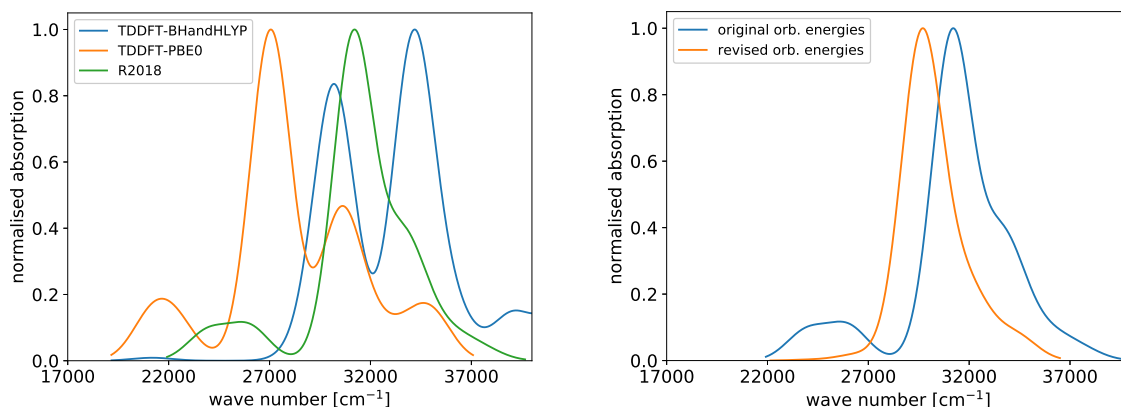


Figure 34: Left-hand side: Calculated absorption spectrum of only the PCTM part, comparing the results of TDDFT-PBE0, TDDFT-BH-LYP (25 roots) and R2018 with short selection threshold (21 roots). The transitions have been broadened by 1000 cm^{-1} FWHM. All transitions have been normalised with regard to the strongest transition of each calculation. Right-hand side: DFT/MRCI-R2018 calculations comparing the results of unaltered BHandHLYP orbital energies to a test calculation where the energies of the highest 11 occupied and lowest 12 unoccupied orbitals have been replaced with *revised* energies. The two calculations are identical in every other aspect.

tinguishable difference. To further the investigation, the energies of the two sets of orbitals have to be compared. Due to the different amount of exact exchange, the orbital energies are not directly comparable between the two functionals. It was found [201] that there is a high correlation ($r^2 > 0.99$) between the energies of BHandHLYP and PBE0 orbitals of the molecules of the training set shown in Fig. 4. The energies of the doubly occupied BHandHLYP orbitals can be modelled via linear regression from the corresponding PBE0 orbital energies as

$$E_i^{BHandHLYP} = 1.08E_i^{PBE0} - 0.58 \quad (75)$$

and the vacant orbitals as

$$E_i^{BHandHLYP} = 1.01E_i^{PBE0} + 0.49 \quad (76)$$

with the intercept in eV. For the singly occupied orbitals, no difference in energies was found [201]. The orbital energies of a ROKS-PBE0 Dalton 2018.0 calculation are then transformed to the expected BHandHLYP energies as in Eq. (75) and (76). The resulting energies of vacant orbitals are 0.4–0.8 eV lower, while the energies of doubly occupied orbitals are up to 0.2 eV lower compared to the energies of the *original* ROKS BHandHLYP calculation. In other words, the energy gap between the HOMO and the SOMO is raised from 3.21 eV to 3.40 eV and the gap between the SOMO and the LUMO is lowered from 4.40 eV to 3.96 eV, while all other occupied and unoccupied orbital energies follow a similar trend. This difference between the *original* and *revised* BHandHLYP orbital energies might explain the systematic blue-shift of the DFT/MRCI and TDDFT-PBE0 spectra, provided that the *revised* energies are, in fact, an improvement over the *original* energies.

In a next step bearing orbital degeneracies in mind, the energies of the 11 highest doubly occupied orbitals and of the 12 lowest unoccupied orbitals are replaced by the *revised* energies in the *oneint* file. Subsequently, a new DFT/MRCI-R2018 calculation is carried out. In this calculation, the 23 orbital energies calculated from a PBE0 reference calculation are used in combination with the two-electron integrals and remaining *original* orbital energies that are left unaltered. The spectrum of this run is shown in Fig. 34 (right). The largest peak is shifted from 31200 cm^{-1} to approx. 29600 cm^{-1} , resulting in a considerable red-shift closer to the experimental value. The small band at 24000 cm^{-1} becomes less intense and its character more strongly mixed, while the transition energy does not change. The results reaffirm the assumption, that the *original* BHandHLYP energies could be the cause of the shift in the spectra of TDDFT-PBE0 and DFT/MRCI-R2018.

6.5 TTM-1Cz Radical

The (4-N-carbazolyl-2,6-dichlorophenyl)bis(2,4,6-trichlorophenyl)methyl (TTM-1Cz) radical is an OLED emitter first described by Peng et al. [16], with a high stability and

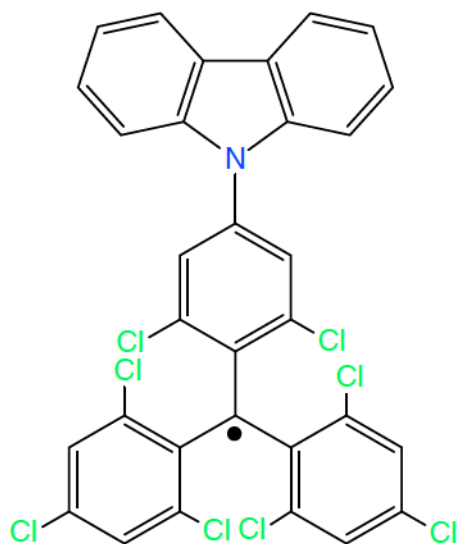


Figure 35: Chemical structure of the TTM-1Cz radical.

quantum yield. TTM-1Cz is a polychlorinated triphenylmethyl radical, just like the PCTM moiety of the TARA-PCTM radical in Sec. 6.4. Both molecules have a similar structure and similar photophysical properties.

The geometry and orbital setup are identical to the one of the TARA-PCTM calculation in Sec. 6.4.1. The DFT/MRCI-R2017 and DFT/MRCI-R2018 runs were carried out with a short selection threshold ($0.8 E_h$) and corresponding parameters with 80 roots in total. Instead of the regular *mrci* program version, which is limited to 50 roots, a purpose-built version has been employed.

The corresponding spectrum is shown in Fig. 36 (left) in comparison to the experiment. The calculated spectrum is systematically blue-shifted. For this reason, a constant shift of -0.6 eV was applied to compare the profile of the spectrum. With the applied shift, both the R2017 and R2018 spectra match to the experimental one fairly well.

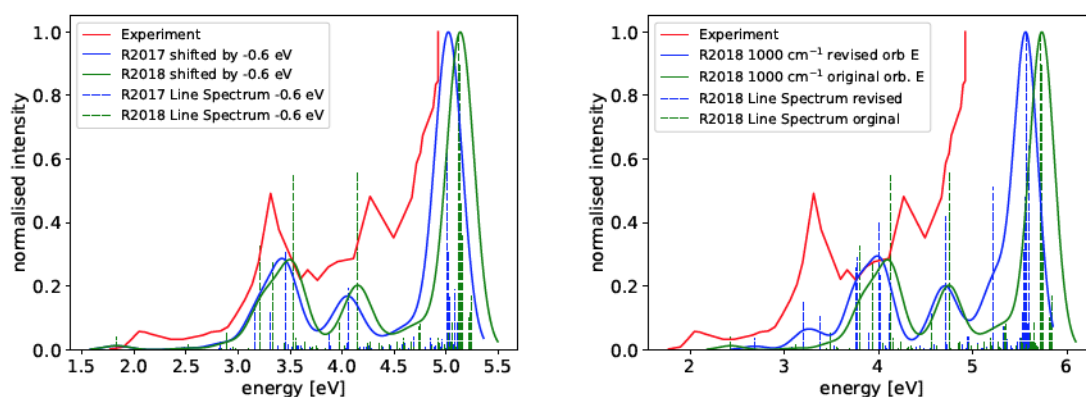


Figure 36: Left-hand site: Shifted DFT/MRCI-R2017 and DFT/MRCI-R2018 absorption spectra of TTM-1Cz in vacuum in comparison to experimental [16] data measured in chloroform. Due to the strong difference between calculation and experiment the spectra are shifted by -0.6 eV. The calculated transitions have been broadened with a FWHM of 1000 cm^{-1} . Right-hand site: Comparison of two DFT/MRCI-R2018 calculations, one with the *original* BHandHLYP energies and one with the 10 highest occupied and 10 lowest unoccupied orbital energies replaced with *revised* energies.

Several tries have been started to get a better description of the TTM-1Cz radical, including a PCM calculation, Grimme’s D3 correction with Becke-Johnson damping [202], applying larger basis sets or replacing the ECP of chlorine with an all-electron basis set. Besides the latter shifting the D_1 energy from 2.43 eV to 2.66 eV and thus leading to a better match to the experiment with the -0.6 eV shift, no significant effect could be observed. Due to the systematic shift, a possible explanation is an artificial lowering of the ground state compared to the excited states, caused by an improper description in the BHandHLYP orbitals.

Due to the structural similarities to the PCTM and similar results of the DFT/MRCI calculations, the BHandHLYP orbital energies are revised from ROKS-PBE0 energies using Eq. (75) and (76) as described in Sec. 6.4.2. As in the PCTM radical it is found that the revised orbital energies deviate considerably from the original BHandHLYP energies. The energies of the 10 highest occupied and 10 lowest unoccupied orbitals have been replaced by revised energies of the corresponding orbitals, while the SOMO energy remains unchanged. The revised orbital energies are found to be 0.1–0.4 eV lower in case of occupied orbitals and 0.5–0.7 eV lower in case of unoccupied orbitals. Since the SOMO energy is unchanged, the gap between the doubly occupied orbitals and the SOMO increases and the gap between the SOMO and the unoccupied orbitals decreases. The resulting spectrum in comparison to the previously calculated one that employed the *original* BHandHLYP energies can be found in Fig. 36 (right). In the DFT/MRCI-R2018 calculation based on the 20 *revised* orbital energies, the experimental band at 3.3 eV is well matched, contrary to the previous calculation based on the *original* energies, where the band was missing. Additionally, a general red-shift is noticeable in the new calculation based on the revised energies, with the exception of the D_1 state, which is blue-shifted. At higher energies, the contribution of non-replaced *original* orbital energies becomes more pronounced. It is evident from the DFT/MRCI-R2018 spectrum based on the *revised* orbital energies that in the same manner as the PCTM radical, the results are improved. Although these results are rudimentary, they indicate shortcomings of the BHandHLYP functional.

6.6 PAH-DTDA Radicals

The following results regarding the absorption are the based on the calculations of Takin Haj Hassani Sohi, who did the first application of the R2017 Hamiltonian in his Bachelor’s thesis [203] under my supervision. In order to present the findings obtained with the R2017 Hamiltonian, his results on the absorption are shown below. These results are expanded by unpublished calculations on the emission.

The three molecules phenanthrene-DTDA, pyrene-DTDA and anthracene-DTDA (Fig. 37) are stable radicals that show blue-light emission at room temperature after excitation. Their structure is made up of a polyatomic hydrocarbon (PAH) linked to a 1,2,3,5-dithiadiazolyl (DTDA) radical.

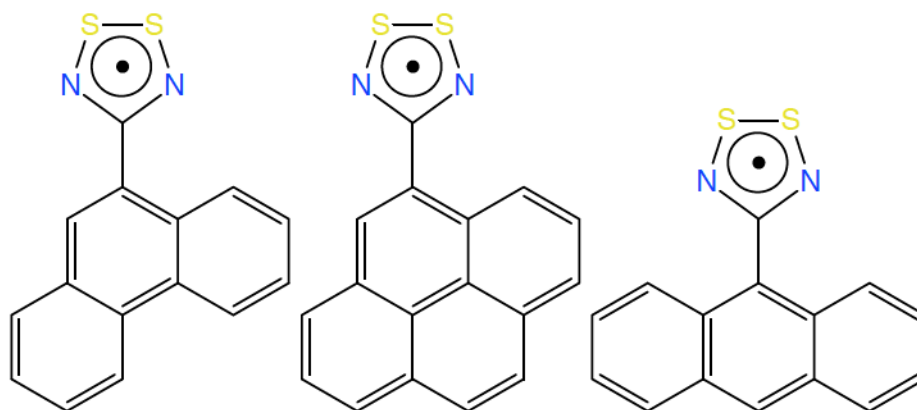


Figure 37: Chemical structures of phenanthrene-DTDA (left), pyrene-DTDA (middle) and anthracene-DTDA (right)

6.6.1 Computational Details

All geometry optimisations, vibrational analyses and TDDFT calculations were carried out with the Gaussian 16 program [185]. The ground states have been optimised with restricted open-shell DFT (RODFT) and the D_1 excited states with UTDDFT. The PBE0 [130, 131] functional has been employed in all optimisations. For carbon and hydrogen, the def-SV(P) basis sets [153] and for nitrogen and sulphur the def2-SVPD basis sets [186] were utilised. For the four-index V_{ijkl} integrals, the resolution-of-the-identity (RI) approximation [66, 187, 188] was employed with SVP [189] as the auxiliary basis for carbon and hydrogen, def2-SVPD [190] for nitrogen and sulphur. The (TD)DFT calculations were carried out in a polarisable continuum model [191] (PCM) with acetonitrile (MeCN) as the solvent. The BHandHLYP [126, 127] orbitals have been optimised using Dalton 2016.1 [95, 167]. The orbitals have been converted from Dalton to Turbomole format using the *d2tm* interface [169]. The DFT/MRCI calculations were carried out with the DFT/MRCI program [66, 69] using the R2017 Hamiltonian [169]. For the absorption, 80 roots with a selection threshold of 1.0 E_h have been calculated using a purpose-built *mrci* version to circumvent the default limitation to 50 roots. For the emission, 10 roots have been calculated using the standard *mrci* version.

6.6.2 Results

The lowest excited states of all three DTDA radicals are dark with an oscillator strength of zero or almost zero. The spectra are heavily dominated by a few very bright transitions. Among phenanthrene-DTDA and pyrene-DTDA, seven transitions have an oscillator strength of larger than 0.1, while in anthracene-DTDA there are only four. All these bright transitions correspond to local PAH excitations from a doubly occupied to a vacant orbital, with no involvement of the SOMO, which is located on the DTDA ring. The absorption spectra in comparison with the experiment [204] can be found in Fig. 38.

The experimental emission wavelength was found to be 410 nm (3.02 eV) for phenanthrene-DTDA and 440 nm (2.82 eV) for the other two radicals in MeCN [204]. Thus, all three radicals were found to be blue-light emitters. In the solid state, a red-shift to 420 nm,

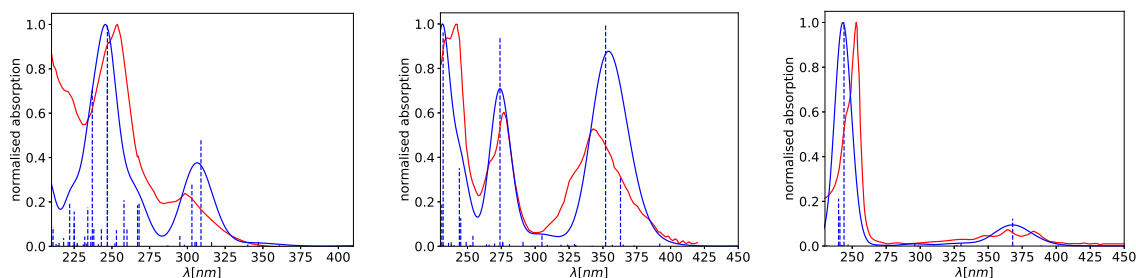


Figure 38: Calculated absorption spectra of phenanthrene-DTDA (left), pyrene-DTDA (middle) and anthracene-DTDA (right) in comparison with the experiment (red line). The spectra were measured in MeCN at room temperature. The calculations were carried out with PCM in MeCN. The line spectra (blue, dashed) were broadened by 1000 cm^{-1} (blue, solid). All data has been normalised. The figures were replotted using the data of Takin Haj Hassani Sohi's Bachelor's Thesis [203].

509 nm and 490 nm was observed, respectively [204]. In the calculations, the emission is a more challenging case. In the TDDFT-PBE0 D_1 geometry optimisations, the resulting energies do not fit the experiment. In phenanthrene-DTDA, the first root lies at 2010 nm (0.62 eV) in MeCN (PCM) and is nearly unchanged in vacuum. In the DFT/MRCI calculation, the energy is even lower at 0.45 eV. The same holds true for the other two radicals.

The D_1 state of pyrene-DTDA has a high amount of spin contamination with $S^2 \approx 2.7$, which corresponds to an unphysical triplet-coupled doublet state with the sum of the expected S^2 -value of a doublet and a triplet [205]. Upon a new optimisation at this minimum, the 'true' D_1 state is obtained, which is energetically identical to that of phenanthrene-DTDA. The D_1 emission energy of anthracene-DTDA is similar and lies at 0.61 eV in the TDDFT-PBE0 and at 0.47 eV in the DFT/MRCI-R2017 calculation. In all states, the character consists almost completely of a SOMO \rightarrow LUMO transition. All states are minima on the potential energy surface (PES). The results are shown in Tab. 17.

It is evident that the first calculated state in the absorption spectrum is energetically far below the emission energy. While the states are dark and thus neither visible in the experimental nor calculated spectra, the states should be the emissive state according to Kasha's rule [101], at least if there is emission. The difference density of the D_1 at the D_1 minimum shows an intra-DTDA transition without any involvement from the PAH part (Fig. 39). The difference density at the minimum of the D_0 state is virtually unchanged.

Table 17: Vertical experimental and calculated emission energy of the three DTDA radicals in comparison to the first excited state of the absorption. All energies are in eV. The emission was calculated at the corresponding excited state geometries and the absorption at the ground state geometries.

Radical	Exp. Em.[204]	TDDFT-PBE0 Em.	R2017 Em.	R2017 Abs. [203]
phenanthrene-DTDA	3.02	0.62	0.45	1.64
pyrene-DTD	2.82	0.62	0.45	1.86
anthracene-DTDA	2.82	0.61	0.47	1.88

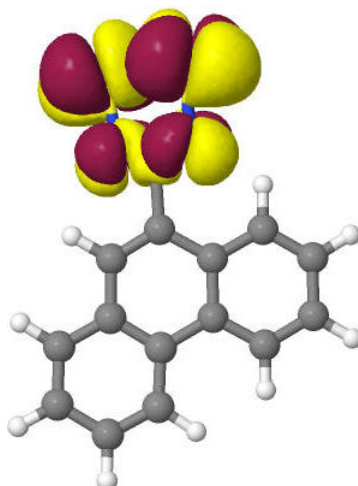


Figure 39: Difference densities with an $|\text{isovalue}|$ of 0.001 of the D_1 state of phenanthrene-DTDA at the D_1 geometry. A loss of electron density with respect to the D_0 state is shown in red and a gain in yellow.

Since the observed emission energy is a lot higher than the calculated one and also above several (dark) states in the absorption spectra, the question arises whether the emission stems from a doublet state at all. In order to answer this question or at least give more insight, the first excited states of the free ligands phenanthrene, pyrene and anthracene have been optimised. These states lie energetically closer to the observed emission of the DTDA radicals, at 3.48 eV, 3.33 and 3.00 eV, respectively. While replacing the DTDA radical with a single hydrogen certainly alters the properties of the emission to a greater extent, a decoupled singlet emission located on the DTDA-bound PAH still might explain the emission. An anion-cation ion-pair similar to the possible alternative proposed in Sec. 6.2 can safely be excluded in this case as both anion and cation show a similarly low emission energy as the neutral radical.

7 Conclusion

The aim of this thesis was the familiarisation with the DFT/MRCI method and open-shell systems, the development of a Dalton interface for ROKS orbitals, the collection of experimental reference data on open-shell excited states and the development and implementation of an open-shell extension to the R2016 Hamiltonian. Additionally, the parameters of the new Hamiltonian had to be trained and the resulting parameter set had to be assessed using the experimental reference data. This target was accomplished with the successful test of the R2017 Hamiltonian and the following publication. The new Hamiltonian proves to be not only capable of calculating open-shell systems but also closed-shell systems employing the same set of parameters in all calculations. The accuracy for closed-shell systems is identical to the R2016 and original Hamiltonians and the accuracy for open-shell systems is nearly identical at 0.15 eV and 0.16 eV, respectively.

A benchmark calculations of the original, R2016 and R2017 Hamiltonians on transition metal complexes discerned problems in these species. A systematic underestimation of the electronic excitation energies was discovered for the R2016 and R2017 Hamiltonians in inorganic and to a lesser extent in organic transition metal complexes. It was found that these deviations arise from an imbalanced treatment of correlation energies caused by a too strong damping of off-diagonal matrix elements. A new damping function was developed and implemented. In combination with the equation for diagonal matrix elements of the R2017, the new R2018 Hamiltonian was developed and parametrised. The parametrisation was carried out with the set of the R2017 Hamiltonian and the addition of twelve excited states of ruthenocene, Cu and Cu⁺. This new Hamiltonian greatly improves the accuracy of spectral properties of transition metal complexes. It was found that the improvement is attributed to the new damping function, with only slight improvements due to the new states included in the fitting set. For organometallic complexes, the resulting RMSE is the lowest among all Hamiltonians. The RMSE is lowered to 0.15 eV, compared to 0.20 and 0.25 eV for the original and R2016 Hamiltonians, respectively. For inorganic complexes, the R2018 Hamiltonian yields a similar accuracy as the original one, with a considerable improvement over the redesigned Hamiltonians R2016 and R2017. While improving the accuracy of electronic excitation energies of transition metal complexes, the R2018 retains the good description of organic molecules, both open-shell and closed-shell. For this reason the R2018 Hamiltonian should be considered the default choice for computing these systems.

Over the course of this thesis, two interfaces were successfully developed. One is the *d2tm* interface between Turbomole format and Dalton. The interface generates a Dalton input starting from a basis set file and coordinates in Turbomole format with support for symmetry via symmetry generators that do not rotate the molecule. After a successful Dalton run, the interface automatically generates the necessary input for integral calculations using the *oneint* and *ritraf* programs. Besides DFT calculations with restricted open-shell orbitals, the interface supports restricted orbitals and Hartree-Fock calculations with both types of orbitals. The second interface is implemented within the *mrci* program and supports the interface files that are requested in the ORCA run. Input files in Turbomole

format for a later run with programs like *proper* and *SpockCI* are automatically generated and can also be requested without a full run. Freezing orbitals by manual specification as well as via an energy threshold is also supported, as well as the frozen-core approximation for ab-initio MRCI runs.

The new R2017 and R2018 Hamiltonians were applied to several fluorescence emitters with both odd and even numbers of electrons.

The three closed-shell phosphorescent (C \wedge N)Pt(acac) platinum complexes of increasing size (ppy)Pt(acac), (bzq)Pt(acac) and (dbq)Pt(acac) were investigated using the R2018 Hamiltonian with additional spin-orbit coupling on top of the R2018 wave function with *SpockCI*. The resulting emission energies, phosphorescence lifetimes and spectral shapes are in good agreement with the experiment. The counter-intuitive blue-shift of the largest of the three complexes and the variation in the phosphorescence lifetimes, that were observed in the experiment and reproduced in the calculations, are explained. The shift is caused by the effective π system, which does not extend to the size of the ligand in case of the largest complex, leaving the second largest (bzq)Pt(acac) complex as the one with the largest effective π system and the most red-shifted emission among the three complexes. The largest π system also leads to the largest LC contribution, which in turn leads to the slower phosphorescence rate that was experimentally observed and computationally reproduced. In the largest complex (dbq)Pt(acac), the difference density of the emitting T₁ state is very similar to that of the (ppy)Pt(acac), stretching across the ppy ligand.

The zinc tripyrrindione complex is a stable fluorescent radical, where the emission found to be at a higher energy than the lowest absorption bands in the experiment. DFT/MRCI calculations using the R2018 Hamiltonian reproduce the absorption spectrum very well. The calculations confirm the observations regarding the emission energy with the vertical absorption energy of the D₁ and D₂ state lying below this value. The D₃-D₀ transition in the calculation matches the experimental bright absorption and emission in both energy and oscillator strength. Since this D₃ emission violates Kasha's rule, other means of emission were investigated. While the first excited states of a reduced [Zn(TD1)(H)] species and an exciplex-formation with THF lie below the emission energy, the free ligand H₃TD1 lies energetically too high. The formation of an anion-cation ion-pair formation has been considered. The S₁ emission energy of both ions matches the experimental emission very well. However, the high ionisation potential for creating the cation in combination with a too low electron affinity for creating the anion makes this formation unlikely. Thus, these alternatives were ultimately excluded due to a mismatch in the emission energy or deemed unlikely due to energy barriers. This leaves the non-Kasha emission from the D₃ state as the most likely among all considered possibilities.

The Blatter radical was investigated regarding absorption and emission using the R2017 Hamiltonian. The results are in good agreement to the experiment, especially the large peaks below 300 nm. The calculations indicate that the D₁ state is not the emitting state. The state shows a strong Stokes shift that was also reproduced in a FC spectrum using the VIBES program in combination with the adiabatic energy from the R2017 runs. The D₂ state is predicted to be the emissive state. The calculations indicate a non-Kasha emission

with similar findings as in the zinc tripyrindione complex.

The three DTDA-based radicals phenanthrene-DTDA, pyrene-DTDA and anthracene-DTDA were investigated using the R2017 Hamiltonian. The absorption was studied by Takin Haj Hassani Sohi in his Bachelor's thesis. The calculated absorption spectra of all three radicals are in good agreement with the experimental spectra. Additional calculations regarding the emission show a very low-lying energy of the optimised D_1 state, ruling out emission from this state. Due to the high experimental emission energy at 2.82–3.02 eV with several excited states below this energy, the emission from any doublet state seems unlikely. A possible explanation lies in the singlet emission from the PAH due to similar emission energies of the free PAH molecules, but the proof remains to be seen.

In the study of tris(trichlorophenyl)methyl radicals or related structures, a systematic overestimation in the absorption energies was found. Since applying a constant shift to the transition of the TTM-1Cz radical of approximately -0.6 eV results in a spectrum that is in good agreement with the experimental spectrum, it is possible that the ground state is artificially lowered with regard to the excited state. This trend is also noticeable in the set of TARA-PCTM radicals. While the first excited state, which is a CT state, is in excellent agreement with the experiment in both absorption and emission, the absorption band at 26000 cm^{-1} is missing in the calculations. This absorption band corresponds to an intra-PCTM excitation. The same band is recovered in an TDDFT-PBE0 calculation, but is also missing in TDDFT-BHandHLYP. *Revised* BHandHLYP energies calculated from a ROKS-PBE0 calculation indicate that the energy gap between the doubly occupied orbitals and the SOMO is lower than expected and the gap between the SOMO and the unoccupied orbitals is higher than expected. A trial R2018 calculation employing the *revised* BHandHLYP energies for the frontier orbitals show improvements for both the TTM-1Cz and PCTM radical over the *original* BHandHLYP energies. While these tests indicate shortcomings of the BHandHLYP functional for these triphenylmethyl radicals, a remedy is not available at the moment.

Apart from these systematic deviations involving chlorinated triphenylmethyl radicals, all calculations have shown that the new Hamiltonians R2017 and R2018 are able to reproduce and predict photophysical properties with good accuracy, with the R2017 Hamiltonian being only suited for organic molecules due to its damping function. In this thesis and the included publications, the R2018 Hamiltonian was employed in calculations of singlet, doublet, triplet and quartet multiplicity of transition metal complexes and organic molecules, for ionisation potentials and electron affinities and to large systems using a shorter selection. These applications demonstrate the universality of the R2018 Hamiltonian.

References

- [1] S. X. Jin, J. Li, J. Z. Li, J. Y. Lin and H. X. Jiang, *Appl. Phys. Lett.*, 2000, **76**, 631–633.
- [2] K. Zhang, D. Peng, K. M. Lau and Z. Liu, *J. Soc. Inf. Disp.*, 2017, **25**, 240–248.
- [3] Z.-K. Tan, R. S. Moghaddam, M. L. Lai, P. Docampo, R. Higler, F. Deschler, M. Price, A. Sadhanala, L. M. Pazos, D. Credgington, F. Hanusch, T. Bein, H. J. Snaith and R. H. Friend, *Nat. Nanotechnol.*, 2014, **9**, 687–692.
- [4] H. Cho, S.-H. Jeong, M.-H. Park, Y.-H. Kim, C. Wolf, C.-L. Lee, J. H. Heo, A. Sadhanala, N. Myoung, S. Yoo, S. H. Im, R. H. Friend and T.-W. Lee, *Science*, 2015, **350**, 1222–1225.
- [5] N. Wang, L. Cheng, R. Ge, S. Zhang, Y. Miao, W. Zou, C. Yi, Y. Sun, Y. Cao, R. Yang, Y. Wei, Q. Guo, Y. Ke, M. Yu, Y. Jin, Y. Liu, Q. Ding, D. Di, L. Yang, G. Xing, H. Tian, C. Jin, F. Gao, R. H. Friend, J. Wang and W. Huang, *Nat. Photonics*, 2016, **10**, 699–704.
- [6] C. W. Tang and S. A. VanSlyke, *Appl. Phys. Lett.*, 1987, **51**, 913–915.
- [7] J. H. Burroughes, D. D. C. Bradley, A. R. Brown, R. N. Marks, K. Mackay, R. H. Friend, P. L. Burns and A. B. Holmes, *Nature*, 1990, **347**, 539–541.
- [8] T. Tsujimura, *OLED Display Fundamentals and Applications*, John Wiley & Sons, Inc., Hoboken, NJ, 2nd edn., 2017.
- [9] L. J. Rothberg and A. J. Lovinger, *J. Mater. Res.*, 1996, **11**, 3174–3187.
- [10] Y. Ma, H. Zhang, J. Shen and C. Che, *Synth. Met.*, 1998, **94**, 245–248.
- [11] M. A. Baldo, D. F. O’Brien, Y. You, A. Shoustikov, S. Sibley, M. E. Thompson and S. R. Forrest, *Nature*, 1998, **395**, 151–154.
- [12] C. Adachi, M. A. Baldo, S. R. Forrest and M. E. Thompson, *Appl. Phys. Lett.*, 2000, **77**, 904–906.
- [13] A. Endo, M. Ogasawara, A. Takahashi, D. Yokoyama, Y. Kato and C. Adachi, *Adv. Mater.*, 2009, **21**, 4802–4806.
- [14] H. Uoyama, K. Goushi, K. Shizu, H. Nomura and C. Adachi, *Nature*, 2012, **492**, 234–238.
- [15] T. J. Penfold, E. Gindensperger, C. Daniel and C. M. Marian, *Chem. Rev.*, 2018, **118**, 6975–7025.
- [16] Q. Peng, A. Obolda, M. Zhang and F. Li, *Angew. Chem. Int. Ed.*, 2015, **54**, 7091–7095.
- [17] Y. Gao, A. Obolda, M. Zhang and F. Li, *Dyes Pigm.*, 2017, **139**, 644–650.

- [18] X. Ai, E. W. Evans, S. Dong, A. J. Gillett, H. Guo, Y. Chen, T. J. H. Hele, R. H. Friend and F. Li, *Nature*, 2018, **563**, 536–540.
- [19] *Stable Radicals*, ed. R. G. Hicks, John Wiley & Sons, Ltd, Chichester, UK, 2010.
- [20] V. Gamero, D. Velasco, S. Latorre, F. López-Calahorra, E. Brillas and L. Juliá, *Tetrahedron Lett.*, 2006, **47**, 2305–2309.
- [21] Y. Hattori, T. Kusamoto and H. Nishihara, *Angew. Chem. Int. Ed.*, 2014, **53**, 11845–11848.
- [22] T. Kusamoto, S. Kimura, Y. Ogino, C. Ohde and H. Nishihara, *Chem.: Eur. J.*, 2016, **22**, 17725–17733.
- [23] S. Kimura, A. Tanushi, T. Kusamoto, S. Kochi, T. Sato and H. Nishihara, *Chem. Sci.*, 2018, **9**, 1996–2007.
- [24] A. Abdurahman, Q. Peng, O. Ablikim, X. Ai and F. Li, *Mater. Horiz.*, 2019, **6**, 1265–1270.
- [25] Y. Hattori, T. Kusamoto and H. Nishihara, *RSC Adv.*, 2015, **5**, 64802–64805.
- [26] H. M. Blatter and H. Lukaszewski, *Tetrahedron Lett.*, 1968, **9**, 2701–2705.
- [27] G. Karecla, P. Papagiorgis, N. Panagi, G. A. Zissimou, C. P. Constantinides, P. A. Koutentis, G. Itskos and S. C. Hayes, *New J. Chem.*, 2017, **41**, 8604–8613.
- [28] Y. Beldjoudi, M. A. Nascimento, Y. J. Cho, H. Yu, H. Aziz, D. Tonouchi, K. Eguchi, M. M. Matsushita, K. Awaga, I. Osorio-Roman, C. P. Constantinides and J. M. Rawson, *J. Am. Chem. Soc.*, 2018, **140**, 6260–6270.
- [29] Y. Beldjoudi, A. Arauzo, J. Campo, E. L. Gavey, M. Pilkington, M. A. Nascimento and J. M. Rawson, *J. Am. Chem. Soc.*, 2019, **141**, 6875–6889.
- [30] R. Gautam, S. J. Petritis, A. V. Astashkin and E. Tomat, *Inorg. Chem.*, 2018, **57**, 15240–15246.
- [31] R. Beaulac, G. Bussière, C. Reber, C. Lescop and D. Luneau, *New J. Chem.*, 2003, **27**, 1200–1206.
- [32] R. Beaulac, D. Luneau and C. Reber, *Chem. Phys. Lett.*, 2005, **405**, 153–158.
- [33] C. Lescop, D. Luneau, G. Bussière, M. Triest and C. Reber, *Inorg. Chem.*, 2000, **39**, 3740–3741.
- [34] D. R. Hartree, *Math. Proc. Cambridge Philos. Soc.*, 1928, **24**, 111–132.
- [35] J. C. Slater, *Phys. Rev.*, 1930, **35**, 210–211.
- [36] V. Fock, *Z. Phys.*, 1930, **61**, 126–148.
- [37] C. C. J. Roothaan, *Rev. Mod. Phys.*, 1951, **23**, 69–89.
- [38] G. D. Purvis and R. J. Bartlett, *J. Chem. Phys.*, 1982, **76**, 1910–1918.

- [39] K. Raghavachari, G. W. Trucks, J. A. Pople and M. Head-Gordon, *Chem. Phys. Lett.*, 1989, **157**, 479–483.
- [40] O. Christiansen, H. Koch and P. Jørgensen, *Chem. Phys. Lett.*, 1995, **243**, 409–418.
- [41] O. Christiansen, H. Koch and P. Jørgensen, *J. Chem. Phys.*, 1995, **103**, 7429–7441.
- [42] M. Head-Gordon, R. J. Rico, M. Oumi and T. J. Lee, *Chem. Phys. Lett.*, 1994, **219**, 21–29.
- [43] J. Schirmer, *Phys. Rev. A*, 1982, **26**, 2395–2416.
- [44] B. O. Roos, P. R. Taylor and P. E. Siegbahn, *Chem. Phys.*, 1980, **48**, 157–173.
- [45] J. Olsen, B. O. Roos, P. Jørgensen and H. J. A. Jensen, *J. Chem. Phys.*, 1988, **89**, 2185–2192.
- [46] P.-Å. Malmqvist, A. Rendell and B. O. Roos, *J. Phys. Chem.*, 1990, **94**, 5477–5482.
- [47] C. Møller and M. S. Plesset, *Phys. Rev.*, 1934, **46**, 618–622.
- [48] K. Hirao, *Chem. Phys. Lett.*, 1992, **190**, 374–380.
- [49] K. Andersson, P.-Å. Malmqvist, B. O. Roos, A. J. Sadlej and K. Wolinski, *J. Phys. Chem.*, 1990, **94**, 5483–5488.
- [50] K. Andersson, P.-Å. Malmqvist and B. O. Roos, *J. Chem. Phys.*, 1992, **96**, 1218–1226.
- [51] E. Runge and E. K. U. Gross, *Phys. Rev. Lett.*, 1984, **52**, 997–1000.
- [52] E. K. U. Gross and W. Kohn, *Phys. Rev. Lett.*, 1985, **55**, 2850–2852.
- [53] E. Gross and W. Kohn, in *Advances in Quantum Chemistry*, Elsevier, 1990, pp. 255–291.
- [54] M. E. Casida, in *Recent Advances in Density Functional Methods*, WORLD SCIENTIFIC, 1995, pp. 155–192.
- [55] M. Kolb, *Ph.D. thesis*, Bergische Universität-Gesamthochschule Wuppertal, 1991.
- [56] M. Kolb and W. Thiel, *J. Comput. Chem.*, 1993, **14**, 37–44.
- [57] W. Weber, *Ph.D. thesis*, Universität Zürich, 1996.
- [58] W. Weber and W. Thiel, *Theor. Chem. Acc.*, 2000, **103**, 495–506.
- [59] M. Scholten, *Ph.D. thesis*, Heinrich-Heine-Universität Düsseldorf, 2003.
- [60] P. O. Dral, X. Wu, L. Spörkel, A. Koslowski, W. Weber, R. Steiger, M. Scholten and W. Thiel, *J. Chem. Theory Comput.*, 2016, **12**, 1082–1096.
- [61] M. R. Silva-Junior and W. Thiel, *J. Chem. Theory Comput.*, 2010, **6**, 1546–1564.
- [62] I. Dokukina, C. M. Marian and O. Weingart, *Photochem. Photobiol.*, 2017, **93**, 1345–1355.

- [63] L. Gagliardi, D. G. Truhlar, G. L. Manni, R. K. Carlson, C. E. Hoyer and J. L. Bao, *Acc. Chem. Res.*, 2016, **50**, 66–73.
- [64] M. Roemelt, D. Maganas, S. DeBeer and F. Neese, *J. Chem. Phys.*, 2013, **138**, 204101.
- [65] D. Maganas, S. DeBeer and F. Neese, *Inorg. Chem.*, 2014, **53**, 6374–6385.
- [66] S. Grimme and M. Waletzke, *J. Chem. Phys.*, 1999, **111**, 5645–5655.
- [67] C. M. Marian, A. Heil and M. Kleinschmidt, *WIREs Comput. Mol. Sci.*, 2019, e1394.
- [68] S. Grimme, *Chem. Phys. Lett.*, 1996, **259**, 128–137.
- [69] M. Kleinschmidt, C. M. Marian, M. Waletzke and S. Grimme, *J. Chem. Phys.*, 2009, **130**, 044708.
- [70] M. Kleinschmidt, J. Tatchen and C. M. Marian, *J. Comput. Chem.*, 2002, **23**, 824–833.
- [71] M. Kleinschmidt and C. M. Marian, *Chem. Phys.*, 2005, **311**, 71–79.
- [72] M. Kleinschmidt, J. Tatchen and C. M. Marian, *J. Chem. Phys.*, 2006, **124**, 124101.
- [73] I. Lyskov, M. Kleinschmidt and C. M. Marian, *J. Chem. Phys.*, 2016, **144**, 034104.
- [74] V. Rai-Constapel, M. Kleinschmidt, S. Salzmann, L. Serrano-Andrés and C. M. Marian, *Phys. Chem. Chem. Phys.*, 2010, **12**, 9320.
- [75] J. P. Götze and W. Thiel, *Chem. Phys.*, 2013, **415**, 247–255.
- [76] C. M. Marian, S. Nakagawa, V. Rai-Constapel, B. Karasulu and W. Thiel, *J. Phys. Chem. B*, 2014, **118**, 1743–1753.
- [77] V. Rai-Constapel, T. Villnow, G. Ryseck, P. Gilch and C. M. Marian, *J. Phys. Chem. A*, 2014, **118**, 11708–11717.
- [78] J. Wilke, M. Wilke, C. Brand, J. D. Spiegel, C. M. Marian and M. Schmitt, *J. Phys. Chem. A*, 2017, **121**, 1597–1606.
- [79] S. Maity, A. Gelessus, V. Daskalakis and U. Kleinekathöfer, *Chem. Phys.*, 2019, **526**, 110439.
- [80] A. Reiffers, C. T. Ziegenbein, L. Schubert, J. Diekmann, K. A. Thom, R. Kühnemuth, A. Griesbeck, O. Weingart and P. Gilch, *Phys. Chem. Chem. Phys.*, 2019, **21**, 4839–4853.
- [81] M. Kleinschmidt, C. van Wüllen and C. M. Marian, *J. Chem. Phys.*, 2015, **142**, 094301.
- [82] A. Heil, K. Gollnisch, M. Kleinschmidt and C. M. Marian, *Mol. Phys.*, 2015, 1–16.
- [83] J. D. Spiegel, M. Kleinschmidt, A. Larbig, J. Tatchen and C. M. Marian, *J. Chem. Theory Comput.*, 2015, **11**, 4316–4327.

- [84] J. D. Spiegel, I. Lyskov, M. Kleinschmidt and C. M. Marian, *Chem. Phys.*, 2017, **482**, 265–276.
- [85] N. Elfers, I. Lyskov, J. D. Spiegel and C. M. Marian, *J. Phys. Chem. C*, 2016, **120**, 13901–13910.
- [86] D. Escudero and W. Thiel, *J. Chem. Phys.*, 2014, **140**, 194105.
- [87] V. Jovanović, I. Lyskov, M. Kleinschmidt and C. M. Marian, *Mol. Phys.*, 2016, **115**, 109–137.
- [88] B. Shi, D. Nachtigallová, A. J. A. Aquino, F. B. C. Machado and H. Lischka, *Phys. Chem. Chem. Phys.*, 2019, **21**, 9077–9088.
- [89] B. Shi, D. Nachtigallová, A. J. A. Aquino, F. B. C. Machado and H. Lischka, *J. Chem. Phys.*, 2019, **150**, 124302.
- [90] B. Shi, D. Nachtigallová, A. J. A. Aquino, F. B. C. Machado and H. Lischka, *J. Phys. Chem. Lett.*, 2019, 5592–5597.
- [91] A. Warshel and M. Levitt, *J. Mol. Biol.*, 1976, **103**, 227–249.
- [92] S. Salzmann, M. R. Silva-Junior, W. Thiel and C. M. Marian, *J. Phys. Chem. B*, 2009, **113**, 15610–15618.
- [93] I. Dokukina and O. Weingart, *Phys. Chem. Chem. Phys.*, 2015, **17**, 25142–25150.
- [94] S. Nakagawa, O. Weingart and C. M. Marian, *J. Phys. Chem. B*, 2017, **121**, 9583–9596.
- [95] K. Aidas, C. Angeli, K. L. Bak, V. Bakken, R. Bast, L. Boman, O. Christiansen, R. Cimraglia, S. Coriani, P. Dahle, E. K. Dalskov, U. Ekström, T. Enevoldsen, J. J. Eriksen, P. Ettenhuber, B. Fernández, L. Ferrighi, H. Fliegl, L. Frediani, K. Hald, A. Halkier, C. Hättig, H. Heiberg, T. Helgaker, A. C. Hennum, H. Hettema, E. Hjerstenæs, S. Høst, I.-M. Høyvik, M. F. Iozzi, B. Jansík, H. J. Aa. Jensen, D. Jonsson, P. Jørgensen, J. Kauczor, S. Kirpekar, T. Kjærgaard, W. Klopper, S. Knecht, R. Kobayashi, H. Koch, J. Kongsted, A. Krapp, K. Kristensen, A. Ligabue, O. B. Lutnæs, J. I. Melo, K. V. Mikkelsen, R. H. Myhre, C. Neiss, C. B. Nielsen, P. Norman, J. Olsen, J. M. H. Olsen, A. Osted, M. J. Packer, F. Pawłowski, T. B. Pedersen, P. F. Provasi, S. Reine, Z. Rinkevicius, T. A. Ruden, K. Ruud, V. V. Rybkin, P. Sałek, C. C. M. Samson, A. S. de Merás, T. Saue, S. P. A. Sauer, B. Schimelpfennig, K. Sneskov, A. H. Steindal, K. O. Sylvester-Hvid, P. R. Taylor, A. M. Teale, E. I. Tellgren, D. P. Tew, A. J. Thorvaldsen, L. Thøgersen, O. Vahtras, M. A. Watson, D. J. D. Wilson, M. Ziolkowski and H. Ågren, *WIREs Comput. Mol. Sci.*, 2014, **4**, 269–284.
- [96] F. Neese, *WIREs Comput. Mol. Sci.*, 2012, **2**, 73–78.
- [97] F. Neese, *WIREs Comput. Mol. Sci.*, 2018, **8**, e1327.
- [98] J. Franck and E. G. Dymond, *Trans. Faraday Soc.*, 1926, **21**, 536.

- [99] E. Condon, *Phys. Rev.*, 1926, **28**, 1182–1201.
- [100] E. U. Condon, *Phys. Rev.*, 1928, **32**, 858–872.
- [101] M. Kasha, *Discuss. Faraday Soc.*, 1950, **9**, 14.
- [102] M. Sauer, J. Hofkens and J. Enderlein, *Handbook of Fluorescence Spectroscopy and Imaging*, WILEY-VCH Verlag GmbH & Co. KGaA, Weinheim, 2011.
- [103] L. H. Thomas, *Math. Proc. Cambridge Philos. Soc.*, 1927, **23**, 542–548.
- [104] E. Fermi, *Z. Phys.*, 1928, **48**, 73–79.
- [105] P. A. M. Dirac, *Math. Proc. Cambridge Philos. Soc.*, 1930, **26**, 376–385.
- [106] D. Cremer, *Mol. Phys.*, 2001, **99**, 1899–1940.
- [107] J. C. Slater, *Phys. Rev.*, 1951, **81**, 385–390.
- [108] P. Hohenberg and W. Kohn, *Phys. Rev.*, 1964, **136**, B864–B871.
- [109] W. Kohn, A. D. Becke and R. G. Parr, *J. Phys. Chem.*, 1996, **100**, 12974–12980.
- [110] W. Kohn and L. J. Sham, *Phys. Rev.*, 1965, **140**, A1133–A1138.
- [111] R. G. Parr and W. Yang, *Density-Functional Theory of Atoms and Molecules*, Oxford University Press (New York), 1989.
- [112] Á. Nagy, *Phys. Rep.*, 1998, **298**, 1–79.
- [113] K. Jankowski, K. Nowakowski, I. Grabowski and J. Wasilewski, *J. Chem. Phys.*, 2009, **130**, 164102.
- [114] D. Maurice and M. Head-Gordon, *Int. J. Quantum Chem.*, 1995, **56**, 361–370.
- [115] M. Roemelt and F. Neese, *J. Phys. Chem. A*, 2013, **117**, 3069–3083.
- [116] M. Filatov and S. Shaik, *Chem. Phys. Lett.*, 1998, **288**, 689–697.
- [117] M. Filatov and S. Shaik, *J. Chem. Phys.*, 1999, **110**, 116–125.
- [118] C. C. J. Roothaan, *Rev. Mod. Phys.*, 1960, **32**, 179–185.
- [119] M. Schulte and I. Frank, *Chem. Phys.*, 2010, **373**, 283–288.
- [120] F. Illas, I. de P. R. Moreira, J. M. Bofill and M. Filatov, *Theor. Chem. Acc.*, 2006, **116**, 587–597.
- [121] J. C. Stoddart, N. H. March and D. Wiid, *Int. J. Quantum Chem.*, 1971, **5**, 745–762.
- [122] U. von Barth and L. Hedin, *J. Phys. C: Solid State Phys.*, 1972, **5**, 1629–1642.
- [123] O. Gunnarsson and B. I. Lundqvist, *Phys. Rev. B*, 1976, **13**, 4274–4298.
- [124] C. R. Jacob and M. Reiher, *Int. J. Quantum Chem.*, 2012, **112**, 3661–3684.

- [125] L. Goerigk, A. Hansen, C. Bauer, S. Ehrlich, A. Najibi and S. Grimme, *Phys. Chem. Chem. Phys.*, 2017, **19**, 32184–32215.
- [126] A. D. Becke, *J. Chem. Phys.*, 1993, **98**, 1372–1377.
- [127] C. Lee, W. Yang and R. G. Parr, *Phys. Rev. B*, 1988, **37**, 785.
- [128] A. D. Becke, *Phys. Rev. A*, 1988, **38**, 3098–3100.
- [129] S. H. Vosko, L. Wilk and M. Nusair, *Can. J. Phys.*, 1980, **58**, 1200–1211.
- [130] C. Adamo and V. Barone, *J. Chem. Phys.*, 1999, **110**, 6158–6170.
- [131] J. P. Perdew, K. Burke and M. Ernzerhof, *Phys. Rev. Lett.*, 1996, **77**, 3865.
- [132] J. P. Perdew, K. Burke and M. Ernzerhof, *Phys. Rev. Lett.*, 1997, **78**, 1396–1396.
- [133] A. Heil, M. Kleinschmidt and C. M. Marian, *J. Chem. Phys.*, 2018, **149**, 164106.
- [134] A. Heil and C. M. Marian, *Inorg. Chem.*, 2019, **58**, 6123–6136.
- [135] H. S. Yu, X. He, S. L. Li and D. G. Truhlar, *Chem. Sci.*, 2016, **7**, 5032–5051.
- [136] H. S. Yu, X. He, S. L. Li and D. G. Truhlar, *Chem. Sci.*, 2016, **7**, 6278–6279.
- [137] A. Heil and C. M. Marian, *Phys. Chem. Chem. Phys.*, 2019, **accepted**, DOI:10.1039/c9cp04244j.
- [138] E. A. Hylleraas, *Z. Phys.*, 1928, **48**, 469–494.
- [139] D. Cremer, *WIREs Comput. Mol. Sci.*, 2013, **3**, 482–503.
- [140] P.-O. Löwdin, *Phys. Rev.*, 1955, **97**, 1509–1520.
- [141] I. Shavitt, in *Methods of Electronic Structure Theory*, ed. H. F. S. III, Plenum Press, 1977, ch. The Method of Configuration Interaction, pp. 189–275.
- [142] O. Sinanoğlu, *Proc. Natl. Acad. Sci. U.S.A.*, 1961, **47**, 1217–1226.
- [143] H. J. Silverstone and O. Sinanoğlu, *J. Chem. Phys.*, 1966, **44**, 3608–3617.
- [144] C. Hollister and O. Sinanoglu, *J. Am. Chem. Soc.*, 1966, **88**, 13–21.
- [145] D. Cremer, M. Filatov, V. Polo, E. Kraka and S. Shaik, *Int. J. Mol. Sci.*, 2002, **3**, 604–638.
- [146] H. Weyl, *Z. Phys.*, 1927, **46**, 1–46.
- [147] J. Mulder, *Mol. Phys.*, 1966, **10**, 479–488.
- [148] J. Paldus, *J. Chem. Phys.*, 1974, **61**, 5321–5330.
- [149] I. Shavitt, *Mol. Phys.*, 1998, **94**, 3–17.
- [150] R. W. Wetmore and G. A. Segal, *Chem. Phys. Lett.*, 1975, **36**, 478–483.
- [151] G. A. Segal, R. W. Wetmore and K. Wolf, *Chem. Phys.*, 1978, **30**, 269–297.

- [152] R. J. Buenker, S. D. Peyerimhoff and W. Butscher, *Mol. Phys.*, 1978, **35**, 771–791.
- [153] A. Schäfer, H. Horn and R. Ahlrichs, *J. Chem. Phys.*, 1992, **97**, 2571–2577.
- [154] D. Andrae, U. Häußermann, M. Dolg, H. Stoll and H. Preuß, *Theor. Chim. Acta*, 1990, **77**, 123–141.
- [155] Z. Li and W. Liu, *J. Chem. Theory Comput.*, 2015, **12**, 238–260.
- [156] *IUPAC. Compendium of Chemical Terminology, 2nd ed. (the "Gold Book")*, ed. A. D. McNaught and A. Wilkinson, Blackwell Scientific Publications, Oxford, 2nd edn., 1997, ch. photoelectron spectroscopy (PES).
- [157] A. Einstein, *Ann. Phys.*, 1905, **322**, 132–148.
- [158] F. I. Vilesov, B. L. Kurbatov and A. N. Terenin, *Sov. Phys. Dokl.*, 1961, **6**, 490.
- [159] D. W. Turner and M. I. A. Jobory, *J. Chem. Phys.*, 1962, **37**, 3007–3008.
- [160] C. Nordling, E. Sokolowski and K. Siegbahn, *Phys. Rev.*, 1957, **105**, 1676–1677.
- [161] C. R. Brundle and D. W. Turner, *Proc. Royal Soc. A*, 1968, **307**, 27–36.
- [162] V. Blanchet and A. Stolow, *J. Chem. Phys.*, 1998, **108**, 4371–4374.
- [163] A. Assion, M. Geisler, J. Helbing, V. Seyfried and T. Baumert, *Phys. Rev. A*, 1996, **54**, R4605–R4608.
- [164] T. Shida, Y. Nosaka and T. Kato, *J. Phys. Chem.*, 1978, **82**, 695–698.
- [165] M. V. Ivanov, D. Wang, D. Zhang, R. Rathore and S. A. Reid, *Phys. Chem. Chem. Phys.*, 2018, **20**, 25615–25622.
- [166] *Dalton, a molecular electronic structure program, Release v2015.0 (2015)*, see <http://daltonprogram.org>.
- [167] *Dalton, a molecular electronic structure program, Release v2016.1 (2016)*, see <http://daltonprogram.org>.
- [168] *Dalton, a molecular electronic structure program, Release v2018.0 (2018)*, see <http://daltonprogram.org>.
- [169] A. Heil and C. M. Marian, *J. Chem. Phys.*, 2017, **147**, 194104.
- [170] J. A. Nelder and R. Mead, *Comput. J.*, 1965, **7**, 308–313.
- [171] A. Springer, *M.Sc. thesis*, Heinrich-Heine-Universität Düsseldorf, 2016.
- [172] H. U. Güdel and C. J. Ballhausen, *Theor. Chim. Acta*, 1972, **25**, 331–337.
- [173] A. Bossi, A. F. Rausch, M. J. Leitl, R. Czerwieniec, M. T. Whited, P. I. Djurovich, H. Yersin and M. E. Thompson, *Inorg. Chem.*, 2013, **52**, 12403–12415.
- [174] J. Brooks, Y. Babayan, S. Lamansky, P. I. Djurovich, I. Tsyba, R. Bau and M. E. Thompson, *Inorg. Chem.*, 2002, **41**, 3055–3066.

- [175] A. Swain, B. Cho, R. Gautam, C. J. Curtis, E. Tomat and V. Huxter, *J. Phys. Chem. B*, 2019, **123**, 5524–5535.
- [176] R. Gautam, J. J. Loughrey, A. V. Astashkin, J. Shearer and E. Tomat, *Angew. Chem. Int. Ed.*, 2015, **54**, 14894–14897.
- [177] F. Ciccullo, N. Gallagher, O. Geladari, T. Chasse, A. Rajca and M. Casu, *ACS Appl. Mater. Interfaces*, 2016, **8**, 1805–1812.
- [178] A. A. Berezin, C. P. Constantinides, C. Drouza, M. Manoli and P. A. Koutentis, *Org. Lett.*, 2012, **14**, 5586–5589.
- [179] J. A. Grant, Z. Lu, D. E. Tucker, B. M. Hockin, D. S. Yufit, M. A. Fox, R. Katakya, V. Chechik and A. C. O'Donoghue, *Nat. Commun.*, 2017, **8**, 1–6.
- [180] A. C. Savva, S. I. Mirallai, G. A. Zissimou, A. A. Berezin, M. Demetriades, A. Kourtellaris, C. P. Constantinides, C. Nicolaidis, T. Trypiniotis and P. A. Koutentis, *J. Org. Chem.*, 2017, **82**, 7564–7575.
- [181] J. Z. Low, G. Kladnik, L. L. Patera, S. Sokolov, G. Lovat, E. Kumarasamy, J. Repp, L. M. Campos, D. Cvetko, A. Morgante and L. Venkataraman, *Nano Lett.*, 2019, **19**, 2543–2548.
- [182] K. A. Hutchison, G. Srdanov, R. Menon, J.-C. P. Gabriel, B. Knight and F. Wudl, *J. Am. Chem. Soc.*, 1996, **118**, 13081–13082.
- [183] M. Demetriou, A. A. Berezin, P. A. Koutentis and T. Krasia-Christoforou, *Polym. Int.*, 2014, **63**, 674–679.
- [184] J. Areephong, K. Mattson, N. Treat, S. Poelma, J. Kramer, H. Sprafke, A. Latimer, J. R. de Alaniz and C. Hawker, *Polym. Chem.*, 2016, **7**, 370–374.
- [185] M. J. Frisch, G. W. Trucks, H. B. Schlegel, G. E. Scuseria, M. A. Robb, J. R. Cheeseman, G. Scalmani, V. Barone, G. A. Petersson, H. Nakatsuji, X. Li, M. Caricato, A. V. Marenich, J. Bloino, B. G. Janesko, R. Gomperts, B. Mennucci, H. P. Hratchian, J. V. Ortiz, A. F. Izmaylov, J. L. Sonnenberg, D. Williams-Young, F. Ding, F. Lipparini, F. Egidi, J. Goings, B. Peng, A. Petrone, T. Henderson, D. Ranasinghe, V. G. Zakrzewski, J. Gao, N. Rega, G. Zheng, W. Liang, M. Hada, M. Ehara, K. Toyota, R. Fukuda, J. Hasegawa, M. Ishida, T. Nakajima, Y. Honda, O. Kitao, H. Nakai, T. Vreven, K. Throssell, J. A. Montgomery, Jr., J. E. Peralta, F. Ogliaro, M. J. Bearpark, J. J. Heyd, E. N. Brothers, K. N. Kudin, V. N. Staroverov, T. A. Keith, R. Kobayashi, J. Normand, K. Raghavachari, A. P. Rendell, J. C. Burant, S. S. Iyengar, J. Tomasi, M. Cossi, J. M. Millam, M. Klene, C. Adamo, R. Cammi, J. W. Ochterski, R. L. Martin, K. Morokuma, O. Farkas, J. B. Foresman and D. J. Fox, *Gaussian 16 Revision B.01*, 2016, Gaussian Inc. Wallingford CT.
- [186] D. Rappoport and F. Furche, *J. Chem. Phys.*, 2010, **133**, 134105.
- [187] O. Vahtras, J. Almlöf and M. Feyereisen, *Chem. Phys. Lett.*, 1993, **213**, 514–518.
- [188] F. Weigend and M. Häser, *Theor. Chem. Acc.*, 1997, **97**, 331–340.

- [189] F. Weigend, M. Häser, H. Patzelt and R. Ahlrichs, *Chem. Phys. Lett.*, 1998, **294**, 143–152.
- [190] A. Hellweg and D. Rappoport, *Phys. Chem. Chem. Phys.*, 2015, **17**, 1010–1017.
- [191] S. Miertuš, E. Scrocco and J. Tomasi, *Chem. Phys.*, 1981, **55**, 117–129.
- [192] M. Etinski, J. Tatchen and C. M. Marian, *J. Chem. Phys.*, 2011, **134**, 154105.
- [193] M. Etinski, J. Tatchen and C. M. Marian, *Phys. Chem. Chem. Phys.*, 2014, **16**, 4740.
- [194] A. Baiardi, J. Bloino and V. Barone, *J. Chem. Theory Comput.*, 2013, **9**, 4097–4115.
- [195] A. Heckmann, S. Dümmler, J. Pauli, M. Margraf, J. Köhler, D. Stich, C. Lambert, I. Fischer and U. Resch-Genger, *J. Phys. Chem. C*, 2009, **113**, 20958–20966.
- [196] S. Dapperheld, E. Steckhan, K.-H. G. Brinkhaus and T. Esch, *Chem. Ber.*, 1991, **124**, 2557–2567.
- [197] *TURBOMOLE V7.1 2016, a development of University of Karlsruhe and Forschungszentrum Karlsruhe GmbH, 1989-2007, TURBOMOLE GmbH, since 2007; available from*
<http://www.turbomole.com>.
- [198] F. Furche and R. Ahlrichs, *J. Chem. Phys.*, 2002, **117**, 7433–7447.
- [199] J. Neugebauer, M. Reiher, C. Kind and B. A. Hess, *J. Comput. Chem.*, 2002, **23**, 895–910.
- [200] G. Igel-Mann, H. Stoll and H. Preuss, *Mol. Phys.*, 1988, **65**, 1321–1328.
- [201] D. Dombrowski, private communication.
- [202] S. Grimme, S. Ehrlich and L. Goerigk, *J. Comput. Chem.*, 2011, **32**, 1456–1465.
- [203] T. Haj Hassani Sohi, *Bachelor's Thesis*, Heinrich-Heine-Universität Düsseldorf, 2018.
- [204] Y. Beldjoudi, *Ph.D. thesis*, University of Windsor, 2016.
- [205] A. Ipatov, F. Cordova, L. J. Doriol and M. E. Casida, *J. Mol. Struct. THEOCHEM*, 2009, **914**, 60–73.

Included Papers

Reproduced from [169], with the permission of AIP Publishing.

THE JOURNAL OF CHEMICAL PHYSICS **147**, 194104 (2017)



DFT/MRCI Hamiltonian for odd and even numbers of electrons

Adrian Heil and Christel M. Marian^{a)}

Institute of Theoretical and Computational Chemistry, Heinrich-Heine-University Düsseldorf, Universitätsstraße 1, 40225 Düsseldorf, Germany

(Received 4 September 2017; accepted 30 October 2017; published online 16 November 2017)

DFT/MRCI is a well-established method of Grimme and Waletzke [J. Chem. Phys. **111**, 5645 (1999)] combining density functional theory and multireference configuration interaction. It was later redesigned by Lyskov, Kleinschmidt, and Marian [J. Chem. Phys. **144**, 034104 (2016)] to provide a better treatment of bi-chromophores while treating all other systems as well as Grimme's version did by computing individual energy shifts for each state function of a configuration. But all previous operators lack the ability to compute states with an odd number of electrons (doublet and quartet states). Here we present a general Hamiltonian based on Lyskov's redesign which calculates excited singlet, doublet, triplet, and quartet states of systems that have up to one open shell in the parent determinant. The multiplicity-independent correction parameters provide an extra correction for the open shell in the parent determinant. The Hamiltonian in combination with two parameter sets for different selection thresholds has been tested and compared to experimental vertical excitation and ionization energies yielding similar statistics for all multiplicities with a root mean square deviation smaller than 0.2 eV while maintaining the good computational performance of the Hamiltonians of Grimme and Lyskov. *Published by AIP Publishing.* <https://doi.org/10.1063/1.5003246>

I. INTRODUCTION

The DFT/MRCI method is a powerful method that shows great efficiency for calculating excited states. It combines density functional theory (DFT), which gives generally good results in systems where the dynamic electron correlation is the dominating part of the electron correlation,¹ with multireference configuration interaction (MRCI) which provides non-dynamic correlation.^{2–5} Kohn-Sham orbitals are used to construct configuration state functions (CSFs) and to modify the MRCI matrix elements by means of Coulomb-like and exchange-like integrals. In the original version,³ different parameter sets were used for singlet and triplet calculations. DFT/MRCI has been shown to work well with excitations from one-electron transitions⁶ and even certain types of double excitations which are ubiquitous in extended π -systems like polyenes⁷ and mini-carotenes.⁸ However, the original version is problematic for electronic states that are mainly characterized by four open-shell configurations, which is caused by an inconsistent parameterization of singlet and triplet multiplicities.⁹ This inconsistency also leads to artificially low-lying states when calculating aromatic compounds containing a nitro group.¹⁰ Lyskov *et al.*⁹ redesigned the Hamiltonian to treat those electronic states as well as the electronic states of dimers and bichromophores, which play an important role in excitation energy transfer¹¹ and singlet fission.¹²

The advantage of DFT/MRCI is its fast computational speed combined with a root mean square deviation (RMSD)

smaller than 0.2 eV,^{3,9} which makes it possible to calculate excited states of large molecules. One important application is the investigation of organic light emitting diodes (OLEDs), which can be computed via DFT/MRCI with a high accuracy despite being large systems, often containing transition metals as a center.^{13–15} Closed-shell emitters experience spin statistics (25% singlet, 75% triplet) at the electron-hole-recombination. In conventional fluorescence emitters containing only light atoms, the internal quantum yield is 25% at most due to non-radiating decay of the triplets. Introducing heavy atoms leads to phosphorescence from the excited triplet state through spin-orbit coupling, thus increasing the internal quantum yield up to 100%.¹⁶ Alternatively, internal high quantum yields close to 1 can be reached by singlet harvesting in thermally activated delayed fluorescence (TADF) which typically are Cu(I) complexes or metal-free donor-acceptor systems.^{17,18} A major disadvantage of phosphorescent and TADF emitters is their long radiative lifetime (typically in the microsecond regime) which makes them sensitive to photodegradation and other quenching processes.

A different class of molecules that has been recently proposed as a new kind of OLED emitter are persistent radicals which do not experience spin statistics like closed-shell emitters do.¹⁹ In those systems, both the ground state and excited states are doublets, and relaxation to a quartet would require unpairing of an electron pair.²⁰ There are many families of stable radicals, for example, those based on triphenylmethyl, phenalenyl, nitroxide, verdazyl, and dithiazolyl.²¹ Not many of them exhibit fluorescence due to quenching by the radicals itself and most of those that do are based on triaryl methyl $\text{Ar}_3\text{C}^\bullet$.^{19,22,23} Other examples are fluorescent systems based on triphenylmethyl like TTM-1Cz.¹⁹ This system contains

^{a)}Electronic mail: Christel.Marian@hhu.de

343 electrons, so a method like DFT/MRCI that can handle excited states of open-shell molecules of this size with the same performance in terms of computational speed and accuracy is desirable. There are developments that aim to reach this goal using either unrestricted time-dependent density functional theory (TD-DFT) or spin restricted TD-DFT, but while there have been some improvements by using spin restricted TD-DFT, difficulties like excitation from any occupied orbital to the vacant shell or the limitation to single excitations remain.^{24,25} Other methods like MRCISD-Q or EOM-CCSD have limitations to small- to medium-sized systems due to their high computational cost.

The DFT/MRCI method in its current state is dependent on a closed-shell anchor configuration based on restricted Kohn-Sham BHandHLYP²⁶ orbitals and parameterized for electronic states with an even number of electrons. If one wants to extend the DFT/MRCI method to open-shell systems with a one-open-shell anchor configuration, three options come to mind: (i) taking the closed-shell anchor and adding or removing one electron, (ii) using unrestricted Kohn-Sham orbitals, and (iii) using restricted open-shell Kohn-Sham (ROKS) orbitals. Attempts to use option (i) fail badly because adding or removing electrons significantly changes the DFT orbital energies on which DFT/MRCI is dependent. Option (ii) is not attractive because unrestricted DFT (UDFT) orbitals require a different CI implementation, namely, unrestricted configuration interaction (UCI), which is not fully developed and leads to rather bad results.²⁷ Additionally, the resulting wave functions are not eigenfunctions of the \hat{S}^2 operator. Thus, the only viable option is (iii). ROKS orbitals provide spin-restricted orbitals in a doubly occupied case with the addition of an open shell for the unpaired electron(s).

The aim of the present work is to extend the operator developed by Lyskov *et al.* for systems that need an open-shell anchor configuration in a way that all multiplicities can be calculated using the same parameters and Hamiltonian without losing the advantages of high computational efficiency and reliability.

II. THEORY

Using restricted open-shell Kohn-Sham DFT proves to be a viable option for generating the orbitals needed for the DFT/MRCI method but has the disadvantage that ROKS is not implemented in many programs and needs additional corrections in DFT/MRCI.⁵ The advantages are that the resulting wave functions are eigenfunctions of the \hat{S}^2 operator and are easily implemented in our current MRCI framework. In this method, all doubly occupied orbitals are spin-restricted orbitals, and for the open-shell spin orbital, an average occupation is assumed.²⁸

The Hamiltonian in the second quantization with \hat{E}_i^j as a one-electron excitation operator is

$$\hat{\mathcal{H}} = \sum_{ij} h_{ij} \hat{E}_i^j + \frac{1}{2} \sum_{ijkl} V_{ijkl} (\hat{E}_i^j \hat{E}_k^l - \delta_{jk} \hat{E}_i^l). \quad (1)$$

With \bar{w}_i as the occupation of the i -th component of the reference vector, the Hamiltonian can be reordered to

$$\begin{aligned} \hat{\mathcal{H}} = & E_{SCF} - \sum_i F_{ii} \bar{w}_i + \frac{1}{2} \sum_{ij} \left(V_{ijij} - \frac{1}{2} V_{ijji} \right) \bar{w}_i \bar{w}_j \\ & + \sum_{ij} F_{ij} \hat{E}_i^j - \sum_{ijk} \left(V_{ikjk} - \frac{1}{2} V_{ikkj} \right) \bar{w}_k \hat{E}_i^j \\ & + \frac{1}{2} \sum_{ijkl} V_{ijkl} (\hat{E}_i^j \hat{E}_k^l - \delta_{jk} \hat{E}_i^l) \end{aligned} \quad (2)$$

with $V_{ijij} = \langle ij|ij \rangle$ as a Coulomb-like integral and $V_{ijji} = \langle ij|ji \rangle$ as an exchange-like integral.

Since matrix elements between configurations that differ in more than two occupations are zero, three different cases occur: two-electron and one-electron differences between two configurations $|w\rangle$ and $|w'\rangle$ and an equivalent spatial occupation (diagonal). The expressions for one-electron and two-electron differences have been published by Wetmore and Segal and can be found in their articles.^{29,30} The CI matrix is diagonal dominant and we therefore focus on the diagonal matrix elements H_{nn} ,

$$\begin{aligned} H_{nn} = & E_{SCF} + \sum_i F_{ii} \Delta_i + \frac{1}{2} \sum_{i \neq j} V_{ijij} \Delta_i \Delta_j \\ & + \frac{1}{2} \sum_{i \neq j} V_{ijji} \left(-\frac{1}{2} \Delta_i \Delta_j + \frac{1}{2} w_i w_j - w_i + \eta_{ij}^i \right) \\ & + \frac{1}{2} \sum_i V_{iiii} \left(\frac{1}{2} \Delta_i^2 + \frac{1}{2} w_i w_i - w_i \right), \end{aligned} \quad (3)$$

where $\Delta_i = w_i - \bar{w}_i$ is the occupation difference between the configuration and parent determinant and $\eta_{ij}^i = \langle \mathbf{w} | E_i^j E_j^i | \mathbf{w}' \omega' \rangle = (E_j^i | \mathbf{w} \rangle)^\dagger \cdot E_j^i | \mathbf{w}' \omega' \rangle$ is the spin coupling.

Like in the original DFT/MRCI ansatz by Grimme and Waletzke as well as Lyskov's redesign, the BHandHLYP²⁶ functional with 50% Hartree-Fock exchange was found to be appropriate if mainly excited states are considered,³

$$E_{XC}^{BHLYP} = 0.5 E_X^{HF} + 0.5 (E_X^{B88} + E_X^{LDA}) + E_C^{LYP}. \quad (4)$$

For convenience, the one-electron basis from which the configuration space is generated is canonical. In contrast to Hartree-Fock, the Fock matrix in DFT has the form

$$F_{ij}^{KS} = h_{ij} + \left\langle i \left| \frac{\delta E_{xc}[\rho]}{\delta \phi} \right| j \right\rangle + \sum_k V_{ikjk} \bar{w}_k. \quad (5)$$

In the DFT/MRCI formalism, the Kohn-Sham orbital energies are used instead of the diagonal elements of the Fock matrix. The parameters were chosen in the fashion outlined by Lyskov *et al.*⁹ The resulting operator with its respective Coulomb and exchange shifts was built from the configuration energies of doublet and quartet states in Eq. (3). We found the resulting Coulomb shift to be identical to the one for a closed-shell anchor configuration save for an additional correction to a diagonal Coulomb-like integral V_{ssss} with s as the open shell in the parent determinant. In the exchange shift, a similar picture has emerged. The shift matches the one developed for a closed-shell anchor configuration with the addition of open-shell specific correction terms. In both the Coulomb and exchange shifts, the additional terms for open shells in the parent determinant have no effect in the case of a system

without open shells. Thus the operator can be used for systems with odd and even numbers of electrons in the same way. The resulting Hamiltonian for diagonal elements is then

$$\begin{aligned} \langle \boldsymbol{w} | \hat{\mathcal{H}}^{\text{DFT}} - E^{\text{DFT}} | \boldsymbol{w} \rangle = & \langle \boldsymbol{w} | \hat{\mathcal{H}} - E^{\text{HF}} | \boldsymbol{w} \rangle \\ & - \sum_c^{n_{\text{exc}}} (F_{cc}^{\text{HF}} - F_{cc}^{\text{KS}}) \\ & + \sum_a^{n_{\text{exc}}} (F_{aa}^{\text{HF}} - F_{aa}^{\text{KS}}) \\ & + \Delta E_{\text{coul}} - \Delta E_{\text{exch}}. \end{aligned} \quad (6)$$

In relation to Lyskov's Hamiltonian, the Coulomb shift has to be extended to correct the aforementioned diagonal integral V_{ssss} , which has to be considered, as can be seen from Eq. (3), whenever a shell is completely filled or completely emptied. In the case of a closed-shell determinant, this happens when double creation or double annihilation acts on the same shell. In the case of the open shell in the parent determinant, this happens with every occupation change. But since only a single creation or annihilation can occur, only half of the integral is added to the configuration energy. Therefore, only half of that integral needs to be corrected. The Coulomb shift is

$$\begin{aligned} \Delta E_{\text{coul}} = \text{PJ} \left(- \sum_{\substack{i,j \in c \\ i>j}} V_{ijij} - \sum_{\substack{i,j \in a \\ i>j}} V_{ijij} + \sum_{i \in c} \sum_{i \in a} V_{ijij} \right. \\ \left. + \frac{1}{2} \sum_{i \in s} V_{iiii} |\Delta w_i| \right). \end{aligned} \quad (7)$$

The other terms can be considered as electron-electron repulsion and hole-hole repulsion (first and second terms) and electron-hole attraction (third term).

For the exchange shift, we need additional terms to account for the different exchange interaction between the electron in the open shell in the parent determinant and annihilated/created electrons. For that reason, we need a different exchange shift than that for a closed-shell system,

$$\Delta E_{\text{exc}} = \text{PF} \left(\frac{1}{2} \sum_{i \in c} \sum_{j \in a} V_{ijij} - \sum_{\substack{i,j \in c \\ j \in s}} V_{ijij} - \sum_{\substack{i,j \in a \\ j \in s}} V_{ijij} + \sum_{\substack{i,j \in o \\ i>j}} V_{ijij} \eta_{ij}^{\text{ji}} \right). \quad (8)$$

The dynamic electron correlation is already treated by the Kohn-Sham operators in large parts, so the additional dynamic correlation added by MRCI leads to double counting. As introduced by Lyskov,⁹ one way to treat this occurrence is by means of damping the contributions of the coupled configurations by evaluating the vertical excitation energies of n-acenes and mini-n-carotenes with respect to different damping functions. The optimal form was found to be

$$H_{nn'} = \frac{p_1}{1 + (p_2 \cdot \boldsymbol{\epsilon})^5 \arctan(p_2 \cdot \boldsymbol{\epsilon})^5} H_{nn'}^{\text{CI}} \quad (9)$$

with a dependency on the energy difference $\boldsymbol{\epsilon}$, as in the original DFT/MRCI. In the case of two coupled degenerate configurations, the coupling is only scaled by the parameter p_1 . The energy difference is computed as a mean of the state energies when an electron configuration consists of more

than one CSF. As in the original work³ as well as Lyskov's redesign,⁹ the selection of important configurations is based on the estimation of the configuration energies. This is done by examining the energy difference between the sum of created and annihilated orbital energies in regard to the reference,

$$\boldsymbol{\epsilon} \approx \sum_{i \in c} F_{ii}^{\text{KS}} - \sum_{i \in a} F_{ii}^{\text{KS}}. \quad (10)$$

A configuration is included in the secular equation if the sum of the excitation energy of the highest root in the reference space and the energy cutoff δE_{sel} is higher than $\boldsymbol{\epsilon}$.

A. Additional corrections to the MRCI matrix elements

The calculation of CI matrix elements involves a diagonal Coulomb integral V_{iiii} in Eq. (3) in the case of completely emptying or filling the corresponding orbital i . In a closed-shell case, this means that the integral has a contribution to that matrix element in two cases:

- Orbital i is doubly occupied in the parent determinant and both electrons are annihilated in excitation;
- the orbital i is empty in the parent determinant and two electrons are created in excitation. Single excitation and thus creation or annihilation of one electron do not lead to a contribution of that integral to the matrix element.

But there is a difference in the case of open-shell orbitals in the parent determinant. Given the relevant part of Eq. (3), which is

$$\frac{1}{2} V_{iiii} \left(\frac{1}{2} \Delta w_i \Delta w_i + \frac{1}{2} w_i w_i - w_i \right) \quad (11)$$

with $\Delta w_i = w_i - \bar{w}_i$, w_i is the current occupation and \bar{w}_i is the occupation in the parent determinant, one can calculate the four cases for a closed-shell determinant, starting from a doubly occupied shell or an empty shell:

- case I: $w_i = 0, \bar{w}_i = 2 : \frac{1}{2} V_{iiii} (\frac{1}{2}(2) - 2 + \frac{1}{2}0^2 - 0) = V_{iiii}$,
- case II: $w_i = 1, \bar{w}_i = 2 : \frac{1}{2} V_{iiii} (\frac{1}{2}(1) - 2 + \frac{1}{2}1^2 - 1) = 0$,
- case III: $w_i = 1, \bar{w}_i = 0 : \frac{1}{2} V_{iiii} (\frac{1}{2}(1) - 0 + \frac{1}{2}1^2 - 1) = 0$,
- case IV: $w_i = 2, \bar{w}_i = 0 : \frac{1}{2} V_{iiii} (\frac{1}{2}(2) - 0 + \frac{1}{2}2^2 - 2) = V_{iiii}$.

It can be seen that only in double annihilation or double creation cases (I and IV), this integral contributes to the configuration energy. One would expect analogous results in open-shell cases, this means that single annihilation or single creation of the singly occupied orbital will lead to a contribution of this integral. And since it is only half of the annihilation/creation, one would expect that contribution to be half of that of the double annihilation/creation of the closed-shell case. But calculating the two cases leads to

- case V: $w_i = 0, \bar{w}_i = 1 : \frac{1}{2} V_{iiii} (\frac{1}{2}(1) - 2 + \frac{1}{2}0^2 - 0) = \frac{1}{4} V_{iiii}$;
- case VI: $w_i = 2, \bar{w}_i = 1 : \frac{1}{2} V_{iiii} (\frac{1}{2}(1) - 2 + \frac{1}{2}2^2 - 2) = \frac{1}{4} V_{iiii}$.

Hence, it can be seen that the contribution is half of what one would expect. Furthermore, the equation includes the occupation part of the configuration $\frac{1}{2} w_i w_i - w_i$, so there is one more case that has to be checked, namely, the case without any change in occupation,

- case VII: $w_i = 1, \bar{w}_i = 1 : \frac{1}{2} V_{iiii} (\frac{1}{2}(0) + \frac{1}{2}1^2 - 1) = -\frac{1}{4} V_{iiii}$.

So, according to Eq. (3), no change in occupation with respect to the parent determinant leads to lowering of the configuration energy by one-fourth of the corresponding diagonal integral of the open shell. This results in lowering of the configuration energy by $\frac{1}{4}V_{ssss}$ with s as the singly occupied orbital every time an open shell exists in the parent determinant, no matter if there is a change in the occupation of this orbital in the configuration or not. Because this problem occurs in all configurations of an open-shell system, vertical excitation energies are not affected. Therefore, as long as the number of electrons remains unchanged, only the total energy of all states is affected and each state is shifted by the same amount. This shift leads to an underestimation of ionization potentials as well as an overestimation of electron affinities. The contribution of $\frac{1}{4}V_{ssss}$ is typically about 1.5–3 eV for systems we tested. In order to avoid this problem, this contribution is added to the energy of every configuration when an open-shell anchor configuration is used.

B. Computational details

The Hamiltonian can handle in principle all multiplicities, but depending on the anchor configuration, a different approach was chosen for setting up the calculation and providing the one- and two-electron integrals.

For molecules with a closed-shell anchor configuration, the geometries were taken from Ref. 9. The ground state geometries of all molecules were calculated with Turbomole 6.5^{31,32} using the B3LYP functional³³ with Grimme’s D3 correction³⁴ including Becke and Johnson damping.³⁵ A valence split triple zeta basis with polarization functions def2-TZVPP³⁶ was used. The RKS orbitals used for integral computation for the DFT/MRCI run were generated using the TZVP basis set,³⁷ for all non-hydrogen atoms’ augmentation functions from the aug-cc-pVTZ basis set³⁸ were added.

For molecules with an open-shell anchor configuration, the geometries were optimized with Turbomole 7.1^{31,39} using the TZVP basis set.³⁷ Depending on the nature of the excitation, two schemes have been followed: (i) In the case of photoelectron spectra (PES) as an experimental reference, the neutral ground state was optimized using spin-restricted Kohn-Sham DFT. (ii) In the case of electronic absorption spectra (EAS), the molecules have an open-shell ground state that can be cationic, anionic, or neutral (radical). The optimization was carried out using UDFT with Grimme’s D3 correction.³⁴ The ROKS orbitals employed in the DFT/MRCI calculation were computed with Dalton 2016.1^{40,41} using the TZVP basis set.³⁷ Likewise, the singlet calculations used for the ionization potentials were carried out with Dalton 2016.1 to ensure a better comparability. For all non-hydrogen atoms, augmentation functions from the aug-cc-pVTZ basis set³⁸ were added with the exception of some cases. Those were either linear dependency issues during the calculation in some molecules which could be resolved using the def2-TZVPD basis set⁴² or size issues in the case of 2,3-benzofluorene⁺ and ovalene⁺ that led to the use of the SV(P) basis set.⁴³ For BeH, the basis set def2-QZVPP³⁶ was used because of a general problem calculating molecules containing beryllium in connection with diffuse functions.

The Dalton calculations have been carried out using an interface between Dalton and Turbomole (d2tm) we developed for this purpose. It provides a conversion between the files from a geometry optimization by Turbomole to Dalton input including symmetry and provides MO coefficients and orbital energies and occupation numbers in the Turbomole format after the Dalton calculation has finished.

For both RKS and ROKS, the resolution-of-the-identity (RI) approach^{3,44} was employed for the calculation of four index integrals V_{ijkl} using the TZVP auxiliary basis.⁴⁵ For the DFT/MRCI run, the reference space has been generated using all configurations with coefficients larger than 0.003, starting from a reference space of 9 or 10 electrons (depending on the occupancy of the highest occupied shell) in 10 orbitals with a selector $\delta E_{\text{sel}} = 1.0E_h$, unless the total number of electrons is fewer than 9 or 10.

C. Optimization of the parameter sets

For the optimization of the parameter sets, we used singlet, doublet, and triplet excitations of different molecules and compared them to a set of experimental reference energies. For singlet and triplet states, the set used by Lyskov *et al.*⁹ was employed. In this set, the excited states were first computed using Grimme’s standard DFT/MRCI (denoted as DFT/MRCI-S) as reference states (with reference CI vectors). For doublet states, we used MRCI with a Hartree-Fock reference^{2,8} to calculate reference CI vectors. The overlap with these reference vectors is used to ensure that the excited-state wave functions maintain an appropriate structure. The simplex algorithm⁴⁶ was used to minimize the RMS error of the new parameter set in combination with the new Hamiltonian by varying the different parameters independently and iteratively. The molecular structures of the fitting set as well as the experimental and computed energies can be found in Table SII of the [supplementary material](#). It is worth mentioning that for the fitting of the doublet states, other basis sets have been used than those mentioned in Sec. II B due to the high computational demand of the *ab initio* MRCI. A list of basis sets used for each molecule is shown in Table SI of the [supplementary material](#).

III. RESULTS AND DISCUSSION

A. Hamiltonian and parameters

Fitting has been carried out with 121 states in total (42 singlets, 52 doublets, and 27 triplets) and includes a diverse set of excitations of small- to medium-sized molecules, including $\pi \rightarrow \pi^*$, $n \rightarrow \pi^*$, and $\pi \rightarrow Ryd$ transitions. The complete list of all calculated excited state energies with experimental references can be found in the [supplementary material](#). Optimized

TABLE I. Optimized DFT/MRCI parameters and the RMSD of the states used for fitting.

$\delta E_{\text{sel}} (E_h)$	p_J	p_F	p_1	$p_2(E_h^+)$	RMSD (eV)	MAE (eV)	MaxAE (eV)
1.0	0.5030	0.3587	0.5639	1.8571	0.1820	0.1447	0.5776
0.8	0.5008	0.3570	0.5735	1.9266	0.1855	0.1487	0.5776

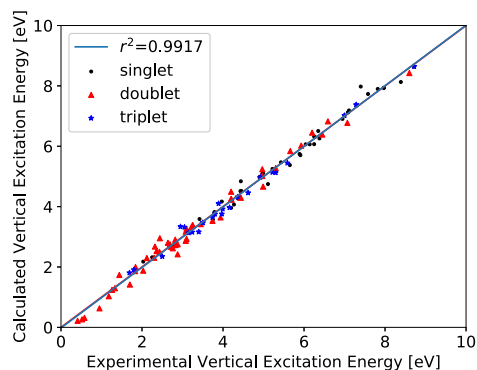


FIG. 1. Correlation between experimental and calculated vertical excitation energies in the fitting set. The red line corresponds to the bisector, and the blue line is the linear regression. Both lines lie on top of each other due to high correlation.

parameters p_1 , p_2 , p_F , and p_J can be found in Table I. The minimization has been done for two sets of parameters: one with $E_{\text{sel}} = 1.0E_h$ and one with $E_{\text{sel}} = 0.8E_h$ (tight parameter set). It can be seen from Table I that both parameter sets yield an RMSD of below 0.2 eV and the difference between both sets is less than 4 meV. From just the results of the fitting procedure, both sets seem to be able to handle a calculation with similar precision. Additionally, an assessment of the parameters has been done to check the results of the fitting.

For a selector $\delta E_{\text{sel}} = 1.0E_h$, the correlation diagram of the calculated values at the minimum of the fitting versus the experimental values is shown in Fig. 1. The correlation diagram for the tight parameters has been omitted since it is virtually identical.

The parameter p_2 influences the shape of the damping function, and it can be seen in Fig. 2 that for $\delta E_{\text{sel}} = 1.0E_h$ the value of the function is effectively zero. The value of p_2 needed for a truncation at $0.8E_h$ is approximately $p_2 = 2.19E_h^+$, but the minimization of the parameters puts the ideal value for p_2 at $1.93E_h^+$. The shape of the resulting damping function is also shown in Fig. 2. A parameterization with a fixed p_2 at $2.19E_h^+$ has been done, resulting in an RMSD of 0.1934 eV, which is almost 0.01 eV higher than the minimum found with a variable p_2 parameter. For this reason, we decided against using the formally more correct parameter and instead chose the parameter which resulted in the smaller error.

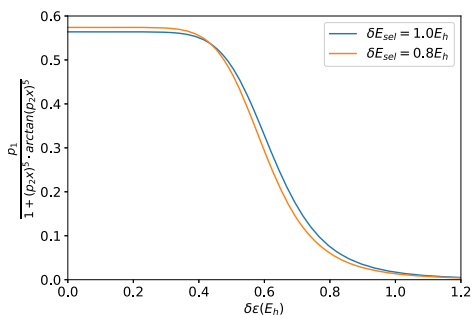


FIG. 2. Damping decay for both selection thresholds $\delta E_{\text{sel}} = 1.0E_h$ and $\delta E_{\text{sel}} = 0.8E_h$ as a function of the energy difference, depending on the parameters p_1 and p_2 .

TABLE II. Results of the assessment of the DFT/MRCI parameters for $\delta E_{\text{sel}} = 1.0E_h$ and tight parameters for $\delta E_{\text{sel}} = 0.8E_h$ for systems with doublet multiplicity.

$\delta E_{\text{sel}} (E_h)$	RMSD (eV)	MAE (eV)	Mean (eV)	Min (eV)	Max (eV)
1.0	0.16	0.13	0.01	-0.44	0.42
0.8	0.17	0.13	0.02	-0.45	0.45

B. Assessment of the parameters

150 vertically excited electronic doublet states have been calculated and compared with experimental data to assess the performance of the Hamiltonian and the parameters. Since the Hamiltonian has been designed and parameterized for odd and even numbers of electrons, 160 excited states with an even number of electrons (93 singlets and 67 triplets) have been calculated for assessment as well. The states differ from the ones used for fitting. For comparison of the singlet and triplet states, the corresponding set of molecules with computed and experimental energies has been taken from the work of Lyskov *et al.*⁹ The detailed results are shown in Tables SIII and SIV of the [supplementary material](#) and a statistical evaluation in Tables II and III in this article. The addition of those states also helps in verifying the success of the new implementation for open shells since all multiplicities were fitted simultaneously with the same parameters. Therefore adding wrongly assigned doublet states during fitting or having faulty terms in the operator itself would have caused a negative impact on the energy differences of the singlet and triplet states compared to the experimental energies. By comparing the results not only to experiment but also to Lyskov's parameters and results as well, we can safely determine if something like this has happened.

So far, the number of experimental quartet states available in the literature, besides some diatomics with degenerate HOMO and HOMO-1 orbitals, in which the HOMO is singly occupied (SOMO), is quite low and consists mostly of adiabatic transitions. Also problematic is the absence of a general assessment set for doublet states in the literature.²⁴ That is why an extensive search for those states was carried out to include a diverse set of systems and excitation, i.e., $\pi \rightarrow \pi^*$, $n \rightarrow \pi^*$, and $\pi \rightarrow \text{Ryd}$, experimentally measured both via PES and EAS. PES follows essentially the one-photon-one-electron principle. Therefore, starting from a closed-shell ground state of the neutral molecule, only cationic states are accessible via PES that differ from the neutral molecule by a single excitation. This means that—in addition to the cationic ground state—excited states can be reached which correspond to an excitation from a doubly occupied to the singly occupied orbital (SOMO) of the cationic ground state ($D \rightarrow S$

TABLE III. Results of the assessment of the DFT/MRCI parameters for $\delta E_{\text{sel}} = 1.0E_h$ and tight parameters for $\delta E_{\text{sel}} = 0.8E_h$ for systems with 93 singlet, 150 doublet, and 93 triplet states.

$\delta E_{\text{sel}} (E_h)$	RMSD (eV)	MAE (eV)	Mean (eV)	Min (eV)	Max (eV)
1.0	0.16	0.12	0.02	-0.44	0.42
0.8	0.16	0.13	0.03	-0.45	0.45

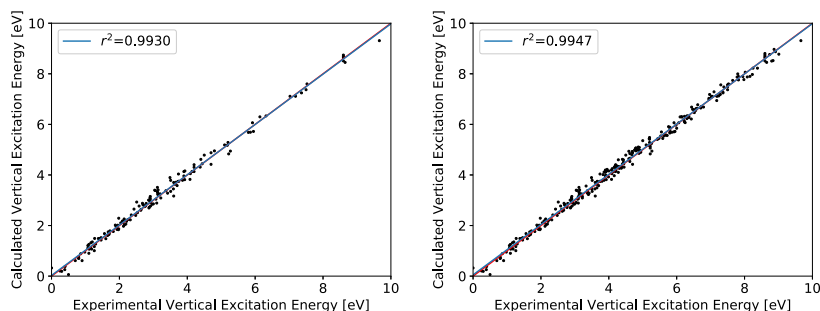


FIG. 3. Correlation between experimental and calculated vertical excitation energies in the assessment set. The red line corresponds to the bisector, and the blue line is the linear regression. Both lines lie on top of each other due to high correlation. On the left, the 150 doublet states are shown, and on the right, all singlet, doublet, and triplet states are shown.

excitation). For a more diverse assessment (and fitting) set, the excitations to the unoccupied (virtual) orbitals $D \rightarrow V$ and $S \rightarrow V$ should be considered as well since their configurations lead to different matrix elements. Those excitations are not accessible via PES; therefore, states acquired by EAS have to be included, but they are rarer than PES states due to the radical nature of systems and the concomitant instability in solution. Also, since the energy difference between the highest doubly occupied orbital and the singly occupied orbital is much lower than that between the occupied and unoccupied orbitals, many states consist of $D \rightarrow S$ excitations as well and excited states mainly characterized by the excitation from the highest doubly occupied orbital (DOMO) to the singly occupied orbital (SOMO) may be well below 1 eV.

1. Singlets and triplets

The assessment of 160 states with $\delta E_{\text{sel}} = 1.0E_h$ resulted in an RMSD of 0.15 eV, which is consistent with the results of Lyskov *et al.*⁹ The new parameters (Table I) show a minimal improvement by 4 meV which is due to larger fitting set by adding the doublet states. The results confirm that the doublet states are suitable because they did not worsen the results of the singlet and triplet states. State-by-state comparison of the assessment states show that both our new and Lyskov's parameter sets yield almost identical results with the new parameters having a lower mean deviation of 0.03 eV in contrast to 0.06 eV. The mean absolute error (MAE) is 0.12 eV for both parameter sets.

For the tight parameters with $E_{\text{sel}} = 0.8E_h$, the RMSD is 7 meV higher than the normal parameter set; thus, for most cases, the tight parameter might be sufficient, at least in the case of the assessment settings using the TZVP basis set.

Different types of orbital classes were involved in the excitations presented in the assessment set. We found out that all three major excitation classes (with more than 5 states in the

assessment) had a similar error, with $\pi \rightarrow \pi^*$ (108 states) and $n \rightarrow \pi^*$ (20 states) having an RMSD of 0.15 eV and $\pi \rightarrow Ryd$ (26 states) having an RMSD of 0.16 eV.

2. Doublets

The assessment of 150 doublet states for $\delta E_{\text{sel}} = 1.0E_h$ yields an RMSD of 0.16 eV, which is almost identical to the results of the 160 closed-shell states in this and Lyskov's parameterization. The mean is at 0.01 eV with a MAE of 0.13 eV. Therefore it can be assumed that both closed-shell and open-shell systems can be calculated with comparable accuracy. The correlation of the experimental and computed states listed in the [supplementary material](#) is shown in Fig. 3. Additionally, the error distribution (Fig. 4) is almost normal. Of all excitation classes assessed, the $n \rightarrow \pi^*$ (25 states) excitations have a slightly higher RMSD of 0.2 eV as compared to $\pi \rightarrow \pi^*$ (106 states) with an RMSD of 0.15 eV. The remaining states which consist of various classes (17 states) are within 0.15 eV identical to the latter. The higher deviation of the $n \rightarrow \pi^*$ excitations is mainly caused by three states: 1^2A_1 of dibenzofuran and $1^2A'$ and $3^2A'$ of ethyl fluoride. All three excitations are transitions from a doubly occupied to the singly occupied orbital $D \rightarrow S$.

For the tight parameters ($\delta E_{\text{sel}} = 0.8E_h$), the RMSD is 6 meV higher, providing a similar picture as in the case of singlets and triplets. So again we can say that at least in our test settings, the tight parameter set seems to be sufficient while saving a high amount of computational time and memory requirements.

3. Singlets, doublets, and triplets combined

All 310 states combined, consisting of 93 singlets, 150 doublets, and 67 triplets, yield an RMSD of 0.16 eV with a mean absolute error (MAE) of 0.12 eV. The mean is at 0.02 eV and the differences range from -0.44 eV as the negative

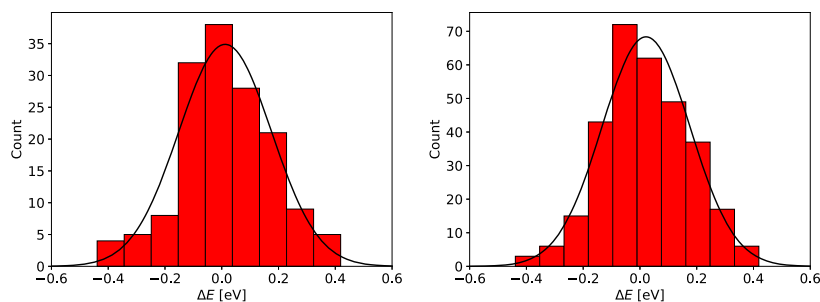


FIG. 4. Histogram of the error ($E_{\text{calc}} - E_{\text{exp}}$) with $\delta E_{\text{sel}} = 1.0E_h$ of all calculated doublet states from a sample of 150 states (left) and all calculated singlet, doublet, and triplet states from a sample of 310 states (right).

maximum to 0.42 eV as the positive maximum. The standard deviation is 0.16 eV, and the distribution of the energy differences is approximately normal (Fig. 4). The correlation of the experimental state energies compared to the calculated ones is shown in Fig. 3. For the tight parameter set, the results are almost identical, with the same RMSD and a very small increase of the MAE and mean by 0.01 eV to 0.13 eV and 0.03 eV, respectively.

4. Quartets

As mentioned above, experimental quartet states are very rare in the literature. We calculated two adiabatic quartet states with a $\sigma \rightarrow \pi^*$ excitation for CH and NH^+ . This choice is not ideal because both molecules have a $^2\Pi$ ground state with $3\sigma^2 1\pi^1$ occupation and the program cannot handle non-Abelian molecular point groups. Therefore, only one of the two possible occupations, $3\sigma^2 1\pi_x^1$ or $3\sigma^2 1\pi_y^1$, can be chosen as the anchor configuration in DFT/MRCI. Consequently, the two components of the ground state are not properly degenerate. For CH, the $^2\Pi_y$ component of the $^2\Pi$ state is located about 0.04 eV above the $^2\Pi_x$ component. The $^4\Sigma^-$ state with $3\sigma^1 1\pi_x^1 1\pi_y^1$ occupation is at 0.74 eV in the experiment⁴⁷ and at 0.69 eV in our calculation or at 0.67 eV if the energies of the two $^2\Pi$ components are averaged. The symmetry breaking is even larger in the case of NH^+ where the $^2\Pi_y$ component is found about 0.08 eV above the $^2\Pi_x$ component in the DFT/MRCI calculation. The experimentally determined adiabatic excitation energy of $^4\Sigma^-$ of NH^+ is 0.04 eV,⁴⁸ while our calculated energy is 0.22 eV relative to $^2\Pi_y$ or 0.18 eV relative to the averaged $^2\Pi$ ground state energy. Although the resulting absolute deviations from experiment are well below 0.2 eV, which is in good agreement with the statistics of the singlet, doublet, and triplet calculations, the percentage error of the (very small) $^4\Sigma^-$ excitation energy of the NH^+ radical is quite obvious. Alternative test cases for quartets which do not pose a degeneracy problem would be highly desirable.

5. Ionization potentials

By means of the newly developed and parameterized Hamiltonian, ionization potentials of selected molecules have been calculated (Table IV). The calculation was done at the singlet ground state geometry for both the singlet and doublet calculations, and the ionization potential then is the difference of the total energies of the ground states of the neutral molecule (singlet) and the cationic molecule (doublet). The DFT/MRCI energies are within 0.15 eV compared to the DFT(BHandHLYP) Δ_{SCF} energies. Since the Kohn-Sham orbital energies enter the expressions for the diagonal matrix

TABLE IV. Ionization potentials for selected molecules. All calculations have been carried out at the B3-LYP singlet ground state geometry. For all IPs, the BHandHLYP functional has been used. Energies are in eV.

Molecule	DFT/MRCI	Expt.	DFT
1,2,3,4-tetrafluorobenzene	9.71	9.8 ^a	9.83
1,2,4,5-tetrafluorobenzene	9.54	9.5 ^a	9.64
Adenine	8.18	8.47 ^b	8.32
Thymine	8.99	9.19 ^b	9.07
Ethylene	10.33	10.5 ^c	10.27
Ethyl fluoride	12.45	12.4 ^a	12.62
Nitrous oxide	12.57	12.89 ^d	12.86
Fulvene	8.12	8.36 ^c	8.16
Methylene fluoride	13.64	13.3 ^a	13.66
Tetrafluoroethylene	10.65	10.69 ^a	10.64
<i>cis</i> -1,2-difluoroethylene	10.43	10.62 ^a	10.42
<i>trans</i> -1,2-difluoroethylene	10.41	10.63 ^a	10.39

^aReference 49.

^bReference 50.

^cReference 51.

^dReference 52.

^eReference 53.

elements in the DFT/MRCI formalism [see Eq. (6)], a dependence of the DFT/MRCI IPs on the DFT level is to be expected. In cases where the DFT ionization potentials have a relatively high deviation to the experiment, the DFT/MRCI calculations show a similar deviation. This can be seen, for example, in fulvene and methylene fluoride, where both DFT and DFT/MRCI differ by approximately 0.3 eV from the experiment.

6. Dimer

A dimer system consisting of an ethylene radical (doublet ground state) and tetrafluoroethylene (singlet ground state) placed 100 Ångström apart has been excited (Fig. 5). In this system, the local excitations of the monomers define the eigenstates of the dimer as $|s_1, m_1\rangle \otimes |s_2, m_2\rangle$ which can be decomposed to linear combinations of local one-electron excitations,

$$|S, M, s_1, s_2\rangle = \sum_{m_1, m_2} c_{m_1, m_2}^{S, M} |s_1, m_1\rangle |s_2, m_2\rangle. \quad (12)$$

For solutions of the spin-free Hamiltonian without external electromagnetic fields, all components M of a total spin moment S for fixed s_1 and s_2 are energetically degenerate.⁹ The energies of the dimer states $|S, 0, m_1, m_2\rangle$ can be expressed as a sum of their local excitations. To test this behavior in the case of a doublet dimer consisting of a closed-shell monomer with local singlet and triplet excitations (tetrafluoroethylene) and a monomer with an open shell with local doublet and quartet

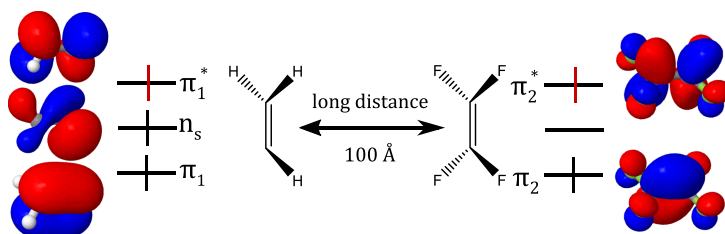


FIG. 5. Model dimer of ethylene radical and tetrafluoroethylene with simultaneous $\pi \rightarrow \pi^*$ excitation. The ethylene radical is an open-shell system with the doublet ground state. Tetrafluoroethylene has a singlet ground state.

TABLE V. Monomer $\pi \rightarrow \pi^*$ vertical excitation energies of ethylene-radical and tetrafluoroethylene and their dimer states $\pi_1\pi_2 \rightarrow \pi_1^*\pi_2^*$. The sum of two monomer energies results in the expected energy in the dimer. All energies are in eV.

		Singlet		Doublet		Triplet		Quartet		Sextet	
		Computed	Expected	Computed	Expected	Computed	Expected	Computed	Expected	Computed	Expected
Monomer	$ s1\rangle$			5.0620				3.9946			
	$ s2\rangle$	8.8861				5.1421					
Dimer	$ s1\rangle$		5.0626	5.0620			3.9948	3.9946			
	$ s2\rangle$		8.9156	8.8861			5.1432	5.1421			
	$ S, 0, \frac{3}{2}, 1\rangle$		9.1432	9.1367			9.1461	9.1367	9.1373	9.1367	
	$ S, 0, \frac{1}{2}, 1\rangle$		10.2158	10.2041			10.218	10.2041			
	$ S, 0, \frac{3}{2}, 0\rangle$						12.944	12.8807			
	$ S, 0, \frac{1}{2}, 0\rangle$		13.9893	13.9481							

TABLE VI. Monomer $\pi \rightarrow \pi^*$ vertical excitation energies of tetrafluoroethylene and the D-S and S-V transitions of the ethylene-radical and the resulting dimer states $n_s\pi_2 \rightarrow \pi_1^*\pi_2^*$ and $\pi_1\pi_2 \rightarrow n_s^*\pi_2^*$, with s marking the singly occupied orbital in the parent determinant. The D-S and S-V excitations on the radical can only compose a doublet state, but via combination doublet and quartet excitations are possible on the dimer. The sum of two monomer energies results in the expected energy in the dimer. All energies are in eV. The energies regarding the tetrafluoroethylene monomer $|s2\rangle$ can be found in Table V.

		$\pi_1 \rightarrow n_s^*$ transition (D \rightarrow S)				$n_s \rightarrow \pi_1^*$ transition (S \rightarrow V)			
		Doublet		Quartet		Doublet		Quartet	
		Computed	Expected	Computed	Expected	Computed	Expected	Computed	Expected
Monomer	$ s1\rangle$	2.4508				5.3642			
Dimer	$ s1\rangle$	2.4515	2.4508			5.3654	5.3642		
	$ S, 0, \frac{1}{2}, 1\rangle$	7.5835	7.5929	7.5961	7.5929	10.4833	10.5063	10.5291	10.5063
	$ S, 0, \frac{1}{2}, 0\rangle$	11.3646	11.3369			14.2737	14.2503		

excitations (ethylene radical), three different kinds of excitation have to be considered depending on the shells involved in the doublet and quartet excitations. For excitations from a doubly occupied π -orbital to a vacant one $\pi_1 \rightarrow \pi_1^*$ on the ethylene radical and $\pi_2 \rightarrow \pi_2^*$ on tetrafluoroethylene, the resulting monomer and dimer excitations are shown in Table V. Additionally, the other two possible single excitations in a doublet system are shown in Table VI. They consist of either an excitation from a doubly to the singly occupied orbital $\pi_1 \rightarrow \pi_s$ or from the singly occupied orbital to a vacant one $\pi_s \rightarrow \pi_1^*$. All symmetry considerations are retained for all three monomer excitations in the ethylene radical combined with the excitation of tetrafluoroethylene.

IV. CONCLUSION

We have presented an extension of Lyskov's DFT/MRCI Hamiltonian to molecules with an open-shell anchor configuration while maintaining the good performance and reliability for systems with a closed-shell anchor. The newly parameterized Hamiltonian yields energies in good agreement with experimental excitation data for singlets, doublets, and triplets with statistical errors of below 0.2 eV. The proposed parameterization extends the standard and Lyskov's DFT/MRCI approaches to systems with open shells like cations, anions, and radicals. It provides a framework for the calculation of ionization potentials on an MRCI-level of theory and for systems with an odd number of electrons like large organic light

emitting diodes based on persistent radicals without losing any of the advantages of the previous Hamiltonians for systems with an even number of electrons. Such applications will be presented in forthcoming work.

SUPPLEMENTARY MATERIAL

See [supplementary material](#) for full expressions of all Hamiltonian matrix elements in the current DFT/MRCI approach, calculated data of vertical excitation energies in comparison with experimental data for fitting and assessment, structural formula of the molecules, and the geometry data used in the calculation in the Cartesian format.

ACKNOWLEDGMENTS

Financial support by the Deutsche Forschungsgemeinschaft (DFG) Project No. MA1051/14-2 is gratefully acknowledged.

¹K. Sharkas, A. Savin, H. J. A. Jensen, and J. Toulouse, *J. Chem. Phys.* **137**, 044104 (2012).

²S. Grimme, *Chem. Phys. Lett.* **259**, 128 (1996).

³S. Grimme and M. Waletzke, *J. Chem. Phys.* **111**, 5645 (1999).

⁴E. V. Beck, E. A. Stahlberg, L. W. Burggraf, and J.-P. Blaudeau, *Chem. Phys.* **349**, 158 (2008).

⁵M. Roemelt, D. Maganas, S. DeBeer, and F. Neese, *J. Chem. Phys.* **138**, 204101 (2013).

⁶M. R. Silva-Junior, M. Schreiber, S. P. Sauer, and W. Thiel, *J. Chem. Phys.* **129**, 104103 (2008).

- ⁷C. M. Marian and N. Gilka, *J. Chem. Theory Comput.* **4**, 1501 (2008).
- ⁸M. Kleinschmidt, C. M. Marian, M. Waletzke, and S. Grimme, *J. Chem. Phys.* **130**, 044708 (2009).
- ⁹I. Lyskov, M. Kleinschmidt, and C. M. Marian, *J. Chem. Phys.* **144**, 034104 (2016).
- ¹⁰J.-M. Mewes, V. Jovanović, C. M. Marian, and A. Dreuw, *Phys. Chem. Chem. Phys.* **16**, 12393 (2014).
- ¹¹J. D. Spiegel, I. Lyskov, M. Kleinschmidt, and C. M. Marian, *Chem. Phys.* **482**, 265 (2017).
- ¹²N. Elfers, I. Lyskov, J. D. Spiegel, and C. M. Marian, *J. Phys. Chem. C* **120**, 13901 (2016).
- ¹³J. Föllner, M. Kleinschmidt, and C. M. Marian, *Inorg. Chem.* **55**, 7508 (2016).
- ¹⁴C. M. Marian, *J. Phys. Chem. C* **120**, 3715 (2016).
- ¹⁵A. Heil, K. Gollnisch, M. Kleinschmidt, and C. M. Marian, *Mol. Phys.* **114**, 407 (2016).
- ¹⁶H. Yersin, "Triplet emitters for oled applications. mechanisms of exciton trapping and control of emission properties," in *Transition Metal and Rare Earth Compounds: Excited States, Transitions, Interactions III* (Springer Berlin Heidelberg, Berlin, Heidelberg, 2004), pp. 1–26.
- ¹⁷M. J. Leitl, D. M. Zink, A. Schinabeck, T. Baumann, D. Volz, and H. Yersin, *Top. Curr. Chem.* **374**, 25 (2016).
- ¹⁸R. Czerwieńiec, M. J. Leitl, H. H. Homeier, and H. Yersin, *Coord. Chem. Rev.* **325**, 2 (2016).
- ¹⁹Q. Peng, A. Obolda, M. Zhang, and F. Li, *Angew. Chem., Int. Ed.* **54**, 7091 (2015).
- ²⁰M. A. Baldo, D. O'Brien, Y. You, A. Shoustikov *et al.*, *Nature* **395**, 151 (1998).
- ²¹I. Ratera and J. Veciana, *Chem. Soc. Rev.* **41**, 303 (2012).
- ²²Y. Hattori, T. Kusamoto, and H. Nishihara, *Angew. Chem., Int. Ed.* **53**, 11845 (2014).
- ²³G. N. Lewis, D. Lipkin, and T. T. Magel, *J. Am. Chem. Soc.* **66**, 1579 (1944).
- ²⁴Z. Li and W. Liu, *J. Chem. Theory Comput.* **12**, 238 (2015).
- ²⁵Z. Li and W. Liu, *J. Chem. Theory Comput.* **12**, 2517 (2016).
- ²⁶A. D. Becke, *J. Chem. Phys.* **98**, 1372 (1993).
- ²⁷W. D. Edwards and M. C. Zerner, *Theor. Chim. Acta* **72**, 347 (1987).
- ²⁸M. Filatov and S. Shaik, *Chem. Phys. Lett.* **288**, 689 (1998).
- ²⁹R. W. Wetmore and G. A. Segal, *Chem. Phys. Lett.* **36**, 478 (1975).
- ³⁰G. A. Segal, R. W. Wetmore, and K. Wolf, *Chem. Phys.* **30**, 269 (1978).
- ³¹O. Treutler and R. Ahlrichs, *J. Chem. Phys.* **102**, 346 (1995).
- ³²"TURBOMOLE V6.5 2013, a development of University of Karlsruhe and Forschungszentrum Karlsruhe GmbH, 1989–2007, TURBOMOLE GmbH, since 2007; available from <http://www.turbomole.com>." (as of 2017).
- ³³A. D. Becke, *J. Chem. Phys.* **98**, 5648 (1993).
- ³⁴S. Grimme, J. Antony, S. Ehrlich, and H. Krieg, *J. Chem. Phys.* **132**, 154104 (2010).
- ³⁵S. Grimme, S. Ehrlich, and L. Goerigk, *J. Comput. Chem.* **32**, 1456 (2011).
- ³⁶F. Weigend and R. Ahlrichs, *Phys. Chem. Chem. Phys.* **7**, 3297 (2005).
- ³⁷A. Schäfer, C. Huber, and R. Ahlrichs, *J. Chem. Phys.* **100**, 5829 (1994).
- ³⁸F. Weigend, A. Köhn, and C. Hättig, *J. Chem. Phys.* **116**, 3175 (2002).
- ³⁹"TURBOMOLE V7.1 2016, a development of University of Karlsruhe and Forschungszentrum Karlsruhe GmbH, 1989–2007, TURBOMOLE GmbH, since 2007; available from <http://www.turbomole.com>." (as of 2017).
- ⁴⁰K. Aidas, C. Angeli, K. L. Bak, V. Bakken, R. Bast, L. Boman, O. Christiansen, R. Cimraglia, S. Coriani, P. Dahle, E. K. Dalskov, U. Ekström, T. Enevoldsen, J. J. Eriksen, P. Ettenhuber, B. Fernández, L. Ferrighi, H. Fliegl, L. Frediani, K. Hald, A. Halkier, C. Hättig, H. Heiberg, T. Helgaker, A. C. Hennum, H. Hettner, E. Hjertenæs, S. Host, I.-M. Høyvik, M. F. Iozzi, B. Jansik, H. J. Aa. Jensen, D. Jonsson, P. Jørgensen, J. Kauczor, S. Kirpekar, T. Kjærgaard, W. Klopper, S. Knecht, R. Kobayashi, H. Koch, J. Kongsted, A. Krapp, K. Kristensen, A. Ligabue, O. B. Lutnæs, J. I. Melo, K. V. Mikkelsen, R. H. Myhre, C. Neiss, C. B. Nielsen, P. Norman, J. Olsen, J. M. H. Olsen, A. Osted, M. J. Packer, F. Pawłowski, T. B. Pedersen, P. F. Provasi, S. Reine, Z. Rinkevicius, T. A. Ruden, K. Ruud, V. V. Rybkin, P. Salek, C. C. M. Samson, A. S. de Merás, T. Saue, S. P. A. Sauer, B. Schimmelpfennig, K. Sneskov, A. H. Steindal, K. O. Sylvester-Hvid, P. R. Taylor, A. M. Teale, E. I. Tellgren, D. P. Tew, A. J. Thorvaldsen, L. Thøgersen, O. Vahtras, M. A. Watson, D. J. D. Wilson, M. Ziolkowski, and H. Ågren, *Wiley Interdiscip. Rev.: Comput. Mol. Sci.* **4**, 269 (2014).
- ⁴¹"Dalton, a molecular electronic structure program, release dalton2016.1 (2015), see <http://daltonprogram.org>."
- ⁴²D. Rappoport and F. Furche, *J. Chem. Phys.* **133**, 134105 (2010).
- ⁴³A. Schäfer, H. Horn, and R. Ahlrichs, *J. Chem. Phys.* **97**, 2571 (1992).
- ⁴⁴O. Vahtras, J. Almlöf, and M. Feyereisen, *Chem. Phys. Lett.* **213**, 514 (1993).
- ⁴⁵F. Weigend, M. Häser, H. Patzelt, and R. Ahlrichs, *Chem. Phys. Lett.* **294**, 143 (1998).
- ⁴⁶J. A. Nelder and R. Mead, *Comput. J.* **7**, 308 (1965).
- ⁴⁷A. Kasdan, E. Herbst, and W. Lineberger, *Chem. Phys. Lett.* **31**, 78 (1975).
- ⁴⁸R. Colin and A. Douglas, *Can. J. Phys.* **46**, 61 (1968).
- ⁴⁹G. Bieri, L. Åsbrink, and W. von Niessen, *J. Electron Spectrosc. Relat. Phenom.* **23**, 281 (1981).
- ⁵⁰K. B. Bravaya, O. Kostko, S. Dolgikh, A. Landau, M. Ahmed, and A. I. Krylov, *J. Phys. Chem. A* **114**, 12305 (2010).
- ⁵¹M. Allan, E. Heilbronner, and G. Kaupp, *Helv. Chim. Acta* **59**, 1949 (1976).
- ⁵²J. Lorquet and C. Cadet, *Int. J. Mass Spectrom. Ion Phys.* **7**, 245 (1971).
- ⁵³H. Rosenstock, J. Dannacher, and J. Liebman, *Radiat. Phys. Chem.* **20**, 7 (1982).

Erratum: “DFT/MRCI Hamiltonian for odd and even numbers of electrons” [J. Chem. Phys. 147, 194104 (2017)]

Cite as: J. Chem. Phys. 150, 219902 (2019); doi: 10.1063/1.5109648

Submitted: 10 May 2019 • Accepted: 14 May 2019 •

Published Online: 4 June 2019



View Online



Export Citation



CrossMark

Adrian Heil and Christel M. Marian^{a)}

AFFILIATIONS

Institute of Theoretical and Computational Chemistry, Heinrich-Heine-University Düsseldorf, Universitätsstraße 1, 40225 Düsseldorf, Germany

^{a)}Electronic mail: Christel.Marian@hhu.de

<https://doi.org/10.1063/1.5109648>

Equation (8) of Ref. 1 is missing a factor of $\frac{1}{2}$ in the second and third terms. Correctly, Eq. (8) should read as

$$\Delta E_{\text{exch}} = P_{\text{F}} \left(\frac{1}{2} \sum_{i \in c} \sum_{j \in a} V_{ijji} - \frac{1}{2} \sum_{\substack{i \in c \\ j \in c, s}} V_{ijji} - \frac{1}{2} \sum_{\substack{i \in a \\ j \in a, s}} V_{ijji} + \sum_{\substack{i, j \in o \\ i \neq j}} V_{ijji} \eta_{ij}^{ij} \right). \quad (8)$$

This error is only a typo in the equation. All published results are unaffected, since the Hamiltonian has been implemented correctly.

An additional change involves the notation of the indices in the second and third terms to accentuate that the index j is addressing created (second term) or annihilated (third term) electrons in an orbital s that is singly occupied in the anchor configuration.

REFERENCE

¹ A. Heil and C. M. Marian, J. Chem. Phys. 147, 194104 (2017).

Supplementary Material

Adrian Heil, Christel M. Marian*

*Institute of Theoretical and Computational Chemistry,
Heinrich-Heine-University Düsseldorf, Universitätsstraße 1, 40225 Düsseldorf, Germany*

* Christel.Marian@hhu.de

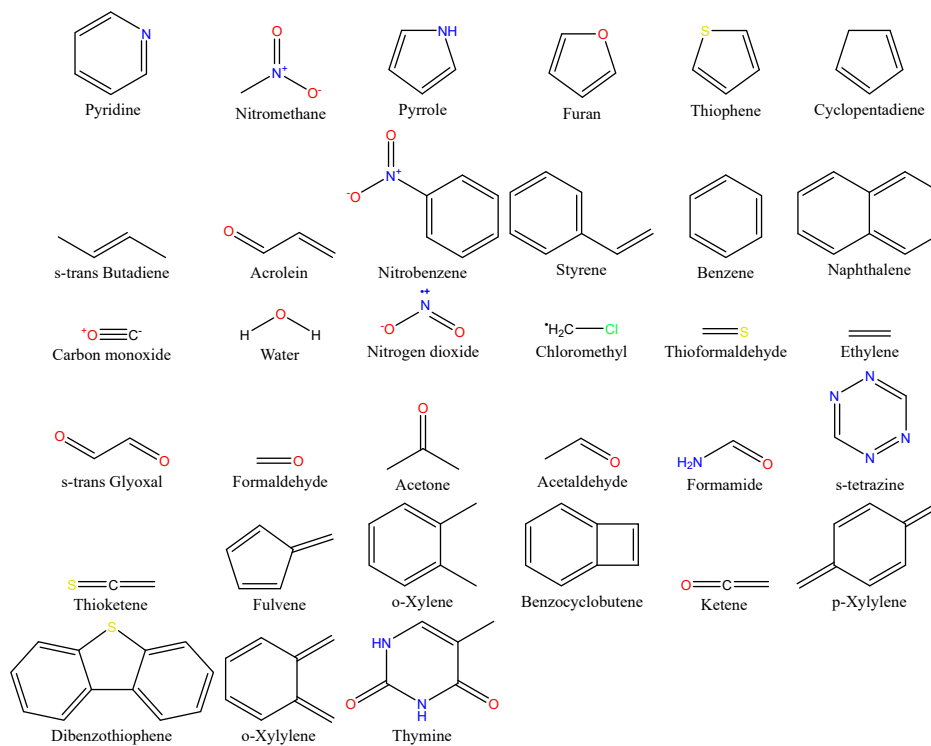


Figure S1. Molecules used in the fitting set

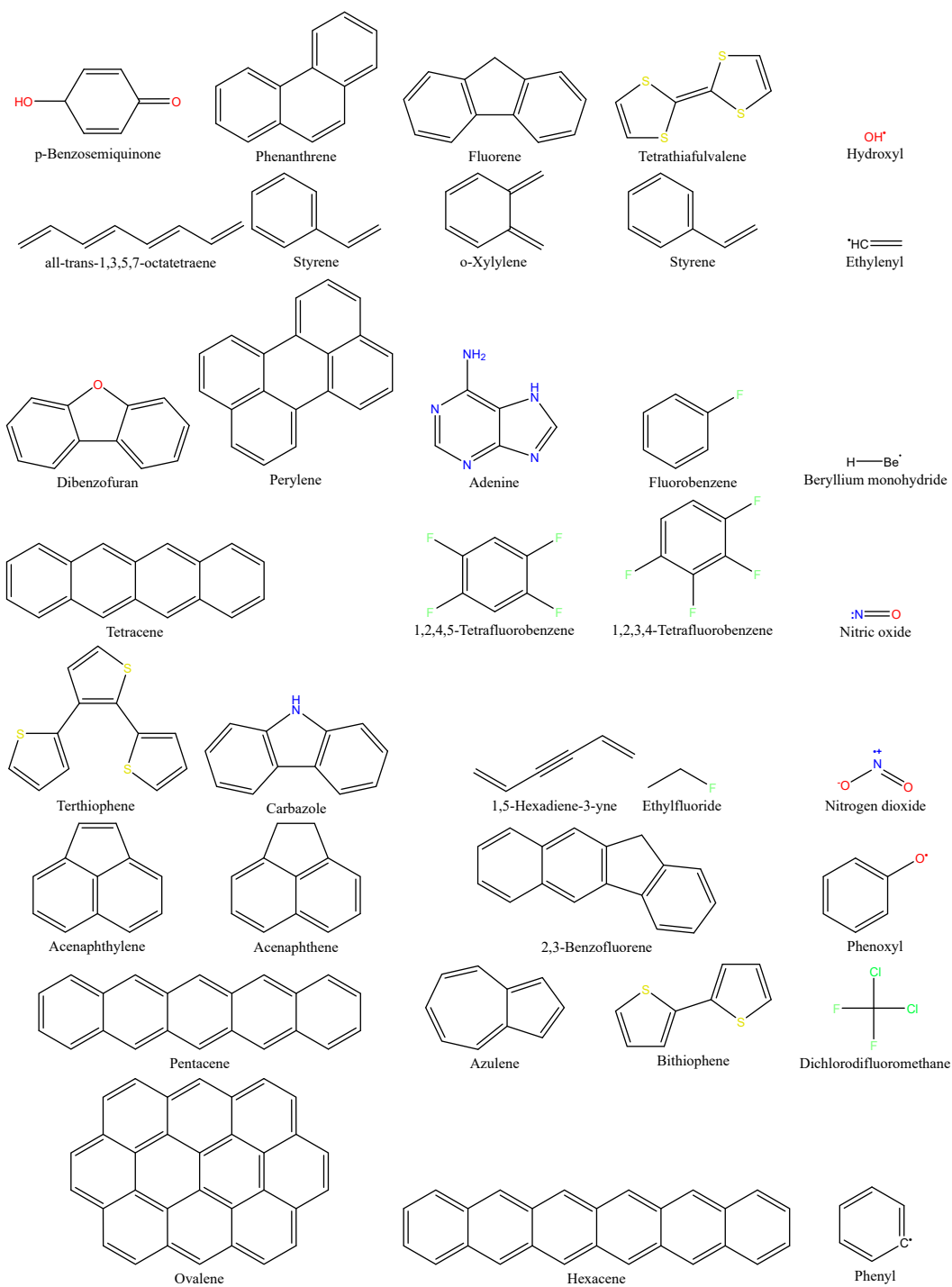


Figure S2. Molecules with doublet states used for assessment

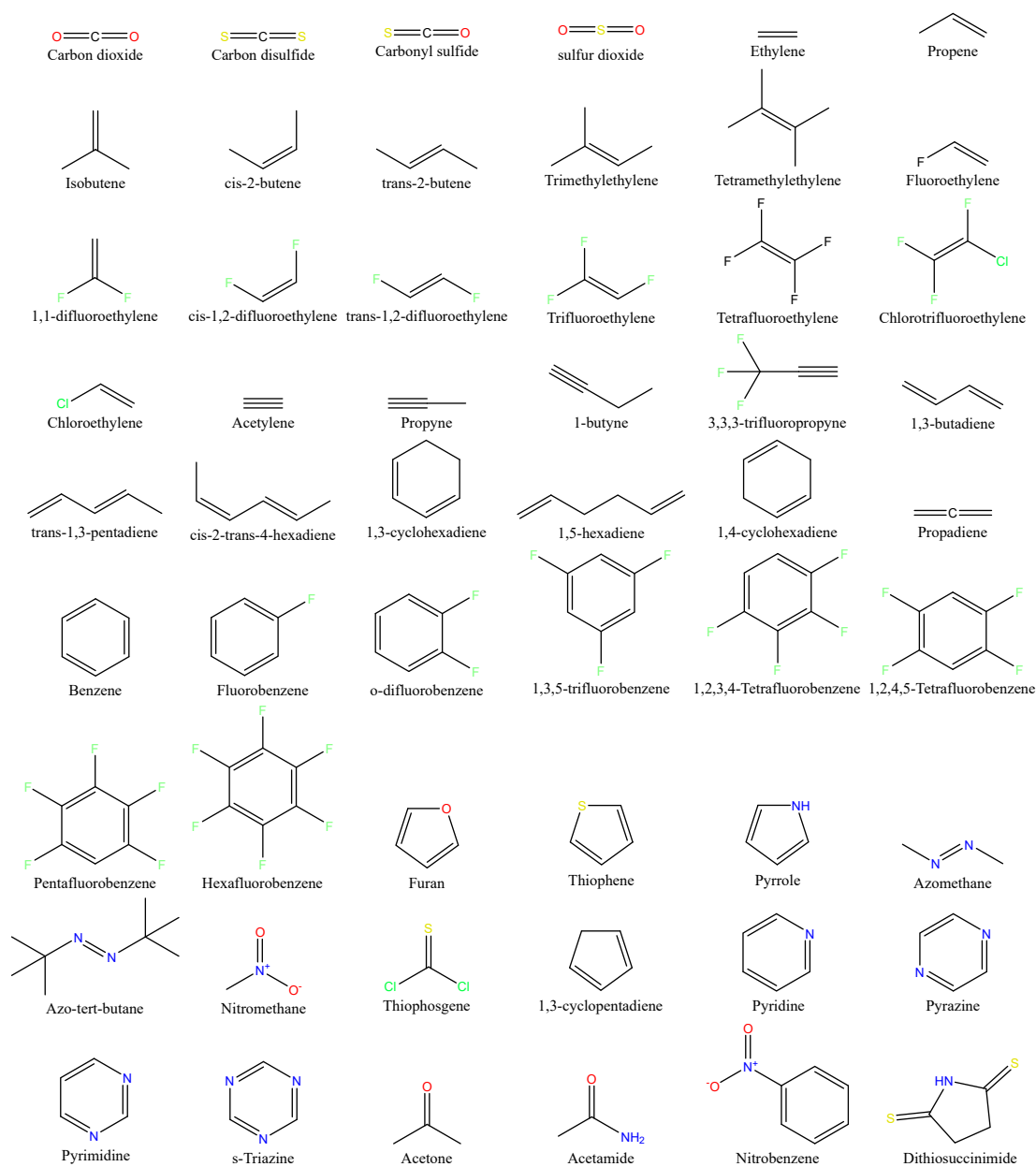


Figure S3. Molecules with singlet and/ or triplet states used for assessment

Table S1. Basis sets used in the fitting of the doublet states

Molecule	Basis set
Benzocyclobutene	SV(P) ^a
s-trans Butadiene cation	TZVP ^b
Methylidine	QZVPP ^c
Chloromethyl	def2-TZVPD ^d
Dibenzothiophene	SV(P) ^a
Ethylene	TZVPP ^b
Fulvene	SV(P) ^a
Ketene	TZVP ^b
Thioketene	def2-TZVPD ^d
Formaldehyde	aug-cc-pVTZ ^e
Water	TZVPP ^b
Naphthalene cation	SV(P) ^a
Nitrogen dioxide	aug-cc-pVTZ ^e
o-Benzoquinone	SV(P) ^a
o-Xylene	SV(P) ^a
o-Xylylene cation	SV(P) ^a
p-Xylylene	SV(P) ^a
Thymine	SV(P) ^a

^a Ref. [1], ^b Ref. [2], ^c Ref. [3], ^d Ref. [4], ^e Ref. [5]

Table S2: Vertical excitation energies and molecular states with singlet, doublet and triplet multiplicities used for parameter optimization. Note that the molecule name corresponds to the geometry used in doublet case, o-Xylylene+ refers to electronic absorption of the cation, o-Xylene refers to photoelectron spectroscopy from the neutral molecule, therefore the neutral ground state geometry was used. All energies are given in eV. The energies of Lyskov's parameterization are given as reference for closed shell system

State	Type	Experiment	DFTMRCI-R	DFT/MRCI-A	DFT/
Pyridine	C ₅ H ₅ N				
1 ¹ B ₂	$n \rightarrow \pi^*$	444 ^a , 445 ^b	4.86	4.84	
1 ¹ B ₁	$n \rightarrow \pi^*$	499 ^a , 499 ^c	5.13	5.11	
2 ¹ A ₁	$\pi \rightarrow \pi^*$	638 ^a , 630 ^a , 638 ^c , 632 ^d	6.31	6.26	
Nitromethane	H ₃ C – NO ₂				
2 ¹ A'	$\pi \rightarrow \pi^*$	625 ^e , 6.23 ^e , 623 ^f	6.34	6.32	
1 ³ A''	$n \rightarrow \pi^*$	380 ^f	3.79	3.75	
Pyrrole	C ₄ H ₄ NH				
1 ³ B ₁	$\pi \rightarrow \pi^*$	421 ^g , 421 ^h , 42 ⁱ	4.21	4.20	
Furan	C ₄ H ₄ O				
1 ¹ B ₁	$\pi \rightarrow \pi^*$	604 ^g , 606 ^h , 604 ^j	6.09	6.06	
3 ¹ A ₁	$\pi \rightarrow \pi^*$	782 ^h , 78 ^j	7.90	7.90	
1 ³ B ₁	$\pi \rightarrow \pi^*$	40 ⁱ , 399 ^h	3.94	3.92	
1 ³ A ₁	$\pi \rightarrow \pi^*$	52 ⁱ , 522 ^h	5.15	5.14	
Thiophene	C ₄ H ₄ S				
2 ¹ A ₁	$\pi \rightarrow \pi^*$	548 ^h , 543 ^g , 552 ^k	5.48	5.47	
1 ³ B ₁	$\pi \rightarrow \pi^*$	37 ⁱ , 374 ^g , 375 ^h	3.77	3.64	
1 ³ A ₁	$\pi \rightarrow \pi^*$	462 ^h , 46 ⁱ , 4.7 ^k	4.58	4.46	
Cyclopentadiene	C ₅ H ₅				
1 ¹ B ₂	$\pi \rightarrow \pi^*$	522 ^g , 526 ^l , 533 ^m	5.29	5.25	
1 ³ B ₂	$\pi \rightarrow \pi^*$	315 ^g , 310 ^l	3.16	3.13	

Continu

s-trans Butadiene	C_4H_6				
1^1B_u	$\pi \rightarrow \pi^*$	591 ^g , 59 ^h , 5.92 ^o	5.75	5.71	
2^1A_g	$\pi \rightarrow \pi^*$	627 ^P	6.32	6.31	
1^3B_u	$\pi \rightarrow \pi^*$	324 ^g , 322 ^o , 32 ⁿ	3.18	3.15	
1^3A_g	$\pi \rightarrow \pi^*$	492 ^g , 491 ^o , 495 ⁿ	4.99	4.98	
s-trans Butadiene cation	$C_4H_6^+$				
1^2A_u	$\pi \rightarrow \pi^*$	232 ^{ah}	-	2.68	
2^2A_u	$\pi \rightarrow \pi^*$	420 ^{ah}	-	4.49	
Acrolein	C_3H_4O				
$1^1A''$	$n \rightarrow \pi^*$	376 ^q , 3.75 ^r , 3.71 ^s	3.58	3.57	
$1^3A''$	$n \rightarrow \pi^*$	308 ^s , 305 ^t	3.33		
Nitrobenzene	$C_6H_5NO_2$				
2^1A_1	$\pi \rightarrow \pi^*$	517 ^u , 511 ^v	4.78	4.75	
Styrene	$H_5C_6CH = CH_2$				
$2^1A'$	$\pi \rightarrow \pi^*$	443 ^w , 4.43 ^x	4.53	4.51	
$1^3A'$	$\pi \rightarrow \pi^*$	340 ^w	3.19	3.16	
Benzene	C_6H_6				
1^1B_{3u}	$\pi \rightarrow \pi^*$	480 ^y , 4.90 ^z , 489 ^A	5.00	4.98	
1^1B_{2u}	$\pi \rightarrow \pi^*$	625 ^y , 603 ^z	6.12	6.07	
2^1B_{3u}	$\pi \rightarrow \pi^*$	695 ^{y,A} , 687 ^z	6.92	6.91	
1^3B_{2u}	$\pi \rightarrow \pi^*$	390 ^y , 389 ^A	4.13	4.10	
2^3B_{3u}	$\pi \rightarrow \pi^*$	559 ^y , 569 ^A	5.49	5.44	
Naphthalene	$C_{10}H_8$				
1^1B_{3u}	$\pi \rightarrow \pi^*$	40 ^B , 397 ^C	4.18	4.17	
1^1B_{2u}	$\pi \rightarrow \pi^*$	445 ^B , 445 ^C	4.55	4.52	
2^1B_{3u}	$\pi \rightarrow \pi^*$	589 ^B , 589 ^C	5.76	5.74	
2^1B_{2u}	$\pi \rightarrow \pi^*$	614 ^C	6.09	6.07	
Naphthalene cation	$C_{10}H_8^+$				
1^2B_{3g}	$\pi \rightarrow \pi^*$	184 ^{ad}	-	2.00	
1^2B_{2g}	$\pi \rightarrow \pi^*$	269 ^{ad}	-	2.75	
2^2B_{2g}	$\pi \rightarrow \pi^*$	325 ^{ad}	-	3.39	
Carbon monoxide	CO				
2^1A	$n \rightarrow \pi^*$	839 ^D	8.16	8.13	
Water	H_2O				
1^1B_2	$n \rightarrow \tilde{R}$	75 ^E , 74 ^F	7.99	7.98	
1^2A_1	$\sigma \rightarrow n^*$	211 ^{aa}	-	1.96	
1^2B_1	$n \rightarrow n^*$	593 ^{aa}	-	6.02	
Nitrogen dioxide	NO_2				
1^2B_2	$n \rightarrow n^*$	281 – 285 ^{ab}	-	2.73	
1^2B_1	$n \rightarrow n^*$	31 ^{ab}	-	3.27	
Chloromethyl	CH_2Cl				
1^2A_1	$\pi \rightarrow \tilde{R}$	499 ^{ac}	-	4.66	
2^1B_2	$\pi \rightarrow \pi^*$	620 ^{ac}	-	6.45	
3^2B_2	$\pi \rightarrow \tilde{R}$	659 ^{ac}		6.83	
Thioformaldehyde	$H_2C = S$				
1^1A_2	$n \rightarrow \pi^*$	203 ^G	2.22	2.18	
1^3A_2	$n \rightarrow \pi^*$	180 ^G	1.95	1.91	

Continu

Ethylene	$\text{H}_2\text{C} = \text{CH}_2$				
1^1B_{1u}	$\pi \rightarrow \bar{R}$	711 ^H , 7.11 ^I	7.20	7.19	
1^2B_{1g}	$\sigma \rightarrow \pi^*$	23 ^{ai}	-	2.31	
1^2A_g	$\sigma \rightarrow \pi^*$	42 ^{ai}	-	4.26	
1^2B_{3u}	$\sigma \rightarrow \pi^*$	53 ^{ai}	-	5.28	
1^2B_{2u}	$\sigma \rightarrow \pi^*$	86 ^{ai}	-	8.42	
1^3B_{2u}	$\pi \rightarrow \pi^*$	436 ^J	4.36	4.32	
Ethylene dimer	$2x[\text{H}_2\text{C} = \text{CH}_2]$				
2^1A	$\pi \rightarrow \pi^*\pi^*$	$2xE(1^3\text{B}_{2u})$	8.71	8.64	
3^3A	$\pi \rightarrow \pi^*\pi^*$	$2xE(1^3\text{B}_{2u})$	8.71	8.64	
s-trans Glyoxal	$\text{HOC} - \text{COH}$				
1^1A_u	$n \rightarrow \pi^*$	28 ^K	2.71	2.68	
1^1B_g	$n \rightarrow \pi^*$	42 ^K	3.97	3.96	
1^3A_u	$n \rightarrow \pi^*$	25 ^K	2.37	2.35	
Formaldehyde	$\text{H}_2\text{C} = \text{O}$				
1^1A_2	$n \rightarrow \pi^*$	379 ^L , 394 ^M	3.83	3.81	
1^1B_1	$n \rightarrow \bar{R}$	709 ^N , 7.09 ^O , 710 ^P	7.11	7.13	
2^1B_1	$n \rightarrow \bar{R}$	797 ^N , 7.98 ^O , 798 ^P	7.93	7.93	
1^2B_2	$\pi \rightarrow \pi^*$	322 ^{ae}	-	3.32	
1^2A_1	$n \rightarrow \pi^*$	497 ^{ae}	-	5.01	
1^3A_2	$n \rightarrow \pi^*$	350 ^L , 350 ^M	3.49	3.47	
Formaldehyde dimer	$2x[\text{H}_2\text{C} = \text{O}]$				
2^1A	$n \rightarrow \pi^*\pi^*$	$2xE(1^3\text{A}_2)$	7.09	7.03	
5^1A	$n \rightarrow \pi^*\pi^*$	$2xE(1^1\text{A}_2)$	7.80	7.73	
1^3A	$n \rightarrow \pi^*\pi^*$	$2xE(1^3\text{A}_2)$	7.09	7.02	
4^3A	$n \rightarrow \pi^*\pi^*$	$E(1^3\text{A}_1) + E(1^1\text{A}_2)$	7.44	7.37	
5^3A	$n \rightarrow \pi^*\pi^*$	$E(1^3\text{A}_2) + E(1^1\text{A}_2)$	7.44	7.37	
Acetone	$\text{C}_3\text{H}_6\text{O}$				
1^1A_2	$n \rightarrow \pi^*$	438 ^L , 437 ^Q	4.26	4.27	
1^1B_2	$n \rightarrow \bar{R}$	636 ^L , 635 ^Q , 636 ^R	6.47	6.51	
1^3A_2	$n \rightarrow \pi^*$	418 ^L , 416 ^Q	3.97	3.97	
Acetaldehyde	$\text{C}_2\text{H}_4\text{O}$				
$1^1\text{A}''$	$n \rightarrow \pi^*$	427 ^L	4.09	4.07	
$1^3\text{A}''$	$n \rightarrow \pi^*$	397 ^L , 391 ^R	3.78	3.76	
Formamide	HCONH_2				
$1^1\text{A}''$	$n \rightarrow \pi^*$	565 ^S	5.38	5.38	
$1^3\text{A}''$	$n \rightarrow \pi^*$	530 ^T	5.14	5.13	
s-Tetrazine	$\text{C}_2\text{H}_2\text{N}_4$				
1^1B_{1u}	$n \rightarrow \pi^*$	235 ^U , 2.25 ^X , 234 ^W	2.36	2.32	
1^1A_u	$n \rightarrow \pi^*$	360 ^U , 342 ^V	3.62	3.59	
1^1B_{3u}	$\pi \rightarrow \pi^*$	492 ^U , 50 ^W	5.11	5.09	
1^3B_{1u}	$n \rightarrow \pi^*$	169 ^{U,X} , 170 ^Y	1.85	1.81	
1^3A_u	$n \rightarrow \pi^*$	295 ^X	3.37	3.34	
Thioketene	H_2CCS				
1^2B_1	$n \rightarrow \pi^*$	243 ^{af}	-	2.50	
2^2B_2	$\pi \rightarrow \pi^*$	325 ^{af}	-	3.37	
1^2A_1	$n \rightarrow \pi^*$	566 ^{af}	-	5.84	

Continu

Fulvene	$C_5H_4 = CH_2$			
1^2B_2	$\pi \rightarrow \pi^*$	118 ^{ag}	-	1.03
1^2B_1	$\sigma \rightarrow \pi^*$	374 ^{ag}	-	3.53
3^2B_2	$\pi \rightarrow \pi^*$	444 ^{ag}	-	4.29
o-Xylene	$C_6H_4(CH_3)_2$			
1^2A_2	$\pi \rightarrow \pi^*$	052 ^{aj}	-	0.26
1^2A_1	$\sigma \rightarrow \pi^*$	244 ^{aj}	-	2.80
2^2B_1	$\sigma \rightarrow \pi^*$	264 ^{aj}	-	2.95
1^2B_2	$\pi \rightarrow \pi^*$	310 ^{aj}	-	2.93
Benzocyclobutene	C_8H_8			
1^2A_2	$\pi \rightarrow \pi^*$	058 ^{aj}	-	0.31
1^2A_1	$\sigma \rightarrow \pi^*$	212 ^{aj}	-	2.30
1^2B_2	$\sigma \rightarrow \pi^*$	276 ^{aj}	-	2.62
2^2B_1	$\pi \rightarrow \pi^*$	308 ^{aj}	-	2.87
Ketene	H_2CCO			
1^2B_1	$n \rightarrow \pi^*$	421 ^{ak}	-	4.23
2^2B_2	$\pi \rightarrow \pi^*$	497 ^{ak}	-	5.24
3^2B_1	$n \rightarrow \pi^*$	645 ^{ak}	-	6.39
1^2A_1	$n \rightarrow \pi^*$	707 ^{ak}	-	6.77
p-Xylylene	$C_6H_4(CH_2)_2$			
1^2B_{2g}	$\pi \rightarrow \pi^*$	183 ^{al}	-	1.86
Dibenzothiophene	$C_{12}H_8S$			
1^2A_2	$\pi \rightarrow \pi^*$	041 ^{am}	-	0.22
2^2A_2	$\pi \rightarrow \pi^*$	133 ^{am}	-	1.30
3^2B_2	$\pi \rightarrow \pi^*$	203 ^{am}	-	1.88
4^2B_2	$\pi \rightarrow \pi^*$	272 ^{am}	-	2.67
1^2A_1	$\cancel{g} \rightarrow \pi^*$	345 ^{am}	-	3.42
o-Xylylene cation	$C_6H_4(CH_2)_2^+$			
1^2B_2	$\pi \rightarrow \pi^*$	144 ^{aj}	-	1.74
2^2A_2	$\pi \rightarrow \pi^*$	236 ^{aj}	-	2.53
2^2B_2	$\pi \rightarrow \pi^*$	282 ^{aj}	-	2.90
Thymine	$C_5H_6N_2O_2$			
$1^2A'$	$\cancel{g} \rightarrow \pi^*$	095 ^{an}	-	0.63
$2^2A''$	$\pi \rightarrow \pi^*$	126 ^{an}	-	1.24
$2^2A'$	$\cancel{g} \rightarrow \pi^*$	170 ^{an}	-	1.42
$3^2A''$	$\pi \rightarrow \pi^*$	308 ^{an}	-	3.17
Methylidyne radical	CH^\bullet			
$A^2\Delta$	$(1\sigma)^2(2\sigma)^2(3\sigma)^1(1\pi_x)^2$	288 ^{ap}	-	2.42
$A^2\Delta$	$(1\sigma)^2(2\sigma)^2(3\sigma)^1(1\pi_y)^2$	288 ^{ap}	-	2.75
$C^2\Sigma^+$	$(1\sigma)^2(2\sigma)^2(3\sigma)^1(1\pi_x)^2, (1\sigma)^2(2\sigma)^2(3\sigma)^1(1\pi_y)^2$	394 ^{ap}	-	3.64

^a Ref. [6], ^b Ref. [7], ^c Ref. [8], ^d Ref. [9], ^e Ref. [10], ^f Ref. [11], ^g Ref. [12], ^h Ref. [13], ⁱ Ref. [14], ^j Ref. [15]

^k Ref. [16], ^l Ref. [17], ^m Ref. [18], ⁿ Ref. [19], ^o Ref. [20], ^p Ref. [21], ^q Ref. [22], ^r Ref. [23], ^s Ref. [24], ^t Ref. [25]

^u Ref. [26], ^v Ref. [27], ^w Ref. [28], ^x Ref. [29], ^y Ref. [30], ^z Ref. [31], ^A Ref. [32], ^B Ref. [33], ^C Ref. [34], ^D Ref. [35]

^E Ref. [36], ^F Ref. [37], ^G Ref. [38], ^H Ref. [39], ^I Ref. [40], ^J Ref. [41], ^K Ref. [42], ^L Ref. [43], ^M Ref. [44], ^N Ref. [45]

^O Ref. [46], ^P Ref. [47], ^Q Ref. [48], ^R Ref. [49], ^S Ref. [50], ^T Ref. [51], ^U Ref. [52], ^V Ref. [53], ^W Ref. [54], ^X Ref. [55]

^{aa} Ref. [56], ^{ab} Ref. [57], ^{ac} Ref. [58], ^{ad} Ref. [59], ^{ae} Ref. [60], ^{af} Ref. [56], ^{ag} Ref. [60], ^{ah} Ref. [61], ^{ai} Ref. [62], ^{aj} Ref. [63]

^{ak} Ref. [64], ^{al} Ref. [65], ^{am} Ref. [66], ^{an} Ref. [67]

Table S3: Vertical excitation energies of selected doublet states (in eV), comparison between experimental data and our new all-multiplicity Hamiltonian with $\delta E_{\text{sel}} = 10E_h$ and $\delta E_{\text{sel}} = 08E_h$ (tight) parameters. Neutral molecules were calculated at their neutral singlet ground state geometry and are experimentally measured by photoelectronspectroscopy. Charged molecules (cations and anions) are calculated at their corresponding cation or anion geometry of their doublet ground state, experimentally measured by electronic absorption spectroscopy.

State	Exp. DFT/MRCI-A	tight DFT/MRCI-A	
p-Benzosemiquinone anion^a			
$1^2B_{1u}(\pi \rightarrow \pi^*)$	2.87	2.69	2.68
$1^2A_u(\pi \rightarrow \pi^*)$	3.22	3.09	3.10
$2^2B_{1u}(\pi \rightarrow 3p_z)$	3.92	3.81	3.84
Perylene cation^b			
$1^2B_{3g}(\pi \rightarrow \pi^*)$	1.56	1.68	1.70
$1^2B_{2g}(\pi \rightarrow \pi^*)$	1.69	1.64	1.66
$2^2B_{3g}(\pi \rightarrow \pi^*)$	1.93	1.85	1.87
$2^2B_{2g}(\pi \rightarrow \pi^*)$	2.32	2.22	2.25
$4^2B_{3g}(\pi \rightarrow \pi^*)$	3.73	3.75	3.80
Fluorene cation^c			
$1^2B_1(\pi \rightarrow \pi^*)$	0.86	0.88	0.88
$2^2A_2(\pi \rightarrow \pi^*)$	1.18	1.07	1.06
$2^2B_1(\pi \rightarrow \pi^*)$	1.93	1.95	1.95
$1^2B_2(\sigma \rightarrow \pi^*)$	3.13	3.23	3.24
$3^2B_1(\pi \rightarrow \pi^*)$	3.64	3.83	3.81
$4^2B_1(\pi \rightarrow \pi^*)$	4.08	3.63	3.63
Tetrathiafulvalene^d			
$1^2B_{2g}(\pi \rightarrow \pi^*)$	2.14	2.22	2.22
$1^2B_{3g}(\pi \rightarrow \pi^*)$	2.51	2.93	2.93
$2^2B_{2g}(\pi \rightarrow \pi^*)$	2.86	3.01	3.01
$2^2B_{3g}(\pi \rightarrow \pi^*)$	3.67	3.71	3.71
1,5-Hexadiene-3-yne^e			
$1^2B_u(n \rightarrow \pi^*)$	1.16	1.32	1.31
$1^2B_g(\pi \rightarrow \pi^*)$	2.19	2.06	2.05
$2^2A_u(\pi \rightarrow \pi^*)$	3.20	3.25	3.22
$1^2A_g(n \rightarrow \pi^*)$	4.14	4.14	4.13
$2^2B_u(\pi \rightarrow \pi^*)$	4.44	4.44	4.45
$5^2A_g(\pi \rightarrow \pi^*)$	6.14	6.30	6.33
$7^2A_g(\pi \rightarrow \pi^*)$	7.19	7.11	7.13
all-trans 1,3,5,7-octatetraene cation^f			
$1^2A_u(\pi \rightarrow \pi^*)$	1.67	1.75	1.73
$2^2A_u(\pi \rightarrow \pi^*)$	2.77	2.77	2.78
$2^2B_g(\pi \rightarrow \pi^*)$	2.97	2.84	2.83
all-trans 1,3,5,7-octatetraene^g			
$1^2A_u(\pi \rightarrow \pi^*)$	1.82	1.76	1.75
$2^2B_g(\pi \rightarrow \pi^*)$	3.10	2.89	2.87
$1^2A_g(n \rightarrow \pi^*)$	3.93	4.16	4.16
o-Xylylene^h			
$1^2B(\pi \rightarrow \pi^*)$	1.90	1.96	1.94
$2^2(Ar \rightarrow \pi^*)$	2.35	2.42	2.41

Continued on next page

State	Exp. DFT/MRCI-A	tight DFT/MRCI-A	
$2^2B(\pi \rightarrow \pi^*)$	2.79	2.87	2.88
$3^2A(\pi \rightarrow \pi^*)$	3.74	4.04	4.05
$5^2B(\pi \rightarrow \pi^*)$	4.40	4.62	4.63
Styrene^h			
$2^2A(\pi \rightarrow \pi^*)$	0.80	0.75	0.74
$3^2A(\pi \rightarrow \pi^*)$	2.09	2.18	2.17
$1^2A'(\sigma \rightarrow \pi^*)$	3.04	3.40	3.40
$2^2A'(\sigma \rightarrow \pi^*)$	3.70	3.58	3.59
$3^2A'(\sigma \rightarrow \pi^*)$	4.38	4.31	4.32
Carbazoleⁱ			
$1^2A_2(\pi \rightarrow \pi^*)$	0.39	0.26	0.25
$2^2A_2(\pi \rightarrow \pi^*)$	1.46	1.43	1.42
$2^2B_2(\pi \rightarrow \pi^*)$	2.15	2.03	2.02
$3^2B_2(\pi \rightarrow \pi^*)$	3.19	3.21	3.20
Dibenzofuran^j			
$1^2B_2(\pi \rightarrow \pi^*)$	0.25	0.20	0.20
$2^2A_2(\pi \rightarrow \pi^*)$	1.26	1.01	1.00
$2^2B_2(\pi \rightarrow \pi^*)$	1.97	1.84	1.83
$1^2A_1(\sigma \rightarrow \pi^*)$	3.12	3.51	3.53
Dichlorodifluoromethane^k			
$1^2A_2(n \rightarrow n^*)$	0.3	0.19	0.18
$1^2B_2(n \rightarrow n^*)$	0.9	0.61	0.60
$1^2A_1(n \rightarrow n^*)$	1.2	1.35	1.34
Adenine^l			
$1^2A'(\sigma \rightarrow \pi^*)$	0.98	0.95	0.96
$2^2A''(\pi \rightarrow \pi^*)$	1.07	1.21	1.21
$2^2A'(\sigma \rightarrow \pi^*)$	1.98	1.87	1.88
$3^2A''(\pi \rightarrow \pi^*)$	2.04	2.11	2.12
$3^2A'(\sigma \rightarrow \pi^*)$	2.88	2.72	2.74
Fluorobenzene^m			
$1^2A''(\pi \rightarrow \pi^*)$	0.4	0.38	0.38
$1^2B_1(\pi \rightarrow \pi^*)$	2.9	3.10	3.10
$2^2B_2(\sigma \rightarrow \pi^*)$	2.9	2.95	2.92
$1^2A_1(\sigma \rightarrow \pi^*)$	3.6	3.70	3.71
$2^2B_1(\sigma \rightarrow \pi^*)$	4.5	4.78	4.80
$3^2B_1(\sigma \rightarrow \pi^*)$	5.2	5.28	5.29
$2^2A_1(\sigma \rightarrow \pi^*)$	5.8	5.68	5.69
2,3-Benzofluorene cationⁿ			
$2^2A''(\pi \rightarrow \pi^*)$	0.80	0.70	0.70
$4^2A''(\pi \rightarrow \pi^*)$	1.72	1.79	1.79
$6^2A''(\pi \rightarrow \pi^*)$	2.70	2.83	2.84
$8^2A''(\pi \rightarrow \pi^*)$	3.06	3.39	3.42
$11^2A''(\pi \rightarrow \pi^*)$	3.49	3.90	3.94
Tetracene cation^j			
$1^2B_{3g}(\pi \rightarrow \pi^*)$	1.43	1.49	1.50
$1^2B_{2g}(\pi \rightarrow \pi^*)$	1.65	1.61	1.61
$4^2B_{3g}(\pi \rightarrow \pi^*)$	3.14	3.41	3.46

Continued on next page

State	Exp. DFT/MRCI-A	tight DFT/MRCI-A	
1,2,4,5-Tetrafluorobenzene			
$1^2B_{3g}(\pi \rightarrow \pi^*)$	0.7	0.61	0.61
$1^2B_{1u}(\pi \rightarrow \pi^*)$	3.0	2.85	2.83
$1^2B_{3u}(n \rightarrow \pi^*)$	4.2	4.30	4.32
$1^2A_g(n \rightarrow \pi^*)$	4.2	4.13	4.14
$1^2B_{1g}(n \rightarrow \pi^*)$	5.1	5.19	5.21
1,2,3,4-Tetrafluorobenzene^m			
$1^2B_2(\pi \rightarrow \pi^*)$	0.0	0.32	0.32
$2^2B_2(\pi \rightarrow \pi^*)$	2.7	2.81	2.78
$1^2A_1(n \rightarrow \pi^*)$	3.9	3.96	4.13
$1^2B_1(n \rightarrow \pi^*)$	3.9	4.13	3.95
$2^2A_1(n \rightarrow \pi^*)$	4.8	4.95	4.95
Ethylfluoride^m			
$1^2A'(\sigma \rightarrow \pi^*)$	0.5	0.06	0.05
$2^2A'(\sigma \rightarrow \pi^*)$	1.6	1.48	1.49
$2^2A''(\pi \rightarrow \pi^*)$	2.1	2.12	2.13
$3^2A'(\sigma \rightarrow \pi^*)$	3.6	3.17	3.18
$3^2A''(\pi \rightarrow \pi^*)$	4.7	4.88	4.89
$4^2A'(\sigma \rightarrow \pi^*)$	4.7	4.42	4.43
$5^2A'(\sigma \rightarrow \pi^*)$	8.6	8.51	8.52
Hydroxyl radical^o			
$A^2\Sigma^+(\sigma \rightarrow \pi^*)$	4.09	4.05	4.05
$B^2\Sigma^+(\sigma \rightarrow 3\sigma)$	8.65	8.45	8.46
Acenaphthylene cation^p			
$1^2A_2(\pi \rightarrow \pi^*)$	0.80	0.70	0.71
$2^2B_2(\pi \rightarrow \pi^*)$	1.15	1.12	1.12
$2^2A_2(\pi \rightarrow \pi^*)$	2.53	2.51	2.51
Acenaphthene cation^j			
$2^2B_1(\pi \rightarrow \pi^*)$	1.88	2.02	2.01
$2^2A_2(\pi \rightarrow \pi^*)$	2.74	2.75	2.73
Bithiophene cation^q			
$2^2A_u(\pi \rightarrow \pi^*)$	2.10	2.13	2.12
$3^2A_u(\pi \rightarrow \pi^*)$	2.92	2.93	2.94
Phenanthrene cation^q			
$2^2A_2(\pi \rightarrow \pi^*)$	1.38	1.49	1.49
$2^2B_2(\pi \rightarrow \pi^*)$	1.95	2.01	2.02
$3^2B_2(\pi \rightarrow \pi^*)$	2.63	2.60	2.61
$3^2A_2(\pi \rightarrow \pi^*)$	2.91	3.15	3.18
$4^2B_2(\pi \rightarrow \pi^*)$	3.13	3.29	3.33
$4^2A_2(\pi \rightarrow \pi^*)$	3.59	3.45	3.48
Beryllium monohydride^o			
$A^2\Pi(n \rightarrow \pi^*)$	2.48	2.40	2.39
$B^2\Pi(n \rightarrow 3p_x)$	6.32	6.33	6.34
Ethylenyl^r			
$1^2A''(\pi \rightarrow n^*)$	3.08	3.04	3.02
$6^2A'(\sigma \rightarrow n^*)$	7.37	7.25	7.23
$7^2A'(\sigma \rightarrow n^*)$	7.53	7.60	7.59

Continued on next page

State	Exp. DFT/MRCI-A		tight DFT/MRCI-A
Nitric oxide^j			
$A^2\Sigma^+(\pi \rightarrow 3\phi)$	5.92	6.06	6.11
$D^2\Sigma^+(\pi \rightarrow 3p_z)$	7.03	7.11	7.15
Nitrogen dioxide^s			
$2^2B_1(\pi \rightarrow \pi^*)$	5.22	4.83	4.80
$2^2A_1(\phi \rightarrow 3\phi)$	7.50	7.37	7.38
$5^2B_1(\phi \rightarrow 3p_x)$	8.60	8.63	8.66
$3^2B_2(\phi \rightarrow 3p_y)$	8.60	8.74	8.78
$5^2A_1(\phi \rightarrow 3p_z)$	8.60	8.68	8.72
$7^2B_1(\phi \rightarrow 3\phi)$	9.66	9.31	9.34
Azulene cation^j			
$2^2A_2(\pi \rightarrow \pi^*)$	2.58	2.77	2.76
$3^2B_2(\pi \rightarrow \pi^*)$	3.37	3.38	3.36
Azulene^t			
$1^2B_2(\pi \rightarrow \pi^*)$	1.07	1.11	1.10
$2^2A_2(\pi \rightarrow \pi^*)$	2.64	2.64	2.63
$3^2B_2(\pi \rightarrow \pi^*)$	3.42	3.28	3.27
Pentacene cation^j			
$1^2B_{1u}(\pi \rightarrow \pi^*)$	1.26	1.17	1.16
$1^2A_u(\pi \rightarrow \pi^*)$	1.30	1.27	1.27
$3^2A_u(\pi \rightarrow \pi^*)$	2.91	3.05	3.08
Tertiophene cation^q			
$1^2B_2(\pi \rightarrow \pi^*)$	1.46	1.52	1.52
$3^2B_2(\pi \rightarrow \pi^*)$	2.25	2.24	2.25
Styrene cation^h			
$3^2A''(\pi \rightarrow \pi^*)$	2.14	2.26	2.25
$5^2A''(\pi \rightarrow \pi^*)$	3.75	3.75	3.73
Ovalene cationⁱ			
$1^2A_u(\pi \rightarrow \pi^*)$	1.0	1.25	1.26
$1^2B_{1u}(\pi \rightarrow \pi^*)$	1.27	1.49	1.49
$3^2B_{1u}(\pi \rightarrow \pi^*)$	2.21	2.17	2.19
$4^2A_u(\pi \rightarrow \pi^*)$	2.68	2.88	2.93
Hexacene^t			
$1^2B_{3g}(\pi \rightarrow \pi^*)$	1.11	1.07	1.07
$1^2B_{1u}(\pi \rightarrow \pi^*)$	1.7	1.68	1.69
$2^2A_u(\pi \rightarrow \pi^*)$	2.12	1.97	1.99
$5^2B_{2g}(\pi \rightarrow \pi^*)$	2.92	2.91	2.96
$3^2B_{3g}(\pi \rightarrow \pi^*)$	2.92	2.77	2.81
$5^2A_u(\pi \rightarrow \pi^*)$	3.51	3.35	3.42
$9^2B_{1u}(\pi \rightarrow \pi^*)$	3.51	3.79	3.88
$7^2B_{3g}(\pi \rightarrow \pi^*)$	3.86	3.79	3.86
Phenoxy^u			
$1^2B_1(\pi \rightarrow \pi^*)$	1.10	0.90	0.89
$1^2A_2(\pi \rightarrow \pi^*)$	1.98	2.29	2.27
$2^2B_2(\pi \rightarrow \pi^*)$	3.12	3.33	3.31
$2^2A_2(\pi \rightarrow \pi^*)$	4.20	4.40	4.41
$4^2B_2(\pi \rightarrow \pi^*)$	5.18	5.17	5.19

Continued on next page

State	Exp. DFT/MRCI-A	tight DFT/MRCI-A
$3^2A_2(\pi \rightarrow \pi^*)$	5.95	5.72
Phenyl^v		
$1^2B_2(\pi \rightarrow \pi^*)$	2.43	2.65
$3^2A_1(\pi \rightarrow \pi^*)$	5.27	4.94
$3^2B_1(\pi \rightarrow \pi^*)$	5.86	5.69

^a Ref. [68], ^b Ref. [59], ^c Ref. [69], ^d Ref. [70], ^e Ref. [60], ^f Ref. [61], ^g Ref. [71], ^h Ref. [63], ⁱ Ref. [72], ^j Ref. [66]

^k Ref. [73], ^l Ref. [67], ^m Ref. [74], ⁿ Ref. [75], ^o Ref. [76], ^p Ref. [77], ^q Ref. [78], ^r Ref. [79], ^s Ref. [80], ^t Ref. [81]

^u Ref. [82], ^v Ref. [83]

Table S4: Vertical excitation energies of selected singlet and triplet states (in eV) compared between experimental data, the original parameterization (DFT/MRCI-S), Lyskov's redesign parameters and our new all-multiplicity-operator (DFT/MRCI-M)

State	Exp. DFT/MRCI-S	DFT/MRCI-R	DFT/MRCI-A	DFT/MRCI-A (tight)
Carbon dioxide^a				
$1^1\Delta_u(\pi \rightarrow \pi^*)$	8.6	8.75	8.80	8.83
Carbon disulfide^a				
$3^3\Delta_u(\pi \rightarrow \pi^*)$	3.36	3.39	3.37	3.38
$1^1\Delta_u(\pi \rightarrow \pi^*)$	3.91	4.02	4.02	3.99
$1^1\Pi_g(\pi \rightarrow \pi^*)$	6.79	6.71	6.69	6.77
Carbonyl sulfide^a				
$3^3\Sigma_u^+(\pi \rightarrow \pi^*)$	4.94	4.86	4.95	4.90
$1^1\Delta_u(\pi \rightarrow \pi^*)$	5.53	5.57	5.59	5.54
$1^1\Pi_g(\pi \rightarrow 3\ddagger)$	7.36	7.29	7.31	7.28
$1^1\Sigma_u^+(\pi \rightarrow \pi^*)$	8.02*	8.26	8.11	8.06
Sulfur dioxide^a				
$3^3B_2(n \rightarrow \pi^*)$	3.40	3.23	3.27	3.23
$1^1A_2(n \rightarrow \pi^*)$	4.31	4.28	4.29	4.26
Ethylene^a				
$3^3B_{3u}(\pi \rightarrow \pi^*)$	4.32	4.25	4.35	4.32
$1^1B_{1u}(\pi \rightarrow 3\ddagger)$	728 *	7.23	7.20	7.19
$1^1B_{3u}(\pi \rightarrow \pi^*)$	7.6	7.64	7.51	7.46
$1^1B_{3g}(\sigma \rightarrow \pi^*)$	8.25	8.21	8.25	8.22
$1^1B_{1u}(\pi \rightarrow 3\cancel{\ddagger})$	891 *	8.94	8.89	8.87
Propene^a				
$3^3A'(\pi \rightarrow \pi^*)$	4.28	4.14	4.35	4.10
$1^1A''(\pi \rightarrow 3\ddagger)$	6.6	6.61	6.64	6.63
$1^1A'(\pi \rightarrow \pi^*)$	7.17	7.22	7.16	7.13
Isobutene^a				
$3^3A_1(\pi \rightarrow \pi^*)$	4.22	4.04	4.30	4.29
$1^1B_1(\pi \rightarrow 3\ddagger)$	6.1	6.26	6.29	6.30
$1^1A_1(\pi \rightarrow \pi^*)$	671 *	6.69	6.67	6.66
$1^1A_1(\pi \rightarrow \pi^*)$	7.78	7.88	7.88	7.87
cis-2-Butene^a				
$3^3B_2(\pi \rightarrow \pi^*)$	4.21	4.27	4.41	4.38
$1^1B_2(\pi \rightarrow \pi^*)$	7.10	7.40	7.32	7.29
trans-2-Butene^a				
$3^3B_u(\pi \rightarrow \pi^*)$	4.24	4.18	4.37	4.35

Continued on next page

State	Exp.	DFT/MRCI-S	DFT/MRCI-R	DFT/MRCI-A	DFT/MRCI-A (tight)
$^1A_u(\pi \rightarrow 3\ddagger)$	6.3	6.31	6.33	6.33	6.33
$^1B_u(\pi \rightarrow \pi^*)$	6.95	7.12	7.06	7.03	7.03
Trimethylethylene^a					
$^3A'(\pi \rightarrow \pi^*)$	4.16	4.02	4.31	4.30	4.30
$^1A''(\pi \rightarrow 3\ddagger)$	5.76	5.87	5.91	5.91	5.91
$^1A'(\pi \rightarrow \pi^*)$	6.47	6.59	6.60	6.59	6.60
$^1A'(\pi \rightarrow \pi^*)$	6.97*	7.20	7.19	7.18	7.19
Tetramethylethylene^a					
$^3A_r(\pi \rightarrow \pi^*)$	4.10	4.07	4.27	4.25	4.25
$^1A_r(\pi \rightarrow 3\ddagger)$	5.55	5.67	5.70	5.70	5.70
$^1A_r(\pi \rightarrow \pi^*)$	6.57	6.65	6.64	6.62	6.62
Fluoroethylene^a					
$^3A'(\pi \rightarrow \pi^*)$	4.40	4.34	4.46	4.43	4.43
$^1A''(\pi \rightarrow 3\ddagger)$	7.02	7.09	7.09	7.07	7.07
$^1A'(\pi \rightarrow \pi^*)$	7.50	7.66	7.53	7.49	7.49
$^1A''(\pi \rightarrow 3p)$	8.08	7.88	7.89	7.88	7.88
$^1A''(\pi \rightarrow 3d)$	8.87	9.02	8.98	8.97	8.97
1,1-difluoroethylene^a					
$^3A_1(\pi \rightarrow \pi^*)$	4.63	4.47	4.68	4.66	4.66
$^1B_2(\pi \rightarrow 3\ddagger)$	6.95	6.98	6.99	6.98	6.99
$^1A_1(\pi \rightarrow \pi^*)$	7.50	7.67	7.59	7.57	7.57
$^1A_2(\pi \rightarrow 3p)$	8.23	7.93	7.98	7.97	7.98
cis-1,2-difluoroethylene^a					
$^3B_1(\pi \rightarrow \pi^*)$	4.43	4.43	4.53	4.49	4.50
$^1B_2(\pi \rightarrow 3\ddagger)$	6.52	6.43	6.48	6.47	6.47
$^1B_1(\pi \rightarrow \pi^*)$	7.82	7.96	7.80	7.76	7.76
$^1A_1(\pi \rightarrow 3p)$	8.38	8.29	8.24	8.22	8.22
$^1B_2(\pi \rightarrow 3d)$	9.01	8.81	8.79	8.78	8.78
trans-1,2-difluoroethylene^a					
$^3B_u(\pi \rightarrow \pi^*)$	4.18	4.27	4.37	4.34	4.34
$^1B_g(\pi \rightarrow 3\ddagger)$	6.44	6.60	6.70	6.68	6.69
$^1B_u(\pi \rightarrow \pi^*)$	7.39	7.68	7.53	7.48	7.48
Trifluoroethylene^a					
$^3A'(\pi \rightarrow \pi^*)$	4.43	4.39	4.61	4.60	4.60
$^1A''(\pi \rightarrow 3\ddagger)$	6.56	6.47	6.56	6.55	6.55
$^1A'(\pi \rightarrow \pi^*)$	7.65	7.85	7.77	7.74	7.74
$^1A''(\pi \rightarrow 3p)$	7.98	7.79	7.78	7.77	7.77
$^1A''(\pi \rightarrow 3d)$	8.74	8.77	8.78	8.76	8.77
Tetrafluoroethylene^a					
$^3B_{2u}(\pi \rightarrow \pi^*)$	4.68	4.85	4.84	4.80	4.80
$^1B_{1u}(\pi \rightarrow 3\ddagger)$	6.62	6.81	6.80	6.78	6.78
$^1B_{2u}(\pi \rightarrow \pi^*)$	8.84	8.79	8.58	8.52	8.52
Chlorotrifluoroethylene^a					
$^3A'(\pi \rightarrow \pi^*)$	4.43	4.41	4.51	4.48	4.48
$^1A''(\pi \rightarrow 3\ddagger)$	6.51	6.54	6.59	6.58	6.58
Chloroethylene^a					
$^3A'(\pi \rightarrow \pi^*)$	4.08	4.08	4.22	4.19	4.20

Continued on next page

State	Exp.	DFT/MRCI-S	DFT/MRCI-R	DFT/MRCI-A	DFT/MRCI-A (tight)
$^1A'(\pi \rightarrow \pi^*)$	6.72*	6.82	6.73	6.70	6.71
Acetylene^a					
$^3\Sigma_u^+(\pi \rightarrow \pi^*)$	5.2	5.23	5.43	5.41	5.42
$^3\Delta_u(\pi \rightarrow \pi^*)$	6.0	5.72	5.87	5.85	5.85
$^1\Pi_u(\pi \rightarrow 3\phi)$	8.16*	7.96	7.91	7.90	7.90
Propyne^a					
$^3A'(\pi \rightarrow \pi^*)$	5.2	5.16	5.48	5.48	5.49
$^3A'(\pi \rightarrow \pi^*)$	5.8	5.62	5.89	5.89	5.89
$^1A'(\pi \rightarrow 3\phi)$	7.18	6.91	6.94	6.94	6.95
1-butyne^a					
$^3A'(\pi \rightarrow \pi^*)$	5.2	5.11	5.45	5.45	5.46
$^3A'(\pi \rightarrow \pi^*)$	5.8	5.57	5.85	5.85	5.86
3,3,3-trifluoropropyne^a					
$^3A'(\pi \rightarrow \pi^*)$	5.0	5.27	5.39	5.36	5.36
$^3A'(\pi \rightarrow \pi^*)$	5.8	5.75	5.81	5.78	5.78
$^1A'(\pi \rightarrow 3\phi)$	8.80	8.55	8.52	8.50	8.51
1,3-butadiene^a					
$^3B_u(\pi \rightarrow \pi^*)$	3.22	3.13	3.18	3.15	3.17
$^3A_g(\pi \rightarrow \pi^*)$	4.91	4.84	4.99	4.98	5.03
$^1B_u(\pi \rightarrow \pi^*)$	592 *	5.88	5.75	5.70	5.71
trans-1,3-pentadiene^a					
$^3A'(\pi \rightarrow \pi^*)$	3.14	3.14	3.19	3.16	3.18
$^3A'(\pi \rightarrow \pi^*)$	4.87	4.83	4.99	4.98	5.03
$^1A'(\pi \rightarrow \pi^*)$	5.80	5.83	5.70	5.66	5.66
cis-2-trans-4-hexadiene^a					
$^3A'(\pi \rightarrow \pi^*)$	3.11	3.12	3.17	3.14	3.15
$^3A'(\pi \rightarrow \pi^*)$	4.8	4.93	5.02	5.01	5.05
$^1A'(\pi \rightarrow \pi^*)$	5.69	5.71	5.61	5.58	5.59
1,3-cyclohexadiene^a					
$^3B(\pi \rightarrow \pi^*)$	2.94	2.89	2.95	2.92	2.93
$^1B(\pi \rightarrow \pi^*)$	4.94	5.06	4.96	4.92	4.92
1,5-hexadiene^a					
$^3A(\pi \rightarrow \pi^*)$	4.25	4.00	4.29	4.29	4.33
1,4-cyclohexadiene^a					
$^3B_{2g}(\pi \rightarrow \pi^*)$	4.29	4.15	4.35	4.34	4.35
$^1B_{3g}(\pi \rightarrow \pi^*)$	6.15	6.27	6.30	6.30	6.31
$^1B_{3g}(\pi \rightarrow \pi^*)$	7.95	7.88	7.89	7.89	7.90
Propadiene (allene)^a					
$^3A_1(\pi \rightarrow \pi^*)$	4.28	4.38	4.61	4.60	4.61
$^1A_1(\pi \rightarrow \pi^*)$	7.24	7.16	7.14	7.13	7.14
Benzene^a					
$^3B_{2u}(\pi \rightarrow \pi^*)$	3.90	4.12	4.13	4.11	4.14
$^3B_{3u}(\pi \rightarrow \pi^*)$	5.59	5.51	5.49	5.44	5.45
$^1B_{3u}(\pi \rightarrow \pi^*)$	4.80	5.04	5.00	4.97	5.01
$^1B_{2u}(\pi \rightarrow \pi^*)$	6.25	6.23	6.12	6.07	6.08
Fluorobenzene^a					
$^3A_1(\pi \rightarrow \pi^*)$	3.90	4.16	4.19	4.16	4.17

Continued on next page

State	Exp.	DFT/MRCI-S	DFT/MRCI-R	DFT/MRCI-A	DFT/MRCI-A (tight)
$^3B_1(\pi \rightarrow \pi^*)$	5.72	5.63	5.61	5.56	5.57
$^1B_1(\pi \rightarrow \pi^*)$	4.78	5.02	5.00	4.98	5.01
$^1A_1(\pi \rightarrow \pi^*)$	6.23	6.26	6.15	6.10	6.11
o-difluorobenzene^a					
$^3B_1(\pi \rightarrow \pi^*)$	3.92	4.17	4.19	4.16	4.17
$^3A_1(\pi \rightarrow \pi^*)$	5.67	5.65	5.63	5.58	5.58
$^1A_1(\pi \rightarrow \pi^*)$	4.76	5.04	5.01	4.99	5.02
$^1B_1(\pi \rightarrow \pi^*)$	6.22	6.30	6.19	6.14	6.15
1,3,5-trifluorobenzene^a					
$^3A_1(\pi \rightarrow \pi^*)$	3.95	4.23	4.25	4.22	4.23
$^3B_2(\pi \rightarrow \pi^*)$	5.62	5.61	5.59	5.54	5.54
$^1B_2(\pi \rightarrow \pi^*)$	4.87	5.13	5.12	5.10	5.13
$^1A_1(\pi \rightarrow \pi^*)$	6.20	6.34	6.24	6.19	6.19
1,2,3,4-tetrafluorobenzene^a					
$^3A_1(\pi \rightarrow \pi^*)$	3.95	4.19	4.20	4.17	4.17
$^1A_1(\pi \rightarrow \pi^*)$	4.85	5.07	5.04	5.02	5.05
$^1B_1(\pi \rightarrow \pi^*)$	6.43	6.37	6.27	6.21	6.22
1,2,4,5-tetrafluorobenzene^a					
$^3B_{2u}(\pi \rightarrow \pi^*)$	4.0	4.18	4.18	4.16	4.19
$^1B_{3u}(\pi \rightarrow \pi^*)$	4.69	4.97	4.95	4.93	4.95
$^1B_{2u}(\pi \rightarrow \pi^*)$	6.3	6.40	6.28	6.23	6.24
Pentafluorobenzene^a					
$^3A_1(\pi \rightarrow \pi^*)$	3.90	4.26	4.22	4.19	4.20
$^1B_1(\pi \rightarrow \pi^*)$	4.79	5.09	5.07	5.06	5.08
$^1A_1(\pi \rightarrow \pi^*)$	6.36	6.44	6.33	6.27	6.28
Hexafluorobenzene^a					
$^3B_{2u}(\pi \rightarrow \pi^*)$	3.86	4.18	4.15	4.11	4.16
$^1B_{3u}(\pi \rightarrow \pi^*)$	4.80	5.15	5.10	5.07	5.10
$^1B_{2u}(\pi \rightarrow \pi^*)$	6.36	6.51	6.38	6.32	6.33
Furan^a					
$^3B_1(\pi \rightarrow \pi^*)$	3.99	3.82	3.94	3.92	3.93
$^3A_1(\pi \rightarrow \pi^*)$	5.22	4.99	5.15	5.14	5.16
$^1B_1(\pi \rightarrow \pi^*)$	6.06	6.15	6.09	6.06	6.07
$^1A_1(\pi \rightarrow \pi^*)$	7.82	7.95	7.90	7.89	7.90
Thiophene^a					
$^3B_1(\pi \rightarrow \pi^*)$	366 *	3.75	3.78	3.75	3.76
$^3A_1(\pi \rightarrow \pi^*)$	4.62	4.55	4.56	4.53	4.55
$^1A_1(\pi \rightarrow \pi^*)$	5.48	5.50	5.47	5.45	5.47
$^1A_1(\pi \rightarrow \pi^*)$	7.05	7.10	7.11	7.11	7.13
Pyrrole^a					
$^3B_1(\pi \rightarrow \pi^*)$	4.21	4.04	4.21	4.20	4.21
$^1A_2(\pi \rightarrow 3\sharp)$	5.22	5.11	5.07	5.06	5.07
$^1B_1(\pi \rightarrow \pi^*)$	5.98	6.01	5.98	5.97	5.98
Azomethane^a					
$^3B_g(n \rightarrow \pi^*)$	2.75	2.62	2.79	2.75	2.76
$^1B_g(n \rightarrow \pi^*)$	3.50	3.44	3.48	3.44	3.45
$^1B_u(n \rightarrow 3\flat)$	6.71	6.92	6.97	6.65	6.66

Continued on next page

State	Exp.	DFT/MRCI-S	DFT/MRCI-R	DFT/MRCI-A	DFT/MRCI-A (tight)
$^1B_u(\pi \rightarrow \pi^*)$	7.8	8.07	8.02	8.00	8.01
Azo-tert-butane^a					
$^3B_g(n \rightarrow \pi^*)$	2.67	2.30	2.61	2.60	2.61
$^3B_u(\pi \rightarrow \pi^*)$	4.9	4.70	5.08	5.09	5.10
$^1B_g(n \rightarrow \pi^*)$	3.37	3.10	3.28	3.28	3.28
$^1B_u(n \rightarrow 3p)$	7.3	7.39	7.53	7.56	7.58
Nitromethane^a					
$^3A''(\sigma \rightarrow \pi^*)$	3.8	3.69	3.79	3.75	3.77
$^1A''(\sigma \rightarrow \pi^*)$	4.45	4.35	4.36	4.31	4.32
$^1A'(\pi \rightarrow \pi^*)$	6.23	6.31	6.34	6.32	6.34
Thiophosgene^a					
$^3A_1(\pi \rightarrow \pi^*)$	3.1	3.08	3.10	3.06	3.06
$^1A_2(\sigma \rightarrow \pi^*)$	2.61	2.65	2.68	2.64	2.64
$^1A_1(\pi \rightarrow \pi^*)$	4.89	4.91	4.88	4.86	4.87
1,3-cyclopentadiene^a					
$^3B_2(\pi \rightarrow \pi^*)$	3.1	3.11	3.16	3.13	3.14
$^1B_2(\pi \rightarrow \pi^*)$	5.26	5.39	5.29	5.25	5.25
Pyridine^b					
$^1A_2(n \rightarrow \pi^*)$	5.43	5.39	5.43	5.41	5.46
Pyrazine^b					
$^3B_{1u}(n \rightarrow \pi^*)$	3.33	3.55	3.61	3.56	3.60
$^3B_{2g}(n \rightarrow \pi^*)$	4.59	4.87	4.96	4.94	4.97
$^1B_{1u}(n \rightarrow \pi^*)$	3.83	4.03	4.04	4.01	4.05
$^1B_{2g}(n \rightarrow \pi^*)$	5.19	5.33	5.45	5.43	5.48
Pyrimidine^c					
$^1A_2(n \rightarrow \pi^*)$	4.62	4.83	4.86	4.85	4.88
s-Triazine^c					
$^1B_2(n \rightarrow \pi^*)$	4.59	4.62	4.66	4.64	4.66
Acetone^d					
$^3A_2(n \rightarrow \pi^*)$	4.16	3.70	3.97	3.97	3.98
$^1A_2(n \rightarrow \pi^*)$	4.37	4.11	4.26	4.27	4.27
Acetamide^e					
$^1A(n \rightarrow \pi^*)$	5.44	5.27	5.43	5.43	5.45
Nitrobenzene^f					
$^1A_2(n \rightarrow \pi^*)$	3.65	3.32	3.52	3.49	3.53
Dithiosuccinimide^g					
$^3B_1(n \rightarrow \pi^*)$	2.63	2.44	2.58	2.56	2.59
$^1B_1(n \rightarrow \pi^*)$	2.77	2.65	2.73	2.71	2.73
$^1A_2(n \rightarrow \pi^*)$	3.04	2.84	2.93	2.91	2.93

^a For experimental energies see Ref. [84] and references therein.

^b Ref. [85], ^c Ref. [8], ^d Ref. [48], ^e Ref. [86], ^f Ref. [26], ^g Ref. [87]

* Band maximum.

ADDITIONAL DETAILS FOR IMPLEMENTATION

Besides the diagonal matrix elements (same space part, same spin coupling) discussed in the main part of this article, three off-diagonal classes exist: a) same space part, different spin coupling, b) one-electron difference in space part and c) two-electron difference in space part. [88] For DFT/MRCI one therefore needs the equations for the CI matrix elements [89] as well as the corresponding DFT/MRCI corrections.

Case a): The same equation as in the diagonal case with same spin coupling is used.

$$H_n = E_{\mathcal{E}} + \sum_i F_i \mathcal{A}_i + \frac{1}{2} \sum_{\substack{j \\ \neq i}} V_j \mathcal{A}_i \mathcal{A}_j + \frac{1}{2} \sum_{\substack{j \\ \neq i}} V_j \left(-\frac{1}{2} \mathcal{A}_i \mathcal{A}_j + \frac{1}{2} w_i w_j - w_i + \eta_j^j \right) + \frac{1}{2} \sum_i V_i \left(\frac{1}{2} \mathcal{A}_i \mathcal{A}_j + \frac{1}{2} w_i w_i - w_i \right) \quad (1)$$

Only the part depending on the exchange-like integral in conjunction with η_j^j contributes to this off-diagonal element. For different spin coupling, we arrive at the correction

$$H_n^{\text{MC}} = -p_F H_n \quad (2)$$

Case b): For matrix elements between two configurations differing in one electron occupation

$$H_n' = F_j \eta_i^j + \sum_{k \neq i} V_k \mathcal{A}'_k \eta_i^j + \sum_{k \neq i} V_k \left(-\frac{1}{2} \mathcal{A}'_k \eta_i^j + \frac{1}{2} w'_k \eta_i^j - n_i^j + \eta_k^k \right) + V_j \left(\frac{1}{2} \mathcal{A}'_i + \frac{1}{2} w'_i \right) \eta_i^j - V_j \left(\frac{1}{2} \mathcal{A}'_j + \frac{1}{2} w'_i - \eta_i^j \right) \quad (3)$$

we use a damping function to avoid double counting of the electron correlation

$$H_n^{\text{MC}}, = \frac{p_1}{1 - \delta_j} H_n' \quad (4)$$

Case c): For matrix elements between two configurations differing in a two electron occupation

$$H_n'' = \left(V_k \eta_k^j + V_k \eta_k^j + \delta_k + \delta_j \right) \quad (5)$$

the same damping function as in the one electron difference is used

$$H_n^{\text{MC}} = \frac{p_1}{1 - \delta_j} H_n'' \quad (6)$$

References

-
- [1] A. Schäfer, H. Horn, and R. Ahlrichs, *J. Chem. Phys.* **97**, 2571 (1992).
- [2] A. Schäfer, C. Huber, and R. Ahlrichs, *J. Chem. Phys.* **100**, 5829 (1994).
- [3] F. Weigend, F. Furche, and R. Ahlrichs, *J. Chem. Phys.* **119**, 12753 (2003).
- [4] D. Rappoport and F. Furche, *J. Chem. Phys.* **133**, 134105 (2010).
- [5] F. Weigend, A. Köhn, and C. Hättig, *J. Chem. Phys.* **116**, 3175 (2002).
- [6] I. C. Walker, M. H. Palmer, and A. Hopkirk, *Chem. Phys.* **141**, 365 (1990).
- [7] E. Villa, A. Amirav, and E. C. Lim, *J. Phys. Chem.* **92**, 5393 (1988).
- [8] A. Bolvinos, P. Tsekeris, J. Philis, E. Pantos, and G. Andritsopoulos, *J. Mol. Spectrosc.* **103**, 240 (1984).
- [9] E. van Veen and F. Plantenga, *Chem. Phys. Lett.* **30**, 28 (1975).
- [10] I. C. Walker and M. A. Fluendy, *Int. J. Mass Spectrom.* **205**, 171 (2001).
- [11] W. M. Flicker, O. A. Mosher, and A. Kuppermann, *J. Chem. Phys.* **72**, 2788 (1980).
- [12] K. R. Asmis, *Electron-Molecule Collisions: A Novel Instrument for Measuring Inelastic Differential Cross Sections at 180° Angle and Applications*, Ph.D. thesis, University of Freiburg, Switzerland (1996).
- [13] W. M. Flicker, O. A. Mosher, and A. Kuppermann, *J. Chem. Phys.* **64**, 1315 (1976).
- [14] E. V. Veen, *Chem. Phys. Lett.* **41**, 535 (1976).
- [15] M. H. Palmer, I. C. Walker, C. C. Ballard, and M. F. Guest, *Chem. Phys.* **192**, 111 (1995).
- [16] M. H. Palmer, I. C. Walker, and M. F. Guest, *Chem. Phys.* **241**, 275 (1999).
- [17] R. P. Frueholz, W. M. Flicker, O. A. Mosher, and A. Kuppermann, *J. Chem. Phys.* **70**, 2003 (1979).
- [18] L. W. Pickett, E. Paddock, and E. Sackter, *J. Am. Chem. Soc.* **63**, 1073 (1941).
- [19] J. P. Doering, *J. Chem. Phys.* **70**, 3902 (1979).
- [20] O. A. Mosher, W. M. Flicker, and A. Kuppermann, *J. Chem. Phys.* **59**, 6502 (1973).
- [21] W. C. Price and A. D. Walsh, *Proc. R. Soc. Lond. A* **174**, 220 (1940).
- [22] A. D. Walsh, *Trans. Faraday Soc.* **41**, 498 (1945).
- [23] R. S. Becker, K. Inuzuka, and J. King, *J. Chem. Phys.* **52**, 5164 (1970).
- [24] K. Inuzuka, *Bull. Chem. Soc. Jpn.* **34**, 6 (1961).
- [25] J. Hollas, *Spectrochim. Acta.* **19**, 1425 (1963).
- [26] S. Nagakura, M. Kojima, and Y. Maruyama, *J. Mol. Spectrosc.* **13**, 174 (1964).
- [27] T. Ari, H. Güven, and N. Ecevit, *J. Electron Spectrosc. Relat. Phenom.* **73**, 13 (1995).
- [28] P. Swiderek, M.-J. Fraser, M. Michaud, and L. Sanche, *J. Chem. Phys.* **100**, 70 (1994).
- [29] K. Kimura and S. Nagakura, *Theor. Chim. Acta* **3**, 164 (1965).
- [30] R. P. Frueholz, W. M. Flicker, O. A. Mosher, and A. Kuppermann, *J. Chem. Phys.* **70**, 3057 (1979).
- [31] A. Hiraya and K. Shobatake, *J. Chem. Phys.* **94**, 7700 (1991).
- [32] J. P. Doering, *J. Chem. Phys.* **67**, 4065 (1977).
- [33] R. Huebner, S. Meiczarek, and C. Kuyatt, *Chem. Phys. Lett.* **16**, 464 (1972).
- [34] G. George and G. Morris, *J. Mol. Spectrosc.* **26**, 67 (1968).
- [35] E. N. Lassettre and A. Skerbele, *J. Chem. Phys.* **54**, 1597 (1971).
- [36] S. Trajmar, W. Williams, and A. Kuppermann, *J. Chem. Phys.* **54**, 2274 (1971).
- [37] A. Chutjian, R. I. Hall, and S. Trajmar, *J. Chem. Phys.* **63**, 892 (1975).
- [38] R. Judge, C. Drury-Lessard, and D. Moule, *Chem. Phys. Lett.* **53**, 82 (1978).
- [39] D. G. Wilden and J. Comer, *J. Phys. B: At. Mol. Phys.* **13**, 1009 (1980).
- [40] R. McDiarmid, *J. Phys. Chem.* **84**, 64 (1980).
- [41] M. Allan, *Chem. Phys. Lett.* **225**, 156 (1994).
- [42] G. Verhaart and H. Brongersma, *Chem. Phys. Lett.* **72**, 176 (1980).
- [43] K. N. Walzl, C. F. Koerting, and A. Kuppermann, *J. Chem. Phys.* **87**, 3796 (1987).
- [44] S. Taylor, D. G. Wilden, and J. Comer, *Chem. Phys.* **70**, 291 (1982).
- [45] M. Suto, X. Wang, and L. C. Lee, *J. Chem. Phys.* **85**, 4228 (1986).
- [46] J. E. Mentall, E. P. Gentieu, M. Krauss, and D. Neumann, *J. Chem. Phys.* **55**, 5471 (1971).
- [47] M. J. Weiss, C. E. Kuyatt, and S. Mielczarek, *J. Chem. Phys.* **54**, 4147 (1971).
- [48] W. M. St. John, R. C. Estler, and J. P. Doering, *J. Chem. Phys.* **61**, 763 (1974).
- [49] E. V. Veen, W. V. Dijk, and H. Brongersma, *Chem. Phys.* **16**, 337 (1976).
- [50] H. Basch, M. B. Robin, and N. A. Kuebler, *J. Chem. Phys.* **47**, 1201 (1967).
- [51] R. H. Staley, L. B. Harding, W. G. III, and J. Beauchamp, *Chem. Phys. Lett.* **36**, 589 (1975).
- [52] M. H. Palmer, H. McNab, D. Reed, A. Pollacchi, I. C. Walker, M. F. Guest, and M. R. Siggel, *Chem. Phys.* **214**, 191 (1997).
- [53] K. Innes, *J. Mol. Spectrosc.* **129**, 140 (1988).
- [54] C. Fridh, L. Åsbrink, B. Jonsson, and E. Lindholm, *Int. J. Mass Spectrom. Ion. Phys.* **9**, 485 (1972).
- [55] K. Innes, I. Ross, and W. R. Moomaw, *J. Mol. Spectrosc.* **132**, 492 (1988).

- [56] W. Meyer, *Int. J. Quantum Chem.* **5**, 341 (1971).
- [57] P. A. Benioff, *J. Chem. Phys.* **68**, 3405 (1978).
- [58] S. V. Levchenko and A. I. Krylov, *J. Chem. Phys.* **115**, 7485 (2001).
- [59] P. A. Benioff, *J. Chem. Phys.* **68**, 3405 (1978).
- [60] H. Rosenstock, J. Dannacher, and J. Liebman, *Radiat. Phys. Chem.* **20**, 7 (1982).
- [61] J. H. Starcke, M. Wormit, and A. Dreuw, *J. Chem. Phys.* **131**, 144311 (2009).
- [62] M. Allan, E. Heilbronner, and G. Kaupp, *Helv. Chim. Acta* **59**, 1949 (1976).
- [63] S. V. Levchenko and A. I. Krylov, *J. Chem. Phys.* **115**, 7485 (2001).
- [64] K. Wolinski and P. Pulay, *J. Chem. Phys.* **90**, 3647 (1989).
- [65] M. Allan, E. Heilbronner, and G. Kaupp, *Helv. Chim. Acta* **59**, 1949 (1976).
- [66] S. Hirata, M. Head-Gordon, J. Szczepanski, and M. Vala, *J. Phys. Chem. A* **107**, 4940 (2003).
- [67] K. B. Bravaya, O. Kostko, S. Dolgikh, A. Landau, M. Ahmed, and A. I. Krylov, *J. Phys. Chem. A* **114**, 12305 (2010).
- [68] R. A. Wheeler, *J. Chem. Phys.* **97**, 1533 (1993).
- [69] J. Szczepanski, J. Banisaukas, M. Vala, S. Hirata, R. J. Bartlett, and M. Head-Gordon, *J. Phys. Chem. A* **106**, 63 (2002).
- [70] S. Hirata, T. J. Lee, and M. Head-Gordon, *J. Chem. Phys.* **111**, 8904 (1999).
- [71] T. Jones and J. Maier, *Int. J. Mass Spectrom. Ion Phys.* **31**, 287 (1979).
- [72] B. Rušćić, B. Kovač, L. Klasinc, and H. Güsten, *Z. Naturforsch. A* **33**, 1006 (1978).
- [73] M. Lewerenz, B. Nestmann, P. J. Bruna, and S. D. Peyerimhoff, *J. Mol. Struct. THEOCHEM* **123**, 329 (1985).
- [74] G. Bieri, L. Åsbrink, and W. V. Niessen, *J. Electron Spectrosc. Relat. Phenom.* **23**, 281 (1981).
- [75] J. Banisaukas, J. Szczepanski, M. Vala, and S. Hirata, *J. Phys. Chem. A* **108**, 3713 (2004).
- [76] D. Maurice and M. Head-Gordon, *Int. J. Quantum Chem.* **56**, 361 (1995).
- [77] J. Banisaukas, J. Szczepanski, J. Eyler, M. Vala, S. Hirata, M. Head-Gordon, J. Oomens, G. Meijer, and G. von Helden, *J. Phys. Chem. A* **107**, 782 (2003).
- [78] M. Rubio, E. Ortí, R. Pou-Amérigo, and M. Merchán, *J. Phys. Chem. A* **105**, 9788 (2001).
- [79] A. M. Mebel, Y.-T. Chen, and S.-H. Lin, *Chem. Phys. Lett.* **275**, 19 (1997).
- [80] S.-K. Shih, S. D. Peyerimhoff, and R. J. Buenker, *Chem. Phys. Lett.* **46**, 201 (1977).
- [81] R. Boschi, E. Clar, and W. Schmidt, *J. Chem. Phys.* **60**, 4406 (1974).
- [82] J. G. Radziszewski, M. Gil, A. Gorski, J. Spanget-Larsen, J. Waluk, and B. J. Mróz, *J. Chem. Phys.* **115**, 9733 (2001).
- [83] J. G. Radziszewski, *Chem. Phys. Lett.* **301**, 565 (1999).
- [84] A. Kuppermann, W. M. Flicker, and O. A. Mosher, *Chem. Rev.* **79**, 77 (1979).
- [85] Y. Okuzawa, M. Fujii, and M. Ito, *Chem. Phys. Lett.* **171**, 341 (1990).
- [86] E. B. Nielsen and J. A. Schellman, *J. Phys. Chem.* **71**, 2297 (1967).
- [87] S. C. J. Meskers, T. Polonski, and H. P. J. M. Dekkers, *J. Phys. Chem.* **99**, 1134 (1995).
- [88] S. Grimme and M. Waletzke, *J. Chem. Phys.* **111**, 5645 (1999).
- [89] G. A. Segal, R. W. Wetmore, and K. Wolf, *Chem. Phys.* **30**, 269 (1978).

Reproduced from [133], with the permission of AIP Publishing.

THE JOURNAL OF CHEMICAL PHYSICS **149**, 164106 (2018)



On the performance of DFT/MRCI Hamiltonians for electronic excitations in transition metal complexes: The role of the damping function

Adrian Heil, Martin Kleinschmidt, and Christel M. Marian^{a)}

Institute of Theoretical and Computational Chemistry, Heinrich-Heine-University Düsseldorf, Düsseldorf, Germany

(Received 31 July 2018; accepted 4 October 2018; published online 26 October 2018)

The combination of density functional theory and multireference configuration interaction (DFT/MRCI) is a well-established semi-empirical method suitable for computing spectral properties of large molecular systems. To this day, three different Hamiltonians and various parameter set combinations exist. These DFT/MRCI variants are well tried and tested when it comes to electronic excitations of organic molecules. For transition metal complexes, systematic benchmarks against experimental data are missing, however. Here we present an assessment of the DFT/MRCI variants and of time-dependent, linear-response density functional theory (TDDFT) for a diverse set of ligand-centered, metal-to-ligand charge transfer, metal-centered, and ligand-to-metal charge transfer (LMCT) excitations on 21 *3d* and *4d* complexes comprising 10 small inorganic and 11 larger metalorganic compounds with closed-shell ground states. In the course of this assessment, we realized that the excitation energies of transition metal complexes can be very sensitive with respect to the details of the damping function that scales off-diagonal matrix elements. This scaling is required in DFT/MRCI to avoid double counting of dynamic electron correlation. These insights lead to a new Hamiltonian, denoted R2018, with improved performance on transition metal compounds, while the results for organic molecules are nearly unaffected by the modified damping function. Two parameter sets were optimized for this Hamiltonian: One set is to be used in conjunction with the standard configuration selection threshold of $1.0 E_h$ and a second set is for use with a selection threshold of $0.8 E_h$ which leads to shorter wave function expansions. The R2018 Hamiltonian in standard parameterization achieves root-mean-square errors (RMSEs) of merely 0.15 eV for the metalorganic complexes, followed by 0.20 eV for the original DFT/MRCI ansatz, and 0.25 eV for the redesigned DFT/MRCI approach. In comparison, TDDFT gives a much larger RMSE of 0.46 eV for metalorganic complexes. None of the DFT/MRCI variants yields convincing results for small oxides and fluorides which exhibit LMCT transitions. Here, TDDFT performs better. If the oxides and fluorides are excluded from the inorganic test set, satisfactory agreement can be achieved, with RMSE values between 0.26 eV and 0.30 eV for DFT/MRCI and 0.34 eV for TDDFT. The performance of the original and the new DFT/MRCI Hamiltonians deteriorates only slightly, when a tighter selection threshold is chosen, thus enabling the computation of reliable spectral properties even for large metalorganic complexes. *Published by AIP Publishing.* <https://doi.org/10.1063/1.5050476>

I. INTRODUCTION

Transition metal systems pose a particular challenge for computational chemistry methods, especially when it comes to electronic excitation.^{1–3} Due to the different radial extents of the valence *nd* and $(n + 1)s$ shells, differential electron correlation plays a vital role in the description of *s* – *d* transitions.⁴ In early transition metals, additionally, correlation between the outer core (*ns*, *np*) and the valence electrons has to be taken into account.⁵ Core-valence correlation plays a lesser role in late transition metals where relativistic effects are particularly pronounced.^{6,7} Moreover, the occurrence of (near) degeneracies often requires a multiconfigurational treatment.² Additional

challenges arise from the sheer size of transition metal complexes, which range from small complexes containing hydride or oxide ligands to large complexes with organic ligands, such as bipyridine, phenylpyridine, or phenanthrene, easily comprising more than 200 electrons. Electronic transitions in transition metal complexes can be grouped into five categories: metal-centered (MC), ligand-centered (LC), metal-to-ligand charge transfer (MLCT), ligand-to-metal charge transfer (LMCT), and ligand-to-ligand charge transfer (LLCT). Providing a balanced description for all these excitation types at reasonable cost represents a major challenge for all quantum chemical methods.

Particularly powerful methods for computing electronic spectra of transition metal complexes are complete active space self-consistent field methods with second-order perturbation corrections (CASSCF/CASPT2)^{8,9} or variants thereof such

^{a)}Electronic mail: christel.marian@hhu.de

as restricted active space expansions (RASSCF/RASPT2)¹⁰ and CASSCF/NEVPT2,¹¹ where the latter acronym stands for n -electron valence state perturbation theory. Although the computational expense of RASPT2 and NEVPT2 is somewhat reduced compared to CASPT2, numerous examples can be found where convergence of the results on the choice of active space is difficult to reach.^{3,12,13} Time-dependent, linear-response density functional theory (TDDFT)^{14–16} on the other hand requires a lot less computational time and power, but the results depend strongly on the underlying density functional and the excitation type.^{17–22} Symmetry-adapted cluster theory with configuration interaction (SAC-CI)^{23,24} starts from a Hartree-Fock reference, but includes multi-reference configuration effects through unlinked terms. It converges faster than ordinary CI expansions. SAC-CI has been applied to large transition metal complexes with good success,^{25,26} but it needs much higher computational resources than does TDDFT.

Another well-established quantum chemical method suitable for computing spectral properties of large molecular systems is the combined density functional theory and multireference configuration interaction (DFT/MRCI) method.^{27–30} By combining information from Kohn-Sham (KS) orbitals with a MRCI ansatz, both dynamical and non-dynamical electron correlation can be accounted for while limiting the number of configuration state functions (CSFs) through configuration selection. To avoid double counting of electron correlation, the MRCI matrix elements are parameterized. Coulomb and exchange integrals are scaled by two global empirically fitted parameters, and off-diagonal matrix elements are damped by a function that explicitly depends on the energy separation of the interacting configurations. To this day, three different Hamiltonians and various parameter set combinations exist. The method was originally developed by Grimme and Waletzke,²⁷ which in the following is referred to as the original Hamiltonian. It has a statistical error below 0.2 eV for organic molecules.³¹ To improve the performance of the method on dimer systems and bichromophores in singlet fission or triplet-triplet upconversion, a redesigned Hamiltonian was introduced by Lyskov *et al.*²⁹ (referred to as R2016), maintaining the accuracy of locally excited singlet and triplet excitations of organic molecules. This Hamiltonian was later extended by Heil and Marian³⁰ to systems with an odd number of electrons, making it possible to calculate excited states of all multiplicities with the same parameter set. It also permits to calculate ionization potentials or electron affinities. This Hamiltonian is referred to as R2017.

DFT/MRCI is well tried and tested when it comes to electronic excitation of organic molecules, and even several examples have been reported where good accuracy and cost-effectiveness were reached for transition metal complexes as well.^{20,32–35} While Escudero and Thiel²⁰ carried out benchmark calculations assessing the performance of the original Hamiltonian on 3d and 4d metal complexes against CASPT2 results, there is no such benchmark study to date that evaluates and compares all DFT/MRCI Hamiltonians. Here, we set out for an assessment of the original and redesigned DFT/MRCI variants against 67 experimental absorption

energies of organic and inorganic transition metal complexes measured in the gas phase or in apolar environments. The benchmark set contains a variety of excitation types, most of them being of MLCT and LC type or mixtures thereof, but a few MC and LMCT transitions are also engaged in the test. For comparison with the DFT/MRCI results and as an additional test, all transitions were calculated with TDDFT employing the hybrid Perdew-Burke-Ernzerhof (PBE0) exchange-correlation functional too.

Because the findings of our initial assessments left some room for improving the performance of the DFT/MRCI method on transition metal systems, we devised and parameterized a novel Hamiltonian, the R2018 Hamiltonian. It uses the same expressions as the R2016 (in the case of closed-shell ground states) and R2017 Hamiltonians for calculating diagonal elements, but differs from the latter by the functional form of the off-diagonal damping. As will be seen below, the shape and course of the damping function is a critical parameter in calculations on transition metal complexes, whereas electronic excitation energies of organic molecules are not very sensitive with respect to the chosen type of damping.

II. THEORY

In the following, we present the general aspects of the DFT/MRCI method with particular focus on the differences between the various Hamiltonians. For a detailed description of the DFT/MRCI method, see Refs. 27, 29, 30, and 36.

The DFT/MRCI method uses a one-particle basis of KS orbitals from an anchor configuration with closed-shell electronic structure (even numbers of electrons) or with one open shell (odd numbers of electrons) to build up n -electron wave functions. The evaluation of MRCI matrix elements follows the scheme as outlined by Segal, Wetmore, and Wolf.^{37,38} As the Hamiltonian contains at most two-electron operators, only configurations differing in two or less occupation numbers result in non-vanishing matrix elements. For this reason, the expressions can be simplified and divided into three cases: (i) equivalent spatial occupation (diagonal), (ii) one-electron difference (off-diagonal), and (iii) two-electron difference (off-diagonal).

To make use of the dynamic electron correlation contained in the underlying Becke's half-and-half exchange in a combination with the Lee-Yang-Parr correlation (BH-LYP)^{39,40} density functional, KS orbital energies are introduced into the DFT/MRCI Hamiltonian and its matrix elements are parameterized to avoid double counting of electron correlation. Spin symmetry is exploited by forming spin-adapted linear combinations of determinants, the CSFs. For this reason, case (i) can be further subdivided into the following: genuinely diagonal matrix elements with the same space part and same spin coupling and off-diagonal matrix elements between CSFs with identical space parts but different spin couplings. Cases (ii) and (iii) represent genuinely off-diagonal terms which are scaled in similar fashions in DFT/MRCI, depending explicitly on the energy separation of the interacting configurations.

A. Diagonal elements

A genuinely diagonal matrix element in the DFT/MRCI Hamiltonian can be expressed as

$$\begin{aligned} \langle \omega w | \hat{\mathcal{H}}^{DFT} - E^{DFT} | \omega w \rangle \\ = \langle \omega w | \hat{\mathcal{H}} - E^{HF} | \omega w \rangle - \sum_{i \in c}^{n_{exc}} (F_{ii}^{HF} - F_{ii}^{KS}) \\ + \sum_{i \in a}^{n_{exc}} (F_{ii}^{HF} - F_{ii}^{KS}) + \Delta E_{coul} - \Delta E_{exch} \end{aligned} \quad (1)$$

with n_{exc} being the number of excitations and c and a labeling created and annihilated electrons. F_{ii}^{HF} is a one-electron matrix element, which is also contained in the energy,

$$E^{HF} = \sum_i \bar{w}_i F_{ii}^{HF} - \frac{1}{2} \sum_{ik} \bar{w}_i \bar{w}_k (V_{ikik} - \frac{1}{2} V_{ikki}) \quad (2)$$

with \bar{w}_i as the occupation number. Therefore it can be replaced by the KS orbital energy F_{ii}^{KS} in the DFT/MRCI method. The two-electron contributions ΔE_{coul} and ΔE_{exch} are scaled by empirically fitted parameters. Two different schemes exist for correcting these energy contributions, the original and the redesigned ansatz.

1. Corrections in the original Hamiltonian

In the original work by Grimme and Waletzke,²⁷ the Coulomb and exchange corrections are given by

$$\Delta E_{coul} - \Delta E_{exch} = \frac{1}{n_{exc}} \sum_{i \in c}^{n_{exc}} \sum_{j \in a}^{n_{exc}} (p_J V_{ijij} - m p [N_o] V_{ijji}) \quad (3)$$

with p_J as a scaling parameter for Coulomb integrals $V_{ijij} = \langle ij|ij \rangle$. The Hamiltonian takes on different forms depending on the multiplicity m and the number of open shells N_o . The parameterization is limited to singlets and triplets and the scaling factors of the exchange terms are given by

$${}^1 p [N_o] = {}^1 p [0] + N_o {}^1 \alpha \quad (4)$$

and

$${}^3 p [N_o] = N_o {}^3 \alpha, \quad (5)$$

respectively. The parameters p_J , ${}^1 p [0]$, and ${}^1 \alpha$ were fitted to energetically match experimental singlet excitation energies of a set of small organic molecules²⁷ and the triplet parameters p_J and ${}^3 \alpha$ were fitted independently.

2. Corrections in the redesigned Hamiltonian

A new, multiplicity independent Hamiltonian was introduced by Lyskov *et al.*,²⁹ in which the parameters for singlets and triplets are identical. This was motivated by problems in photoexcited dimers, where two triplets can form an overall singlet-coupled triplet pair. Since this Hamiltonian was set up in conjunction with a closed-shell anchor configuration, it was only suitable for multiplicities with an even number of electrons (singlets, triplets, quintets, . . .), and it was later extended by Heil and Marian³⁰ for systems with an open-shell anchor configuration. This made it possible to calculate all

multiplicities using one and the same parameter set, thus additionally enabling the calculation of ionization potentials and electron affinities.

The scaling parameters are divided into a spin-independent Coulomb scaling p_J and an exchange scaling, which amounts to p_X for the spin-dependent part with the spin-coupling η_{ij}^{ji} and to $\frac{p_X}{2}$ for the spin-independent part. With c and a as created and annihilated electrons and o as open shells in the occupation vector w , the energy correction for R2016 is given by

$$\begin{aligned} \Delta E_{coul} - \Delta E_{exch} = p_J \left(- \sum_{\substack{i,j \in c \\ i>j}}^{n_{exc}} V_{ijij} - \sum_{\substack{i,j \in a \\ i>j}}^{n_{exc}} V_{ijij} + \sum_{i \in c}^{n_{exc}} \sum_{j \in a}^{n_{exc}} V_{ijij} \right) \\ - p_X \left(\frac{1}{2} \sum_{i \in c}^{n_{exc}} \sum_{j \in a}^{n_{exc}} V_{ijji} + \sum_{\substack{i,j \in o \\ i>j}}^{N_o} V_{ijji} \eta_{ij}^{ji} \right). \end{aligned} \quad (6)$$

For an anchor configuration with open shell s , three new sums appear as corrections in R2017,

$$\begin{aligned} \Delta E_{coul} - \Delta E_{exch} \\ = p_J \left(- \sum_{\substack{i,j \in c \\ i>j}}^{n_{exc}} V_{ijij} - \sum_{\substack{i,j \in a \\ i>j}}^{n_{exc}} V_{ijij} + \sum_{i \in c}^{n_{exc}} \sum_{j \in a}^{n_{exc}} V_{ijij} + \frac{1}{2} \sum_{i \in s}^{n_{single}} V_{iiii} |\Delta w_i| \right) \\ - p_X \left(\frac{1}{2} \sum_{i \in c}^{n_{exc}} \sum_{j \in a}^{n_{exc}} V_{ijji} - \sum_{\substack{i,j \in c \\ j \in s}}^{n_{exc}} V_{ijji} - \sum_{\substack{i,j \in a \\ j \in s}}^{n_{exc}} V_{ijji} + \sum_{\substack{i,j \in o \\ i>j}}^{N_o} V_{ijji} \eta_{ij}^{ji} \right). \end{aligned} \quad (7)$$

Comparing Eqs. (6) and (7), it is easily seen that both are equivalent in cases without an open shell in the parent determinant.

B. Off-diagonal elements with same spatial occupation

In the original Hamiltonian, the off-diagonal elements with the same spatial occupation but different spin coupling are not scaled and therefore have the form

$$\langle \omega w | \hat{\mathcal{H}}^{DFT} | \omega' w \rangle = \langle \omega w | \hat{\mathcal{H}}^{CI} | \omega' w \rangle. \quad (8)$$

By contrast, these matrix elements are scaled by $1 - p_X$ in the redesigned Hamiltonian, with p_X being the exchange correction parameter,

$$\langle \omega w | \hat{\mathcal{H}}^{DFT} | \omega' w \rangle = \langle \omega w | (1 - p_X) \hat{\mathcal{H}}^{CI} | \omega' w \rangle. \quad (9)$$

C. Off-diagonal elements with different occupation

In DFT/MRCI Hamiltonians, the genuine off-diagonal elements are scaled by a function that depends on the energy difference between two CSFs. The general idea underlying this way of scaling is to avoid double counting of dynamic correlation (interaction of configurations with large energy separation) that has been taken care of by the DFT part while

static correlation between near degenerate configurations is scaled by p_1 . The different damping functions employed in the DFT/MRCI variants are displayed in Fig. 1 and their functional forms are given below. A steeper function profile leads to a stronger damping, which in turn decreases the correlation contributions, especially in the ground state.

1. Original Hamiltonian

For the original Hamiltonian,²⁷ an exponential damping was chosen,

$$H_{nm'} = p_1 \cdot \exp(-p_2 \cdot \Delta E^4) \cdot H_{nm'}^{CI}. \quad (10)$$

Since the parameter p_1 depends on the correction of the diagonal elements, the damping of the original Hamiltonian leads to a function that is too steep and is therefore underestimating vertical excitation energies on the average in both organic molecules and transition metal complexes.

2. R2016 and R2017 Hamiltonian

The redesigned damping²⁹ employed in the R2016 and R2017 Hamiltonians has the form

$$H_{nm'} = \frac{p_1}{1 + p_2 \cdot \Delta E^5 \arctan(p_2 \cdot \Delta E^5)} H_{nm'}^{CI}. \quad (11)$$

During our tests (Sec. III), we observed that some excitation energies in transition metal complexes are vastly underestimated by the redesigned Hamiltonian. We could trace this failure mainly back to the damping function. The original Hamiltonian provided better results, but still left some room for improvement.

3. R2018 Hamiltonian

By comparing the results of all Hamiltonians and parameter sets, we found that less damping in the region beginning at $0.45 E_h$ results in a more accurate calculation (closer to experimental energies) for vertical energies of the critical cases. Since the original Hamiltonian provides more accurate results for transition metal complexes, its damping function [Eq. (10)] should perform better than the damping function of the redesigned Hamiltonians R2016 and R2017 [Eq. (11)]. This, however, is not the case as the original damping function

leads to even stronger damping in the redesigned Hamiltonians. This is because in its current form, the damping functions depend on two parameters. p_2 shapes the profile of the damping function and depends on the function itself. p_1 scales the damping function. This includes interaction between degenerate or near-degenerate configurations, which are unaffected by an energy-dependent damping. Thus, p_1 is to some degree independent of the profile of the damping function. In a parameterization, p_1 depends heavily on the diagonal correction. Using the original damping [Eq. (10)] in a redesigned Hamiltonian results in a p_1 parameter value that is nearly identical to the one currently employed in R2016 and R2017. As can be seen in Fig. 1, the function of the original Hamiltonian begins to decrease at $\sim 0.2 E_h$. When starting at the p_1 values of the redesigned Hamiltonians, this leads to an even stronger damping. Based on these insights, we took several functions into consideration that provide the necessary profile. The ideal function that increases the vertical excitation energies close to the experimental energies without overestimating them was found to be

$$H_{nm'} = p_1 \cdot \exp(-p_2 \cdot \Delta E^6) \cdot H_{nm'}^{CI}, \quad (12)$$

which improved the vertical excitation energies of transition metal complexes while keeping the good accuracy of the DFT/MRCI method in organic systems. For a statistical evaluation of 160 singlet and triplet states of various organic molecules, see Tables S6 and S10, and for ionization potentials of 30 organic molecules, see Table S14 in the [supplementary material](#). Expression (12) provides less damping in a broader energy range (Fig. 1) and a steeper decline while reaching a lower function value at the energy of the selection threshold ($1.0 E_h$ or $0.8 E_h$).

D. Parameter optimization

The parameter optimization for the new Hamiltonian was carried out as described in Refs. 29 and 30. A set of four parameters (p_1 , p_2 , p_J , and p_X) was varied by the Nelder-Mead simplex algorithm⁴¹ to find the parameters with the lowest root mean-square error (RMSE). The fitting set of Ref. 30, consisting of 42 singlet, 52 doublet, and 27 triplet states of organic molecules, was extended by one singlet state (b^1E_{1g}) and one triplet state (a^3E_{1g}) of ruthenocene as well as the four lowest singlet and four lowest triplet states of the Cu^+ cation and the two lowest doublet states of the Cu atom. Two unique parameter sets were optimized: one for the standard selection threshold (Table I) and one for a shorter selection (Table II).

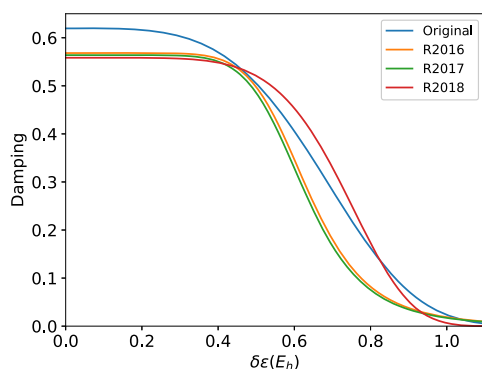


FIG. 1. Damping functions of all Hamiltonians optimized for a selection threshold of $1.0 E_h$.

TABLE I. All parameter sets optimized for a selection threshold of $\Delta E = 1.0 E_h$. p_X refers to the redesigned Hamiltonians and $p[0]$ to the original Hamiltonian.

Reference		p_1	p_2	p_J	$p_X, p[0]$	α
Original	Singlet	0.619 5	3.2719	0.5102	0.5945	0.1058
	Triplet			0.4930		
R2016		0.568 2	18.2960	0.5079	0.3559	...
R2017		0.563 9	22.0912	0.5030	0.3587	...
R2018		0.558 411	4.4717	0.5089	0.3624	...

TABLE II. All parameter sets optimized for a selection threshold of $\Delta E = 0.8 E_h$. p_X refers to the redesigned Hamiltonians and $p[0]$ to the original Hamiltonian.

Reference		p_1	p_2	p_J	$p_X, p[0]$	α
Original	Singlet	0.6290	8.0000	0.1190	0.6110	0.5030
	Triplet					
R2016		0.5798	50.0000	0.5035	0.3681	...
R2017		0.5735	26.5414	0.5008	0.3570	...
R2018		0.5777	11.4991	0.5058	0.3596	...

E. Computational details

Ground-state geometries of the benchmark molecules were optimized using Turbomole 7.1^{42,43} with the PBE0 functional,^{44,45} save for the structures of $\text{Cr}(\text{CO})_6$ and MnO_4^- which were provided by Escudero.²⁰ The BH-LYP^{39,40} KS orbitals and orbital energies for the DFT/MRCI single-point calculations were determined using the `dscf`⁴² module of Turbomole. For the first-row transition metals, we employed the scalar relativistic `ecp-10-mdf`⁴⁶ effective core potential and basis set, and for the second-row transition elements, the `ecp-28-mwb` Wood-Boring effective core potential (ECP) with the corresponding valence basis.⁴⁷ For organic ligands, we used the `def-SV(P)` basis set,⁴⁸ and for inorganic ligands `def2-TZVPD`⁴⁹ for all non-hydrogen atoms and `def2-SVP` for hydrogen.

In all DFT/MRCI calculations, the resolution-of-the-identity (RI) approach^{27,50} was employed for the computation of four-index integrals V_{ijkl} using the TZVP auxiliary basis⁵¹ for first- and second-row transition metals. For inorganic complexes, the `def2-TZVPD` auxiliary basis⁵² was used for all non-hydrogen atoms and `def2-SVP` for hydrogen. For organic complexes, the `def-SV(P)` auxiliary basis⁵¹ was used for all ligand atoms.

The TDDFT⁵³ reference calculations were carried out with the PBE0 functional at the same geometry as the DFT/MRCI calculations. The PBE0 functional was chosen because previous calculations by Escudero and Thiel found this functional to provide the best results.²⁰ For triplet states, the Tamm-Dancoff approximation⁵⁴ (TDA) was employed.

III. RESULTS

In previous articles, three different Hamiltonians and corresponding parameter sets had been introduced.^{27,29,30} We evaluated all published sets as well as the new R2018 Hamiltonian and parameter sets with regard to their performance on electronic excitations of transition metal complexes. To this end, we collected 67 experimental absorption energies and oscillator strengths of organic and inorganic transition metal complexes measured in the gas phase or in apolar environments. The group of inorganic complexes contains 10 compounds (Fig. 2), consisting of metal fluorides, oxides, carbonyls, amines, and aqua complexes with a total of 27 uniquely assigned transitions. The set of 11 organometallic complexes (Fig. 3) comprises Rh and Ru complexes with chelating pyridine and phenanthroline ligands, various Zn

porphyrins, and Fe, Co, and Ru cyclopentadienyl complexes with 40 experimentally known electronic excitation energies. The benchmark set contains a variety of excitation types, most of them being $d \rightarrow \pi^*$ (MLCT), $d \rightarrow d^*/\pi^*$ (MC/MLCT), $\pi \rightarrow d^*/\pi^*$ (MLCT/LC), and $\pi \rightarrow \pi^*$ (LC) transitions. For a list of all states including experimental and calculated energies, excitation type, and experimental environment, see Table III for inorganic and Table IV for organic complexes. The experimental and calculated oscillator strength and degree of degeneracy in symmetry-broken states can be found in Table S1 in [supplementary material](#) for all transitions.

Previous benchmarks for organic molecules^{30,36} had shown that a selection threshold of $0.8 E_h$ (short or tight selection) in combination with a parameter set especially optimized for this threshold provides results of similar quality as the standard parameterization with selection threshold $1.0 E_h$, but at significantly reduced computational cost. Therefore, the benchmark calculations on the 67 excited states of 21 transition metal complexes were carried out for both combinations of the parameter set and selection threshold. Due to problems with the assignment of two transitions in MnO_4^- (see Sec. III B 1 for more details), the test set contains only 65 states in the case of all redesigned Hamiltonians (R2016, R2017, and R2018). We focus our analysis on the standard selection first. The results of the short selection will be discussed in Sec. III D.

A. Performance of the standard parameterizations

Diagrams showing the correlation of the computed vs. experimental data are displayed for all DFT/MRCI Hamiltonians in Fig. 4. The corresponding root mean square errors (RMSEs) and mean absolute errors (MAEs) are presented graphically in Fig. 5. Further results of the statistical analysis such as mean absolute error (MAE), mean error, and maximum absolute error (MaxAE) can be found in the [supplementary material](#).

Our tests reveal that out of the three older Hamiltonians (original, R2016, and R2017), the original one by Grimme and Waletzke shows by far the best performance on the transition metal compounds (correlation coefficient of 0.9270). With a RMSE of 0.35 eV and a MAE of 0.24 eV, the agreement is not as good as for purely organic molecules (compare Tables S3 and S6 in the [supplementary material](#)), but this is to be expected because of the more pronounced electron correlation effects in the d shell. The correlation diagrams also show that some excitation energies of inorganic transition metal complexes are vastly underestimated by the R2016 and R2017 Hamiltonians (for details, see below). The significantly worse performance of these Hamiltonians could be traced back to the form of the damping function for off-diagonal matrix elements (Fig. 1). The exponential function of R2018 in Eq. (12) provides less damping than the inverse tangent in Eq. (11) in an energy range up to approximately $0.9 E_h$ while having a lower function value at the selection threshold. Our new R2018 Hamiltonian that combines the treatment of diagonal elements of the redesigned Hamiltonian R2017 (and R2016 for closed-shell molecules) with a new type of damping performs better than all other DFT/MRCI Hamiltonians (correlation

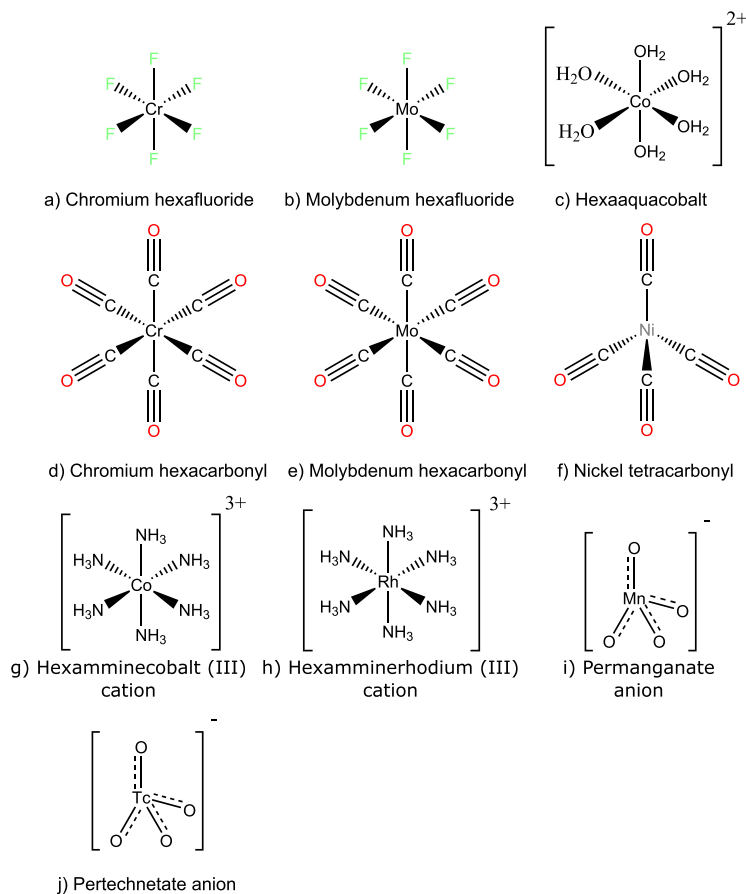


FIG. 2. Inorganic transition metal complexes used for the benchmark calculations.

coefficient 0.9272, RMSE 0.33 eV, and MAE 0.23 eV). In comparison, TDDFT-PBE0 yields a RMSE of 0.41 eV and a MAE of 0.32 eV, thus giving slightly less reliable results on the average than R2018 and the original Hamiltonian.

To learn more about the problems encountered, the results deserve a closer look. We find a large variation of the performance not only between different Hamiltonians but also between different types of transition metal complexes and last but not least between different types of excitations. In the following, we analyze the strengths and weaknesses of all examined DFT/MRCI Hamiltonians in a more detailed way. The excitation energies and excitation types of all states can be found in Table S1 in the [supplementary material](#).

B. Inorganic transition metal complexes

At first glance, the DFT/MRCI energies of the inorganic transition metal complexes show higher deviations from experiment than the organometallic compounds. Further analysis shows the problematic systems (at least in our test cases) to be limited to fluoride and oxide complexes, which perform poorly in the case of the original and new redesigned Hamiltonian and even worse in the case of the old redesigned ones. In all cases, the transitions are predominantly composed of oxygen or fluorine $2p$ lone-pair to metal nd LMCT transitions admixed with

local excitations on the anionic ligands. TDDFT-PBE0 does not show noteworthy differences between LMCT transitions and non-LMCT states, which can be seen in the RMSE of 0.32 and 0.34 eV, respectively. The main outliers in this set arise from CrF_6 , MoF_6 , and MnO_4^- , especially in the old redesigned Hamiltonians, which also show a large deviation in the case of TcO_4^- .

In the following, we present a detailed analysis of the aforementioned critical cases. Let us emphasize that almost all DFT/MRCI results are in good agreement with experiment and that the following examples which proved to be difficult for at least one of the Hamiltonians are known exceptions. The experimental energies and environments for all 27 states and the corresponding results of all four DFT/MRCI Hamiltonians can be found in Table III.

1. Oxides

The MnO_4^- anion proved to be a test for the limits of the DFT/MRCI method. Molecular orbitals which are important in the MRCI expansion of the considered states are sketched in Fig. 6. The calculation was set up with an active space comprising 10 electrons in 10 orbitals with up to two-electron excitations for creating the initial reference space. The active orbitals are then determined iteratively. This leads to configurations that include 24 electrons in 17 orbitals, which is consistent with

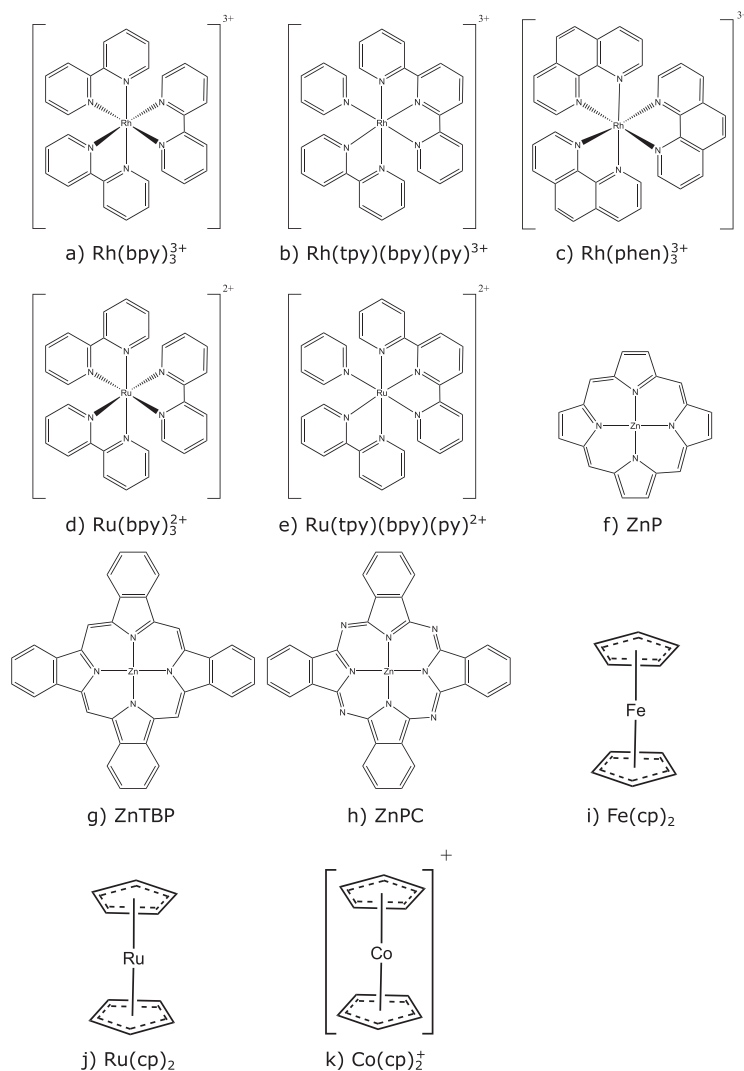


FIG. 3. Organometallic complexes used as benchmark molecules.

the active space previously employed in multiconfiguration pair-density functional theory (MC-PDFT)⁵⁵ and CASPT2⁵⁶ calculations. The highest occupied molecular orbital (HOMO) is threefold degenerate ($1t_1$) and is composed of lone-pair oxygen $2p$ orbitals. The lowest unoccupied molecular orbital (LUMO) is twofold degenerate ($2e$) and has significant manganese $3d$ orbital contributions combined in an antibonding fashion with oxygen $2p$ orbitals. Single excitations between these orbitals give rise to several LMCT electronic states, among them one (1^1T_2) with a strong absorption peaking at about 2.4 eV in experiment.⁵⁷ This state could be identified in all DFT/MRCI calculations. Its energy is well described by the original DFT/MRCI (2.52 eV) and somewhat overestimated by the new DFT/MRCI Hamiltonian (2.70 eV) and TDDFT-PBE0 (2.79 eV), whereas the other Hamiltonians place it at 1.82 eV (R2016) and 1.64 eV (R2017). The second state at 3.6 eV in the experiment is a 1^1T_2 state too, arising mainly from mixtures of $1t_1 \rightarrow 3t_2$ and $2t_2 \rightarrow 2e$ excitations. Like $2e$, $3t_2$ exhibits large amplitudes for Mn $3d$ and antibonding contributions from oxygen $2p$. $2t_2$ is mainly formed by oxygen $2p$ orbitals, but has

small contributions from Mn $3d$ as well. DFT/MRCI utilizes only Abelian point-group symmetries, here C_{2v} . In this subgroup, the 2^1T_2 state is split into A_1 , B_1 , and B_2 components. We find the singly excited B_1 and B_2 states, whereas the energetically matching A_1 state is dominated by a double excitation in the R2016, R2017, and R2018 calculations. Due to this fact, we decided to exclude the 2^1T_2 state from the statistical analysis of the redesigned Hamiltonians. The same difficulties were observed for the 4^1T_2 state and hence this state was omitted too when analyzing the results of the redesigned Hamiltonians. Like 1^1T_2 , the 3^1T_2 state is made up from $2t_2 \rightarrow 2e$ and $1t_1 \rightarrow 3t_2$ excitations. Here, R2018 severely overshoots, whereas R2016 and R2017 underestimate the excitation energy but not as drastically as in the 1^1T_2 case. The original Hamiltonian performs well, deviating from the experiment by less than 0.3 eV in any state. TDDFT-PBE0 yields somewhat larger deviations than the original DFT/MRCI Hamiltonian, but performs significantly better than the redesigned Hamiltonians. MC-PDFT, a different multiconfigurational method employing DFT, yields results similar to the original Hamiltonian and

TABLE III. Experimental and calculated energies of all 10 inorganic complexes for the four DFT/MRCI Hamiltonians. For missing values for permanganate, see text. All energies are in eV.

State	Type	Expt.	Original	R2016	R2017	R2018
CrF ₆						
¹ T _{1u}	$\pi \rightarrow d/\pi^*$	3.31 ^a	2.28	1.61	1.48	2.86
¹ T _{1u}	$\pi \rightarrow d/\pi^*$	3.88 ^a	2.86	1.96	1.83	3.30
¹ T _{1u}	$\pi \rightarrow d/\pi^*$	4.77 ^a	3.85	3.05	2.94	4.29
MoF ₆						
¹ T _{1u}	$\pi \rightarrow d/\pi^*$	5.90 ^b	5.13	4.86	4.85	5.02
² ¹ T _{1u}	$\pi \rightarrow d/\pi^*$	6.54 ^b	5.66	5.24	5.25	5.44
³ ¹ T _{1u}	$\pi \rightarrow d/\pi^*$	7.12 ^b	6.33	5.81	5.83	6.05
Mo(CO) ₆						
¹ T _{1u}	$d/\pi \rightarrow \pi^*$	4.32 ^c	4.46	4.33	4.29	4.41
¹ T _{1u}	$d/\pi \rightarrow \pi^*$	5.44 ^c	5.70	5.45	5.42	5.53
Cr(CO) ₆						
¹ T _{1u}	$d/\pi \rightarrow \pi^*$	4.43 ^c	4.73	4.60	4.56	4.72
¹ T _{1u}	$d/\pi \rightarrow \pi^*$	5.41 ^c	5.72	5.54	5.49	5.66
Ni(CO) ₄						
¹ T ₂	$\sigma/d \rightarrow \pi^*$	4.54 ^d	4.40	4.09	3.95	4.91
¹ T ₂	$\sigma/d \rightarrow \pi^*$	5.17 ^d	5.44	4.66	4.59	5.56
Co(H ₂ O) ₆ ²⁺						
¹ ³ T _g (t _g ² e _g ¹)	$\pi/d \rightarrow \sigma^*/d^*$	0.99 ^e	0.88	1.38	1.35	1.44
² ³ T _g (t _g ² e _g ¹)	$\pi/d \rightarrow \sigma^*/d^*$	1.55 ^e	1.35	1.78	1.75	1.82
¹ ¹ T _g (t _g ² e _g ¹)	$\pi/d \rightarrow \sigma^*/d^*$	2.06 ^e	1.72	1.99	1.95	2.04
² ¹ T _g (t _g ² e _g ¹)	$\pi/d \rightarrow \sigma^*/d^*$	3.09 ^e	2.65	2.81	2.78	2.85
Co(NH ₃) ₆ ³⁺						
¹ T _{1g}	$d \rightarrow \sigma^*/d^*$	2.70 ^f	2.67	2.69	2.62	2.90
¹ T _{2g}	$d \rightarrow \sigma^*/d^*$	3.40 ^f	3.63	3.58	3.49	3.76
Rh(NH ₃) ₆ ³⁺						
¹ T _{1g}	$d \rightarrow \sigma^*/d^*$	3.96 ^f	3.78	3.78	3.73	3.83
¹ T _{2g}	$d \rightarrow \sigma^*/d^*$	4.88 ^f	4.49	4.45	4.39	4.48
MnO ₄ ⁻						
¹ T ₂	$\pi \rightarrow d^*/\pi^*$	2.4 ^g	2.52	1.82	1.64	2.70
² ¹ T ₂	$\pi \rightarrow d/\pi^*/\sigma^*$	3.6 ^g	3.75			
³ ¹ T ₂	$\pi \rightarrow d^*/\pi^*$	4.1 ^g	4.33	3.90	3.65	4.95
⁴ ¹ T ₂	$\pi \rightarrow d^*/\pi^*$	5.5 ^g	5.80			
TcO ₄ ⁻						
¹ T ₂	$\pi \rightarrow d^*/\pi^*$	4.35 ^h	3.93	3.57	3.48	4.05
² ¹ T ₂	$d/\pi \rightarrow d^*/\pi^*$	5.1 ^h	4.89	4.45	4.36	4.98
³ ¹ T ₂	$\pi \rightarrow d^*/\pi^*/\sigma^*$	6.6 ⁱ	5.91	5.63	5.57	6.15

^aReference 58 (in N₂ matrix).^bReference 62 (in gas phase).^cReference 63 (in gas phase).^dReference 64 (in matrix).^eReference 65 (in powder).^fReference 66 (in aqueous solution).^gReference 57 (in KClO₄ at 4 K).^hReference 67 (in KClO₄ at 4 K).ⁱReference 68 (in vacuo).

performs better than all redesigned Hamiltonians for the first three T₂ states.⁵⁵

In the heavier TcO₄⁻ homologue, the results of the R2016 and R2017 DFT/MRCI calculations exhibit similar but less pronounced trends, i.e., all LMCT transitions are energetically underestimated. In contrast to the MnO₄⁻ case, the R2018 Hamiltonian is found to perform better than the original Hamiltonian.

TABLE IV. Experimental and calculated energies of all 11 organic complexes for the four DFT/MRCI Hamiltonians. All energies are in eV. All band maxima consist of singlet states.

State	Type	Expt.	Original	R2016	R2017	R2018
Ru(bpy) ₃						
Band max.	$d \rightarrow \pi^*$	2.88 ^a	2.92	2.81	2.81	2.92
	$d \rightarrow d^*$	4.00 ^a	3.94	4.28	4.26	3.94
	$\pi \rightarrow \pi^*$	4.38 ^a	4.37	4.26	4.26	4.41
	$d \rightarrow \pi^*$	5.02 ^a	4.98	4.86	4.86	5.08
Ru(tpy)(bpy)(py) ²⁺						
Band max.	$d \rightarrow \pi^*$	2.66 ^b	2.76	2.67	2.64	2.77
	$d \rightarrow \pi^*$	2.99 ^b	3.02	3.04	3.02	3.14
	$d \rightarrow \pi^*$	3.99 ^b	4.04	3.92	3.92	4.09
	$d/\pi \rightarrow \pi^*$	4.40 ^b	4.38	4.32	4.32	4.49
	$d/\pi \rightarrow \pi^*$	5.30 ^b	5.02	5.02	5.02	5.23
Rh(bpy) ₃ ³⁺						
Band max.	$\pi \rightarrow \pi^*$	3.88 ^c	3.89	3.82	3.81	3.99
	$\pi \rightarrow \pi^*$	4.04 ^c	3.94	3.88	3.86	4.05
	$d/\pi \rightarrow \pi^*$	5.15 ^c	5.12	5.10	5.10	5.32
Rh(phen) ₃ ³⁺						
Band max.	$\pi \rightarrow \pi^*$	4.44 ^d	4.44	4.35	4.34	4.53
Rh(tpy)(bpy)(py) ²⁺						
Band max.	$\pi \rightarrow \pi^*$	3.46 ^e	3.50	3.56	3.55	3.60
	$\pi \rightarrow \pi^*$	3.65 ^e	3.85	3.91	3.90	3.73
	$\pi \rightarrow \pi^*$	4.00 ^e	4.08	4.11	4.09	4.08
	$d/\pi \rightarrow \pi^*$	4.37 ^e	4.28	4.31	4.31	4.29
ZnP						
¹ E _u	$\pi \rightarrow \pi^*$	2.18 ^f	2.19	2.17	2.16	2.20
² ¹ E _u	$\pi \rightarrow \pi^*$	3.13 ^f	3.25	3.18	3.17	3.19
⁴ ¹ E _u	$\pi \rightarrow \pi^*$	4.07 ^f	4.04	4.02	4.01	4.15
ZnTBP						
¹ E _u	$\pi \rightarrow \pi^*$	1.98 ^g	1.93	1.89	1.87	1.95
² ¹ E _u	$\pi \rightarrow \pi^*$	3.06 ^g	3.03	2.94	2.92	3.01
³ ¹ E _u	$\pi \rightarrow \pi^*$	3.87 ^g	3.73	3.68	3.66	3.81
⁸ ¹ E _u	$\pi \rightarrow \pi^*$	4.89 ^g	4.61	4.55	4.53	4.76
ZnPC						
¹ E _u	$\pi \rightarrow \pi^*$	1.89 ^h	1.81	1.82	1.81	1.84
² ¹ E _u	$\pi \rightarrow \pi^*$	3.71 ^h	3.50	3.53	3.59	3.72
³ ¹ E _u	$\pi \rightarrow \pi^*$	3.74 ^h	3.60	3.60	3.63	3.67
¹ A _{2u}	$\pi \rightarrow \pi^*$	3.99 ^h	3.91	3.90	4.03	4.10
Ferrocene						
^a ³ E _{1g}	$d \rightarrow d^*/\pi^*$	2.34 ⁱ	2.04	1.97	1.89	2.15
^a ¹ E _{1g}	$d \rightarrow d^*/\pi^*$	2.8 ^j	2.92	2.72	2.64	2.93
¹ E _{2g}	$d \rightarrow d^*/\pi^*$	2.81 ^j	2.69	2.51	2.44	2.69
^b ¹ E _{1g}	$d \rightarrow d^*/\pi^*$	3.82 ^{i,j}	3.99	3.72	3.63	4.02
Ruthenocene						
^a ³ E _{1g}	$d \rightarrow d^*/\pi^*$	3.22 ⁱ	3.02	3.04	2.99	3.19
^a ¹ E _{1g}	$d \rightarrow d^*/\pi^*$	3.66 ⁱ	3.55	3.49	3.44	3.62
¹ E _{2g}	$d \rightarrow d^*/\pi^*$	4.03 ⁱ	3.56	3.48	3.42	3.63
^b ¹ E _{1g}	$d \rightarrow d^*/\pi^*$	4.54 ⁱ	4.16	4.05	3.99	4.18
Cobaltocene						
^a ³ E _{1g}	$d \rightarrow d^*/\pi^*$	2.70 ^k	2.26	2.08	1.97	2.43
^a ¹ E _{1g}	$d \rightarrow d^*/\pi^*$	3.01 ^k	2.57	2.53	2.40	2.86
¹ E _{2g}	$d \rightarrow d^*/\pi^*$	3.27 ^k	2.85	2.77	2.65	3.12
^b ¹ E _{1g}	$d \rightarrow d^*/\pi^*$	4.12 ^k	4.08	3.79	3.66	4.19

^aReference 60 (in vacuo).^bReference 69 (in CH₃CN at room temperature).^cReference 61 (in MeOH at 293 K).^dReference 70 (in MeOH at room temperature).^eReference 71 (in 10⁻³M HClO₄ aqueous solution).^fReference 72 (in MeOH).^gReference 73 (in gas phase).^hReference 74 (in argon matrix).ⁱReference 75 (in EPA).^jReference 76 (in gas phase).^kReference 75 (in aqueous solution).

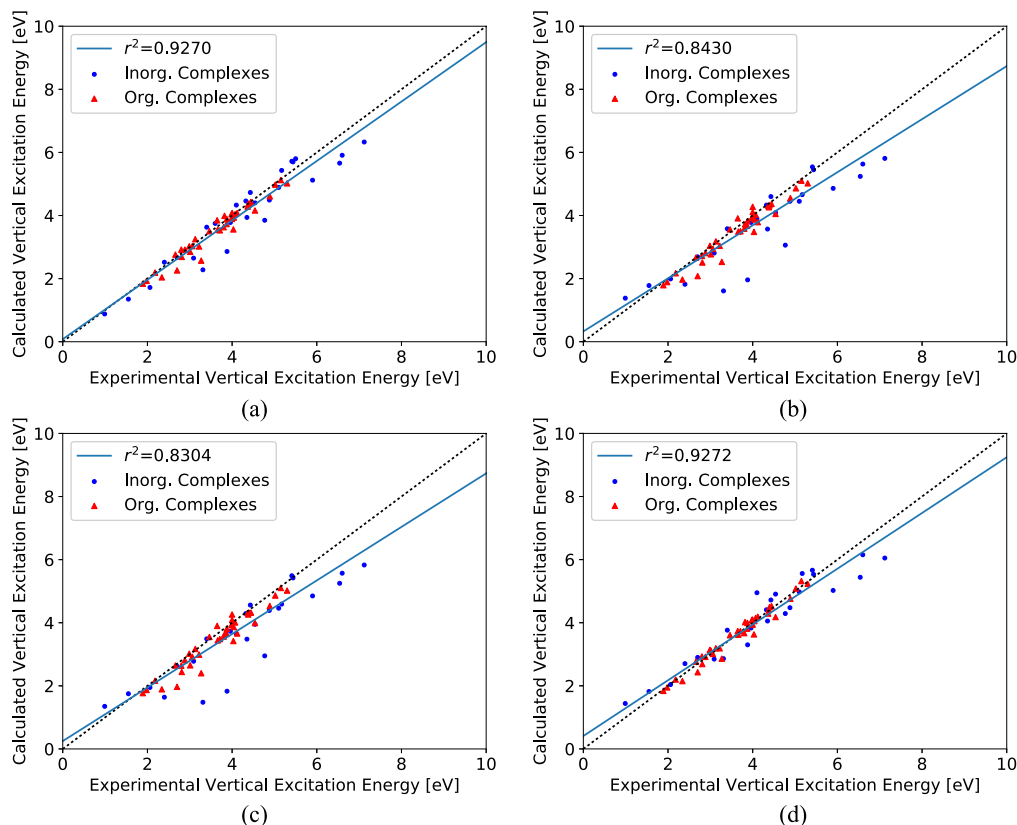


FIG. 4. Correlation of the DFT/MRCI excitation energies of 21 transition metal complexes with the experimental reference data. (a) Original, (b) R2016, (c) R2017, and (d) R2018 Hamiltonians parameterized for a selection threshold of $1.0 E_h$.

2. Fluorides

Another difficult molecule is CrF_6 . There were problems with every set of parameters and Hamiltonians. In the case of the original Hamiltonian, the calculated energies were too low compared to experimental data,⁵⁸ which had been measured in an N_2 matrix. Similar to the permanganate case, the low-lying CrF_6 transitions stem from excitations of an electron from a

lone-pair $2p$ orbital on fluorine to d/π^* -type orbitals with large amplitudes on the metal atom (Fig. 7).

The deviations from the experimental reference data are visualized for all DFT/MRCI approaches in Fig. 8. For the original Hamiltonian, the calculated excitation energies are systematically too low by ~ 1 eV. The results for the redesigned Hamiltonians R2016 and R2017 are even worse. The energies are underestimated by 1.7 eV–1.9 eV in the case of R2016

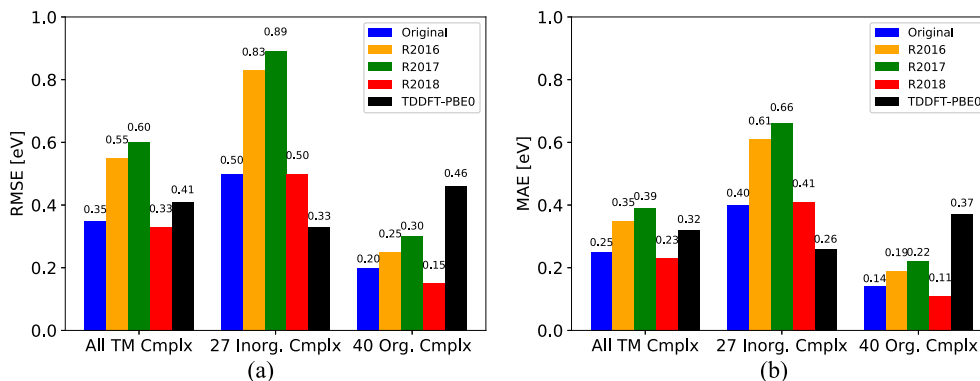
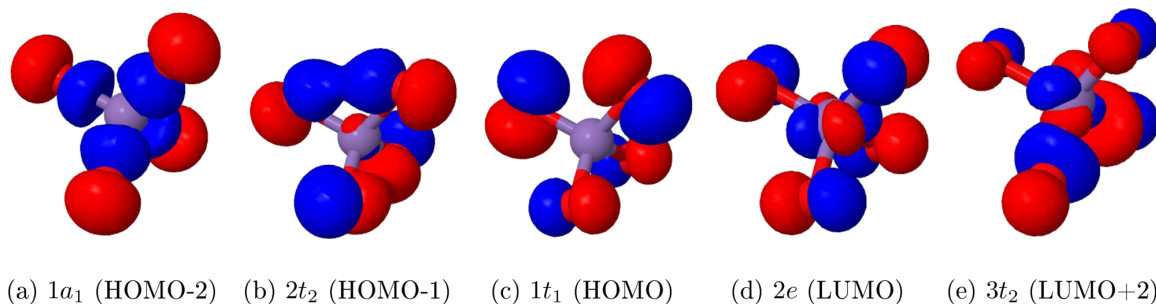
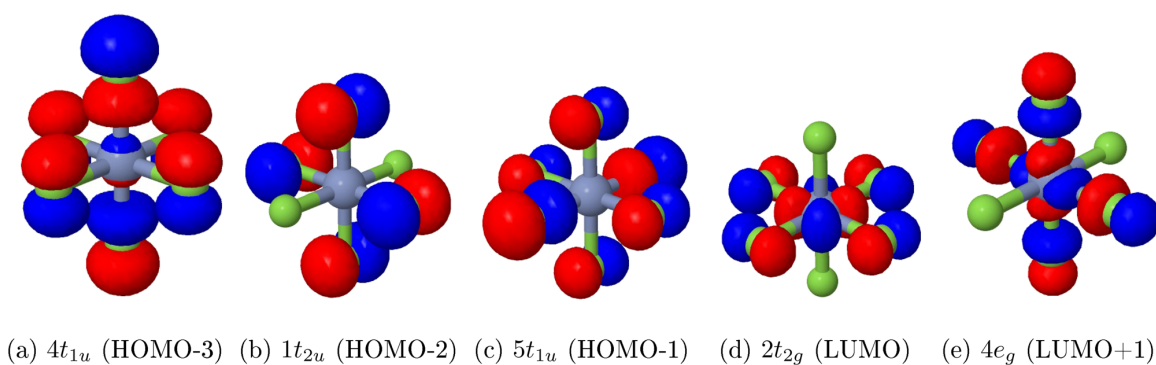


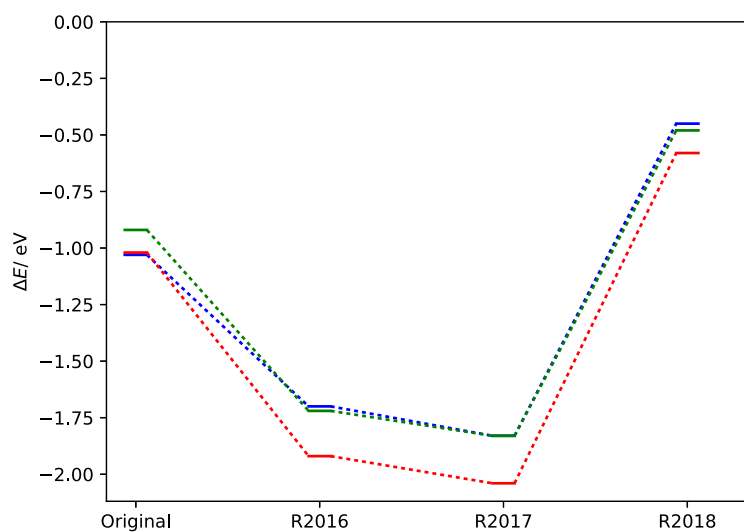
FIG. 5. RMSE and MAE for all four DFT/MRCI Hamiltonians using the standard selection and parameter set, compared to TDDFT-PBE0. The left block shows all 67 (65) excited states, which are comprised of 27 (25) states of inorganic complexes (middle) and 40 states of organic complexes (right).

FIG. 6. Molecular orbitals of MnO_4^- involved in the investigated transitions.FIG. 7. Molecular orbitals of CrF_6 involved in the investigated transitions.

and by 1.8–2.1 eV with R2017. Additionally, we notice a high amount of artificially low-lying doubly excited states that start at root 29 in C_{2v} symmetry with R2016 and at root 36 with R2017. By employing the redesigned Hamiltonian R2018 which uses a different scaling for off-diagonal elements (Sec. II C), we managed to increase the vertical energies dramatically. The energies are still 0.5–0.6 eV too low but much better than all previous results. The problem of low-lying

doubly excited states still persists and seems to occur irrespective of the chosen damping function.

The problems in MoF_6 are analogous to those encountered in CrF_6 , energy-wise. Contrary to CrF_6 , we do not find any artificially low-lying doubly excited states, but all Hamiltonians and parameter sets underestimate the excitation energies compared to the experiment (in the gas phase). The best results are gained using the original Hamiltonian, but

FIG. 8. Excitation energies for three experimentally known states of CrF_6 as the difference to the experiment, calculated with a selection threshold of $\Delta E = 1.0 E_h$.

the deviations are still high (roughly -0.85 eV on the average). With the redesigned Hamiltonian R2018, the results are slightly worse with deviations ranging from -0.88 eV to -1.10 eV. With R2016 and R2017, the computed energies are even lower.

The results of MoF_6 and TcO_4^- suggest that the damping function plays a minor role for compounds of second-row transition elements. The reasons for the failure of the redesigned Hamiltonians to describe LMCT transitions of these small oxides and fluorides are not completely clear at present. Problems of the R2016 Hamiltonian with low-lying double excitations from non-bonding lone-pair orbitals to π^* orbitals had already been observed in benchmark calculations on unsaturated organic molecules.⁵⁹ The modified damping function in the R2018 Hamiltonian does not solve the problems encountered for $n^2 \rightarrow \pi^{*2}$ transitions in aldehydes and ketones, either.

3. Aqua, ammine, and carbonyl complexes

When we just look at the aqua, ammine, and carbonyl complexes in our assessment set (16 states in 6 molecules) with $d/\pi \rightarrow d^*/\sigma^*$, $d \rightarrow d^*/\sigma^*$, and $d/\pi \rightarrow \pi^*$ excitations, all four Hamiltonians are seen to perform well. We do not find large differences in the statistical data of the four DFT/MRCI Hamiltonians, which range from 0.26 eV to 0.30 eV (RMSE) and from 0.22 eV to 0.25 eV (MAE). So, at least within our assessment set, it is safe to say that any of the four Hamiltonians yields satisfactory results for these types of compounds. A noticeable distinction between the Hamiltonians is regarding the mean. While the redesigned Hamiltonians are close to zero (-0.07 – -0.06 eV), the original Hamiltonian seems to underestimate the excitation energies, resulting in -0.18 eV as the mean.

C. Metal organic complexes

Transition metal complexes with organic ligands are calculated with high accuracy using DFT/MRCI. We find that R2018 performs best in our benchmark set of 40 states in 11 molecules, yielding a RMSE of 0.15 eV, with the original

Hamiltonian as a second at 0.20 eV. Lyskov's redesigned Hamiltonian R2016 yields slightly less satisfactory results with a RMSE of 0.25 eV. The redesigned Hamiltonian R2017, while performing very well on excitations in purely organic molecules (see Table S6 in the [supplementary material](#)), exhibits the largest RMSE (0.30 eV) among the DFT/MRCI Hamiltonians in the standard parameterization for spectral transitions in organometallic complexes. Overall, we see the same tendency as in the inorganic complexes. The accuracy of the results correlates directly with the profile of the damping function for the off-diagonal elements. The functions exerting stronger damping underestimate the excitation energies. The mean error is negative, up to -0.18 eV in the case of R2017. By applying the new damping function with R2018, the mean increases to -0.01 eV. TDDFT-PBE0 performs poorly in comparison to all DFT/MRCI Hamiltonians, arriving at a RMSE of 0.46 eV with a MAE of 0.37 eV.

The molecules of our benchmark set can be grouped into three categories, which are zinc porphyrins, metallocenes, and large complexes containing nitrogen-bonded heterocycles such as phenanthroline or various counts of pyridine. The metallocenes consist exclusively of MC/MLCT states, while the other two categories contain MLCT, LC, MLCT/LC, and one MC state. (For a list of all transitions, see Table S1). The corresponding RMSEs and MAEs are presented graphically in Fig. 9. The experimental energies and environments for all 40 states and the corresponding results of all four DFT/MRCI Hamiltonians can be found in Table IV.

1. Zinc porphyrins

The smallest zinc porphyrin in our test set consists of Zn^{2+} ligated to the unsubstituted anionic porphyrin macrocycle (ZnP). In addition, we included spectral data of zinc tetrabenzoporphyrin (ZnTBP) and zinc phthalocyanine (ZnPC). We investigated a total of 11 states, which are exclusively LC $\pi \rightarrow \pi^*$ transitions. All Hamiltonians yield good RMSE values, ranging from 0.08 eV (R2018) to 0.18 (R2017). The same goes for the MAE, which ranges from 0.07 eV (R2018) to 0.18 eV (R2017) and the mean, from -0.01 (R2018) to -0.14 eV (R2017). In all cases, the results of R2016 are very

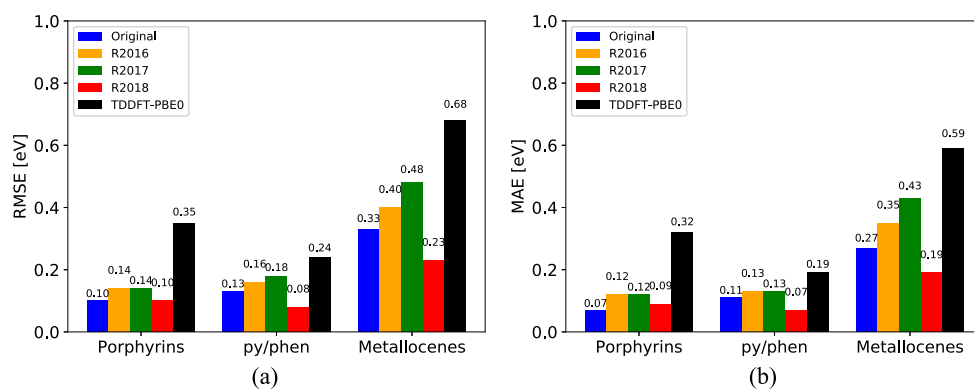


FIG. 9. RMSE and MAE of the 40 excited states of organic complexes for all four DFT/MRCI Hamiltonians using the standard selection and parameter set, compared to TDDFT-PBE0. The results are divided into three groups: zinc porphyrins (left), large Ru and Rh complexes with pyridine and phenanthroline ligands (middle), and metallocenes (right).

close to those of R2017, while the original Hamiltonian lies between the R2018 and R2017. TDDFT-PBE0 overestimates the transition energies, having both the MAE and mean at 0.19 eV, while the RMSE is 0.24 eV.

2. Metallocenes

The three metallocenes $\text{Fe}(\text{cp})_2$, $\text{Ru}(\text{cp})_2$, and $\text{Co}(\text{cp})_2^+$, in total 12 MC/MLCT states including one triplet state per complex, yield somewhat higher deviations from experiment compared to other organometallic complexes. The RMSE ranges from 0.23 eV in the case of the new R2018 Hamiltonian to 0.33 eV for the original Hamiltonian and to 0.40 and 0.48 eV for the redesigned Hamiltonians R2016 and R2017, respectively. The MAE follows the same trend, ranging from 0.20 eV (R2018) to 0.44 eV (R2017). The mean is -0.12 eV in the case of R2018 and -0.23 eV for the original Hamiltonian. The means of the other redesigned Hamiltonians are -0.35 eV for R2016 and -0.44 eV for R2017. The transition energies are underestimated in comparison to the experiment by a higher degree than in the other organometallic complexes, the results being more similar to those of the inorganic ones. Triplet states of closed-shell molecules as well as MC states are generally rare in the literature due to their spectroscopic properties. Since we decided to compare our results to experimental data, such states are not well represented in our assessment set. In metallocenes, however, all states have MC character and three states exhibit a triplet multiplicity. All four Hamiltonians yield good results in computing the triplet states in addition to the performance on the MC/MLCT states discussed above.

TDDFT-PBE0 is having difficulties in calculating the excitation energies of metallocenes, which can be seen in the RMSE at 0.68 eV. The mean is -0.29 eV, so the excitation energies are underestimated compared to experiment.

In our parameter optimization for the new R2018 Hamiltonian, we included the third singlet and the triplet state of ruthenocene. Usually it would be good practice to exclude those states from any benchmark, but since excluding both states (0.40 and 0.15 eV deviation from experiment) lowers the RMSE, we decided to keep them in the assessment set.

For ferrocene, we found additional experimental data measured in gas phase, while all other experimental energies were measured in EPA (diethyl ether/isopentane/ethanol). The a^1E_{1g} and $^1E_{2g}$ states of ferrocene split up under the influence of the EPA environment, while they have almost the same energy in gas phase. The excitation energies of the b^1E_{1g} state are identical in both environments. For ruthenocene, only spectra in EPA were recorded and the spectrum of cobaltocene was measured in water. We use these solution data of ruthenocene and cobaltocene in the assessment, being well aware that the excitation energies are not strictly comparable.

3. Pyridine and phenanthroline complexes

In this class of compounds, we investigated the complexes $\text{Ru}(\text{bpy})_2^{2+}$, $\text{Ru}(\text{tpy})(\text{bpy})(\text{py})^{2+}$, $\text{Rh}(\text{bpy})_3^{3+}$, $\text{Rh}(\text{phen})_3^{3+}$, and $\text{Rh}(\text{tpy})(\text{bpy})(\text{py})^{3+}$. For a comparison with experimental data, we used the spectra and compared the position of band

maxima with the calculated transitions, which were broadened by a Gaussian of width 750 cm^{-1} at half maximum. In the case of $\text{Ru}(\text{bpy})_3^{2+}$, the $d \rightarrow d^*$ transition, which was listed in the experiment,⁶⁰ was assigned by picking the explicit state, since it was covered by the strong $\pi \rightarrow \pi^*$ band at 4.38 eV. A similar occurrence was found in $\text{Rh}(\text{bpy})_3^{3+}$, where the first and second transitions mentioned in the experimental literature⁶¹ are separated by only 0.16 eV. In some cases, our calculations did not cover the complete spectrum, since our program is limited to 50 roots per multiplicity. We avoided third-row transition metal complexes due to expected magnetic relativistic effects mainly caused by spin-orbit coupling.

Our benchmark shows that all Hamiltonians and parameter sets generate excellent results in those systems which are comprised of LC, MLCT, and MLCT/LC states. The redesigned R2016 and R2017 Hamiltonians show a RMSE of 0.14 eV and an MAE of 0.12 eV, while the original Hamiltonian and the newly designed Hamiltonian R2018 arrive at a remarkable 0.10 eV, with MAEs of 0.07 and 0.09 eV, respectively. The MC state in $\text{Ru}(\text{bpy})_3^{2+}$ is very well described by the original and R2018 Hamiltonian with a deviation of 0.06 eV, while R2016 and R2017 overestimate the energy, but remain below 0.3 eV.

TDDFT-PBE0 on the other hand yields a RMSE of 0.35 eV with a MAE of 0.32 eV and a mean of 0.31 eV. Therefore it can be said to systematically overestimate the excitation energies.

D. Performance of the short parameterizations

A smaller selection threshold causes fewer configurations and thus leads to a significant lowering of calculation times. The central processing unit (CPU) time and number of CSFs for some molecules can be found in Table V. Generally we observe a speed up of calculation times which is tenfold or more for most molecules. Previous tests on organic molecules revealed a minimal decrease in computational accuracy in comparison to experimental vertical excitation energies if the tighter selection threshold is employed instead of the standard parameterization.³⁰ In the case of the R2018 Hamiltonian, error compensation leads to results which are the best of all combinations and thresholds tested. (See Tables S7 and S10 of the [supplementary material](#).) In the context of this article, we investigate whether the same holds true for transition metal complexes.

TABLE V. Number of CSFs and calculation times for selected molecules using the R2018 Hamiltonian with short ($0.8 E_h$) and standard ($1.0 E_h$) selection. For each molecule, the same type and number of CPUs has been employed in short and standard calculations.

Molecule	Symmetry used	Roots calc.	Time		CSFs	
			Short	Standard	Short	Standard
$\text{Rh}(\text{phen})_3^{3+}$	C_1	50	5 h	122 h	3 437 047	45 288 577
ZnPC	D_{2h}	17	4 m	88 m	2 447 089	34 776 646
ZnP	D_{2h}	17	13 s	250 s	147 282	1 584 839
$\text{Cr}(\text{CO})_6$	C_{2v}	41	44 s	192 s	97 433	766 969

There are two ways of carrying out the calculations with a short selection: by using the standard parameters (Table I) and by using the parameters optimized for the short selection (Table II).

1. Parameters optimized for $0.8 E_h$ selection threshold (short selection)

Using the parameters fitted for the short selection threshold, we observed similar trends as for the standard selection. The six non-LMCT inorganic complexes and the organic complexes are calculated with satisfactory accuracy. The overall RMSE for the 67 (65) states is 0.42 eV for the new R2018 Hamiltonian, 0.43 eV for the original Hamiltonian, 0.60 eV for R2016, and 0.55 eV for R2017. The correlation diagrams and the results of the statistical evaluations are displayed in Figs. 10 and 11, respectively.

The results of the redesigned Hamiltonians R2016 and R2017 are surprising at first glance. Both are identical in their formulation for closed-shell systems and differ slightly with regard to the parameters. However, the statistical data are easy to explain. Choosing a smaller selection threshold leads to higher excitation energies due to smaller correlation contributions, especially in excited states. The parameter p_2 of the damping function in R2016 was designed to cut the CI expansion at $0.8 E_h$, which leads to a steeper function profile (Fig. 12). As already mentioned for the standard

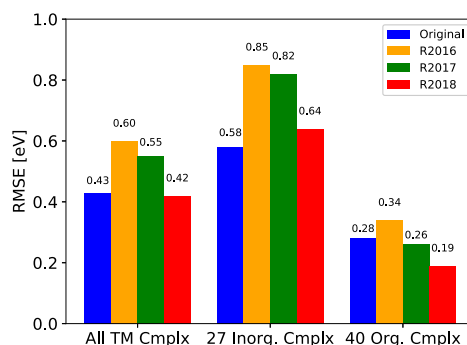


FIG. 11. RMSE for all four DFT/MRCI Hamiltonians using the short (tight) selection and parameter set. The left block shows all 67 (65) excited states, which are comprised of 27 (25) states of inorganic complexes (middle) and 40 states of organic complexes (right).

parameterization, the performance of the DFT/MRCI Hamiltonians on transition metal complexes depends strongly on the profile of the damping function. If the interaction between configurations is damped too much, the energies of excited states are lowered. In the case of R2016, we therefore obtain an increase in energy by lowering the selection threshold and a decrease by increasing the damping, but both effects do not cancel each other completely. So, on the average, we worsen the results in this case. The same effects are operative for

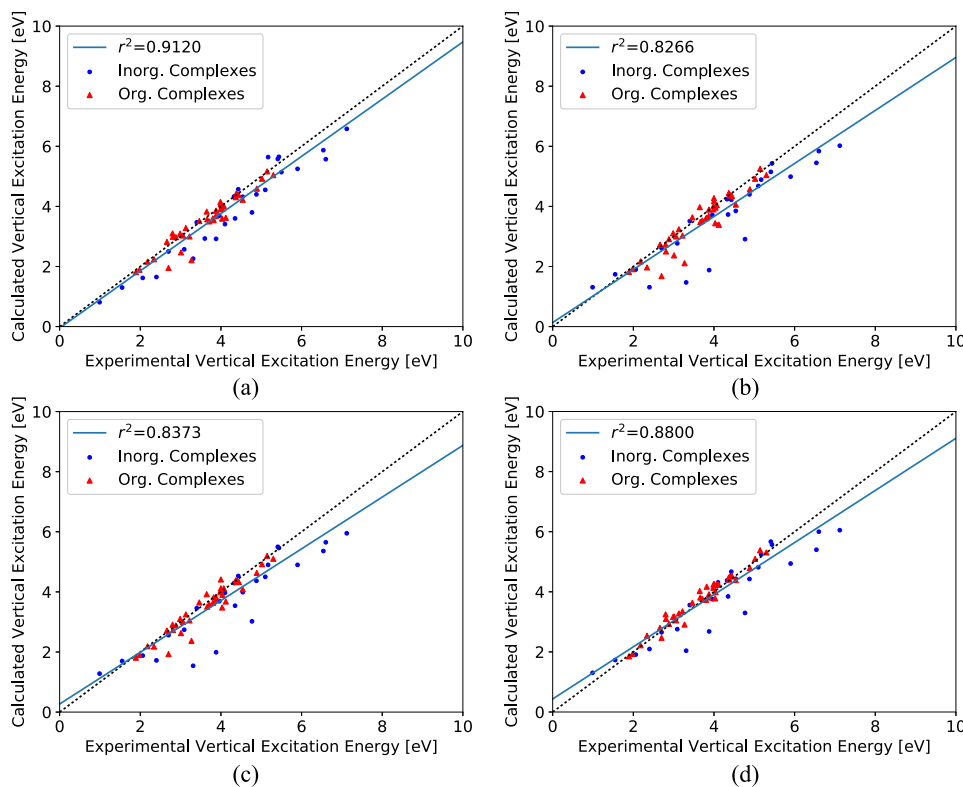


FIG. 10. Correlation of the DFT/MRCI excitation energies of 21 transition metal complexes with the experimental reference data. (a) Original, (b) R2016, (c) R2017, and (d) R2018 Hamiltonians parameterized for a selection threshold of $0.8 E_h$.

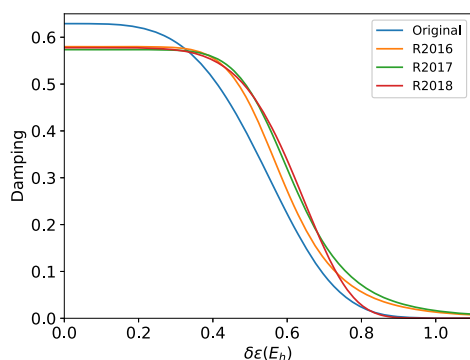


FIG. 12. Damping functions of all Hamiltonians optimized for a selection threshold of $0.8 E_h$.

the R2017 parameterization. In this case, however, the results improve compared to R2016 when using the lower selection threshold because here the damping function is almost identical to the one optimized for the standard selection ($1.0 E_h$). So, all energies are increased and, since most energies are underestimated, the errors cancel partially and we get slightly better results.

For inorganic complexes, the RMSEs of the 27 (25) vertical excitation energies are at 0.58 eV for the original and 0.64 eV for the R2018 Hamiltonians and 0.85 eV and 0.80 eV for R2016 and R2017, respectively. By excluding the LMCT states (oxides and fluorides), the results are 0.23 eV for R2018, 0.32 eV for the R2017, 0.35 eV for the original Hamiltonian, and 0.40 eV for R2016. The energies are underestimated more strongly by R2016 compared to the standard selection and compared to R2017, which explains the larger error. The results of R2018 are better than those of all other Hamiltonians using the short selection, but also outperform all Hamiltonians (incl. R2018) with the standard selection.

For organic complexes, the RMSEs of the 40 vertical excitation energies are 0.19 eV for R2018, 0.26 eV for R2017, 0.28 eV for the original, and 0.34 eV for R2016 Hamiltonians (Table S9 of the [supplementary material](#)). This is very similar to the inorganic complexes (without the LMCT states), where the order of the Hamiltonians is identical, but the excitation energies for organic complexes are lowered by 0.03–0.05 eV on the average.

2. Engaging standard parameters with a small selection threshold

The parameters optimized for a short selection (*vide supra*) showed unsatisfactory results for the R2016 and original Hamiltonians because the damping is steeper than in the standard parameter set. This leads to an underestimation of the excitation energies of transition metal complexes. For this reason, we decided to assess the combination of short selection and standard parameters too. At this point we want to underline that for organic molecules, the short parameter set is the preferable choice for all Hamiltonians.

The overall RMSE for the 67 (65) states is 0.41 eV for the original Hamiltonian, 0.47 eV for R2016, 0.50 eV for R2017, and 0.49 eV for the new 2018 Hamiltonian. The lower damping

leads to an increased mean in all Hamiltonians. In the case of the original Hamiltonian, the mean increases by 0.32 eV, while for R2016, it increases by 0.18 eV and for R2017 by 0.07 eV. In the case of R2018, the lower damping raises the mean from -0.07 eV to 0.25 eV, which explains the highest RMSE among the four Hamiltonians, since the damping is too weak for this selection threshold. (See Tables S11–S13 in the [supplementary material](#) for further details.)

From these results, we conclude that for the older three Hamiltonians, original, R2016, and R2017, the standard parameter sets should be engaged, even in conjunction with the short selection. By contrast, the short parameter set, which was optimized for (but is not limited to) transition metal complexes, should be used in R2018 when setting the selection threshold to $0.8 E_h$. This choice enables calculations on very large transition metal complexes, for which calculations with the standard selection threshold are too expensive or technically not feasible.

IV. CONCLUSION

DFT/MRCI is a well-established method for calculating electronic excitations in organic molecules. The benchmark calculations presented here show that DFT/MRCI is a valuable tool for computing spectra of large transition metal organic complexes with closed-shell ground states too. To date, four different variants of the DFT/MRCI Hamiltonian have been developed: the original DFT/MRCI Hamiltonian of Grimme and Waletzke,²⁷ the redesigned DFT/MRCI Hamiltonian R2016 for systems with even numbers of electrons by Lyskov *et al.*,²⁹ its extension to radicals (R2017) by Heil and Marian,³⁰ and the multiplicity independent R2018 Hamiltonian with the modified damping function developed in this work. For all four Hamiltonians, parameter sets are available that have been optimized in conjunction with a configuration selection threshold of $1.0 E_h$ (standard parameterization) and with a tighter configuration selection threshold of $0.8 E_h$ (short parameterization) that saves considerable computation time.

The diverse and vastly different excitations that are possible in transition metal complexes lead to a larger scattering of the results compared to purely organic compounds. Good performance of the original and redesigned DFT/MRCI Hamiltonians is observed for LC, MLCT, and mixed LC/MLCT transitions. The excitation energies of the MC transitions in metallocenes appear to be somewhat underestimated, but the term ordering is correct. Triplet excitations are rare due to our focus on experimental energies, but show good accuracy in metallocenes. Small inorganic transition metal complexes with LMCT and LC/LMCT excitations are the most critical ones. The assessment of the DFT/MRCI variants reveals a somewhat better but far from satisfactory performance of the original DFT/MRCI Hamiltonian on these states. Therefore, caution is advised when dealing with those types of states. Huge (more than 1 eV) errors of the R2016 and R2017 Hamiltonians for the LMCT/LC states of oxides and fluorides could partially be traced back to the damping function for the off-diagonal matrix elements. For compounds composed of main group elements only, the steeper descent of this damping function as compared

to the exponential damping had not caused significant differences in the statistical analysis.²⁹ This is not the situation in the compact $3d$ shell where differential electron correlation effects are stronger. These insights prompted us to reparameterize the multiplicity-independent DFT/MRCI Hamiltonian matrix elements in conjunction with an exponential form of the damping function.

This new Hamiltonian, dubbed R2018, is generally applicable and shows the best overall performance of all DFT/MRCI variants, especially for metal organic complexes yielding a RMSE of 0.15 eV when employing standard selection and parameters. The original Hamiltonian shows good accuracy as well; the RMSE for metal organic complexes is 0.20 eV. However, the original Hamiltonian lacks the advantages of multiplicity-independent parameterization that motivated the development of the redesigned Hamiltonian(s) recommended for dimers and excimers. The older redesigned Hamiltonians R2016 and R2017 yield higher deviations from experiment for organic complexes than the other two. We find the new R2018 Hamiltonian to be the best overall choice in both the standard and short selections when combined with the corresponding parameter set. With the exception of fluoride and oxide complexes, the average absolute error is below 0.3 eV for inorganic complexes for all four Hamiltonians. None of the Hamiltonians perform well for the LMCT oxide and fluoride complexes, but the original and R2018 Hamiltonians handle them better.

The short selection with the associated parameter set performs well for inorganic (0.23 eV) and organic (0.19 eV) complexes with the R2018 Hamiltonian when excluding the aforementioned oxides and fluorides, which have a higher deviation in this case. For R2017, R2016, and the original Hamiltonian, we find higher deviations as these operators tend to underestimate the excitation energies. For those Hamiltonians, the standard parameters should be used in applications on transition metal complexes in combination with the tighter selection threshold of $0.8 E_h$. This choice leads to better results, especially in the case of R2016, which yields a 0.19 eV RMSE for organic complexes when using this combination.

All DFT/MRCI variants outperform TDDFT-PBE0 greatly on metal organic complexes and slightly in the case of non-LMCT inorganic complexes. For LMCT transitions, TDDFT-PBE0 is a favorable choice over DFT/MRCI.

SUPPLEMENTARY MATERIAL

See [supplementary material](#) for all experimental and calculated transition energies for the standard and short selection threshold and parameter set and statistical evaluation data for RMSE, MAE, mean, and maximum absolute error (MaxAE).

ACKNOWLEDGMENTS

We would like to thank Daniel Escudero for sharing his geometry parameters of the optimized $\text{Cr}(\text{CO})_6$ and MnO_4^- structures. Financial support by the Deutsche Forschungsgemeinschaft (DFG) Project No. MA1051/14-2 is gratefully acknowledged.

- ¹ *Quantum Chemistry: The Challenge of Transition Metals and Coordination Chemistry*, edited by A. Veillard (D. Reidel Publishing Company, Dordrecht, 1986).
- ² S. R. Langhoff and C. W. Bauschlicher, *Annu. Rev. Phys. Chem.* **39**, 181 (1988).
- ³ K. Pierloot, Q. M. Phung, and A. Domingo, *J. Chem. Theory Comput.* **13**, 537 (2017).
- ⁴ C. W. Bauschlicher, S. P. Walch, and H. Partridge, *J. Chem. Phys.* **76**, 1033 (1982).
- ⁵ S. Vancollie, H. Zhao, V. T. Tran, M. F. A. Hendrickx, and K. Pierloot, *J. Chem. Theory Comput.* **7**, 3961 (2011).
- ⁶ C. M. Marian, M. R. A. Blomberg, and P. E. M. Siegbahn, *J. Chem. Phys.* **91**, 3589 (1989).
- ⁷ C. Marian, *Chem. Phys. Lett.* **173**, 175 (1990).
- ⁸ K. Andersson, P. A. Malmqvist, B. O. Roos, A. J. Sadlej, and K. Wolinski, *J. Phys. Chem.* **94**, 5483 (1990).
- ⁹ B. O. Roos, K. Andersson, M. P. Fülscher, P.-Å. Malmqvist, L. Serrano-Andrés, K. Pierloot, and M. Merchán, "Multiconfigurational perturbation theory: Applications in electronic spectroscopy," in *Advances in Chemical Physics* (Wiley-Blackwell, 1996), pp. 219–331.
- ¹⁰ P. Å. Malmqvist, K. Pierloot, A. R. M. Shahi, C. J. Cramer, and L. Gagliardi, *J. Chem. Phys.* **128**, 204109 (2008).
- ¹¹ C. Angeli, R. Cimraglia, and J.-P. Malrieu, *J. Chem. Phys.* **117**, 9138 (2002).
- ¹² K. Pierloot, *Mol. Phys.* **101**, 2083 (2003).
- ¹³ M. Kepenekian, V. Robert, B. Le Guennic, and C. De Graaf, *J. Comput. Chem.* **30**, 2327 (2009).
- ¹⁴ M. Petersilka, U. J. Gossmann, and E. K. U. Gross, *Phys. Rev. Lett.* **76**, 1212 (1996).
- ¹⁵ M. E. Casida, "Time-dependent density functional response theory for molecules," in *Recent Advances in Density Functional Methods* (World Scientific, 1995), pp. 155–192.
- ¹⁶ R. Bauernschmitt and R. Ahlrichs, *Chem. Phys. Lett.* **256**, 454 (1996).
- ¹⁷ C. J. Cramer and D. G. Truhlar, *Phys. Chem. Chem. Phys.* **11**, 10757 (2009).
- ¹⁸ M. Kepenekian, A. Calborean, V. Vetere, B. Le Guennic, V. Robert, and P. Maldivi, *J. Chem. Theory Comput.* **7**, 3532 (2011).
- ¹⁹ D. Escudero and L. González, *J. Chem. Theory Comput.* **8**, 203 (2012).
- ²⁰ D. Escudero and W. Thiel, *J. Chem. Phys.* **140**, 194105 (2014).
- ²¹ F. Vlahović, M. Perić, M. Gruden-Pavlović, and M. Zlatar, *J. Chem. Phys.* **142**, 214111 (2015).
- ²² C. Latouche, D. Skouteris, F. Palazzetti, and V. Barone, *J. Chem. Theory Comput.* **11**, 3281 (2015).
- ²³ H. Nakatsuji and K. Hirao, *J. Chem. Phys.* **68**, 2053 (1978).
- ²⁴ H. Nakatsuji, *Chem. Phys. Lett.* **67**, 334 (1979).
- ²⁵ H. Nakatsuji, Y. Tokita, J. Hasegawa, and M. Hada, *Chem. Phys. Lett.* **256**, 220 (1996).
- ²⁶ Y. Tokita and H. Nakatsuji, *J. Phys. Chem. B* **101**, 3281 (1997).
- ²⁷ S. Grimme and M. Waletzke, *J. Chem. Phys.* **111**, 5645 (1999).
- ²⁸ M. Kleinschmidt, C. M. Marian, M. Waletzke, and S. Grimme, *J. Chem. Phys.* **130**, 044708 (2009).
- ²⁹ I. Lyskov, M. Kleinschmidt, and C. M. Marian, *J. Chem. Phys.* **144**, 034104 (2016).
- ³⁰ A. Heil and C. M. Marian, *J. Chem. Phys.* **147**, 194104 (2017).
- ³¹ M. R. Silva-Junior, M. Schreiber, S. P. A. Sauer, and W. Thiel, *J. Chem. Phys.* **129**, 104103 (2008).
- ³² M. Kleinschmidt, C. van Wüllen, and C. M. Marian, *J. Chem. Phys.* **142**, 094301 (2015).
- ³³ A. Heil, K. Gollnisch, M. Kleinschmidt, and C. M. Marian, *Mol. Phys.* **114**, 407 (2016).
- ³⁴ J. Föller, M. Kleinschmidt, and C. M. Marian, *Inorg. Chem.* **55**, 7508 (2016).
- ³⁵ J. Föller and C. M. Marian, *J. Phys. Chem. Lett.* **8**, 5643 (2017).
- ³⁶ C. M. Marian, A. Heil, and M. Kleinschmidt, *Wiley Interdiscip. Rev.: Comput. Mol. Sci.* e1394 (2018).
- ³⁷ R. W. Wetmore and G. A. Segal, *Chem. Phys. Lett.* **36**, 478 (1975).
- ³⁸ G. A. Segal, R. W. Wetmore, and K. Wolf, *Chem. Phys.* **30**, 269 (1978).
- ³⁹ A. D. Becke, *J. Chem. Phys.* **98**, 1372 (1993).
- ⁴⁰ C. Lee, W. Yang, and R. G. Parr, *Phys. Rev. B* **37**, 785 (1988).
- ⁴¹ J. A. Nelder and R. Mead, *Comput. J.* **7**, 308 (1965).
- ⁴² O. Treutler and R. Ahlrichs, *J. Chem. Phys.* **102**, 346 (1995).
- ⁴³ TURBOMOLE V7.1 2016, a development of University of Karlsruhe and Forschungszentrum Karlsruhe GmbH, 1989-2007, TURBOMOLE GmbH, since 2007; available from <http://www.turbomole.com>.
- ⁴⁴ J. P. Perdew, K. Burke, and M. Ernzerhof, *Phys. Rev. Lett.* **77**, 3865 (1996).
- ⁴⁵ C. Adamo and V. Barone, *J. Chem. Phys.* **110**, 6158 (1999).
- ⁴⁶ M. Dolg, U. Wedig, H. Stoll, and H. Preuss, *J. Chem. Phys.* **86**, 866 (1987).

- ⁴⁷D. Andrae, U. Häußermann, M. Dolg, H. Stoll, and H. Preuß, *Theor. Chim. Acta* **77**, 123 (1990).
- ⁴⁸A. Schäfer, H. Horn, and R. Ahlrichs, *J. Chem. Phys.* **97**, 2571 (1992).
- ⁴⁹D. Rappoport and F. Furche, *J. Chem. Phys.* **133**, 134105 (2010).
- ⁵⁰O. Vahtras, J. Almlöf, and M. Feyereisen, *Chem. Phys. Lett.* **213**, 514 (1993).
- ⁵¹F. Weigend, M. Häser, H. Patzelt, and R. Ahlrichs, *Chem. Phys. Lett.* **294**, 143 (1998).
- ⁵²A. Hellweg and D. Rappoport, *Phys. Chem. Chem. Phys.* **17**, 1010 (2015).
- ⁵³F. Furche and R. Ahlrichs, *J. Chem. Phys.* **117**, 7433 (2002).
- ⁵⁴S. Hirata and M. Head-Gordon, *Chem. Phys. Lett.* **314**, 291 (1999).
- ⁵⁵P. Sharma, D. G. Truhlar, and L. Gagliardi, *J. Chem. Theory Comput.* **14**, 660 (2018).
- ⁵⁶J. Su, W.-H. Xu, C.-F. Xu, W. H. E. Schwarz, and J. Li, *Inorg. Chem.* **52**, 9867 (2013).
- ⁵⁷S. L. Holt and C. J. Ballhausen, *Theor. Chim. Acta* **7**, 313 (1967).
- ⁵⁸E. G. Hope, P. J. Jones, W. Levason, J. S. Ogden, M. Tajik, and J. W. Turff, *J. Chem. Soc., Dalton Trans.* **1985**, 1443.
- ⁵⁹V. Jovanović, I. Lyskov, M. Kleinschmidt, and C. M. Marian, *Mol. Phys.* **115**, 109 (2017).
- ⁶⁰M.-B. S. Kirketerp and S. B. Nielsen, *Int. J. Mass Spectrom.* **297**, 63 (2010).
- ⁶¹M. Maestri, D. Sandrini, V. Balzani, U. Maeder, and A. V. Zelewsky, *Inorg. Chem.* **26**, 1323 (1987).
- ⁶²R. McDiarmid, *J. Chem. Phys.* **61**, 3333 (1974).
- ⁶³H. B. Gray and N. A. Beach, *J. Am. Chem. Soc.* **85**, 2922 (1963).
- ⁶⁴A. Lever, G. Ozin, A. Hanlan, W. Power, and H. B. Gray, *Inorg. Chem.* **18**, 2088 (1979).
- ⁶⁵D. A. Johnson and A. G. Sharpe, *J. Chem. Soc. A* **1966**, 798.
- ⁶⁶P. C. Ford, *Coord. Chem. Rev.* **44**, 61 (1982).
- ⁶⁷H. U. Güdel and C. J. Ballhausen, *Theor. Chim. Acta* **25**, 331 (1972).
- ⁶⁸P. Mullen, K. Schwochau *et al.*, *Chem. Phys. Lett.* **3**, 49 (1969).
- ⁶⁹S. C. Rasmussen, S. E. Ronco, D. A. Mlsna, M. A. Billadeau, W. T. Pennington, J. W. Kolis, and J. D. Petersen, *Inorg. Chem.* **34**, 821 (1995).
- ⁷⁰D. Sandrini, M. Maestri, V. Balzani, U. Maeder, and A. V. Zelewsky, *Inorg. Chem.* **27**, 2640 (1988).
- ⁷¹M. E. Frink, S. D. Sprouse, H. A. Goodwin, R. J. Watts, and P. C. Ford, *Inorg. Chem.* **27**, 1283 (1988).
- ⁷²H. Sekino and H. Kobayashi, *J. Chem. Phys.* **86**, 5045 (1987).
- ⁷³L. Edwards, M. Gouterman, and C. B. Rose, *J. Am. Chem. Soc.* **98**, 7638 (1976).
- ⁷⁴T. C. VanCott, J. L. Rose, G. C. Misener, B. E. Williamson, A. E. Schrimpf, M. E. Boyle, and P. N. Schatz, *J. Phys. Chem.* **93**, 2999 (1989).
- ⁷⁵H. B. Gray, Y. S. Sohn, and N. Hendrickson, *J. Am. Chem. Soc.* **93**, 3603 (1971).
- ⁷⁶A. T. Armstrong, F. Smith, E. Elder, and S. P. McGlynn, *J. Chem. Phys.* **46**, 4321 (1967).

Erratum: “On the performance of DFT/MRCI Hamiltonians for electronic excitations in transition metal complexes: The role of the damping function” [J. Chem. Phys. 149, 164106 (2018)]

Cite as: J. Chem. Phys. 150, 219903 (2019); doi: 10.1063/1.5109649

Submitted: 10 May 2019 • Accepted: 17 May 2019 •

Published Online: 4 June 2019



Adrian Heil, Martin Kleinschmidt, and Christel M. Marian^{a)}

AFFILIATIONS

Institute of Theoretical and Computational Chemistry, Heinrich-Heine-University Düsseldorf, Düsseldorf, Germany

^{a)}Electronic mail: Christel.Marian@hhu.de

<https://doi.org/10.1063/1.5109649>

Equation (7) of Ref. 1 is missing a factor of $\frac{1}{2}$ in the second and third terms of the last line. Correctly, Eq. (7) should read as

$$\begin{aligned} \Delta E_{\text{coul}} - \Delta E_{\text{exch}} = pJ & \left(- \sum_{\substack{i,j \in c \\ i > j}}^{n_{\text{exc}}} V_{ijij} - \sum_{\substack{i,j \in a \\ i > j}}^{n_{\text{exc}}} V_{ijij} + \sum_{i \in c} \sum_{j \in a}^{n_{\text{exc}} n_{\text{exc}}} V_{ijij} + \frac{1}{2} \sum_{i \in s}^{n_{\text{single}}} V_{iiii} |\Delta w_i| \right) \\ & - pX \left(\frac{1}{2} \sum_{i \in c} \sum_{j \in a}^{n_{\text{exc}} n_{\text{exc}}} V_{ijji} - \frac{1}{2} \sum_{\substack{i \in c \\ j \in c, s}}^{n_{\text{exc}}} V_{ijji} - \frac{1}{2} \sum_{\substack{j \in a \\ j \in a, s}}^{n_{\text{exc}}} V_{ijji} + \sum_{\substack{i, j \in o \\ i > j}}^{N_o} V_{ijji} \eta_{ij}^{ij} \right). \end{aligned} \quad (7)$$

This error is only a typo in the equation. All published results are unaffected, since the Hamiltonian has been implemented correctly.

An additional change involves the notation of the indices in the second and third terms of the last line of Eq. (7) to accentuate that the index j is addressing created (second term) or annihilated (third term) electrons in an orbital s that is singly occupied in the anchor configuration.

REFERENCE

¹ A. Heil, M. Kleinschmidt, and C. M. Marian, J. Chem. Phys. 149, 164106 (2018).

Supplementary Material

Adrian Heil, Martin Kleinschmidt, Christel M. Marian

September 17, 2018

Institute of Theoretical and Computational Chemistry, Heinrich-Heine-University Düsseldorf, Universitätsstraße 1, 40225 Düsseldorf, Germany

Table S1: Vertical excitation energies of transition metal complexes (in eV) in comparison to experiment. Oscillator strengths in parentheses. All DFT/MRCI calculations were performed using the respective standard parameter set and a selection threshold of $1.0 E_h$. Original denotes the ansatz by Grimme and Waletzke [1], R2016 marks the redesigned Hamiltonian by Lyskov et al. [2], R2017 refers to variant proposed by Heil and Marian [3], and R2018 to the parameterization in the present work. Some molecules exhibit non-Abelian symmetry. In DFT/MRCI, which can handle only Abelian point-group symmetries, all components of spatially degenerate state are listed to show the level of degeneracy. For comparison to the experimentally derived energies, the average energy is given as well. Blank cells in the average column are due to some states not assignable.

Molecule	State/ Transition	Type	Experiment (Oscil. str.)	Original		R2016		R2017		R2018		TDDFT	
				states	av.	states	av.	states	av.	states	av.	PBE0	
CrF ₆	¹ T _{1u}	$\pi \rightarrow d/\pi^*$	3.31 (middle) [4]	2.28 (0.0048)		1.61 (0.0022)		1.48 (0.0022)		2.85 (0.0046)		2.86	3.16
				2.28 (0.0046)	2.28	1.61 (0.0019)	1.61	1.48 (0.0020)	1.48	2.85 (0.0046)			
				2.28 (0.0046)		1.61 (0.0019)		1.48 (0.0020)		2.88 (0.0068)			
	¹ T _{1u}	$\pi \rightarrow d/\pi^*$	3.88 (strong) [4]	2.86 (0.0600)		1.96 (0.0678)		1.84 (0.0593)		3.29 (0.11)		3.30	3.93
				2.86 (0.0613)	2.86	1.96 (0.0684)	1.96	1.83 (0.0602)	1.83	3.29 (0.11)			
				2.86 (0.0613)		1.96 (0.0684)		1.83 (0.0602)		3.32 (0.11)			
	¹ T _{1u}	$\pi \rightarrow d/\pi^*$	4.77 (strong) [4]	3.85 (0.0387)		3.06 (0.0282)		2.95 (0.0325)		4.27 (0.029)		4.29	4.96
				3.85 (0.0385)	3.85	3.05 (0.0272)	3.05	2.94 (0.0318)	2.94	4.30 (0.027)			
				3.85 (0.0385)		3.05 (0.0272)		2.94 (0.0317)		4.30 (0.027)			
MoF ₆	¹ T _{1u}	$\pi \rightarrow d/\pi^*$	5.90 (weak) [5]	5.12 (0.00959)		4.86 (0.01405)		4.85 (0.01529)		5.02 (0.012)		5.02	5.42
				5.13 (0.00933)	5.13	4.86 (0.01405)	4.86	4.85 (0.01515)	4.85	5.02 (0.012)			
				5.13 (0.00933)		4.86 (0.01405)		4.85 (0.01516)		5.03 (0.012)			
	² T _{1u}	$\pi \rightarrow d/\pi^*$	6.54 (middle) [5]	5.66 (0.08970)		5.24 (0.13919)		5.25 (0.13795)		5.44 (0.13)		5.44	5.97
				5.66 (0.08974)	5.66	5.24 (0.13919)	5.24	5.25 (0.13794)	5.25	5.44 (0.13)			
				5.66 (0.08961)		5.24 (0.13930)		5.25 (0.13819)		5.44 (0.13)			
	² T _{1u}	$\pi \rightarrow d/\pi^*$	7.12 (strong) [5]	6.33 (0.22026)		5.81 (0.16592)		5.83 (0.16237)		6.05 (0.21)		6.05	7.12
				6.33 (0.22029)	6.33	5.81 (0.16596)	5.81	5.83 (0.16172)	5.83	6.05 (0.21)			
				6.33 (0.22340)		5.81 (0.16689)		5.83 (0.16298)		6.05 (0.21)			
Mo(CO) ₆	¹ T _{1u}	$d/\pi \rightarrow \pi^*$	4.32 (0.139) [6]	4.46 (0.080)		4.33 (0.10)		4.29 (0.10)		4.41		4.41	4.41
				4.46 (0.080)	4.46	4.33 (0.10)	4.33	4.29 (0.10)	4.29	4.41			
				4.46 (0.080)		4.33 (0.10)		4.29 (0.10)		4.41			
	¹ T _{1u}	$d/\pi \rightarrow \pi^*$	5.44 (1.78) [6]	5.70 (1.07)		5.45 (1.02)		5.42 (1.02)		5.53 (1.06)		5.53	6.15
				5.70 (1.07)	5.70	5.45 (1.02)	5.45	5.42 (1.02)	5.42	5.53 (1.06)			
				5.71 (1.07)		5.45 (1.02)		5.42 (1.02)		5.54 (1.06)			
Cr(CO) ₆	¹ T _{1u}	$d/\pi \rightarrow \pi^*$	4.43 (0.19) [6]	4.73 (0.078)		4.6 (0.084)		4.55 (0.086)		4.72 (0.093)		4.72	4.72
				4.73 (0.078)	4.73	4.6 (0.084)	4.60	4.56 (0.086)	4.56	4.72 (0.093)			
				4.73 (0.078)		4.6 (0.084)		4.56 (0.086)		4.72 (0.093)			
	¹ T _{1u}	$d/\pi \rightarrow \pi^*$	5.41 (1.45) [6]	5.72 (0.78)		5.54 (0.78)		5.49 (0.78)		5.66 (0.80)		5.66	6.19
				5.72 (0.78)	5.72	5.54 (0.78)	5.54	5.49 (0.78)	5.49	5.66 (0.80)			
				5.72 (0.78)		5.54 (0.78)		5.49 (0.78)		5.67 (0.80)			
Ni(CO) ₄	¹ T ₂	$\sigma/d \rightarrow \pi^*$	4.54 [7]	4.39 (0.1236)		4.08 (0.0894)		3.94 (0.0985)		4.90 (0.12)		4.91	4.92
				4.40 (0.1289)	4.40	4.10 (0.0875)	4.09	3.96 (0.0969)	3.95	4.91 (0.12)			

Molecule	State/ Transition	Type	Experiment (Oscil. str.)	Original		R2016		R2017		R2018		TDDFT
				states	av.	states	av.	states	av.	states	av.	PBE0
Co(H ₂ O) ₆ ²⁺	¹ T ₂	σ/d → π*	5.17 [7]	4.40 (0.1289)		4.10 (0.0875)		3.96 (0.0969)		4.91 (0.12)		
				5.42 (0.2064)	5.44	4.65 (0.1994)	4.66	4.58 (0.1914)	4.59	5.56 (0.22)	5.56	5.16
				5.45 (0.2034)		4.67 (0.1961)		4.60 (0.1878)		5.56 (0.22)		
	¹ T ₂	σ/d → π*	5.17 [7]	5.45 (0.2034)		4.67 (0.1961)		4.60 (0.1878)		5.56 (0.22)		
Co(NH ₃) ₆ ²⁺	¹ T _{2g} (t _{2g} ⁵ e _g ¹)	π/d → σ*/d*	0.99 [8]	0.85		1.36		1.33		1.42		
				0.88	0.88	1.37	1.38	1.34	1.35	1.43	1.44	0.93
	¹ T _{2g} (t _{2g} ⁵ e _g ¹)	π/d → σ*/d*	1.55 [8]	0.91		1.41		1.38		1.47		
	² T _{2g} (t _{2g} ⁵ e _g ¹)	π/d → σ*/d*	1.55 [8]	1.32		1.75		1.72		1.81		
1.36				1.35	1.79	1.78	1.76	1.75	1.81	1.82	1.42	
¹ T _{2g} (t _{2g} ⁵ e _g ¹)	π/d → σ*/d*	2.06 [8]	1.37		1.80		1.77		1.84			
Co(NH ₃) ₆ ³⁺	¹ T _{1g}	d → σ*/d*	2.70 [9]	1.70		1.97		1.94		2.03		
				1.75	1.72	1.99	1.99	1.95	1.95	2.04	2.04	1.95
	¹ T _{2g}	d → σ*/d*	3.09 [8]	1.72		2.00		1.96		2.05		
	² T _{2g} (t _{2g} ⁵ e _g ¹)	π/d → σ*/d*	3.09 [8]	2.65		2.80		2.76		2.83		
2.62				2.65	2.81	2.81	2.78	2.78	2.85	2.85	2.97	
² T _{2g} (t _{2g} ⁵ e _g ¹)	π/d → σ*/d*	3.09 [8]	2.67		2.83		2.79		2.86			
Rh(NH ₃) ₆ ³⁺	¹ T _{1g}	d → σ*/d*	2.70 [9]	2.66 (0.00005)		2.68 (0.00004)		2.61 (0.00003)		2.89 (0.00003)		
				2.68 (0.00006)	2.67	2.70 (0.00004)	2.69	2.62 (0.00004)	2.62	2.90 (0.00004)	2.90	2.49
				2.68 (0.00002)		2.70 (0.00001)		2.63 (0.00001)		2.91 (0.00001)		
	¹ T _{2g}	d → σ*/d*	3.40 [9]	3.62 (0.00001)		3.57 (0.00001)		3.49 (0.00001)		3.76 (0.00001)		
				3.63 (0.00004)	3.63	3.58 (0.00003)	3.58	3.49 (0.00003)	3.49	3.76 (0.00003)	3.76	3.57
¹ T _{2g}	d → σ*/d*	3.40 [9]	3.65 (0.00003)		3.59 (0.00002)		3.50 (0.00002)		3.77 (0.00002)			
Rh(NH ₃) ₆ ³⁺	¹ T _{1g}	d → σ*/d*	3.96 [9]	3.77		3.77		3.72		3.82		
				3.78	3.78	3.78	3.78	3.72	3.73	3.83	3.83	3.85
	¹ T _{2g}	d → σ*/d*	4.88 [9]	3.80		3.80		3.74		3.84		
	¹ T _{2g}	d → σ*/d*	4.88 [9]	4.47		4.44		4.38		4.47		
4.49				4.49	4.45	4.45	4.39	4.39	4.48	4.48	4.53	
¹ T _{2g}	d → σ*/d*	4.88 [9]	4.51		4.45		4.39		4.48			
MnO ₄ ⁻	¹ T ₂ (1t ₁ → 2e)	π → d*/π*	2.4 (strong) [10]	2.47 (0.010)		1.80 (0.0042)		1.61 (0.0029)		2.70 (0.015)		
				2.54 (0.008)	2.52	1.80 (0.0042)	1.82	1.61 (0.0029)	1.64	2.70 (0.015)	2.70	2.79
				2.54 (0.008)		1.85 (0.0066)		1.69 (0.0055)		2.71 (0.016)		
	² T ₂ (1t ₁ → 3t ₂ , 2t ₂ → 2e)	π → d*/π*/σ*	3.6 (medium) [10]	3.74 (0.0014)								
				3.75 (0.0009)	3.75							3.91
³ T ₂ (2t ₂ → 2e, 1t ₁ → 3t ₂)	π → d*/π*	4.1 (strong) [10]	4.33 (0.023)		3.85 (0.0044)		3.58 (0.0025)		4.95 (0.033)			
			4.33 (0.023)	4.33	3.93 (0.010)	3.90	3.69 (0.0070)	3.65	4.95 (0.024)	4.95	4.41	
³ T ₂ (2t ₂ → 2e, 1t ₁ → 3t ₂)	π → d*/π*	4.1 (strong) [10]	4.33 (0.023)		3.93 (0.010)		3.69 (0.0070)		4.95 (0.024)			

Molecule	State/ Transition	Type	Experiment (Oscil. str.)	Original		R2016		R2017		R2018		TDDFT
				states	av.	states	av.	states	av.	states	av.	PBE0
TeO ₄ ⁻	4 ¹ T ₂ (1a ₁ → 3t ₂ , 2t ₂ → 3t ₂)	π → d*/π*	5.5 (medium) [10]	5.73 (0.0012) 5.83 (0.0004) 5.83 (0.0004)	5.80							5.70
	1 ¹ T ₂ (1t ₁ → 2e, 2t ₂ → 2e)	π → d*/π*	4.35 [11]	3.92 (0.0168) 3.95 (0.0144) 3.95 (0.0144)	3.93	3.54 (0.015) 3.58 (0.015) 3.58 (0.015)		3.46 (0.015) 3.49 (0.015) 3.49 (0.015)		4.04 (0.020) 4.06 (0.019) 4.06 (0.019)	4.05	4.68
	2 ¹ T ₂ (1t ₁ → 2e, 2t ₂ → 2e)	d/π → d*/π*	5.1 [11]	4.88 (0.035) 4.90 (0.034) 4.90 (0.034)	4.89	4.44 (0.031) 4.44 (0.031) 4.48 (0.033)		4.35 (0.032) 4.35 (0.032) 4.39 (0.034)		4.97 (0.046) 4.97 (0.046) 4.99 (0.048)	4.98	5.59
	3 ¹ T ₂ (1t ₁ → 3t ₂ , 2t ₂ → 3t ₂)	π → d*/π*/σ*	6.6 [12]	5.91 (0.0068) 5.91 (0.0068) 5.92 (0.0064)	5.91	5.62 (0.0078) 5.62 (0.0078) 5.64 (0.0071)		5.56 (0.0078) 5.56 (0.0078) 5.58 (0.0072)		6.15 (0.010) 6.15 (0.010) 6.16 (0.0094)	6.15	6.62
Ru(bpy) ₃	band max.	d → π*	2.88 [13]		2.92		2.81		2.81		2.92	3.12
		d → d*	4.00 [13]		3.94		4.28		4.26		3.94	4.02
		π → π*	4.38 [13]		4.37		4.26		4.26		4.41	4.73
		d → π*	5.02 [13]		4.98		4.86		4.86		5.08	5.23
Ru(tpy)(bpy)(py) ²⁺	band max.	d → π*	2.66 [14]		2.76		2.67		2.64		2.77	3.07
		d → π*	2.99 [14]		3.02		3.04		3.02		3.14	3.27
		d → π*	3.99 [14]		4.04		3.92		3.92		4.09	4.28
		d/π → π*	4.40 [14]		4.38		4.32		4.32		4.49	4.70
		d/π → π*	5.30 [14]		5.02		5.02		5.02		5.23	5.19
Rh(bpy) ₃ ³⁺	band max.	π → π*	3.88 [15]		3.89		3.82		3.81		3.99	4.37
		π → π*	4.04 [15]		3.94		3.88		3.86		4.05	4.44
		d/π → π*	5.15 [15]		5.12		5.10		5.10		5.32	5.77
Rh(phen) ₃ ³⁺	band max.	π → π*	4.44 [16]		4.44		4.35		4.34		4.53	4.75
Rh(tpy)(bpy)(py) ²⁺	band max.	π → π*	3.46 [17]		3.50		3.56		3.55		3.60	3.83
		π → π*	3.65 [17]		3.85		3.91		3.90		3.73	4.04
		π → π*	4.00 [17]		4.08		4.11		4.09		4.08	4.43
		d/π → π*	4.37 [17]		4.28		4.31		4.31		4.29	4.63
ZnP	1 ¹ E _u	π → π*	2.18 (0.005) [18]	2.19 (0.005) 2.19 (0.005)	2.19	2.17 (0.0044) 2.17 (0.0044)	2.17	2.16 (0.0043) 2.16 (0.0043)	2.16	2.20 (0.0058) 2.20 (0.0058)	2.20	2.46
	2 ¹ E _u	π → π*	3.13 (0.98) [18]	3.25 (1.25) 3.25 (1.25)	3.25	3.18 (1.30) 3.18 (1.30)	3.18	3.17 (1.31) 3.17 (1.31)	3.17	3.19 (1.36) 3.19 (1.36)	3.19	3.58
	4 ¹ E _u	π → π*	4.07 (0.2) [18]	4.04 (0.25) 4.04 (0.25)	4.04	4.02 (0.23) 4.02 (0.23)	4.02	4.01 (0.23) 4.01 (0.23)	4.01	4.15 (0.23) 4.15 (0.23)	4.15	4.42
ZnTBP	1 ¹ E _u	π → π*	1.98 (0.3) [19]	1.93 (0.22) 1.93 (0.22)	1.93	1.89 (0.24) 1.89 (0.24)	1.89	1.87 (0.24) 1.87 (0.24)	1.87	1.95 (0.26) 1.95 (0.26)	1.95	2.20
	2 ¹ E _u	π → π*	3.06 (1.6) [19]	3.03 (1.54)	3.03	2.94 (1.54)	2.94	2.92 (1.54)	2.92	3.01 (1.57)	3.01	3.32

Molecule	State/ Transition	Type	Experiment (Oscil. str.)	Original		R2016		R2017		R2018		TDDFT	
				states	av.	states	av.	states	av.	states	av.	PBE0	
	3^1E_u	$\pi \rightarrow \pi^*$	3.87 (0.4) [19]	3.03 (1.54) 3.73 (0.034)	3.73	2.94 (1.54) 3.68 (0.031)	3.68	2.92 (1.54) 3.66 (0.032)	3.66	3.01 (1.57) 3.81 (0.030)	3.81	3.87	
	8^1E_u	$\pi \rightarrow \pi^*$	4.89 (0.4) [19]	4.61 (0.18) 4.61 (0.18)		4.61		4.55 (0.15) 4.55 (0.15)		4.55			4.53 (0.15) 4.53 (0.15)
ZnPC	1^1E_u	$\pi \rightarrow \pi^*$	1.89 [20]	1.81 (0.54) 1.81 (0.54)	1.81	1.82 (0.60) 1.82 (0.60)	1.82	1.81 (0.59) 1.81 (0.59)	1.81	1.84 (0.59) 1.84 (0.59)	1.84	2.20	
	2^1E_u	$\pi \rightarrow \pi^*$	3.71 [20]	3.50 3.50		3.50		3.53 3.53		3.53			3.59 3.59
	3^1E_u	$\pi \rightarrow \pi^*$	3.74 [20]	3.60 (0.25) 3.60 (0.25)	3.60	3.60 (0.41) 3.60 (0.41)	3.60	3.63 (0.34) 3.63 (0.34)	3.63	3.67 (0.77) 3.67 (0.77)	3.67	3.83	
	1^1A_{2u}	$\pi \rightarrow \pi^*$	3.99 [20]	3.91 3.91		3.91		3.90 3.90		3.90			4.03 4.03
Ferrocene	a^3E_{1g}	$d \rightarrow d^*/\pi^*$	2.34 [21]	2.04 2.04	2.04	1.97 1.97	1.97	1.89 1.89	1.89	2.15 2.15	2.15	1.26	
	a^1E_{1g}	$d \rightarrow d^*/\pi^*$	2.8 [22]	2.92 2.92		2.92		2.72 2.72		2.72			2.64 2.64
	$^1E_{2g}$	$d \rightarrow d^*/\pi^*$	2.81 [22]	2.69 2.69	2.69	2.51 2.51	2.51	2.44 2.44	2.44	2.69 2.69	2.69	2.39	
	b^1E_{1g}	$d \rightarrow d^*/\pi^*$	3.82 [21, 22]	3.99 3.99		3.99		3.72 3.72		3.72			3.62 3.63
Ruthenocene	a^3E_{1g}	$d \rightarrow d^*/\pi^*$	3.22 [21]	3.02 3.02	3.02	3.04 3.04	3.04	2.99 2.99	2.99	3.19 3.19	3.19	3.09	
	a^1E_{1g}	$d \rightarrow d^*/\pi^*$	3.66 [21]	3.55 3.55		3.55		3.49 3.49		3.49			3.44 3.44
	$^1E_{2g}$	$d \rightarrow d^*/\pi^*$	4.03 [21]	3.56 3.56	3.56	3.48 3.48	3.48	3.42 3.42	3.42	3.63 3.63	3.63	3.65	
	b^1E_{1g}	$d \rightarrow d^*/\pi^*$	4.54 [21]	4.16 4.16		4.16		4.05 4.05		4.05			3.99 3.99
Cobaltocene	a^3E_{1g}	$d \rightarrow d^*/\pi^*$	2.70 [21]	2.26 2.26	2.26	2.08 2.08	2.08	1.97 1.97	1.97	2.43 2.43	2.43	1.70	
	a^1E_{1g}	$d \rightarrow d^*/\pi^*$	3.01 [21]	2.57 2.57		2.57		2.53 2.53		2.53			2.40 2.40
	$^1E_{2g}$	$d \rightarrow d^*/\pi^*$	3.27 [21]	2.85 2.85	2.85	2.77 2.77	2.77	2.65 2.65	2.65	3.12 3.12	3.12	2.81	
	b^1E_{1g}	$d \rightarrow d^*/\pi^*$	4.12 [21]	4.08 4.08		4.08		3.79 3.79		3.79			3.66 3.66

Table S2: Vertical excitation energies of transition metal complexes (in eV) in comparison to experiment. Oscillator strengths in parentheses. All DFT/MRCI calculations were performed using the respective tight (or short) parameter set and a selection threshold of $0.8 E_h$. Original denotes the ansatz by Grimme and Waletzke [1], R2016 marks the redesigned Hamiltonian by Lyskov et al. [2], R2017 refers to variant proposed by Heil and Marian [3], and R2018 to the parameterization in the present work. Some molecules exhibit non-Abelian symmetry. In DFT/MRCI, which can handle only Abelian point-group symmetries, all components of spatially degenerate state are listed to show the level of degeneracy. For comparison to the experimentally derived energies, the average energy is given as well. Blank cells in the average column are due to some states not assignable.

Molecule	State/ Transition	Type	Experiment (Oscil. str.)	Original		R2016		R2017		R2018	
				states	av.	states	av.	states	av.	states	av.
CrF ₆	¹ T _{1u}	$\pi \rightarrow d/\pi^*$	3.31 (middle) [4]	2.26 (0.00515)		1.47 (0.0017)		1.53 (0.0024)		2.04 (0.0024)	
				2.26 (0.0050)	2.26	1.47 (0.0017)	1.47	1.54 (0.0023)	1.54	2.04 (0.0024)	2.04
				2.26 (0.0050)		1.47 (0.0020)		1.54 (0.0023)		2.04 (0.0024)	
	¹ T _{1u}	$\pi \rightarrow d/\pi^*$	3.88 (strong) [4]	2.91 (0.045)		1.88 (0.052)		1.99 (0.062)		2.68 (0.095)	
				2.92 (0.046)	2.92	1.88 (0.052)	1.88	1.99 (0.062)	1.99	2.68 (0.095)	2.68
				2.92 (0.046)		1.89 (0.051)		1.99 (0.061)		2.68 (0.095)	
	¹ T _{1u}	$\pi \rightarrow d/\pi^*$	4.77 (strong) [4]	3.80 (0.025)		2.91 (0.03)		3.02 (0.037)		3.29 (0.027)	
				3.80 (0.027)	3.80	2.91 (0.03)	2.91	3.02 (0.037)	3.02	3.30 (0.034)	3.30
				3.80 (0.027)		2.91 (0.03)		3.02 (0.038)		3.30 (0.034)	
MoF ₆	¹ T _{1u}	$\pi \rightarrow d/\pi^*$	5.90 (weak) [5]	5.25 (0.0089)		4.99 (0.010)		4.90 (0.012)		4.94 (0.010)	
				5.25 (0.0089)	5.25	4.99 (0.010)	4.99	4.90 (0.012)	4.90	4.94 (0.010)	4.94
				5.25 (0.0089)		4.99 (0.010)		4.90 (0.012)		4.94 (0.010)	
	² T _{1u}	$\pi \rightarrow d/\pi^*$	6.54 (middle) [5]	5.87 (0.069)		5.45 (0.11)		5.36 (0.14)		5.40 (0.11)	
				5.87 (0.069)	5.87	5.45 (0.11)	5.45	5.36 (0.14)	5.36	5.40 (0.11)	5.40
				5.87 (0.069)		5.45 (0.11)		5.36 (0.14)		5.40 (0.11)	
	³ T _{1u}	$\pi \rightarrow d/\pi^*$	7.12 (strong) [5]	6.58 (0.22)		6.02 (0.18)		5.95 (0.19)		6.05 (0.24)	
				6.58 (0.22)	6.58	6.02 (0.18)	6.02	5.95 (0.19)	5.95	6.05 (0.24)	6.05
				6.58 (0.22)		6.02 (0.18)		5.95 (0.19)		6.05 (0.24)	
Mo(CO) ₆	¹ T _{1u}	$d/\pi \rightarrow \pi^*$	4.32 (0.139) [6]	4.33 (0.073)		4.24 (0.089)		4.29 (0.10)		4.38 (0.092)	
				4.33 (0.073)	4.33	4.24 (0.089)	4.24	4.29 (0.10)	4.29	4.38 (0.093)	4.38
				4.33 (0.073)		4.24 (0.089)		4.29 (0.10)		4.38 (0.093)	
	¹ T _{1u}	$d/\pi \rightarrow \pi^*$	5.44 (1.78) [6]	5.65 (1.12)		5.43 (1.08)		5.46 (1.05)		5.57 (1.07)	
				5.65 (1.12)	5.65	5.43 (1.08)	5.43	5.46 (1.05)	5.46	5.57 (1.07)	5.46
				5.65 (1.12)		5.43 (1.08)		5.46 (1.05)		5.57 (1.07)	
Cr(CO) ₆	¹ T _{1u}	$d/\pi \rightarrow \pi^*$	4.43 (0.19) [6]	4.57 (0.08)		4.22 (0.086)		4.53 (0.081)		4.67 (0.075)	
				4.57 (0.08)	4.57	4.22 (0.086)	4.22	4.53 (0.081)	4.53	4.67 (0.075)	4.72
				4.57 (0.08)		4.22 (0.086)		4.53 (0.081)		4.67 (0.075)	
	¹ T _{1u}	$d/\pi \rightarrow \pi^*$	5.41 (1.45) [6]	5.58 (0.86)		5.15 (0.79)		5.50 (0.84)		5.67 (0.86)	
				5.58 (0.86)	5.58	5.15 (0.79)	5.15	5.50 (0.84)	5.50	5.67 (0.86)	5.66
				5.58 (0.86)		5.15 (0.79)		5.50 (0.84)		5.67 (0.86)	
Ni(CO) ₄	¹ T ₂	$\sigma/d \rightarrow \pi^*$	4.54 [7]	4.31 (0.12)		3.84 (0.11)		3.98 (0.11)		4.42 (0.11)	
				4.32 (0.13)	4.32	3.86 (0.11)	3.85	4.00 (0.12)	3.99	4.44 (0.12)	4.43

Molecule	State/ Transition	Type	Experiment (Oscil. str.)	Original		R2016		R2017		R2018	
				states	av.	states	av.	states	av.	states	av.
Co(H ₂ O) ₆ ²⁺	¹ T ₂	σ/d → π*	5.17 [7]	4.32 (0.13)		3.86 (0.11)		4.00 (0.12)		4.44 (0.12)	
				5.62 (0.18)	5.64	4.87 (0.14)	4.89	4.88 (0.16)	5.24 (0.19)		
				5.65 (0.17)	5.65 (0.17)	4.90 (0.13)	4.90 (0.13)	4.91 (0.15)	5.25 (0.18)		
	¹ T ₂ (t ₂ ⁵ e _g ¹)	π/d → σ*/d*	0.99 [8]	0.78		1.29		1.26		1.28	
				0.81	0.81	1.31	1.31	1.28	1.3		
² T ₂ (t ₂ ⁵ e _g ¹)	π/d → σ*/d*	1.55 [8]	1.26		1.7		1.66		1.69		
			1.3	1.30	1.75	1.74	1.71	1.74			
¹ T ₂ (t ₂ ⁵ e _g ¹)	π/d → σ*/d*	2.06 [8]	1.59		1.88		1.86		1.89		
			1.62	1.62	1.89	1.90	1.88	1.91			
² T ₂ (t ₂ ⁵ e _g ¹)	π/d → σ*/d*	3.09 [8]	2.58		2.74		2.72		2.73		
			2.53	2.57	2.77	2.77	2.75	2.76			
Co(NH ₃) ₆ ³⁺	¹ T _{1g}	d → σ*/d*	2.70 [9]	2.48 (0.00003)		2.59 (0.00003)		2.55 (0.00003)		2.64 (0.00003)	
				2.50 (0.00004)	2.50	2.61 (0.00004)	2.61	2.56 (0.00004)	2.66 (0.00004)		
				2.51 (0.00002)	2.51 (0.00002)	2.62 (0.00001)	2.62	2.57 (0.00001)	2.66 (0.00001)		
	¹ T _{2g}	d → σ*/d*	3.40 [9]	3.46 (0.00000)		3.50 (0.00000)		3.45 (0.00000)		3.55 (0.00000)	
				3.46 (0.00002)	3.47	3.50 (0.00002)	3.51	3.45 (0.00002)	3.56 (0.00002)		
Rh(NH ₃) ₆ ³⁺	¹ T _{1g}	d → σ*/d*	3.96 [9]	3.67		3.71		3.68		3.74	
				3.68	3.69	3.72	3.72	3.69	3.75		
				3.71	3.71	3.74	3.74	3.71	3.77		
	¹ T _{2g}	d → σ*/d*	4.88 [9]	4.38		4.38		4.36		4.41	
				4.41	4.40	4.40	4.40	4.37	4.43		
MnO ₄ ⁻	¹ T ₂ (1t ₁ → 2e)	π → d*/π*	2.4 (strong) [10]	1.52 (0.0091)		1.14 (0.0051)		1.67 (0.0031)		2.09 (0.0074)	
				1.72 (0.0069)	1.65	1.39 (0.0020)	1.31	1.67 (0.0031)	1.72		
				1.72 (0.0069)	1.72 (0.0069)	1.39 (0.0020)	1.39 (0.0020)	1.81 (0.0084)	2.11 (0.0095)		
	² T ₂ (1t ₁ → 3t ₂ , 2t ₂ → 2e)	π → d/π*/σ*	3.6 (medium) [10]	2.93 (0.0066)							
				2.93 (0.0057)	2.93						
³ T ₂ (2t ₂ → 2e, 1t ₁ → 3t ₂)	π → d*/π*	4.1 (strong) [10]	3.4 (0.013)		3.29 (0.0041)		3.87 (0.011)		4.26 (0.013)		
			3.4 (0.013)	3.41	3.44 (0.0057)	3.39	4.02 (0.0059)	3.97			
			3.42 (0.011)		3.44 (0.0057)		4.02 (0.0059)		4.42 (0.011)		

Molecule	State/ Transition	Type	Experiment (Oscil. str.)	Original		R2016		R2017		R2018	
				states	av.	states	av.	states	av.	states	av.
TeO ₄ ⁻	4 ¹ T ₂ (1a ₁ → 3t ₂ , 2t ₂ → 3t ₂)	π → d*/π*	5.5 (medium) [10]	5.14 (0.0013) 5.14 (0.0011) 5.14 (0.0011)	5.14						
	1 ¹ T ₂ (1t ₁ → 2e, 2t ₂ → 2e)	π → d*/π*	4.35 [11]	3.55 (0.017) 3.63 (0.013) 3.63 (0.013)	3.60	3.70 (0.017) 3.74 (0.016) 3.74 (0.016)	3.73	3.51 (0.017) 3.56 (0.016) 3.56 (0.016)	3.54	3.82 (0.019) 3.86 (0.017) 3.86 (0.017)	3.85
	2 ¹ T ₂ (1t ₁ → 2e, 2t ₂ → 2e)	d/π → d*/π*	5.1 [11]	4.52 (0.034) 4.57 (0.034) 4.57 (0.034)	4.55	4.68 (0.038) 4.68 (0.038) 4.69 (0.040)	4.68	4.48 (0.037) 4.48 (0.037) 4.54 (0.039)	4.50	4.81 (0.041) 4.82 (0.040) 4.82 (0.040)	4.82
Ru(bpy) ₃	band max.	d → π*	2.88 [13]	5.56 (0.0069)	5.57	5.84 (0.012)	5.84	5.65 (0.011)	5.65	6.00 (0.012)	6.00
		d → d*	4.00 [13]	5.56 (0.0069)	5.57	5.84 (0.012)	5.84	5.65 (0.011)	5.65	6.00 (0.012)	6.00
		π → π*	4.38 [13]	5.58 (0.0062)	5.58	5.85 (0.011)	5.85	5.66 (0.010)	5.66	6.00 (0.011)	6.00
Ru(tpy)(bpy)(py) ²⁺	band max.	d → π*	2.66 [14]		2.97		2.91		2.88		2.93
		d → d*	4.00 [13]		4.09		4.28		4.41		4.15
		π → π*	4.38 [13]		4.43		4.37		4.34		4.40
		d → π*	5.02 [13]		4.92		4.92		4.92		5.09
		d/π → π*	2.66 [14]		2.82		2.73		2.71		2.80
Rh(bpy) ₃ ³⁺	band max.	d → π*	2.99 [14]		3.09		3.11		3.10		3.16
		d → π*	3.99 [14]		4.15		4.01		3.99		4.13
		d/π → π*	4.40 [14]		4.40		4.40		4.40		4.51
		d/π → π*	5.30 [14]		5.04		5.04		5.10		5.31
		π → π*	3.88 [15]		3.86		3.89		3.83		3.92
Rh(phen) ₃ ³⁺	band max.	π → π*	4.04 [15]		3.92		3.96		3.90		3.99
		π → π*	5.15 [15]		5.17		5.25		5.20		5.38
		d/π → π*	4.44 [16]		4.37		4.35		4.33		4.53
Rh(tpy)(bpy)(py) ²⁺	band max.	π → π*	3.46 [17]		3.51		3.64		3.65		3.64
		π → π*	3.65 [17]		3.83		3.97		3.92		4.03
		π → π*	4.00 [17]		4.08		4.18		4.12		4.26
		d/π → π*	4.37 [17]		4.31		4.44		4.38		4.48
ZnP	1 ¹ E _u	π → π*	2.18 (0.005) [18]		2.16		2.17		2.19		2.22
	2 ¹ E _u	π → π*	3.13 (0.98) [18]		3.28		3.24		3.25		3.28
	4 ¹ E _u	π → π*	4.07 (0.2) [18]		4.02		4.04		4.12		4.26
ZnTBP	1 ¹ E _u	π → π*	1.98 (0.3) [19]		1.89		1.91		1.90		1.93
	2 ¹ E _u	π → π*	3.06 (1.6) [19]		3.03		3.00		3.00		3.05

Molecule	State/ Transition	Type	Experiment (Oscil. str.)	Original		R2016		R2017		R2018	
				states	av.	states	av.	states	av.	states	av.
	3^1E_u	$\pi \rightarrow \pi^*$	3.87 (0.4) [19]		3.68		3.68		3.72		3.81
	8^1E_u	$\pi \rightarrow \pi^*$	4.89 (0.4) [19]		4.59		4.57		4.63		4.79
ZnPC	1^1E_u	$\pi \rightarrow \pi^*$	1.89 [20]		1.81		1.82		1.81		1.85
	2^1E_u	$\pi \rightarrow \pi^*$	3.71 [20]		3.50		3.53		3.59		3.77
	3^1E_u	$\pi \rightarrow \pi^*$	3.74 [20]		3.60		3.60		3.63		3.73
	1^1A_{2u}	$\pi \rightarrow \pi^*$	3.99 [20]		3.91		3.90		4.03		4.24
Ferrocene	a^3E_{1g}	$d \rightarrow d^*/\pi^*$	2.34 [21]		2.24		1.97		2.18		2.54
	a^1E_{1g}	$d \rightarrow d^*/\pi^*$	2.8 [22]		3.10		2.73		2.91		3.25
	$^1E_{2g}$	$d \rightarrow d^*/\pi^*$	2.81 [22]		2.99		2.50		2.73		3.10
	b^1E_{1g}	$d \rightarrow d^*/\pi^*$	3.82 [21, 22]		3.54		3.62		3.82		4.17
Ruthenocene	a^3E_{1g}	$d \rightarrow d^*/\pi^*$	3.22 [21]		3.00		3.03		3.05		3.35
	a^1E_{1g}	$d \rightarrow d^*/\pi^*$	3.66 [21]		3.57		3.48		3.51		3.81
	$^1E_{2g}$	$d \rightarrow d^*/\pi^*$	4.03 [21]		3.59		3.44		3.48		3.78
	b^1E_{1g}	$d \rightarrow d^*/\pi^*$	4.54 [21]		4.22		4.06		4.09		4.39
Cobaltocene	a^3E_{1g}	$d \rightarrow d^*/\pi^*$	2.70 [21]		1.95		1.68		1.93		2.47
	a^1E_{1g}	$d \rightarrow d^*/\pi^*$	3.01 [21]		2.47		2.37		2.63		3.18
	$^1E_{2g}$	$d \rightarrow d^*/\pi^*$	3.27 [21]		2.21		2.11		2.37		2.91
	b^1E_{1g}	$d \rightarrow d^*/\pi^*$	4.12 [21]		3.62		3.39		3.68		4.23

Statistical evaluation

Standard selection and matching parameters

Table S3: Statistical data for the performance of TDDFT-PBE0, the original Hamiltonian and the three redesigned Hamiltonians R2016, R2017 and R2018 on the test suite including all transition metal complexes. The DFT/MRCI calculations were performed with the standard parameter set and a selection threshold of $1.0 E_h$. All values are in eV.

	Original 67 states	R2016	R2017	R2018	TDDFT-PBE0 67 states
RMSE	0.35	0.55	0.60	0.33	0.41
MAE	0.25	0.35	0.39	0.23	0.32
Mean	-0.15	-0.29	-0.34	-0.04	0.09
MaxAE	1.03	1.92	2.05	1.10	1.14

Table S4: Statistical data for the performance of TDDFT-PBE0, the original Hamiltonian and the three redesigned Hamiltonians R2016, R2017 and R2018 on the inorganic transition metal complexes. The DFT/MRCI calculations were performed with the standard parameter set and a selection threshold of $1.0 E_h$. All values are in eV.

	Original 27 states	R2016	R2017	R2018	TDDFT-PBE0 27 states
RMSE	0.50	0.83	0.89	0.50	0.33
MAE	0.40	0.61	0.66	0.41	0.26
Mean	-0.23	-0.52	-0.59	-0.09	0.09
MaxAE	1.03	1.92	2.05	1.10	0.78

Table S5: Statistical data for the performance of TDDFT-PBE0, the original Hamiltonian and the three redesigned Hamiltonians R2016, R2017 and R2018 on 40 singlet and triplet excitation energies of metal organic complexes. The DFT/MRCI calculations were performed with the standard parameter set and a selection threshold of $1.0 E_h$. All values are in eV.

	Original	R2016	R2017	R2018	TDDFT-PBE0
RMSE	0.20	0.25	0.30	0.15	0.46
MAE	0.14	0.19	0.22	0.11	0.37
Mean	-0.09	-0.15	-0.18	-0.01	0.10
MaxAE	0.70	0.74	0.87	0.41	1.14

Table S6: Statistical data of 160 vertical excitation energies (93 singlets, 67 triplets) of organic molecules for the original Hamiltonian and the three redesigned Hamiltonians R2016, R2017 and R2018 with the standard parameter set and a selection threshold of $1.0 E_h$. All values are in eV. The geometries, experimental references and the values for Original and R2016 have been taken from Ref. [2], values for R2017 from Ref. [3].

	Original	R2016	R2017	R2018
RMSE	0.16	0.15	0.15	0.17
MAE	0.13	0.12	0.12	0.13
Mean	0.02	0.06	0.03	0.06
MaxAE	0.46	0.39	0.36	0.49

Short selection and matching parameters

Table S7: Statistical data for the performance of the original Hamiltonian and the three redesigned Hamiltonians R2016, R2017 and R2018 on the test suite including all transition metal complexes. The DFT/MRCI calculations were performed with the parameter set optimized for a short selection and a selection threshold of $0.8 E_h$ (tight selection). All values are in eV.

	Original 67 states	R2016	R2017	R2018
		65 states		
RMSE	0.43	0.60	0.55	0.42
MAE	0.31	0.37	0.33	0.27
Mean	-0.23	-0.32	-0.27	-0.08
MaxAE	1.06	2.00	1.89	1.47

Table S8: Statistical data for the performance of the original Hamiltonian and the three redesigned Hamiltonians R2016, R2017 and R2018 on the inorganic transition metal complexes. The DFT/MRCI calculations were performed with the parameter set optimized for a short selection and a selection threshold of $0.8 E_h$ (tight selection). All values are in eV.

	Original 27 states	R2016	R2017	R2018
		25 states		
RMSE	0.58	0.85	0.82	0.64
MAE	0.49	0.59	0.55	0.43
Mean	-0.41	-0.58	-0.54	-0.34
MaxAE	1.05	2.00	1.89	1.47

Table S9: Statistical data for the performance of the original Hamiltonian and the three redesigned Hamiltonians R2016, R2017 and R2018 on the test suite including 40 states of transition metal organic complexes. The DFT/MRCI calculations were performed with the parameter set optimized for a short selection and a selection threshold of $0.8 E_h$ (tight selection). All values are in eV.

	Original	R2016	R2017	R2018
RMSE	0.28	0.34	0.26	0.19
MAE	0.19	0.23	0.18	0.15
Mean	-0.11	-0.15	-0.10	0.08
MaxAE	0.80	1.02	0.77	0.45

Table S10: Statistical data of 160 vertical excitation energies (93 singlets, 67 triplets) of organic molecules for the original Hamiltonian and the three redesigned Hamiltonians R2016, R2017 and R2018 with the short parameter set and a selection threshold of $0.8 E_h$. All values are in eV. The geometries and experimental references have been taken from Ref. [2], values for R2017 from Ref. [3].

	Original	R2016	R2017	R2018
RMSE	0.18	0.16	0.16	0.15
MAE	0.15	0.13	0.13	0.12
Mean	-0.03	0.02	0.04	0.03
MaxAE	0.43	0.39	0.38	0.39

Short Selection and Standard parameters

Table S11: Statistical data for the performance of the original Hamiltonian and the three redesigned Hamiltonians R2016, R2017 and R2018 on the test suite including all transition metal complexes. The DFT/MRCI calculations were performed with the parameter set optimized for a standard selection and a selection threshold of $0.8 E_h$ (tight selection). All values are in eV.

	Original 67 states	R2016	R2017	R2018
		65 states		
RMSE	0.41	0.47	0.50	0.49
MAE	0.33	0.29	0.30	0.41
Mean	0.09	-0.14	-0.20	-0.25
MaxAE	1.07	1.64	1.75	1.50

Table S12: Statistical data for the performance of the original Hamiltonian and the three redesigned Hamiltonians R2016, R2017 and R2018 on the inorganic transition metal complexes. The DFT/MRCI calculations were performed with the parameter set optimized for a standard selection and a selection threshold of $0.8 E_h$ (tight selection). All values are in eV.

	Original 27 states	R2016	R2017	R2018
		25 states		
RMSE	0.54	0.71	0.76	0.58
MAE	0.49	0.59	0.55	0.47
Mean	-0.08	-0.38	-0.45	0.06
MaxAE	1.07	1.64	1.75	1.50

Table S13: Statistical data for the performance of the original Hamiltonian and the three redesigned Hamiltonians R2016, R2017 and R2018 on the test suite including 40 states of transition metal organic complexes. The DFT/MRCI calculations were performed with the parameter set optimized for a standard selection and a selection threshold of $0.8 E_h$ (tight selection). All values are in eV.

	Original	R2016	R2017	R2018
RMSE	0.29	0.19	0.24	0.42
MAE	0.24	0.14	0.17	0.37
Mean	0.20	0.01	-0.05	0.37
MaxAE	0.64	0.61	0.77	0.73

Ionization Potentials

Table S14: Ionization potentials (in eV) of various molecules. All calculations have been performed at the B3-LYP optimized singlet ground state geometry. ΔE_{SCF} values refer to singlet ground-state RKS B3LYP and doublet ground-state ROKS B3LYP energies. At the DFT/MRCI level, RKS orbitals and orbital energies of the neutral ground state have been applied.

Molecule	exp. IP	R2017	R2018	ΔE_{SCF} (BH-LYP)
1,2,3,4-Tetrafluorobenzene	9.8 [23]	9.71	9.72	9.83
1,2,4,5-Tetrafluorobenzene	9.5 [23]	9.54	9.54	9.64
Adenine	8.47 [24]	8.18	8.46	8.32
Thymine	9.19 [24]	8.99	8.98	9.07
Ethylene	10.5 [25]	10.33	10.34	10.27
Ethyl fluoride	12.4 [23]	12.45	12.42	12.62
Nitrous oxide	12.89 [26]	12.57	12.60	12.86
Fulvene	8.36 [27]	8.12	8.14	8.16
Methylene fluoride	13.3 [23]	13.64	13.63	13.66
Tetrafluoroethylene	10.69 [23]	10.65	10.68	10.64
cis-1,2-Difluoroethylene	10.62 [23]	10.43	10.45	10.42
trans-1,2-Difluoroethylene	10.63 [23]	10.41	10.43	10.39
p-Xylylene	7.87 [28]	7.43	7.47	7.52
Fluorobenzene	9.4 [23]	9.10	9.12	9.24
o-Benzoquinone	9.6 [29]	9.27	9.23	9.95
Tetracene	7.04 [30]	6.52	6.51	6.62
Acenaphthylene	8.22 [30]	7.76	7.76	7.92
Anthracene	7.47 [30]	7.05	7.05	7.17
Azulene	7.43 [30]	7.11	7.12	7.23
Naphthalene	8.15 [30]	7.84	7.83	7.97
Pyrene	7.41 [30]	7.08	7.08	7.24
Formaldehyde	10.87 [31]	10.64	10.63	10.81
Guanine	8.24 [32]	7.92	7.85	8.03
Cytosine	8.94 [32]	8.62	8.80	8.93
Furan	9.0 [33]	8.71	8.73	8.80
Pyrrole	8.21 [33]	8.01	8.03	8.15
Benzene	9.3 [34]	9.02	9.03	9.18
Tetracyanoethylene	11.79 [34]	11.48	11.44	11.67
Ethanol	10.7 [35]	10.26	10.23	10.63
Benzonitrile	9.8 [34]	9.49	9.47	9.678

References

- [1] S. Grimme, M. Waletzke, A combination of Kohn–Sham density functional theory and multi-reference configuration interaction methods, *J. Chem. Phys.* 111 (13) (1999) 5645–5655. doi:10.1063/1.479866.
- [2] I. Lyskov, M. Kleinschmidt, C. M. Marian, Redesign of the DFT/MRCI Hamiltonian, *J. Chem. Phys.* 144 (3) (2016) 034104. doi:10.1063/1.4940036.
- [3] A. Heil, C. M. Marian, DFT/MRCI Hamiltonian for odd and even numbers of electrons, *J. Chem. Phys.* 147 (19) (2017) 194104. doi:10.1063/1.5003246.
- [4] E. G. Hope, P. J. Jones, W. Levason, J. S. Ogden, M. Tajik, J. W. Turff, Spectroscopic studies on the higher binary fluorides of chromium: CrF₄, CrF₅, and CrF₆, both in the solid state and isolated in inert gas matrices, *J. Chem. Soc., Dalton Trans.* (7) (1985) 1443. doi:10.1039/dt9850001443.
- [5] R. McDiarmid, Assignments in the ultraviolet spectra of MoF₆ and WF₆, *J. Chem. Phys.* 61 (8) (1974) 3333–3339.
- [6] H. B. Gray, N. A. Beach, The electronic structures of octahedral metal complexes. I. metal hexacarbonyls and hexacyanides, *J. Am. Chem. Soc.* 85 (19) (1963) 2922–2927. doi:10.1021/ja00902a014.
- [7] A. Lever, G. Ozin, A. Hanlan, W. Power, H. B. Gray, Electronic absorption spectra of metal tetracarbonyls, *Inorg. Chem.* 18 (8) (1979) 2088–2090.
- [8] D. A. Johnson, A. G. Sharpe, The preparation of cobalt(III) sulphate and its alums, and the magnetic, spectroscopic, and crystallographic properties of the Co(H₂O)₆³⁺ ion, *J. Chem. Soc. A* (1966) 798doi:10.1039/j19660000798.
- [9] P. C. Ford, The ligand field photosubstitution reactions of d⁶ hexacoordinate metal complexes, *Coord. Chem. Rev.* 44 (1) (1982) 61–82. doi:10.1016/s0010-8545(00)80517-2.
- [10] S. L. Holt, C. J. Ballhausen, Low temperature absorption spectra of KMnO₄ in KClO₄, *Theor. Chim. Acta* 7 (4) (1967) 313–320. doi:10.1007/bf00537508.
- [11] H. U. Güdel, C. J. Ballhausen, Low temperature absorption spectra of TcO₄⁻ and ReO₄⁻ in KClO₄, *Theor. Chim. Acta* 25 (4) (1972) 331–337. doi:10.1007/bf00526564.
- [12] P. Mullen, K. Schwochau, et al., Vacuo ultraviolet spectra of permanganate, pertechnetate and perrhenate, *Chem. Phys. Lett.* 3 (1) (1969) 49–51.
- [13] M.-B. S. Kirketerp, S. B. Nielsen, Absorption spectrum of isolated tris(2,2'-bipyridine)ruthenium(II) dications in vacuo, *Int. J. Mass Spectrom.* 297 (1-3) (2010) 63–66. doi:10.1016/j.ijms.2010.05.019.
- [14] S. C. Rasmussen, S. E. Ronco, D. A. Mlsna, M. A. Billadeau, W. T. Pennington, J. W. Kolis, J. D. Petersen, Ground- and excited-state properties of ruthenium(II) complexes containing tridentate azine ligands, Ru(tpy)(bpy)l²⁺, where l is a polymerizable acetylene, *Inorg. Chem.* 34 (4) (1995) 821–829. doi:10.1021/ic00108a013.
- [15] M. Maestri, D. Sandrini, V. Balzani, U. Maeder, A. V. Zelewsky, Absorption spectra, electrochemical behavior, luminescence spectra, and excited-state lifetimes of mixed-ligand ortho-metalated rhodium(III) complexes, *Inorg. Chem.* 26 (8) (1987) 1323–1327. doi:10.1021/ic00255a025.
- [16] D. Sandrini, M. Maestri, V. Balzani, U. Maeder, A. V. Zelewsky, Spectroscopic and electrochemical properties of new mixed-ligand orthometalated rhodium(III) complexes, *Inorg. Chem.* 27 (15) (1988) 2640–2643. doi:10.1021/ic00288a016.
- [17] M. E. Frink, S. D. Sprouse, H. A. Goodwin, R. J. Watts, P. C. Ford, Synthesis and excited-state properties of rhodium(III) terpyridine complexes, *Inorg. Chem.* 27 (7) (1988) 1283–1286. doi:10.1021/ic00280a039.
- [18] H. Sekino, H. Kobayashi, A screened potential molecular-orbital calculation of the π-electron systems of metalloporphyrin, metallochlorin, and metallobacteriochlorin, *J. Chem. Phys.* 86 (9) (1987) 5045–5052. doi:10.1063/1.452681.
- [19] L. Edwards, M. Gouterman, C. B. Rose, Synthesis and vapor spectrum of zinc tetrabenzporphine, *J. Am. Chem. Soc.* 98 (24) (1976) 7638–7641. doi:10.1021/ja00440a031.
- [20] T. C. VanCott, J. L. Rose, G. C. Misener, B. E. Williamson, A. E. Schrimpf, M. E. Boyle, P. N. Schatz, Magnetic circular dichroism and absorption spectrum of zinc phthalocyanine in an argon matrix between 14700 and 74000 cm⁻¹, *J. Phys. Chem.* 93 (8) (1989) 2999–3011. doi:10.1021/j100345a028.
- [21] H. B. Gray, Y. S. Sohn, N. Hendrickson, Electronic structure of metallocenes, *J. Am. Chem. Soc.* 93 (15) (1971) 3603–3612. doi:10.1021/ja00744a011.
- [22] A. T. Armstrong, F. Smith, E. Elder, S. P. McGlynn, Electronic absorption spectrum of ferrocene, *J. Chem. Phys.* 46 (11) (1967) 4321–4328. doi:10.1063/1.1840547.
- [23] G. Bieri, L. Åsbrink, W. V. Niessen, 30.4-nm He(II) photoelectron spectra of organic molecules, *J. Electron Spectrosc. Relat. Phenom.* 23 (2) (1981) 281–322. doi:10.1016/0368-2048(81)80036-9.

- [24] A. B. Trofimov, J. Schirmer, V. B. Kobychyev, A. W. Potts, D. M. P. Holland, L. Karlsson, Photoelectron spectra of the nucleobases cytosine, thymine and adenine, *J. Phys. B: At., Mol. Opt. Phys.* 39 (2) (2005) 305–329. doi:10.1088/0953-4075/39/2/007.
- [25] A. Baker, C. Baker, C. Brundle, D. Turner, The electronic structures of methane, ethane, ethylene and formaldehyde studied by high-resolution molecular photoelectron spectroscopy, *Int. J. Mass Spectrom. Ion Phys.* 1 (4) (1968) 285 – 301. doi:[https://doi.org/10.1016/0020-7381\(68\)85005-3](https://doi.org/10.1016/0020-7381(68)85005-3).
URL <http://www.sciencedirect.com/science/article/pii/0020738168850053>
- [26] J. Lorquet, C. Cadet, Excited states of gaseous ions, *Int. J. Mass Spectrom. Ion Phys.* 7 (3) (1971) 245–254. doi:10.1016/0020-7381(71)80020-7.
- [27] H. Rosenstock, J. Dannacher, J. Liebman, The role of excited electronic states in ion fragmentation: $C_6H_6^+$, *Radiat. Phys. Chem.* 20 (1) (1982) 7–28. doi:10.1016/0146-5724(82)90056-5.
- [28] M. Allan, E. Heilbronner, G. Kaupp, The photoelectron spectrum of dibenzo-p-quinodimethane, *Helv. Chim. Acta* 59 (6) (1976) 1949–1952. doi:10.1002/hlca.19760590608.
- [29] P. Schang, R. Gleiter, A. Rieker, The He(I) photoelectron spectrum of cyclobutene-1,2-dione and o-benzoquinone, *Ber. Bunsenges. Phys. Chem.* 82 (6) (1978) 629–633. doi:10.1002/bbpc.197800131.
- [30] R. Boschi, E. Clar, W. Schmidt, Photoelectron spectra of polynuclear aromatics. III. the effect of nonplanarity in sterically overcrowded aromatic hydrocarbons, *J. Chem. Phys.* 60 (11) (1974) 4406–4418. doi:10.1063/1.1680919.
- [31] J. E. Mentall, E. P. Gentieu, M. Krauss, D. Neumann, Photoionization and absorption spectrum of formaldehyde in the vacuum ultraviolet, *The Journal of Chemical Physics* 55 (12) (1971) 5471–5479. doi:10.1063/1.1675711.
- [32] N. Hush, A. S. Cheung, Ionization potentials and donor properties of nucleic acid bases and related compounds, *Chem. Phys. Lett.* 34 (1) (1975) 11–13. doi:10.1016/0009-2614(75)80190-4.
- [33] G. Bieri, L. Åsbrink, W. von Niessen, 30.4-nm He(II) photoelectron spectra of organic molecules, *J. Electron Spectrosc. Relat. Phenom.* 27 (2) (1982) 129–178. doi:10.1016/0368-2048(82)85059-7.
- [34] G. Bieri, L. Åsbrink, 30.4-nm He(II) photoelectron spectra of organic molecules, *J. Electron Spectrosc. Relat. Phenom.* 20 (1) (1980) 149–167. doi:10.1016/0368-2048(80)85013-4.
- [35] W. V. Niessen, L. Cederbaum, J. Schirmer, G. Diercksen, W. Kraemer, Ionization energies of some molecules found in interstellar clouds calculated by a green's function method, *J. Electron Spectrosc. Relat. Phenom.* 28 (1) (1982) 45–78. doi:10.1016/0368-2048(82)80016-9.

Received: 3 August 2018 | Revised: 14 September 2018 | Accepted: 18 September 2018

DOI: 10.1002/wcms.1394



ADVANCED REVIEW

The DFT/MRCI method

Christel M. Marian | Adrian Heil | Martin Kleinschmidt

Institute of Theoretical and Computational Chemistry, Heinrich Heine Universität Düsseldorf, Düsseldorf

Correspondence

Christel M. Marian, Institute of Theoretical and Computational Chemistry, Heinrich Heine Universität Düsseldorf, Universitätsstraße 1, 40225 Düsseldorf, Germany.
Email: christel.marian@hhu.de

Funding information

Deutsche Forschungsgemeinschaft, Grant/Award Numbers: MA 1051-14/2, MA 1051-14/1

In the past two decades, the combined density functional theory and multireference configuration interaction (DFT/MRCI) method has developed from a powerful approach for computing spectral properties of singlet and triplet excited states of large molecules into a more general multireference method applicable to states of all spin multiplicities. In its original formulation, it shows great efficiency in the evaluation of singlet and triplet excited states which mainly originate from local one-electron transitions. Moreover, DFT/MRCI is one of the few methods applicable to large systems that yields the correct ordering of states in extended π -systems where double excitations play a significant role. A recently redesigned DFT/MRCI Hamiltonian extends the application range of the method to bi-chromophores such as hydrogen-bonded or π -stacked dimers and loosely coupled donor–acceptor systems. In conjunction with a restricted–open shell Kohn–Sham optimization of the molecular orbitals, even electronically excited doublet and quartet states can be addressed. After a short outline of the general ideas behind this semi-empirical method and a brief review of alternative approaches combining density functional and multireference wavefunction theory, formulae for the DFT/MRCI Hamiltonian matrix elements are presented and the adjustments of the two-electron contributions are discussed. The performance of the DFT/MRCI variants on excitation energies of organic molecules and transition metal compounds against experimental or ab initio reference data is analyzed and case studies are presented which show the strengths and limitations of the method. Finally, an overview over the properties available from DFT/MRCI wavefunctions and further developments is given.

ABBREVIATIONS: ACRXTN, 3-(9,9-dimethylacridin-10[9H]-yl)-9H-xanthen-9-one; AO, atomic orbital; CASSCF, Complete active space self-consistent field; CASPT2, Complete active space second-order perturbation theory; CCSD(T), Coupled-cluster with singles and doubles and perturbative treatment of triples; CC2, Coupled-cluster with approximate treatment of doubles; CD, Circular dichroism; CI, Configuration interaction; CIPSI, configuration interaction by perturbation with multiconfigurational zeroth-order wave functions selected by iterative process; CSF, Configuration state function; CT, Charge transfer; DCM, Dichloromethane; DFT, Density functional theory; EA, Electron affinity; FBP, Free-base porphyrin; FWHM, Full width at half maximum; GGA, Generalized gradient approximation; HF, Hartree-Fock; HOMO, Highest occupied molecular orbital; INDO/S, Intermediate neglect of differential overlap/screened approximation; IP, Ionization potential; ISC, Intersystem crossing; IVO, Improved virtual orbital; KS, Kohn-Sham; LC, Ligand-centered; LE, Local excitation; LMCT, Ligand to metal charge transfer; LUMO, Lowest unoccupied molecular orbital; lr-WFT, Long-range wave function theory; LSDA, Local spin density approximation; MAD, Mean absolute deviation; MaxAD, Maximum absolute deviation; MC, Metal-centered; MC-PDFT, Multiconfiguration pair-density functional theory; MCSCF, Multiconfiguration self-consistent field; MLCT, Metal to ligand charge transfer; MNDO, Modified neglect of differential overlap; MO, Molecular orbital; MP2, Møller-Plesset second-order perturbation theory; MRCI, Multireference configuration interaction; MRD-CI, Multireference double excitation configuration interaction; NEVPT2, n-electron valence state perturbation theory; NO, Natural orbital; PPP, Pariser-Parr-Pople; QM/MM, Quantum mechanics / molecular mechanics; RAS, Restricted active space; rISC, Reverse intersystem crossing; RMSD, Root mean square deviation; RKS, Restricted Kohn-Sham; ROKS, Restricted open-shell Kohn-Sham; SCF, Self-consistent field; SOC, Spin-orbit coupling; SOMO, Singly occupied molecular orbital; sr-DFT, Short-range density functional theory; SSC, Spin-spin coupling; TADF, Thermally activated delayed fluorescence; TDDFT, Time-dependent density functional theory; TDHF, Time-dependent Hartree-Fock; TDM, Transition dipole moment; UV, ultraviolet; WFT, Wave function theory

This is an open access article under the terms of the Creative Commons Attribution-NonCommercial-NoDerivs License, which permits use and distribution in any medium, provided the original work is properly cited, the use is non-commercial and no modifications or adaptations are made.

© 2018 The Authors. *WIREs Computational Molecular Science* published by Wiley Periodicals, Inc.

WIREs Comput Mol Sci. 2019;9:e1394.
<https://doi.org/10.1002/wcms.1394>

wires.wiley.com/compmolsci | 1 of 31

This article is categorized under:

Electronic Structure Theory > Density Functional Theory

Electronic Structure Theory > Semiempirical Electronic Structure Methods

Software > Quantum Chemistry

KEYWORDS

assessment, benchmark, excited states, multireference, parameterization

1 | INTRODUCTION

Understanding electronic excitation of molecules and excited-state processes is of fundamental importance for bolstering further developments in many areas of science and technology, ranging from biological and medicinal issues (photosynthesis, visual perception, ultraviolet (UV)-degradation and protection, photodynamic therapy) over classical photochemistry to modern aspects of materials sciences (photolithography, photovoltaics, efficient display, and lighting technologies). The computational characterization of the involved molecular states is a challenging task for quantum chemistry. Contrary to other problems in computational chemistry, classical approaches which neglect electronic wave functions entirely cannot be employed when it comes to electronic excitation. Modeling of molecular excited-state processes does not only need a rigorous quantum treatment of the photoactive part. It turns out that electron correlation is indispensable if a qualitatively correct theoretical description is to be obtained. Moreover, as a consequence of near-degeneracy effects, most electronically excited states exhibit genuine multiconfiguration character. Ab initio multiconfiguration electron correlation methods, that is, electronic structure methods that do not rely on empirical knowledge, can only be applied to small- and medium-sized molecules due to their high technical and computational complexity.^{1–3} To address electronically excited states of larger molecular systems, approximations are inevitable.

In recent years, time-dependent, linear-response density functional theory (TDDFT)^{4–7} has emerged as a reasonably accurate method for the calculation of excited-state properties of molecules.^{8–12} Because of its low computational costs and numerical complexity, TDDFT is applicable to fairly large systems (50–500 atoms) for which traditional wavefunction-based methods are not feasible. Although TDDFT is a formally exact theory, it is in practice an approximate method due to the approximate nature of the exchange-correlation (XC) functionals used. The usually employed adiabatic approximation^{4,5} in TDDFT in combination with conventional (ground state) functionals is expected to work well for energetically low-lying states of typical closed-shell, large-gap molecules. However, one of the most serious disadvantages of TDDFT (similar to the closely related time-dependent Hartree-Fock (TDHF)) is the inadequate treatment of excited states with significant double-excitation character. Typically, such states appear in the spectroscopically accessible excitation energy range (<7 eV) when molecules are unsaturated or exhibit other orbital near degeneracies.¹³ This is illustrated in Figure 1 for two prototypical

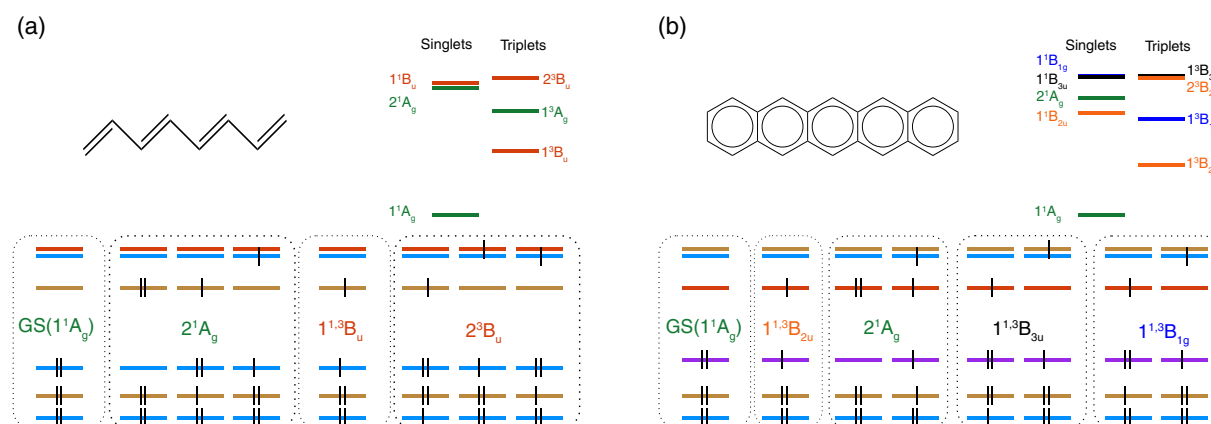


FIGURE 1 Schematic of the low-lying singlet and triplet excited-state energies of (a) *all-trans*-octatetraene (b) pentacene and the leading configurations of the corresponding wave functions. Both examples stress the importance of double excitations and multiconfiguration expansions for a qualitatively correct description of the spectral properties of these compounds

organic molecules. Although double-excitations have vanishing one-photon transition moments and hence are usually “dark” in routine absorption measurements, they are photochemically active and can couple with the more common single-excitation dominated states, thereby influencing their properties. For a more detailed discussion of excited states in molecules and their character see References 1,14–16.

The aim in the development of the currently reviewed DFT/MRCI method was to provide a general-purpose method for computing electronic spectra of large molecules and excited-state properties of $\pi\pi^*$, $n\pi^*$, Rydberg, charge transfer (CT), and even doubly excited states in a balanced manner.¹⁷ The approach should be similar to TDDFT in that it was mostly of “black-box” character, that is, applied straightforwardly starting from a ground state self-consistent field (SCF) solution. In particular, “hand-selection” of orbital or reference spaces that is common in complete active space self-consistent field (CASSCF) methods with second-order perturbation corrections (CASPT2)^{1,18} or variants thereof was to be avoided. Instead, the reference space was to automatically adjust to the requirements of the given problem. Another important consideration in the conceptual design of the new method was to alleviate the steep scaling of its computational expense with the number of variably occupied (i.e., active) orbitals in the reference space.

To achieve these objectives, Grimme and Waletzke opted for a configuration-driven multireference configuration interaction (MRCI) ansatz with iterative reference space generation, individual configuration selection, and truncation of the CI space.¹⁷ Improved convergence properties with respect to dynamic electron correlation compared to older configuration-driven MRCI methods such as multireference double excitation configuration interaction (MRD-CI)^{19–21} or configuration interaction by perturbation with multiconfigurational zeroth-order wave functions selected by iterative process (CIPSI)^{22,23} were to be accomplished by combining elements from density functional theory (DFT) and MRCI. The newly devised DFT/MRCI method was to be computationally more efficient than ab initio MRCI with full singles and doubles but simultaneously more accurate and with wider application range than MRCI expansions based on heavily parameterized semi-empirical Hamiltonians such as Pariser-Parr-Pople (PPP), intermediate neglect of differential overlap/ screened approximation (INDO/S), or modified neglect of differential overlap (MNDO)-type methods.^{8,24–26}

The original DFT/MRCI method¹⁷ was devised for electronic singlet and triplet states as these are the most common spin multiplicities encountered in organic molecules. Further technical developments included the extension of the method to spin-dependent Hamiltonians^{27–30} and the parallelization of the code,³¹ thus significantly widening its application range. Benchmarks of electronic excitation energies of small- to medium-sized organic molecules against CASPT2 results³² showed the superiority of the DFT/MRCI method compared to TDDFT in conjunction with typical density functionals. It turned out, however, that the original DFT/MRCI ansatz was not well suited for describing loosely coupled multichromophore systems. The problem could be traced back to the multiplicity-dependent parametrization of the Hamiltonian which fails for singlet-coupled triplet pairs (¹TT) with four open shells. The recently presented redesigned DFT/MRCI Hamiltonian is independent of the spin multiplicity and is particularly well suited for investigating the spectral properties of dimers and donor–acceptor systems.³³ An extension of this Hamiltonian also covers radicals with an odd number of electrons.³⁴ The latest method development focuses on the particular requirements for a balanced description of static and dynamic electron correlation in transition metal complexes.³⁵ While the statistical analysis shows somewhat larger errors for first- and second-row transition metal complexes in comparison to organic molecules, the overall performance of DFT/MRCI on these compounds is satisfactory.^{35,36}

2 | APPROACHES COMBINING DENSITY FUNCTIONAL AND WAVEFUNCTION THEORY

2.1 | The idea behind DFT/MRCI

In DFT/MRCI, Kohn–Sham (KS) orbitals are utilized as the one-electron basis from which the configuration space is constructed. This choice was motivated by the desire to generate a more compact MRCI expansion than in the basis of Hartree–Fock (HF) orbitals. Virtual HF orbitals, in particular, are known to be too diffuse because their Fock operators contain electron repulsion terms of an n -electron mean field instead of an $(n - 1)$ -electron one. Determinants based on improved virtual orbitals^{37,38} or natural orbitals^{39–41} typically recover larger parts of the correlation energy in truncated CI expansions, and even KS orbitals had been employed for that purpose before.^{42,43} In contrast to these approaches, DFT/MRCI does not only employ KS MOs but also incorporates KS orbital energies into the Hamiltonian. Dynamic electron correlation is well accounted for by DFT whereas HF-based MRCI needs long expansions of doubly or even higher excited configurations to capture this effect. In contrast, MRCI is well suited to describe static electron correlation which arises from near-degeneracies and is not covered by KS-DFT. Because MRCI has no principle limitations to describe dynamic electron correlation as well, one has to take appropriate measures to prevent double counting of this effect in mixed DFT and MRCI approaches. Before going into more details on how this is achieved in DFT/MRCI, we will briefly review alternative approaches combining elements from density functional and multiconfiguration wavefunction theory (WFT).

2.2 | Alternative approaches

The most widespread combination of DFT and elements of WFT is found in hybrid and double-hybrid density functionals. We refrain here from giving an overview over these functionals because they are typically employed in genuine single-determinant (TD)DFT calculations where HF and/or Møller-Plesset second-order perturbation theory (MP2) data are merely used to modify the XC functional. For a review on double-hybrid density functionals see Reference 44. This leaves us with three major classes of mixed multiconfiguration WFT-DFT approaches: (a) Density embedding of a correlated wave function (WFT-in-DFT), (b) multiconfiguration pair-density functional theory (MC-PDFT), and (c) range-separated multiconfiguration DFT (sr-DFT-Ir-WFT).

Although WFT-in-DFT combines elements of multiconfiguration wave function theory—mostly CASSCF and MRCI—with DFT, it pursues a strategy completely different from DFT/MRCI. WFT-in-DFT embedding^{45–51} is an ansatz aiming at multiscale modeling of complex systems, reminiscent of quantum mechanics/molecular mechanics (QM/MM)^{52,53} and ONIOM-type⁵⁴ approaches. The projector-based embedding method^{49–51} uses localized KS-DFT MOs to partition the system. Subsystem density and Fock matrices are then constructed and used to define a nonlocal embedding potential. The active subsystem can be treated by high-level WFT methods such as a coupled-cluster (CC) expansion with singles and doubles and perturbative treatment of triples (CCSD(T)). Carter et al.^{45–48} devised CASSCF-in-DFT and MRCI-in-DFT methods to study reactions of small molecules on metal surfaces where the failure of common density functionals to treat charge-transfer (CT) and local excitations (LE) in a balanced manner is an important issue. Similar to the more familiar DFT-in-DFT embedding,^{55,56} the system under consideration is partitioned into two subsystems: A small subsystem (subsystem I) consisting of the chemically active or photoresponsive part is addressed by means of correlated WFT methods and the environment (subsystem II) as well as the interaction between the two subsystems is treated with simpler, cost-effective (periodic) DFT methods. In the original formulation, KS orbitals of the total system were not available so that approximate kinetic energy functionals had to be employed.^{45,46} Later developments of the density functional embedding theory delivered an ab initio embedding potential of the cluster and eliminated the need to use approximate kinetic energy density functionals.^{47,48}

While WFT-in-DFT methods aim at a multiscale description of large systems, MC-PDFT as well as sr-DFT-Ir-WFT methods pursue similar objectives as DFT/MRCI. In the beginning, the combinations of generalized valence bond theory in perfect-pairing approximation^{57,58} or minimal CASSCF or CASCI with DFT^{59–64} were mostly thought to provide a proper description of bond dissociation processes in the electronic ground state. Later approaches used larger active spaces and additionally addressed electronically excited states^{65–69} or strived for correcting the long-range behavior of TDDFT in describing CT states.⁷⁰

It was noted early on that a multideterminantal situation required a reformulation of the standard density functionals. Furthermore, a clear separation between DFT and WFT contributions was needed to avoid double counting of electron correlation effects.⁷¹

As long as the wave function is represented by a single determinant, density functionals can be formulated in terms of the individual spin densities $\rho_\alpha(\vec{r})$ and $\rho_\beta(\vec{r})$ or equivalently by the spinless density $\rho(\vec{r}) = \rho_\alpha(\vec{r}) + \rho_\beta(\vec{r})$ and the spin magnetization density $m(\vec{r}) = \rho_\alpha(\vec{r}) - \rho_\beta(\vec{r})$. In multideterminantal situations, spin-DFT features a symmetry dilemma and $m(\vec{r})$ is no longer a proper descriptor. To preserve the multiplet spin degeneracies, a formulation of the density functional in terms of $\rho(\vec{r})$ and the spinless on-top pair density was advised.^{72–74}

$$P_2(\vec{r}) = N(N-1) \int |\Psi(\vec{x}_1, \vec{x}_2, \vec{x}_3, \dots, \vec{x}_N)|^2 d\sigma_1 d\sigma_2 d\vec{x}_1 \dots d\vec{x}_N \Big|_{\vec{r}_1 = \vec{r}_2 = \vec{r}} \quad (1)$$

Several work groups used the ratio of the reference density and the total density as a measure of the active space in the construction of the residual correlation density^{59,60} Alternatively, natural orbitals and their occupation numbers were engaged to define electron densities in conjunction with multideterminantal wave functions.⁷⁵

Instead of directly employing the on-top pair density (1) as auxiliary parameter, recent developments in MC-PDFT methodology^{67,68,76} utilize a normalized form of the on-top density

$$R(\vec{r}) = \frac{2P_2(\vec{r})}{|\rho(\vec{r})|^2} \quad (2)$$

which is strictly equal to 1 in the closed-shell HF case. The on-top density functionals, as proposed by Gagliardi et al, are translated from common XC functionals in local spin-density approximation or generalized gradient approximation by setting $m(\vec{r}) = \rho(\vec{r})(1-R(\vec{r}))^{(1/2)}$ if $R \leq 1$ and to $m(\vec{r}) = 0$ if $R > 1$ in the density functional. In all these approaches, the density $\rho(\vec{r})$ and possibly the density gradient $\nabla\rho(\vec{r})$ as well as the on-top pair density $P_2(\vec{r})$ are obtained from the CASSCF wave function.^{67,68}

Another way to avoid double counting of the correlation energy in combined density functional and multiconfiguration wave function approaches is to employ a range separation of the two-electron interaction. The short-range interaction is covered by density functional theory (sr-DFT) whereas long-range interactions are described by multiconfiguration wavefunction theories (lr-WFT). This separation is motivated on the one hand by the short-rangedness of dynamical correlation which is well covered by DFT whereas local exchange density functionals exhibit unphysical asymptotic behavior at large interelectronic distances. Static correlation effects on the other hand, caused by near-degeneracies of the ground and low-lying excited states, are well accounted for by short multiconfiguration expansions.

Several models for decomposing the contributions into short- and long-range parts were proposed in the course of time.^{59,71,77,78} The most convenient splitting of the interaction Hamiltonian is achieved with the help of the error function⁶¹

$$\frac{1}{r_{12}} = \underbrace{\frac{1 - \operatorname{erf}(\mu r_{12})}{r_{12}}}_{\text{short range}} + \underbrace{\frac{\operatorname{erf}(\mu r_{12})}{r_{12}}}_{\text{long range}} \quad (3)$$

where the error function occurring in Equation (3) is defined as

$$\operatorname{erf}(x) = \frac{2}{\sqrt{\pi}} \int_0^x e^{-u^2} du \quad (4)$$

To ensure maximal separation between long-range and dynamic correlations in multideterminant range-separated DFT, the parameter μ has to be chosen in an optimal way. Recipes for defining an optimal μ for multiconfiguration self-consistent field (MCSCF) wave functions in conjunction with short-range DFT (MC-srDFT) have been given by Jensen et al.^{65,79} Also a time-dependent extension of MC-srDFT, TD-MC-srDFT, was presented in which short-range TDDFT is combined with long-range MCSCF.⁷⁰

First results of the MC-PDFT and sr-DFT–lr-WFT methods look promising. The computational costs of MC-PDFT and MC-srDFT scale with the system size in the same way as CASSCF but the results are of much higher quality.^{65–80} This scaling might nevertheless be too steep when investigating chemical reactions or electronic excitations of transition metal complexes as these typically require large active spaces. One way out is to combine sr-DFT with density matrix renormalization group approaches that can handle larger active spaces in the lr-MC-WFT part.⁸¹ DFT/MRCI does not have these restrictions, but a clear separation between DFT and WFT contributions to electron correlation is difficult to achieve in this approach.

3 | THE CI HAMILTONIAN

In order to acquire a detailed understanding of the approximations made in DFT/MRCI, it is useful to study the CI matrix elements of an unmodified Hamiltonian first. Readers who are more interested in the performance of the DFT/MRCI approaches and sample applications than in the underlying theory may skip the following two sections.

In second quantization, a spin-independent electronic Hamiltonian can be written as

$$\hat{\mathcal{H}} = \sum_{ij} h_{ij} \hat{E}_i^j + \frac{1}{2} \sum_{ijkl} V_{ijkl} (\hat{E}_i^j \hat{E}_k^l - \delta_{jk} \hat{E}_i^l) \quad (5)$$

where h_{ij} denotes a one-electron integral,

$$\hat{E}_i^j \equiv \hat{a}_{i\alpha}^\dagger \hat{a}_{j\alpha} + \hat{a}_{i\beta}^\dagger \hat{a}_{j\beta} \quad (6)$$

is a spin-traced one-electron (de)excitation operator that annihilates an electron in orbital j and recreates it in orbital i and where we have used the Dirac notation for the two-electron four-index integral $V_{ijkl} \equiv \langle i(1)k(2) | \frac{1}{r_{12}} | j(1)l(2) \rangle$. To make optimal use of spin symmetry in the evaluation of Hamiltonian matrix elements, the one-electron basis from which the determinants are constructed is generated in spin-restricted SCF calculations, that is, the molecular orbitals (MOs) are equal for α and β electrons. The advantage of this choice is that spin-adapted linear combinations of Slater determinants can be formed, so-called configuration state functions (CSFs), which are eigenfunctions of the \hat{S}^2 operator and hence represent true electron spin multiplets. In the following, a CSF is characterized by a spatial occupation number vector w and a spin-coupling pattern ω . In the absence of spin-dependent operators, the Hamiltonian matrix is block-diagonal for each multiplicity and separate MRCI calculations can be performed for singlets, doublets, triplets, etc. Let \bar{w}_i denote the occupation of the i th MO in the SCF determinant. The Hamiltonian (5) can then be rearranged to^{82,83}

$$\hat{H}^{\text{CI}} = E^{\text{SCF}} - \sum_i F_{ii} \bar{w}_i + \frac{1}{2} \sum_{ij} \left(V_{ijij} - \frac{1}{2} V_{ijji} \right) \bar{w}_i \bar{w}_j + \sum_{ij} F_{ij} \hat{E}_i^j - \sum_{ijk} \left(V_{ikjk} - \frac{1}{2} V_{ikkj} \right) \bar{w}_k \hat{E}_i^j + \frac{1}{2} \sum_{ijkl} V_{ikjl} \left(\hat{E}_i^j \hat{E}_k^l - \delta_{jk} \hat{E}_i^l \right) \quad (7)$$

where the Fock matrix and in particular its diagonal elements F_{ii} , that is, the MO energies, are introduced.

$$F_{ij} = h_{ij} + \sum_k \bar{w}_k \left(V_{ikjk} - \frac{1}{2} V_{ikkj} \right) \quad (8)$$

Note that the MO energies are also contained in the total SCF energy E^{SCF} and that the terms partially cancel. Equation (7) offers a good starting point for semi-empirical modifications of the Hamiltonian such as DFT/MRCI.

Let n , n' , and n'' denote configurations, that is, spatial occupation number vectors. Because the Hamiltonian contains only one- and two-electron operators, it may couple configurations which differ in two occupations at most. CI matrix elements can therefore be grouped into three categories⁸³:

1. Diagonal spatial occupations

$$\begin{aligned} H_{nn}^{\text{CI}} &= E^{\text{SCF}} + \sum_i F_{ii} \Delta w_i + \frac{1}{2} \sum_{i \neq j} V_{ijij} \Delta w_i \Delta w_j \\ &+ \frac{1}{2} \sum_{i \neq j} V_{ijji} \left(-\frac{1}{2} \Delta w_i \Delta w_j + \frac{1}{2} w_i w_j - w_i + \eta_{ij}^i \right) \\ &+ \frac{1}{2} \sum_i V_{iiii} \left(\frac{1}{2} \Delta w_i \Delta w_i + \frac{1}{2} w_i w_i - w_i \right) \end{aligned} \quad (9)$$

2. One-electron difference

$$\begin{aligned} H_{nn'}^{\text{CI}} &= F_{ij} \eta_i^j + \sum_{k \neq i, j} V_{ikjk} \Delta w'_k \eta_i^j \\ &+ \sum_{k \neq i, j} V_{ikkj} \left(-\frac{1}{2} \Delta w'_k \eta_i^j + \frac{1}{2} w'_k \eta_i^j - \eta_i^j + \eta_{ik}^{kj} \right) \\ &+ V_{ijij} \left(\frac{1}{2} \Delta w'_i + \frac{1}{2} w'_i \right) \eta_i^j - V_{ijij} \left(\frac{1}{2} \Delta w'_j + \frac{1}{2} w'_j - 1 \right) \eta_i^j \end{aligned} \quad (10)$$

3. Two-electron differences

$$H_{nn''}^{\text{CI}} = \left(V_{ikjl} \eta_{ik}^{jl} + V_{iklj} \eta_{ik}^{lj} \right) \left[(1 + \delta_{ik})(1 + \delta_{jl}) \right]^{-1} \quad (11)$$

where $\Delta w_i = w_i - \bar{w}_i$ is the occupation difference between the configuration and the SCF configuration in the i th MO and

$$\eta_i^j = \langle \omega w | E_i^j | \omega' w' \rangle \quad (12)$$

$$\begin{aligned} \eta_{ik}^{jl} &= \langle \omega w | E_i^j E_k^l | \omega'' w'' \rangle \\ &= \left(E_j^l | \omega w \rangle \right)^\dagger \cdot E_k^l | \omega'' w'' \rangle \end{aligned} \quad (13)$$

are one- and two-electron spin couplings, respectively. These spin couplings are nothing more than weighting coefficients for one- and two-electron integrals. They depend on the excitation pattern and the open-shell structure of the determinants, but not on the actual problem and may therefore be precomputed and stored. Note in particular that the two-electron weighting coefficients (13) are just products of one-electron terms.

Although Equations (9)–(11) look cumbersome at first sight, they have the advantage that all excitations are expressed with respect to a common closed-shell anchor configuration which allows for efficient configuration comparison and matrix element evaluation algorithms in a configuration-driven CI.^{82,83}

4 | DESIGN OF THE DFT/MRCI HAMILTONIAN

The DFT/MRCI Hamiltonian comes in various flavors: The original formulation by Grimme and Waletzke¹⁷ employs different parameter sets for singlet and triplet excitations whereas the redesigned effective Hamiltonians^{33–35} use identical parameter sets for all multiplicities. We have chosen here a formulation that emphasizes the commonalities of these approaches and discusses their particularities where necessary.

To exploit spin symmetry in the evaluation of Hamiltonian matrix elements, the one-electron basis for all MRCI calculations on systems with even numbers of electrons—even for triplets—is generated in restricted Kohn–Sham (RKS) optimization of a closed-shell anchor configuration. For systems with odd numbers of electrons, restricted open-shell Kohn–Sham (ROKS) calculations are performed for an anchor configuration with one open shell. While RKS is the standard procedure for closed-shell SCF calculations, a ROKS ansatz for doublets⁸⁴ is implemented only in a few quantum chemistry program packages and needs additional corrections in MRCI approaches.^{34,85}

4.1 | Diagonal Hamiltonian matrix elements

Let E^{DFT} be the total KS energy of the anchor configuration and \bar{w}_i the occupation number of the i th MO with orbital energy F_{ii}^{KS} . A diagonal element of the effective DFT/MRCI Hamiltonian is given by

$$\langle \omega w | \hat{\mathcal{H}}^{\text{DFT}} - E^{\text{DFT}} | \omega w \rangle = \langle \omega w | \hat{\mathcal{H}} - E^{\text{HF}} | \omega w \rangle - \sum_{i \in c}^{n_{\text{exc}}} (F_{ii}^{\text{HF}} - F_{ii}^{\text{KS}}) + \sum_{i \in c}^{n_{\text{exc}}} (F_{ii}^{\text{HF}} - F_{ii}^{\text{KS}}) + \Delta E_{\text{coul}} - \Delta E_{\text{exch}} \quad (14)$$

Herein, HF-like orbital energies are replaced by their KS counterparts, n_{exc} is the excitation class with respect to the anchor configuration (1 for single excitations, 2 for double excitations etc.), with a referring to the annihilated and c to the created electrons. Although the denominations E^{HF} and F_{ii}^{HF} are a bit misleading, we have kept this nomenclature because it had been used in the original literature.^{17,33,34} It should be stressed, however, that E^{HF} is not the total HF energy in the given atomic orbital (AO) basis and F_{ii}^{HF} is not a true HF orbital energy. Instead, F_{ii}^{HF} represents an effective one-electron matrix element constructed in a HF-like manner from the given KS orbital basis:

$$F_{ii}^{\text{HF}} = h_{ii} + \sum_k \bar{w}_k \left(V_{ikik} - \frac{1}{2} V_{ikki} \right) \quad (15)$$

Correspondingly,

$$E^{\text{HF}} = \sum_i \bar{w}_i F_{ii}^{\text{HF}} - \frac{1}{2} \sum_{ik} \bar{w}_i \bar{w}_k \left(V_{ikik} - \frac{1}{2} V_{ikki} \right). \quad (16)$$

Because the orbital energy gap between occupied and unoccupied MOs is typically much smaller in KS than in HF theories, the two-electron contributions to the diagonal Hamiltonian matrix elements, ΔE_{coul} and ΔE_{exch} , need to be adjusted appropriately. The original and redesigned DFT/MRCI Hamiltonians use different approaches to achieve these goals.

4.2 | Coulomb and exchange integral corrections in the original DFT/MRCI Hamiltonian

In the original work by Grimme and Waletzke, the two-electron terms in Equation (14) are given by

$$\Delta E_{\text{coul}}^{\text{orig}} - \Delta E_{\text{exch}}^{\text{orig}} = \frac{1}{n_{\text{exc}}} \sum_{i \in c}^{n_{\text{exc}}} \sum_{j \in a}^{n_{\text{exc}}} (p_J V_{ijij} - {}^m p [N_o] V_{ijji}) \quad (17)$$

where m labels the spin multiplicity (1 or 3). The parameter p_J , which scales the electron–hole Coulomb interaction, depends, of course, strongly on the amount of nonlocal (“exact”) exchange in the underlying KS functional. For the BHLYP functional^{86,87} used here, a value close to $p_J = 0.5$ is expected.¹⁷ Grimme and Waletzke assumed the exchange integral correction ${}^m p [N_o]$ to vary linearly with the number of open shells N_o and arrived at the following expressions for singlet and triplet CSFs

$${}^1 p [N_o] = {}^1 p [0] + N_o {}^1 \alpha \quad (18)$$

$${}^3 p [N_o] = N_o {}^3 \alpha \quad (19)$$

Together with two additional parameters used for damping the off-diagonal matrix elements (see below), the parameters p_J , 1p [0], and ${}^1\alpha$ were optimized to fit experimental singlet excitation energies of a representative set of molecules in a least-squares sense. The parameters p_J and ${}^3\alpha$ for triplet states were fitted independently.

4.3 | Coulomb and exchange shifts in the redesigned DFT/MRCI Hamiltonians

In some cases, for example in photoexcited dimers, where two triplet-excited molecules can form an overall singlet-coupled triplet pair (1TT), the use of independent (and thus different) parameter sets for singlet and triplet states is not practical as it can lead to artifacts.^{33,88} On these grounds, a novel DFT/MRCI Hamiltonian was designed that is based on the same general ideas as the original approach, but requires the parameter sets to be independent of the spin multiplicity. Lyskov et al.³³ realized that experimental singlet-triplet energy splittings of states with two non-degenerate open shells i and j (where static correlation effects can be disregarded in first approximation) correlate nearly linearly with the size of the HF-type exchange integrals in the basis of BHLYP MOs. This observation made it possible to obtain these splittings by introducing a multiplicity independent scaling factor (p_X) in front of the spin-coupling coefficients η_{ij}^{ij} of the exchange-type integrals V_{ijji} . Moreover, it turned out that the prefactor of the spin-independent exchange terms in Equation (9) can, in good approximation, be set to $1/2 p_X$. The Coulomb-like two-electron terms which are spin-independent, too, are uniformly scaled by a factor p_J , yielding the following expression for diagonal Hamiltonian matrix elements of systems with an even number of electrons (singlets, triplets, quintets, ...) generated from a closed-shell anchor configuration

$$\begin{aligned} \Delta E_{coul}^{red-even} - \Delta E_{exch}^{red-even} = & p_J \left(- \sum_{\substack{i,j \in c \\ i > j}}^{n_{exc}} V_{ijij} - \sum_{\substack{i,j \in a \\ i > j}}^{n_{exc}} V_{ijij} + \sum_{i \in c} \sum_{j \in a}^{n_{exc}} V_{ijij} \right) \\ & - p_X \left(\frac{1}{2} \sum_{i \in c} \sum_{j \in a}^{n_{exc}} V_{ijji} + \sum_{\substack{i,j \in o \\ i > j}}^{N_o} V_{ijji} \eta_{ij}^{ij} \right) \end{aligned} \quad (20)$$

where a and c are defined as before and o denotes open shells in the occupation vector w . To achieve a consistent treatment of states with different multiplicities, Lyskov et al.³³ added a few dimers with large intermolecular separations to the fitting set of the redesigned Hamiltonian, in the following denoted by R2016, which otherwise contained experimental data on small- and medium-sized molecules mainly from gas-phase photoelectron spectra.

The terms in Equation (9) involving the diagonal two-electron integrals V_{iiii} cancel unless two electrons are annihilated or created simultaneously in MO i in which case the total prefactor of the integral reduces to 1. For a system with an odd number of electrons and singly occupied MOs in the anchor configuration, in the following labeled by s , this is different. Every occupation change in s results in the addition of $\frac{1}{2} V_{ssss}$ to the configuration energy whereas a simplistic application of Equation (9) yields a prefactor of $\frac{1}{4}$ for this integral. Because this correction affects only the contributions from the diagonal two-electron integrals V_{ssss} of the singly occupied MOs in the anchor configuration (which do not exist in the closed-shell anchor for even numbers of electrons), a common expression for diagonal DFT/MRCI matrix elements of molecules with even or odd numbers of electrons can be set up³⁴:

$$\begin{aligned} \Delta E_{coul}^{red} - \Delta E_{exch}^{red} = & p_J \left(- \sum_{\substack{i,j \in c \\ i > j}}^{n_{exc}} V_{ijij} - \sum_{\substack{i,j \in a \\ i > j}}^{n_{exc}} V_{ijij} + \sum_{i \in c} \sum_{j \in a}^{n_{exc}} V_{ijij} + \sum_{i \in s}^{n_{single}} \frac{1}{2} V_{iiii} |\Delta w_i| \right) \\ & - p_X \left(\frac{1}{2} \sum_{i \in c} \sum_{j \in a}^{n_{exc}} V_{ijji} - \sum_{\substack{i,j \in c \\ j \in s}}^{n_{exc}} V_{ijji} - \sum_{\substack{i,j \in a \\ j \in s}}^{n_{exc}} V_{ijji} + \sum_{\substack{i,j \in o \\ i > j}}^{N_o} V_{ijji} \eta_{ij}^{ij} \right) \end{aligned} \quad (21)$$

However, there is one more correction to be made in the case of an open-shell anchor configuration³⁴: Equation (9) gives a nonvanishing contribution from V_{ssss} integrals even if no change of occupation occurs, that is, if $\Delta w_i = 0$, resulting in an energy shift of the configuration by $-\frac{1}{4} V_{ssss}$. As long as the number of electrons in the system does not change, excitation energies are unaffected by this diagonal shift because it is identical for all configurations. The problem manifests itself if ionization potentials or electron affinities are to be computed. As a remedy, $\frac{1}{4} V_{ssss}$ is added to each diagonal element in the CI

matrix when an open-shell anchor configuration is used. Equation (21) represents the diagonal correction for the R2017 and R2018 Hamiltonians.

4.4 | Off-diagonal matrix elements among CSFs of the same configuration

Configurations with up to two open shells are represented by a single CSF per multiplicity. For configurations with more than two open shells, typically several CSFs with the same S^2 -eigenvalue can be formed.

In the original DFT/MRCI approach, matrix elements between different CSFs but equal space parts are evaluated with the unmodified CI Hamiltonian.

$$\langle \omega w | \hat{\mathcal{H}}^{\text{DFT}} | \omega' w' \rangle = \langle \omega w | \hat{\mathcal{H}}^{\text{CI}} | \omega' w' \rangle \quad (22)$$

Because $\hat{\mathcal{H}}$ is spin independent, all CSFs are eigenfunctions of \hat{S}_z with the same total M_S quantum number. Therefore, a spin flip in one orbital must be accompanied by a reverse spin flip in another orbital. The matrix element in Equation (22) is therefore a weighted sum of exchange-type integrals. For an extension of the formalism to spin-dependent Hamiltonians.^{28,30}

To maintain a consistent energy splitting between the CSFs, a scaling factor of $(1 - p_x)$ was introduced in the redesigned Hamiltonians.³³

$$\langle \omega w | \hat{\mathcal{H}}^{\text{DFT}} | \omega' w' \rangle = \langle \omega w | (1 - p_x) \hat{\mathcal{H}}^{\text{CI}} | \omega' w' \rangle \quad (23)$$

4.5 | Matrix elements of configurations with unequal spatial occupations

In DFT, dynamic electron correlation is introduced through the exchange correlation functional, here the BLYP functional.^{86,87} In an ab initio CI treatment, this type of correlation is described by (double and higher) excitations into energetically high-lying orbitals. To avoid double counting of dynamic correlation in DFT/MRCI, such excitations have to be avoided or their contributions have to be scaled down, at least. In DFT/MRCI, all MOs with orbital energy higher than $2 E_h$ are discarded. In addition, a damping function for off-diagonal matrix elements was introduced in the original DFT/MRCI which depends exponentially on the energy difference between the diagonal elements of the involved CSFs $\Delta E_{ww'}$.

$$\langle \omega w | \hat{\mathcal{H}}^{\text{DFT}} | \omega' w' \rangle = \langle \omega w | \hat{\mathcal{H}}^{\text{CI}} | \omega' w' \rangle p_1 e^{-p_2 \Delta E_{ww'}^4} \quad (24)$$

If more than one CSF belongs to a configuration, the mean value of their energies is employed. As may be seen in Figure 2, the value of the exponential function stays close to p_1 up to an energy difference of $\Delta E_{ww'} \approx 0.3 E_h$. In this way, near-degenerate configurations can interact strongly. For energy differences larger than $1 E_h$ its value is close to 0. Therefore, it appears appropriate that configurations with a mean energy above a certain energy threshold are discarded. This threshold

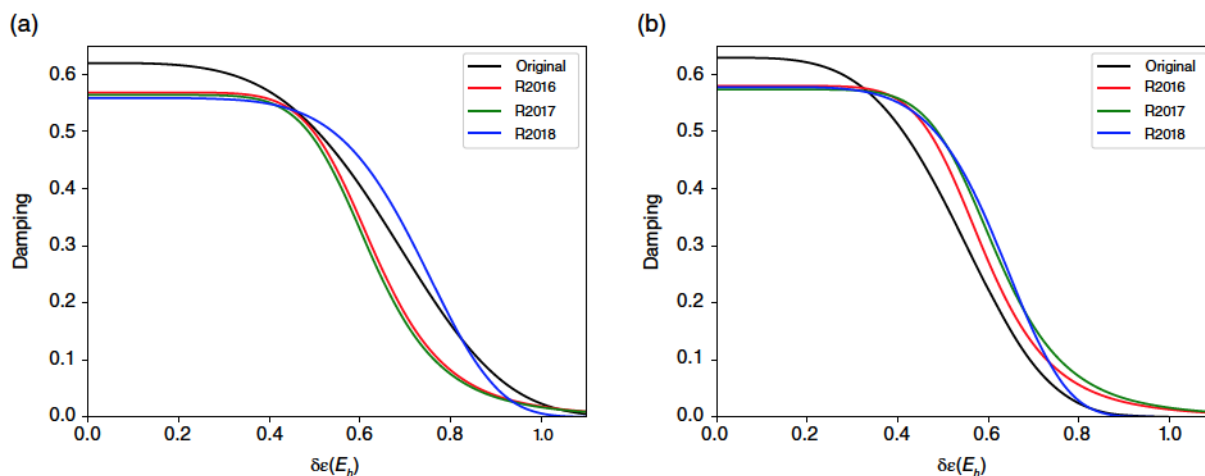


FIGURE 2 Damping functions used to scale down the off-diagonal matrix elements with unequal spatial configurations in the original, R2016, R2017, and R2018 Hamiltonians for (a) the standard parametrization in conjunction with a configuration selection threshold $esel = 1.0 E_h$ (b) the tight (or short) parametrization in conjunction with $esel = 0.8 E_h$

($t_{sel} = esel + E_{max}^{ref} - E^{DFT}$) varies from case to case as it depends on the eigenvalue of the highest desired root in the reference space, E_{max}^{ref} . The original DFT/MRCI parameters were optimized for a value of $esel = 1 E_h$.

In the redesigned DFT/MRCI Hamiltonians, the orbital and configuration selection criteria are unchanged from the original parametrization. The damping functions for the off-diagonal matrix elements have slightly different shapes (Figure 2), however. The damping function of the R2016 and R2017 Hamiltonians

$$\langle \omega w | \hat{\mathcal{H}}^{DFT} | \omega' w' \rangle = \langle \omega w | \hat{\mathcal{H}}^{CI} | \omega' w' \rangle \frac{p_1}{1 + (p_2 \Delta E_{\omega w'})^5 \arctan(p_2 \Delta E_{\omega w'})^5} \quad (25)$$

remains nearly constant until the energy difference has reached a value of approximately $0.4 E_h$ and then drops off more steeply than the exponential function used in the original DFT/MRCI (Figure 2a). A second set of parameters that was optimized in conjunction with a smaller configuration threshold of $0.8 E_h$ (Figure 2b) leads to even shorter CI expansions. The standard deviations obtained with these two parameter sets are similar in magnitude for organic molecules.^{33,34} It turned out, however, that the steeper decay of the damping function in Equation (25) as compared to Equation (24) leads to less satisfactory results in compounds containing *3d* elements such as Cu and Fe, in particular when combined with the smaller selection threshold. For that reason, further parameter sets were optimized in conjunction with the multiplicity independent DFT/MRCI Hamiltonian, but engaging a damping function for the off-diagonal terms with shallower slope (Figure 2).³⁵

$$\langle \omega w | \hat{\mathcal{H}}^{DFT} | \omega' w' \rangle = \langle \omega w | \hat{\mathcal{H}}^{CI} | \omega' w' \rangle p_1 e^{-p_2 \Delta E_{\omega w'}^6} \quad (26)$$

In addition to excitation energies of organic compounds, the fitting set for this DFT/MRCI Hamiltonian, denoted by R2018 in the following, comprised four singlet and four triplet states of the Cu^+ ion, two doublet states of the Cu atom and one singlet and triplet state of ruthenocene.³⁵ The performance of this modified Hamiltonian is comparable to the other multiplicity-independent DFT/MRCI Hamiltonians for purely organic compounds, but the accuracy is dramatically improved for electronic states of transition metal compounds.

5 | PERFORMANCE OF THE DFT/MRCI APPROACHES

5.1 | Organic molecules with closed-shell ground states

5.1.1 | Benchmark studies

The original DFT/MRCI parameters had been fitted to a set of experimental singlet and triplet excitation energies of small to medium-sized organic molecules comprising $\pi\pi^*$, $n\pi^*$, and Rydberg vertical transitions. For this fitting set of 37 singlet and 13 triplet excitation energies, a mean value close to zero (-0.02 eV for singlets, -0.06 for triplets) was obtained, that is, the DFT/MRCI results scatter around the experimental data with a root mean square deviation (RMSD) below 0.2 eV (0.15 eV for singlets, 0.14 for triplets).

In 2008, Thiel et al. started a series of benchmarks for electronically excited states of 28 small- and medium-sized organic molecules including, among other short polyenes, aromatic hydrocarbons, heterocycles, carbonyl compounds, and nucleobases. In their first paper, they investigated the performance of CASPT2 and CC methods and proposed a benchmark set with best theoretical estimates of all together 146 singlet and 71 triplet excitations.⁸⁹ Later, they used this benchmark set to assess the accuracy of TDDFT results in conjunction with various density functionals and the performance of DFT/MRCI in its original form.³² The statistical evaluation of these benchmark calculations shows that DFT/MRCI performs best among the DFT-based approaches, giving the lowest mean absolute deviations (MADs) of vertical excitation energies from the chosen *ab initio* reference data. In particular, DFT/MRCI gives reliable results for the low-lying 1A_g states of polyenes which have considerable double excitation character that increases with the number of conjugated double bonds. The statistical data are similar for singlet and triplet DFT/MRCI excitation energies, but the MADs depend on the chosen reference data. In comparison to CASPT2 values from the literature (no IPEA shift), mean values close to zero (0.02 eV) result in MAD values of 0.29 eV for singlets and 0.17 eV for triplets. If instead multistate (MS)-CASPT2 values generated with the recommended IPEA shift of $0.25 E_h$ are employed for validation, mean values of -0.19 eV (singlets) and -0.24 eV (triplets) are obtained with similar MADs as above, that is, on the average DFT/MRCI excitation energies are systematically lower than MS-CASPT2 values. The IPEA shift is a particular type of level shift that had been introduced in Fock-type operators of CASPT2 to lessen problems with intruder states.⁹⁰ Intruder states have a zeroth-order energy that is close to or even lower than the reference energy of the electronically excited state to be studied. They arise mainly due to limitations of the active space in the underlying CASSCF treatment. Unfortunately, CASPT2 results can be very sensitive with respect to the choice of the active space and to the magnitude of the level shift. In extreme cases, for example in free-base porphyrin (FBP) and

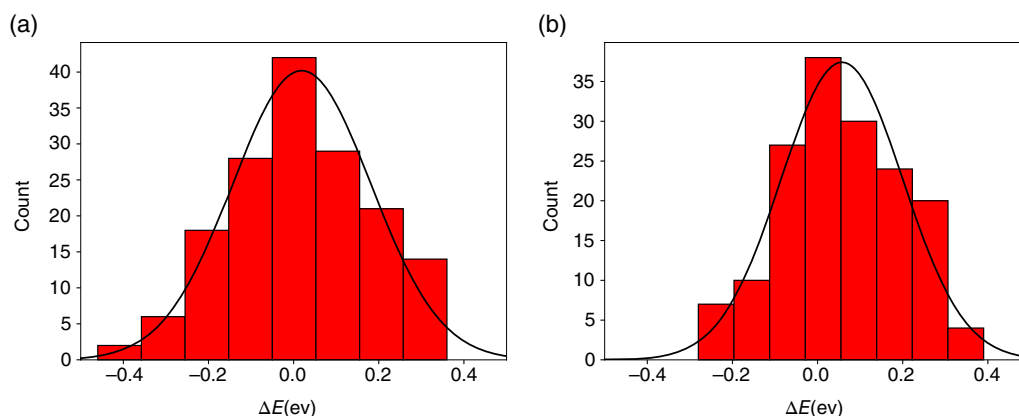


FIGURE 3 Histogram of the error distributions ($E_{\text{calc}} - E_{\text{exp}}$) of 160 singlet and triplet states of small- and medium-sized organic molecules from experimental data using (a) the original and (b) the redesigned R2016 DFT/MRCI Hamiltonian using standard parameters and a selection threshold of $\delta E_{\text{sel}} = 1.0 E_h$

metalloporphyrins,^{91,92} the recommended IPEA shift of $0.25 E_h$ affects the excitation energies of low-lying bright $\pi\pi^*$ states by up to 1 eV compared to the values obtained without application of a level shift where the latter values are in much better agreement with experimental data. For these reasons it appears more appropriate to benchmark the performance of the DFT/MRCI variants against carefully chosen experimental data or more reliable ab initio methods.

Lyskov et al.³³ added dimer states with large intermolecular separations to the fitting set of the redesigned Hamiltonian which otherwise contained experimental data on small- and medium-sized molecules mainly from gas-phase photoelectron spectra. The robustness of the original and redesigned Hamiltonians was tested on a benchmark set of 160 vertical singlet and triplet excitation energies of $\pi\pi^*$, $n\pi^*$, and Rydberg states of small- and medium-sized organic molecules not employed in the fitting. For a fair comparison, the assessment set did not comprise excitation energies of dimers and multichromophores.

Figure 3 shows the error distributions of the performance test. Detailed data and technical parameters of the calculations can be found in Reference 33. The errors are normally distributed with mean values close to 0 and standard deviations of approximately 0.15 eV. Maximum absolute deviations are below 0.5 eV. If instead a smaller configuration selection threshold of $\delta E_{\text{sel}} = 0.8 E_h$ and the corresponding optimized DFT/MRCI parameters are used, the deviations from experiment become only marginally larger (Table 1) while speeding up the computations significantly.

5.1.2 | Success stories

Electronically excited states of porphyrins are intrinsically multiconfigurational in character. They are often discussed in terms of the Gouterman four-orbital model,⁹³ comprising the highest occupied molecular orbital (HOMO) and the nearly degenerate HOMO-1, the lowest unoccupied molecular orbital (LUMO) and LUMO+1. In D_{4h} -symmetric metalloporphyrins, the HOMO transforms according to the a_{1u} irreducible representation, HOMO-1 is a_{2u} -symmetric and LUMO and LUMO+1 form a degenerate e_g pair. The latter splits into nearly degenerate b_{2g} and b_{3g} MOs in D_{2h} -symmetric compounds such as FBP, the smallest macrocycle related to all porphyrinoids. The four Gouterman orbitals of FBP are displayed in Figure 4c–f.

In porphyrinoids, the bands in the long wavelength region (> 500 nm) of the absorption spectrum are denominated Q_x and Q_y bands where the subindex x or y denotes the orientation of the transition dipole moment (TDM). The much brighter B_x and B_y transitions together form the so-called Soret band peaking around 400 nm. Following the common convention, the

TABLE 1 Statistical data showing the deviations of 160 vertical singlet and triplet DFT/MRCI excitation energies (eV) of small and medium sized organic molecules from experimental data. An overview over the state characteristics and the experimental reference data can be found in Reference 33

	Standard parameters		Short parameters	
	(esel = 1.0 E_h)		(esel = 0.8 E_h)	
	Original	R2016	Original	R2016
RMSD	0.16	0.15	0.18	0.16
MAD	0.13	0.12	0.15	0.13
Mean	0.01	0.06	-0.03	0.02
MaxAD	0.46	0.39	0.43	0.39

RMSD: root mean square deviation; MAD: Mean absolute deviation; MaxAD: Maximum absolute deviation.

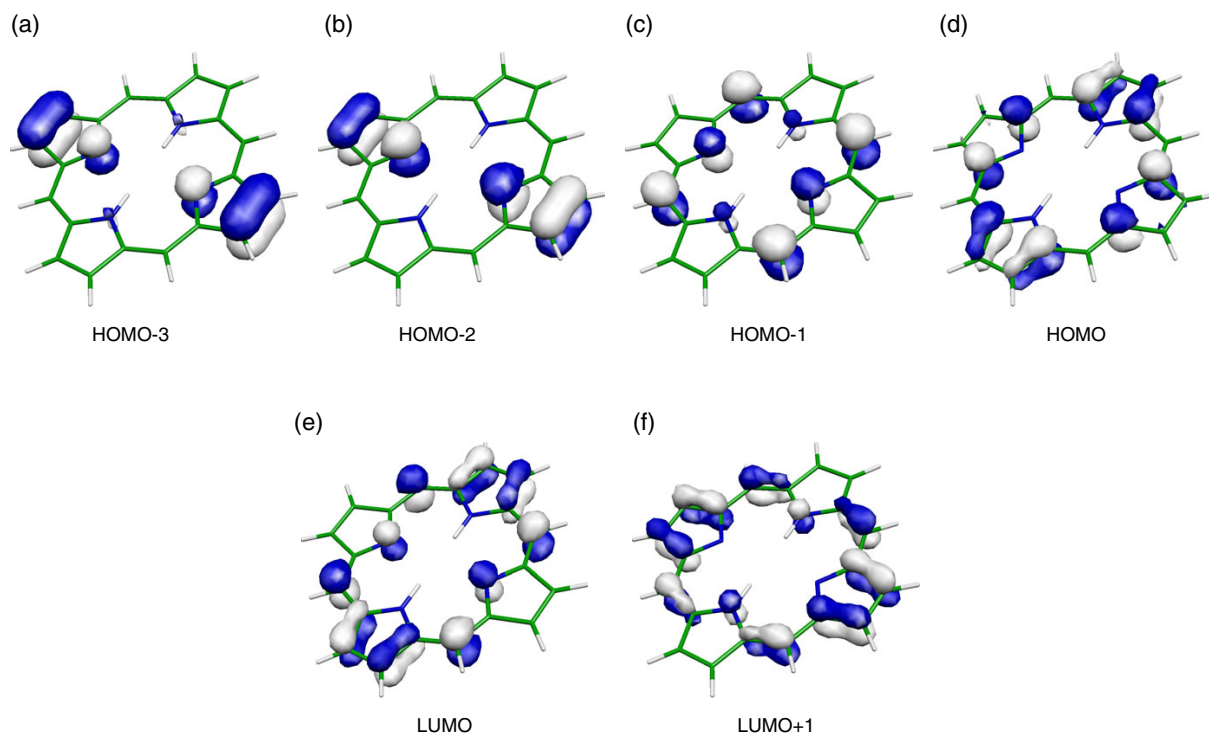


FIGURE 4 Frontier MOs of free-base porphyrin. In addition to the four Gouterman orbitals (c)–(f), at least two further high-lying occupied orbitals (a) and (b) are required for a qualitatively correct description of the Soret band. (a) HOMO-3, (b) HOMO-2, (c) HOMO-1, (d) HOMO, (e) LUMO, and (f) LUMO+1

macrocycle is situated in the xy plane. In FBP and related compounds, the x axis coincides with the pyrrolic hydrogen bonds. In contrast, the x -axis bisects the reduced pyrrol ring(s) in chlorin and bacteriochlorin while the y axis coincides with the N-H bonds. As a consequence of these axis conventions, the lowest electronic transition which is polarized along the N-H bonds is called the Q_x band in FBP whereas it is denominated Q_y in chlorin and bacteriochlorin.

Shortly after the DFT/MRCI method had become available, Parusel and Grimme investigated the singlet excited states of a series of porphyrin derivatives, that is, FBP, chlorin, bacteriochlorin, tetrazaporphyrins, metalloporphyrins, chlorophyll a as well as pheophytin a .^{94,95} The DFT/MRCI calculations (original Hamiltonian) accurately reproduce not only the experimental absorption energies, but also the transition intensities. To achieve good agreement with the peak positions in the experimental spectrum (errors of 0.2 eV at most), it was necessary to allow for double and even triple excitations with respect to the

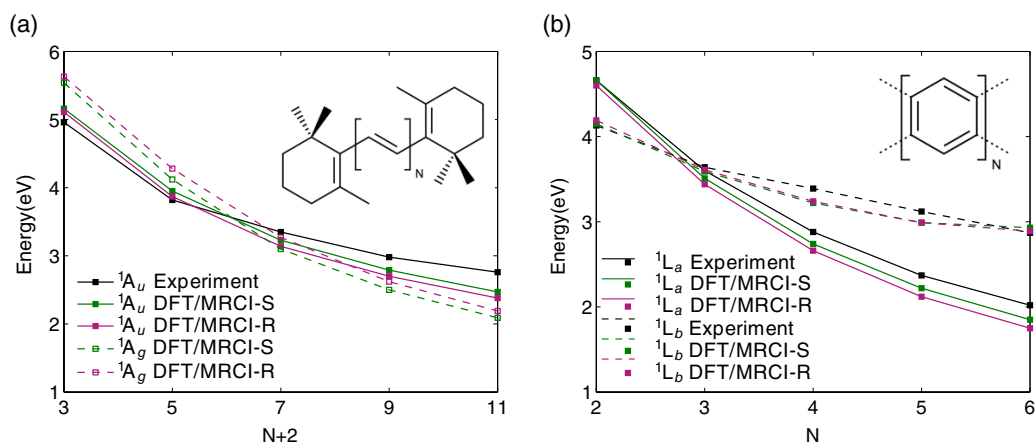


FIGURE 5 Performance of the original DFT/MRCI (DFT/MRCI-S) and redesigned R2016 DFT/MRCI (DFT/MRCI-R) methods on excitation energies of extended π -systems in comparison with experimental results: (a) carotenes, (b) polyacenes (Reprinted with permission from Reference 33. Copyright 2016 AIP Publishing)

ground-state determinant and to include further orbitals (Figure 4a and b) beyond the four Gouterman orbitals into the active space. The calculation of dipole transition intensities in porphyrins requires a balanced description of degenerate (or nearly degenerate) configurations. In the Q_x band of FBP, the HOMO→LUMO+1 and HOMO-1 → LUMO contributions to the TDM nearly cancel at the equilibrium geometry whereas they add up in the B_x band. The same is true for the HOMO→LUMO and HOMO-1 → LUMO+1 contributions to the TDM of the Q_y and B_y bands. Increasing the intensities of the Q bands necessitates either vibronic coupling to asymmetric stretching vibrations or asymmetric substitution. Both effects are well reproduced by DFT/MRCI calculations.^{94–96} Due to the lack of dynamic correlation, CASSCF severely overestimates the excitation energies of porphyrins, even if large active spaces are employed.^{91,92} Inclusion of dynamical correlation via many-body perturbation theory in CASPT2 calculations considering 16 electrons in 14 orbitals leads to good agreement with experiment if no IPEA shift is applied,⁹¹ with a MAD of 0.27 eV between calculated and experimental excitation energies of the eight lowest optically allowed $^1B_{2u}$ and $^1B_{3u}$ states of FBP. The agreement is even better for the D_{4h} -symmetric magnesium porphyrin (0.09 eV) and zinc porphyrin (0.10 eV). The excitation energies are typically increased by about 0.7–0.8 eV if the recommended IPEA shift of 0.25 E_h is used instead, resulting in MADs of 0.58, 0.77, and 0.77 eV, respectively, for these compounds. Similar observations were made for an iron porphyrin derivative.⁹² In this complex, metal-centered (MC) excitations and metal-to-ligand charge transfer (MLCT) excitations are among the low-lying singlet states in addition to the ligand-centered (LC) transitions. The effect of the IPEA shift was found to strongly depend on the nature of the electronic transition⁹²: MC states are only moderately affected (<0.5 eV), MLCT states experience blue shifts of 0.5–1.0 eV, singly excited LC states are shifted by about 1 eV, and doubly excited states are shifted by ≥ 0.9 eV.

Triplet states of FBP were investigated later by means of DFT/MRCI in our group.^{29,97} In this case, only the adiabatic excitation energy of the T_1 state and the $S_1 - T_1$ energy gap may be compared with experimental values, showing deviations of 0.10 eV at most. In contrast, TDDFT-B3LYP places the T_1 state much too low in energy while strongly overestimating the adiabatic S_1 excitation energy, thus yielding a completely erroneous singlet-triplet energy gap.^{97,98} The latter quantity is important when studying singlet-triplet intersystem crossing (ISC) in porphyrins which are used as triplet sensitizers in photodynamic therapy of skin diseases.⁹⁹ All-in-all, it appears that DFT/MRCI does an excellent job in computing spectral properties of porphyrins and their derivatives. That does not only apply to the original Hamiltonian. Lately, experimentally known transitions in zinc complexes of porphyrin, tetrabenzoporphyrin, and phthalocyanine were investigated yielding convincing results for all four DFT/MRCI variants.³⁵

Polyenes are another class of molecules where multiconfiguration and double-excitation effects play a significant role. In their benchmark calculations, Silva-Junior et al. had observed DFT/MRCI to give results for butadiene, hexatriene, and octatetraene close to the theoretical best estimates. In fact, DFT/MRCI appears to be one of the very few methods that give the correct order of states in longer polyenes and carotenoids.^{13,31} The linear response methods TDDFT and CC with approximative doubles (CC2) face particular difficulties in describing the low-lying 2^1A_g state because of its considerable double excitation character. As may be seen in Figure 5a, neither of the DFT/MRCI variants has this problem: The optically bright 1^1A_u state (labeled $^1B_u^+$ by the carotenoid scientific community) and the dark 2^1A_g state of carotenoids are described in a balanced manner by these approaches.³³ DFT/MRCI even successfully predicted a level crossing between the $^1B_u^+$ and an additional state of A_u symmetry ($^1B_u^-$) in β -carotene and lutein to occur upon geometry relaxation in the excited state, thus accelerating its radiationless decay to the lower-lying 2^1A_g state.¹⁰⁰

DFT/MRCI provides a balanced description of electronically excited states of polyaromatic hydrocarbons, too, whereas TDDFT in conjunction with standard functionals gives dramatic failures for the short-axis polarized 1L_a state of polyacenes despite the fact that it originates mainly from a HOMO→LUMO single excitation.¹⁰¹ In contrast, TDDFT shows good performance for the long-axis polarized 1L_b state characterized by a linear combination of two nearly equally weighted single excitations, that is, HOMO→LUMO+1 and HOMO-1 → LUMO. This strange behavior has been interpreted in a valence-bond picture where 1L_a features large contributions from ionic structures whereas 1L_b is mainly represented by covalent structures. CC2 reproduces the experimental trends very well,¹⁰¹ and so does DFT/MRCI.^{13,33} Inspection of Figure 5b shows that DFT/MRCI predicts the 1L_a and 1L_b states to swap order between naphthalene ($N = 2$) and anthracene ($N = 3$), in agreement with experiment.

The proper balance between 1L_a and 1L_b states is also essential when modeling the photophysics of indole and its derivatives. DFT/MRCI does not only give the correct energetic ordering of the two states, also the lengths and orientations of the excited-state (transition) dipole moments are in nearly perfect agreement with experiment.^{102,103} This is of particular importance for the analysis of protein properties using tryptophan as intrinsic sensor for the hydrophobicity of a protein pocket, as the fluorescent properties of the indole derivative tryptophan are very sensitive with regard to the polarity and proticity of the micro-environment.¹⁰⁴ In contrast to DFT/MRCI, TDDFT-B3LYP places the more ionic and optically brighter 1L_a state erroneously below 1L_b even in apolar environments.¹⁰⁵

There are many other success stories to be told where DFT/MRCI in its original form was used to unravel excited-state reaction paths and to assign electronic transitions. Consider, for example, the nucleobases which constitute the building blocks of DNA and RNA. Although these molecules are quite small, the balanced theoretical treatment of their $n\pi^*$ and $\pi\pi^*$ excited states poses a significant challenge to quantum chemical excited-state methods.¹⁰⁶ DFT/MRCI performs very well for the monomeric nucleobases^{32,107–113} and several predictions as to their photophysical behavior were confirmed later by experiment. The interplay of $n\pi^*$ and $\pi\pi^*$ excited states strongly influences the photophysical properties of the xanthone family of dyes, too. DFT/MRCI calculations could successfully explain the solvent dependence of delayed fluorescence in xanthone¹¹⁴ and predict the occurrence of delayed fluorescence in thioxanthone in methanol solution.^{115,116} Computed ISC rate constants allowed to discriminate between alternative relaxation pathways. Further, theoretically determined excited-state absorption spectra of thioxanthone in various solvents (methanol, tetrafluoroethanol, cyclohexane) made it possible to unambiguously assign the measured spectral signatures of the transient species, thus aiding to disentangle the complex kinetic schemes of the photorelaxation processes in this molecule.^{116–118} Also flavins have a rich photochemistry which depends critically on the solvent or protein environment. DFT/MRCI calculations engaging hybrid solvent models^{119–122} or QM/MM models of protein environments^{123–125} substantially added to the understanding of excited-state reactions of flavins in solution and in light-oxygen-voltage domains of blue-light receptors.

5.1.3 | Critical cases

The reason for starting a redesign of the DFT/MRCI Hamiltonian was an obvious failure of the original DFT/MRCI approach in describing electronically excited states of dimers and weakly coupled donor–acceptor systems. The problems associated with a spin multiplicity-dependent parametrization of the DFT/MRCI Hamiltonian become apparent when studying a small test example, namely the ethylene–tetrafluoroethylene dimer (Figure 6).³³ This model system had been employed already by Dreuw and Head-Gordon for demonstrating the problematic long-range behavior of various density functionals in TDDFT calculations.¹²⁶

At very large internuclear separations, the $\pi_1\pi_2 \rightarrow \pi_1^*\pi_2^*$ transition energies of the dimer states can be expressed as a sum of the energies of the local transitions $\pi_1 \rightarrow \pi_1^*$ and $\pi_2 \rightarrow \pi_2^*$ (Table 2). The first two dimer states of singlet and triplet multiplicity, shown in Table 2, correspond to local one-electron excitations on one monomer while the other one remains in the electronic ground state. Among the doubly excited states, we expect the product states composed of the local triplet one-electron excitations (TT) to be the lowest ones. Ideally, the resulting singlet, triplet and quintet dimer states should be energetically degenerated. As may be seen in Table 2, this is not the case for the original DFT/MRCI parametrization. Instead, the energies of the singlet-coupled triplet pairs are vastly underestimated while parameters for quintet states are not available. As a remedy of this problem, Lyskov et al.³³ presented a redesigned DFT/MRCI Hamiltonian which preserves this degeneracy by employing a multiplicity-independent ansatz.

Although this example may appear rather academic, it shows the fundamental problems encountered in hydrogen-bonded or π -stacked dimers and in weakly coupled donor–acceptor complexes. Such systems play a significant role in photobiology,^{106,127,128} photovoltaics,^{129–131} and in third-generation electroluminescent emitters that are based on thermally activated delayed fluorescence (TADF).^{132–135} For their modeling, the use of a multiplicity independent Hamiltonian is mandatory in a DFT/MRCI treatment.^{88,136–139}

Contrary to monomeric nucleobases, strange results are obtained for a hydrogen-bonded adenine–thymine Watson–Crick base pair if the original DFT/MRCI Hamiltonian is employed. In these calculations, the first excited singlet state corresponds to a double excitation with $\pi\pi' \rightarrow \pi^*\pi'^*$ structure. It is located about 0.85 eV lower in energy than the corresponding triplet state. This result is obviously wrong. Analysis of the wavefunction shows that it is made up of local triplet $\pi \rightarrow \pi^*$ and $\pi' \rightarrow \pi'^*$ single excitations which are overall coupled to a state with singlet spin multiplicity. The parameter $^1p[N_o]$ used to scale the exchange interaction in Equation (17) adopts values larger than 1 for $N_o = 4$ leading to artificially low-lying singlet states. Although the corresponding parameter for triplet states $^3p[N_o]$ is much smaller, the energy of the doubly excited triplet state is underestimated,

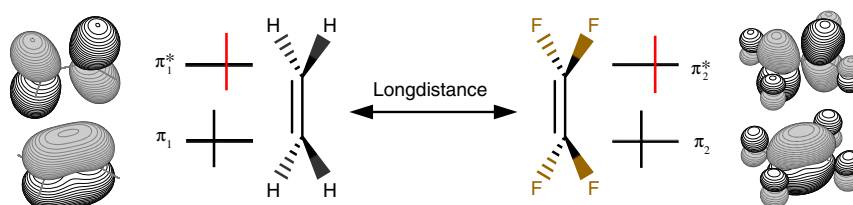


FIGURE 6 Sketch of the ethylene–tetrafluoroethylene dimer and the orbitals involved in the low-lying excitations (Reprinted with permission from Reference 33. Copyright 2016 AIP Publishing)

TABLE 2 DFT/MRCI $\pi \rightarrow \pi^*$ vertical excitation energies of ethylene, tetrafluoroethylene and of their $\pi_1\pi_2 \rightarrow \pi_1^*\pi_2^*$ dimer states (eV) according to Lyskov et al.³³

	Excitation	Original			R2016		
		Singlet	Triplet	Quintet	Singlet	Triplet	Quintet
Monomer	$\pi_1 \rightarrow \pi_1^*$	8.05	4.42	—	7.82	4.38	—
	$\pi_2 \rightarrow \pi_2^*$	8.99	4.90	—	8.70	4.81	—
Dimer	$\pi_1 \rightarrow \pi_1^*$	7.84	4.29	—	7.82	4.38	—
	$\pi_2 \rightarrow \pi_2^*$	8.72	4.79	—	8.70	4.81	—
	$\pi_1\pi_2 \rightarrow \pi_1^*\pi_2^*$ TT	2.19	9.32	n.a.	9.17	9.18	9.20
	$\pi_1\pi_2 \rightarrow \pi_1^*\pi_2^*$ ST	—	9.56	—	—	12.66	—
	$\pi_1\pi_2 \rightarrow \pi_1^*\pi_2^*$ TS	—	10.26	—	—	13.13	—
	$\pi_1\pi_2 \rightarrow \pi_1^*\pi_2^*$ SS	13.56	—	—	16.59	—	—

too. In contrast, the redesigned DFT/MRCI Hamiltonians yield a balanced description of monomer and dimer excitations. In the case of π -stacked dimers, it may be necessary to add a semiempirical dispersion correction, such as Grimme's D3 correction,^{140,141} to obtain a properly bound ground state.¹³⁸ The dispersion corrections mainly affect the molecular geometry. For a given nuclear arrangement, the D3 corrections have no impact on the MOs and the DFT/MRCI Hamiltonian and hence on the electronic spectrum.

A few problems of this kind have been encountered even in small and medium-sized monomeric systems. A simultaneous twist of the CH₂ end groups about the double bonds in *all-trans*-butadiene, for example, leads to electronic decoupling of the chromophore subunits and a break-down of the original DFT/MRCI approach whereas the redesigned DFT/MRCI yields qualitatively correct results.³³ The original DFT/MRCI also finds artificially low-lying singlet states in *o*-benzynes and in nitrobenzene which are dominated by $\pi\pi' \rightarrow \pi^*\pi'^*$ double excitations with four open shells.¹⁴² These states are described well by the redesigned DFT/MRCI. In contrast, the latter has difficulties in describing double excitations from nonbonding MOs appropriately, be it doubly excited closed-shell $n^2 \rightarrow \pi^{*2}$ configurations (in formaldehyde, thioformaldehyde, and dithiosuccinimide) or open-shell $nn' \rightarrow \pi^*\pi'^*$ singlet and triplet excitations.¹⁴² Such states appear at much too low excitation energies in the R2016 DFT/MRCI whereas the original DFT/MRCI gives results close to ab initio multireference Møller-Plesset second-order perturbation theory. The reasons for the failure of the R2016 DFT/MRCI approach for this kind of excitations are not completely clear at this point. It thus appears wise to regard DFT/MRCI results for doubly excited states of the above described types with some reservation.

5.2 | Radicals with doublet ground states

To preserve the multiplicity independence of the R2017 DFT/MRCI Hamiltonian, the parameters in the Hamiltonian matrix elements Equations (21)–(25) were fitted to a collection of experimental excitation energies of 42 singlets, 52 doublets, and 27 triplets (121 states in total) of small- to medium-sized monomers and a few dimers, including mainly $\pi\pi^*$, some $n\pi^*$, and a few Rydberg transitions.³⁴ Experimental optical spectra of radicals in the gas phase or apolar solvents are scarce. Therefore,

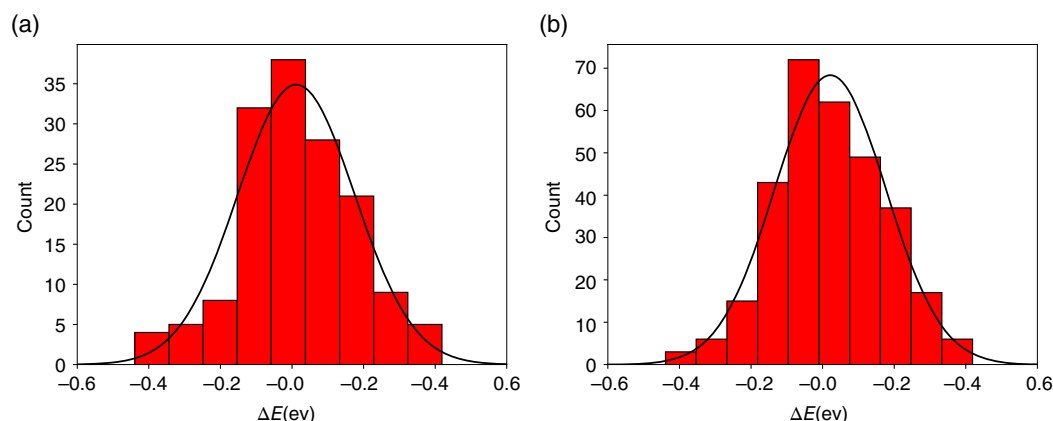


FIGURE 7 Histogram of the error ($E_{\text{calc}} - E_{\text{exp}}$) of the R2017 DFT/MRCI approach with $\delta E_{\text{set}} = 1.0 E_h$. (a) All doublet states from a sample of 150 states, (b) all singlet, doublet and triplet states from a sample of 310 states in total (Reprinted with permission from Reference 34. Copyright 2017 AIP Publishing)

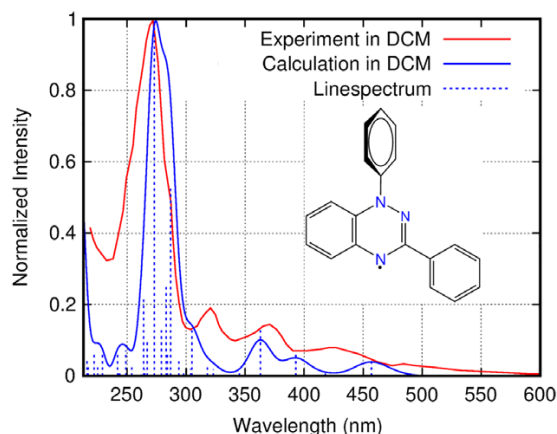


FIGURE 8 Chemical structure and absorption spectrum of the Blatter radical in dichloromethane (DCM) solution. The data points of the experimental spectrum were read from Reference 143

Heil and Marian utilized data from photoelectron spectroscopy in addition to optical data for assessing the performance of the method on doublet and quartet excitation energies.³⁴

Comparison of Figures 3b and 7b convincingly demonstrates that the good performance of the redesigned Hamiltonian does not deteriorate upon the inclusion of organic molecules with odd numbers of electrons.

An example where individual transitions could not be identified, is 1,3-diphenyl-1,4-dihydro-1,2,4-benzotriazin-4-yl, the Blatter radical (Figure 8, inset). Blatter-type compounds are persistent radicals which have attracted attention because of their potential application as building blocks of metal-free magnets.^{144,145} But also their optical properties are interesting. Being chemically stable compounds with doublet multiplicity, these radicals might be able to harvest singlet and triplet excitons in OLEDs without the necessity to involve ISC. For the calculations, the R2017 DFT/MRCI Hamiltonian and the polarizable continuum solvation model¹⁴⁶ were employed. By and large, the DFT/MRCI method reproduces the experimental UV/Vis spectrum quite well. In the short wavelength region <300 nm (local phenyl excitations from doubly occupied MOs to virtual MOs) a nearly perfect match of theory and experiment is found (Figure 8). The lower part of the spectrum ($\lambda > 300$ nm) stems from excitations of the singly occupied MO (SOMO) to virtual MOs or from doubly occupied MOs to the SOMO. These transitions appear to be systematically blue-shifted by about 0.15 eV with respect to experiment. Nevertheless, the calculations allow for a qualitative assignment of the major bands in the UV/Vis spectrum.

DFT/MRCI and DFT (ΔE^{SCF}) have the tendency to underestimate vertical ionization potentials (IPs). This is to be expected because electron correlation is typically larger in n -electron systems than in the corresponding cations featuring only $n - 1$ electrons. In contrast to excitation energies of systems where the number of electrons is conserved, the errors in the calculated IPs are therefore not normally distributed. Overall, ΔE^{SCF} values obtained with the BHLYP functional are somewhat closer to experiment than IPs based on DFT/MRCI energy differences, presumably due to partial error cancellation because a ROKS ansatz was used in the BHLYP calculations on the radical cations and hence spin polarization was neglected (Table 3).

5.3 | Molecules with high-spin ground states

By construction, the anchor configuration in the DFT/MRCI program is required to be a closed-shell Slater determinant for molecules with an even number of electrons or a Slater determinant with a single open shell for molecules with an odd number of electrons. This requirement has a technical background as it allows for very efficient configuration comparison and matrix

TABLE 3 Statistical data showing the deviations of 30 calculated vertical ionization potentials of organic molecules from experimental data.³⁵ All calculations were carried out at the B3LYP optimized geometries of the neutral ground states. Throughout, a spin-restricted ansatz was used for the BHLYP calculations on the radical cations

Error	BHLYP (ΔE^{SCF})	R2017 DFT/MRCI
RMSD	0.21	0.30
MAD	0.18	0.28
Mean	-0.11	-0.25
MaxAD	0.42	0.52

RMSD: root mean square deviation; MAD: Mean absolute deviation; MaxAD: Maximum absolute deviation.

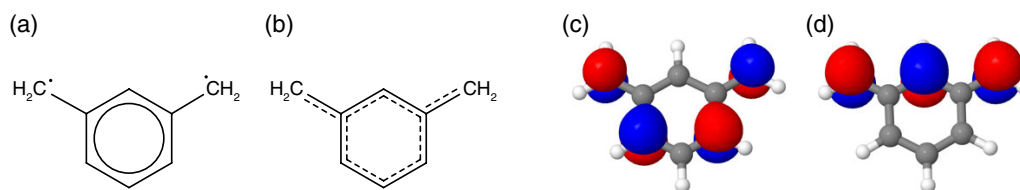


FIGURE 9 Chemical structure of *m*-xylylene in the biradical ground state (a) and the first excited singlet state (b). Density plots of the $2a_2$ (c) and $3b_2$ (d) MOs are shown for an isovalue of 0.05

element evaluation algorithms in a configuration-driven CI⁸³ and a good load balancing scheme in the parallelized execution of the program.³¹ On the downside, atoms and molecules with high-spin ground states pose a particular challenge to the DFT/MRCI approach.

5.3.1 | The *meta*-Xylylene case

An example where DFT/MRCI works well despite a triplet ground-state structure is *m*-xylylene (Figure 9). The 3B_1 ground state is a biradical (Figure 9a) with $\dots 2a_2^1 3b_2^1$ occupation while the 1A_1 symmetric first excited singlet state (Figure 9b) has multiconfiguration character with the $\dots 2a_2^2 3b_2^0$ and $\dots 2a_2^0 3b_2^2$ configurations as the leading terms. For the orbital shapes see Figures 9c and d. From anion photoelectron spectroscopy, a 0_0^0 energy of 9.6 ± 0.2 kcal/mol (corresponding to ca. 0.42 ± 0.01 eV) was deduced for the 1A_1 state and an upper limit of 21.5 kcal/mol (ca. 0.93 eV) was estimated for the 0_0^0 energy of the second excited singlet state, 1B_1 .^{147,148} Vertical excitation energies are not known experimentally but have to be higher than the adiabatic ones, of course. Calculation of the triplet–singlet energy gap by quantum chemical methods appears to be notoriously difficult. The vertical 3B_1 – 1A_1 energy gap, computed at the ab initio MRCI level by Mañeru et al.,¹⁴⁹ depends strongly on the underlying MO basis and the active space, ranging from roughly 1.06 eV when 3B_1 -CASSCF (8,8) MOs are employed to about 0.24 eV for 1A_1 -CASSCF (8,8) MOs. Within the DFT/MRCI approach, a closed-shell determinant with $\dots 3b_2^2 2a_2^0$ or $\dots 3b_2^0 2a_2^2$ occupation can be chosen as anchor configuration. The other leading determinant of the 1A_1 wavefunction then corresponds to a closed-shell double excitation. In either case, nearly the same vertical triplet–singlet splittings are obtained, 0.68/0.75 eV for the original DFT/MRCI approach and 0.71/0.69 eV for the R2016 Hamiltonian using a TZVP¹⁵⁰ basis set. In this particular example, static electron correlation, that is well accounted for by the MRCI expansion, appears to play the dominant role. Notably, the use of different MOs does not lead to significantly different results. Part of this balanced description within DFT/MRCI is attributed to the fact that the active orbitals in the reference space are iteratively determined and that their number is not limited by the structure of the underlying one-particle basis.

5.3.2 | The *hexa*-Aquanadium(III) ion

Transition metal complexes with partially filled *d*-subshells are much more critical cases. $V(\text{H}_2\text{O})_6^{3+}$, for example, has a 3T_g electronic ground state with configuration $t_g^2 e_g^0$ which is moderately distorted by Jahn–Teller coupling with the 3E_g components lying approximately 0.24 eV above the spatially nondegenerate 3A_g component.¹⁵¹ Absorption bands have been determined for the corresponding 1T_g state and two excited 3T_g states with configuration $t_g^1 e_g^1$.¹⁵²

For the sake of investigating possible problems of the DFT/MRCI approaches with the high-spin ground state, we computed vertical excitation energies for a perfectly T_h -symmetric structure with V–O bond distances of 199 pm using a TZVP AO basis.¹⁵⁰ Ideally, threefold degenerate levels should therefore be obtained in this case study. As may be seen from the entries in Table 4, the averaged DFT/MRCI excitation energies fit the experimental ones quite well, with the original

TABLE 4 Vertical DFT/MRCI excitation energies (in eV) of $[V(\text{H}_2\text{O})_6]^{3+}$ for a T_h -symmetric structure using KS orbitals from a b_{3g}^2 anchor configuration. In parentheses, the excitation class (s:Single, d:Double) with respect to the anchor configuration is given. Results for the original¹⁷ and R2016.³³ Hamiltonians are shown together with mean experimental excitation energies of the Jahn–teller distorted components^{151,152}

State	Original DFT/MRCI				R2016 DFT/MRCI				Exp. Average
	B_{1g}	B_{2g}	B_{3g}	Average	B_{1g}	B_{2g}	B_{3g}	Average	
$1^3T_g (t_g^2 e_g^0)$	0.00 (s)	0.00 (s)	0.46 (d)	0.15	0.45 (s)	0.45 (s)	0.00 (d)	0.30	0.16
$1^1T_g (t_g^2 e_g^0)$	1.19 (s)	1.20 (s)	1.52 (d)	1.30	1.36 (s)	1.37 (s)	0.84 (d)	1.19	1.32
$2^3T_g (t_g^1 e_g^1)$	2.23 (d)	2.26 (d)	1.56 (s)	2.02	1.97 (d)	1.97 (d)	2.00 (s)	1.98	2.33
$3^3T_g (t_g^1 e_g^1)$	3.06 (d)	3.08 (d)	2.91 (s)	3.02	2.70 (d)	2.68 (d)	3.44 (s)	2.94	3.35

DFT/MRCI parametrization doing somewhat better than the R2016 ansatz. However, we also notice large energetic splittings between the ideally degenerate components. These results point toward possible shortcomings of the current DFT/MRCI approaches.

The DFT/MRCI program can handle D_{2h} molecular point groups and subgroups thereof. A T_g state has B_{1g} , B_{2g} , and B_{3g} components in D_{2h} subgroup symmetry. Forcing the b_{3g} component of the t_g orbital to be doubly occupied in the closed-shell anchor determinant leads to largely different Fock matrix elements entering the Hamiltonian. The KS orbital energies of the occupied b_{3g} and the empty b_{1g} and b_{2g} components differ by more than 7 eV. Even the lower-lying doubly occupied t_u and t_g shells are split by about 0.7 and 0.4 eV, respectively. This artificial symmetry breaking is not fully recovered by the truncated MRCI expansion. Herein, it is irrelevant whether the initial reference space was generated by all single and double excitations of 2 or 14 active electrons to the five lowest unoccupied MOs. After one iteration of selecting the most important configurations to become reference configurations, the reference spaces are nearly identical.

For each state listed in Table 4, the leading configuration of the CI expansion exhibits two open shells, but the excitation class differs among the components, indicated by (s) for a single excitation with respect to the (arbitrarily chosen) b_{3g}^2 anchor configuration or (d) for a double excitation. For example, the leading term of the B_{1g} component of the electronic ground state can be reached from the b_{3g}^2 anchor configuration by a $b_{3g} \rightarrow b_{2g}$ single excitation. Likewise, the leading configuration of the B_{2g} component corresponds to a $b_{3g} \rightarrow b_{1g}$ single excitation whereas a $b_{3g}^2 \rightarrow b_{1g}b_{2g}$ double excitation is required to generate the leading configuration of the B_{3g} component. Interestingly, the original DFT/MRCI ansatz places the singly excited states systematically below the doubly excited ones whereas the contrary is true for the redesigned Hamiltonian.

Summarizing, the example of the hexa-aquavanadium(III) ion shows that DFT/MRCI does not even approximately preserve the degeneracies of the electronic states in highly symmetric molecules with high-spin ground states. This problem becomes particularly apparent in transition metal complexes with partially filled shells, but it is also present, though to a lesser extent, in linear molecules composed of main group elements such as O_2 . It originates mainly from the technical requirement of a closed-shell anchor configuration which invariably leads to symmetry breaking. Application of the current DFT/MRCI variants to such cases is therefore not recommended. On these grounds, the following performance tests of the DFT/MRCI approaches in transition metal compounds are limited to systems with a closed-shell electronic ground state where transitions have been identified unambiguously.

5.4 | Transition metal complexes with closed-shell ground states

5.4.1 | Benchmark studies

Escudero and Thiel assessed the performance of the original DFT/MRCI method and TDDFT in conjunction with the CAM-B3LYP, PBE0, PBE functionals on a total of 42 singlet and triplet excitation energies of 7 first- and second-row transition metal complexes against CASPT2 results.³⁶ They do not present statistical data, but conclude that DFT/MRCI performs reasonably well for all complexes save for the permanganate ion. In particular, DFT/MRCI is said to systematically underestimate the energies of the lowest singlet and triplet excited states, but to provide the correct order of states in comparison to CASPT2 and a balanced description of excited states with different character, in contrast to the TDDFT results for the tested functionals.

Springer¹⁵³ repeated these calculations using exactly the same set of molecular states and geometries but added DFT/MRCI excitation energies obtained with the R2016 Hamiltonian and performed a statistical analysis, the results of which are shown in Table 5. While the RMSD from the reference data are larger than for organic molecules, the overall performance of the DFT/MRCI variants on transition metal compounds appears to be satisfactory.

Validation of DFT/MRCI excitation energies against CASPT2 results always bears a risk, however, of being biased. The requirement to employ reference data that are converged with respect to the size of the active space is particularly demanding

TABLE 5 Statistical data showing the deviations of vertical DFT/MRCI excitation energies (in eV) of 7 first- and second-row transition metal complexes with respect to CASPT2 literature data.³⁶ Results for the original¹⁷ and R2016³³ Hamiltonians are shown

Error	Original DFT/MRCI			R2016 DFT/MRCI		
	All 42	MC	MLCT	All 37 ^a	MC	MLCT
RMSD	0.40	0.42	0.21	0.33	0.29	0.29
MAD	-0.06	0.18	0.04	0.13	0.13	0.15
Max (-) deviation	0.79	0.63	0.34	0.44	0.31	0.27
Max (+) deviation	0.76	0.76	0.53	0.54	0.54	0.54

RMSD: root mean square deviation; MAD: Mean absolute deviation

^a Five excited states of MnO_4^- could not be unambiguously assigned.

TABLE 6 Statistical data showing the deviations of 67 vertical DFT/MRCI and TDDFT excitation energies (in eV) of 21 first- and second-row transition metal complexes with respect to experimental data.³⁵ DFT/MRCI results were obtained with standard parameters and selection threshold $1 E_h$

	Original	R2016 ^a	R2017 ^a	R2018 ^a	TDDFT-PBE0
RMSD	0.35	0.55	0.60	0.33	0.41
MAD	0.25	0.33	0.39	0.23	0.32
Mean	-0.15	-0.29	-0.34	-0.04	0.09
MaxAD	1.03	1.92	2.05	1.10	1.14

RMSD: root mean square deviation; MAD: Mean absolute deviation; MaxAD: Maximum absolute deviation.

^a Two excited states of MnO_4^- could not be unambiguously assigned.

in the case of transition metal compounds. Moreover, startling results were reported for iron and zinc porphyrin complexes where the computed CASPT2 excitation energies are found to be very sensitive with respect to the level shift used in the calculations.^{91,92} Heil et al. therefore decided to assess the performance of the DFT/MRCI variants against a set of 67 carefully selected experimental excitation energies of 21 transition metal complexes with closed-shell ground states.³⁵ In addition to small inorganic complexes (fluorides, oxides, carbonyls, ammine, and aqua complexes), larger organometallic compounds (metallocenes, pyridine and phenanthroline complexes as well as metalloporphyrins) were considered. See Reference 35 for detailed information on the chemical compositions and selected electronic states. Two of the molecules in the set, namely MnO_4^- and $Cr(CO)_6$, had also been investigated by Escudero and Thiel.³⁶ The data set comprised in total 67 LC $\pi \rightarrow \pi^*$, MLCT $d \rightarrow \pi^*$ and mixed MLCT/LC $d/\pi \rightarrow \pi^*$ transitions, some ligand-to-metal charge transfer (LMCT) mixed with LC excitations $\pi \rightarrow d^*/\pi^*$ as well as MC $d \rightarrow d^*$ excited states. In the case of the redesigned Hamiltonians, the set only included 65 states, because two states in MnO_4^- could not be assigned to their experimental counterparts. This is due to a large number of artificially low-lying doubly excited states in the spectrum of these Hamiltonians. In the assessment set, triplet and MC transitions are somewhat underrepresented because their optical transitions are very weak and only limited experimental reference data are available. In the DFT/MRCI runs, various combinations of parameter sets and selection thresholds were tested. We present here only the results for the standard parameter sets in conjunction with $esel = 1.0 E_h$ and for the tight (or short) parameter sets in conjunction with $esel = 0.8 E_h$. For further details on the calculations see Reference 35.

On the average, the excitation energies of the complete set showed quite large deviations from the experimental reference values (Table 6). In particular, the redesigned Hamiltonians R2016 and R2017 performed significantly inferior to the original DFT/MRCI. A first rough classification grouping the results into sets of 27 excitation energies of small inorganic complexes and 40 organometallic complexes (Figure 10) revealed the small inorganic complexes to be the most problematic ones. Astoundingly, even TDDFT in conjunction with the PBE0 functional^{154,155} performed statistically better than all DFT/MRCI variants on the latter group of complexes. An in-depth analysis found the DFT/MRCI results on the carbonyl, aqua, and ammine complexes to be unsuspecting whereas huge deviations were observed for the electronic excitations of the fluorides and oxides. The 13 experimentally known $n \rightarrow d^*/\pi^*$ transitions in CrF_6 , MoF_6 , MnO_4^- , and TcO_4^- yielded a RMSD of 0.67 eV for the original Hamiltonian with a MaxAD of 1.03 eV. Using the redesigned Hamiltonians instead, only 11 of

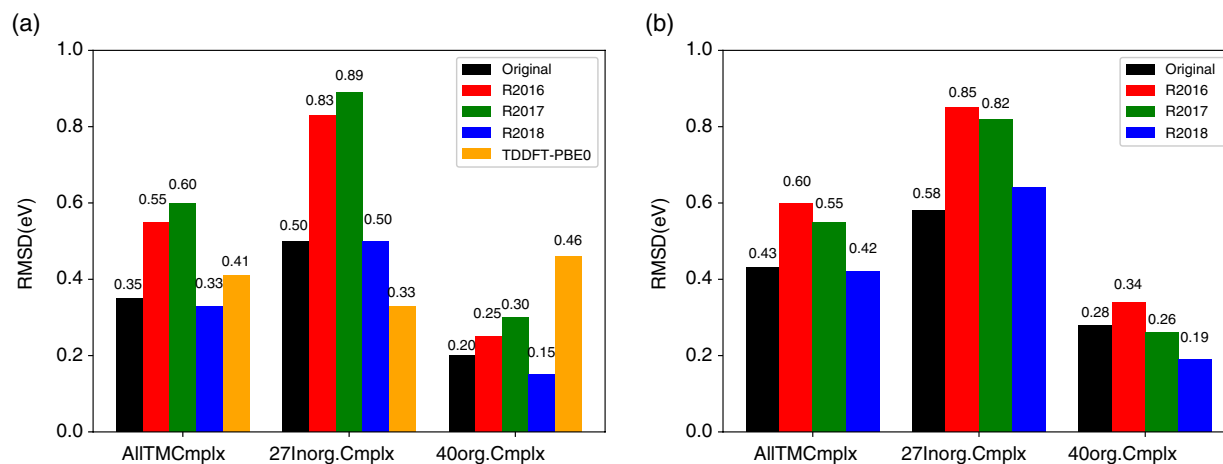


FIGURE 10 Histogram of the error distributions ($E_{calc} - E_{exp}$) of 67 DFT/MRCI and TDDFT singlet and triplet excitation energies (in eV) of 21 first- and second-row transition metal complexes with respect to experimental data. DFT/MRCI results on the 27 inorganic and 40 organometal complexes were obtained with (a) standard parameters and selection threshold $1 E_h$ (b) tight parameters and selection threshold $0.8 E_h$ ³⁵

TABLE 7 Number of CSFs and calculation times for selected molecules using the R2018 Hamiltonian with short ($0.8 E_h$) and standard ($1.0 E_h$) selection. For all molecules, the same type of CPUs has been employed

Molecule	Symm. Used	Roots Calc.	CPUs	CPU time		CSFs	
				Short	Standard	Short	Standard
Rh(phenantroline) $_3^{3+}$	C_1	50	9	5 h	122 h	3,437,047	45,288,577
Zinc phthalocyanine	D_{2h}	17	30	4 m	88 m	2,447,089	34,776,646
Zinc porphyrin	D_{2h}	17	30	13 s	250 s	147,282	1,584,839

13 transitions could be assigned with RMSD of 1.22/1.29 eV for the R2016/R2017 Hamiltonians, respectively, and MaxAD values of 1.92/2.05 eV. Their excitation energies come out much too low as may be seen from mean values of -0.46 eV for the original and $-1.11/-1.19$ eV for the R2016/2017 Hamiltonians.

This observation led to a modified DFT/MRCI Hamiltonian, hereafter dubbed R2018, which sought to combine the advantages of the original and redesigned approaches.³⁵ It differs from the R2017 Hamiltonian by the functional form of the off-diagonal damping, compare Equations (25) and (26). Lyskov et al. had tested several damping functions when redesigning the DFT/MRCI Hamiltonian and had found only little variation of the statistical data in their fitting and assessment sets comprising predominately organic compounds.³³ Choosing an exponential damping function (Equation 26) which depends on the sixth power of the energy difference between configurations, Heil et al. noticed a dramatic improvement of the excitation energies of the $3d$ transition metal oxides and fluorides.³⁵ With a mean value of -0.39 eV, a RMSD of 0.67 eV and a MaxAD of 1.10 eV, the performance of the R2018 Hamiltonian is not optimal for these compounds, but much better than that of the R2016 and R2017 Hamiltonians and even slightly superior to that of the original Hamiltonian. Note that the previously observed good performance of the redesigned Hamiltonians on the organic molecules and radicals did not deteriorate when changing the functional form of the off-diagonal damping. The improvement of the LC $\pi \rightarrow \pi^*$ and MLCT $d \rightarrow \pi^*$ excitation energies of organometallic complexes, brought about by the R2018 parametrization, was less dramatic but clearly noticeable (Figure 10). For these types of transitions, the performance of TDDFT-PBE0 is much poorer than that of any DFT/MRCI variant. Excitation energies of MC transitions are not easily compared to experiment because they are dipole forbidden and require vibronic coupling to gain some intensity. As can be seen from the metallocenes and the hexammine complexes, satisfactory agreement with experimental data was achieved for the original and R2018 Hamiltonians.³⁵

Although the computational cost of a DFT/MRCI calculation is typically small in comparison to ab initio calculations of similar quality, it may happen that the configuration space comprises several hundred million CSFs, in particular if the UV/Vis spectrum of transition metal complexes with extended organic ligands is to be determined. To save computational resources, it may therefore be advisable or even mandatory to employ a tighter selection threshold leading to significantly shorter wave functions and hence resource requirements (Table 7).

As may be seen from a comparison of the RMSD values in Figures 10a and b, this is easily possible for organometallic complexes without significant loss of accuracy. For the R2016 and R2017 Hamiltonians, statistically the best results are obtained by combining standard parameters with a selection threshold of $0.8 E_h$.³⁵ We do not recommend this choice, however, because the seemingly good performance benefits from error compensation. The entries in Table 6 show that the mean

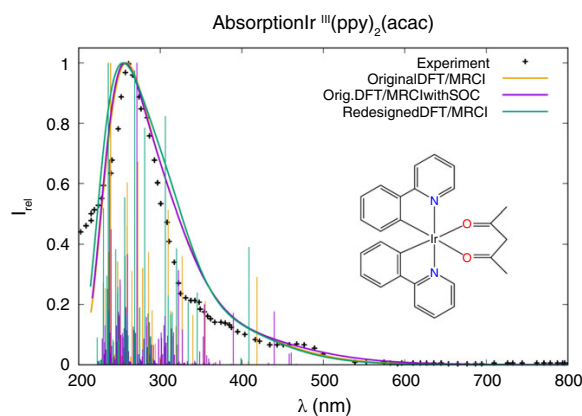


FIGURE 11 Calculated absorption spectra of $\text{Ir}^{\text{III}}(\text{ppy})_2(\text{acac})$. Green: Spin-orbit free DFT/MRCI (R2016 Hamiltonian), yellow: Spin-orbit free DFT/MRCI (original Hamiltonian), purple: DFT/MRCI (original Hamiltonian) including spin-orbit coupling effects. The envelopes of the line spectra were plotted with a Gaussian broadening of 3,000/cm FWHM. The data points of the experimental spectrum were taken from Reference 159

energy is too low for these Hamiltonians in transition metal complexes. Reducing the size of the configuration space by lowering the selection threshold leads in turn to an increase of the transition energies and hence partial error cancellation.

5.4.2 | Case studies

Due to the high density of excited states in large transition metal complexes, it is often difficult or even impossible to make a one-to-one assignment of spectral bands. Several examples of octahedral transition metal complexes with ground-state occupation t_{2g}^6 can be found where DFT/MRCI provides excellent descriptions of electronic absorption spectra.^{36,156,157} In third-row transition metal complexes where direct photoexcitation of triplet MLCT states can be observed in the long wavelength tails of the absorption spectra,^{158–160} spin-orbit coupling (SOC) ought to be incorporated in the quantum chemical treatment for a meaningful comparison with experiment.

In Figure 11, theoretical absorption spectra of iridium(III)-bis[(2-phenylpyridinato)-N,C^{2'}] (acetylacetonate), in short Ir^{III}(ppy)₂(acac), are shown together with experimental data points taken from Reference 159. The scalar relativistic spectra computed with the original and redesigned DFT/MRCI methods, respectively, are nearly indistinguishable. The spectral envelope does not change markedly when SOC is included at the level of quasi-degenerate perturbation theory (presented here only for the original DFT/MRCI parametrization). This is particularly true in the short wavelength region where absorption properties are dominated by LC transitions. A closer look at the spectral region between 500 and 400 nm reveals, however, that the intensity of the S₁ absorption is greatly reduced with respect to the scalar relativistic spectrum. Instead, triplet excitations with mixed MLCT/LC character dominate the low-energy tail of the absorption spectra up to about 400 nm where the first transition with prevailing singlet multiplicity is found. In all those transitions, electron density is transferred from the metal center and the phenyl rings toward the pyridine rings. The spin-orbit mixed transitions (purple lines in Figure 11) are seen to match well with shoulders at the long wavelength edge of the measured absorption spectrum. A similarly good performance is observed for properties other than energies such as ISC rate constants and phosphorescence lifetimes.¹⁵⁷

Also d^6 metallocenes exhibit a closed-shell ground state and their UV/Vis spectra were studied in the seminal paper by Grimme and Waletzke.¹⁷ The DFT/MRCI excitation energies of ferrocene (FeCp₂) are too small by about 0.15 eV on the average in comparison to experiment. On these grounds, the theoretical values were blue-shifted by that amount in Figure 12.¹⁷ The oscillator strengths are seen to agree very well with the intensities of the UV/Vis spectra¹⁶¹ and thus allow for an assignment of the bands.

Likewise, convincing DFT/MRCI results were obtained for Cu and Au complexes with closed-shell d^{10} ground states whereas TDDFT spectra are often less satisfactory.^{162,163} Consider, for example, the absorption spectrum of the cationic three-coordinate 1,3-bis(2,6-diisopropylphenyl)imidazol-2-ylidene-Cu(I)-1,10-phenanthroline complex. DFT/MRCI calculations (original parametrization) incorporating scalar relativistic effects through an effective core potential reproduce the experimental spectrum very well (Figure 13a). The experimental spectrum had been measured in dichloromethane.¹⁶⁴ Föller et al.¹⁶² found solvent effects and the influence of the counterion on the computed spectra to be negligible and used theoretical results for the isolated cationic complex for comparison with experiment. Environment effects on MLCT and LMCT transitions can be very strong causing large spectral shifts in polar media. For examples see References 163,165,166.

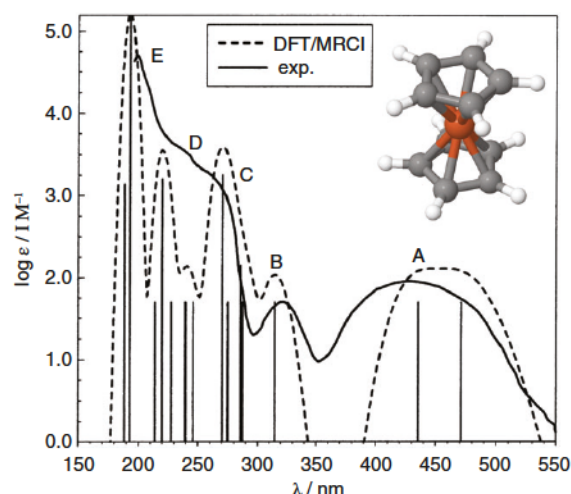


FIGURE 12 UV/Vis spectrum of ferrocene. Experimental data had been taken from Reference 161. The DFT/MRCI excitation energies (original parametrization) were blue-shifted by 0.15 eV for a better match with experiment (Reprinted with permission from Reference 17. Copyright 1999 AIP Publishing)

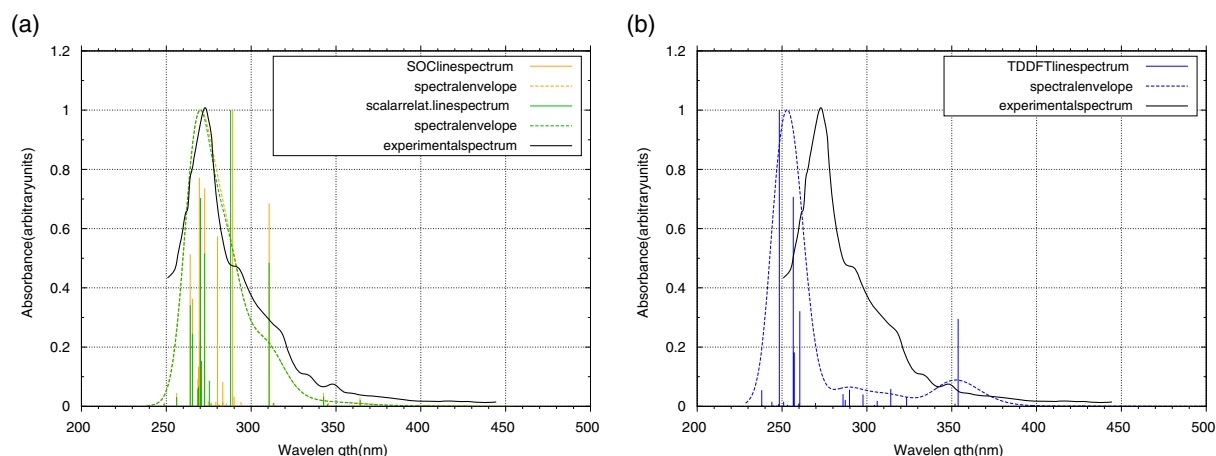


FIGURE 13 Absorption spectra of the three-coordinate 1,3-bis(2,6-diisopropylphenyl)imidazol-2-ylidene-Cu(I)-1,10-phenanthroline complex. The experimental data points were read from Figure 3 of Reference 164. (a) DFT/MRCI (original parametrization), green: Scalar relativistic, gold: Including spin-orbit coupling effects; (b) TDDFT in conjunction with the PBE0 functional. All line spectra were broadened with Gaussians of 1,500/cm FWHM. Herein, no shifts were applied (Reprinted with permission from Reference 162. Copyright 2016 ACS Publications)

At the long wavelength edge, weak MLCT transitions can be identified between 420 and 400 nm. In the region between 400 and 300 nm, mixed MLCT/LC excitations with small to medium oscillator strengths are found whereas the short wavelength region between 300 and 250 nm is dominated by strong LC $\pi\pi^*$ transitions. DFT/MRCI appears to describe the MLCT and LC transitions in a balanced way, in contrast to TDDFT/PBE0 (Figure 13b) which assigns too small oscillator strengths to the transitions in the spectral region between 290 and 340 nm. Although SOC plays an essential role in the photophysics of this compound, its effects on the absorption properties are hardly visible in the spectrum (compare yellow and green lines in Figure 13a).

The presented examples show that DFT/MRCI is a valuable tool for computing spectra of large transition metal organic complexes with closed-shell ground states. Incorporation of scalar relativistic effects—be it through effective core potentials or by adding correction terms to the all-electron Hamiltonian—is desirable for first-row transition metal compounds. For second- and third-row transition elements, their inclusion is mandatory. Property modules allow the computation of transition probabilities between electronic states and hence provide information on decay mechanisms following photonic or electrical excitation.

5.4.3 | Properties

The good performance of the DFT/MRCI method is not limited to excitation energies. Routinely, one-electron electric dipole and quadrupole as well as magnetic (transition) moments can be determined. Numerous examples corroborate the high quality of related properties such as oscillator strengths of radiative transitions.^{17,32} Monomer transition densities may also be used to compute excitonic couplings for resonant excitation energy transfer between donor and acceptor chromophores.^{167,168} More sensitive with respect to the quality of the wave function is the rotatory strength as it does not only depend on the lengths of the electric and magnetic dipole transition vectors, but also on their relative orientation. The rotatory strength is a necessary ingredient computing circular dichroism (CD) spectra. Diedrich et al.¹⁶⁹ performed a systematic investigation of quantum chemical methods to predict electronic CD spectra, employing TDDFT, multireference MP2 (MRMP2), and CC2 besides DFT/MRCI. They concluded that none of the methods performed reliably for all molecules in the test suite. The best overall performance was achieved by the DFT/MRCI and CC2 methods, although some outliers were observed for those methods, too. In particular, systems with Rydberg-valence mixing and an iron complex turned out to be rather difficult cases.

Spin-dependent properties are available within the spin-orbit coupling kit Spock^{27–29} and its extension to spin–spin coupling treatment Spock.Sistr.³⁰ Spock provides electronic SOC matrix elements of DFT/MRCI wavefunctions required for the computation of ISC and reverse ISC rate constants.^{96,139,170} Spin-orbit mixed DFT/MRCI wavefunctions either from a quasi-degenerate perturbation theory (QDPT) or a variational multireference spin-orbit configuration interaction treatment are further used to determine second-order spin-dependent properties such as phosphorescence lifetimes and g -matrices.^{29,171} Jovanović et al. tested the performance of the DFT/MRCI variants on SOC matrix elements in comparison to MRMP2 and CASPT2 results in diatomic and small polyatomic molecules including higher excitations.¹⁴² Generally, very good agreement between the methods is found. The few outliers result from rotations of DFT/MRCI vectors between high-lying near-degenerate electronic states. Although these rotations change the properties of the individual states, their overall contributions to second-order properties such as phosphorescence lifetimes remain nearly constant. Electronic spin–spin coupling (SSC)

matrix elements are presently available only for small to medium-sized molecules because SSC is a two-electron property and the spatial part of the Hamiltonian contains a second-rank tensor with six different types of integrals in Cartesian representation. A resolution of the identity (RI)-approximation for SSC is implemented in combination with the ORCA suite of programs and appears to work very well.¹⁷² Technical improvements as well as process parallelization will be required to extend the application range of Spock.Sistr to larger molecules.

6 | TECHNICALITIES AND AVAILABILITY

6.1 | Technical aspects

6.1.1 | One-particle bases and integrals

For systems with an even number of electrons, typically the Turbomole program suite¹⁷³ has been employed for generating the RKS MOs as well as the one- and two-electron integrals required to set up the DFT/MRCI matrix. Alternatively, the ORCA program package^{174,175} may be used for these purposes. ROKS MOs for systems with an odd number of electrons are calculated utilizing Dalton.¹⁷⁶ For further details on the interfaces between these program packages and the parallelized version of the DFT/MRCI program³¹ see below.

Due to the fact that the KS orbital energies enter the expressions for the parameterized diagonal Hamiltonian matrix elements (Equation 14), DFT/MRCI requires the MO basis, from which the configuration space is constructed, to be canonical. Presently, optimized parameter sets are available in conjunction with the BHLYP hybrid XC functional^{86,87} only. To enable the computation of electronic spectra even of large molecular systems, a RI approximation^{17,177} is employed for the construction of the two-electron integrals. Herein, auxiliary basis sets are used that have been optimized for MP2 or other WFT approaches.^{178,179} In the beginning of a DFT/MRCI run, three-index two-electron integrals are read in and stored from which the required four-index two-electron integrals are constructed later on-the-fly. The maximum number of one-particle basis functions is currently limited to 1,200, not including the frozen core and anticore orbitals.

6.1.2 | Reference space generation and configuration selection

The reference space of a DFT/MRCI calculation is generated iteratively. Typically, in a first calculation the reference space is created in a restricted-active-space (RAS) like manner by including all single and double excitations out of a user-chosen set of occupied orbitals into a set of unoccupied orbitals. Single and double excitations with respect to these reference configurations span the CI space of this first DFT/MRCI calculation after configuration selection. All configurations of the CI vectors which exceed a certain weight in the CI vector (default: squared coefficient >0.003) are included in the reference space for the next iteration. In most cases, two to three iterations are sufficient to reach convergence. To speed up this procedure, the iterations may be done with a lower selection threshold, and only the final run is then done with a higher one. In 3-(9,9-dimethylacridin-10(9H)-yl)-9H-xanthen-9-one, for example, the nonbonding n orbital on the carbonyl oxygen, involved in the low-lying $n\pi^*$ transitions, is not active in the first iteration because this MO lies energetically as low as HOMO-10 in the ground-state BHLYP KS calculation.¹³⁶ Nevertheless, the $n\pi^*$ configuration pops up in the singlet and triplet wave functions of the first iteration with significant weights and is henceforth included in the reference space. The adaptive reference space generation scheme is one of the major advantages of DFT/MRCI compared to CASSCF/CASPT2. CAS methods often suffer from restrictions in the number of orbitals and electrons that can be included in the active space. In the DFT/MRCI method, there are no restrictions as to how many orbitals may be active in the reference configurations. However, the complete diagonalization of the reference Hamiltonian matrix limits the number of reference configurations currently to 1,000. In the reference space, at most sixfold excitations with respect to the anchor configuration are allowed yielding up to eight-fold excitations in the final CI space. The number of open shells per configuration is restricted to 10, featuring 252 determinants in each CSF.

Also the selection threshold is handled in an adaptive manner. The reference space energy of the highest root requested in the final MRCI procedure is added to the user-supplied selection threshold *esel*. For this reason, the dimension of the CI matrix and the final results vary slightly with the number of desired roots that is limited to 50 in the current version. The program can handle D_{2h} point group symmetries and all subgroups thereof. To speed up the configuration selection of the single and double excitations out of all reference configurations, the expected excitation energy of every configuration is approximated by summing up the (negative) orbital energies of the annihilated and created orbitals. If this energy is higher than the selection threshold, this configuration is discarded, otherwise it is included in the CI space. Typically, more than 99% of all configurations are discarded.

6.1.3 | Iterative diagonalization of the CI space

The CI space is iteratively diagonalized by computing the requested number of roots in a multi-root Davidson algorithm.^{180,181} Simultaneous optimization of multiple roots is found to converge faster than a consecutive diagonalization procedure. If the requirements for storing all CI vectors and σ vectors simultaneously in random access memory are too heavy, the diagonalization is performed in several sweeps. The DFT/MRCI program is written in the FORTRAN 90 programming language. The parallelized version³¹ utilizes the distributed memory parallelization standard *Message Passing Interface*. Only the on-the-fly generation of the Hamiltonian matrix and its multiplication with the σ vector have been parallelized, as these are by far the most time demanding steps.

6.1.4 | Gradients

The iterative improvement of the reference space makes the DFT/MRCI method a very flexible tool for computing many electronic states even of large molecules simultaneously. A disadvantage of this flexibility is the nonexistent invariance of the energy with respect to orbital rotations which makes the method unsuitable for formulating an analytical gradient using a Z-vector approach. DFT/MRCI gradients can be determined numerically via finite differences and a similar procedure can be used to locate minimum energy conical intersection points.¹⁸² During these searches, the configuration space has to be frozen. After a number of steps (typically 20–30), the CI space is updated and the search for a stationary point is restarted. In a similar way, (spin-)vibronic coupling matrix elements can be determined by numerical differentiation. As these numerical procedures scale very inefficiently with the number of nuclear degrees of freedom, they should be applied only in cases where derivatives of the DFT/MRCI energy or wave function are absolutely necessary.

6.2 | Interfaces to other quantum chemistry programs

Originally, the DFT/MRCI program had been interfaced to an early version of the Turbomole program package,^{183,184} from which the necessary DFT energy of the anchor configuration, BHLYP KS MOs and the MO integrals were obtained.¹⁷ In particular the use of the RI approximation for the on-the-fly construction of the four-index two-electron integrals¹⁷⁷ turned out to be essential for the application of the DFT/MRCI approach to large molecular systems. This interface is still functional in later program versions of DFT/MRCI and Turbomole (at least up to version 7.1) and is currently the most employed one, but it requires a potential DFT/MRCI user to hold a license of the meanwhile commercially distributed Turbomole package.¹⁷³

For radicals with a doublet ground state, ROKS was found to be the most suitable starting point. Turbomole offers the possibility to generate ROHF orbitals but lacks a ROKS option. This option exists in the Dalton program package.¹⁷⁶ For that reason, an interface was written which converts ROKS orbitals and orbital energies from Dalton to Turbomole format.³⁴ The reformatted ROKS orbitals may then be used to generate one-electron and RI-integrals by means of the Turbomole interface and to start a DFT/MRCI run for systems with an odd number of electrons.

The big success of the DFT/MRCI method and numerous requests for obtaining the code prompted us recently to make the program available to a broader scientific community. For this reason, an interface to the ORCA program package was created, starting with version 4.0. ORCA is a general purpose quantum chemical program^{174,175} which is available free of charge to the academic scientific community. The ORCA interface provides KS MOs, one- and two-electron integrals and the necessary basis set information for subsequent property calculations. The DFT/MRCI program with the integrated ORCA interface, including the original¹⁷ and redesigned R2016,³³ R2017,³⁴ and R2018³⁵ Hamiltonians and parametrizations is available upon request on our home page.¹⁸⁵ For the academic scientific community, its use is free of charge.

7 | CONCLUSIONS

7.1 | Summary

In the past two decades, the DFT/MRCI method has developed from a powerful approach for computing spectral properties of singlet and triplet excited states of large molecules into a more general multireference method applicable to states of all spin multiplicities. Property modules allow the computation of probabilities for transitions between electronic states and hence provide information on decay mechanisms following photonic or electric excitation. DFT/MRCI shows great efficiency in the evaluation of $\pi\pi^*$, $n\pi^*$, Rydberg, and CT excitations. Even doubly excited states are described in a balanced manner. High flexibility is achieved through iterative refinement of the reference space. On the one hand, this flexibility is an advantage over complete active space approaches as it allows computation of states of different character in a nearly automated way. On the other hand, the individual selection of configurations prevents an easy implementation of analytic gradients which may be considered the greatest drawback of the DFT/MRCI method.

TABLE 8 Recommended DFT/MRCI Hamiltonians for excited-state calculations on molecules with closed-shell or single-open shell ground states

System type	States	Recommended Hamiltonian
Ordinary organic molecules	Singlets, triplets	Original, R2016, R2017, R2018
Organic radicals	Doublets, quartets	R2017, R2018
Donor–acceptor systems and dimers	Singlets, triplets	R2016, R2017, R2018
	All multiplets	R2017, R2018
Transition metal complexes with		
(a) Closed-shell ground states	Singlets, triplets	Original, R2018
	All multiplets	R2018
(b) Open-shell ground states	All multiplets	None

Assessment of its performance on organic molecules against experimental excitation energies shows root-mean-square deviations of all DFT/MRCI variants well below 0.2 eV and mean values close to zero. This applies even to parameter sets optimized for a tighter than the standard selection threshold that leads to shorter wave function expansions and hence lower computational expense. In spite of the excellent general performance, a few weaknesses of the Hamiltonians become apparent. The original DFT/MRCI features difficulties in describing weakly coupled donor–acceptor systems and hydrogen-bonded or π -stacked dimers. A multiplicity independent redesigned DFT/MRCI Hamiltonian takes care of this problem and thus extends the application range of the DFT/MRCI method. In conjunction with a restricted-open shell KS optimization of the MOs, also electronically excited doublet and quartet states can be addressed.

In transition metal organic complexes, good performance of the original and redesigned DFT/MRCI Hamiltonians is observed for LC, MLCT, and mixed LC/MLCT transitions. The excitation energies of the MC transitions in metallocenes appear to be somewhat underestimated, but the term ordering is correct. Small inorganic transition metal complexes with LMCT and LC/LMCT excitations are the most critical ones. The assessment of the DFT/MRCI variants reveals a somewhat better but far from satisfactory performance of the original DFT/MRCI Hamiltonian on these states. These insights led to a reparametrization of the multiplicity-independent DFT/MRCI Hamiltonian matrix elements. The resulting Hamiltonian, dubbed R2018, is generally applicable and shows the best overall performance of all DFT/MRCI variants.³⁵ Application of the current DFT/MRCI variants to transition metal complexes with open-shell ground states is not recommended. The problems observed for such compounds originate mainly from the technical requirement of a closed-shell or one-open-shell anchor configuration in the DFT/MRCI program which inevitably leads to symmetry breaking of degeneracies. Table 8 gives an overview over the DFT/MRCI Hamiltonians and their recommended fields of application.

7.2 | Future directions

All parametrizations of the DFT/MRCI Hamiltonian so far have been based on MOs and MO energies from KS-DFT calculations employing the BLYP functional. With scaling factors for the Coulomb and exchange integrals independent of the interelectronic distance, the DFT/MRCI method inherits some properties from the underlying functional, in particular its long-range behavior. Although DFT/MRCI is much more robust than TDDFT/BLYP and yields a significantly more balanced description of valence and CT (or Rydberg) excited state than most linear response TDDFT calculations, its performance on CT states is far from ideal. Especially excited-state energies of extended push-pull donor–acceptor complexes are underestimated. New parametrizations, based for example on modern range-separated functionals, might therefore improve the long-range behavior of the method. Alternatively, the parameters introduced into the DFT/MRCI Hamiltonian could be made to vary with the interelectronic separation.

A reparametrization might also help to get rid of a few problematic cases in the redesigned DFT/MRCI approaches which are related to double excitations from nonbonding MOs to antibonding ones. The difficulties encountered in describing the electronic spectra of CrF₆, MoF₆, MnO₄[−], and TcO₄[−] presumably have a similar origin. Inclusion of doubly excited states in the fitting set (being well aware that these states are optically dark in most kinds of spectroscopy and experimental data may not be available or reliable) might be an option worthwhile trying.

Off-diagonal Fock matrix elements are presently omitted in the semiempirical Hamiltonian, but there is no principle hindrance to reintroduce them. When investigating spatially extended molecules or excimers, DFT/MRCI calculations engaging a localized one-particle basis might be preferable. Research on singlet fission and triplet–triplet upconversion, for example, where transitions between singlet excitons and singlet–coupled triplet pairs play a central role, would certainly profit from such a development. Presently, there are hardly any electronic structure methods around that are apt for modeling these excited-state processes: available methods either cannot handle double excitations appropriately or are computationally too expensive to be applied to dimers of prototypical singlet-fission materials such as pentacene. While the redesigned DFT/MRCI

Hamiltonians describe single and double excitations in polyacene dimers and related compounds well, diabaticization of the interaction potentials is not an easy task in a delocalized basis. Localized orbitals would not only help reducing the CI space, they would also allow for an easier distinction between local and charge-transfer excitations that is needed to determine excitonic couplings between weakly interacting dimers or multimers.

ACKNOWLEDGMENTS

We would like to thank Stefan Grimme for providing us with the original DFT/MRCI program and for fruitful discussions on its further development. We would also like to thank Frank Neese and his team for their technical help in interfacing the DFT/MRCI program to the ORCA program package. Financial support by the Deutsche Forschungsgemeinschaft for two projects focusing on the development and assessment of the multiplicity independent redesigned DFT/MRCI Hamiltonians (MA 1051-14/1 and MA 1051-14/2) is gratefully acknowledged.

CONFLICT OF INTEREST

The authors have declared no conflicts of interest for this article.

RELATED WIREs ARTICLES

[Spin-orbit coupling and intersystem crossing in molecules](#)

[Double-hybrid density functionals](#)

[Subsystem density-functional theory](#)

[Software update: The ORCA program system, version 4.0](#)

[The Dalton quantum chemistry program system](#)

REFERENCES

1. Roos BO, Andersson K, Fülcher MP, et al. Multiconfigurational perturbation theory: Applications in electronic spectroscopy. *Adv Chem Phys.* 1996;93:219–331. <https://doi.org/10.1002/9780470141526.ch5>
2. Szalay PG, Müller T, Gidofalvi G, Lischka H, Shepard R. Multiconfiguration self-consistent field and multireference configuration interaction methods and applications. *Chem Rev.* 2012;112:108–181. <https://doi.org/10.1021/cr200137a>
3. Lischka H, Nachtigallová D, Aquino AJA, et al. Multireference approaches for excited states of molecules. *Chem Rev.* 2018;118:7293–7361. <https://doi.org/10.1021/acs.chemrev.8b00244>
4. Petersilka M, Gossmann UJ, Gross EKV. Excitation energies from time-dependent density-functional theory. *Phys Rev Lett.* 1996;76:1212–1215. <https://doi.org/10.1103/PhysRevLett.76.1212>
5. Casida ME. Time-dependent density functional response theory for molecules In: Recent advances in density functional methods, part I. *World Sci.*, Singapore. 1995;155–192. https://doi.org/10.1142/9789812830586_0005
6. Bauernschmitt R, Ahlrichs R. Treatment of electronic excitations within the adiabatic approximation of time dependent density functional theory. *Chem Phys Lett.* 1996;256:454–464. [https://doi.org/10.1016/0009-2614\(96\)00440-X](https://doi.org/10.1016/0009-2614(96)00440-X)
7. Burke K. Perspective on density functional theory. *J Chem Phys.* 2012;136:150901. <https://doi.org/10.1063/1.4704546>
8. Silva-Junior MR, Thiel W. Benchmark of electronically excited states for semiempirical methods: MNDO, AM1, PM3, OM1, OM2, OM3, INDO/S, and INDO/S2. *J Chem Theory Comput.* 2010;6:1546–1564. <https://doi.org/10.1021/ct100030j>
9. Cohen AJ, Mori-Sánchez P, Yang W. Challenges for density functional theory. *Chem Rev.* 2012;112:289–320. <https://doi.org/10.1021/cr200107z>
10. Peach MJG, Tozer DJ. Overcoming low orbital overlap and triplet instability problems in TDDFT. *J Phys Chem A.* 2012;116:9783–9789. <https://doi.org/10.1021/jp308662x>
11. Adamo C, Jacquemin D. The calculations of excited-state properties with time-dependent density functional theory. *Chem Soc Rev.* 2013;42:845–856. <https://doi.org/10.1039/C2CS35394F>
12. Escudero D, Laurent AD, Jacquemin D. Time-dependent density functional theory: A tool to explore excited states. In: Leszczynski HJ, Kaczmarek-Kedziera A, Puzyn T, Papadopoulos MG, Reis H, Shukla MK, editors. *Handbook of computational chemistry*. Cham, Switzerland: Springer International Publishing, 2017; p. 927–961. https://doi.org/10.1007/978-3-319-27282-5_43
13. Marian CM, Gilka N. Performance of the density functional theory/multireference configuration interaction method on electronic excitation of extended π -systems. *J Chem Theory Comput.* 2008;4:1501–1515. <https://doi.org/10.1021/ct8001738>
14. Klessinger M, Michl J. *Excited States and Photochemistry of Organic Molecules*. New York, Weinheim, Cambridge: VCH, 1995.
15. Grimme S. Calculation of the electronic spectra of large molecules. *Rev Comput Chem.* 2004;3:153–218. <https://doi.org/10.1002/0471678856.ch3>
16. Olivucci M. (Ed.) *Computational PhotoChemistry*. Amsterdam: Elsevier, 2005.
17. Grimme S, Waletzke M. A combination of Kohn–Sham density functional theory and multi-reference configuration interaction methods. *J Chem Phys.* 1999;111:5645–5655. <https://doi.org/10.1063/1.479866>
18. Andersson K, Malmqvist PA, Roos BO, Sadlej AJ, Wolinski K. Second-order perturbation theory with a CASSCF reference function. *J Phys Chem.* 1990;94:5483–5488. <https://doi.org/10.1021/j100377a012>
19. Buenker RJ, Peyerimhoff SD. Individualized configuration selection in CI calculations with subsequent energy extrapolation. *Theor Chim Acta.* 1974;35:33–58. <https://doi.org/10.1007/PL00020553>
20. Krebs S, Buenker RJ. A new table-direct configuration interaction method for the evaluation of Hamiltonian matrix elements in a basis of linear combinations of spin-adapted functions. *J Chem Phys.* 1995;103:5613–5629. <https://doi.org/10.1063/1.470544>

21. Hanrath M, Engels B. New algorithms for an individually selecting MR-CI program. *Chem Phys*. 1997;225:197–202. [https://doi.org/10.1016/S0301-0104\(97\)00241-3](https://doi.org/10.1016/S0301-0104(97)00241-3)
22. Huron B, Malrieu JP, Rancurel P. Iterative perturbation calculations of ground and excited state energies from multiconfigurational zeroth-order wavefunctions. *J Chem Phys*. 1973;58:5745–5759. <https://doi.org/10.1063/1.1679199>
23. Cimiraglia R, Persico M. Recent advances in multireference second order perturbation CI: The CIPSI method revisited. *J Comput Chem*. 1986;8:39–47. <https://doi.org/10.1002/jcc.540080105>
24. Tavan P, Schulten K. The low-lying electronic excitations in long polyenes: A PPP-MRD-CI study. *J Chem Phys*. 1986;85:6602–6609. <https://doi.org/10.1063/1.451442>
25. Ridley JE, Zerner MC. Triplet states via intermediate neglect of differential overlap: Benzene, pyridine and the diazines. *Theor Chim Acta*. 1976;42:223–236. <https://doi.org/10.1007/BF00574445>
26. Koslowski A, Beck ME, Thiel W. Implementation of a general multireference configuration interaction procedure with analytic gradients in a semiempirical context using the graphical unitary group approach. *J Comput Chem*. 2003;24:714–726. <https://doi.org/10.1002/jcc.10210>
27. Kleinschmidt M, Tatchen J, Marian CM. Spin-orbit coupling of DFT/MRCI wavefunctions: Method, test calculations, and application to thiophene. *J Comput Chem*. 2002;23:824–833. <https://doi.org/10.1002/jcc.10064>
28. Kleinschmidt M, Marian CM. Efficient generation of matrix elements for one-electron spin-orbit operators. *Chem Phys*. 2005;311:71–79. <https://doi.org/10.1016/j.chemphys.2004.10.025>
29. Kleinschmidt M, Tatchen J, Marian CM. SPOCK-CI: A multireference spin-orbit configuration interaction method for large molecules. *J Chem Phys*. 2006;124:124101. <https://doi.org/10.1063/1.2173246>
30. Gilka N, Taylor PR, Marian CM. Electron spin-spin coupling from multireference configuration interaction wave functions. *J Chem Phys*. 2008;129:044102. <https://doi.org/10.1063/1.2948402>
31. Kleinschmidt M, Marian CM, Waletzke M, Grimme S. Parallel multireference configuration interaction calculations on mini- β -carotenes and β -carotene. *J Chem Phys*. 2009;130:044708. <https://doi.org/10.1063/1.3062842>
32. Silva-Junior MR, Schreiber M, Sauer SPA, Thiel W. Benchmarks for electronically excited states: Time-dependent density functional theory and density functional theory based multireference configuration interaction. *J Chem Phys*. 2008;129:104103. <https://doi.org/10.1063/1.2973541>
33. Lyskov I, Kleinschmidt M, Marian CM. Redesign of the DFT/MRCI Hamiltonian. *J Chem Phys*. 2016;144:034104. <https://doi.org/10.1063/1.4940036>
34. Heil A, Marian CM. DFT/MRCI Hamiltonian for odd and even numbers of electrons. *J Chem Phys*. 2017;147:194104. <https://doi.org/10.1063/1.5003246>
35. Heil A, Kleinschmidt M, Marian CM. On the performance of DFT/MRCI Hamiltonians for electronic excitations in transition metal complexes: The role of the damping function. *J Chem Phys*. 2018;149. <https://doi.org/10.1063/1.5050476>
36. Escudero D, Thiel W. Assessing the density functional theory-based multireference configuration interaction (DFT/MRCI) method for transition metal complexes. *J Chem Phys*. 2014;140:194105. <https://doi.org/10.1063/1.4875810>
37. Huzinaga S, Arnau C. Virtual orbitals in Hartree-Fock theory. *Phys Rev A*. 1970;1:1285–1288. <https://doi.org/10.1103/PhysRevA.1.1285>
38. Potts DM, Taylor CM, Chaudhuri RK, Freed KF. The improved virtual orbital-complete active space configuration interaction method, a “packageable” efficient *ab initio* many-body method for describing electronically excited states. *J Chem Phys*. 2001;114:2592–2600. <https://doi.org/10.1063/1.1337053>
39. Bender CF, Davidson ER. A natural orbital based energy calculation for helium hydride and lithium hydride. *J Phys Chem*. 1966;70:2675–2685. <https://doi.org/10.1021/j100880a036>
40. Thunemann KH, Römelt J, Peyerimhoff SD, Buenker RJ. A study of the convergence in iterative natural orbital procedures. *Int J Quantum Chem*. 1977;11:743–752. <https://doi.org/10.1002/qua.560110506>
41. Maganas D, DeBeer S, Neese F. Pair natural orbital restricted open-shell configuration interaction (PNO-ROCIS) approach for calculating X-ray absorption spectra of large chemical systems. *J Phys Chem A*. 2018;122:1215–1227. <https://doi.org/10.1021/acs.jpca.7b10880>
42. Hupp T, Engels B, Della Sala F, Görling A. Orbitals from a self-interaction free Kohn–Sham potential as a single electron basis for *ab initio* methods. *Chem Phys Lett*. 2002;360:175–181. [https://doi.org/10.1016/S0009-2614\(02\)00786-8](https://doi.org/10.1016/S0009-2614(02)00786-8)
43. Hupp T, Engels B. Advantages and limitations of Kohn–Sham orbitals as single electron basis for multireference configuration interaction and multireference perturbation theory. *J Chem Phys*. 2003;119:591–11 601. <https://doi.org/10.1063/1.1624593>
44. Goerigk L, Grimme S. Double-hybrid density functionals. *WIREs Comput Mol Sci*. 2014;4:576–600. <https://doi.org/10.1002/wcms.1193>
45. Klüner T, Govind N, Wang YA, Carter EA. Periodic density functional embedding theory for complete active space self-consistent field and configuration interaction calculations: Ground and excited states. *J Chem Phys*. 2002;116:42–54. <https://doi.org/10.1063/1.1420748>
46. Huang P, Carter EA. Advances in correlated electronic structure methods for solids, surfaces, and nanostructures. *Annu Rev Phys Chem*. 2008;59:261–290. <https://doi.org/10.1146/annurev.physchem.59.032607.093528>
47. Huang C, Pavone M, Carter EA. Quantum mechanical embedding theory based on a unique embedding potential. *J Chem Phys*. 2011;134:154110. <https://doi.org/10.1063/1.3577516>
48. Libisch F, Huang C, Carter EA. Embedded correlated wavefunction schemes: Theory and applications. *Acc Chem Res*. 2014;47:2768–2775. <https://doi.org/10.1021/ar500086h>
49. Manby FR, Stella M, Goodpaster JD, Miller TF. A simple, exact density-functional-theory embedding scheme. *J Chem Theory Comput*. 2012;8:2564–2568. <https://doi.org/10.1021/ct300544e>
50. Goodpaster JD, Barnes TA, Manby FR, Miller TF. Density functional theory embedding for correlated wavefunctions: Improved methods for open-shell systems and transition metal complexes. *J Chem Phys*. 2012;137:224113. <https://doi.org/10.1063/1.4770226>
51. Goodpaster JD, Barnes TA, Manby FR, Miller TF. Accurate and systematically improvable density functional theory embedding for correlated wavefunctions. *J Chem Phys*. 2014;140:18A507. <https://doi.org/10.1063/1.4864040>
52. Senn HM, Thiel W. QM/MM methods for biomolecular systems. *Angew Chem Int Ed*. 2009;48:1198–1229. <https://doi.org/10.1002/anie.200802019>
53. Boulanger E, Harvey JN. QM/MM methods for free energies and photochemistry. *Curr Opin Struct Biol*. 2018;49:72–76. <https://doi.org/10.1016/j.sbi.2018.01.003>
54. Chung LW, Sameera WMC, Ramozzi R, et al. The ONIOM method and its applications. *Chem Rev*. 2015;115:5678–5796. <https://doi.org/10.1021/cr5004419>
55. Wesolowski TA, Shedge S, Zhou X. Frozen-density embedding strategy for multilevel simulations of electronic structure. *Chem Rev*. 2015;115:5891–5928. <https://doi.org/10.1021/cr500502v>
56. Jacob CR, Neugebauer J. Subsystem density-functional theory. *WIREs Comput Mol Sci*. 2014;4:325–362. <https://doi.org/10.1002/wcms.1175>
57. Kraka E. Homolytic dissociation energies from GVB-LSDC calculations. *Chem Phys*. 1992;161:149–153. [https://doi.org/10.1016/0301-0104\(92\)80183-V](https://doi.org/10.1016/0301-0104(92)80183-V)
58. Kurzweil Y, Lawler KV, Head-Gordon M. Analysis of multi-configuration density functional theory methods: Theory and model application to bond-breaking. *Mol Phys*. 2009;107:2103–2110. <https://doi.org/10.1080/00268970903160597>
59. Miehl B, Stoll H, Savin A. A correlation-energy density functional for multideterminantal wavefunctions. *Mol Phys*. 1997;91:527–536. <https://doi.org/10.1080/002689797171418>

60. Gräfenstein J, Cremer D. The combination of density functional theory with multi-configuration methods – CAS-DFT. *Chem Phys Lett.* 2000;316:569–577. [https://doi.org/10.1016/S0009-2614\(99\)01326-3](https://doi.org/10.1016/S0009-2614(99)01326-3)
61. Pollet R, Savin A, Leininger T, Stoll H. Combining multideterminantal wave functions with density functionals to handle near-degeneracy in atoms and molecules. *J Chem Phys.* 2002;116:1250–1258. <https://doi.org/10.1063/1.1430739>
62. Stoll H. On the coupling of multi-configuration self-consistent-field and density-functional information. *Chem Phys Lett.* 2003;376:141–147. [https://doi.org/10.1016/S0009-2614\(03\)00908-4](https://doi.org/10.1016/S0009-2614(03)00908-4)
63. Takeda R, Yamanaka S, Yamaguchi K. CAS-DFT based on odd-electron density and radical density. *Chem Phys Lett.* 2002;366:321–328. [https://doi.org/10.1016/S0009-2614\(02\)01576-2](https://doi.org/10.1016/S0009-2614(02)01576-2)
64. Nakata K, Ukai T, Yamanaka S, Takada T, Yamaguchi K. CASSCF version of density functional theory. *Int J Quantum Chem.* 2006;106:3325–3333. <https://doi.org/10.1002/qua.21151>
65. Fromager E, Toulouse J, Jensen HJA. On the universality of the long-/short-range separation in multiconfigurational density-functional theory. *J Chem Phys.* 2007;126:047111 doi:10.1063/1.2566459.
66. Dong G, Ryde U, Jensen HJA, Hedegård ED. Exploration of H₂ binding to the [NiFe]-hydrogenase active site with multiconfigurational density functional theory. *Phys Chem Chem Phys.* 2018;20:794–801. <https://doi.org/10.1039/C7CP06767D>
67. Li Manni G, Carlson RK, Luo S, et al. Multiconfiguration pair-density functional theory. *J Chem Theory Comput.* 2014;10:3669–3680. <https://doi.org/10.1021/ct500483t>
68. Gagliardi L, Truhlar DG, Li Manni G, Carlson RK, Hoyer CE, Bao JL. Multiconfiguration pair-density functional theory: A new way to treat strongly correlated systems. *Acc Chem Res.* 2017;50:66–73. <https://doi.org/10.1021/acs.accounts.6b00471>
69. Sharma P, Truhlar DG, Gagliardi L. Active space dependence in multiconfiguration pair-density functional theory. *J Chem Theory Comput.* 2018;14:660–669. <https://doi.org/10.1021/acs.jctc.7b01052>
70. Fromager E, Knecht S, Jensen HJA. Multi-configuration time-dependent density-functional theory based on range separation. *J Chem Phys.* 2013;138:084101. <https://doi.org/10.1063/1.4792199>
71. Stoll, H. and Savin, A. (1985) *Density Functionals for correlation energies of atoms and molecules*, Plenum, New York, pp 177–207, doi:https://doi.org/10.1007/978-1-4757-0818-9_7
72. Perdew JP, Savin A, Burke K. Escaping the symmetry dilemma through a pair-density interpretation of spin-density functional theory. *Phys Rev A.* 1995;51:4531–4541. <https://doi.org/10.1103/PhysRevA.51.4531>
73. Becke AD, Savin A, Stoll H. Extension of the local-spin-density exchange-correlation approximation to multiplet states. *Theor Chim Acta.* 1995;91:147–156. <https://doi.org/10.1007/BF01114982>
74. Perdew JP, Ernzerhof M, Burke K, Savin A. On-top pair-density interpretation of spin density functional theory with applications to magnetism. *Int J Quantum Chem.* 1997;61:197–205. [https://doi.org/10.1002/\(SICI\)1097-461X\(1997\)61:2<197::AID-QUA2>3.0.CO;2-R](https://doi.org/10.1002/(SICI)1097-461X(1997)61:2<197::AID-QUA2>3.0.CO;2-R)
75. Pérez-Jiménez ÁJ, Pérez-Jordá JM. Combining multiconfigurational wave functions with correlation density functionals: A size-consistent method based on natural orbitals and occupation numbers. *Phys Rev A.* 2007;75(012):503. <https://doi.org/10.1103/PhysRevA.75.012503>
76. Gusarov S, Malmqvist PÅ, Lindh R, Roos BO. Correlation potentials for a multiconfigurational-based density functional theory with exact exchange. *Theor Chem Acc.* 2004;112:84–94. <https://doi.org/10.1007/s00214-004-0568-1>
77. Savin A, Flad HJ. Density functionals for the Yukawa electron-electron interaction. *Int J Quantum Chem.* 1995;56:327–332. <https://doi.org/10.1002/qua.560560417>
78. Sharkas K, Savin A, Jensen HJA, Toulouse J. A multiconfigurational hybrid density-functional theory. *J Chem Phys.* 2012;137:044104. <https://doi.org/10.1063/1.4733672>
79. Hedegård ED, Toulouse J, Jensen HJA. Multiconfigurational short-range density-functional theory for open-shell systems. *J Chem Phys.* 2018;148:214103. <https://doi.org/10.1063/1.5013306>
80. Hedegård ED, Heiden F, Knecht S, Fromager E, Jensen HJA. Assessment of charge-transfer excitations with time-dependent, range-separated density functional theory based on long-range MP2 and multiconfigurational self-consistent field wave functions. *J Chem Phys.* 2013;139:184308.
81. Hedegård ED, Knecht S, Kielberg JS, Jensen HJA, Reiher M. Density matrix renormalization group with efficient dynamical electron correlation through range separation. *J Chem Phys.* 2015;142:224108. <https://doi.org/10.1063/1.4922295>
82. Wetmore RW, Segal GA. Efficient generation of configuration interaction matrix elements. *Chem Phys Lett.* 1975;36:478–483. [https://doi.org/10.1016/0009-2614\(75\)80284-3](https://doi.org/10.1016/0009-2614(75)80284-3)
83. Segal GA, Wetmore RW, Wolf K. Efficient methods for configuration interaction calculations. *Chem Phys.* 1978;30:269–297. [https://doi.org/10.1016/0301-0104\(78\)85124-6](https://doi.org/10.1016/0301-0104(78)85124-6)
84. Filatov M, Shaik S. Spin-restricted density functional approach to the open-shell problem. *Chem Phys Lett.* 1998;288(5):689–697. [https://doi.org/10.1016/S0009-2614\(98\)00364-9](https://doi.org/10.1016/S0009-2614(98)00364-9)
85. Roemelt M, Maganas D, DeBeer S, Neese F. A combined DFT and restricted open-shell configuration interaction method including spin-orbit coupling: Application to transition metal L-edge X-ray absorption spectroscopy. *J Chem Phys.* 2013;138:204101. <https://doi.org/10.1063/1.4804607>
86. Becke AD. A new mixing of Hartree-Fock and local density-functional theories. *J Chem Phys.* 1993;98:1372–1377. <https://doi.org/10.1063/1.464304>
87. Lee C, Yang W, Parr RG. Development of the Colle-Salvetti correlation-energy formula into a functional of the electron density. *Phys Rev B.* 1988;37:785–789. <https://doi.org/10.1103/PhysRevB.37.785>
88. Spiegel JD, Lyskov I, Kleinschmidt M, Marian CM. Charge-transfer contributions to the excitonic coupling matrix element in BODIPY-based energy transfer casettes. *Chem Phys.* 2017;482:265–276. <https://doi.org/10.1016/j.chemphys.2016.10.004>
89. Schreiber M, Silva-Junior MR, Sauer SPA, Thiel W. Benchmarks for electronically excited states: CASPT2, CC2, CCSD, and CC3. *J Chem Phys.* 2008;128:134110. <https://doi.org/10.1063/1.2889385>
90. Ghigo G, Roos BO, Malmqvist PÅ. A modified definition of the zeroth-order hamiltonian in multiconfigurational perturbation theory (CASPT2). *Chem Phys Lett.* 2004;396:142–149. <https://doi.org/10.1016/j.cplett.2004.08.032>
91. Kerridge A. A RASSCF study of free base, magnesium and zinc porphyrins: Accuracy versus efficiency. *Phys Chem Chem Phys.* 2013;15:2197–2209. <https://doi.org/10.1039/C2CP43982D>
92. Ben Amor N, Soupart A, Heitz MC. Methodological CASPT2 study of the valence excited states of an iron-porphyrin complex. *J Mol Model.* 2017;23:53. <https://doi.org/10.1007/s00894-017-3226-y>
93. Gouterman M, Wagnière GH, Snyder LC. Spectra of porphyrins: Part II. Four orbital model. *J Mol Spectrosc.* 1963;11:108–127. [https://doi.org/10.1016/0022-2852\(63\)90011-0](https://doi.org/10.1016/0022-2852(63)90011-0)
94. Parusel ABJ, Grimme S. DFT/MRCI calculations on the excited states of porphyrin, hydroporphyrins, tetraporphyrins and metalloporphyrins. *J Porphyr Phthalocya.* 2001;05:225–232. <https://doi.org/10.1002/jpp.310>
95. Parusel ABJ, Grimme S. A theoretical study of the excited states of chlorophyll *a* and pheophytin *a*. *J Phys Chem B.* 2000;104:5395–5398. <https://doi.org/10.1021/jp000346w>

96. Etinski M, Tatchen J, Marian CM. Thermal and solvent effects on the triplet formation in cinnoline. *Phys Chem Chem Phys*. 2014;16:4740–4751. <https://doi.org/10.1039/C3CP53247J>
97. Perun S, Tatchen J, Marian CM. Singlet and triplet excited states and intersystem crossing in free-base porphyrin: TDDFT and DFT/MRCI study. *Chem Phys Chem*. 2008;9:282–292. <https://doi.org/10.1002/cphc.200700509>
98. Loboda O, Tunell I, Minaev B, Ågren H. Theoretical study of triplet state properties of free-base porphyrin. *Chem Phys*. 2005;312:299–309. <https://doi.org/10.1016/j.chemphys.2004.11.041>
99. Fritsch C, Goerz G, Ruzicka T. Photodynamic therapy in dermatology. *Arch Dermatol*. 1998;134:207–214. <https://doi.org/10.1001/archderm.134.2.207>
100. Ostroumov E, Müller MG, Marian CM, Kleinschmidt M, Holzwarth AR. Electronic coherence provides a direct proof for energy-level crossing in photoexcited lutein and β -carotene. *Phys Rev Lett*. 2009;103(108):302. <https://doi.org/10.1103/PhysRevLett.103.108302>
101. Parac M, Grimme S. A TDDFT study of the lowest excitation energies of polycyclic aromatic hydrocarbons. *Chem Phys*. 2003;292:11–21.
102. Brand C, Küpper J, Pratt DW, et al. Vibronic coupling in indole: I. theoretical description of the 1L_a – 1L_b interaction and the electronic spectrum. *Phys Chem Chem Phys*. 2010;12:4968–4979. <https://doi.org/10.1039/C001776K>
103. Küpper J, Pratt DW, Leo Meerts W, Brand C, Tatchen J, Schmitt M. Vibronic coupling in indole: II. Investigation of the 1L_a – 1L_b interaction using rotationally resolved electronic spectroscopy. *Phys Chem Chem Phys*. 2010;12:4980–4988. <https://doi.org/10.1039/C001778G>
104. Ghisaidoobe ABT, Chung SJ. Intrinsic tryptophan fluorescence in the detection and analysis of proteins: A focus on Förster resonance energy transfer techniques. *Int J Mol Sci*. 2014;15:22518–22538. <https://doi.org/10.3390/ijms15122518>
105. Schmitt M, Brause R, Marian CM, Salzmann S, Meerts WL. Electronically excited states of tryptamine and its microhydrated complex. *J Chem Phys*. 2006;125:309. <https://doi.org/10.1063/1.2354494>
106. Improtà R, Santoro F, Blancafort L. Quantum mechanical studies on the photophysics and the photochemistry of nucleic acids and nucleobases. *Chem Rev*. 2016;116:3540–3593. <https://doi.org/10.1021/acs.chemrev.5b00444>
107. Marian C, Schneider F, Kleinschmidt M, Tatchen J. Electronic excitation and singlet-triplet coupling in uracil tautomers and uracil-water complexes. *Eur Phys J D*. 2002;20:357–367. <https://doi.org/10.1140/epjd/e2002-00158-3>
108. Marian CM. A new pathway for the rapid decay of electronically excited adenine. *J Chem Phys*. 2005;122:104314. <https://doi.org/10.1063/1.1861452>
109. Tomić K, Tatchen J, Marian CM. Quantum chemical investigation of the electronic spectra of the keto, enol, and keto–imine tautomers of cytosine. *J Phys Chem A*. 2005;109:8410–8418. <https://doi.org/10.1021/jp051510o>
110. Marian CM. The guanine tautomer puzzle: Quantum chemical investigation of ground and excited states. *J Phys Chem A*. 2007;111:1545–1553. <https://doi.org/10.1021/jp068620v>
111. Etinski M, Fleig T, Marian CM. Intersystem crossing and characterization of dark states in the pyrimidine nucleobases uracil, thymine, and 1-methylthymine. *J Phys Chem A*. 2009;113:11809–11816. <https://doi.org/10.1021/jp902944a>
112. Parac M, Doerr M, Marian CM, Thiel W. QM/MM calculation of solvent effects on absorption spectra of guanine. *J Comput Chem*. 2009;31:90–106. <https://doi.org/10.1002/jcc.21233>
113. Lan Z, Lu Y, Fabiano E, Thiel W. QM/MM nonadiabatic decay dynamics of 9H-adenine in aqueous solution. *ChemPhysChem*. 2011;12:1989–1998. <https://doi.org/10.1002/cphc.201001054>
114. Rai-Constapel V, Etinski M, Marian CM. Photophysics of xanthone: A quantum chemical perusal. *J Phys Chem A*. 2013;117:3935–3944. <https://doi.org/10.1021/jp401755j>
115. Rai-Constapel V, Salzmann S, Marian CM. Isolated and solvated thioxanthone: A photophysical study. *J Phys Chem A*. 2011;115:8589–8596. <https://doi.org/10.1021/jp2022456>
116. Villnow T, Ryseck G, Rai-Constapel V, Marian CM, Gilch P. Chimeric behavior of excited thioxanthone in protic solvents: I. experiments. *J Phys Chem A*. 2014;118:11696–11707. [doi:10.1021/jp5099393](https://doi.org/10.1021/jp5099393)
117. Rai-Constapel V, Villnow T, Ryseck G, Gilch P, Marian CM. Chimeric behavior of excited thioxanthone in protic solvents: II. Theory. *J Phys Chem A*. 2014;118(11):708–11 717. <https://doi.org/10.1021/jp5099415>
118. Mundt R, Villnow T, Ziegenbein CT, Gilch P, Marian CM, Rai-Constapel V. Thioxanthone in apolar solvents: Ultrafast internal conversion precedes fast intersystem crossing. *Phys Chem Chem Phys*. 2016;18:6637–6647. <https://doi.org/10.1039/c5cp06849e>
119. Salzmann S, Tatchen J, Marian CM. The photophysics of flavins: What makes the difference between gas phase and aqueous solution? *J Photochem Photobiol A*. 2008;198:221–231. <https://doi.org/10.1016/j.jphotochem.2008.03.015>
120. Salzmann S, Martinez-Junza V, Zorn B, et al. Photophysical properties of structurally and electronically modified flavin derivatives determined by spectroscopy and theoretical calculations. *J Phys Chem A*. 2009;113:9365–9375. <https://doi.org/10.1021/jp905724b>
121. Marian CM, Nakagawa S, Rai-Constapel V, Karasulu B, Thiel W. Photophysics of flavin derivatives absorbing in the blue-green region: Thioflavins as potential cofactors of photoswitches. *J Phys Chem B*. 2014;118(7):1743–1753. <https://doi.org/10.1021/jp4098233>
122. Karasulu B, Thiel W. Photoinduced intramolecular charge transfer in an electronically modified flavin derivative: Roseoflavin. *J Phys Chem B*. 2015;119:928–943. <https://doi.org/10.1021/jp506101x>
123. Salzmann S, Silva-Junior MR, Thiel W, Marian CM. Influence of the LOV domain on low-lying excited states of flavin: A combined quantum-mechanics/molecular-mechanics investigation. *J Phys Chem B*. 2009;113:15610–15618. <https://doi.org/10.1021/jp905599k>
124. Silva-Junior MR, Mansurova M, Gärtner W, Thiel W. Photophysics of structurally modified flavin derivatives in the blue-light photoreceptor ytvA: A combined experimental and theoretical study. *ChemBiochem*. 2013;14:1648–1661. <https://doi.org/10.1002/cbic.201300217>
125. Nakagawa S, Weingart O, Marian CM. Dual photochemical reaction pathway in flavin-based photoreceptor LOV domain: A combined quantum-mechanics/molecular-mechanics investigation. *J Phys Chem B*. 2017;121:9583–9596. <https://doi.org/10.1021/acs.jpcc.7b09207>
126. Dreuw A, Head-Gordon M. Single-reference ab initio methods for the calculation of excited states of large molecules. *Chem Rev*. 2005;105:4009–4037. <https://doi.org/10.1021/cr0505627>
127. Polívka T, Sundström V. Ultrafast dynamics of carotenoid excited states—from solution to natural and artificial systems. *Chem Rev*. 2004;104:2021–2072. <https://doi.org/10.1021/cr020674n>
128. Middleton CT, de La Harpe K, Su C, Law YK, Crespo-Hernández CE, Kohler B. DNA excited-state dynamics: From single bases to the double helix. *Annu Rev Phys Chem*. 2009;60:217–239. <https://doi.org/10.1146/annurev.physchem.59.032607.093719>
129. Smith MB, Michl J. Singlet fission. *Chem Rev*. 2010;110:6891–6936. <https://doi.org/10.1021/cr1002613>
130. Casanova D. Theoretical modeling of singlet fission. *Chem Rev*. 2018;118:7164–7207. <https://doi.org/10.1021/acs.chemrev.7b00601>
131. Singh-Rachford TN, Castellano FN. Photon upconversion based on sensitized triplet–triplet annihilation. *Coord Chem Rev*. 2010;254:2560–2573. <https://doi.org/10.1016/j.ccr.2010.01.003>
132. Adachi C. Third-generation organic electroluminescence materials. *Jpn J Appl Phys*. 2014;53:060101. <https://doi.org/10.7567/JJAP.53.060101>
133. Yang Z, Mao Z, Xie Z, et al. Recent advances in organic thermally activated delayed fluorescence materials. *Chem Soc Rev*. 2017;46:915–1016. <https://doi.org/10.1039/C6CS00368K>

134. Bui TT, Goubard F, Ibrahim-Ouali M, Gignes D, Dumur F. Recent advances on organic blue thermally activated delayed fluorescence (TADF) emitters for organic light-emitting diodes (OLEDs). *Beilstein J Org Chem*. 2018;14:282–308. <https://doi.org/10.3762/bjoc.14.18>
135. Yersin H. (Ed.) *Highly efficient OLEDs: Materials based on thermally activated delayed fluorescence*. Weinheim: Wiley VCH, 2018.
136. Marian CM. Mechanism of the triplet-to-singlet upconversion in the assistant dopant ACRXTN. *J Phys Chem C*. 2016;120:3715–3721. <https://doi.org/10.1021/acs.jpcc.6b00060>
137. Lyskov I, Marian CM. Climbing up the ladder: Intermediate triplet states promote the reverse intersystem crossing in the efficient TADF emitter ACRSA. *J Phys Chem C*. 2017;121:21145–21153. <https://doi.org/10.1021/acs.jpcc.7b06187>
138. Elfers N, Lyskov I, Spiegel JD, Marian CM. Singlet fission in quinoidal oligothiophenes. *J Phys Chem C*. 2016;120:13901–13910. <https://doi.org/10.1021/acs.jpcc.6b02263>
139. Penfold TJ, Gindensperger E, Daniel C, Marian CM. Spin-vibronic mechanism for intersystem crossing. *Chem Rev*. 2018;118:6975–7025. <https://doi.org/10.1021/acs.chemrev.7b00617>
140. Grimme S, Antony J, Ehrlich S, Krieg H. A consistent and accurate ab initio parametrization of density functional dispersion correction (DFT-D) for the 94 elements H–Pu. *J Chem Phys*. 2010;132:154104. <https://doi.org/10.1063/1.3382344>
141. Grimme S. Density functional theory with London dispersion corrections. *WIREs Comput Mol Sci*. 2011;1:211–228. <https://doi.org/10.1002/wcms.30>
142. Jovanović V, Lyskov I, Kleinschmidt M, Marian CM. On the performance of DFT/MRCI-R and MR-MP2 in spin-orbit coupling calculations on diatomics and polyatomic organic molecules. *Mol Phys*. 2017;115:109–137. <https://doi.org/10.1080/00268976.2016.1201600>
143. Karcia G, Papagiorgis P, Panagi N, et al. Emission from the stable Blatter radical. *New J Chem*. 2017;41:8604–8613. <https://doi.org/10.1039/C7NJ00677B>
144. Blatter HM, Lukaszewski H. A new stable free radical. *Tetrahedron Lett*. 1968;9:2701–2705. [https://doi.org/10.1016/S0040-4039\(00\)89678-1](https://doi.org/10.1016/S0040-4039(00)89678-1)
145. Ciccullo F, Gallagher NM, Geladari O, Chassé T, Rajca A, Casu MB. A derivative of the Blatter radical as a potential metal-free magnet for stable thin films and interfaces. *ACS Appl Mater Interfaces*. 2016;8:1805–1812. <https://doi.org/10.1021/acsmi.5b09693>
146. Miertuš S, Scrocco E, Tomasi J. Electrostatic interaction of a solute with a continuum. A direct utilization of ab initio molecular potentials for the prevision of solvent effects. *Chem Phys*. 1981;55:117–129. [https://doi.org/10.1016/0301-0104\(81\)85090-2](https://doi.org/10.1016/0301-0104(81)85090-2)
147. Wenthold PG, Kim JB, Lineberger WC. Photoelectron spectroscopy of m-xylylene anion. *J Am Chem Soc*. 1997;119:1354–1359. <https://doi.org/10.1021/ja9623830>
148. Lineberger CW, Borden WT. The synergy between qualitative theory, quantitative calculations, and direct experiments in understanding, calculating, and measuring the energy differences between the lowest singlet and triplet states of organic diradicals. *Phys Chem Chem Phys*. 2011;13:11792–11813. <https://doi.org/10.1039/C0CP02786C>
149. Mañeru DR, Pal AK, Moreira IdPR, Datta SN, Illas F. The triplet-singlet gap in the m-xylylene radical: A not so simple one. *J Chem Theory Comput*. 2014;10:335–345. <https://doi.org/10.1021/ct400883m>
150. Schäfer A, Horn H, Ahlrichs R. Fully optimized contracted Gaussian basis sets for atoms Li to Kr. *J Chem Phys*. 1992;97:2571–2577. <https://doi.org/10.1063/1.463096>
151. Best SP, Clark RJ. The identification of an electronic Raman transition for the hexa-aquavanadium(III) ion. A direct spectroscopic determination of the trigonal field splitting of the ${}^3T_{1g}$ ground term. *Chem Phys Lett*. 1985;122:401–405. [https://doi.org/10.1016/0009-2614\(85\)80245-1](https://doi.org/10.1016/0009-2614(85)80245-1)
152. Johnson DA, Nelson PG. Ligand field stabilization energies of the hexaaqua 3+ complexes of the first transition series. *Inorg Chem*. 1999;38:4949–4955. <https://doi.org/10.1021/ic990426i>
153. Springer A. Validierung der DFT/MRCI-Methode für Übergangsmetallkomplexe [Master's thesis]. Heinrich-Heine Universität Düsseldorf; 2016. Available from: <http://www.theochem.hhu.de> (as of 2018)
154. Perdew JP, Burke K, Ernzerhof M. Generalized gradient approximation made simple. *Phys Rev Lett*. 1996;77:3865–3868. <https://doi.org/10.1103/PhysRevLett.77.3865>
155. Adamo C, Barone V. Toward reliable density functional methods without adjustable parameters: The PBE0 model. *J Chem Phys*. 1999;110:6158–6170. <https://doi.org/10.1063/1.478522>
156. Kleinschmidt M, van Wüllen C, Marian CM. Intersystem-crossing and phosphorescence rates in fac-Ir^{III}(ppy)₃: A theoretical study involving multi-reference configuration interaction wavefunctions. *J Chem Phys*. 2015;142:094301. <https://doi.org/10.1063/1.4913513>
157. Heil A, Gollnisch K, Kleinschmidt M, Marian CM. On the photophysics of four heteroleptic iridium(III) phenylpyridyl complexes investigated by relativistic multi-configuration methods. *Mol Phys*. 2016;114:407–422. <https://doi.org/10.1080/00268976.2015.1076902>
158. Lamansky S, Djurovich P, Murphy D, et al. Synthesis and characterization of phosphorescent cyclometalated iridium complexes. *Inorg Chem*. 2001;40:1704–1711. <https://doi.org/10.1021/ic0008969>
159. Liu Z, Nie D, Bian Z, et al. Photophysical properties of heteroleptic iridium complexes containing carbazole-functionalized β -diketonates. *ChemPhysChem*. 2008;9:634–640. <https://doi.org/10.1002/cphc.200700648>
160. Yersin H, Rausch AF, Czerniowiec R, Hofbeck T, Fischer T. The triplet state of organo-transition metal compounds. Triplet harvesting and singlet harvesting for efficient OLEDs. *Coord Chem Rev*. 2011;255:2622–2652. <https://doi.org/10.1016/j.ccr.2011.01.042>
161. Sohn YS, Hendrickson N, Gray HB. Electronic structure of metallocenes. *J Am Chem Soc*. 1971;93:3603–3612. <https://doi.org/10.1021/ja00744a011>
162. Föllner J, Kleinschmidt M, Marian CM. Phosphorescence or thermally activated delayed fluorescence? Intersystem crossing and radiative rate constants of a three-coordinate copper(I) complex determined by quantum-chemical methods. *Inorg Chem*. 2016;55:7508–7516. <https://doi.org/10.1021/acs.inorgchem.6b00818>
163. Föllner J, Marian CM. Rotationally assisted spin-state inversion in carbene-metal-amides is an artifact. *J Phys Chem Lett*. 2017;8:5643–5647. <https://doi.org/10.1063/1.5003246>
164. Krylova VA, Djurovich PI, Conley BL, et al. Control of emission colour with N-heterocyclic carbene (NHC) ligands in phosphorescent three-coordinate Cu(I) complexes. *Chem Commun*. 2014;50:7176–7179. <https://doi.org/10.1039/C4CC02037E>
165. Escudero D, Jacquemin D. Computational insights into the photodeactivation dynamics of phosphors for OLEDs: A perspective. *Dalton Trans*. 2015;44:8346–8355. <https://doi.org/10.1039/C4DT03804E>
166. Jacquemin D, Escudero D. Thermal equilibration between excited states or solvent effects: Unveiling the origins of anomalous emissions in heteroleptic Ru(II) complexes. *Phys Chem Chem Phys*. 2018;20:11559–11563. <https://doi.org/10.1039/C8CP01101J>
167. Spiegel JD, Kleinschmidt M, Larbig A, Tatchen J, Marian CM. Quantum-chemical studies on excitation energy transfer processes in BODIPY-based donor-acceptor systems. *J Chem Theory Comput*. 2015;11:4316–4327. <https://doi.org/10.1021/acs.jctc.5b00501>
168. Spiegel JD, Fulle S, Kleinschmidt M, Gohlke H, Marian CM. Failure of the IDA in FRET systems at close inter-dye distances is moderated by frequent low κ^2 values. *J Phys Chem B*. 2016;120:8845–8862. <https://doi.org/10.1021/acs.jpbc.6b05754>
169. Diedrich C, Grimme S. Systematic investigation of modern quantum chemical methods to predict electronic circular dichroism spectra. *J Phys Chem A*. 2003;107:2524–2539. <https://doi.org/10.1021/jp0275802>
170. Marian CM. Spin-orbit coupling and intersystem crossing in molecules. *WIREs Comput Mol Sci*. 2012;2:187–203. <https://doi.org/10.1002/wcms.83>
171. Tatchen J, Kleinschmidt M, Marian CM. Calculating electron paramagnetic resonance g-matrices for triplet state molecules from multireference spin-orbit configuration interaction wave functions. *J Chem Phys*. 2009;130:154106. <https://doi.org/10.1063/1.3115965>

172. Ganyushin D, Gilka N, Taylor PR, Marian CM, Neese F. The resolution of the identity approximation for calculations of spin-spin contribution to zero-field splitting parameters. *J Chem Phys.* 2010;132:144111. <https://doi.org/10.1063/1.3367718>
173. TURBOMOLE. *A development of University of Karlsruhe and Forschungszentrum Karlsruhe GmbH, 1989-2007.* TURBOMOLE GmbH, Karlsruhe, 2007 Available from: <http://www.turbomole.com>
174. Neese F. The ORCA program system. *WIREs Comput Mol Sci.* 2012;2:73–78. <https://doi.org/10.1002/wcms.81>
175. Neese F. Software update: The ORCA program system, version 4.0. *WIREs Comput Mol Sci.* 2017;8:e1327. <https://doi.org/10.1002/wcms.1327>
176. Aidas K, Angeli C, Bak KL, et al. The Dalton quantum chemistry program system. *WIREs Comput Mol Sci.* 2016;4:269–284. <https://doi.org/10.1002/wcms.1172>
177. Vahtras O, Almlöf J, Feyereisen M. Integral approximations for LCAO-SCF calculations. *Chem Phys Lett.* 1993;213:514–518. [https://doi.org/10.1016/0009-2614\(93\)89151-7](https://doi.org/10.1016/0009-2614(93)89151-7)
178. Weigend F, Häser M, Patzelt H, Ahlrichs R. RI-MP2: Optimized auxiliary basis sets and demonstration of efficiency. *Chem Phys Lett.* 1998;294:143–152. [https://doi.org/10.1016/S0009-2614\(98\)00862-8](https://doi.org/10.1016/S0009-2614(98)00862-8)
179. Hellweg A, Rappoport D. Development of new auxiliary basis functions of the Karlsruhe segmented contracted basis sets including diffuse basis functions (def2-SVPD, def2-TZVPPD, and def2-QVPPD) for RI-MP2 and RI-CC calculations. *Phys Chem Chem Phys.* 2015;17:1010–1017. <https://doi.org/10.1039/c4cp04286g>
180. Davidson ER. The iterative calculation of a few of the lowest eigenvalues and corresponding eigenvectors of large real-symmetric matrices. *J Comput Phys.* 1975;17:37–94. [https://doi.org/10.1016/0021-9991\(75\)90065-0](https://doi.org/10.1016/0021-9991(75)90065-0)
181. Liu B. *Numerical algorithms in Chemistry Algebraic methods. [Workshop, August 9–11, 1978].* Berkeley, CA: Lawrence Berkeley National Laboratory, 1978.
182. Pohler L, Kleinschmidt M, Etinski M, Marian CM. In search of the dark state of 5-methyl-2-hydroxypyrimidine using a numerical DFT/MRCI gradient. *Mol Phys.* 2012;110:2429–2438. doi:10.1080/00268976.2012.695030.
183. Ahlrichs R, Bär M, Häser M, Horn H, Kölmel C. Electronic structure calculations on workstation computers: The program system Turbomole. *Chem Phys Lett.* 1989;162:165–169. [https://doi.org/10.1016/0009-2614\(89\)85118-8](https://doi.org/10.1016/0009-2614(89)85118-8)
184. von Arnim M, Ahlrichs R. Performance of parallel TURBOMOLE for density functional calculations. *J Comput Chem.* 1998;19:1746–1757. [https://doi.org/10.1002/\(SICI\)1096-987X\(19981130\)19:15\(1746::AID-JCC7\)3.0.CO;2-N](https://doi.org/10.1002/(SICI)1096-987X(19981130)19:15(1746::AID-JCC7)3.0.CO;2-N)
185. The DFT/MRCI program; 2018. Available from: <http://www.theochem.hhu.de> (as of 2018)

How to cite this article: Marian CM, Heil A, Kleinschmidt M. The DFT/MRCI method. *WIREs Comput Mol Sci.* 2019;9:e1394. <https://doi.org/10.1002/wcms.1394>

DOI: 10.1002/wcms.1437

CORRIGENDUM**WILEY**

The DFT/MRCI method

In Marian et al.,¹ typographical errors have been published in Equations (14) and (21).

Equation (14) was mistakenly referring to the created electrons in the second sum over the orbital energies. The correct Equation (14) is presented below:

$$\begin{aligned} \langle \omega w | \hat{\mathcal{H}}^{\text{DFT}} - E^{\text{DFT}} | \omega w \rangle = & \langle \omega w | \hat{\mathcal{H}} - E^{\text{HF}} | \omega w \rangle - \sum_{i \in c}^{n_{\text{exc}}} (F_{ii}^{\text{HF}} - F_{ii}^{\text{KS}}) \\ & + \sum_{i \in a}^{n_{\text{exc}}} (F_{ii}^{\text{HF}} - F_{ii}^{\text{KS}}) + \Delta E_{\text{coul}} - \Delta E_{\text{exch}} \end{aligned} \quad (14)$$

Equation (21) was missing a factor of 1/2 in the second and third terms of the last line. The correct Equation (21) is presented below:

$$\begin{aligned} \Delta E_{\text{coul}}^{\text{red}} - \Delta E_{\text{exch}}^{\text{red}} = & p_J \left(- \sum_{\substack{i,j \in c \\ i > j}}^{n_{\text{exc}}} V_{ijj} - \sum_{\substack{i,j \in a \\ i > j}}^{n_{\text{exc}}} V_{ijj} + \sum_{i \in c}^{n_{\text{exc}}} \sum_{j \in a}^{n_{\text{exc}}} V_{ijj} + \sum_{i \in s}^{n_{\text{single}}} \frac{1}{2} V_{iii} | \Delta w_i | \right) \\ & - p_X \left(\frac{1}{2} \sum_{i \in c}^{n_{\text{exc}}} \sum_{j \in a}^{n_{\text{exc}}} V_{ijj} - \frac{1}{2} \sum_{\substack{i \in c \\ j \in c,s}}^{n_{\text{exc}}} V_{ijj} - \frac{1}{2} \sum_{\substack{i \in a \\ j \in a,s}}^{n_{\text{exc}}} V_{ijj} + \sum_{\substack{i,j \in o \\ i > j}}^{N_o} V_{ijj} \eta_{ij}^i \right) \end{aligned} \quad (21)$$

An additional change involves the notation of the indices in the second and third terms of the last line of Equation (21) to accentuate that the index j is addressing created (second term) or annihilated (third term) electrons in an orbital s that is singly occupied in the anchor configuration.

Both errors in Equations (14) and (21) are typos in the equations. All published results are unaffected since the Hamiltonian has been implemented correctly.

We apologize for these errors.

REFERENCE


1. Marian CM, Heil A, Kleinschmidt M. The DFT/MRCI method. *WIREs Comput Mol Sci*. 2019;9:e1394. <https://doi.org/10.1002/wcms.1394>.

Reprinted with permission from [134]. Copyright 2019 American Chemical Society.

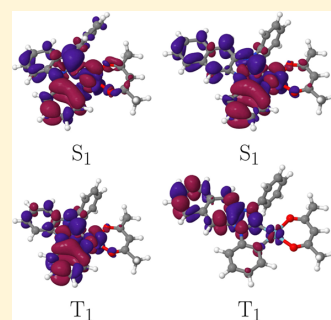
Structure–Emission Property Relationships in Cyclometalated Pt(II) β -Diketonate Complexes

Adrian Heil and Christel M. Marian*[✉]

Institut für Theoretische Chemie und Computerchemie, Heinrich-Heine-Universität Düsseldorf, Universitätsstr. 1, D-40225 Düsseldorf, Germany

 Supporting Information

ABSTRACT: Extending the ligand π -system of phosphorescent ($C^{\wedge}C^*$) or ($C^{\wedge}N$) cyclometalated platinum(II) β -diketonate complexes can lead to large and seemingly abrupt variations of the photophysical properties such as triplet quantum yields and phosphorescence lifetimes. Quantum chemical studies using methods including elements from density functional theory (DFT) and multireference configuration interaction (MRCI) as well as spin–orbit coupling (SOC) provide a rationale for these observations. In the Franck–Condon region, the first excited singlet states (S_1) of these complexes are characterized by mixed metal-to-ligand charge-transfer (MLCT) and ligand-centered (LC) excitations. With increasing extension of the effective π -system, the lowest-lying triplet state yields more and more LC character, thus leading to a decrease of the phosphorescence rate constant. The ability to undergo efficient intersystem crossing from S_1 to T_1 is not diminished as the S_1 state largely retains its character. In the N-heterocyclic carbene (NHC) complexes investigated here, at least two triplet states are found energetically below the S_1 state. Out-of-plane distortion enhances the probability for nonradiative decay of the triplet population. In the smaller compounds emitting in the violet or blue spectral region, the phosphorescent state is separated from the lowest-lying dark metal-centered (MC) triplet state by a small barrier only, explaining their experimentally observed low photoluminescence quantum yields in liquid solution. The semiempirical DFT/MRCI-R2018 Hamiltonian employed in our studies proves well-suited for investigating the absorption and emission properties of these platinum(II) complexes. Generally, good agreement is observed between our calculated data and the experimental findings.



INTRODUCTION

Phosphorescent platinum complexes have been employed as emitters in electroluminescent devices for approximately two decades.^{1–8} The recombination of holes and electrons in organic light-emitting diodes (OLEDs) generates singlet and triplet excited states with a ratio of 25% and 75%, respectively. To achieve 100% internal quantum yield, singlet as well as triplet excitons must be harvested for luminescence. In OLEDs based on phosphorescent dopants (PhOLEDs), excited singlet states typically undergo fast intersystem crossing to lower-lying triplet states at a rate that outcompetes fluorescence and internal conversion to the electronic ground state. The limited photostability of present-day PhOLEDs continues to put pressing challenges before researchers to develop efficient and stable deep-blue phosphors with sufficiently long operational lifetime to make technical application meaningful.⁷

Optimal conditions for the use of Pt(II) complexes as electroluminescent dopants in PhOLEDs are—besides photostability and color purity—high triplet quantum yields and fast phosphorescence with radiative lifetimes of a few microseconds at most. In this way, chances are high that phosphorescence outcompetes nonradiative triplet decay processes.² One necessary condition for achieving this goal is well-dosed spin–orbit coupling (SOC) of the lowest triplet to the singlet

manifold. Incorporation of a heavy metal atom is not a guarantee for this condition to be fulfilled, however. Many iridium and platinum complexes are known with low phosphorescence quantum yields at room temperature (RT). In some of them, a metal-centered (MC) dd^* excited triplet state can be reached that deactivates quickly to the electronic ground state,^{9–12} or even worse, leads to bond cleavage¹³—a common reason for the instability of PhOLEDs, in particular of those emitting in the blue spectral region. Other iridium and platinum complexes exhibit ligand-centered (LC) T_1 – S_0 transitions and, hence, too small SOC to make the spin-forbidden radiative transition really efficient.^{14,15} Furthermore, because of their square-planar coordination, Pt(II) complexes tend to form aggregates that either quench the emission or shift it toward long wavelengths.¹⁶ Dual emission from such complexes in the blue and yellow wavelength regions has been used to generate white light.^{17,18} However, for OLED displays, color purity is an essential asset. To prevent excimer formation, bulky, sterically demanding ligands have been designed.³

As a measure of the phosphorescence efficiency, the magnitude of the zero-field splitting (ZFS) of the T_1 state

Received: February 11, 2019

Published: April 25, 2019

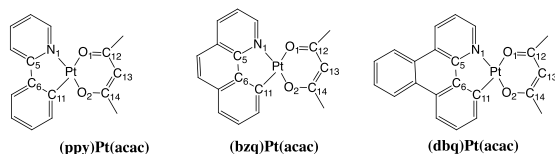
Inorganic Chemistry

Article

has been proposed.³ It was argued that the metal-to-ligand charge transfer (MLCT) character and the phosphorescence rate constant are directly related to this quantity. However, the ZFS of spatially nondegenerate states is determined predominantly by second-order spin-orbit interaction, whereas phosphorescence rate constants are controlled additionally by the oscillator strengths of the spin-allowed electric dipole transitions from which the intensity is borrowed.¹⁹ Given the larger electric dipole transition moment of an LC $\pi\pi^*$ state and the stronger SOC of an MLCT state, a mixture of LC and MLCT characters and the absence of low-lying MC dd^* states appears to be favorable for reaching high phosphorescence efficiencies.³

Complexes with one C[^]N main ligand and one ancillary β -diketonato ligand represent the most developed type of electroluminescent phosphors, with good emission properties and tunable color.⁴ The pronounced σ -donor effect of the phenyl ring and the π -accepting character of the pyridine ring in 2-phenylpyridyl (ppy) complexes result in a strong ligand field for the coordinated metal, thus raising the energy of the quenching dd^* states.⁸ In an attempt to tune the emission properties of (C[^]N)Pt(II)(O[^]O) complexes (O[^]O = dipivalylmethanoate (dpm), acetylacetonate (acac)) by enlarging the π -system of the main ligand from ppy over benzo[*h*]quinolinyl (bzq) to dibenzo[*fh*]quinolinyl (dbq), an unsystematic variation of the emission behavior was observed.²⁰ (For chemical structures, see Chart 1.) Contrary

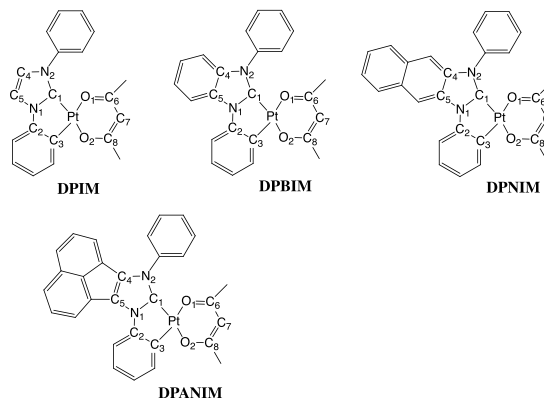
Chart 1. Chemical Structures of Pyridine-Based Platinum Complexes Investigated in This Work



to expectations, the complex with the most extended π -system shows the most blue-shifted 0–0 transition. Also, the phosphorescence quantum yields and rate constants do not follow a simple trend. The authors tried to rationalize this behavior on the basis of spin densities in the triplet states obtained from time-dependent density functional theory (TDDFT) calculations. The respective T₁ states appear to have mixed MLCT/LC character involving the (C[^]N) ligand. The question why (bzq)Pt(dpm) exhibits a much longer phosphorescence lifetime than the other compounds, remained open so far and shall be investigated in the present work.

N-heterocyclic carbenes (NHCs) are typically strong σ -donors and weak π -acceptors.²¹ Bidentate phenyl-imidazolylidene-based complexes show substantially blue-shifted emission, compared to the corresponding ppy-based ones.⁷ The beneficial effect of carbene ligands on the photophysical properties of Pt(II) complexes was impressively demonstrated by Strassner and co-workers, who synthesized and characterized a series of OLED phosphors emitting in the green-blue spectral region.^{6,22–25} The emission wavelengths of (C[^]C[^]*)-Pt(II)(acac) complexes could be tuned by extending the NHC π -system from imidazol-2-ylidene over benzo[*d*]imidazol-2-ylidene to naphtho[2,3-*d*]imidazol-2-ylidene.²³ (For chemical structures, see Chart 2.) The phosphorescence quantum yield increases continuously in this series. In contrast, no measurable

Chart 2. Chemical Structures of Imidazol-ylidene-Based Platinum Complexes Investigated in This Work



quantum yield was observed when the NHC backbone was extended further to an acenaphtho ring system. Remarkably, the highest luminescence quantum yield was found for the (C[^]C[^]*)Pt(II)(acac) complex with the longest phosphorescence lifetime. The reasons causing these variations are currently unclear and shall be elucidated in this work.

The present theoretical investigation strives for a better understanding of the factors that influence the emission behavior of cyclometalated platinum(II) β -diketonate complexes. To this end, we performed combined density functional theory (DFT) and multireference configuration interaction calculations (MRCI) on low-lying singlet and triplet excited states including scalar relativistic and SOC effects. Rate constants, determined for fluorescence, phosphorescence, and intersystem crossing (ISC) transitions, allow one to decide upon competitive excitation decay processes.

THEORY

In heavy transition-metal compounds, where direct SOC between an initial and a final state of a nonradiative transition is substantial, spin-vibronic interactions can often be neglected.²⁶ ISC rate constants may then be computed according to a Fermi golden rule expression in Condon approximation. This means that the vibrational and electronic contributions can be separated. The temperature dependence of the transition probability is included through a Boltzmann distribution of the vibrational population of the initial state. In this approximation, the rate constant for an ISC proceeding from an excited singlet state S to a triplet state T may be expressed as²⁷

$$k_{\text{ISC}}^{\text{FC},\text{T}} = \frac{2\pi}{\hbar Z} \sum_i |\langle T_1 | \hat{H}_{\text{SO}} | S \rangle|^2 \sum_{j,k} e^{-(E_{S_j} - E_{S_0})/k_{\text{B}}T} |\langle \nu_{\text{TK}} | \nu_{\text{Sj}} \rangle|^2 \delta(E_{S_j} - E_{\text{TK}}) \quad (1)$$

where j and k label the vibrational wave functions ν of the S and T states, respectively, and Z is the partition function, which is defined as

$$Z = \sum_j e^{-(E_{S_j} - E_{S_0})/k_{\text{B}}T} \quad (2)$$

with E_{S_0} being the zero vibrational energy of the singlet state. For obtaining the total ISC rate constant, we sum over all triplet sublevels i , which is equivalent to summing over all

Cartesian or tensor components of \hat{H}_{SO} . Important parameters entering eq 1 are the mutual spin–orbit coupling matrix elements (SOCMEs) of the initial and final electronic states, the Franck–Condon (FC) overlaps of their vibrational wave functions and their energy differences. To achieve effective SOC, the configurations are required to be singly excited, with respect to each other, preferably related by local excitations at the metal center involving a change of magnetic angular momentum quantum number, such as $d_{yz} \rightarrow d_{xy}$, for example.^{26,28} This means, in particular, that the initial and final states of an ISC ideally should not exhibit the same spatial wave function characteristics. These rules bear similarity with the ones formulated by El-Sayed²⁹ for organic molecules. With regard to the FC overlaps, two limiting cases for radiationless transitions were outlined.³⁰ The weak coupling limit applies to nested states with similar minimum geometries. In this case, the transition probability decreases exponentially with the magnitude of the adiabatic energy gap between the states. This relation is generally known as the energy gap law. The strong coupling limit refers to pairs of states with significantly displaced minimum geometries. In this case, there are good chances for a crossing of the potential energy hypersurfaces (PEHs) to occur where the overlap of the vibrational wave functions is large. In the strong coupling limit, the probability for ISC typically shows a Gaussian-type behavior with an inverted region in which the probability increases with increasing energy difference before falling off rapidly. While both limiting cases can be favorable for promoting ISC between the excited states, a low degree of molecular distortion in the excited state, with respect to the ground state, is beneficial for achieving high luminescence quantum yields and high color purity, as it prevents strong vibronic coupling and, hence, lessens nonradiative decay of the emission.

In contrast to ISC, phosphorescence is a higher-order property in the framework of perturbation theory, involving coupling to intermediate states. Although the use of Rayleigh–Schrödinger perturbation theory (RSPT) is not advisable in practical calculations,^{31,32} it provides much qualitative insight into the factors that control the phosphorescence efficiency. Unfortunately, incomplete or even incorrect formulas for estimating phosphorescence rate constants via sum-over-states expressions are widespread in the literature.^{3,20,33} Within the framework of RSPT, phosphorescence intensity for a transition between an excited triplet state and a singlet ground state is borrowed from spin-allowed radiative transitions between the initial or final states on the one side and intermediate states on the other side, weighted by coefficients that are dependent on the SOCME and the energy difference between the states.¹⁹

$$k_p(i) = \frac{4e^2}{3c^3\hbar^4} (E(T_i) - E(S_0))^3 \times \left[\sum_{m=0}^{\infty} \frac{\langle S_m | \hat{H}_{\text{SO}} | T_{i,i} \rangle}{E(S_m) - E(T_i)} \langle S_0 | \sum_j e_j^\dagger | S_m \rangle + \sum_{n=1}^{\infty} \frac{\langle S_0 | \hat{H}_{\text{SO}} | T_{n,i} \rangle}{E(T_n) - E(S_0)} \langle T_{n,i} | \sum_j e_j^\dagger | T_{i,i} \rangle \right]^2 \quad (3)$$

Contrary to what is found in most publications, triplet admixtures to the electronic ground-state wave function cannot be neglected in heavy transition-metal compounds. Because of their huge SOCMEs, ³MC states possess remarkably large coefficients in the first-order perturbed

ground-state wave function. To a lesser extent, this also applies to contributions from ³MLCT states. Moreover, if the length form of the electric dipole operator is to be used, the sum over singlet states must include the ground state ($m = 0$) and the sum over triplet states must include the first excited triplet state ($n = 1$).^{34,35} For this reason, also the difference of the static dipole moments of the initial and final states, multiplied by their mutual SOCME, adds to the phosphorescence transition dipole moment. This contribution is particularly pronounced for ³MLCT states. Importantly, the products of the perturbation expansion coefficients and dipole (transition) moments must be summed up *before* squaring.¹⁹

In practice, we will not use eq 3 for two reasons. First, the sum-over-states expression is not easily converged, with respect to the number of intermediate states, because the SOCMEs are complex-valued in general and the summands can have any phase. Therefore, admixing intermediate-state wave function character to the perturbation expansion can not only lend intensity to the spin-forbidden transition, it can also take intensity away. This complication can be avoided by employing either response theory, which is equivalent to summing over infinitely many intermediate states^{31,36} or by using a variational procedure instead.^{32,37,38} Second, the excitation energies of the spin–orbit mixed states of third-row transition-metal compounds can differ markedly from the ones of the unperturbed singlet and triplet states used in the denominators of eq 3. Typically, the ground state is stabilized to a higher extent than the first excited triplet states, thus leading to an increase of their excitation energies.^{39,40} These higher-order effects are well accounted for in multireference spin–orbit configuration interaction (MRSOCI)³² calculations to be described in more detail in the *Methods* section.

METHODS AND COMPUTATIONAL DETAILS

The ground-state geometries of the isolated molecules were optimized with Kohn–Sham density functional theory (KS-DFT)⁴¹ employing the TURBOMOLE program package version 7.0,⁴² whereas full linear response time-dependent density functional theory (TDDFT)⁴³ was utilized for the singlet excited-state geometries. For the geometry optimization of the excited triplet states, TDDFT in Tamm–Dancoff approximation (TDDFT-TDA)⁴⁴ was chosen to avoid triplet instabilities. The PBE0 hybrid functional^{45,46} with a Hartree–Fock exchange ratio of 0.25 was engaged in all geometry optimizations. For all nonmetal atoms, the def-SV(P)⁴⁷ basis set and, for Pt, the def-SV(P) valence basis set of the TURBOMOLE library, together with the multielectron fit Wood–Boring effective core potential (ECP),⁴⁸ were chosen. For the (C[^]C*)Pt(II)(acac) complexes with the freely rotatable *N*-phenyl group, empirical dispersion corrections were added using the Grimme D3 expression with Becke–Johnson damping.⁴⁹

Single-point calculations to generate spin–orbit free vertical excitation spectra were performed with the semiempirical DFT/MRCI method,^{50,51} using the standard parameter set of the recently redesigned, multiplicity-independent R2018 Hamiltonian,⁵² which is particularly well-suited for transition-metal compounds. Herein, molecular orbitals (MOs) from Kohn–Sham calculations employing the BH-LYP functional^{53,54} were engaged. Reference space generation started with all double excitations from the five highest occupied MOs to the five lowest unoccupied MOs. In a second step, the reference wave function was improved to include all configurations with squared coefficients ≥ 0.003 in any of the desired 10 singlet or triplet roots with a selection threshold of 1 E_h .

Spin–orbit coupling matrix elements (SOCMEs) of the DFT/MRCI wave functions were calculated with the spin–orbit coupling kit Spock developed in our laboratory.^{55,56} Herein, we employed the Wood–Boring SOC-ECP⁴⁸ on platinum and an atomic mean-field

Table 1. DFT/MRCI and DFT/MRSOCI Excitation Energies and Radiative Rate Constants of Low-Lying Singlet and Triplet States of Various (C[^]N) Cyclometalated Pt(II) Complexes^a

molecule	state	character	DFT/MRCI, ΔE_{adia} (eV)	DFT/MRSOCI			$k_{\text{F}}/k_{\text{P}}$	k_{ISC} (s ⁻¹)
				ΔE_{adia} (eV)	ΔE_{0-0} (eV)	ΔE_{vert} (eV)		
(ppy)Pt(acac)	S ₁	LC(ppy)/MLCT	3.00	2.93	2.83	2.73	1.2×10^7	1×10^{12}
	T ₁	LC(ppy)/MLCT	2.61	2.70	2.60	2.43	3.6×10^4	
	T _{MC}	MC	2.34	2.30		0.16		
(bzq)Pt(acac)	S ₁	LC(bzq)/MLCT	2.78	2.75	2.65	2.56	1.4×10^7	8×10^{12}
	T ₁	LC(bzq)/MLCT	2.47	2.58	2.46	2.31	2.4×10^3	
	T _{MC}	MC	2.26	2.21		0.09		
(dbq)Pt(acac)	S ₁	LC(dbq)/MLCT	2.87	2.83	2.74	2.63	1.1×10^7	2×10^{12}
	T ₁	LC(dbq)/MLCT	2.64	2.72	2.61	2.50	4.1×10^4	
	T _{MC}	MC	2.30	2.25		0.11		

^a ΔE_{vert} describes a vertical electronic transition, i.e., without change of the geometry. ΔE_{adia} is the difference between the electronic energies of two states at their corresponding relaxed geometries. ΔE_{0-0} corresponds to the adiabatic excitation energy including the difference between the zero-point energies (ZPE) of both states, resulting in the 0–0 vibronic transition energy.

approximation of the Breit–Pauli spin–orbit operator on all other centers.^{57–59} The excitation energies and transition dipole moments for the absorption spectrum including SOC were obtained in the framework of quasi-degenerate perturbation theory (SOC-QDPT). The rate constants of spin-allowed (k_{P}) and spin-forbidden (k_{F}) radiative transitions from an electronically excited state A to the ground state X were computed according to

$$k_{\text{rad}}(A, X) = \frac{4\alpha}{3c^2 \hbar^3} (E_A - E_X)^3 |\mu_{\text{el}}(A, X)|^2 \quad (4)$$

Herein, α is the fine-structure constant, e the electronic charge, c the speed of light, \hbar the reduced Planck constant, and μ_{el} the electric dipole transition moment in length form as required for spin-forbidden radiative transitions. The μ_{el} were determined employing multiplicity-mixed DFT/MRSOCI³² wave functions at the TDDFT or TDDFT-TDA optimized minimum geometry of the respective excited state A. Typically, five roots—one for the ground state, three for the sublevels of the first triplet, and one for the first excited singlet—were calculated at the T₁ and the S₁ geometries. Phosphorescence rate constants were averaged over all triplet sublevels, i.e.,

$$k_{\text{p,av}} = \frac{k_{\text{p,I}} + k_{\text{p,II}} + k_{\text{p,III}}}{3} \quad (5)$$

Vibrational frequencies and wave functions were generated for DFT, TDDFT, and TDDFT-TDA potentials, respectively, in harmonic oscillator approximation employing a finite difference technique as implemented in the SNF⁶⁰ program. The FC profiles of the emission from the T₁ states were obtained using a Fourier transform approach, including temperature and Duschinsky effects,⁶¹ as implemented in the VIBES program.^{27,62} Herein, a time interval of 300 fs and a grid of 16 384 points were chosen. The time correlation function was damped with a Gaussian function of 100 cm⁻¹ width at half maximum. The temperature was set to 77 K. All spectra were normalized to one. Rate constants for ISC of the respective S₁ states to all energetically proximate triplet states were computed for two temperatures, 298 and 77 K, in Condon approximation (eq 1). For the integration of the time correlation function in the VIBES program,^{27,62} a finer grid (time interval 3 ps and 165 536 grid points) and a smaller damping (10 cm⁻¹ width at half-maximum) were chosen. We refrained from computing rate constants for T₁ → S₀ ISC, because the harmonic oscillator approximation appears inappropriate for very large energy separations between the initial and final states.

Admittedly, geometry optimization and computation of spectral properties at different levels of theory is a weakness of the protocol. Unfortunately, an analytical gradient is not available for the DFT/MRCI or DFT/MRSOCI approaches. For this reason, we had to fall

back on linear response methods for geometry optimizations, and vibrational frequency calculations. Note that the order of electronic states, computed at the TDDFT or TDDFT-TDA and DFT/MRCI levels of theory, may differ. TDDFT or TDDFT-TDA minimum geometries were assigned to electronic states such that the largest amplitude in the response calculation matches the leading configuration of the DFT/MRCI expansion.

RESULTS AND DISCUSSION

(C[^]N)Pt(II)(acac) Complexes. Experimental investigations on three (C[^]N)Pt(II)(acac) complexes (Chart 1) revealed an unsystematic variation of their photophysical properties.²⁰ In the following, we will start analyzing the results of our theoretical studies on these complexes with the smallest complex in the series, which contains a ppy ligand. Enlarging the π -system by substituting bzq for ppy resulted in a red shift in the experimental 0–0 emission wavelength. In the largest complex, dbq is chosen as the (C[^]N) ligand, thus further extending the π -system. Unexpectedly, the experimental 0–0 emission wavelength is blue-shifted in comparison to both smaller complexes bearing the ppy or bzq ligand. An overview over the vertical, adiabatic, and 0–0 energies at the excited-state minima and of the calculated rate constants is provided in Table 1. A comparison to TDA-PBE0 results and experimental energies and phosphorescence lifetimes can be found in Table 2.

(ppy)Pt(acac). Bossi et al.²⁰ report a photoluminescence (PL) quantum yield of 0.33 for the complex (ppy)Pt(dpm) = (2-phenylpyridine) platinum(II) (dipivolylmethanoate) at an emission energy of 2.56 eV at RT in cyclohexane. At 77 K in 2-methyltetrahydrofuran (2-MeTHF), the 0–0 emission energy is slightly blue-shifted to 2.58 eV, while the radiative lifetime is increased from 7.1 μ s to 8.7 μ s. For our calculation, we exchanged the dpm ligand for acac, which does not significantly alter the photophysical properties of the complex according to Bossi et al. In earlier work, Brooks et al.⁶³ had observed the emission of (ppy)Pt(acac) to occur with a maximum at 2.55 eV in 2-MeTHF at RT. At 77 K, this complex emits phosphorescence with a lifetime of 9.0 μ s and a band maximum at 480 nm corresponding to an energy of 2.58 eV. For test calculations on the spectral properties of the larger (ppy)Pt(dpm) complex (see below). The (ppy)Pt(acac) complex exhibits quadratically planar Pt coordination in the

Table 2. TDA-PBE0 and DFT/MRSOCI 0-0 Energies ΔE_{0-0} , as Well as Averaged Phosphorescence Lifetimes (τ_p) of the Emitting Triplet State of Various (C^N) Cyclometalated Pt(II) Complexes in Comparison to Corresponding Experimental Values²⁰

molecule	state	TDA-PBE0, ^a ΔE_{0-0}	ΔE_{0-0} (eV)		τ_p (μ s)	
			DFT/MRSOCI	exp., 77 K	DFT/MRSOCI	exp., 77 K
(ppy) Pt(acac)	T ₁	2.47	2.60	2.59	12.2	8.7
(bzq) Pt(acac)	T ₁	2.32	2.46	2.50	109	125
(dbq) Pt(acac)	T ₁	2.50	2.61	2.64	9.7	7.0

^aNote that the TDA-PBE0 excitation energies are computed at the scalar relativistic level and do not include spin-orbit coupling effects.

ground state and in the S₁ and T₁ excited states. Relevant bond lengths and angles are shown in Table S1 in the Supporting Information. Bossi et al. found two unique molecules in a unit cell which form head-to-tail dimers. For comparison with our calculations, we averaged the bond lengths of both molecules.

Vertically, only one triplet was found below the S₁ state, which we denominate T₁. Adiabatically, a further triplet state, T_{MC} is placed below S₁, which actually forms the global minimum on the triplet PEH in the isolated complex. Differences between the electron density distributions in the excited states and in the ground state, in short difference densities, are shown in Figure 1. The electronic structures of

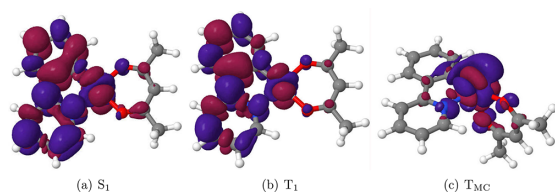


Figure 1. Difference densities (isovalue = 0.001) of low-lying excited states of (ppy)Pt(acac). A loss of electron density, with respect to the S₀ state, is indicated in red, and a gain in electron density is indicated in blue.

the S₁ and T₁ states are dominated by intraligand $\pi\pi^*$ excitations located on the ppy ligand admixed with $d(\text{Pt}) \rightarrow \pi^*(\text{ppy})$ MLCT and small MC contributions. In agreement with experiment, the calculated emission bands (Figure 2) show a high degree of vibronic structure, which is typical for LC transitions. The MC contributions to the excited-state wave functions are nevertheless large enough to make S₁ \leftrightarrow T₁ ISC efficient. The SOCME connecting the S₁ and T₁ states is ~ 101 cm⁻¹. ISC at RT and 77 K outcompetes fluorescence with a calculated rate constant of $k_{\text{ISC}} \approx 1 \times 10^{12}$ s⁻¹, compared to $k_f \approx 1 \times 10^7$ s⁻¹. Therefore, it is conceivable that fluorescence is completely quenched in this complex. For the larger (ppy)Pt(dpm) complex, the ISC rate constant is nearly unchanged with $k_{\text{ISC}} \approx 8 \times 10^{11}$ s⁻¹ at 77 K and $\approx 1 \times 10^{12}$ s⁻¹ at RT. Including SOC, we arrive at a T₁ 0–0 emission energy of 2.60 eV (477 nm) for (ppy)Pt(acac) and of 2.61 eV (475 nm) for (ppy)Pt(dpm), which compares very well to the experimentally reported emission wavelengths of 480 nm for

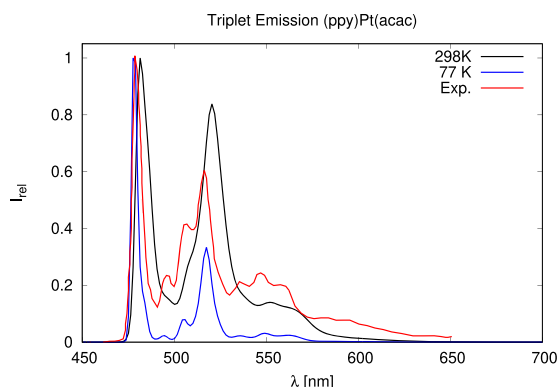


Figure 2. Triplet emission of (ppy)Pt(acac) calculated at 77 and 298 K (RT) in comparison with experimental data measured at 77 K in 2-MeTHF.²⁰

the (ppy)Pt(acac) complex at 77 K in 2-MeTHF⁶³ and of 479 nm for (ppy)Pt(dpm) under the same conditions.²⁰

The averaged phosphorescence lifetime of 12 μ s of the DFT/MRSOCI calculation on (ppy)Pt(acac) is slightly larger than the experimental value of 9.0 μ s at 77 K in 2-MeTHF.⁶³ The corresponding values for the (ppy)Pt(dpm) complex ($\tau_{\text{calc}} = 11$ μ s, $\tau_{\text{exp}} = 8.7$ μ s at 77 K in 2-MeTHF²⁰) are essentially the same. The oscillator strength stems mainly from the upper triplet sublevel, the lower two emit radiation with rate constants an order of magnitude smaller than the third one. (For rate constants and energetic splittings of the individual triplet sublevels, see Table S9 in the Supporting Information.) While the calculated lifetimes are in good agreement with the experimental findings, this is not the case for the ZFS. The DFT/MRSOCI calculations yield a small ZFS between the first two sublevels, which are mainly composed of $m_s = \pm 1$ spin components of the T₁ state. Both couple strongly to a nearby dark singlet MLCT state with $d_z^2 \rightarrow \pi^*(\text{ppy})$ character. The third triplet sublevel is dominated by the $m_s = 0$ spin component of the T₁ state, which borrows intensity from the next-higher optically bright MLCT/LC state. From their experiments, Bossi et al.²⁰ deduced a significantly smaller energy separation of 11.5 cm⁻¹ between the first and third triplet sublevels, compared to a computed ZFS of 87 cm⁻¹ in (ppy)Pt(acac) and 89 cm⁻¹ in (ppy)Pt(dpm). However, it is well-known that ZFSs of iridium and platinum complexes may vary significantly with the local environment.³

The calculations have shown that substitution of acac for dpm has minor effects on the photophysical properties of the (ppy)Pt(dpm) complex, in agreement with experimental observations.^{20,63} Therefore, we continue our computational study engaging the acac ligand instead of dpm.

As mentioned previously, the lowest point on the triplet PEH is found for an electronic structure with MC excitation character, denoted T_{MC}. At this minimum, Pt exhibits a quasi-octahedral coordination with three equatorial bonds (Pt–N₁, Pt–C₁₁, and Pt–O₂), one axial Pt–O₁ bond, as well as two voids in directions along which the highest charge density of the singly occupied $d(\text{Pt})$ orbitals is located (Figure 1c). This nuclear arrangement is very unfavorable for the electronic ground state, with the result that the T₁ and S₀ potentials are separated by an energy gap of merely ~ 1300 cm⁻¹. In view of the strong SOC between these states (sum of squared matrix

elements $\sim 117\,000\text{ cm}^{-2}$), we expect fast nonradiative depletion of the triplet population, once the T_{MC} state has been reached.^{10,13} To obtain an estimate of the height of the barrier, separating the minimum of the phosphorescent T_1 LC/MLCT state from the lower-lying T_{MC} minimum, we proceeded as follows. We computed a minimum energy path (MEP) by fixing the $C_{11}\text{--Pt--O}_2\text{--C}_{14}$ dihedral angle (see Chart 1 for atom labeling) at a predefined value and performed constrained optimizations of all other internal coordinates in the first excited triplet state at the TDDFT-TDA level of theory. Coordinate driving started close to the minimum of the T_1 LC/MLCT state at a torsion angle of 170° and proceeded in steps of 10° (or 5° near the crossing point of the PEHs) toward the T_{MC} minimum where the angle is $\sim 270^\circ$. DFT/MRCI single-point calculations along this MEP yield the energy profile depicted in Figure S1. The curvature of the energy profile is seen to change abruptly at $\sim 220^\circ$, where the electronic structure of the T_1 state switches from a LC/MLCT to a MC excitation. We consider the maximum of this energy profile, 0.17 eV above the T_1 LC/MLCT minimum at the DFT/MRCI level of theory (0.15 eV for TDDFT-TDA), a viable estimate of the transition state separating these minima. To overcome this barrier, substantial out-of-plane distortion of the acac ligand by $\sim 40^\circ$ is required. Sterical hindrance of this torsional motion by a rigid matrix environment or by a neighboring complex in the crystalline state is expected to aggravate the nonadiabatic transition to the MC state.^{12,20,64}

(bzq)Pt(acac). For *(bzq)Pt(dpm)* = (benzo[h]quinoline) platinum(II) (dipivoly) methanoate), the experimental PL quantum yield is 0.29.²⁰ Bossi et al. report a 0–0 emission energy of 2.46 eV at RT in cyclohexane and 2.50 eV at 77 K in 2-MeTHF, while the phosphorescence lifetime changes from $\sim 100\ \mu\text{s}$ at RT to $125\ \mu\text{s}$ at 77 K. Remarkably, this lifetime is ~ 15 times longer than in the ppy complex, despite the nearly equal PL quantum yields. With a value of $E_{0-0} = 495\text{ nm}$ at 77 K, the emission wavelength is red-shifted with respect to the (ppy)Pt(dpm) complex, which is to be expected due to the increased π -system of the ligand. As before, we exchanged the dpm ligand for acac in our study.

Like the ppy complex, *(bzq)Pt(acac)* exhibits quadratically planar Pt coordination in the ground state and in the S_1 and T_1 excited states. Relevant bond lengths and angles are shown in Table S2 in the Supporting Information. Unlike the crystal structures of (ppy)Pt(acac) and (dbq)Pt(acac), the measurements on *(bzq)Pt(acac)* yield identical bond lengths for Pt–O₁ and Pt–O₂, which is not reproduced in our calculations. Here, the Pt–O₁ bond, which is *trans* to the Pt–C₁₁ bond, is significantly longer than the Pt–O₂ bond opposite the Pt–N₁ bond. According to Bossi et al., the *(bzq)Pt(acac)* complex does not stack up with another molecule in a head-to-tail fashion in the crystalline state. Interestingly, the measurements yield also nearly equal Pt–C₁₁ and Pt–N₁ bond lengths for this complex.

The differences between the electron density distributions in the excited states and in the ground state are shown in Figure 3. Both, the S_1 and T_1 states, are characterized by intraligand $\pi\pi^*$ excitations located on the bzq ligand admixed with MLCT and MC excitations. The participation of $d(\text{Pt})$ density in the transition is significantly more pronounced for the S_1 than for the T_1 excitation. This observation agrees with the trend in the phosphorescence rate constant, which is an order of magnitude smaller than for the other complexes. Our computed phosphorescence lifetime amounts to $\sim 109\ \mu\text{s}$, in good

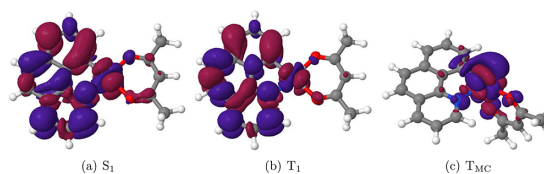


Figure 3. Difference densities (isovalue = 0.001) of low-lying excited states of *(bzq)Pt(acac)*. A loss of electron density, with respect to the S_0 state, is indicated in red, and a gain in electron density in blue.

agreement with the experimental value of $125\ \mu\text{s}$ at 77 K.²⁰ We obtain an energy of 2.46 eV (503 nm) for the 0–0 transition, in excellent agreement with experiment. Also, the shape of the emission spectrum at RT agrees very well with the experimental RT spectrum, while the peak maxima are slightly red-shifted (Figure 4). The much slower phosphorescence in

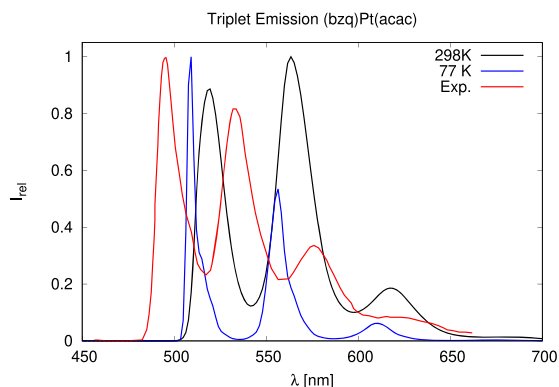


Figure 4. Triplet emission of *(bzq)Pt(acac)* calculated at 77 and 298 K (RT), in comparison with experimental data measured at 77 K in 2-MeTHF.²⁰

this complex does not automatically mean that ISC is less efficient. In contrast, the SOCME between the S_1 and T_1 states is, by far, the largest among the three complexes with a value of 260 cm^{-1} . ISC outcompetes fluorescence by more than 5 orders of magnitude, with rate constants of $k_{\text{ISC}} \approx 8 \times 10^{12}\text{ s}^{-1}$ at RT, compared to $k_{\text{F}} \approx 1 \times 10^7\text{ s}^{-1}$. The ISC rate is only slightly lower at 77 K.

Experimentally, only one transition could be assigned to a 0–0 band at cryogenic temperatures. For this reason, Bossi et al.²⁰ concluded that the ZFS must be $< 2\text{ cm}^{-1}$. Our calculations do not support this assumption. The computed ZFS of this compound shows a similar pattern as for the ppy complex (see Table S9 in the Supporting Information).

The minimum of the emitting triplet state, T_1 , is separated from the lower T_{MC} potential well by a barrier of 0.19 eV at the DFT/MRCI level (0.17 eV for TDDFT-TDA). Similar to that observed in the ppy complex, the crossing point along the minimum energy path is found for an out-of-plane distortion of $\sim 40^\circ$ (Figure S1 in the Supporting Information).

(dbq)Pt(acac). For *(dbq)Pt(dpm)* = (dibenzo[f,h]-quinoline) platinum(II) (dipivoly) methanoate), the experimental PL quantum yield is 0.20, making it the lowest quantum yield of the three (C[^]N)-Pt-complexes. The experimental 0–0 emission energy is 2.60 eV in cyclohexane at RT and 2.64 eV in 2-MeTHF at 77 K.²⁰ The same trend as in

(ppy)Pt(dpm) is observable, with respect to the lifetime, which increases from 3.8 μs to 7.0 μs when lowering the temperature from RT to 77 K. The emission energy is blue-shifted with respect to both (ppy)Pt(dpm) and (bzq)Pt(dpm), despite having the largest π -system of the three complexes. As with the other two complexes, we exchanged the dpm ligand for acac.

The complex is quadratically planar-coordinated about the Pt in the ground state and in the lowest singlet and triplet states. Bossi et al. found two unique molecules in a unit cell which are related to head-to-tail dimers, just like for the (ppy)Pt(acac) complex. For comparison with our calculations, we averaged the bond lengths of both molecules. Relevant bond lengths and angles are shown in Table S3 in the Supporting Information. Contrary to the S_1 state, there is a slight deviation from planarity in the T_1 state in the O_2 -Pt- C_{11} - C_6 dihedral angle by 0.1° .

The difference densities of the lowest-lying excited states are shown in Figure 5. As for (ppy)Pt(acac) and (bzq)Pt(acac),

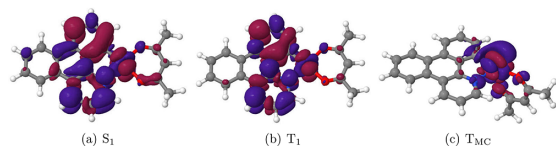


Figure 5. Difference densities (isovalue = 0.001) of low-lying excited states of (dbq)Pt(acac). A loss of electron density with respect to the S_0 state is indicated in red, and a gain in electron density is shown in blue.

the S_1 and T_1 states of the (dbq)Pt(acac) complex are dominated by intraligand $\pi\pi^*$ excitations on the dbq ligand admixed with $d(\text{Pt}) \rightarrow \pi^*(\text{dbq})$ MLCT and small MC contributions. Bossi et al. noticed a blue-shift in the triplet emission energy, compared to the two smaller complexes. This trend is also noticeable in our calculations which yield a 0–0 emission energy of 2.61 eV. As may be seen in Figure 5b, the difference density closely resembles the one in the ppy complex (Figure 1b). In particular, it does not involve the additional aromatic ring at all. This is opposed to the situation in the medium-sized complex (bzq)Pt(acac), where the density changes across the bzq ligand upon electronic excitation. A similar conclusion was presented by Bossi et al. on the basis of spin densities resulting from TDDFT calculations. While the shapes of the computed and measured emission spectra agree very well (Figure 6), the blue-shift of the emission wavelength is somewhat less pronounced in the quantum chemical calculations.

The SOC between the T_1 and S_1 amounts to 134 cm^{-1} , making it larger than for (ppy)Pt(acac) but only the half amount of the coupling in the (bzq)Pt(acac) complex. Nevertheless, ISC outcompetes fluorescence by 5 orders of magnitude at room temperature and by 4 orders of magnitude at 77 K. The ISC rate constant changes from $k_{\text{ISC}} \approx 2 \times 10^{12} \text{ s}^{-1}$ at RT to $k_{\text{ISC}} \approx 2 \times 10^{11} \text{ s}^{-1}$ at 77 K, while the fluorescence rate constant is $k_{\text{F}} \approx 1 \times 10^7 \text{ s}^{-1}$. Our computed phosphorescence lifetime (9.7 μs) is similar to the one obtained for the ppy complex, in agreement with the experimental trend. As for the other complexes, the $m_s = 0$ spin component dominates the uppermost triplet substate, which exhibits the highest phosphorescence rate constant (Table S9). While the computed ZFS of the two lower-lying substates (7 cm^{-1}) agrees well with experiment (5.5 cm^{-1}),²⁰

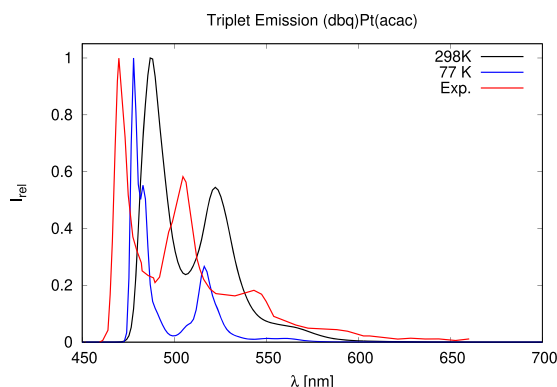


Figure 6. Triplet emission of (dbq)Pt(acac) calculated at 77 and 298 K (RT), in comparison with experimental data measured at 77 K in 2-MeTHF.²⁰

the calculations yield a nearly twice as large ZFS between the first and the third substates compared to the experimentally derived value.

Similar to that observed in (ppy)Pt(acac), the potential well of the T_1 state is separated by a shallow barrier only from the lower-lying T_{MC} state, but the nonadiabatic transition requires out-of-plane distortion of the complex. According to our calculations, a torsion of the acac ligand about the Pt- O_2 bond by 35° is sufficient to reach the crossing point. Among the three ($C^{\wedge}N$)-Pt-complexes, (dbq)Pt(acac) exhibits the smallest barrier (0.15 eV at the DFT/MRCI level, 0.12 eV for TDDFT-TDA) toward nonradiative decay via the T_{MC} state.

($C^{\wedge}C^*$)Pt(II)(acac) Complexes. While the electronic structures of the lowest excited states of the three ($C^{\wedge}N$)-Pt(II)(acac) complexes were similar at least, this is not the case for the ($C^{\wedge}C^*$)Pt(II)(acac) complexes investigated in this work (Chart 2). In the following, we will analyze the results of our theoretical studies on these complexes, beginning with the largest complex in this series and proceeding then to the smallest one. This is motivated by the observation that the excited-state energy landscape becomes more and more complicated the smaller the NHC π -backbone is. An overview over the adiabatic and vertical excitation energies at the excited-state minima and of the rate constants computed in this work is provided in Table 3. TDA-PBE0 and experimental vertical excitation energies and decay lifetimes can be found in Table 4.

DPANIM. Tronnier et al. report a luminescence quantum yield of DPANIM = (SP-4-3)[7,9-diphenyl-7H-acenaphtho-[1,2-*d*]imidazol-2-ylidene- $\kappa\text{C}2,\kappa\text{C}2'$](2,4-pentanedionato- $\kappa\text{O}2,\kappa\text{O}4$) platinum(II) below the detection limit of their apparatus.²³ According to our quantum chemical studies, this complex exhibits a quadratically planar Pt coordination in the electronic ground state and in the low-lying electronically excited states. (For essential geometry parameters of these minima, see Table S4.) Adiabatically, only one triplet minimum is found below the S_1 state. Because of the multiconfigurational nature of the excited-state wave functions, a molecular orbital picture alone is not conclusive. Difference densities of the low-lying electronic states are displayed in Figure 7. The electronic structures of S_1 and T_1 are dominated by intraligand (NHC) $\pi\pi^*$ excitations admixed with $\text{Pt}(d_{yz}) \rightarrow \pi_{\text{NHC}}^*$ MLCT contributions. They closely resemble each other,

Table 3. DFT/MRCI and DFT/MRSOCI Excitation Energies and Radiative Rate Constants of Low-Lying Singlet and Triplet States of Various (C[^]C*) Cyclometalated Pt(II) Complexes^a

molecule	state	character	DFT/MRCI, ΔE_{adia} (eV)	DFT/MRSOCI		$k_{\text{f}}/k_{\text{p}}$	k_{ISC} (s ⁻¹)
				ΔE_{adia} (eV)	ΔE_{vert} (eV)		
DPIM	S ₁	MLCT/LC(NHC)	3.33	3.23	2.70	1.6×10^6	1×10^{12}
	T ₁	MLCT/LC(NHC)	3.02	3.10	2.68	1.0×10^5	
	T ₁ '	MLCT/LC(acac)	3.09	3.21	2.81	2.0×10^5	
	T _{MC}	MC	2.59	2.57	0.59	0.3×10^3	
DPBIM	S ₁	MLCT/LC(NHC)	3.17	3.10	2.41	0.9×10^6	2×10^{12}
	T ₁	MLCT/LC(NHC)	2.95	3.04	2.65	1.1×10^5	
	T ₁ '	MLCT/LC(acac)	3.09	3.22	2.83	2.1×10^5	
	T _{MC}	MC	2.65	2.64	0.61	0.5×10^3	
DPNIM	S ₁	MLCT/LC(NHC)	3.08	3.06	2.79	0.7×10^6	6×10^{11}
	T ₁	LC(NHC)/MLCT	2.47	2.62	2.35	3.3×10^3	
	T ₂	MLCT/LC(NHC)	2.97				
	T _{MC}	MC	2.58	2.57	0.52	0.4×10^3	
DPANIM	S ₁	LC(NHC)/MLCT	2.26	2.28	1.94	5.0×10^6	1×10^9
	T ₁	LC(NHC)/MLCT	1.79	1.91	1.55	1.2×10^3	
	T ₂	LC(NHC)/MLCT	2.49				
	T _{MC}	MC	2.63	2.60	0.59	0.4×10^3	

^aFor a definition of ΔE_{vert} , ΔE_{adia} , and ΔE_{0-0} , see Table 1.

Table 4. TDA-PBE0 and DFT/MRSOCI Vertical Excitation Energies, as Well as Averaged Phosphorescence Lifetimes (τ_{p}) of the Emitting Triplet State of Various (C[^]C*) Cyclometalated Pt(II) Complexes and Comparison to Experimental Emission Maxima and Decay Lifetimes τ_0 ^{2,3}

molecule	state	ΔE_{vert} (eV)		exp, ΔE_{em} (eV)	DFT/MRSOCI, τ_{p} (μs)	exp, τ_0 (μs)
		TDA-PBE0, ^a	DFT/MRSOCI			
DPIM	T ₁	2.56	2.68	2.78	10.0	18.3
DPBIM	T ₁	2.55	2.65	2.71	8.9	9.2
DPNIM	T ₁	2.17	2.35	2.41	300	404.6
DPANIM ^b	T ₁	1.39	1.55	/	820	/

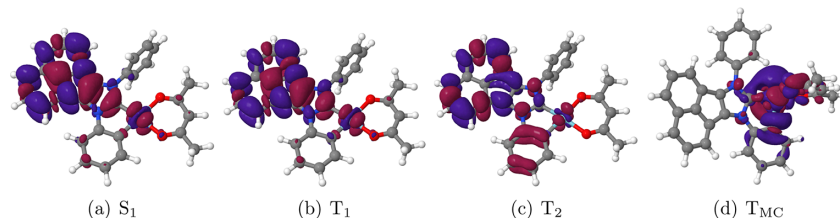
^aNote that the TDA-PBE0 excitation energies are computed at the scalar relativistic level and do not include spin-orbit coupling effects.

^bFor DPANIM, no experimental data are available.

but are sufficiently different to allow for a small SOCME with an absolute value of $\sim 31 \text{ cm}^{-1}$. With rate constants of $k_{\text{ISC}} \approx 1 \times 10^9 \text{ s}^{-1}$, compared to $k_{\text{f}} \approx 5 \times 10^6 \text{ s}^{-1}$ at RT, S₁ \leftrightarrow T₁ ISC nevertheless outcompetes fluorescence by ~ 3 orders of magnitude. This dominance of the ISC process over fluorescence and the absence of large geometrical displacements,

with respect to the electronic ground state, leads us to conclude that the triplet quantum yield should be close to 1. So, why is the measured PL quantum yield of this complex so low? This could have two reasons: (a) phosphorescence cannot compete against nonradiative deactivation of the triplet state or (b) the emission wavelength is outside the observation window. We tend toward explanation (b). Phosphorescence is slow, indeed, with a thermally averaged lifetime of $\sim 800 \mu\text{s}$ at RT, but there is no reason to believe that the radiationless T₁ \rightarrow S₀ decay is very efficient. Their mutual SOC is small at the T₁ minimum (sum over squared SOCMEs $\approx 680 \text{ cm}^{-2}$), compared to a vertical energy gap of $\sim 12\,500 \text{ cm}^{-1}$. Moreover, both structures are planar and vibronic coupling is expected to be insignificant. The T_{MC} state, located adiabatically 2.63 eV above the electronic ground state at the DFT/MRCI level, is energetically not accessible from the relaxed T₁ state with LC/MLCT character. It would be interesting to see whether phosphorescence can be detected at 77 K in the near-infrared with a band maximum at $\sim 800 \text{ nm}$. For a computed triplet emission spectrum, see Figure 8.

DPNIM. For DPNIM = (SP-4-3)[1,3-diphenyl-1H-naphtho-[2,3-*d*]imidazol-2-ylidene- $\kappa\text{C}2,\kappa\text{C}2'$](2,4-pentanedionato- $\kappa\text{O}2,\kappa\text{O}4$) platinum(II), a phosphorescence quantum yield of 0.81 was measured in poly(methyl methacrylate) (PMMA)

**Figure 7.** Difference densities (isovalue = 0.001) of low-lying excited states of DPANIM. A loss of electron density with respect to the S₀ state is indicated in red, and a gain in electron density is shown in blue.

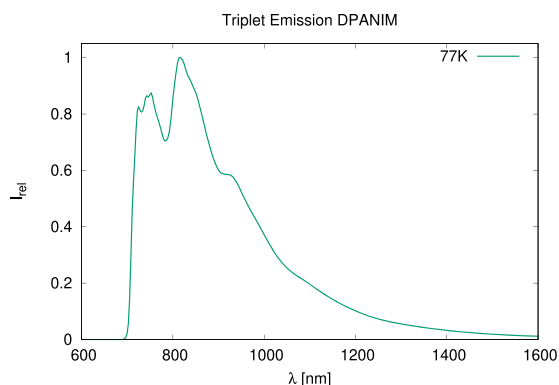


Figure 8. Calculated phosphorescence emission spectrum of DPANIM at 77K. Intensities relative to peak maximum are shown.

films.²³ This is the highest value of all compounds in this series. Remarkably, this high phosphorescence quantum yield goes along with a radiative lifetime of ca. 400 μ s, indicating a high degree of LC character in the T_1 state. In turn, this raises a question about the mechanism of the efficient triplet population. Like DPANIM, DPNIM has nearly C_s symmetric nuclear arrangements in its low-lying electronically excited states. (For the most important geometry parameters, see Table S5.) Two triplet minima were located energetically below the S_1 state in DPNIM. The electronic structures of S_1 and T_2 are dominated by interligand ($\text{Ph} \rightarrow \text{NHC}$) LLCT and $\text{Pt}(d_{xz}) \rightarrow \pi_{\text{NHC}}^*$ MLCT excitations (Figure 9). In contrast, T_1 originates predominantly from local excitations of the NHC π -system with small MLCT contributions of $\text{Pt}(d_{yz}) \rightarrow \pi_{\text{NHC}}^*$ type. Accordingly, the largest geometry shifts are found for C–C bonds in the NHC backbone. Because of the reorientation of the open d shell on Pt ($d_{yz} \leftrightarrow d_{xz}$), $|\langle T_1 | \hat{H}_{\text{SO}} | S_1 \rangle| \approx 72 \text{ cm}^{-1}$ is larger than for DPANIM, leading to very efficient ISC with $k_{\text{ISC}} \approx 6 \times 10^{11} \text{ s}^{-1}$ at RT. Phosphorescence, on the other hand, is long-lived (calculated high-temperature averaged lifetime $\tau_{\text{p,av}} \approx 300 \mu\text{s}$ at 525 nm in vacuo, measured $\tau_0 \approx 405 \mu\text{s}$ at RT in PMMA²³), because of the predominant LC character of the transition. The vibrational fine structure of the calculated emission spectrum has a spacing of ca. 1500 cm^{-1} and stems predominantly from progressions of C–C stretching vibrations in the naphthalene rings attached to the NHC core. Note the nearly perfect agreement of the theoretical and experimental spectra (Figure 10). Direct SOC between T_1 and S_0 is small (sum over squared SOCMEs $\approx 5070 \text{ cm}^{-2}$), relative to the vertical emission energy of 19 000 cm^{-1} . In this complex, the T_{MC} and $T_{\text{LC(NHC)/MLCT}}$ states exhibit nearly equal adiabatic excitation energies. At the DFT/MRCI level of theory, the

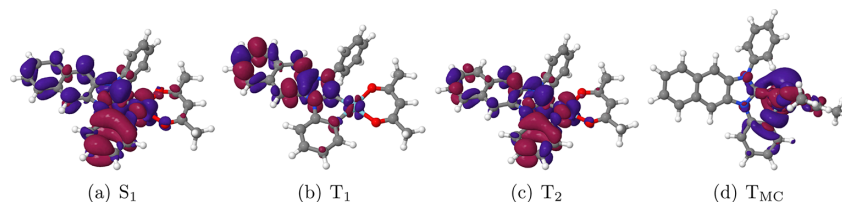


Figure 9. Difference densities (isovalue = 0.001) of low-lying excited states of DPNIM. A loss of electron density with respect to the S_0 state is indicated in red, and a gain in electron density is shown in blue.

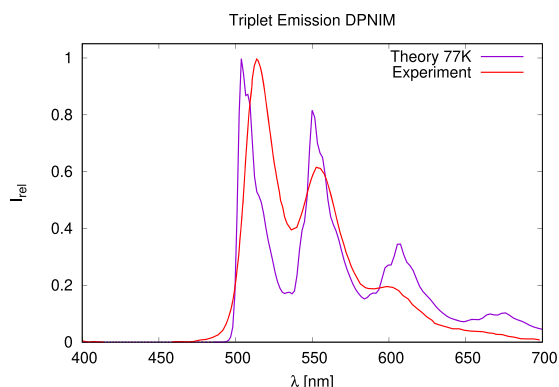


Figure 10. Calculated phosphorescence emission spectrum of DPNIM at 77 K, in comparison with experimental data measured at RT in PMMA.²³

T_{MC} minimum is found to lie 0.11 eV higher in energy, whereas it is located slightly below the $T_{\text{LC(NHC)/MLCT}}$ minimum (by 0.05 eV) if SOC is taken into account variationally. Hence, we do not expect a strong driving force toward pyramidalization. Nevertheless, we computed a MEP between the two minima in a similar fashion as described in detail for (ppy)Pt(acac). As the reaction coordinate, the $\text{C}_3\text{–Pt–O}_2\text{–C}_8$ dihedral angle (for atom labeling see Chart 2) was chosen. The DFT/MRCI energy profile connecting the two states is depicted in Figure S2 in the Supporting Information. The $T_{\text{LC(NHC)/MLCT}}$ minimum is separated by a barrier of 0.20 eV height from the T_{MC} minimum. Accordingly, we do not expect fast nonradiative deactivation of the phosphorescence emission. The lack of a strong driving force toward pyramidalization, in conjunction with the additional energy barrier, could explain the exceptionally high photoluminescence quantum yield of 0.81 observed by Tronnier et al.²³ for this complex.

DPBIM. In DPBIM = (SP-4-3)[1,3-diphenyl-1H-benzo[*d*]-imidazol-2-ylidene- $\kappa\text{C}2,\kappa\text{C}2'$](2,4-pentanedionato- $\kappa\text{O}2,\kappa\text{O}4$) platinum(II), the C_s -symmetric nuclear arrangement is a saddle point on the S_1 PEH, placed ~ 0.12 eV above two out-of-plane distorted minima. While the local Pt coordination is still approximately square planar, the NHC ligand is slightly kinked at the C_1 center. The electronic structure (Figure 11a) resembles the one of DPNIM (Figure 9a), but with larger MLCT and MC contributions. The Pt– C_3 and the opposite Pt– O_1 bonds shorten markedly upon excitation, whereas the Pt– C_1 and the Pt– O_2 bonds are noticeably elongated. Population of the π_{NHC}^* orbital further leads to elongation of the carbene $\text{C}_1\text{–N}_1$ and $\text{C}_1\text{–N}_2$ bonds and to a contraction of

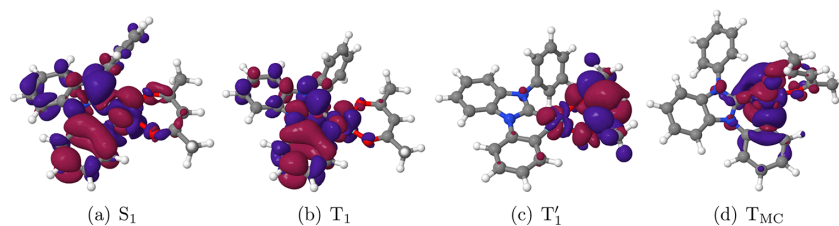


Figure 11. Difference densities (isovaluel = 0.001) of low-lying excited states of DPBIM. A loss of electron density with respect to the S_0 state is indicated in red, and a gain in electron density is shown in blue.

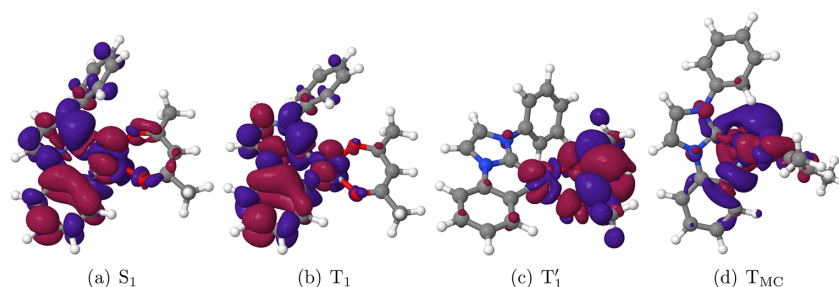


Figure 12. Difference densities (isovaluel = 0.001) of low-lying excited states of DPIM. A loss of electron density with respect to the S_0 state is indicated in red, and a gain in electron density is shown in blue.

the N_1-C_2 bond connecting the Pt-ligated phenyl and imidazol-ylidene rings. (See also Table S6 for important bond lengths and angles.) The kink is less pronounced in the equilibrium nuclear arrangements of the corresponding triplet state, T_1 . The electronic structure is a mixture of LLCT ($Ph \rightarrow NHC$), $Pt(d_{xz}) \rightarrow \pi_{NHC}^*$ MLCT and LC excitations, with the LC contributions being slightly larger than in the S_1 state. In contrast to the S_1 geometry parameters, the two Pt–O bonds have similar lengths in the T_1 minimum nuclear arrangements. The energy barrier between the two minima (<0.01 eV) is practically nonexistent. However, these are not the only minima found on the T_1 potential PEH. Another pair of equivalent minima, in the following denoted by T_1' , are located adiabatically ~ 0.15 eV (0.14 eV without SOC and 0.17 eV including SOC) higher in energy and exhibit nuclear arrangements kinked at the oxygen atoms of the acac ligand. Electronically, they correspond to mixtures of MLCT and LC transitions involving mainly the π -system of the acac ligand besides the Pt d -shell. A triplet state with similar characteristics was found in recent theoretical work by Pinter and Strassner⁶⁴ in the related complex MPBIM = (SP-4-3)[1-methyl,3-phenyl-1H-benzo[*d*]imidazol-2-ylidene- $\kappa C2, \kappa C2'$](2,4-pentanedionato- $\kappa O2, \kappa O4$) platinum(II), bearing a methyl instead of a phenyl substituent at N_2 . ISCs from S_1 to the T_1 and T_1' states proceed at rates of $\sim 2 \times 10^{12}$ and 2×10^9 s⁻¹, respectively, and are expected to quantitatively quench fluorescence ($k_f \approx 0.9 \times 10^6$ s⁻¹). The high ISC rate constants also preclude inefficient triplet formation processes as the origin of the lower phosphorescence quantum yield of DPBIM, in comparison to DPNIM. Because of the mixed MLCT/LLCT/LC character of the T_1 electronic state, phosphorescence of DPBIM has a comparatively high rate constant (calculated high-temperature averaged $k_{p,av} \approx 1.1 \times 10^5$ s⁻¹ yielding a phosphorescence lifetime $\tau_{p,av} \approx 8.9$ μ s at 467 nm in vacuo, compared to a measured value of $\tau_0 = 9.2$ μ s at RT in PMMA with $\lambda_{max} = 457$ nm²³). Simultaneously, the larger coefficients of the MLCT

configurations in the T_1 wave function of DPBIM result in much stronger direct SOC between T_1 and S_0 (sum over squared SOCMEs $\sim 300\,000$ cm⁻², vertical emission energy of $\sim 21\,400$ cm⁻¹) than in DPNIM. More importantly, however, we find the T_{MC} minimum to be markedly lower in energy than the other triplet minima. The minimum energy path along the interligand torsional angle (Figure S2) leads from the $T_{MLCT/LC(acac)}$ structure nearly barrierlessly to the $T_{MLCT/LC(NHC)}$ minimum, which is separated from the strongly displaced T_{MC} minimum by a small barrier only (barrier height 0.09 eV at the DFT/MRCI level). We consider the competition between radiative and nonradiative decay of the T_1 state the main reason for the lower phosphorescence quantum yield of DPBIM (measured value = 0.41),²³ compared to DPNIM. The loss of vibrational structure in the experimental emission spectrum of DPBIM is rationalized by the increased MLCT character of the transition combined with the excitation of low-frequency out-of-plane vibrational modes. Because of the double-minimum nature of the excited state, we refrained from computing a Franck–Condon spectrum in harmonic approximation.

DPIM. The electronic and geometric structures of electronically excited DPIM = (SP-4-3)[1,3-diphenyl-1H-imidazol-2-ylidene- $\kappa C2, \kappa C2'$](2,4-pentanedionato- $\kappa O2, \kappa O4$) platinum(II), i.e., the complex with the smallest NHC π -system, are similar to the ones of DPBIM. (See Figure 12a for difference densities and Table S7 in the Supporting Information for important geometry parameters.) The MLCT/LC state involving the acac ligand (T_1') has nearly the same adiabatic excitation energy as in DPBIM, whereas the S_1 and T_1 states with MLCT/LLCT/LC character involving the phenyl-imidazole-ylidene ligand are located at somewhat higher energies, because of the smaller NHC π -system. The energy difference between the T_1 and T_1' minima shrinks to values between 0.07 eV (without SOC) and 0.11 eV (including SOC), suggesting strong vibronic coupling between the two

triplet states. Rate constants for $S_1 \rightarrow T_1$ ISC ($\approx 1 \times 10^{12} \text{ s}^{-1}$) and $S_1 \rightarrow T_1'$ ISC ($\approx 3 \times 10^{10} \text{ s}^{-1}$) are very high. Hence, we expect a nearly quantitative population of the triplet manifold following electronic excitation. Similar to that observed in DPBIM, the T_{MC} forms the global minimum on the triplet PEH. Pyramidalization of the Pt coordination requires a small barrier to be overcome (Figure S2), which is why phosphorescence can be observed at all in liquid solution. Interestingly, Pinter and Strassner⁶⁴ report a PL quantum yield close to unity for the related complex MPIM = (SP-4-3)[1-methyl,3-phenyl-1H-imidazol-2-ylidene- $\kappa C2, \kappa C2'$](2,4-pentanedionato- $\kappa O2, \kappa O4$) platinum(II) in a glassy matrix at 77 K where the out-of-plane distortions are hindered. Rigidification of the environment is expected to enhance the quantum yield of the DPIM emission, too. We determine a purely radiative phosphorescence lifetime of $\tau_{P,av} \approx 10 \mu\text{s}$ for T_1 in the high-temperature limit, in qualitative agreement with the measured $\tau_0 = 18.3 \mu\text{s}$ at RT in PMMA.²³ Consistent with the findings for the other complexes in this series, the computed emission wavelength for the vertical transition at the T_1 minimum (463 nm) is somewhat overestimated, relative to the measured emission maximum of $\lambda_{max} = 446 \text{ nm}$.

CONCLUSIONS

In this work, extensive quantum chemical calculations including relativistic and multiconfiguration effects have been performed on seven neutral cyclometalated Pt(II) acetylacetonate complexes. They are not only able to reproduce experimentally observed emission properties (wavelengths, spectral shapes, phosphorescence lifetimes) with good accuracy, they also provide qualitative insight into the origins of the observed variations upon extension of the ligand π -system.

Analysis of the charge density distributions in the frontier molecular orbitals at the ground-state geometry does not give a clue with regard to excited-state properties of these complexes. Instead, it proves necessary to perform geometry optimizations of the excited-state structures followed by single-point multireference calculations beyond the scalar relativistic level. Even the low-lying excited states exhibit strongly mixed multiconfigurational wave functions. It is the intricate balance of configurations with LC, MLCT, MC, and LLCT character that steers the emission properties of these compounds. Visualizing the differences between the electron density distributions in the excited states and in the ground state is a useful tool for analyzing these contributions. The semi-empirical DFT/MRCI-R2018 Hamiltonian,⁵² recently parametrized and benchmarked on excitation energies of first- and second-row transition-metal complexes besides purely organic compounds, proves well-suited for investigating the absorption and emission properties of platinum(II) complexes, too. Generally good agreement is observed between our calculated data and the experimental findings.

The results of our quantum chemical studies on a series of (C[^]N)Pt(II)(acac) phosphors, synthesized and spectrally characterized by Thompson and co-workers,²⁰ do not only explain why the complex with the largest π -system exhibits the most blue-shifted triplet emission, they also provide a rationale for the wide variation in the radiative rate constants. In the Franck–Condon region, the S_1 and T_1 electronic structures of these complexes are characterized by intraligand $\pi\pi^*$ excitations located on the (C[^]N) ligand admixed with MLCT and MC excitations. As a general trend, we observe

that the LC contributions to the wave functions are larger in the T_1 states than in the corresponding S_1 states. This is easily explained by the larger exchange interactions in the LC $\pi\pi^*$ excitations, compared to MLCT transitions and the concomitant preferential stabilization of 3LC configurations. In the series (ppy)Pt(acac), (bzq)Pt(acac), and (dbq)Pt(acac), the effective π -system is most extended in the (bzq)Pt(acac) complex. Therefore, its T_1 state exhibits a higher percentage of LC contributions and consequently a markedly smaller phosphorescence rate constants than the other two complexes. While phosphorescence borrows intensity from all spin-allowed transitions in the picture of perturbation theory, the electronic part of the $S_1 \rightarrow T_1$ ISC probability is mainly determined by their mutual spin–orbit interaction. Singlet and triplet wave functions with equal spatial parts and differing only in their spin parts do not interact via SOC, even if the heavy-metal center is involved in the electronic excitation. A single replacement of orbitals at the same center and with equal angular momentum but different magnetic quantum numbers ($d \leftrightarrow d'$, for example) when comparing the singlet and triplet configurations is required to make SOC efficient. For this reason, the SOCME between the S_1 and T_1 states of (bzq)Pt(acac) is, by far, the largest among the three complexes and explains the efficient triplet formation. In all compounds, the lowest-lying 3MC state is located adiabatically $\sim 2.25 \text{ eV}$ above the S_0 minimum. Therefore, the emitting triplet states are only metastable with respect to nonradiative deactivation by the T_{MC} state. This transition is accompanied by large out-of-plane motion of the (acac) ligand. Therefore, sterical hindrance by a rigid environment will increase the photoluminescence quantum yield of the complexes compared to fluid solution as empirically found by Bossi et al.²⁰

The photophysics of the (C[^]C[^])Pt(II)(acac) complexes, experimentally investigated by Strassner and co-workers,²³ is particularly more involved. In these compounds, more than one MLCT or LC triplet state is located below the first excited singlet state, in addition to the 3MC state which lies approximately 0.3 eV higher in energy than in the (C[^]N)Pt(II)(acac) compounds. Extension of the π -backbone of the NHC ligand leads to a red shift of the LC $\pi\pi^*$ excitation energy. Together with smaller Pt(d_{xz}) \rightarrow NHC π^* MLCT contributions, $\pi_{NHC} \rightarrow$ NHC π^* excitations form the S_1 , T_1 and T_2 states of DPANIM, the complex with the largest π -backbone. Phosphorescence emission is predicted to be slow, but should be observable in the infrared at low temperatures, because of the absence of low-lying MC states that could quench the emission. In the complex with the second largest NHC π -system, DPNIM, the T_1 state is dominated by LC excitations on the NHC ligand, too, with small Pt(d_{xz}) \rightarrow NHC π^* MLCT contributions. In contrast, the electronic structure of the S_1 state is characterized by LLCT ($\pi_{Ph} \rightarrow \pi_{NHC}^*$ MC Pt(d_{yz}) \rightarrow Pt(d_{xz}) and Pt(d_{yz}) $\rightarrow \pi_{NHC}^*$ MLCT excitations. Despite the dominant LC character of the T_1 state, SOC between (d_{yz}) and (d_{xz}) on Pt leads to efficient $S_1 \rightarrow T_1$ ISC and, hence, high triplet quantum yield while the $T_1 \rightarrow S_0$ radiative transition is a comparatively slow process. We explain the remarkably high photoluminescence quantum yield (0.81) of this complex, measured at 77 K in 2Me-THF,²³ by the lack of a strong driving force toward pyramidalization in the triplet state as the minima of the phosphorescing $^3LC/MLCT$ and the dark 3MC states have nearly equal adiabatic excitation energies and are additionally separated by a small barrier of 0.20 eV height. The two smallest (C[^]C[^])Pt(II)(acac) complexes lose

their C_s -symmetric structures in the low-lying excited states. Because of limitations of the harmonic oscillator approximation, the computation of spectral profiles is not meaningful if the emitting state is out-of-plane distorted with a shallow double-minimum structure while the ground state is close to quadratically planar. Therefore, we refrained from plotting emission spectra of these complexes. Their S_1 and T_1 states are characterized by LLCT ($Ph_\pi \rightarrow NHC_{\pi^*}$, MC $Pt(d_{yz}) \rightarrow Pt(d_{xz})$) and $Pt(d_{yz}) \rightarrow NHC_{\pi^*}$ MLCT excitations, with the MC and MLCT partitions increase as the size of the π -backbone decreases. The higher involvement of MC dd^* excitations in the T_1 state not only accelerates phosphorescence, but also enhances the probability for nonradiative decay of the triplet population. In both complexes, the emitting triplet state is separated only by a small barrier from the lower-lying 3MC state. Rigidification of the molecular environment in the solid state or in matrices is expected to increase the barrier height and, hence, the phosphorescence quantum yields of these compounds.^{23,64} The triplet decay is further promoted by vibronic coupling with another low-lying $^3LC/MLCT$ state engaging the acac auxiliary ligand. The seemingly counter-intuitive experimental finding that the complex with the smallest phosphorescence rate constant exhibits the highest photoluminescence quantum yield is easily explained by (1) the different electronic structures of its S_1 and T_1 states which drive the efficient ISC, (2) the planarity of the emitting T_1 state which reduces vibronic deactivation, and (3) its favorable energetic position, which impedes depletion of the phosphorescence by nonradiative decay via the T_{MC} state.

Summarizing, we have performed elaborate relativistic multiconfiguration interaction studies to gain insight into the involved photophysics of cyclometalated Pt(II) β -diketonate complexes. The semiempirical DFT/MRCI and DFT/MRSOCI methods prove to be useful in easing the computational expenses of such calculations while simultaneously showing good accuracy. The R2018 Hamiltonian, recently designed and parametrized in our laboratory,⁵² appears to be particularly well-suited for investigating the luminescence properties of transition-metal compounds with closed-shell ground states, such as Pt(II) complexes. The excellent agreement between calculated and measured data make us confident that the methods employed in our quantum chemical studies can not only be used to explain trends across series of complexes with varying ligands. They also provide useful tools for reliably predicting the emission properties of yet unknown cyclometalated Pt(II) complexes.

■ ASSOCIATED CONTENT

📄 Supporting Information

The Supporting Information is available free of charge on the ACS Publications website at DOI: 10.1021/acs.inorgchem.9b00403.

Characteristic geometry parameters of the complexes in the ground and low-lying excited states; minimum energy paths connecting the $T_{LC/MLCT}$ and T_{MC} states, zero-field splittings and phosphorescence rate constants of the individual T_1 sublevels, Cartesian coordinates of the S_0 , S_1 , and various T_1 minima including the barriers in the minimum energy paths (PDF)

■ AUTHOR INFORMATION

Corresponding Author

*E-mail: Christel.Marian@hhu.de.

ORCID

Christel M. Marian: 0000-0001-7148-0900

Notes

The authors declare no competing financial interest.

■ ACKNOWLEDGMENTS

Financial support by the Deutsche Forschungsgemeinschaft (DFG) through Project No. MA-1051/14-2 and through funds (No. INST 208/704-1 FUGG) enabling us to purchase the hybrid compute cluster used in this study is gratefully acknowledged. The authors thank Prof. Thomas Strassner (Dresden) for valuable discussions in the framework of the DFG Priority Programme "Light Controlled Reactivity of Metal Complexes" (No. SPP 2102).

■ REFERENCES

- (1) Baldo, M. A.; O'Brien, D. F.; You, Y.; Shoustikov, A.; Sibley, S.; Thompson, M. E.; Forrest, S. R. Highly efficient phosphorescent emission from organic electroluminescent devices. *Nature* **1998**, *395*, 151–154.
- (2) Thompson, M. The Evolution of Organometallic Complexes in Organic Light-Emitting Devices. *MRS Bull.* **2007**, *32*, 694–701.
- (3) Yersin, H.; Rausch, A. F.; Czerwieniec, R.; Hofbeck, T.; Fischer, T. The triplet state of organo-transition metal compounds. Triplet harvesting and singlet harvesting for efficient OLEDs. *Coord. Chem. Rev.* **2011**, *255*, 2622–2652.
- (4) Yang, B. X.; Yao, C.; Zhou, G. Highly Efficient Phosphorescent Materials Based on Platinum Complexes and their Application in Organic Light-Emitting Devices (OLEDs). *Platinum Met. Rev.* **2013**, *57*, 2–16.
- (5) Choy, W. C. H.; Chan, W. K.; Yuan, Y. Recent Advances in Transition Metal Complexes and Light-Management Engineering in Organic Optoelectronic Devices. *Adv. Mater.* **2014**, *26*, 5368–5399.
- (6) Strassner, T. Phosphorescent Platinum(II) Complexes with C^*C^* Cyclometalated NHC Ligands. *Acc. Chem. Res.* **2016**, *49*, 2680–2689.
- (7) Fleetham, T.; Li, G.; Li, J. Phosphorescent Pt(II) and Pd(II) Complexes for Efficient, High-Color-Quality, and Stable OLEDs. *Adv. Mater.* **2017**, *29*, 1601861.
- (8) Cebrián, C.; Mauro, M. Recent advances in phosphorescent platinum complexes for organic light-emitting diodes. *Beilstein J. Org. Chem.* **2018**, *14*, 1459–1481.
- (9) Williams, J. A. G.; Develay, S.; Rochester, D. L.; Murphy, L. Optimising the luminescence of platinum(II) complexes and their application in organic light emitting devices (OLEDs). *Coord. Chem. Rev.* **2008**, *252*, 2596–2611.
- (10) Lam, W. H.; Lam, E. S.-H.; Yam, V. W.-W. Computational Studies on the Excited States of Luminescent Platinum(II) Alkynyl Systems of Tridentate Pincer Ligands in Radiative and Nonradiative Processes. *J. Am. Chem. Soc.* **2013**, *135*, 15135–15143.
- (11) Escudero, D.; Thiel, W. Exploring the Triplet Excited State Potential Energy Surfaces of a Cyclometalated Pt(II) Complex: Is There Non-Kasha Emissive Behavior? *Inorg. Chem.* **2014**, *53*, 11015–11019.
- (12) Riese, S.; Holzapfel, M.; Schmiedel, A.; Gert, I.; Schmidt, D.; Würthner, F.; Lambert, C. Photoinduced Dynamics of Bisdipyrrinato-palladium(II) and Porphodimetheno-palladium(II) Complexes: Governing Near Infrared Phosphorescence by Structural Restriction. *Inorg. Chem.* **2018**, *57*, 12480–12488.
- (13) Wagenknecht, P. S.; Ford, P. C. Metal centered ligand field excited states: Their roles in the design and performance of transition metal based photochemical molecular devices. *Coord. Chem. Rev.* **2011**, *255*, 591–616.

- (14) Hanson, K.; Tamayo, A.; Diev, V. V.; Whited, M. T.; Djurovich, P. I.; Thompson, M. E. Efficient Dipyrrin-Centered Phosphorescence at Room Temperature from Bis-Cyclometalated Iridium(III) Dipyrrinato Complexes. *Inorg. Chem.* **2010**, *49*, 6077–6084.
- (15) Klein, J. H.; Sunderland, T. L.; Kaufmann, C.; Holzapfel, M.; Schmiedel, A.; Lambert, C. Stepwise versus pseudo-concerted two-electron-transfer in a triarylamine-iridium dipyrrin-naphthalene diimide triad. *Phys. Chem. Chem. Phys.* **2013**, *15*, 16024–16030.
- (16) Wong, K. M.-C.; Yam, V. W.-W. Self-Assembly of Luminescent Alkynylplatinum(II) Terpyridyl Complexes: Modulation of Photophysical Properties through Aggregation Behavior. *Acc. Chem. Res.* **2011**, *44*, 424–434.
- (17) D'Andrade, B.; Brooks, J.; Adamovich, V.; Thompson, M.; Forrest, S. White Light Emission Using Triplet Excimers in Electrophosphorescent Organic Light-Emitting Devices. *Adv. Mater.* **2002**, *14*, 1032–1036.
- (18) Reineke, S.; Thomschke, M.; Lüssem, B.; Leo, K. White organic light-emitting diodes: Status and perspective. *Rev. Mod. Phys.* **2013**, *85*, 1245–1293.
- (19) Marian, C. M. In *Reviews in Computational Chemistry*, Vol. 17; Lipkowitz, K., Boyd, D., Eds.; Wiley-VCH: Weinheim, Germany, 2001; pp 99–204.
- (20) Bossi, A.; Rausch, A. F.; Leitl, M. J.; Czerwieńiec, R.; Whited, M. T.; Djurovich, P. I.; Yersin, H.; Thompson, M. E. Photophysical Properties of Cyclometalated Pt(II) Complexes: Counterintuitive Blue Shift in Emission with an Expanded Ligand π System. *Inorg. Chem.* **2013**, *52*, 12403–12415.
- (21) Jacobsen, H.; Correa, A.; Poater, A.; Costabile, C.; Cavallo, L. Understanding the M(NHC) (NHC = N-heterocyclic carbene) bond. *Coord. Chem. Rev.* **2009**, *253*, 687–703.
- (22) Unger, Y.; Meyer, D.; Molt, O.; Schildknecht, C.; Münster, I.; Wagenblast, G.; Strassner, T. Green-Blue Emitters: NHC-Based Cyclometalated [Pt(C[∧]C*)(acac)] Complexes. *Angew. Chem., Int. Ed.* **2010**, *49*, 10214–10216.
- (23) Tronnier, A.; Pöthig, A.; Metz, S.; Wagenblast, G.; Münster, I.; Strassner, T. Enlarging the π System of Phosphorescent (C[∧]C*) Cyclometalated Platinum(II) NHC Complexes. *Inorg. Chem.* **2014**, *53*, 6346–6356.
- (24) Tronnier, A.; Nischan, N.; Metz, S.; Wagenblast, G.; Münster, I.; Strassner, T. Phosphorescent C[∧]C* Cyclometalated Pt^{II} Dibenzofuranyl-NHC Complexes—An Auxiliary Ligand Study. *Eur. J. Inorg. Chem.* **2014**, *2014*, 256–264.
- (25) Pittkowski, R.; Strassner, T. Enhanced quantum yields by sterically demanding aryl-substituted β -diketonate ancillary ligands. *Beilstein J. Org. Chem.* **2018**, *14*, 664–671.
- (26) Penfold, T. J.; Gindensperger, E.; Daniel, C.; Marian, C. M. Spin-Vibronic Mechanism for Intersystem Crossing. *Chem. Rev.* **2018**, *118*, 6975–7025.
- (27) Etinski, M.; Tatchen, J.; Marian, C. M. Time-Dependent Approaches for the Calculation of Intersystem Crossing Rates. *J. Chem. Phys.* **2011**, *134*, 154105.
- (28) Li, E. Y.-T.; Jiang, T.-Y.; Chi, Y.; Chou, P.-T. Semi-quantitative assessment of the intersystem crossing rate: an extension of the El-Sayed rule to the emissive transition metal complexes. *Phys. Chem. Chem. Phys.* **2014**, *16*, 26184–26192.
- (29) El-Sayed, M. Spin-Orbit Coupling and the Radiationless Processes in Nitrogen Heterocyclics. *J. Chem. Phys.* **1963**, *38*, 2834–2838.
- (30) Englman, R.; Jortner, J. The energy gap law for radiationless transitions in large molecules. *Mol. Phys.* **1970**, *18*, 145–164.
- (31) Baryshnikov, G.; Minaev, B.; Ågren, H. Theory and Calculation of the Phosphorescence Phenomenon. *Chem. Rev.* **2017**, *117*, 6500–6537.
- (32) Kleinschmidt, M.; Tatchen, J.; Marian, C. M. SPOCK.CI: A Multireference Spin-Orbit Configuration Interaction Method for Large Molecules. *J. Chem. Phys.* **2006**, *124*, 124101.
- (33) Gernert, M.; Müller, U.; Haehnel, M.; Pflaum, J.; Steffen, A. A Cyclic Alkyl(amino)carbene as Two-Atom π -Chromophore Leading to the First Phosphorescent Linear Cu^I Complexes. *Chem. - Eur. J.* **2017**, *23*, 2206–2216.
- (34) Lohr, L. L., Jr. Spin-forbidden electric-dipole transition moments. *J. Chem. Phys.* **1966**, *45*, 1362–1363.
- (35) Goodman, L.; Laurenzi, B. J. Probability of singlet-triplet transitions. *Adv. Quantum Chem.* **1968**, *4*, 153–169.
- (36) Minaev, B.; Baryshnikov, G.; Ågren, H. Principles of phosphorescent organic light emitting devices. *Phys. Chem. Chem. Phys.* **2014**, *16*, 1719–1758.
- (37) Hess, B. A.; Buenker, R. J.; Marian, C. M.; Peyerimhoff, S. D. Ab-initio calculation of the zero-field splittings of the X³ Σ_g^- and B³ $\Pi_{g,i}$ states of the S₂ molecule. *Chem. Phys.* **1982**, *71*, 79–85.
- (38) Yarkony, D. R. On the use of the Breit-Pauli approximation for evaluating line strengths for spin-forbidden transitions. II. The symbolic matrix element method. *J. Chem. Phys.* **1986**, *84*, 2075–2078.
- (39) Kleinschmidt, M.; van Wüllen, C.; Marian, C. M. Intersystem-crossing and phosphorescence rates in *fac*-Ir^{III}(ppy)₃: A theoretical study involving multi-reference configuration interaction wavefunctions. *J. Chem. Phys.* **2015**, *142*, 094301.
- (40) Heil, A.; Gollnisch, K.; Kleinschmidt, M.; Marian, C. M. On the photophysics of four heteroleptic iridium(III) phenylpyridyl complexes investigated by relativistic multi-configuration methods. *Mol. Phys.* **2016**, *114*, 407–422.
- (41) von Arnim, M.; Ahlrichs, R. Performance of Parallel TURBOMOLE for Density Functional Calculations. *J. Comput. Chem.* **1998**, *19*, 1746–1757.
- (42) TURBOMOLE, a development of University of Karlsruhe and Forschungszentrum Karlsruhe GmbH, 1989–2007, TURBOMOLE GmbH, since 2007; available from <http://www.turbomole.com>.
- (43) Furche, F.; Ahlrichs, R. Adiabatic Time-Dependent Density Functional Methods for Excited State Properties. *J. Chem. Phys.* **2002**, *117*, 7433–7447.
- (44) Hirata, S.; Head-Gordon, M. Time-dependent density functional theory within the Tamm-Dancoff approximation. *Chem. Phys. Lett.* **1999**, *314*, 291–299.
- (45) Perdew, J. P.; Burke, K.; Ernzerhof, M. Generalized Gradient Approximation Made Simple. *Phys. Rev. Lett.* **1996**, *77*, 3865–3868.
- (46) Adamo, C.; Barone, V. Toward Reliable Density Functional Methods without Adjustable Parameters: The PBE0 Model. *J. Chem. Phys.* **1999**, *110*, 6158–6170.
- (47) Schäfer, A.; Horn, H.; Ahlrichs, R. Fully Optimized Contracted Gaussian Basis Sets for Atoms Li to Kr. *J. Chem. Phys.* **1992**, *97*, 2571–2577.
- (48) Andrae, D.; Häußermann, U.; Dolg, M.; Stoll, H.; Preuß, H. Energy-Adjusted Ab Initio Pseudopotentials for the Second and Third Row Transition Elements. *Theor. Chim. Acta* **1990**, *77*, 123–141.
- (49) Grimme, S. Density functional theory with London dispersion corrections. *WIREs Comput. Mol. Sci.* **2011**, *1*, 211–228.
- (50) Grimme, S.; Waletzke, M. A Combination of Kohn-Sham Density Functional Theory and Multi-Reference Configuration Interaction Methods. *J. Chem. Phys.* **1999**, *111*, 5645–5655.
- (51) Marian, C. M.; Heil, A.; Kleinschmidt, M. The DFT/MRCI Method. *WIREs Comp. Mol. Sci.* **2019**, *9*, e1394.
- (52) Heil, A.; Kleinschmidt, M.; Marian, C. M. On the performance of DFT/MRCI Hamiltonians for electronic excitations in transition metal complexes: The role of the damping function. *J. Chem. Phys.* **2018**, *149*, 164106.
- (53) Lee, C.; Yang, W.; Parr, R. G. Development of the Colle-Salvetti Correlation-Energy Formula into a Functional of the Electron Density. *Phys. Rev. B: Condens. Matter Mater. Phys.* **1988**, *37*, 785–789.
- (54) Becke, A. D. A New Mixing of Hartree-Fock and Local Density-Functional Theories. *J. Chem. Phys.* **1993**, *98*, 1372–1377.
- (55) Kleinschmidt, M.; Tatchen, J.; Marian, C. M. Spin-Orbit Coupling of DFT/MRCI Wavefunctions: Method, Test Calculations, and Application to Thiophene. *J. Comput. Chem.* **2002**, *23*, 824–833.

(56) Kleinschmidt, M.; Marian, C. M. Efficient Generation of Matrix Elements for One-Electron Spin-Orbit Operators. *Chem. Phys.* **2005**, *311*, 71–79.

(57) Mitin, A. V.; van Wüllen, C. Two-component relativistic density-functional calculations of the dimers of the halogens from bromine through element 117 using effective core potential and all-electron methods. *J. Chem. Phys.* **2006**, *124*, 064305.

(58) Hess, B. A.; Marian, C. M.; Wahlgren, U.; Gropen, O. A Mean-Field Spin-Orbit Method Applicable to Correlated Wavefunctions. *Chem. Phys. Lett.* **1996**, *251*, 365–371.

(59) Schimmelpfennig, B. *AMFI* (an atomic spin-orbit integral program); University of Stockholm: Stockholm, Sweden, 1996.

(60) Weymuth, T.; Haag, M. P.; Kiewisch, K.; Lubert, S.; Schenk, S.; Jacob, C. R.; Herrmann, C.; Neugebauer, J.; Reiher, M. MOVIPAC: Vibrational Spectroscopy with a Robust Meta-Program for Massively Parallel Standard and Inverse Calculations. *J. Comput. Chem.* **2012**, *33*, 2186–2198.

(61) Baiardi, A.; Bloino, J.; Barone, V. General Time Dependent Approach to Vibronic Spectroscopy Including Franck-Condon, Herzberg-Teller, and Duschinsky Effects. *J. Chem. Theory Comput.* **2013**, *9*, 4097–4115.

(62) Etinski, M.; Tatchen, J.; Marian, C. M. Thermal and Solvent Effects on the Triplet Formation in Cinnoline. *Phys. Chem. Chem. Phys.* **2014**, *16*, 4740–4751.

(63) Brooks, J.; Babayan, Y.; Lamansky, S.; Djurovich, P. I.; Tsyba, I.; Bau, R.; Thompson, M. E. Synthesis and Characterization of Phosphorescent Cyclometalated Platinum Complexes. *Inorg. Chem.* **2002**, *41*, 3055–3066.

(64) Pinter, P.; Strassner, T. Prediction of the Efficiency of Phosphorescent Emitters: A Theoretical Analysis of Triplet States in Platinum Blue Emitters. *Chem. - Eur. J.* **2019**, *25*, 4202–4205.

Supporting Information
for
Structure-Emission Property Relationships in
Cyclometalated Pt(II) β -Diketonate
Complexes

Adrian Heil and Christel M. Marian*

*Institute of Theoretical and Computational Chemistry, Heinrich Heine University
Düsseldorf, Universitätsstr. 1, D-40225 Düsseldorf, Germany*

E-mail: Christel.Marian@hhu.de

April 4, 2019

Table S1: Characteristic bond lengths (pm) and angles ($^{\circ}$) of (ppy)Pt(acac) in the ground and low-lying singlet and triplet states and available experimental bond lengths¹

(ppy)Pt(acac)	Exp.	S ₀	S ₀	S ₁	T ₁	T _{MC}
Pt-C ₁₁	196	197	193	194	201	
Pt-N ₁	198	201	200	200	222	
Pt-O ₁	206	213	212	213	215	
Pt-O ₂	200	203	207	205	222	
C ₁₁ -Pt-N ₁	-	81.2	82.7	82.7	78.8	
O ₁ -Pt-O ₂	-	90.1	89.3	89.8	85.8	
O ₁ -Pt-N ₁ -C ₅	-	180	180	180	172	
O ₂ -Pt-C ₁₁ -C ₆	-	180	180	180	91	

Table S2: Characteristic bond lengths (pm) and angles ($^{\circ}$) of (bzq)Pt(acac) in the ground and low-lying singlet and triplet states and available experimental bond lengths¹

(bzq)Pt(acac)	Exp.	S ₀	S ₀	S ₁	T ₁	T _{MC}
Pt-C ₁₁	199	198	194	203	202	
Pt-N ₁	198	202	202	196	224	
Pt-O ₁	203	213	210	211	215	
Pt-O ₂	203	203	206	204	221	
C ₁₁ -Pt-N ₁	-	82.1	83.0	81.6	79.6	
O ₁ -Pt-O ₂	-	90.8	90.1	90.2	86.0	
O ₁ -Pt-N ₁ -C ₅	-	180	180	180	173	
O ₂ -Pt-C ₁₁ -C ₆	-	180	180	180	90	

Table S3: Characteristic bond lengths (pm) and angles ($^{\circ}$) of (dbq)Pt(acac) in the ground and low-lying singlet and triplet states and available experimental bond lengths¹

(dbq)Pt(acac)	Exp.	S ₀	S ₀	S ₁	T ₁	T _{MC}
Pt-C ₁₁	199	198	193	193	223	
Pt-N ₁	200	202	201	201	202	
Pt-O ₁	208	213	210	212	215	
Pt-O ₂	201	203	206	205	222	
C ₁₁ -Pt-N ₁	-	81.7	82.7	82.9	79.0	
O ₁ -Pt-O ₂	-	90.5	89.8	90.1	85.9	
O ₁ -Pt-N ₁ -C ₅	-	180	180	180	173	
O ₂ -Pt-C ₁₁ -C ₆	-	180	180	179.9	91	

Table S4: Characteristic bond lengths (pm) and angles ($^{\circ}$) of DPANIM in the ground and low-lying singlet and triplet states and available experimental bond lengths²

DPANIM	Exp. S_0	S_0	S_1	T_1	T_2	T_{MC}
Pt-C ₁	195.5	194	191	191	195	199
Pt-C ₃	197.5	199	199	199	196	214
Pt-O ₁	208.6	212	213	213	210	223
Pt-O ₂	204.2	208	207	207	208	211
C ₁ -N ₁		137	139	139	137	137
C ₁ -N ₂		138	136	136	135	136
C ₄ -C ₅		138	144	145	140	138
N ₁ -C ₂		142	141	141	139	142
C ₂ -C ₃		141	141	141	143	140
O ₁ -C ₆		126	126	126	127	126
O ₂ -C ₈		126	127	127	127	126
C ₆ -C ₇		141	141	141	141	141
C ₇ -C ₈		140	140	140	141	141
C ₁ -Pt-C ₃		79.8	80.2	80.3	79.9	79.3
O ₁ -Pt-O ₂		88.3	87.9	87.9	88.2	87.7
O ₁ -Pt-O ₂ -C ₈		0.0	0.0	0.0	0.0	12.9
O ₁ -Pt-C ₁ -N ₁	175.2	180.0	180.0	180.0	180.0	-99.1
O ₁ -Pt-C ₁ -N ₂		0.0	0.0	0.0	0.0	68.6
O ₁ -Pt-O ₂ -C ₃		180.0	180.0	180.0	180.0	98.2
C ₃ -C ₂ -N ₁ -C ₁		0.0	0.0	0.0	0.0	11.9

Table S5: Characteristic bond lengths (pm) and angles ($^{\circ}$) of DPNIM in the ground and low-lying singlet and triplet states and available experimental bond lengths²

DPNIM	Exp. S_0	S_0	S_1	T_1	T_2	T_{MC}
Pt-C ₁	190.6	193	196	193	194	198
Pt-C ₃	196.7	199	193	198	195	214
Pt-O ₁	207.2	213	209	212	211	222
Pt-O ₂	203.4	208	210	208	210	210
C ₁ -N ₁		137	140	138	140	136
C ₁ -N ₂		135	135	136	137	136
C ₄ -C ₅		142	142	139	142	142
N ₁ -C ₂		142	137	141	138	142
C ₂ -C ₃		141	148	141	145	140
O ₁ -C ₆		126	127	126	127	126
O ₂ -C ₈		127	127	127	127	126
C ₆ -C ₇		141	140	141	141	141
C ₇ -C ₈		140	141	140	141	141
C ₁ -Pt-C ₃		79.9	80.4	79.7	80.3	79.3
O ₁ -Pt-O ₂		88.1	88.4	88.3	88.2	87.7
O ₁ -Pt-O ₂ -C ₈		0.0	0.0	0.0	0.0	12.7
O ₁ -Pt-C ₁ -N ₁	-170.6	180.0	180.0	180.0	180.0	-99.6
O ₁ -Pt-C ₁ -N ₂		0.0	0.0	0.0	0.0	66.9
O ₁ -Pt-O ₂ -C ₃		180.0	180.0	180.0	180.0	97.9
C ₃ -C ₂ -N ₁ -C ₁		0.0	0.0	0.0	0.0	11.0

Table S6: Characteristic bond lengths (pm) and angles ($^{\circ}$) of DPBIM in the ground and low-lying singlet and triplet states and available experimental bond lengths²

DPBIM	Exp. S_0	S_0	S_1	T_1	T'_1	T_{MC}
Pt-C ₁	192.5	193	197	194	195	199
Pt-C ₃	198.1	199	193	194	199	214
Pt-O ₁	208.2	213	209	211	211	223
Pt-O ₂	203.8	208	215	210	207	210
C ₁ -N ₁		137	142	142	137	136
C ₁ -N ₂		135	138	138	135	136
C ₄ -C ₅		142	141	142	141	141
N ₁ -C ₂		142	138	135	142	143
C ₂ -C ₃		141	145	148	141	140
O ₁ -C ₆		126	127	126	130	126
O ₂ -C ₈		127	126	126	130	126
C ₆ -C ₇		141	140	141	142	141
C ₇ -C ₈		140	141	141	143	141
C ₁ -Pt-C ₃		79.9	81.0	80.5	79.8	79.2
O ₁ -Pt-O ₂		88.2	87.4	88.2	86.5	87.7
O ₁ -Pt-O ₂ -C ₈		0.0	-4.3	0.0	39.3	12.9
O ₁ -Pt-C ₁ -N ₁	-179.3	180.0	163.0	-178.9	-178.4	-98.7
O ₁ -Pt-C ₁ -N ₂		0.0	19.2	-1.8	-2.8	67.5
O ₁ -Pt-O ₂ -C ₃		180.0	-173.3	179.5	179.8	97.6
C ₃ -C ₂ -N ₁ -C ₁		0.0	-8.2	0.6	1.6	11.3

Table S7: Characteristic bond lengths (pm) and angles ($^{\circ}$) of DPIM in the ground and low-lying singlet and triplet states and available experimental bond lengths²

DPIM	Exp. S_0	S_0	S_1	T_1	T'_1	T_{MC}
Pt-C ₁	195.1	194	198	195	196	200
Pt-C ₃	198.5	199	194	194	200	215
Pt-O ₁	208.4	212	209	212	210	224
Pt-O ₂	203.2	208	215	210	207	211
C ₁ -N ₁		136	141	142	136	136
C ₁ -N ₂		135	138	138	136	136
C ₄ -C ₅		136	135	136	136	136
N ₁ -C ₂		142	137	134	142	143
C ₂ -C ₃		141	145	148	141	140
O ₁ -C ₆		126	127	126	130	126
O ₂ -C ₈		127	126	127	130	126
C ₆ -C ₇		141	140	141	142	141
C ₇ -C ₈		140	141	141	143	141
C ₁ -Pt-C ₃		79.8	81.5	81.1	79.9	79.2
O ₁ -Pt-O ₂		88.7	87.4	88.2	86.5	87.3
O ₁ -Pt-O ₂ -C ₈		0.0	-5.3	-1.0	41.1	9.4
O ₁ -Pt-C ₁ -N ₁	-174.3	180.0	162.3	171.0	-178.0	-98.8
O ₁ -Pt-C ₁ -N ₂		0.0	18.5	2.0	-3.0	74.1
O ₁ -Pt-O ₂ -C ₃		180.0	-172.3	176.3	179.7	97.7
C ₃ -C ₂ -N ₁ -C ₁		0.0	-6.6	-2.5	1.1	5.6

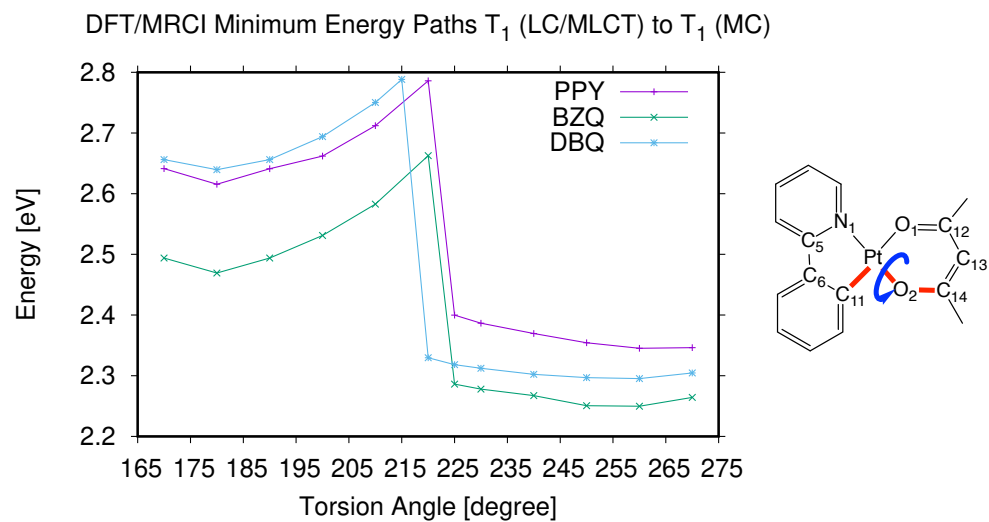


Figure S1: DFT/MRCI energy profiles of the (C[^]N) cyclometalated Pt (acac) complexes calculated along minimum energy paths obtained by constrained optimization with fixed C₁₁-Pt-O₂-C₁₄ dihedral angle. The data points corresponding to the LC or LC/MLCT and MC triplet minima are provided in Table S8.

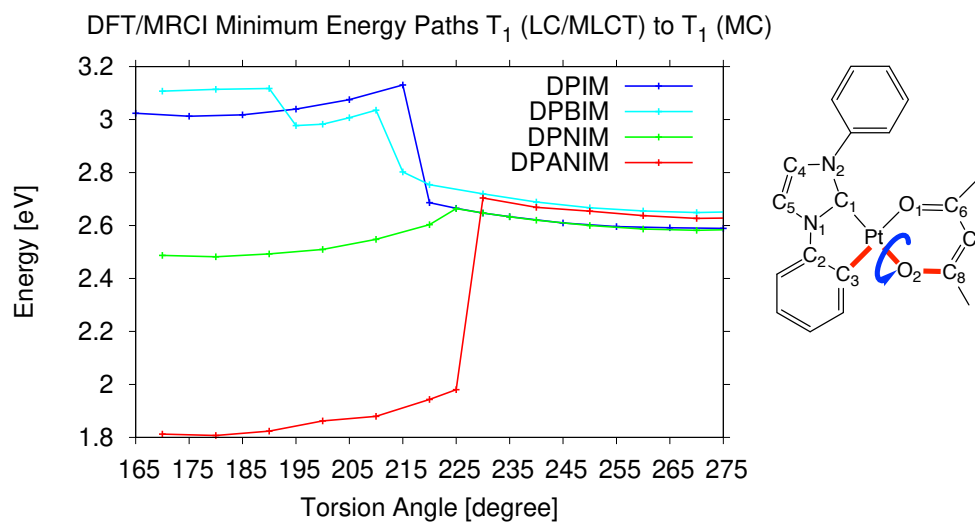


Figure S2: DFT/MRCI energy profiles of the ($C^{\wedge}C^*$) cyclometalated Pt (acac) complexes calculated along minimum energy paths obtained by constrained optimization with fixed C_3 -Pt- O_2 - C_8 dihedral angle. The data points corresponding to the LC or LC/MLCT and MC triplet minima are provided in Table S8.

Table S8: Energy minima and maxima in the energy profiles of all (C[^]N) and C[^]C*) cyclometalated Pt (acac) complexes depicted in Figure S1 and S2

Complex	MLCT min (eV)	MC min (eV)	Barrier (eV)
(ppy)Pt(acac)	2.62 (180°)	2.35 (260°)	2.79 (220°)
(bzq)Pt(acac)	2.47 (180°)	2.25 (260°)	2.66 (220°)
(dbq)Pt(acac)	2.64 (180°)	2.30 (260°)	2.79 (215°)
DPIM	3.01 (180°)	2.59 (275°)	3.13 (215°)
DPBIM	3.11 (180°), 2.98 (195°)	2.65 (275°)	3.12 (190°), 3.04 (220°)
DPNIM	2.48 (180°)	2.58 (270°)	2.66 (225°)
DPANIM	1.81 (180°)	2.62 (270°)	2.70 (230°)

Table S9: Vertical emission energies of the sublevels of the lowest triplet state of all (C[^]N) and C[^]C^{*}) cyclometalated Pt (acac) complexes with zero-field splitting (ZFS) and rate. The ZFS is presented as the difference to the first sublevel.

Complex	T ₁ sublevel	ΔE_{vert} (eV)	ZFS (cm ⁻¹)	rate (s ⁻¹)	Exp. ZFS (cm ⁻¹) ¹	Exp. rate (s ⁻¹) ¹
(ppy)Pt(acac)	I	2.42	0	2.1×10^4	0	1.1×10^4
	II	2.42	7	3.5×10^4	8	5.9×10^4
	III	2.43	87	1.9×10^5	11.5	3.1×10^5
(bzq)Pt(acac)	I	2.30	0	5.5×10^3	0	3.9×10^3
	II	2.30	11	1.0×10^2	< 2	1.5×10^4
	III	2.31	80	2.2×10^4	< 2	6.3×10^4
(dbq)Pt(acac)	I	2.49	0	2.8×10^4	0	1.6×10^4
	II	2.49	7	3.0×10^4	5.5	5.3×10^4
	III	2.50	90	2.5×10^5	46.5	5.9×10^5
DPIM	I	2.67	0	2.4×10^3		
	II	2.67	32	1.6×10^5		
	III	2.68	83	1.3×10^5		
DPBIM	I	2.65	0	2.0×10^3		
	II	2.65	32	1.5×10^5		
	III	2.66	79	1.8×10^5		
DPNIM	I	2.35	0	1.1×10^3		
	II	2.35	8	3.6×10^2		
	III	2.36	60	8.6×10^3		
DPANIM	I	1.54	0	7.6×10^1		
	II	1.54	10	1.9×10^1		
	III	1.55	67	3.6×10^3		

Geometries

(ppy)Pt(acac)

S₀

C	-1.2109940	1.2932442	0.0000000
C	-2.4935365	0.6889803	-0.0000026
C	-3.6590173	1.4686314	-0.0000010
C	-3.5623356	2.8550584	0.0000003
C	-2.3004916	3.4607164	0.0000020
C	-1.1379091	2.6905644	0.0000000
C	-2.4719590	-0.7685213	-0.0000019
N	-1.2183786	-1.2997645	-0.0000049
C	-1.0303500	-2.6251663	-0.0000025
C	-2.0940815	-3.5155704	0.0000016
C	-3.3919466	-3.0007173	0.0000019
C	-3.5789894	-1.6249822	-0.0000000
Pt	0.2973955	0.0231866	-0.0000021
O	1.7239540	1.4715979	0.0000042
C	2.9807100	1.2771473	0.0000015
C	3.6479780	0.0426251	0.0000018
C	3.0558001	-1.2360758	-0.0000017
O	1.8156717	-1.4771135	-0.0000074
H	0.0154287	-2.9462415	-0.0000043
H	-1.9024704	-4.5909449	0.0000036
H	-4.2559086	-3.6718564	0.0000039
H	-4.4685118	3.4677192	0.0000012
H	-2.2262972	4.5535731	0.0000021
H	-0.1553099	3.1718348	0.0000010
H	4.7389185	0.0794921	0.0000035
H	-4.5849732	-1.2010997	0.0000011
H	-4.6471678	0.9971168	-0.0000021
C	3.9468347	-2.4522085	0.0000005
C	3.7895484	2.5476096	-0.0000004
H	4.8736897	2.3613889	-0.0000016
H	3.5233689	3.1481355	-0.8872347
H	3.5233710	3.1481378	0.8872331
H	5.0177138	-2.1995078	0.0000023
H	3.7201213	-3.0684941	0.8875703
H	3.7201241	-3.0684957	-0.8875687

S₁

C	-1.2108340	1.2689900	-0.0000029
C	-2.5186606	0.6476491	-0.0000113
C	-3.6412119	1.4705984	-0.0000187
C	-3.4967670	2.8669735	-0.0000025
C	-2.2330828	3.4768289	0.0000164
C	-1.0955264	2.6754736	0.0000150
C	-2.5025901	-0.8011355	-0.0000123
N	-1.2024821	-1.3276236	-0.0000246
C	-1.0333564	-2.6738671	-0.0000153
C	-2.0933860	-3.5462216	0.0000053
C	-3.4274418	-3.0404340	0.0000177
C	-3.5964549	-1.6596082	0.0000080
Pt	0.2665471	0.0240236	-0.0000273
O	1.7186949	1.5015053	-0.0000252
C	2.9712189	1.3113066	-0.0000071
C	3.6372241	0.0699798	0.0000062
C	3.0403274	-1.2014037	-0.0000041
O	1.7932933	-1.4389882	-0.0000217
H	0.0049533	-3.0147470	-0.0000248
H	-1.8956416	-4.6209197	0.0000118
H	-4.2871999	-3.7129549	0.0000359
H	-4.3961594	3.4909799	-0.0000041
H	-2.1482265	4.5670248	0.0000299
H	-0.0947514	3.1170447	0.0000250
H	4.7280791	0.1024086	0.0000217
H	-4.6022611	-1.2298623	0.0000200
H	-4.6465598	1.0399258	-0.0000346
C	3.9168101	-2.4244573	0.0000046
C	3.7854147	2.5771725	-0.0000017
H	4.8686791	2.3872897	0.0000021
H	3.5205424	3.1781839	-0.8873640
H	3.5205369	3.1781795	0.8873622
H	4.9901995	-2.1837572	0.0000129
H	3.6800295	-3.0377778	0.8868974
H	3.6800432	-3.0377802	-0.8868900

T₁ MLCT

C	-1.1875545	1.2856452	0.0001236
C	-2.5172312	0.6408422	-0.0002662
C	-3.6732070	1.4674352	-0.0011788
C	-3.5327521	2.8365689	-0.0016929
C	-2.2487209	3.4660727	-0.0012618
C	-1.1029299	2.6872803	-0.0003587
C	-2.4960152	-0.7686518	0.0002479
N	-1.1974177	-1.3145601	0.0007506
C	-1.0286718	-2.6389220	0.0014110
C	-2.0941024	-3.5253662	0.0016540
C	-3.4245886	-3.0109551	0.0011305
C	-3.6079704	-1.6507090	0.0004099
Pt	0.2831034	0.0284630	0.0006968
O	1.7232047	1.4908085	0.0012050
C	2.9777258	1.2955061	0.0010413
C	3.6431492	0.0578493	-0.0000338
C	3.0491397	-1.2180817	-0.0006478
O	1.8068993	-1.4601276	0.0001587
H	0.0118831	-2.9771522	0.0017400
H	-1.8983771	-4.5996147	0.0022506
H	-4.2814208	-3.6893706	0.0013175
H	-4.4297996	3.4644863	-0.0024786
H	-2.1837152	4.5575430	-0.0016824
H	-0.1110122	3.1485939	-0.0000365
H	4.7340384	0.0923148	-0.0004579
H	-4.6151121	-1.2263873	0.0000155
H	-4.6723916	1.0231453	-0.0015692
C	3.9358243	-2.4359157	-0.0025506
C	3.7913593	2.5626284	0.0021172
H	4.8747625	2.3726411	0.0017999
H	3.5268566	3.1647358	-0.8845446
H	3.5271110	3.1629638	0.8900634
H	5.0074870	-2.1871477	-0.0024302
H	3.7053826	-3.0526527	0.8836753
H	3.7050632	-3.0499094	-0.8906185

T₁ MC

C	-1.3932614	1.7118992	0.5279329
C	-2.4572010	0.8833552	0.0898545
C	-3.7054886	1.4333124	-0.2389970
C	-3.9166137	2.8038315	-0.1425728
C	-2.8756512	3.6320651	0.2836220
C	-1.6327759	3.0896467	0.6119761
C	-2.1826516	-0.5587148	0.0019267
N	-0.9275604	-0.9325425	0.3217297
C	-0.5434876	-2.2050090	0.2937017
C	-1.4114630	-3.2267834	-0.0720737
C	-2.7196004	-2.8777639	-0.4119079
C	-3.1080017	-1.5448306	-0.3744433
Pt	0.3417868	0.7802589	0.9437634
O	1.3488973	0.8747600	-1.0303812
C	2.5132033	0.4571865	-1.2770485
C	3.4102668	-0.1602821	-0.3815590
C	3.1911048	-0.4179922	0.9836662
O	2.1381598	-0.1687179	1.6380462
H	0.4966719	-2.3995360	0.5754549
H	-1.0682613	-4.2637738	-0.0898456
H	-3.4397858	-3.6475864	-0.7053788
H	-4.8915531	3.2273956	-0.4010724
H	-3.0356852	4.7126505	0.3615269
H	-0.8319285	3.7582941	0.9438400
H	4.3823364	-0.4480945	-0.7859021
H	-4.1303373	-1.2646487	-0.6340613
H	-4.5255113	0.7934111	-0.5784304
C	4.3015070	-1.0473230	1.7894668
C	2.9598624	0.6721481	-2.7053058
H	3.9611714	0.2626738	-2.9079494
H	2.9596128	1.7546860	-2.9215885
H	2.2272975	0.2087762	-3.3881257
H	5.1709966	-1.3305220	1.1771547
H	4.6262553	-0.3351243	2.5687741
H	3.9138189	-1.9374058	2.3140566

T₁ barrier at 220°

C	-1.3207867	1.2856588	0.4972405
C	-2.4696345	0.6296439	-0.0150408
C	-3.6889284	1.3127345	-0.1385608
C	-3.7882874	2.6470004	0.2382699
C	-2.6640615	3.3053385	0.7418945
C	-1.4494704	2.6305454	0.8670974
C	-2.3157534	-0.7814261	-0.4027498
N	-1.0708022	-1.2856201	-0.2850174
C	-0.7880335	-2.5491864	-0.5877905
C	-1.7612498	-3.4260245	-1.0521309
C	-3.0624567	-2.9398182	-1.1898174
C	-3.3430552	-1.6189625	-0.8637016
Pt	0.3544179	0.1725664	0.5754588
O	1.4606661	0.8239708	-1.2384330
C	2.7166630	0.7624215	-1.3484912
C	3.6103401	0.0386610	-0.5320944
C	3.2463660	-0.8593790	0.4868287
O	2.0650509	-1.1090189	0.8659511
H	0.2549539	-2.8519646	-0.4470843
H	-1.5028988	-4.4584369	-1.2991072
H	-3.8622923	-3.5940643	-1.5499490
H	-4.7408980	3.1753839	0.1373689
H	-2.7361939	4.3565009	1.0404550
H	-0.5819810	3.1671569	1.2646686
H	4.6738045	0.1322308	-0.7598864
H	-4.3596401	-1.2345723	-0.9615003
H	-4.5740545	0.8085590	-0.5385648
C	4.3240884	-1.6503696	1.1851377
C	3.2796234	1.5578853	-2.5035640
H	4.3779886	1.5141161	-2.5585223
H	2.9560359	2.6089244	-2.4113548
H	2.8535499	1.1728497	-3.4465113
H	5.3325629	-1.4378829	0.7994464
H	4.2925187	-1.4268853	2.2660418
H	4.1109225	-2.7281071	1.0761275

(bzq)Pt(acac)

S₀

C	3.6168919	2.8001956	-0.0000026
C	3.3061740	1.3979358	-0.0000028
C	1.9420056	1.0391419	0.0000008
C	0.9067935	2.0093975	0.0000052
C	1.2339276	3.3841992	0.0000040
C	2.6263839	3.7429396	0.0000024
N	1.5279646	-0.2579236	0.0000023
C	2.4263642	-1.2365535	-0.0000008
C	3.8019655	-0.9656087	0.0000009
C	4.2447243	0.3480100	-0.0000017
C	0.1642953	4.3028253	0.0000031
C	-1.1410895	3.8307879	-0.0000003
C	-1.4420485	2.4522964	-0.0000009
C	-0.4208320	1.5091473	0.0000032
Pt	-0.4850438	-0.4719436	-0.0000013
O	-2.5123586	-0.5447799	-0.0000071
C	-3.2067056	-1.6108922	-0.0000005
O	-0.3773596	-2.5955198	-0.0000076
C	-1.3891709	-3.3521301	-0.0000001
C	-2.7349752	-2.9329060	0.0000057
H	2.0220514	-2.2528254	-0.0000009
H	4.5079063	-1.7993493	0.0000011
H	5.3158525	0.5741103	-0.0000013
H	0.3676923	5.3782151	0.0000025
H	-1.9656356	4.5518579	-0.0000034
H	-2.4857640	2.1237663	-0.0000040
H	-3.4929324	-3.7181362	0.0000107
H	4.6685362	3.1019805	-0.0000043
H	2.8902980	4.8054870	0.0000034
C	-4.6922036	-1.3633853	-0.0000014
C	-1.0845404	-4.8285337	0.0000001
H	-1.9898205	-5.4538933	0.0000011
H	-0.4749143	-5.0729565	-0.8875812
H	-0.4749129	-5.0729565	0.8875803
H	-5.2783953	-2.2942475	-0.0000008
H	-4.9605627	-0.7638757	0.8872760
H	-4.9605617	-0.7638769	-0.8872799

S₁

C	-3.5869137	-1.5311776	-0.0001121
C	-2.4018043	-0.7784217	0.0002911
N	-1.1410331	-1.3384044	0.0007309
C	-1.0393504	-2.6964269	0.0008542
C	-2.1696323	-3.5002097	0.0005128
C	-3.4635850	-2.9558958	0.0000032
C	-2.4275532	0.6278432	0.0002468
C	-1.1428415	1.2823965	0.0006183
C	-1.1118997	2.6857320	0.0006314
C	-2.3187107	3.4111466	0.0002646
C	-3.5492051	2.7643672	-0.0001684
C	-3.6422214	1.3371603	-0.0002025
Pt	0.3380900	0.0333792	0.0007967
O	1.8421518	-1.4359486	0.0005431
C	3.0898874	-1.2000057	0.0000159
C	3.9635585	-2.4247791	-0.0005830
O	1.7755617	1.5111987	0.0007322
C	3.0276729	1.3154676	0.0001978
C	3.8466061	2.5780890	-0.0001977
C	3.6884910	0.0708020	-0.0001457
H	-0.0253151	-3.1005235	0.0012258
H	-2.0281735	-4.5847788	0.0006492
H	-4.3504826	-3.5922767	-0.0002911
H	-4.4718542	3.3538803	-0.0004929
H	-2.2902863	4.5049268	0.0002979
H	-0.1484140	3.2032893	0.0009265
H	4.7794577	0.1001097	-0.0006154
C	-4.8089495	-0.7952256	-0.0006203
C	-4.8496481	0.5877786	-0.0006669
H	4.9290888	2.3838141	0.0000923
H	3.5845517	3.1797717	-0.8878996
H	3.5841596	3.1806491	0.8867784
H	5.0373918	-2.1862770	-0.0003373
H	3.7251950	-3.0383064	0.8856866
H	3.7254286	-3.0372038	-0.8876916
H	-5.7473835	-1.3591644	-0.0009950
H	-5.8108753	1.1100248	-0.0010761

T₁ MLCT

C	-3.5951546	-1.5308906	-0.0001715
C	-2.3889411	-0.7725883	0.0004581
N	-1.1652007	-1.3296869	0.0010737
C	-1.0420320	-2.6946073	0.0012045
C	-2.1679840	-3.5070078	0.0006684
C	-3.4515015	-2.9610025	-0.0000477
C	-2.4160360	0.6477938	0.0004108
C	-1.1547789	1.2740732	0.0009618
C	-1.1252766	2.6959580	0.0009702
C	-2.3262871	3.4227139	0.0003888
C	-3.5617655	2.7869923	-0.0002392
C	-3.6498732	1.3539782	-0.0002596
Pt	0.3469492	0.0196502	0.0012436
O	1.8562659	-1.4534788	0.0009485
C	3.0989660	-1.2144129	0.0002064
C	3.9836286	-2.4331103	-0.0008362
O	1.7637403	1.4835392	0.0010353
C	3.0221881	1.2979679	0.0003549
C	3.8264394	2.5705182	-0.0004322
C	3.6911539	0.0635922	0.0000523
H	-0.0206882	-3.0787072	0.0017145
H	-2.0296056	-4.5917079	0.0008057
H	-4.3382655	-3.5992349	-0.0005165
H	-4.4835594	3.3769409	-0.0007358
H	-2.2909561	4.5168656	0.0003997
H	-0.1615350	3.2125803	0.0014097
H	4.7819663	0.1005157	-0.0005653
C	-4.7984355	-0.8132313	-0.0008947
C	-4.8374962	0.6168839	-0.0009414
H	4.9109285	2.3866666	-0.0001390
H	3.5596242	3.1696615	-0.8884792
H	3.5592889	3.1711187	0.8865094
H	5.0554309	-2.1848689	-0.0005630
H	3.7524426	-3.0493060	0.8855100
H	3.7525940	-3.0475080	-0.8884902
H	-5.7413207	-1.3685592	-0.0014652
H	-5.8037530	1.1286995	-0.0015496

T₁ MC

C	-1.3469363	1.7465574	0.5452127
C	-2.3860864	0.8803692	0.1095361
C	-3.6779259	1.3474112	-0.2423696
C	-3.9286468	2.7326291	-0.1612421
C	-2.9234421	3.5882881	0.2555689
C	-1.6468012	3.1040116	0.6058811
C	-2.1151125	-0.5253355	0.0246048
N	-0.8715720	-0.9379612	0.3554403
C	-0.5464468	-2.2163823	0.3104567
C	-1.4684468	-3.1988663	-0.0830787
C	-2.7497173	-2.8087908	-0.4327517
C	-3.1087973	-1.4473106	-0.3876409
Pt	0.3924802	0.8132029	0.9658142
O	1.3830871	0.9037093	-1.0094347
C	2.5379746	0.4652504	-1.2667438
C	3.4340209	-0.1635771	-0.3789262
C	3.2259298	-0.4130303	0.9899936
O	2.1838457	-0.1464085	1.6543675
H	0.4805468	-2.4702063	0.5933017
H	-1.1649742	-4.2481623	-0.1119935
H	-3.4908722	-3.5512360	-0.7460929
H	-4.9166302	3.1200939	-0.4287012
H	-3.1225883	4.6633445	0.3174878
H	-0.8851235	3.8195483	0.9322858
H	4.3969814	-0.4678459	-0.7929113
C	-4.4050135	-0.9395391	-0.7310132
C	-4.6700728	0.3971500	-0.6623860
C	4.3354945	-1.0563263	1.7857827
C	2.9699665	0.6670019	-2.7010522
H	3.9690115	0.2553313	-2.9107165
H	2.9663445	1.7474078	-2.9273531
H	2.2301256	0.1965569	-3.3713201
H	5.2007809	-1.3387335	1.1672934
H	4.6669087	-0.3542689	2.5713372
H	3.9448473	-1.9500225	2.3023502
H	-5.1773692	-1.6455339	-1.0506244
H	-5.6639512	0.7702235	-0.9303725

T₁ barrier at 220°

C	-1.0059433	1.3415146	0.5843339
C	-2.1720665	0.6719167	0.1222242
C	-3.4356040	1.3082708	0.0292893
C	-3.5256796	2.6652392	0.4023412
C	-2.3961245	3.3312241	0.8458803
C	-1.1500849	2.6791720	0.9382767
C	-2.0670321	-0.7066543	-0.2607647
N	-0.8476911	-1.2831687	-0.1760929
C	-0.6698946	-2.5518321	-0.4941188
C	-1.7323164	-3.3539225	-0.9393799
C	-2.9924354	-2.7917150	-1.0481286
C	-3.1936173	-1.4396835	-0.7073048
Pt	0.6476932	0.1847761	0.6030056
O	1.6879547	0.7915296	-1.2596759
C	2.9354116	0.6889661	-1.4264465
C	3.8424441	-0.0563082	-0.6455970
C	3.4985028	-0.9338271	0.3982724
O	2.3293165	-1.1426073	0.8342686
H	0.3490608	-2.9405162	-0.3934794
H	-1.5514909	-4.4001201	-1.1981097
H	-3.8399913	-3.3902030	-1.3977666
H	-4.4891674	3.1804328	0.3385199
H	-2.4706423	4.3848715	1.1349208
H	-0.2861656	3.2464051	1.2995301
H	4.8965058	0.0013224	-0.9234804
C	-4.4556583	-0.7640509	-0.7845747
C	-4.5640990	0.5500069	-0.4342687
C	4.5822395	-1.7535818	1.0526354
C	3.4684386	1.4581064	-2.6129406
H	4.5607095	1.3760260	-2.7206177
H	3.1860069	2.5202545	-2.5126263
H	2.9840345	1.0829431	-3.5313881
H	5.5787756	-1.5709162	0.6231337
H	4.6033062	-1.5273318	2.1331560
H	4.3340935	-2.8250003	0.9560047
H	-5.3301045	-1.3229157	-1.1314349
H	-5.5339325	1.0538115	-0.5002288

(dbq)Pt(acac)

S₀

C	3.0656113	1.9953429	-0.0000004
C	2.6855266	0.5803438	0.0000004
C	1.3154399	0.2530229	-0.0000023
C	0.3257799	1.2826619	0.0000014
C	0.6518721	2.6504924	0.0000001
C	2.0687456	3.0132917	0.0000012
N	-0.9613597	0.8414467	0.0000003
C	-1.9679008	1.7116473	0.0000036
C	-1.7301671	3.0866666	0.0000012
C	-0.4231447	3.5555434	0.0000019
C	3.5919922	-0.4959760	-0.0000004
C	3.1223221	-1.8051617	0.0000000
C	1.7505590	-2.1052010	-0.0000025
C	0.8162201	-1.0746691	-0.0000018
C	4.4188223	2.3897684	0.0000004
C	4.7910334	3.7227453	-0.0000016
C	3.8089788	4.7210476	-0.0000000
C	2.4723880	4.3630585	-0.0000001
Pt	-1.1593180	-1.1671821	-0.0000020
O	-1.2116818	-3.1969832	-0.0000056
C	-2.2674402	-3.9065968	0.0000000
O	-3.2870302	-1.0921968	0.0000018
C	-4.0315255	-2.1128534	-0.0000012
C	-3.5957265	-3.4531300	0.0000014
H	-2.9715231	1.2770102	0.0000040
H	-2.5754900	3.7783900	0.0000022
H	-0.2454526	4.6334595	0.0000006
H	4.6701825	-0.3223080	0.0000011
H	3.8485079	-2.6251819	0.0000002
H	1.4133747	-3.1459013	-0.0000020
H	-4.3709333	-4.2212333	0.0000030
H	1.7184904	5.1538075	0.0000005
H	4.0922903	5.7774179	-0.0000006
H	5.8513060	3.9922026	-0.0000015
H	5.1989745	1.6259795	-0.0000001
C	-1.9994715	-5.3885355	0.0000024
C	-5.5117034	-1.8267892	-0.0000033
H	-2.9223448	-5.9872895	0.0000046
H	-1.3963554	-5.6486880	-0.8872408
H	-1.3963535	-5.6486851	0.8872452
H	-6.1254972	-2.7399682	-0.0000047
H	-5.7640001	-1.2204087	0.8875338
H	-5.7639979	-1.2204074	-0.8875401

S₁

C	3.0652629	1.9857025	0.0000076
C	2.6577221	0.5930264	0.0000079
C	1.2915483	0.3017705	-0.0000015
C	0.3040887	1.3262214	-0.0000020
C	0.6440604	2.6767098	0.0000088
C	2.0584340	3.0072448	0.0000077
N	-0.9925401	0.8596320	-0.0000116
C	-2.0122784	1.7679517	0.0000002
C	-1.7471676	3.1233293	0.0000138
C	-0.4315565	3.6207777	0.0000154
C	3.5450755	-0.5240195	0.0000107
C	3.0781228	-1.8374906	0.0000008
C	1.7057454	-2.1119319	-0.0000082
C	0.7860028	-1.0460493	-0.0000076
C	4.4230462	2.3666792	-0.0000008
C	4.8048607	3.6954717	-0.0000113
C	3.8210736	4.6983457	-0.0000088
C	2.4827459	4.3563687	0.0000027
Pt	-1.1442120	-1.1480983	-0.0000138
O	-1.1867456	-3.2118386	-0.0000125
C	-2.2324983	-3.9275263	0.0000000
O	-3.2462926	-1.1114988	-0.0000204
C	-3.9971422	-2.1356715	-0.0000087
C	-3.5663413	-3.4726206	0.0000045
H	-3.0224060	1.3554335	-0.0000030
H	-2.5932618	3.8164166	0.0000227
H	-0.2542442	4.6955487	0.0000244
H	4.6249549	-0.3575909	0.0000205
H	3.7998765	-2.6595034	0.0000008
H	1.3345324	-3.1405208	-0.0000157
H	-4.3420574	-4.2398975	0.0000151
H	1.7336595	5.1503282	0.0000034
H	4.1125684	5.7530669	-0.0000167
H	5.8657040	3.9613975	-0.0000215
H	5.1999912	1.5981679	-0.0000030
C	-1.9645986	-5.4083043	0.0000094
C	-5.4715657	-1.8370454	-0.0000108
H	-2.8866018	-6.0078423	0.0000183
H	-1.3612394	-5.6675125	-0.8874088
H	-1.3612300	-5.6675003	0.8874250
H	-6.0935882	-2.7442994	-0.0000132
H	-5.7157557	-1.2264161	0.8867221
H	-5.7157526	-1.2264124	-0.8867420

S23

T₁ MLCT

C	3.0731636	1.9986501	0.0005367
C	2.6748900	0.5954835	0.0020097
C	1.2889396	0.3028508	0.0011460
C	0.3234862	1.3069715	0.0004554
C	0.6501077	2.6835393	0.0001945
C	2.0750181	3.0202188	-0.0008756
N	-0.9954806	0.8460814	0.0005323
C	-1.9926367	1.7477672	0.0013467
C	-1.7393541	3.1069579	0.0017537
C	-0.4070054	3.5998279	0.0010128
C	3.5435651	-0.5000692	0.0041501
C	3.0750986	-1.8395503	0.0048811
C	1.7138599	-2.1211102	0.0032727
C	0.7803351	-1.0685793	0.0014149
C	4.4287248	2.3852866	-0.0000370
C	4.8065434	3.7161200	-0.0024038
C	3.8273846	4.7193458	-0.0044249
C	2.4898406	4.3682003	-0.0035625
Pt	-1.1508522	-1.1599117	-0.0001133
O	-1.1958810	-3.2128643	-0.0018294
C	-2.2460057	-3.9255637	-0.0026246
O	-3.2657129	-1.1096516	-0.0000098
C	-4.0114739	-2.1339851	0.0000068
C	-3.5773397	-3.4718193	-0.0015778
H	-3.0055529	1.3365241	0.0016822
H	-2.5839350	3.7999759	0.0026100
H	-0.2340192	4.6762242	0.0014493
H	4.6252055	-0.3401841	0.0053971
H	3.8066717	-2.6523588	0.0066673
H	1.3524009	-3.1532894	0.0035024
H	-4.3525114	-4.2397268	-0.0019332
H	1.7371247	5.1590931	-0.0053417
H	4.1166113	5.7741917	-0.0067624
H	5.8679706	3.9811283	-0.0029078
H	5.2074200	1.6189853	0.0011676
C	-1.9796450	-5.4073739	-0.0048545
C	-5.4889316	-1.8432248	0.0021015
H	-2.9032218	-6.0047738	-0.0054993
H	-1.3773341	-5.6667709	-0.8928821
H	-1.3767964	-5.6694578	0.8820138
H	-6.1059318	-2.7540462	0.0011283
H	-5.7363263	-1.2363010	0.8905629
H	-5.7384145	-1.2328117	-0.8833560

T₁ MC

C	-1.4929627	1.7033584	0.5671145
C	-2.5599015	0.8462697	0.1859594
C	-3.8559823	1.3196985	-0.1200053
C	-4.0701301	2.7088863	-0.0448747
C	-3.0374508	3.5611351	0.3165623
C	-1.7595617	3.0687429	0.6204800
C	-2.2877789	-0.5694196	0.1172733
N	-1.0281999	-0.9575304	0.4088377
C	-0.6758926	-2.2311302	0.3846662
C	-1.5937461	-3.2303883	0.0516887
C	-2.8942416	-2.8613420	-0.2572007
C	-3.2809337	-1.5098624	-0.2332069
Pt	0.2577538	0.7821864	0.9485580
O	1.1949454	0.8358910	-1.0572575
C	2.3546945	0.4223700	-1.3317344
C	3.2873272	-0.1623559	-0.4509368
C	3.1124187	-0.3960818	0.9250070
O	2.0776896	-0.1432145	1.6065554
H	0.3657084	-2.4562078	0.6362478
H	-1.2833919	-4.2777380	0.0341961
H	-3.6159143	-3.6379837	-0.5197983
H	-5.0494698	3.1356684	-0.2685600
H	-3.2272812	4.6383861	0.3683655
H	-0.9710812	3.7726253	0.9048118
H	4.2490299	-0.4497009	-0.8797145
C	-4.6243479	-1.0283602	-0.5445384
C	-4.9032848	0.3647064	-0.4921820
C	4.2483043	-1.0105533	1.7063147
C	2.7476134	0.5981992	-2.7806836
H	3.7619283	0.2304220	-2.9980250
H	2.6828863	1.6684015	-3.0426618
H	2.0204645	0.0677015	-3.4194962
H	5.1324581	-1.2230169	1.0865723
H	4.5333177	-0.3264105	2.5246618
H	3.9011377	-1.9454904	2.1800245
C	-6.2105093	0.7923412	-0.8033639
C	-5.6565148	-1.9200037	-0.8993835
C	-7.2086714	-0.1009577	-1.1495071
H	-6.4501260	1.8563053	-0.7717784
C	-6.9308467	-1.4725417	-1.1980238
H	-5.4572622	-2.9930237	-0.9428672
H	-7.7126198	-2.1877522	-1.4694874
H	-8.2117646	0.2675201	-1.3833500

T_1 barrier at 215°

C	-0.3333715	1.3896692	0.6559408
C	-1.5424298	0.7298340	0.3046346
C	-2.7935320	1.3860481	0.2647658
C	-2.8134081	2.7576109	0.5813974
C	-1.6419000	3.4188713	0.9186267
C	-0.4116173	2.7462215	0.9581834
C	-1.4703855	-0.6755863	-0.0182104
N	-0.2464552	-1.2435141	0.0206633
C	-0.0691054	-2.5268207	-0.2406095
C	-1.1464656	-3.3504768	-0.5764213
C	-2.4149774	-2.7937532	-0.6355511
C	-2.6143541	-1.4302358	-0.3560065
Pt	1.3092701	0.2230468	0.6219338
O	2.1733140	0.6903896	-1.3683876
C	3.3903311	0.5311366	-1.6631220
C	4.3613547	-0.1801710	-0.9285183
C	4.1230758	-0.9501169	0.2239593
O	3.0104192	-1.0838243	0.8114842
H	0.9590368	-2.8988123	-0.1801874
H	-0.9823005	-4.4088666	-0.7925227
H	-3.2600611	-3.4318843	-0.9027745
H	-3.7486342	3.3200164	0.5667636
H	-1.6820692	4.4858656	1.1615164
H	0.4907331	3.3013760	1.2330658
H	5.3771524	-0.1827798	-1.3281788
C	-3.9104991	-0.7586799	-0.3967924
C	-3.9948891	0.6279775	-0.0952033
C	5.2602591	-1.7400565	0.8227234
C	3.8054269	1.1851703	-2.9607752
H	4.8748688	1.0524933	-3.1843772
H	3.5689185	2.2622069	-2.9149395
H	3.2062591	0.7604519	-3.7851088
H	6.2056588	-1.6180625	0.2728446
H	5.4045286	-1.4268836	1.8716867
H	4.9867835	-2.8095013	0.8441284
C	-5.2625062	1.2432727	-0.1506368
C	-5.0860425	-1.4586854	-0.7347408
C	-6.4037884	0.5365642	-0.4856142
H	-5.3552712	2.3068015	0.0753273
C	-6.3167655	-0.8294295	-0.7808444
H	-5.0354366	-2.5240277	-0.9692174
H	-7.2127442	-1.3974857	-1.0469697
H	-7.3704672	1.0478163	-0.5187962

DPIM

 S_0

C	-3.7441986	1.2115999	1.9364232
C	-3.6816661	0.0000208	1.2535829
C	-3.7441786	-1.2115795	1.9364135
C	-3.8829431	-1.2085996	3.3221400
C	-3.9541554	0.0000043	4.0146065
C	-3.8829697	1.2086098	3.3221483
N	-3.5325239	0.0000193	-0.1649741
C	-4.5835617	-0.0000026	-1.0727051
C	-4.0347416	-0.0000111	-2.3177298
N	-2.6702075	0.0000068	-2.1399225
C	-2.3475382	0.0000228	-0.8189358
C	-1.5716602	0.0000083	-3.0318571
C	-0.3396117	0.0000219	-2.3472150
C	0.8167702	0.0000232	-3.1292901
C	0.7343913	0.0000143	-4.5259140
C	-0.5036870	0.0000041	-5.1686684
C	-1.6804276	-0.0000006	-4.4157786
Pt	-0.4633030	0.0000310	-0.3589490
O	1.6001723	0.0000295	-0.1003931
C	2.2178334	-0.0000002	1.0065475
C	3.7187887	-0.0000197	0.8779592
O	-0.6781629	0.0000255	1.7516474
C	0.2685421	-0.0000015	2.5865786
C	-0.1644311	-0.0000191	4.0303057
C	1.6448889	-0.0000163	2.2884549
H	4.2314472	-0.0000410	1.8513910
H	4.0321619	-0.8870938	0.3004151
H	4.0321889	0.8870599	0.3004387
H	0.6832336	-0.0000216	4.7321867
H	-0.7979828	0.8844031	4.2160199
H	-0.7979680	-0.8844593	4.2160014
H	-2.6566627	-0.0000077	-4.9099649
H	-0.5599312	0.0000025	-6.2609777
H	1.6524795	0.0000170	-5.1221623
H	1.7908575	0.0000296	-2.6311736
H	-5.6192944	-0.0000105	-0.7428526
H	-4.5040544	-0.0000309	-3.2983501
H	-3.6691153	-2.1473956	1.3770611
H	-3.9285579	-2.1572708	3.8646239
H	-4.0607288	-0.0000026	5.1033556
H	-3.9286052	2.1572773	3.8646389
H	-3.6691594	2.1474300	1.3770814
H	2.3337276	-0.0000398	3.1350997

S₁

C	-3.5613384	0.9325134	2.1263841
C	-2.7257027	0.0384523	1.4373334
C	-2.1726663	-1.0546861	2.1213397
C	-2.4613000	-1.2478275	3.4654792
C	-3.2918752	-0.3595986	4.1561434
C	-3.8397901	0.7284305	3.4739555
N	-2.4647524	0.2291141	0.0735798
C	-3.4233825	0.6706179	-0.8402703
C	-2.9251415	0.5429689	-2.0909443
N	-1.6473225	0.0295882	-1.9662906
C	-1.3347398	-0.1948375	-0.6050014
C	-0.5973202	-0.0354652	-2.8455702
C	0.6791359	-0.1766756	-2.1801408
C	1.8402819	-0.2657282	-2.9807343
C	1.7532091	-0.1803989	-4.3620544
C	0.4949818	-0.0243794	-4.9770787
C	-0.6841963	0.0427975	-4.2321844
Pt	0.6115920	-0.1850769	-0.2431150
O	2.7385050	-0.3698431	0.0060726
C	3.3733708	-0.2015278	1.0807829
C	4.8702001	-0.3282500	0.9622911
O	0.4884291	0.0912312	1.8272858
C	1.4510846	0.1951716	2.6492467
C	1.0238196	0.4675314	4.0654986
C	2.8151515	0.0799635	2.3490766
H	5.3917116	-0.1768361	1.9191422
H	5.1178963	-1.3289240	0.5676056
H	5.2362837	0.4082736	0.2259292
H	1.8688139	0.5099979	4.7689561
H	0.4710985	1.4226190	4.0943512
H	0.3110736	-0.3132495	4.3818654
H	-1.6494449	0.1444939	-4.7344947
H	0.4351782	0.0370053	-6.0680324
H	2.6540794	-0.2301861	-4.9796613
H	2.8040757	-0.3902914	-2.4788750
H	-4.4138785	0.9811803	-0.5171379
H	-3.3780618	0.7789762	-3.0508212
H	-1.5304448	-1.7488228	1.5762292
H	-2.0356736	-2.1134375	3.9828666
H	-3.5093671	-0.5144663	5.2165455
H	-4.4852354	1.4382322	4.0003584
H	-3.9685413	1.8069391	1.6116366
H	3.5144518	0.2009146	3.1781264

T₁

C	-3.5902702	0.9671488	2.1029309
C	-2.7343133	0.0904298	1.4267744
C	-2.1529104	-0.9839945	2.1069725
C	-2.4388991	-1.1805947	3.4528701
C	-3.2989891	-0.3146684	4.1321589
C	-3.8738629	0.7577711	3.4500971
N	-2.4867715	0.2788001	0.0506980
C	-3.4863622	0.4977595	-0.8768063
C	-2.9642347	0.4411055	-2.1294757
N	-1.6084955	0.1873278	-1.9799714
C	-1.2820096	0.0857399	-0.6010566
C	-0.5848336	0.0646774	-2.8433213
C	0.7078261	-0.0981295	-2.1479704
C	1.8506143	-0.2487765	-2.9523184
C	1.7561377	-0.2264493	-4.3336739
C	0.4814923	-0.0523468	-4.9796272
C	-0.6762932	0.0925019	-4.2564095
Pt	0.6193228	-0.0383555	-0.2078235
O	2.7019593	-0.2262970	-0.0004656
C	3.3543321	-0.1745995	1.0821598
C	4.8433225	-0.3382255	0.9204575
O	0.4961304	0.1666242	1.8956042
C	1.4702254	0.1773416	2.7010194
C	1.0850132	0.3885033	4.1419205
C	2.8278828	0.0154069	2.3725996
H	5.3871560	-0.2732810	1.8745970
H	5.0502243	-1.3154049	0.4499193
H	5.2199220	0.4377665	0.2316629
H	1.9478670	0.3745453	4.8246126
H	0.5591939	1.3547402	4.2335012
H	0.3625508	-0.3906094	4.4401709
H	-1.6404863	0.2179480	-4.7558047
H	0.4377978	-0.0396599	-6.0727745
H	2.6516937	-0.3353966	-4.9511809
H	2.8176403	-0.3743860	-2.4574300
H	-4.5198514	0.6346514	-0.5651553
H	-3.4434725	0.5574447	-3.0977048
H	-1.4837472	-1.6574213	1.5682689
H	-1.9878549	-2.0285132	3.9772215
H	-3.5184975	-0.4745093	5.1916099
H	-4.5398281	1.4496783	3.9740944
H	-4.0146094	1.8262949	1.5758630
H	3.5425366	0.0439160	3.1968600

T'_1

C	-2.3447974	1.1567421	2.0930982
C	-2.6809738	-0.0270054	1.4411117
C	-3.2509220	-1.0917699	2.1393953
C	-3.4915363	-0.9649429	3.5057020
C	-3.1581886	0.2173351	4.1665442
C	-2.5841764	1.2729774	3.4588496
N	-2.4645571	-0.1522667	0.0399694
C	-3.4629946	-0.4864099	-0.8654698
C	-2.8962318	-0.4925999	-2.1012802
N	-1.5733077	-0.1659131	-1.9208762
C	-1.2899202	0.0441602	-0.6076545
C	-0.4840290	-0.0489123	-2.8188337
C	0.7202806	0.2471273	-2.1536055
C	1.8628372	0.3893226	-2.9430202
C	1.7927225	0.2354820	-4.3324986
C	0.5815255	-0.0605220	-4.9566862
C	-0.5809517	-0.2058732	-4.1941595
Pt	0.5879208	0.4131584	-0.1667787
O	2.6126126	0.7456491	0.0724776
C	3.2857194	0.1957998	1.0409216
C	4.7422891	-0.0322496	0.7882286
O	0.4437090	0.5751307	1.9260129
C	1.3323182	0.0370939	2.7058867
C	0.8795562	-0.3123612	4.0894219
C	2.6873602	-0.1225994	2.2985853
H	5.2618053	-0.4355018	1.6726844
H	4.8863258	-0.7414696	-0.0504373
H	5.2390421	0.9115732	0.4909343
H	1.6718315	-0.8051420	4.6765153
H	0.5512242	0.5922326	4.6393016
H	0.0015350	-0.9846100	4.0471374
H	-1.5352575	-0.4359060	-4.6768369
H	0.5337185	-0.1787108	-6.0429463
H	2.6983761	0.3498754	-4.9364958
H	2.8138510	0.6276195	-2.4575369
H	-4.4876229	-0.6576427	-0.5450714
H	-3.3292070	-0.6930385	-3.0778079
H	-3.4866347	-2.0211576	1.6136000
H	-3.9333495	-1.7995767	4.0575683
H	-3.3439373	0.3146065	5.2400988
H	-2.3134305	2.1984443	3.9744179
H	-1.8862757	1.9710794	1.5290536
H	3.3746974	-0.4919134	3.0673800

T_{MC}

N	-3.6253749	0.1223649	0.5325016
C	-3.9088349	-1.1764099	0.9299651
C	-2.8192500	-1.9286543	0.6231388
N	-1.9039264	-1.0759882	0.0475580
C	-2.3928919	0.1877833	-0.0276505
C	-0.5632442	-1.3021774	-0.3775070
C	-0.0012979	-2.5728983	-0.4543111
C	1.3301404	-2.6846574	-0.8597484
C	2.0603126	-1.5425941	-1.1873191
C	1.4632453	-0.2777706	-1.1183151
C	0.1418294	-0.1367225	-0.7063466
Pt	-1.1400438	1.5871671	-0.7043046
O	0.0583173	3.0819876	-1.5738082
C	0.8872715	3.8224538	-0.9723101
C	1.6975429	4.7144226	-1.8786101
C	-4.4902029	1.2340606	0.7059167
O	-0.5347239	2.3815472	1.2909780
C	0.4017323	3.2160197	1.4308419
C	0.7776311	3.4920637	2.8681542
C	1.1046725	3.8952707	0.4167626
H	-0.5780763	-3.4707601	-0.2119912
H	1.7940025	-3.6732708	-0.9235994
H	2.0465672	0.6103237	-1.3869876
H	3.1053645	-1.6375673	-1.4999810
H	-2.6203721	-2.9836373	0.7914832
H	-4.8412498	-1.4384919	1.4241191
H	1.8812458	4.5869950	0.7480730
H	1.5339290	4.2849742	2.9708787
H	-0.1276681	3.7726374	3.4332351
H	1.1643157	2.5612564	3.3190107
H	2.4342620	5.3239876	-1.3348178
H	1.0125425	5.3802148	-2.4322647
H	2.2155104	4.0933230	-2.6294321
C	-3.9745440	2.4316516	1.2061550
C	-4.8267645	3.5239808	1.3573343
C	-6.1780181	3.4196553	1.0287169
C	-6.6838616	2.2147092	0.5406488
C	-5.8397539	1.1192673	0.3717867
H	-2.9188728	2.4947087	1.4848771
H	-4.4261059	4.4651538	1.7442293
H	-6.8405791	4.2809561	1.1527610
H	-7.7407354	2.1289830	0.2726954
H	-6.2207144	0.1820912	-0.0433509

T_1 barrier at 215°

C	1.7896431	-0.6465959	3.8627828
C	1.3879684	0.1680575	2.7986673
C	0.3895404	1.1283013	2.9881974
C	-0.1868089	1.2796198	4.2443978
C	0.2155187	0.4759887	5.3138554
C	1.2054887	-0.4865761	5.1167866
N	2.0311572	0.0499509	1.5479644
C	3.4042265	0.0769573	1.4051325
C	3.7218523	0.1788997	0.0883333
N	2.5205325	0.2143694	-0.6043736
C	1.4318324	0.1071997	0.3023487
C	2.2003953	0.3133041	-1.9059809
C	0.7401836	0.2513459	-2.1178540
C	0.2810261	0.3710928	-3.4406274
C	1.1711692	0.5249691	-4.4903422
C	2.5908687	0.5628805	-4.2507501
C	3.1082419	0.4551637	-2.9840094
Pt	-0.3247982	-0.0398578	-0.5210486
O	-2.1284611	-0.1578222	-1.5987659
C	-3.2359261	0.2739322	-1.1598118
C	-4.2697974	0.5518272	-2.2179612
O	-1.5321081	-0.2511276	1.2238374
C	-2.7580024	0.0486775	1.2790381
C	-3.3738298	-0.0539842	2.6500045
C	-3.5755114	0.4276806	0.1945302
H	-5.2351462	0.8737337	-1.7995591
H	-3.8882077	1.3346781	-2.8970132
H	-4.4184473	-0.3575295	-2.8256817
H	-4.3773685	0.3948852	2.7013634
H	-3.4491804	-1.1220335	2.9226222
H	-2.7065672	0.4164692	3.3906169
H	4.1870007	0.4890556	-2.8108810
H	3.2693814	0.6809205	-5.1008541
H	0.8057502	0.6069067	-5.5174114
H	-0.7964491	0.3208671	-3.6207453
H	4.0575461	0.0652116	2.2751884
H	4.6906933	0.2381438	-0.3998881
H	0.0859875	1.7554487	2.1475261
H	-0.9538213	2.0456177	4.3937078
H	-0.2431440	0.5997221	6.2989334
H	1.5206679	-1.1291696	5.9441234
H	2.5481356	-1.4169303	3.6982948
H	-4.5968434	0.7376928	0.4230104

DPBIM

 S_0

C	-1.6492208	-0.0000319	-4.4184478
C	-1.5715166	-0.0000139	-3.0303723
C	-0.3423432	0.0000140	-2.3383220
C	0.8267648	0.0000324	-3.0989191
C	0.7688273	0.0000179	-4.4962963
C	-0.4602045	-0.0000152	-5.1524955
N	-2.6757285	-0.0000203	-2.1422772
C	-4.0533395	-0.0000181	-2.3019033
C	-4.5875649	-0.0000021	-0.9986925
N	-3.5072646	0.0000046	-0.1212665
C	-2.3442961	-0.0000035	-0.8153828
C	-3.6314132	0.0000199	1.2981771
C	-3.6969316	1.2117418	1.9809028
C	-3.8314065	1.2086827	3.3670438
C	-3.8987303	0.0000189	4.0597554
C	-3.8313967	-1.2086766	3.3670565
C	-3.6969204	-1.2117363	1.9808980
Pt	-0.4710701	0.0000169	-0.3538802
O	-0.6709090	0.0000169	1.7618938
C	0.2772090	-0.0000073	2.5948739
C	1.6528280	-0.0000162	2.2928056
C	2.2181325	0.0000108	1.0085952
C	3.7176771	0.0000109	0.8684907
O	1.5918728	0.0000379	-0.0942842
C	-0.1515949	-0.0000264	4.0394201
H	4.2379602	0.0000002	1.8378269
H	4.0263099	-0.8870518	0.2883516
H	4.0263107	0.8870853	0.2883701
H	0.6977579	-0.0000240	4.7391041
H	-0.7846662	0.8842410	4.2266886
H	-0.7846454	-0.8843139	4.2266716
H	-2.6061398	-0.0000570	-4.9413201
H	-0.5039263	-0.0000255	-6.2453662
H	1.6956301	0.0000337	-5.0787539
H	1.7911367	0.0000568	-2.5825792
C	-5.9552584	0.0000152	-0.7530938
C	-4.9049531	-0.0000228	-3.4071927
H	-3.6303983	-2.1476844	1.4206934
H	-3.8787115	-2.1570302	3.9098763
H	-4.0006611	0.0000090	5.1489302
H	-3.8787284	2.1570483	3.9098706
H	-3.6304097	2.1477020	1.4206888
H	2.3450690	-0.0000383	3.1365133
C	-6.7981551	0.0000137	-1.8627101
C	-6.2778121	-0.0000062	-3.1644063
H	-4.5274221	-0.0000346	-4.4287159
H	-6.9642230	-0.0000063	-4.0154927
H	-7.8816214	0.0000284	-1.7153611
H	-6.3411516	0.0000317	0.2688052

S₁

C	-0.2475492	-0.3348142	-4.0734524
C	-0.1911095	-0.3037959	-2.6835775
C	1.0833496	-0.2823666	-1.9946754
C	2.2667086	-0.2922701	-2.7700492
C	2.2035121	-0.3026238	-4.1529254
C	0.9496950	-0.3277729	-4.7934636
N	-1.2604189	-0.2853953	-1.8185061
C	-2.5858541	0.1006268	-1.9598045
C	-3.0978478	0.2253344	-0.6478123
N	-2.0671492	-0.0829808	0.2370183
C	-0.9214397	-0.4343702	-0.4480683
C	-2.2233728	-0.2414707	1.6291272
C	-2.8000368	0.7777899	2.3933456
C	-2.9505555	0.6106484	3.7682338
C	-2.5228448	-0.5636858	4.3872441
C	-1.9406578	-1.5751330	3.6191426
C	-1.7875918	-1.4175594	2.2470170
Pt	1.0007386	-0.2272638	-0.0643089
O	0.8165030	0.0723356	1.9975772
C	1.7487120	0.2846318	2.8332532
C	3.1227337	0.3026238	2.5561847
C	3.7260434	0.0645048	1.3005457
C	5.2296118	0.0829157	1.2051969
O	3.1279663	-0.1738478	0.2174188
C	1.2716583	0.5299318	4.2382246
H	5.7189321	0.2939308	2.1676736
H	5.5789613	-0.8927956	0.8250834
H	5.5337944	0.8445560	0.4663111
H	2.0940143	0.7070711	4.9472099
H	0.5885797	1.3969469	4.2373937
H	0.6722001	-0.3356313	4.5692135
H	-1.1971490	-0.3872723	-4.6046272
H	0.9058249	-0.3539643	-5.8864463
H	3.1179579	-0.2975997	-4.7523669
H	3.2253916	-0.2863605	-2.2437717
C	-4.4344216	0.5389219	-0.4222452
C	-3.3973917	0.3365938	-3.0648464
H	-1.3279523	-2.1956978	1.6330158
H	-1.6049192	-2.5014591	4.0951877
H	-2.6406977	-0.6906548	5.4672489
H	-3.3970534	1.4135209	4.3625962
H	-3.1041108	1.7096999	1.9102598
H	3.7929463	0.5016729	3.3941486
C	-5.2489094	0.7661030	-1.5414010
C	-4.7400778	0.6790613	-2.8334863
H	-3.0231865	0.2582570	-4.0846698
H	-5.3938502	0.8687876	-3.6890423
H	-6.3029845	1.0153156	-1.3897496
H	-4.8360125	0.6009479	0.5904369

T_1

C	-0.2226203	0.0169587	-4.1148207
C	-0.1774111	0.0131192	-2.7025511
C	1.1108675	0.0087533	-1.9794914
C	2.2893349	0.0098668	-2.7542561
C	2.2321280	0.0119528	-4.1332241
C	0.9653300	0.0156768	-4.8083822
N	-1.2283266	0.0120876	-1.8537789
C	-2.6177076	-0.0093718	-1.9978356
C	-3.1431074	-0.0225519	-0.6839720
N	-2.0869268	-0.0079325	0.2012060
C	-0.8854796	0.0204378	-0.4721594
C	-2.2138342	0.0055320	1.6150825
C	-2.2108727	1.2210892	2.2963162
C	-2.3373021	1.2314526	3.6833430
C	-2.4607885	0.0305862	4.3827223
C	-2.4579235	-1.1828389	3.6951396
C	-2.3320813	-1.1978581	2.3075670
Pt	1.0028068	0.0054060	-0.0467624
O	0.8116365	-0.0149334	2.0581930
C	1.7613374	-0.0233979	2.8928016
C	3.1358221	-0.0209770	2.5954808
C	3.7098146	-0.0092391	1.3110157
C	5.2111326	-0.0099663	1.1842632
O	3.0911082	0.0018296	0.2083167
C	1.3251220	-0.0358074	4.3340753
H	5.7232183	-0.0164935	2.1579449
H	5.5241037	-0.8942570	0.6021287
H	5.5260926	0.8804681	0.6127111
H	2.1699258	-0.0529498	5.0389893
H	0.6995886	0.8528252	4.5263583
H	0.6795323	-0.9141421	4.5056626
H	-1.1696162	0.0222477	-4.6531896
H	0.9452282	0.0187120	-5.9021036
H	3.1505954	0.0107807	-4.7265355
H	3.2482825	0.0078973	-2.2288252
C	-4.5178801	-0.0381510	-0.4544435
C	-3.4623102	-0.0163817	-3.1015207
H	-2.3137459	-2.1381487	1.7508123
H	-2.5496736	-2.1254194	4.2427461
H	-2.5577399	0.0406060	5.4724593
H	-2.3368007	2.1836482	4.2220673
H	-2.1004185	2.1493711	1.7303782
H	3.8243555	-0.0293996	3.4421318
C	-5.3570569	-0.0441809	-1.5718192
C	-4.8453525	-0.0345199	-2.8715744
H	-3.0804010	-0.0071203	-4.1216678
H	-5.5278537	-0.0397338	-3.7250754
H	-6.4406498	-0.0560453	-1.4217699
H	-4.9131996	-0.0447129	0.5634585

T'_1

C	-0.1492308	0.1180910	-4.0456058
C	-0.0775487	0.1854747	-2.6595197
C	1.1407758	0.3592012	-1.9719454
C	2.3063310	0.4603771	-2.7316040
C	2.2550205	0.3886688	-4.1278869
C	1.0362600	0.2197778	-4.7801563
N	-1.1808709	0.1009662	-1.7717278
C	-2.5383720	-0.1266205	-1.9384707
C	-3.0873692	-0.1193637	-0.6420719
N	-2.0321867	0.1046323	0.2400759
C	-0.8725120	0.2357490	-0.4467492
C	-2.1844693	0.1939137	1.6527380
C	-1.9300560	1.3977906	2.3041091
C	-2.1069174	1.4780552	3.6821387
C	-2.5392845	0.3640715	4.4009368
C	-2.7898713	-0.8390360	3.7409126
C	-2.6103088	-0.9284942	2.3623425
Pt	1.0071465	0.4542770	0.0137902
O	0.8545631	0.5468621	2.1157657
C	1.7095581	-0.0466994	2.8917966
C	3.0585055	-0.2667231	2.4933572
C	3.6858731	0.0402876	1.2446675
C	5.1311886	-0.2602053	1.0041120
O	3.0515076	0.6371203	0.2796782
C	1.2347840	-0.3875149	4.2702006
H	5.6176666	-0.7071708	1.8863314
H	5.2484269	-0.9597508	0.1532091
H	5.6816016	0.6611168	0.7314424
H	1.9986580	-0.9274411	4.8533486
H	0.9536883	0.5276369	4.8284783
H	0.3220169	-1.0103321	4.2184077
H	-1.0976441	-0.0049088	-4.5688338
H	0.9959807	0.1688183	-5.8719685
H	3.1775242	0.4693895	-4.7113215
H	3.2600233	0.6033416	-2.2152372
C	-4.4470292	-0.2949812	-0.4098414
C	-3.3598521	-0.3358086	-3.0474586
H	-2.7878298	-1.8675457	1.8314558
H	-3.1209185	-1.7172128	4.3025337
H	-2.6779142	0.4319432	5.4838528
H	-1.8992524	2.4191635	4.1989011
H	-1.5788756	2.2567112	1.7281354
H	3.7189695	-0.6820197	3.2622743
C	-5.2600215	-0.4994754	-1.5220650
C	-4.7210894	-0.5231712	-2.8160593
H	-2.9680602	-0.3568801	-4.0631698
H	-5.3837428	-0.6903969	-3.6695514
H	-6.3348653	-0.6437499	-1.3827577
H	-4.8516567	-0.2719849	0.6043896

T_{MC}

C	-5.7656854	1.1287285	0.2132545
C	-4.4456667	1.2009432	0.6605298
C	-3.9467735	2.3700312	1.2371832
C	-4.7861986	3.4763606	1.3596794
C	-6.1091016	3.4122631	0.9239275
C	-6.5982211	2.2368934	0.3528036
N	-3.5926114	0.0752541	0.5163520
C	-3.8599129	-1.2033957	1.0003679
C	-2.7448613	-1.9968646	0.6698309
N	-1.8665341	-1.1570601	-0.0037077
C	-2.3812415	0.1029761	-0.0911558
C	-0.5334540	-1.3468998	-0.4703925
C	0.0421957	-2.5967887	-0.6904511
C	1.3675857	-2.6561281	-1.1273896
C	2.0848712	-1.4846455	-1.3618869
C	1.4716704	-0.2393344	-1.1807091
C	0.1586559	-0.1534806	-0.7301226
Pt	-1.1590849	1.5311815	-0.7290981
O	-0.6430644	2.3245603	1.2872469
C	0.2897104	3.1568641	1.4669914
C	1.0275859	3.8427757	0.4841322
C	0.8477654	3.7910881	-0.9114714
C	1.6812850	4.6967843	-1.7815949
O	0.0343448	3.0595644	-1.5441519
C	0.6063537	3.4276967	2.9188557
H	-0.5220644	-3.5211519	-0.5580765
H	1.8337253	-3.6314004	-1.2951951
H	2.0332883	0.6770336	-1.3947993
H	3.1254231	-1.5401978	-1.6977954
C	-2.6866575	-3.3317575	1.0744283
C	-4.9384530	-1.7062838	1.7217417
H	1.7949879	4.5283666	0.8474178
H	1.4143300	4.1626540	3.0523193
H	-0.3039196	3.7912677	3.4265674
H	0.8908491	2.4785791	3.4051690
H	2.4126400	5.2865847	-1.2095757
H	1.0122880	5.3819624	-2.3311705
H	2.2074494	4.0889893	-2.5374606
H	-2.9114327	2.4015599	1.5880914
H	-4.3984659	4.3966171	1.8056832
H	-6.7627058	4.2832687	1.0263515
H	-7.6316298	2.1850904	-0.0015862
H	-6.1291592	0.2133071	-0.2611477
C	-4.8804503	-3.0436254	2.1051325
C	-3.7705443	-3.8389385	1.7876499
H	-5.7864057	-1.0706755	1.9843183
H	-5.7091311	-3.4755949	2.6727148
H	-3.7470379	-4.8821404	2.1144536
H	-1.8235325	-3.9615704	0.8650901

T_1 barrier at 190°

C	-0.9927908	-0.6968940	3.5541390
C	0.0970412	-0.7219144	2.6872257
C	1.2633434	-0.0197589	2.9808565
C	1.3388291	0.7131782	4.1615002
C	0.2549848	0.7423873	5.0388908
C	-0.9099197	0.0385709	4.7343085
N	0.0272737	-1.4986229	1.4960831
C	0.0481670	-2.8914013	1.4759428
C	0.0391578	-3.2790858	0.1221304
N	0.0156981	-2.0990090	-0.6047878
C	-0.0016290	-1.0165610	0.2314695
C	0.0133648	-1.7869850	-1.9880459
C	0.0476525	-2.7094336	-3.0260237
C	0.0499490	-2.2325835	-4.3411946
C	0.0167855	-0.8634372	-4.5941865
C	-0.0190945	0.0511948	-3.5361035
C	-0.0191235	-0.3943881	-2.2142066
Pt	-0.0971425	0.7394794	-0.5867663
O	-0.2618489	1.8945790	1.1736506
C	-0.1535554	3.1861739	1.2745617
C	-0.1111496	4.0425554	0.1434422
C	-0.1424210	3.7129214	-1.2485873
C	-0.0910199	4.7777613	-2.2978142
O	-0.2318732	2.4915671	-1.6831188
C	-0.1091010	3.7381075	2.6660604
H	0.0743036	-3.7836738	-2.8421173
H	0.0774067	-2.9467004	-5.1692572
H	-0.0524897	1.1276861	-3.7268489
H	0.0175849	-0.5014523	-5.6269754
C	0.0579541	-4.6319573	-0.2204298
C	0.0893386	-3.8147975	2.5142694
H	-0.0675693	5.1141690	0.3664786
H	-0.1588649	4.8394206	2.6807766
H	-0.9482781	3.3373482	3.2657339
H	0.8178346	3.4277712	3.1874821
H	-0.0262065	5.7888433	-1.8640070
H	-0.9892975	4.7353523	-2.9448778
H	0.7816717	4.6297580	-2.9638949
H	2.0980693	-0.0473546	2.2763861
H	2.2510494	1.2689000	4.3960360
H	0.3166806	1.3213681	5.9649190
H	-1.7647068	0.0676363	5.4159950
H	-1.9026144	-1.2431992	3.2926108
C	0.1087054	-5.1629565	2.1634728
C	0.0906408	-5.5600664	0.8189970
H	0.1052667	-3.4875613	3.5560334
H	0.1391100	-5.9225525	2.9493302
H	0.1043002	-6.6258750	0.5751011
H	0.0468063	-4.9674508	-1.2562920

T_1 barrier at 195°

C	-0.7688822	-0.8565519	3.7486570
C	0.1647060	-0.7590810	2.7141172
C	1.2889438	0.0579720	2.8572606
C	1.4840957	0.7599729	4.0411917
C	0.5604771	0.6580740	5.0840070
C	-0.5649026	-0.1508166	4.9327872
N	-0.0190828	-1.4990651	1.5245954
C	-0.0754673	-2.8829331	1.4702479
C	-0.0147550	-3.2759232	0.1133483
N	0.0859267	-2.0982635	-0.6248472
C	0.0916953	-0.9708547	0.2513166
C	0.1221272	-1.8006494	-1.9421124
C	0.2308996	-2.7113534	-3.0159802
C	0.2575897	-2.2118441	-4.2985595
C	0.1796725	-0.8066372	-4.5600095
C	0.0820458	0.0932203	-3.5186511
C	0.0414141	-0.3512715	-2.1796247
Pt	-0.1132376	0.7629538	-0.6059114
O	-0.3038367	1.9378253	1.1384940
C	-0.2286857	3.1991987	1.1980594
C	-0.0728705	4.0781713	0.1111208
C	-0.1064218	3.7216788	-1.2495103
C	-0.0115371	4.8056310	-2.2911133
O	-0.2486862	2.5544613	-1.7154537
C	-0.3322627	3.7650940	2.5892512
H	0.3139703	-3.7839690	-2.8458650
H	0.3493397	-2.9056757	-5.1393598
H	0.0225017	1.1691599	-3.7038042
H	0.1978281	-0.4565616	-5.5957471
C	-0.0534497	-4.6190920	-0.2457543
C	-0.1302999	-3.8329434	2.4875221
H	0.0164593	5.1410094	0.3417777
H	-0.1965638	4.8566937	2.6209468
H	-1.3232825	3.5092481	3.0037359
H	0.4133535	3.2728185	3.2364169
H	0.0847230	5.8111246	-1.8552002
H	-0.9094284	4.7700659	-2.9322029
H	0.8577586	4.6059084	-2.9417034
H	1.9994672	0.1323040	2.0305740
H	2.3711624	1.3908087	4.1534277
H	0.7175007	1.2121459	6.0139640
H	-1.2998665	-0.2266842	5.7397049
H	-1.6621130	-1.4720048	3.6128359
C	-0.1594478	-5.1812234	2.1176345
C	-0.1317648	-5.5718473	0.7780765
H	-0.1456444	-3.5314351	3.5361303
H	-0.2057549	-5.9443266	2.9000443
H	-0.1648738	-6.6330572	0.5189271
H	-0.0244538	-4.9390188	-1.2863736

T_1 barrier at 220°

C	-1.5517153	-1.6467091	3.3864386
C	-0.5418521	-1.1101104	2.5860080
C	0.1902853	-0.0002396	3.0066603
C	-0.1015929	0.5779775	4.2407543
C	-1.1023496	0.0452857	5.0520119
C	-1.8250132	-1.0687512	4.6238307
N	-0.2634671	-1.6953058	1.3229877
C	0.0349041	-3.0404601	1.1169119
C	0.2228091	-3.2010858	-0.2686410
N	0.0180666	-1.9466945	-0.8276557
C	-0.2685120	-1.0280297	0.1406587
C	0.1489665	-1.4665716	-2.1614522
C	0.1248791	-2.2869035	-3.2876285
C	0.2592804	-1.6987574	-4.5471733
C	0.3849109	-0.3158893	-4.6699645
C	0.3619288	0.4948004	-3.5296444
C	0.2480776	-0.0693632	-2.2625688
Pt	-0.2941793	0.8770574	-0.4339967
O	1.5092016	1.6525262	0.6232327
C	1.6105872	2.8631523	0.9738294
C	0.8087389	3.9437895	0.5616313
C	-0.1915876	3.9050274	-0.4279821
C	-0.8754862	5.1860117	-0.8283522
O	-0.5550853	2.8809867	-1.0724720
C	2.7219814	3.1311314	1.9616362
H	-0.0274211	-3.3646115	-3.2092272
H	0.2500188	-2.3326837	-5.4385609
H	0.4320057	1.5833519	-3.6321283
H	0.4936099	0.1355561	-5.6614919
C	0.5977583	-4.4404898	-0.7902440
C	0.1964858	-4.0940057	2.0118184
H	1.0306131	4.9167185	1.0033308
H	2.8466630	4.2011569	2.1856283
H	2.5116381	2.5889419	2.9013014
H	3.6664695	2.7262057	1.5607293
H	-0.5183051	6.0588166	-0.2616966
H	-1.9639863	5.0737689	-0.6829857
H	-0.7122304	5.3580275	-1.9063777
H	0.9752117	0.4025922	2.3607836
H	0.4649904	1.4536556	4.5713431
H	-1.3242158	0.5013801	6.0211340
H	-2.6195076	-1.4838547	5.2506241
H	-2.1322530	-2.5013978	3.0287209
C	0.5499608	-5.3321666	1.4813266
C	0.7504219	-5.4980389	0.1038306
H	0.0628652	-3.9476121	3.0855712
H	0.6850750	-6.1845513	2.1525523
H	1.0434170	-6.4783941	-0.2816892
H	0.7883084	-4.5852345	-1.8527356

DPNIM

S₀

C	-1.6404772	-0.0000384	-4.4038954
C	-1.5599944	-0.0000192	-3.0159764
C	-0.3289903	0.0000073	-2.3271906
C	0.8387191	0.0000230	-3.0888314
C	0.7778861	0.0000072	-4.4862728
C	-0.4523768	-0.0000236	-5.1398586
N	-2.6607280	-0.0000270	-2.1252866
C	-4.0402453	-0.0000233	-2.2842912
C	-4.5726490	-0.0000159	-0.9634261
N	-3.4822298	-0.0000141	-0.0952966
C	-2.3250680	-0.0000132	-0.7984519
C	-3.6015286	-0.0000049	1.3242016
C	-3.6688071	1.2118319	2.0067398
C	-3.8052967	1.2088215	3.3926973
C	-3.8730574	0.0000062	4.0853084
C	-3.8052601	-1.2088296	3.3927029
C	-3.6687705	-1.2118304	2.0067592
Pt	-0.4540035	0.0000112	-0.3423905
O	-0.6474840	0.0000144	1.7742551
C	0.3014396	-0.0000034	2.6061602
C	1.6765385	-0.0000103	2.3012653
C	2.2382760	0.0000133	1.0158308
C	3.7372490	0.0000157	0.8719013
O	1.6091202	0.0000354	-0.0859279
C	-0.1254302	-0.0000179	4.0510850
H	4.2605058	0.0000066	1.8396141
H	4.0443017	-0.8870452	0.2910889
H	4.0443006	0.8870869	0.2911050
H	0.7250204	-0.0000106	4.7492423
H	-0.7584127	0.8839825	4.2397234
H	-0.7583862	-0.8840403	4.2397136
H	-2.5985280	-0.0000660	-4.9245962
H	-0.4980671	-0.0000370	-6.2326767
H	1.7035720	0.0000210	-5.0703755
H	1.8037775	0.0000472	-2.5736741
C	-5.9195857	-0.0000041	-0.7052154
C	-4.8830260	-0.0000182	-3.3734119
H	-3.6030058	-2.1478089	1.4465410
H	-3.8548057	-2.1573663	3.9351248
H	-3.9769342	0.0000148	5.1743073
H	-3.8548715	2.1573635	3.9351071
H	-3.6030763	2.1478031	1.4465373
H	2.3713590	-0.0000275	3.1428723
C	-6.8076094	0.0000017	-1.8090259
C	-6.2831190	-0.0000049	-3.1468973
H	-4.5139504	-0.0000224	-4.3983047
C	-7.1986374	0.0000089	-4.2339255
C	-8.2163795	0.0000197	-1.6260533
H	-6.2990935	0.0000053	0.3191315
C	-8.5561589	0.0000296	-4.0205875
C	-9.0713954	0.0000348	-2.7020048
H	-6.7995200	0.0000056	-5.2528510
H	-9.2433930	0.0000426	-4.8714676
H	-10.1535428	0.0000511	-2.5417322
H	-8.6108128	0.0000244	-0.6051050

S₁

C	-1.6643425	-0.0000469	-4.3656032
C	-1.6050045	-0.0000294	-2.9724732
C	-0.3296572	0.0000044	-2.2717321
C	0.8530530	0.0000278	-3.0470235
C	0.7861064	0.0000144	-4.4259533
C	-0.4703157	-0.0000247	-5.0778299
N	-2.6721337	-0.0000422	-2.1140000
C	-4.0611170	-0.0000236	-2.2786337
C	-4.5861100	-0.0000023	-0.9632997
N	-3.5028582	-0.0000115	-0.0897348
C	-2.3271410	-0.0000365	-0.7541253
C	-3.6283661	-0.0000122	1.3273159
C	-3.6921656	1.2118306	2.0102855
C	-3.8182733	1.2088864	3.3976995
C	-3.8802517	-0.0000085	4.0911436
C	-3.8182227	-1.2088719	3.3976963
C	-3.6921174	-1.2118309	2.0103135
Pt	-0.4157671	0.0000050	-0.3417156
O	-0.5963172	0.0000049	1.7412646
C	0.3538120	-0.0000097	2.5819703
C	1.7256608	-0.0000122	2.2833808
C	2.2977630	0.0000151	0.9969076
C	3.7968789	0.0000250	0.8641236
O	1.6717264	0.0000361	-0.1029499
C	-0.0889612	-0.0000235	4.0183590
H	4.3118865	0.0000065	1.8359937
H	4.1090059	-0.8875305	0.2865505
H	4.1089975	0.8876082	0.2865887
H	0.7526759	-0.0000232	4.7268724
H	-0.7263265	0.8830174	4.1963265
H	-0.7263128	-0.8830779	4.1963133
H	-2.6164411	-0.0000799	-4.8919289
H	-0.5059315	-0.0000393	-6.1709335
H	1.7006818	0.0000335	-5.0251918
H	1.8119977	0.0000547	-2.5224449
C	-5.9513243	0.0000148	-0.7106917
C	-4.8952589	-0.0000264	-3.3809659
H	-3.6382182	-2.1467325	1.4471074
H	-3.8694977	-2.1574127	3.9402387
H	-3.9804588	0.0000056	5.1805800
H	-3.8695842	2.1574009	3.9402121
H	-3.6383065	2.1467086	1.4470968
H	2.4155475	-0.0000277	3.1287257
C	-6.8377614	0.0000159	-1.8237121
C	-6.3110975	-0.0000024	-3.1658697
H	-4.5273310	-0.0000431	-4.4058067
C	-7.2129308	0.0000047	-4.2489298
C	-8.2426114	0.0000371	-1.6573080
H	-6.3401119	0.0000293	0.3090929
C	-8.5906164	0.0000283	-4.0505489
C	-9.1030221	0.0000435	-2.7481428
H	-6.8069900	-0.0000083	-5.2658098
H	-9.2672822	0.0000350	-4.9098852
H	-10.1852282	0.0000607	-2.5849406
H	-8.6466707	0.0000491	-0.6399601

S42

T₁

C	-1.6479889	-0.0000473	-4.3852642
C	-1.5638311	-0.0000239	-2.9950713
C	-0.3286660	0.0000091	-2.3066349
C	0.8364457	0.0000288	-3.0772274
C	0.7694009	0.0000101	-4.4719901
C	-0.4654164	-0.0000298	-5.1239356
N	-2.6622197	-0.0000323	-2.1082006
C	-4.0319999	-0.0000318	-2.2550371
C	-4.5600923	-0.0000157	-0.9680455
N	-3.4879373	-0.0000093	-0.0921980
C	-2.3165240	-0.0000153	-0.7740633
C	-3.6109787	-0.0000039	1.3279447
C	-3.6717770	1.2120995	2.0099423
C	-3.7993257	1.2087710	3.3967727
C	-3.8633477	0.0000031	4.0896849
C	-3.7992765	-1.2087765	3.3967838
C	-3.6717265	-1.2121115	2.0099450
Pt	-0.4355216	0.0000144	-0.3260508
O	-0.6236795	0.0000077	1.7869525
C	0.3296411	-0.0000108	2.6145538
C	1.7033060	-0.0000112	2.3051755
C	2.2629841	0.0000203	1.0177992
C	3.7622586	0.0000295	0.8720497
O	1.6318507	0.0000448	-0.0817054
C	-0.0916939	-0.0000330	4.0613187
H	4.2863779	0.0000034	1.8394061
H	4.0690879	-0.8870065	0.2909217
H	4.0690823	0.8871017	0.2909736
H	0.7613710	-0.0000397	4.7565269
H	-0.7238930	0.8842213	4.2518718
H	-0.7238854	-0.8842973	4.2518469
H	-2.6081078	-0.0000803	-4.9018684
H	-0.5135041	-0.0000478	-6.2165439
H	1.6922645	0.0000256	-5.0605685
H	1.8036203	0.0000562	-2.5662905
C	-5.9498319	0.0000038	-0.7119739
C	-4.9011921	-0.0000335	-3.3861238
H	-3.6076981	-2.1475941	1.4488322
H	-3.8440967	-2.1572298	3.9397617
H	-3.9604251	0.0000016	5.1792713
H	-3.8441829	2.1572320	3.9397484
H	-3.6077879	2.1475915	1.4488120
H	2.3996655	-0.0000304	3.1454921
C	-6.8376187	0.0000125	-1.8244154
C	-6.3051287	-0.0000088	-3.1669427
H	-4.5234983	-0.0000466	-4.4068791
C	-7.2072772	-0.0000028	-4.2477191
C	-8.2316811	0.0000436	-1.6570322
H	-6.3324780	0.0000190	0.3100084
C	-8.6159314	0.0000283	-4.0482114
C	-9.1206712	0.0000527	-2.7706779
H	-6.8066008	-0.0000212	-5.2656257
H	-9.2826761	0.0000336	-4.9146071
H	-10.2000721	0.0000784	-2.5954882
H	-8.6397587	0.0000615	-0.6419888

T_{MC}

C	-5.7413974	1.1168382	0.1679459
C	-4.4242599	1.1691657	0.6267060
C	-3.9294425	2.3126495	1.2557336
C	-4.7700547	3.4122653	1.4221084
C	-6.0908686	3.3663175	0.9779831
C	-6.5754087	2.2174109	0.3516407
N	-3.5735822	0.0466391	0.4497917
C	-3.8497724	-1.2442053	0.9028300
C	-2.7175813	-2.0366661	0.5614307
N	-1.8376471	-1.1742171	-0.0850140
C	-2.3570237	0.0864514	-0.1467979
C	-0.4969524	-1.3455552	-0.5320218
C	0.0926655	-2.5864325	-0.7664365
C	1.4276535	-2.6268853	-1.1757189
C	2.1413742	-1.4459648	-1.3692713
C	1.5153521	-0.2087671	-1.1757106
C	0.1924952	-0.1423334	-0.7523062
Pt	-1.1388498	1.5304272	-0.7437331
O	-0.6503572	2.3128752	1.2810404
C	0.2716941	3.1541295	1.4760344
C	1.0085142	3.8586829	0.5059580
C	0.8403341	3.8173306	-0.8913713
C	1.6639297	4.7449396	-1.7473269
O	0.0436584	3.0778227	-1.5359189
C	0.5743419	3.4148014	2.9325997
H	-0.4677629	-3.5170130	-0.6662979
H	1.9046450	-3.5950303	-1.3539206
H	2.0751895	0.7156154	-1.3571651
H	3.1893437	-1.4872823	-1.6829501
C	-2.6572687	-3.3637176	0.9261471
C	-4.9274498	-1.7552019	1.5836115
H	1.7636794	4.5509631	0.8819961
H	1.3807465	4.1490838	3.0777178
H	-0.3399517	3.7752231	3.4354294
H	0.8549900	2.4627262	3.4151432
H	2.3912893	5.3312085	-1.1668633
H	0.9877932	5.4345059	-2.2826999
H	2.1929377	4.1554953	-2.5154088
H	-2.8957588	2.3301545	1.6123283
H	-4.3851674	4.3119707	1.9104768
H	-6.7462049	4.2309262	1.1169161
H	-7.6068986	2.1808947	-0.0102004
H	-6.1015441	0.2228648	-0.3478823
C	-4.8998215	-3.1227496	1.9496709
C	-3.7552572	-3.9266773	1.6230120
H	-5.7814499	-1.1291373	1.8497999
C	-5.9811714	-3.7233331	2.6488711
C	-3.7493983	-5.2922973	2.0175372
H	-1.7910709	-3.9881650	0.7132531
C	-5.9418041	-5.0478326	3.0118633
C	-4.8128440	-5.8408929	2.6926918
H	-6.8511435	-3.1066203	2.8944822
H	-6.7832439	-5.4931173	3.5504800
H	-4.7900340	-6.8941938	2.9865660
H	-2.8760725	-5.9037474	1.7708325

T₁ barrier at 225°

C	-1.7151256	-1.3522535	3.1569381
C	-0.6736727	-0.7787563	2.4250033
C	0.1225087	0.2229236	2.9797981
C	-0.1365048	0.6555382	4.2793726
C	-1.1684456	0.0836866	5.0221103
C	-1.9555996	-0.9219221	4.4594965
N	-0.4281961	-1.2162925	1.0973728
C	-0.2068131	-2.5439565	0.7287131
C	-0.0340539	-2.5424109	-0.6838355
N	-0.1729017	-1.2158997	-1.0759273
C	-0.4033381	-0.4113926	0.0040063
C	-0.0053963	-0.5792363	-2.3357526
C	-0.0732857	-1.2441623	-3.5584818
C	0.1067332	-0.5081096	-4.7318038
C	0.3202887	0.8682472	-4.6759663
C	0.3407897	1.5253344	-3.4406223
C	0.1836428	0.8104264	-2.2572511
Pt	-0.3036731	1.5454071	-0.3226311
O	1.5548835	2.0329558	0.7962710
C	1.7891865	3.1899224	1.2501647
C	1.0941204	4.3793628	0.9652536
C	0.0593675	4.5376265	0.0237827
C	-0.5029639	5.9136655	-0.2191801
O	-0.4383762	3.6248004	-0.6937599
C	2.9482131	3.2509175	2.2170868
H	-0.2944594	-2.3109410	-3.6194117
H	0.0643110	-1.0203776	-5.6974707
H	0.4806134	2.6111843	-3.4018718
H	0.4645800	1.4355124	-5.6011308
C	0.2594556	-3.7086088	-1.3557838
C	-0.1094606	-3.6897319	1.4797498
H	1.4308829	5.2786476	1.4833626
H	3.1783533	4.2756979	2.5449206
H	2.7160661	2.6323857	3.1027060
H	3.8391794	2.8085297	1.7402521
H	-0.0257001	6.6883116	0.3993958
H	-1.5881247	5.8998313	-0.0166599
H	-0.3795520	6.1688497	-1.2858434
H	0.9320251	0.6563492	2.3862848
H	0.4809489	1.4463832	4.7155459
H	-1.3641769	0.4243090	6.0429466
H	-2.7742709	-1.3660281	5.0329863
H	-2.3439613	-2.1190114	2.6967696
C	0.1686211	-4.9063642	0.8102824
C	0.3582974	-4.9119061	-0.6136672
H	-0.2282216	-3.6709520	2.5650553
C	0.2791085	-6.1323722	1.5198264
C	0.6515482	-6.1458347	-1.2553287
H	0.4357860	-3.7330674	-2.4302103
C	0.5622191	-7.3070762	0.8654708
C	0.7506374	-7.3134907	-0.5378957
H	0.1350661	-6.1230126	2.6045808
H	0.6440898	-8.2414953	1.4281883
H	0.9764323	-8.2530791	-1.0503607
H	0.7975449	-6.1489435	-2.3398709

DPANIM

S₀

C	-1.8341135	-0.0000645	-4.2479994
C	-1.7223707	-0.0000326	-2.8313640
C	-0.4623426	0.0000069	-2.2724253
C	0.6761571	0.0000160	-3.1307334
C	0.5844286	-0.0000141	-4.5239630
C	-0.7284226	-0.0000562	-5.0769332
C	1.9093756	0.0000608	-2.4047440
C	1.4922870	0.0000760	-0.9995682
C	0.1140764	0.0000465	-0.9424306
N	-0.2597459	0.0000738	0.3822688
C	0.8539969	0.0001142	1.1624197
N	1.9298379	0.0001150	0.3082112
C	3.1898148	0.0001594	0.9529369
C	4.4158793	0.0001548	0.3012883
C	5.5804456	0.0002048	1.0715702
C	5.4950468	0.0002571	2.4632389
C	4.2501900	0.0002559	3.1005600
C	3.0684253	0.0002058	2.3580431
Pt	1.2099983	0.0001815	3.0647127
O	1.8227101	0.0002609	5.0541444
C	1.0732137	0.0002729	6.0764828
C	1.8140955	0.0003325	7.3882958
C	-1.6062265	0.0000469	0.8518031
C	-2.2539788	1.2122420	1.0732655
C	-3.5734725	1.2089446	1.5194496
C	-4.2328059	0.0000363	1.7426361
C	-3.5733994	-1.2088103	1.5195342
C	-2.2539616	-1.2120929	1.0733695
O	-0.8001427	0.0001399	3.7501143
C	-1.1702023	0.0001719	4.9567987
C	-2.6640780	0.0001354	5.1577641
C	-0.3307267	0.0002353	6.0873185
H	1.1420810	0.0003453	8.2596866
H	2.4694800	-0.8868445	7.4340252
H	2.4694405	0.8875413	7.4339684
H	-2.9550326	0.0001714	6.2188753
H	-3.0946163	0.8846666	4.6573229
H	-3.0945621	-0.8844663	4.6573988
H	4.4749561	0.0001107	-0.7874530
H	6.5557192	0.0002024	0.5764807
H	6.4111414	0.0002978	3.0623275
H	4.1860716	0.0002948	4.1926792
H	-1.7148267	-2.1473734	0.9045569
H	-4.0872221	-2.1573755	1.6997159
H	-5.2674830	0.0000463	2.0978848
H	-4.0872951	2.1574679	1.6995435
H	-1.7149244	2.1474831	0.9043933
H	-0.8164845	0.0002537	7.0646292
C	1.8130059	0.0000027	-5.2427285
H	-0.8572453	-0.0000816	-6.1634852
H	-2.8337574	-0.0000965	-4.6921123
H	-2.6217877	-0.0000397	-2.2103134
C	3.0106887	0.0000496	-4.5565990
C	3.0789250	0.0000803	-3.1363176
H	1.8040564	-0.0000203	-6.3367437
H	3.9491931	0.0000643	-5.1182541
H	4.0613572	0.0001201	-2.6608566

S₁

C	-1.8579791	-0.0000653	-4.1904408
C	-1.7689341	-0.0000343	-2.8047717
C	-0.4736602	0.0000070	-2.2353383
C	0.6830212	0.0000176	-3.0863358
C	0.5846495	-0.0000131	-4.5040738
C	-0.7245621	-0.0000560	-5.0305395
C	1.9339270	0.0000634	-2.3722688
C	1.5300189	0.0000790	-1.0122953
C	0.0898991	0.0000466	-0.9470254
N	-0.2671328	0.0000674	0.3746280
C	0.8538406	0.0001132	1.1527353
N	1.9467372	0.0001164	0.2880041
C	3.1955542	0.0001589	0.9397566
C	4.4283886	0.0001545	0.2974196
C	5.5821775	0.0002046	1.0806270
C	5.4873592	0.0002560	2.4734891
C	4.2387743	0.0002538	3.1025732
C	3.0685356	0.0002033	2.3451834
Pt	1.2021398	0.0001769	3.0344646
O	1.8107127	0.0002561	5.0124009
C	1.0696936	0.0002725	6.0469392
C	1.8280224	0.0003340	7.3460120
C	-1.6133370	0.0000817	0.8509567
C	-2.2595046	1.2130379	1.0702814
C	-3.5785917	1.2092931	1.5173388
C	-4.2372239	0.0000338	1.7406614
C	-3.5785553	-1.2091612	1.5174327
C	-2.2594631	-1.2129492	1.0703741
O	-0.8079605	0.0001370	3.7334559
C	-1.1770067	0.0001713	4.9391349
C	-2.6683613	0.0001349	5.1444462
C	-0.3303252	0.0002368	6.0678545
H	1.1685615	0.0003508	8.2265639
H	2.4842302	-0.8866962	7.3813880
H	2.4841949	0.8873923	7.3813262
H	-2.9556434	0.0001732	6.2063026
H	-3.0993016	0.8843222	4.6440047
H	-3.0992471	-0.8841249	4.6440844
H	4.4943335	0.0001109	-0.7900670
H	6.5620203	0.0002030	0.5950402
H	6.3993266	0.0002964	3.0784354
H	4.1645524	0.0002906	4.1937214
H	-1.7237023	-2.1487307	0.8941267
H	-4.0939508	-2.1576385	1.6932439
H	-5.2730237	0.0000458	2.0923843
H	-4.0940244	2.1577355	1.6930793
H	-1.7237745	2.1488620	0.8939628
H	-0.8104909	0.0002591	7.0475648
C	1.8107046	0.0000045	-5.2123677
H	-0.8619550	-0.0000810	-6.1159930
H	-2.8482485	-0.0000984	-4.6563413
H	-2.6639242	-0.0000424	-2.1793916
C	3.0344410	0.0000532	-4.5210728
C	3.1310282	0.0000842	-3.1330452
H	1.8022447	-0.0000186	-6.3057943
H	3.9601259	0.0000690	-5.1048561
H	4.1155369	0.0001265	-2.6646895

S47

T₁

C	-1.8599564	-0.0000653	-4.1919870
C	-1.7701581	-0.0000339	-2.8039641
C	-0.4737963	0.0000071	-2.2318548
C	0.6855345	0.0000186	-3.0925570
C	0.5888781	-0.0000124	-4.4934532
C	-0.7306278	-0.0000562	-5.0291038
C	1.9357881	0.0000653	-2.3759634
C	1.5346990	0.0000791	-1.0163648
C	0.0825161	0.0000451	-0.9520045
N	-0.2688407	0.0000683	0.3794862
C	0.8548190	0.0001125	1.1495354
N	1.9496007	0.0001168	0.2870556
C	3.1993960	0.0001601	0.9401095
C	4.4323821	0.0001552	0.2990807
C	5.5865452	0.0002046	1.0832133
C	5.4900848	0.0002560	2.4748708
C	4.2400285	0.0002544	3.1019556
C	3.0707264	0.0002044	2.3436763
Pt	1.2028729	0.0001772	3.0300471
O	1.8119686	0.0002577	5.0105507
C	1.0703147	0.0002730	6.0432713
C	1.8270151	0.0003338	7.3437835
C	-1.6135682	0.0000651	0.8579311
C	-2.2612969	1.2125863	1.0763353
C	-3.5815924	1.2091277	1.5198631
C	-4.2412473	0.0000474	1.7412159
C	-3.5815516	-1.2090161	1.5199549
C	-2.2612545	-1.2124737	1.0764265
O	-0.8063125	0.0001373	3.7285911
C	-1.1755261	0.0001715	4.9349739
C	-2.6674347	0.0001341	5.1392265
C	-0.3304890	0.0002371	6.0636340
H	1.1661966	0.0003510	8.2233599
H	2.4830989	-0.8868048	7.3800673
H	2.4830645	0.8875002	7.3800057
H	-2.9556331	0.0001734	6.2009279
H	-3.0982352	0.8844905	4.6389072
H	-3.0981800	-0.8842956	4.6389888
H	4.5006163	0.0001106	-0.7884338
H	6.5666491	0.0002015	0.5980857
H	6.4007967	0.0002954	3.0815630
H	4.1641380	0.0002910	4.1930049
H	-1.7247572	-2.1483428	0.9028282
H	-4.0970518	-2.1574783	1.6954352
H	-5.2778934	0.0000485	2.0905651
H	-4.0971276	2.1575743	1.6952724
H	-1.7248315	2.1484700	0.9026657
H	-0.8113007	0.0002584	7.0431922
C	1.8150468	0.0000044	-5.2096469
H	-0.8653896	-0.0000820	-6.1147329
H	-2.8507891	-0.0000984	-4.6567112
H	-2.6646787	-0.0000412	-2.1780095
C	3.0357244	0.0000530	-4.5250299
C	3.1289684	0.0000850	-3.1327085
H	1.8024896	-0.0000191	-6.3032210
H	3.9620897	0.0000677	-5.1075859
H	4.1123399	0.0001262	-2.6616351

T_{MC}

C	-5.7825570	1.1025125	0.1767002
C	-4.4531911	1.2079264	0.5869179
C	-3.9649102	2.3885021	1.1487837
C	-4.8279621	3.4741590	1.2931390
C	-6.1603590	3.3784002	0.8937134
C	-6.6373960	2.1904468	0.3377390
N	-3.5850484	0.0976993	0.4242378
C	-3.8457330	-1.1959155	0.8228430
C	-2.7418691	-1.9609918	0.5081155
N	-1.8372579	-1.1113911	-0.0928661
C	-2.3515728	0.1562174	-0.1503846
C	-0.5056855	-1.2896142	-0.5614673
C	0.0453820	-2.5396990	-0.8264625
C	1.3696876	-2.6075587	-1.2632910
C	2.1047849	-1.4376614	-1.4514940
C	1.5114994	-0.1891905	-1.2282272
C	0.1978590	-0.0952363	-0.7782200
Pt	-1.1093819	1.5981843	-0.7380475
O	-0.6140146	2.3501980	1.3019657
C	0.3169098	3.1770730	1.5105113
C	1.0709071	3.8788129	0.5508180
C	0.9119632	3.8521348	-0.8479563
C	1.7662421	4.7658794	-1.6896034
O	0.1037967	3.1378518	-1.5063073
C	0.6143431	3.4206971	2.9715070
H	-0.5500640	-3.4493735	-0.7317265
H	1.8209559	-3.5825145	-1.4691275
H	2.0893722	0.7239033	-1.4108492
H	3.1451973	-1.4970422	-1.7873559
C	-2.9327573	-3.3183348	1.0262456
C	-4.8296490	-1.9854890	1.5455635
H	1.8355603	4.5547067	0.9374826
H	1.4146911	4.1590575	3.1299371
H	-0.3050137	3.7657525	3.4756155
H	0.9009715	2.4639886	3.4415874
H	2.4849130	5.3494255	-1.0954066
H	1.1108598	5.4564398	-2.2486010
H	2.3096816	4.1644028	-2.4383878
H	-2.9241337	2.4423409	1.4803822
H	-4.4509984	4.4030602	1.7303196
H	-6.8312868	4.2338398	1.0136206
H	-7.6786349	2.1135173	0.0118242
H	-6.1350056	0.1762199	-0.2854253
C	-4.2268285	-3.2753777	1.6333019
C	-6.0673378	-1.7912643	2.1222779
C	-6.6959268	-2.8874750	2.7718953
C	-4.8256577	-4.3608935	2.2772550
C	-6.1085162	-4.1351372	2.8521813
C	-2.2296961	-4.5034977	1.1001637
C	-4.0787981	-5.5719292	2.3140082
C	-2.8224165	-5.6232198	1.7449236
H	-6.5648979	-0.8188844	2.0942050
H	-7.6784026	-2.7292364	3.2260191
H	-6.6223614	-4.9531661	3.3657860
H	-4.4990081	-6.4552864	2.8041173
H	-1.2237887	-4.6061759	0.6903572
H	-2.2514221	-6.5549497	1.7903117

T_1 barrier at 230°

C	-1.6623115	-1.3304170	3.1824806
C	-0.6875646	-0.6762602	2.4278590
C	0.0586306	0.3698712	2.9706994
C	-0.1845454	0.7621956	4.2862237
C	-1.1499133	0.1108592	5.0529384
C	-1.8868465	-0.9374592	4.4997367
N	-0.4583304	-1.0826852	1.0882932
C	-0.2726612	-2.3823728	0.6668337
C	-0.0928050	-2.3569871	-0.7001977
N	-0.1906477	-1.0367218	-1.0819710
C	-0.4160129	-0.2449807	0.0130622
C	-0.0533899	-0.3828712	-2.3369910
C	-0.1480475	-1.0505967	-3.5542875
C	0.0004080	-0.3163971	-4.7323730
C	0.2090067	1.0615876	-4.6768925
C	0.2514452	1.7192371	-3.4419933
C	0.1238820	1.0066329	-2.2525353
Pt	-0.3316108	1.7259984	-0.2960137
O	1.5819759	2.1717787	0.7607196
C	1.8751930	3.3269812	1.1807323
C	1.2036500	4.5338922	0.9107887
C	0.1135868	4.7134691	0.0377615
C	-0.4185138	6.1058370	-0.1844416
O	-0.4671113	3.8121831	-0.6296840
C	3.0851017	3.3680178	2.0852397
H	-0.3720390	-2.1181112	-3.5948240
H	-0.0640409	-0.8265084	-5.6979427
H	0.3831335	2.8064302	-3.4092492
H	0.3289458	1.6309520	-5.6043710
C	0.2354340	-3.7052701	-1.1693493
C	-0.0933907	-3.7299000	1.1833283
H	1.5998971	5.4300711	1.3910297
H	3.3538968	4.3888250	2.3960140
H	2.8884136	2.7563875	2.9839406
H	3.9402843	2.9059409	1.5633435
H	0.1274710	6.8713333	0.3869744
H	-1.4861675	6.1321014	0.0952656
H	-0.3638375	6.3437470	-1.2607886
H	0.8255913	0.8580208	2.3628140
H	0.3952737	1.5841788	4.7161177
H	-1.3322938	0.4218820	6.0856012
H	-2.6540525	-1.4444040	5.0919784
H	-2.2531116	-2.1303618	2.7277367
C	0.2043126	-4.4991775	0.0194280
C	-0.1187685	-4.3635593	2.4080166
C	0.1433470	-5.7592320	2.4587555
C	0.4758514	-5.8690994	0.0521417
C	0.4297090	-6.4994645	1.3280511
C	0.5735540	-4.3322458	-2.3512152
C	0.7980663	-6.4853238	-1.1897728
C	0.8468383	-5.7273715	-2.3422632
H	-0.3281150	-3.8168493	3.3306429
H	0.1205137	-6.2579207	3.4321145
H	0.6318905	-7.5716820	1.4092591
H	1.0186575	-7.5563293	-1.2240943
H	0.6526602	-3.7867832	-3.2930176
H	1.1094429	-6.2082284	-3.2888741

References

- (1) Bossi, A.; Rausch, A. F.; Leitl, M. J.; Czerwieniec, R.; Whited, M. T.; Djurovich, P. I.; Yersin, H.; Thompson, M. E. *Inorg. Chem.* **2013**, *52*, 12403–12415.
- (2) Tronnier, A.; Pöthig, A.; Metz, S.; Wagenblast, G.; Münster, I.; Strassner, T. *Inorg. Chem.* **2014**, *53*, 6346–6356.

Reproduced from Ref. [137] with permission from the PCCP Owner Societies.



PCCP

PAPER

View Article Online

View Journal



Cite this: DOI: 10.1039/c9cp04244j

DFT/MRCI-R2018 study of the photophysics of the zinc(II) tripyrrindione radical: non-Kasha emission?

Adrian Heil and Christel M. Marian *

Stable radical-based fluorescent emitters are rare, even more so at room temperature. The zinc(II) tripyrrindione [Zn(TD1•)(H₂O)] complex has recently been described experimentally by Gautam *et al.* [*Inorg. Chem.*, 2018, **57**, 15240] as a new member of the small family of neutral radical emitters with possible applications in electronics and photonics. Upon excitation at the absorption maximum of 599 nm (2.07 eV), strong fluorescence was observed with a maximum at 644 nm (1.93 eV) at room temperature in tetrahydrofuran solution. The fluorescence energy is higher than several low-intensity absorption bands starting at ≈ 930 nm. Here we present a theoretical investigation into the absorption and fluorescence of this zinc complex by means of the recently developed semi-empirical all-multiplicity DFT/MRCI-R2018 method. The DFT/MRCI method combines density functional theory (DFT) in a closed shell or restricted open-shell Kohn–Sham orbital basis and multireference configuration interaction (MRCI). The R2018 Hamiltonian proves to be well-suited for investigating the properties of the radical-based zinc complex. The calculations reveal that the absorption spectrum is dominated by bright transitions to the D₃, D₆ and D₁₁ states. The experimentally observed emission band lies at considerably shorter wavelengths than the lowest absorption band of the radical. This precludes the D₁ → D₀ transition as the origin of the emission. Our calculations indicate a non-Kasha emission, with D₃ as the emissive state. Other ways of explaining the experimentally observed emission, such as ion-pair formation or ligand emission after demetalation, are discussed as well.

Received 30th July 2019,
Accepted 30th August 2019

DOI: 10.1039/c9cp04244j

rsc.li/pccp

1 Introduction

Since the advent of the first organic light emitting diode (OLED) in 1987,¹ many different routes have been followed to enhance their properties in terms of efficiency, colour purity or manufacturing costs. One possible way of increasing the efficiency in electroluminescent devices is by leveraging off the spin statistics. In a closed-shell emitter, the hole–electron recombination results in spin statistics of 25% singlet and 75% triplet states. By being limited to the fluorescence from a singlet state, a purely organic emitter with a low phosphorescence rate will therefore have 25% internal quantum efficiency (IQE) at most. By also enabling phosphorescence, an IQE of almost 100% is possible.^{2–4} A different approach to harvest all excitons *via* thermally activated delayed fluorescence aims at increasing the reverse intersystem crossing (rISC) to repopulate the lowest singlet state from the triplet states,^{5,6} with excellent results.⁷

A promising alternative is the use of persistent open-shell radicals as emitters, as recently proposed by Peng *et al.*⁸ In many of these systems, the spin state of the exciton does not influence the emission properties as the interaction of singlet- and triplet-coupled electron–hole pairs with the open-shell radicals preferentially produces excited doublet states. In principle, quartet states could be generated from the interaction between the triplet exciton and the radical as well. However, the requirement for a quartet state is the presence of three unpaired electrons, while a doublet state can be created with just one unpaired electron. The latter occupation is energetically favoured in most systems. In this manner, a formation ratio of 100% has been reported for the doublet excited state⁹ and 27% external quantum efficiency has been achieved,¹⁰ showing the potential of radical-based emitters. However, while electroluminescent systems with an unpaired electron have many advantages when it comes to the IQE, the main concern is the lack of stability and longevity brought on by their radicalic nature. By addressing this potential weakness, systems with better suitability can be designed.

The most common persistent open-shell emitters are based on triphenylmethyl (or trityl) radicals¹¹ with polychlorinated aryl rings as luminescent dyes.^{8,9,12–15} Other halogens have also

Institut für Theoretische Chemie und Computerchemie, Heinrich-Heine-Universität Düsseldorf, 40225 Düsseldorf, Germany. E-mail: Christel.Marian@hhu.de;
Fax: +49-211-81-13466, +49-211-81-13210

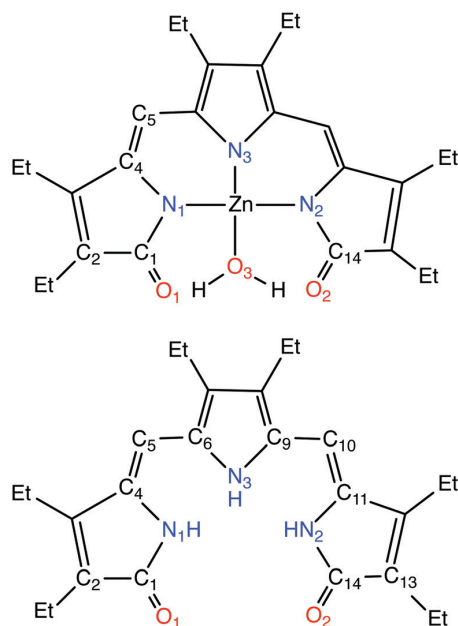


Fig. 1 Chemical structure of [Zn(TD1*)(H₂O)] complex (top) and the H₃TD1 molecule (bottom) including selected atom labels.

been substituted in order to alter properties such as the photostability and the quantum yield of the trityl compounds.¹⁶ Further stable structures include nitroxide radicals,^{17,18} organometallic complexes,¹⁹ Blatter's radical^{20,21} and 1,2,3,5-dithiadiazolyl (DTDA) radicals linked to aromatic molecules.^{22,23}

A new type of stable radical that shows fluorescence at room temperature has recently been reported by Gautam *et al.*²⁴ This emitter is an organometallic Zn(II) complex with tripyrrin-1,14-dione as a dianionic radical, forming the neutral [Zn(TD1*)(H₂O)] complex (Fig. 1, top). While the closed-shell counterparts of luminescent zinc complexes with nitrogen donors are well known in literature,²⁵ open-shell zinc complexes as fluorophores are rare.

Linear oligopyrroles are omnipresent pigments in nature, where they function in the metabolism of heme and chlorophyll²⁶ and in photosynthetic systems²⁷ or as degradation products of bile pigments.²⁷ The hexaethyltripyrindione (H₃TD1) ligand (Fig. 1, bottom) is a synthetic oligopyrrole²⁸ and closely related to the urinary pigment uroerythrin.²⁹

Experimentally, the formation of the [Zn(TD1*)(H₂O)] was monitored by its UV-vis absorption spectrum.²⁴ An intense band close to 600 nm and three weak bands in the wave-length region between 700 and 950 nm were found to be characteristic of metal-bound TD1²⁻. Upon excitation at the absorption maximum of 599 nm (2.07 eV), strong fluorescence was observed with maximum at 644 nm (1.93 eV) at room temperature in tetrahydrofuran solution. Apparently, the emission does not stem from the first-excited doublet state (D₁) and hence violates Kasha's rule.³⁰ Although such violations are well known in literature – the S₂ fluorescence of azulene,³¹ for example, and the D₂ emission of the azaxanthone ketyl radical³² – a closer

look on the electronic structure and the photophysical properties of the [Zn(TD1*)(H₂O)] seems appropriate.

To gain further insight into the origin of the emission band, the DFT/MRCI-R2018³³ Hamiltonian is employed in this work to compute the spectral properties of the H₃TD1 ligand and the metal-bound neutral [Zn(TD1*)(H₂O)] radical as well as its cationic and anionic counterparts. The H₃TD1 ligand can be detected after demetalation of the complex and thus might affect the emission. The DFT/MRCI method combines density functional theory (DFT) and multireference configuration interaction (MRCI),^{34–36} where the dynamical correlation stems from DFT and the static correlation from MRCI. It is empirically parametrised against experimental excitation energies to avoid double counting of electron correlation, since some dynamical correlation is still provided by the MRCI expansion. DFT/MRCI has been shown to yield electronic excitation energies with good accuracy and at reasonable cost.³⁶ For organic molecules of both, open- and closed-shell type, the root mean square deviation (RMSD) from experiment is below 0.2 eV.^{37,38} The RMSD is only slightly larger for transition metal organic complexes with closed-shell ground states.^{33,36,39–42} The following results are the first to be reported for an open-shell transition metal complex.

2 Theory

The DFT/MRCI method for open-shell systems relies on a restricted open-shell Kohn–Sham (ROKS) determinant as the anchor configuration. Within the set of ROKS orbitals, the open shell is commonly called singly occupied orbital (SOMO). Contrary to a restricted orbital setting for closed-shell systems, the highest doubly occupied molecular orbital is called HDOMO instead of HOMO (highest occupied MO) to avoid confusions. This is done because both the SOMO and the HDOMO are occupied and a reference to the highest occupied orbital might be ambiguous.

Within the framework of the DFT/MRCI method, we make use of the newly developed all-multiplicity R2018 Hamiltonian.³³ This Hamiltonian employs the same corrections for diagonal matrix elements as the previously developed R2017 Hamiltonian,³⁸ but treatment of off-diagonal matrix elements is improved over the redesigned R2017³⁸ and R2016³⁷ Hamiltonians, leading to a better description of transition metal complexes.

The MRCI matrix elements are evaluated as outlined by Segal, Wetmore and Wolf.^{43,44} Spin symmetry is exploited by employing configuration state functions (CSF) that are formed as spin-adapted linear combinations of determinants in DFT/MRCI. True diagonal matrix elements, *i.e.* matrix elements of two CSF with the same spatial occupation w and spin pattern ω , are given as

$$\begin{aligned} \langle \omega w | \hat{\mathcal{H}}^{\text{DFT}} - E^{\text{DFT}} | \omega w \rangle = & \langle \omega w | \hat{\mathcal{H}} - E^{\text{HF}} | \omega w \rangle - \sum_{i \in c}^{n_{\text{exc}}} (F_{ii}^{\text{HF}} - F_{ii}^{\text{KS}}) \\ & + \sum_{i \in a}^{n_{\text{exc}}} (F_{ii}^{\text{HF}} - F_{ii}^{\text{KS}}) + \Delta E_{\text{coul}} - \Delta E_{\text{exch}} \end{aligned} \quad (1)$$

with c and a as created and annihilated electrons. The Fock matrix elements F_{ii}^{HF} are replaced by the KS orbital energies F_{ii}^{KS} , with n_{exc} as the number of excitations. The contributions of the two-electron interactions ΔE_{coul} and ΔE_{exch} are scaled by the empirically fitted parameters p_J for Coulomb-type integrals $V_{ijij} = \langle ij|ij \rangle$ and p_X for exchange-like integrals V_{ijji} . For the R2018 (and R2017) Hamiltonian this correction is

$$\begin{aligned} & \Delta E_{\text{coul}} - \Delta E_{\text{exch}} \\ &= p_J \left(- \sum_{\substack{i,j \in c \\ i > j}}^{n_{\text{exc}}} V_{ijij} - \sum_{\substack{i,j \in a \\ i > j}}^{n_{\text{exc}}} V_{ijij} + \sum_{i \in c} \sum_{j \in a}^{n_{\text{exc}}} V_{ijij} + \sum_{i \in s} \frac{1}{2} V_{iiii} |\Delta w_i| \right) \\ & - p_X \left(\frac{1}{2} \sum_{i \in c} \sum_{j \in a}^{n_{\text{exc}}} V_{ijji} - \frac{1}{2} \sum_{\substack{i \in c \\ j \in c,s}}^{n_{\text{exc}}} V_{ijji} - \frac{1}{2} \sum_{\substack{j \in a \\ j \in a,s}}^{n_{\text{exc}}} V_{ijji} + \sum_{\substack{ij \in o \\ i > j}}^{N_o} V_{ijji} \eta_{ij}^{ji} \right) \end{aligned} \quad (2)$$

with s labeling the n_{single} singly occupied orbitals of the anchor configuration and $\Delta w_i = w_i - \bar{w}_i$ as the occupation difference between a configuration and the anchor configuration. The η_{ij}^{ji} are spin coupling coefficients, the CSF. When a ROKS anchor configuration for a molecule with a doublet ground state is used, there is therefore one singly occupied orbital in the s set. V_{iiii} describes a diagonal orbital that is required whenever a shell is doubly occupied or vacant in a configuration but not in the anchor configuration. This condition only requires a single (de)excitation in case of a singly occupied orbital. For a closed shell ground state, eqn (2) is identical to the expression of the R2016 Hamiltonian.³⁷ The index o refers to the N_o open shells in a configuration.

The off-diagonal matrix elements between two configurations with the same spatial occupation but different spin patterns are scaled in the R2018 Hamiltonian as

$$\langle \omega w | \hat{\mathcal{H}}^{\text{DFT}} | \omega' w' \rangle = \langle \omega w | (1 - p_X) \hat{\mathcal{H}}^{\text{CI}} | \omega' w' \rangle. \quad (3)$$

The off-diagonal elements differing in one and two electron occupations are damped by a function that depends on the energy difference between two CSF with the parameter p_2 and scaled by a parameter p_1 . The scaling is carried out to adjust the interaction between near-degenerate configurations. The damping of matrix elements between CSF with a large energy separation avoids double counting of dynamic correlation that is partially included through the KS orbital energies. In the R2018 Hamiltonian these have the form

$$\langle \omega w | \hat{\mathcal{H}}^{\text{DFT}} | \omega' w' \rangle = \langle \omega w | \hat{\mathcal{H}}^{\text{CI}} | \omega' w' \rangle p_1 e^{-p_2 \Delta E_{\omega w' \omega' w' }^6}. \quad (4)$$

The R2018 Hamiltonian has been parametrised against vertical excitation energies of various singlet, doublet and triplet states of organic molecules of the R2017 fitting set³⁸ and additionally in total 10 states of Cu, Cu⁺ and ruthenocene.³³ The standard parameters for the R2018 Hamiltonian shown in Table 1.

The R2018 Hamiltonian was developed to improve the accuracy on transition metal complexes^{33,36} and has recently been employed to cyclometalated Pt(II) β -diketonate complexes

Table 1 Parameters employed in the R2018 calculation with a selection threshold of 1.0 E_h

p_1	p_2	p_J	p_X
0.5584	4.4717	0.5089	0.3624

with good accuracy compared to the experiment.⁴⁵ DFT/MRCI is currently parametrised for the BHandHLYP^{46,47} functional.

3 Computational details

Restricted open-shell calculations provide many advantages, the most important being that the resulting wave function is an eigenfunction to the \hat{S}^2 operator, but ROKS is not very commonly utilised. Thus, an implementation is missing in many quantum chemistry program packages. Especially analytic gradients are missing, which results in time-dependent density functional theory (TD-DFT) based on ROKS orbitals not being applicable for optimising excited state geometries. For this reason, unrestricted Kohn–Sham density functional theory (UDFT) and unrestricted TD-DFT (UTD-DFT) were used for the geometry optimisations and vibrational analyses of the ground and excited states of the [Zn(TD1*)(H₂O)] radical, respectively. Herein, the MN15⁴⁸ functional was chosen due to its known accuracy for transition metal complexes and its high (44%) percentage of Hartree–Fock exchange. The PBE0 functional^{49,50} gave inferior results for the excited states of the [Zn(TD1*)(H₂O)] radical and was employed for test purposes only. The MN15 functional was also employed for optimising the ground and excited states of the [Zn(TD1)(H₂O)]⁺ cation and [Zn(TD1)(H₂O)]⁻ anion. The ground states of various H₃TD1 conformers were optimised using the B3LYP⁵¹ functional with Grimme's D3 dispersion with Becke–Johnson damping⁵² to include London dispersion interaction in the flexible molecular structure. For carbon and hydrogen the def-SV(P) basis sets⁵³ and for nitrogen and oxygen the def2-SVPD⁵⁴ basis sets were utilised. For zinc, the 10-mdf 6s5p3d basis set⁵⁵ was employed in combination with the Stuttgart–Köln MCDHF RSC ECP⁵⁶ for the 10 core electrons. All geometry optimisations and vibrational analyses were performed with the Gaussian 16 program package.⁵⁷

The BHandHLYP^{46,47} ROKS orbitals of [Zn(TD1*)(H₂O)] and the restricted Kohn–Sham (RKS) orbitals of [Zn(TD1)(H₂O)]⁺, [Zn(TD1)(H₂O)]⁻ and H₃TD1 for subsequent DFT/MRCI runs were calculated with Dalton 2018.0^{58,59} and converted from Dalton to Turbomole format with the d2tm interface.³⁸

Vertical excitation and emission energies as well as transition moments were calculated with the DFT/MRCI program^{34,35} using the R2018 Hamiltonian³³ and a selection threshold of 1.0 E_h . The DFT/MRCI calculations on [Zn(TD1*)(H₂O)] and the corresponding cation and anion relaxed states were carried out for 10 excited singlet or doublet states in each of the A' and A'' irreducible representation of the C_s point group plus one root for the ground state. For H₃TD1, the first 10 excited singlet states and the ground state were calculated in C_1 geometry. The resolution-of-the-identity (RI) approximation^{34,60,61} was employed for the four-index V_{ijkl} integrals with SVP⁶² as the auxiliary basis

for carbon and hydrogen, def2-SVPD⁶³ for nitrogen and oxygen and TZVP⁶² for zinc.

Starting from the transition dipole moment in length form μ , the transition rate constant is

$$\Gamma_{\text{rad}} = \frac{\omega^3 n |\mu|^2}{3\pi\epsilon_0 \hbar c^3} \quad (5)$$

with ω as the transition frequency, ϵ_0 the vacuum permittivity, n the refraction index of the medium, c the speed of light and \hbar the reduced Planck's constant. By sorting the constants and assuming a refraction index of $n = 1$, eqn (5) can be simplified to

$$\Gamma_{\text{rad}} = 2.0261 \times 10^{-6} \cdot \bar{\nu}^3 \cdot |\mu_{\text{au}}|^2 \quad (6)$$

with $\bar{\nu}$ as the transition energy in cm^{-1} and μ_{au} as the transition dipole moment in length form in atomic units.

Franck-Condon profiles of the absorption to the D_1 state were calculated with the VIBES program,^{64,65} using a Fourier transform approach and including temperature and Duschinsky effects.⁶⁶ The time correlation function was damped with a Gaussian function of 10 cm^{-1} full width at half maximum (FWHM). The temperature was set to 298 K and the time interval to 300 fs. The grid was expanded over 16 384 points.

4 Results for H₃TD1

4.1 Geometries

The tripyrrin-1,14-dione (H₃TD1) molecule (Fig. 1) is neutral with a closed-shell ground state. Different conformers were optimised and are all minima on the potential energy surface. The main difference between these conformers are the N₃-C₆-C₄-N₁ and N₃-C₉-C₁₁-N₂ dihedral angles. The dihedral angles as well as the angle between the pyrrole entities can be found in Table 2 for the three energetically lowest conformers. It can be seen that the angle between the pyrrole entities shows very little deviation between the different conformers.

4.2 Absorption

The molecule shows a broad absorption band in the experiment with a maximum at approx. 2.64 eV (470 nm) and a shoulder at approx. 2.48 eV (500 nm) with further absorption in the higher energy part of the spectrum. The calculations in C₁ symmetry with DFT/MRCI-R2018 in vacuum show that the absorption stems from a very bright transition to the S₁ state with a HOMO → LUMO configuration. The different orientations of the pyrrole entities influence the energy of the

Table 2 Geometry parameters of characteristic angles describing the differences of H₃TD1 conformers. See Fig. 1 for atom labels. All bond angles in degrees

Angle	Conf. 1	Conf. 2	Conf. 3
N ₃ -C ₆ -C ₄ -N ₁	16.2	22.4	-20.3
N ₃ -C ₉ -C ₁₁ -N ₂	-21.0	22.2	117.7
C ₄ -C ₅ -C ₆	128.4	127.1	127.1
C ₉ -C ₁₀ -C ₁₁	127.3	127.2	126.5

1 and 2 correspond to a *syn-Z*-conformer.⁶⁷

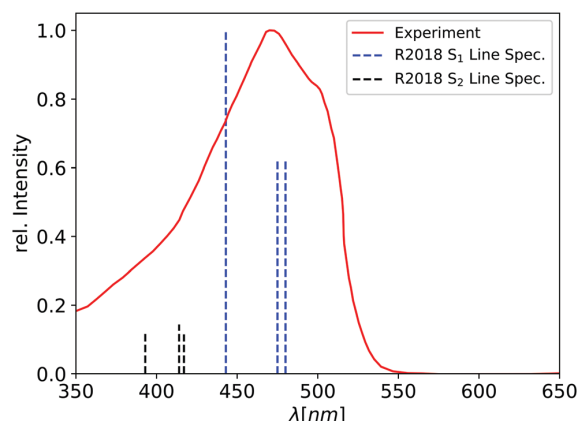


Fig. 2 Absorption spectrum of the H₃TD1 molecule. Calculated transitions to the S₁ state of the three energetically lowest conformers are in blue and to the S₂ state in black. The experimental spectrum²⁴ is red. The experiment and the calculated transitions have been normalised and do not represent the Boltzmann distribution.

Table 3 Differences in the S₀ → S₁ transition energy and oscillator strength $f(L)$ of three H₃TD1 conformers and energy differences of the S₀ ground state relative to conformer 1, calculated with DFT/MRCI-R2018

Conf.	$\Delta E_{S_0 \rightarrow S_1}$ (eV)	$\Delta E_{S_0 \rightarrow S_1}$ (nm)	$f(L)$	ΔE_{GS} (meV)
1	2.58	480	0.647	0
2	2.61	475	0.654	7.6
3	2.80	443	1.044	89.9

transition as well as the transition dipole moment. The resulting vertical energies and oscillator strengths of the three most stable conformers along with the experimental absorption spectrum can be found in Fig. 2. The vertical transition energies to the S₁ state as well as ground state energies relative to 1 are shown in Table 3.

The Boltzmann distribution shows a population of mainly conformer 1 (56%) and 2 (42%), while the energetically higher laying conformer 3 shows only a population of 2%. Due to the high flexibility of the molecule it is possible that more stable conformers exist that are energetically below conformer 3.

We can therefore conclude, that the different peaks stem from the S₁ state of different conformers due to the high flexibility of the molecule which allows rotations about the single bonds at room temperature. The density difference of all three calculated conformers, which also shows the structure of the conformers, is shown in Fig. 3.

The next bright state is the S₂ state. For the 1 conformer the state is located energetically at 2.98 eV (417 nm) with an oscillator strength of 0.12. For conformer 2 the state is located at 3.00 eV (414 nm) with a similar oscillator strength of 0.15 and for 3 at 3.15 eV (393 nm) with 0.13 oscillator strength.

4.3 Emission

The emission of the H₃TD1 molecule was calculated using the DFT/MRCI-R2018 method on the B3LYP-optimised S₁

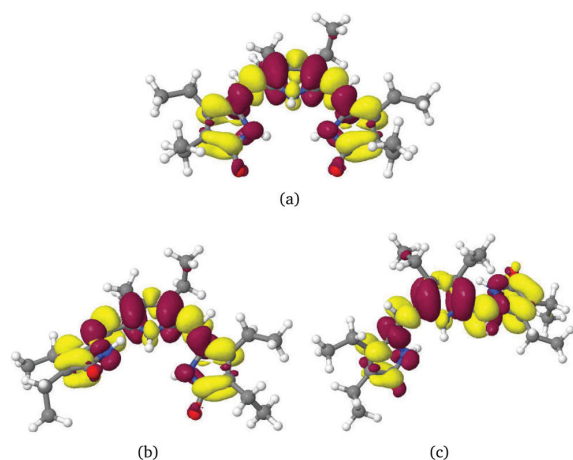


Fig. 3 Difference densities ($|\text{isovalue}| = 0.001$) of the S_1 state of the three energetically lowest conformers of the H_3TD1 ligand at the S_0 geometry. A loss of electron density with respect to the S_0 state is indicated in red, a gain in yellow. The energetically lowest conformer **1** is shown on the top (a), the second lowest **2** on the bottom left (b) and the third lowest **3** on the bottom right (c).

geometries of the two most stable conformers **1–2** that have a considerable population in the Boltzmann distribution. The vertical emission energy was found to be very similar in both conformers at 2.24 eV (553 nm) and 2.25 eV (552 nm), respectively. Both conformers show a strong transition with an oscillator strength of 0.62 and 0.63, respectively. The character of the S_1 state at the S_1 geometry is similar that at the S_0 geometry. A recent measurement by Swain *et al.* found the fluorescence of H_3TD1 in the spectral region about 550 nm in THF.⁶⁸ Consequently, our calculated vertical emission energies are in excellent agreement with the experiment.

5 Results for $[Zn(TD1^*)(H_2O)]$

5.1 Geometries

Gautam *et al.*²⁴ found the complex $[Zn(TD1^*)(H_2O)]$ (Fig. 1) to be a radical in solution at room temperature with one unpaired electron that is localised on the ligand. Our calculations confirm this observation. The SOMO (Fig. 4(b)) is located mostly on the carbon atoms of the aromatic system of the ligand with small contributions on the N_1 and N_2 atoms and none on the N_3 , zinc or the water ligand. The frontier orbitals HOMO, SOMO and LUMO are shown in Fig. 4.

The complex is C_s symmetric with the D_0 ground-state wave function transforming according to A'' . The mirror plane lies along the O_3-Zn-N_3 axis, as the equilibrium nuclear arrangement is not planar. It is quasi quadratically planar coordinated with the zinc atom slightly placed outside the plane of the coordinating nitrogen atoms. The crystal structure (CCDC 1438445)²⁴ shows small deviations from the mirror symmetry, that might be caused by environmental effects. Additionally, some ethyl groups are rotated upwards (*i.e.* the same side as the H_2O ligand) and others are rotated downwards while in the C_s

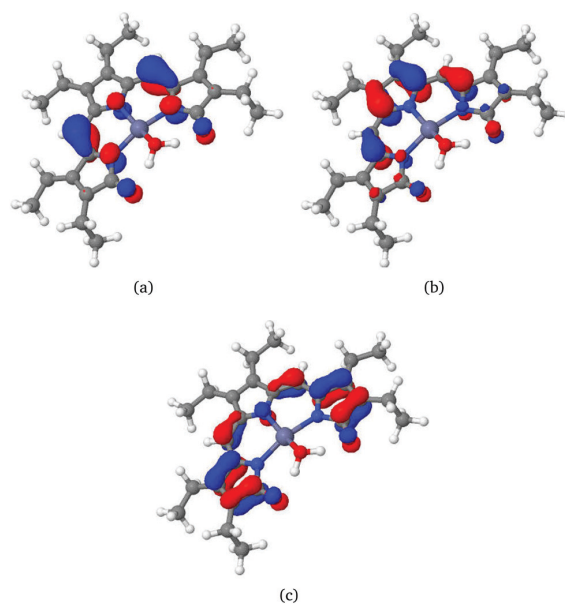


Fig. 4 The frontier orbitals of $[Zn(TD1^*)(H_2O)]$: (a) highest doubly occupied orbital (HOMO), (b) singly occupied orbital (SOMO), (c) lowest unoccupied orbital (LUMO).

structure four ethyl groups are oriented downwards and two are in plane. The orientation of the ethyl groups is expected to have minimal effect on the spectroscopic properties since they are not part of the photo-system and can rotate freely at room temperature. A test calculation in C_1 symmetry with the crystal structure as a starting structure confirms this expectation. The results are very similar regarding geometry and vertical transitions besides a shift of +0.13 eV in the D_2 energy, making the C_s structure the preferred choice by lowering the computational demand.

The calculations yield Zn–N distances of 204, 200 and 200 pm, compared to the experimental distances of 202 pm for all three bond lengths. The carbon–oxygen bonds are 125 pm in the experiment and 123 pm in the ground state calculation. Table 4 contains the geometry parameters of important calculated bond lengths and angles in the ground state and excited states. We decided against comparing to experimental Zn–O parameters due to the dimerisation of the complex in the solid state. According to EPR measurements by Gautam *et al.*,²⁴ each subunit of the $[Zn(TD1^*)(\mu-H_2O)]_2$ coordination dimer features an unpaired electron and hence retains its radical character.

The computed and experimental bond lengths in the electronic ground state are in good agreement, differing by 2 pm at most. The N_1-Zn-N_2 angle shows a larger deviation from the experiment, possibly due to the dimerisation of the complex in the crystal structure.

Geometry optimisation of the lowest-lying excited doublet states led to C_s symmetric D_1 and D_3 minima. Both excited states result from multiconfigurational ligand-centred transitions (*cf. supra*). All attempts to find the minimum of the D_2

Table 4 Selected geometry parameters of the UDFT-MN15 optimised ground state and the UTDDFT-MN15 optimised excited states of the $[\text{Zn}(\text{TD1}^*)(\mu\text{-H}_2\text{O})]$ complex in comparison to the experimental $[\text{Zn}(\text{TD1}^*)(\mu\text{-H}_2\text{O})_2]$ crystal structure. See Fig. 1 for atom labels. All bond lengths are in pm, bond angles in degrees

Bond	D ₀ exp. ²⁴	D ₀ calc.	D ₁ calc.	D ₃ calc.
Zn–N ₁	202	200	201	200
Zn–N ₃	202	204	203	203
C ₁ –O ₁	125	123	124	124
C ₁₄ –O ₂	125	123	124	124
Zn–O ₃	—	209	208	207
N ₁ –C ₁	138	137	139	138
C ₁ –C ₂	148	150	148	148
C ₄ –C ₅	138	139	142	140
O ₃ –Zn–N ₃	—	159	159	155
N ₁ –Zn–N ₃	91	92	92	93
N ₁ –Zn–N ₂	152	163	163	159

state were unsuccessful because D₁ and D₂ undergo a conical intersection along the optimisation path. The D₁ and D₃ geometries closely resemble the ground-state structure. While the zinc bond lengths are not expected to be altered due to the absence of electron density on the zinc center in the HDOMO, SOMO and LUMO (Fig. 4), other bond lengths in the ligand are almost unchanged as well.

5.2 Absorption

Electronic transitions from the electronic ground state to the first 10 excited states in each irreducible representation have been calculated with DFT/MRCI-R2018 at the ground state geometry in vacuum. The resulting line spectra have been Gaussian-broadened with a 1000 cm⁻¹ FWHM. Both are shown in Fig. 5 in comparison to the experimental spectrum²⁴ that was measured in tetrahydrofuran (THF). TDDFT test calculations employing a polarisable continuum solvent model (PCM)^{69–71} with THF as a solvent did not alter the results considerably. The excitation energies of the first 11 excited states shift

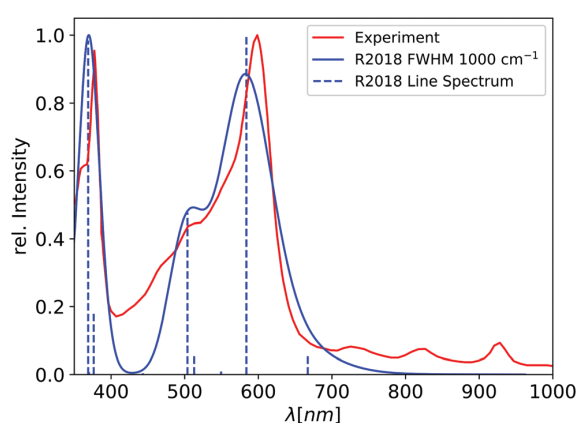


Fig. 5 Absorption spectrum of the $[\text{Zn}(\text{TD1}^*)(\text{H}_2\text{O})]$ radical calculated with DFT/MRCI-R2018 in comparison to experiment.²⁴ The calculated line spectrum has been broadened by Gaussians with a FWHM of 1000 cm⁻¹. The line spectrum and the highest peak maxima have been normalised to 1.

by ± 0.05 eV at most, with the exception of the D₂ state, which is red-shifted by 0.11 eV. The negligible influence of the solvent on the absorption spectrum is to be expected, because all excited states result from ligand-centred transitions with small impact on the static dipole moments.

Experimentally, three small bands with low oscillator strength have been observed in the long wavelength region at 927 nm (1.34 eV), 823 nm (1.51 eV) and 726 nm (1.71 eV) with the latter as a broad peak ranging from 1.69–1.73 eV. These three bands show a minimal blue-shift with increased temperature from 170 K to 290 K by a few meV.²⁴ The first strong absorption band peaks at about 600 nm and displays two shoulders at about 500 and 470 nm before evolving into the next strong absorption peak at 380 nm.

The calculated absorption spectrum is in good agreement with the experiment, in particular in the short wavelength region. In the long wavelength region, the calculated line spectrum comprises only two weak transitions with vertical excitation energies of 1.53 eV (809 nm, D₁) and 1.86 eV (667 nm, D₂). The D₁ state is mainly composed of a HDOMO \rightarrow SOMO and a SOMO \rightarrow LUMO configuration to almost equal contributions. The D₂ on the other hand is dominated by a HDOMO–1 \rightarrow SOMO transition. The density difference of the D₁ and D₂ states with respect to the D₀ state are shown in Fig. 6(a) and (b), respectively.

To make sure that the third band does not originate from a spin-forbidden transition, we computed quartet states as well. The first quartet state Q₁ is located vertically at 2.33 eV (532 nm), above the first four doublet states. It originates almost exclusively

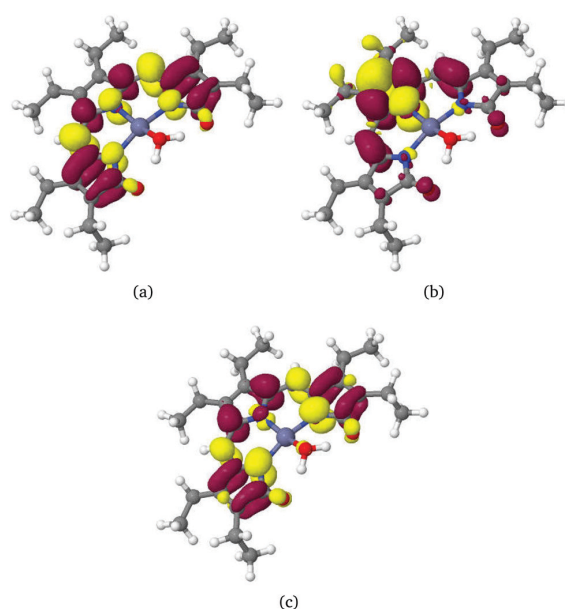


Fig. 6 Difference densities ($|\text{isovalue}| = 0.001$) of low-lying excited states of $[\text{Zn}(\text{TD1}^*)(\text{H}_2\text{O})]$ at the D₀ geometry. A loss of electron density with respect to the D₀ state is indicated in red, a gain in yellow. The dark D₁ (a) is shown on the top left, D₂ (b) on the top right and the bright state D₃ (c) on the bottom.

PCCP

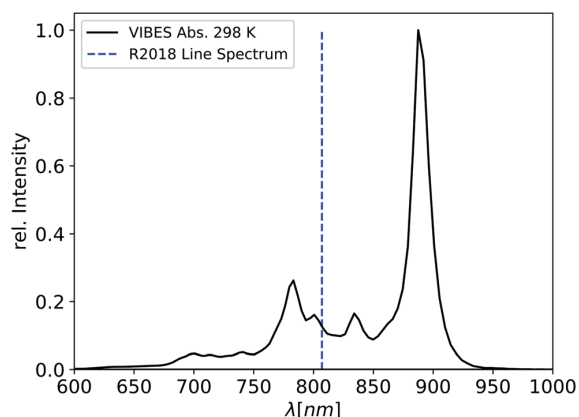


Fig. 7 Franck-Condon absorption spectrum of the D_1 state of the $[\text{Zn}(\text{TD1}^*)(\text{H}_2\text{O})]$ radical based on U(TD-)DT/MN15 vibrational frequencies and the adiabatic energy of the DFT/MRCI-R2018 calculation (black), compared to the vertical transition at the D_0 geometry calculated with DFT/MRCI-R2018 (blue).

from a HDOMO \rightarrow LUMO excitation. Its electronic structure does not match the character of any doublet state within the first 20 excited doublet states, but shows some resemblance to the D_{11} and D_{14} states (*vide infra*). These states share a similar spatial occupation with three open shells that leads to two CSF in doublet and one in quartet multiplicity.

The question of the missing band, found experimentally at 1.34 eV, was resolved when we computed a Franck-Condon spectrum of the $D_1 \leftarrow D_0$ transition (Fig. 7). The vibrational modes with the largest displacement that determine the structure of the spectrum are at 1519, 1245 and 734 cm^{-1} . All three vibrations are A' symmetric and stretched across the photoactive part of the ligand. The highest peak in the Franck-Condon spectrum at 900 nm is the 0-0 transition. It is significantly shifted with respect to the vertical transition energy at the ground-state minimum. The second experimental band with maximum at 823 nm seems to be caused by vibrational progressions of the $D_1 \leftarrow D_0$ transition according to our VIBES calculation.

A similar Franck-Condon analysis could not be performed for the $D_2 \leftarrow D_0$ transition, but the vertical excitation energy (667 nm) suggests that the third band at 726 nm originates from this transition. All in all, the electronic $D_1 \leftarrow D_0$ and $D_2 \leftarrow D_0$ transitions exhibit very low oscillator strength and are therefore hardly visible in the absorption spectrum in Fig. 5. We expect the intensity of these transitions to be enhanced by vibronic interactions like the Q band transitions of porphyrins and metalloporphyrins.⁶⁵ The $\text{H}_3\text{TD1}$ ligand when bound to a metal centre has a high structural similarity to metalloporphyrins, with H_2O instead of a fourth Zn-N bond. Also the electronic structures of the D_1 and D_3 states (*vide infra*) of $[\text{Zn}(\text{TD1}^*)(\text{H}_2\text{O})]$ resemble those of the S_1 and S_3 states of porphyrins³⁶ which form the Q_x and Soret(B) bands, respectively.

The strong absorption band is the transition to the D_3 state in our calculation, at an energy of 2.12 eV (586 nm), which is in good agreement with the 2.07 eV (599 nm) of the experiment.

The state has a multiconfigurational character that is mainly composed of a HDOMO \rightarrow SOMO and SOMO \rightarrow LUMO configuration to nearly equal parts with some contribution from the HDOMO-3 \rightarrow SOMO configuration. The transition is bright, with an oscillator strength of 0.33 in dipole length form. The corresponding transition dipole moment is 6.4 D. The characters of the D_1 and D_3 state are dominated by the same two configurations, which have a negative linear combination in the D_3 state and a positive linear combination in the D_1 state. This is causing the strong transition dipole moment of the D_3 and a cancelling transition dipole moment, resulting in only 0.19 D for the D_1 state. This cancellation is very similar to the Q band transition in zinc porphyrin.³⁶ The density difference of the D_3 state is shown in Fig. 6(c).

The shoulder at ≈ 500 nm corresponds to the transition to the D_6 state at 2.46 eV (504 nm) in our calculation, with a transition dipole moment of 4.6 D. The state is mainly characterised by a HDOMO-3 \rightarrow SOMO transition ($c^2 \approx 0.5$) admixed with some minor contributions from other configurations. The density difference of the D_6 state is shown in Fig. 8(a). The D_6 state, like the D_1 , D_2 and D_3 state, has AA' symmetry.

The bright transition with the highest energy in the absorption spectrum in Fig. 5 stems from the D_{11} state at 3.36 eV (369 nm). The corresponding experimental transition is of similar brightness at roughly 3.31 eV (375 nm). The D_{11} has A'' symmetry and a multiconfigurational character. The HDOMO \rightarrow LUMO configuration possesses three open shells, resulting in two CSF with different spin coupling patterns that contribute to the state with coefficients of 0.48 and 0.42. The third contribution stems from the HDOMO-3 \rightarrow LUMO transition with a coefficient of -0.47. The density difference of the D_{11} state is shown in Fig. 8(b).

The next bright state is the D_{14} at 3.85 eV (322 nm) in our calculation, which is outside the spectral range of the experiment. Its character shows some similarity to that of the D_{11} and Q_1 state with two CSF of the HDOMO \rightarrow LUMO configuration with coefficients of 0.57 and -0.33. The third contribution to this multiconfigurational state is a SOMO \rightarrow LUMO+1 transition with a coefficient of 0.46. The oscillator strengths of the D_{11} and D_{14} state are 0.28 and 0.33, respectively.

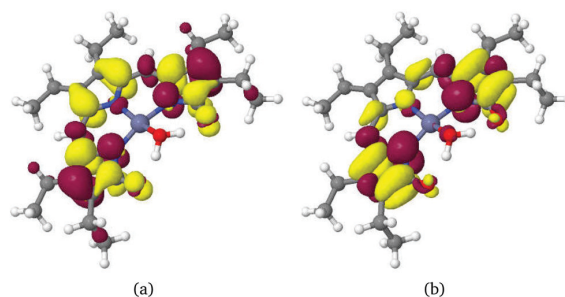


Fig. 8 Difference densities (isovalue = 0.001) of low-lying excited states of $[\text{Zn}(\text{TD1}^*)(\text{H}_2\text{O})]$ at the D_0 geometry. A loss of electron density with respect to the D_0 state is indicated in red, a gain in yellow. The bright states D_6 and D_{11} are on the left and right, respectively.

Table 5 Vertical excitation energies and oscillator strengths of DFT/MRCI-R2018, UTD-DFT-MN15 and UTD-DFT-PBE0 at the UDFT-MN15 optimised D_0 ground state geometry. State assignment is according to the DFT/MRCI results. All UTDDFT states that are energetically above the D_3 state have a high degree of spin contamination and should be considered with caution. All energies are in eV and the oscillator strength in length form is given in parentheses

State	DFT/MRCI-R2018	UTDDFT-MN15	UTDDFT-PBE0
D_1	1.54 (0.0002)	1.70 (0.0005)	1.65 (0.0003)
D_2	1.86 (0.0206)	2.15 (0.0660)	2.03 (0.0373)
D_3	2.12 (0.3314)	2.32 (0.3370)	2.24 (0.2273)
D_6	2.46 (0.1581)	2.66 (0.1089)	2.46 (0.2346)
D_{11}	3.36 (0.3251)	3.56 (0.1049)	3.26 (0.0501)
D_{14}	3.85 (0.2757)	4.14 (0.3715)	3.91 (0.2177)

A comparison of the vertical excitation energies of the discussed states to the UTD-DFT calculations employing the PBE0 and MN15 functional can be found in Table 5.

For the lowest three states the UTD-DFT energies are higher than the experiment while the spin-contamination is of no concern in these states. In the higher states, however, the amount of spin contamination increases drastically. The D_{11} state arrives at $S^2 \approx 1.8$ in the PBE0 calculation and $S^2 \approx 1.5$ in the MN15 calculation, thus producing unreliable results. In contrast, the DFT/MRCI results are unaffected by multiplicity mixing since the wave function is an eigenfunction of the \hat{S}^2 operator.

5.3 Emission

After photoexcitation of the radical complex to the D_3 state at 599 nm (2.07 eV), strong fluorescence with a quantum yield of 23% was observed with maximum at 644 nm (1.93 eV) at room temperature in tetrahydrofuran solution.²⁴ According to Kasha's rule,³⁰ the complex is expected to emit from the D_1 state, but the emission wavelength is much too short considering that the $D_1 \rightarrow D_0$ 0–0 transition has a wavelength around 900 nm. We therefore tested various alternative explanations, *i.e.*,

- non-Kasha emission from the D_3 state of $[\text{Zn}(\text{TD1}^*)(\text{H}_2\text{O})]$,
- formation of an exciplex with a THF molecule,
- emission from a reduced species $[\text{Zn}(\text{TD1})(\text{H})]$,
- disproportionation of the radical to a $[\text{Zn}(\text{TD1})(\text{H}_2\text{O})]^{+}$ – $[\text{Zn}(\text{TD1})(\text{H}_2\text{O})]^{-}$ ion pair with subsequent emission from the cation and/or the anion complex,
- emission from the free ligand $\text{H}_3\text{TD1}$.

5.3.1 Non-Kasha emission from the D_3 state. For the D_3 state, we calculate a vertical emission energy of 1.99 eV (622 nm). The state has a multiconfigurational character and is composed mainly of a SOMO \rightarrow LUMO and HOMO \rightarrow SOMO configuration with some contribution from the HOMO–3 \rightarrow SOMO configuration. The character is nearly identical to that of the D_3 at the D_0 ground state geometry. The Stokes shift amounts to 0.13 eV in our calculation and 0.14 eV in the experiment. The emissive state has a high oscillator strength of 0.29. Disregarding non-radiative decay, we obtain a fluorescence rate constant of this state of $5.0 \times 10^7 \text{ s}^{-1}$, which corresponds to a fluorescence lifetime of 19.9 ns.

Non-Kasha emission from an upper minimum usually occurs if the energy gap between the emitting state and the

lowest excited state is large and the overlap of the vibrational wave functions is small. This is not the case here. The adiabatic energy difference between the D_3 and D_1 states is merely 0.61 eV and the potentials are only slightly displaced. We have no idea why the internal conversion from D_3 to D_1 cannot compete with the radiative decay of the D_3 state. Nonetheless, the overlapping onsets of the experimental absorption and emission spectra and the low Stokes shift strongly suggests that the emitting and absorbing electronic states are the same.

5.3.2 Exciplex formation. In order to investigate the possibility of exciplex formation with a coordinating solvent, a THF molecule was added that coordinates to the zinc ion in a similar fashion as the second H_2O in the crystal structure. THF coordination does not alter the vertical absorption spectrum by more than -0.05 eV, eliminating the possibility of a solvent-induced change of the excited states.

5.3.3 Emission from a neutral reduced species. Emission from a neutral reduced species $[\text{Zn}(\text{TD1})(\text{H})]$, where the water ligand of the $[\text{Zn}(\text{TD1}^*)(\text{H}_2\text{O})]$ radical had been replaced by a hydrogen atom, could be excluded as the origin of the emission as well. The S_1 state of this complex (vertical absorption energy 1.41 eV, 881 nm) has a similar energy as the D_1 state of the open-shell species (*vide supra*). The S_1 wave function is mainly composed of a HOMO \rightarrow LUMO excitation. The HOMO corresponds to the HOMO of $[\text{Zn}(\text{TD1}^*)(\text{H}_2\text{O})]$ (Fig. 4(a)) with a strong similarity of the charge distribution and orbital phases. The main difference is some charge density on the hydrogen atom that is bound to the zinc centre. The LUMO of the closed-shell species is undistinguishable from the SOMO of $[\text{Zn}(\text{TD1}^*)(\text{H}_2\text{O})]$ (Fig. 4(b)) and the same holds true for the LUMO+1 of $[\text{Zn}(\text{TD1})(\text{H})]$ in relation to the LUMO of $[\text{Zn}(\text{TD1}^*)(\text{H}_2\text{O})]$ (Fig. 4(c)). Unlike the D_1 and D_3 states of the radical, the S_1 state of $[\text{Zn}(\text{TD1})(\text{H})]$ is not multiconfigurational.

5.3.4 Emission from a cation–anion pair. Motivated by the observation of cationic and anionic states in the related $[\text{Pd}(\text{TD1}^*)(\text{H}_2\text{O})]$ complex,⁶⁷ we investigated two further redox states of the $[\text{Zn}(\text{TD1}^*)(\text{H}_2\text{O})]$ complex with regard their absorption and emission using the DFT/MRCI-R2018 method.

In the oxidised state of the complex, $[\text{Zn}(\text{TD1})(\text{H}_2\text{O})]^+$, the low-lying bands between 700 and 950 nm, characteristic of metal-bound $\text{TD1}^{2-\bullet}$, disappear. The S_1 state is mainly characterised by a HOMO \rightarrow LUMO transition. The orbitals are visually indistinguishable from the ROKS orbitals of the $[\text{Zn}(\text{TD1}^*)(\text{H}_2\text{O})]$. The HOMO matches the HOMO of the radical (Fig. 4(a)), while LUMO and SOMO (Fig. 4(b)) as well as LUMO+1 and LUMO (Fig. 4(c)) are corresponding orbitals, respectively. The spectroscopic properties of the $S_1 \leftarrow S_0$ absorption in terms of the vertical excitation energy (1.92 eV, 644 nm) and the oscillator strength of the transition (0.45), are in the same ballpark as the corresponding properties of the $D_3 \leftarrow D_0$ transition in the neutral radical state. The emission energy of the S_1 state is 1.73 eV (715 nm) with an oscillator strength of 0.34.

In the $[\text{Zn}(\text{TD1})(\text{H}_2\text{O})]^-$ anion, the first absorption band is blue-shifted to 2.28 eV (543 nm). The oscillator strength (0.59) is stronger than for the radicalic and cationic species.

PCCP

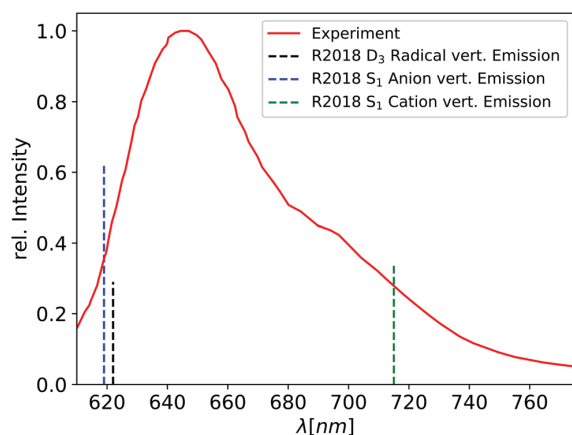


Fig. 9 Calculated line spectra of the D_3 emission of the neutral $[\text{Zn}(\text{TD1}^*)(\text{H}_2\text{O})]$ radical (black, dashed), the S_1 emission of the $[\text{Zn}(\text{TD1})(\text{H}_2\text{O})]^-$ anion (blue, dashed) and the S_1 emission of the $[\text{Zn}(\text{TD1})(\text{H}_2\text{O})]^+$ cation (green, dashed), with intensities corresponding to the oscillator strengths of the transitions. The normalised experimental spectrum²⁴ was measured at room temperature in THF.

The character of the S_1 state is best described by a HOMO \rightarrow LUMO configuration, with the HOMO of the anion corresponding to the SOMO (Fig. 4(b)) of the radical. The LUMO (Fig. 4(c)) in both complexes is very similar as well. The $S_1 \leftarrow S_0$ excitation of the anion is thus comparable to the SOMO \rightarrow LUMO configuration in the D_1 and D_3 states of the radical. The emission of the S_1 state occurs with a vertical energy of 2.00 eV (619 nm) and an oscillator strength of 0.62.

Fig. 9 shows the emission from the anion and cation compared to the neutral radical and the experiment. Considering only the wavelengths and oscillator strengths, the emission might very well originate from the cation–anion pair state. However, the calculations of the monomers show a vertical ionisation potential of 6.02 eV and a vertical electron affinity of -2.18 eV, both at the D_0 geometry. The adiabatic energies are 5.83 eV and -2.30 eV, respectively. Thus, while the emission energies of the cation and anion states fit very well and even explain the shoulder in the experimental spectrum at ≈ 700 nm, the energy balance does not allow the formation of isolated cations and anions in the absence of an external electric potential. In contrast, disproportionation of the radical to a $[\text{Zn}(\text{TD1})(\text{H}_2\text{O})]^+[\text{Zn}(\text{TD1})(\text{H}_2\text{O})]^-$ ion pair in van der Waals distance would be possible due to the compensating effect of their coulombic attraction.

5.3.5 Emission of the tripyrrin-1,14-dione ligand. Another possibility to be considered is the emission of the free ligand after demetalation. The measured⁶⁸ and calculated emission of the $\text{H}_3\text{TD1}$ molecule (see Section 4.3) lies at ≈ 550 nm and is therefore energetically too high. Additionally, the experimental²⁴ fluorescence of $[\text{Zn}(\text{TD1}^*)(\text{H}_2\text{O})]$ was measured after excitation at 599 nm, making the S_1 state of the free ligand energetically inaccessible.

5.3.6 Appraisal of the alternative explanations. While the emission from the D_3 state of the $[\text{Zn}(\text{TD1}^*)(\text{H}_2\text{O})]$ radical is counter-intuitive, it is the only explanation that we can provide

with the experimental and computational data on our hands. The fact that the experimentally observed emission band lies at considerably shorter wavelengths than the lowest absorption band of the radical precludes the $D_1 \rightarrow D_0$ transition of the complex as the origin of the emission. From the possibilities discussed so far in Section 5.3, only two match the experimental spectrum and the energetic requirements. These are the non-Kasha D_3 emission of the neutral $[\text{Zn}(\text{TD1}^*)(\text{H}_2\text{O})]$ radical and the emission from the S_1 state of the closed-shell anion that is part of an ion pair. Due to the high spectral overlap between absorption and emission in the experimental spectrum and the low Stokes shift, we are inclined to predict D_3 to be the emissive state.

6 Conclusions

In this work the newly developed all-multiplicity DFT/MRCI-R2018 Hamiltonian has been employed to an open-shell system with an odd number of electrons after being previously successfully employed to closed-shell platinum complexes.⁴⁵ By using the same parameter set for all calculations and multiplicities involved, we were able to obtain comparable results and IP and EA energies between open-shell and closed-shell species.

The absorption properties of the $[\text{Zn}(\text{TD1}^*)(\text{H}_2\text{O})]$ radical are in good agreement to the experiment. We find the D_3 , D_6 and D_{11} state to be the brightest state in the spectral region above 350 nm within our DFT/MRCI-R2018 calculations. The experimentally observed fluorescence with maximum at 644 nm following the photoexcitation at 599 nm in THF solution is attributed to the non-Kasha emission from the D_3 state. Emissions from the S_1 states of the closed-shell anion and cation, respectively, lie in the same spectral range. However, due to the high ionisation potential of the radical complex, these states are energetically accessible only if the anion and cation form an ion pair. In contrast to DFT/MRCI, the UTDDFT reference calculations show an overestimation of the energies of the lowest three states, including the emissive state at the D_3 geometry, and a high degree of spin-contamination in higher states.

The nature of the emission makes it difficult to assess the suitability of the complex for application as emitters in electroluminescent devices. These doubts do not arise due to the fact that the emitter is a radical, because other dyes, *e.g.* the one developed by Peng *et al.*,⁸ emit from the lowest excited doublet state. Rather, the location of two non-emitting electronic states, D_1 and D_2 , well below the emissive D_3 state suggests that D_1 and D_2 might function as exciton traps, thus diminishing the internal quantum efficiency of the OLED.

In addition to the photophysics of the $[\text{Zn}(\text{TD1}^*)(\text{H}_2\text{O})]$ radical, the absorption and emission characteristics of the unmetalated tripyrrin-1,14-dione ligand has been investigated in this work. The unusual width of the $\text{H}_3\text{TD1}$ spectral peaks is explained through different conformers that are energetically accessible at room temperature causing a variation of the transition energy and oscillator strength of the $S_1 \leftarrow S_0$ absorption and $S_1 \rightarrow S_0$ emission.

Conflicts of interest

There are no conflicts to declare.

Acknowledgements

We thank Rainer Weinkauff (Düsseldorf) for valuable discussions. Financial support by the Deutsche Forschungsgemeinschaft (DFG) through project MA-1051/14-2 and through funds (INST 208/704-1 FUGG) enabling us to purchase the hybrid compute cluster used in this study is gratefully acknowledged.

Notes and references

- C. W. Tang and S. A. VanSlyke, *Appl. Phys. Lett.*, 1987, **51**, 913–915.
- Y. Ma, H. Zhang, J. Shen and C. Che, *Synth. Met.*, 1998, **94**, 245–248.
- M. A. Baldo, D. F. O'Brien, Y. You, A. Shoustikov, S. Sibley, M. E. Thompson and S. R. Forrest, *Nature*, 1998, **395**, 151–154.
- C. Adachi, M. A. Baldo, S. R. Forrest and M. E. Thompson, *Appl. Phys. Lett.*, 2000, **77**, 904–906.
- A. Endo, M. Ogasawara, A. Takahashi, D. Yokoyama, Y. Kato and C. Adachi, *Adv. Mater.*, 2009, **21**, 4802–4806.
- T. J. Penfold, E. Gindensperger, C. Daniel and C. M. Marian, *Chem. Rev.*, 2018, **118**, 6975–7025.
- H. Uoyama, K. Goushi, K. Shizu, H. Nomura and C. Adachi, *Nature*, 2012, **492**, 234–238.
- Q. Peng, A. Obolda, M. Zhang and F. Li, *Angew. Chem., Int. Ed.*, 2015, **54**, 7091–7095.
- Y. Gao, A. Obolda, M. Zhang and F. Li, *Dyes Pigm.*, 2017, **139**, 644–650.
- X. Ai, E. W. Evans, S. Dong, A. J. Gillett, H. Guo, Y. Chen, T. J. H. Hele, R. H. Friend and F. Li, *Nature*, 2018, **563**, 536–540.
- M. Gomberg, *J. Am. Chem. Soc.*, 1900, **22**, 757–771.
- V. Gamero, D. Velasco, S. Latorre, F. López-Calahorra, E. Brillas and L. Juliá, *Tetrahedron Lett.*, 2006, **47**, 2305–2309.
- Y. Hattori, T. Kusamoto and H. Nishihara, *Angew. Chem., Int. Ed.*, 2014, **53**, 11845–11848.
- T. Kusamoto, S. Kimura, Y. Ogino, C. Ohde and H. Nishihara, *Chem. – Eur. J.*, 2016, **22**, 17725–17733.
- S. Kimura, A. Tanushi, T. Kusamoto, S. Kochi, T. Sato and H. Nishihara, *Chem. Sci.*, 2018, **9**, 1996–2007.
- Y. Hattori, T. Kusamoto and H. Nishihara, *RSC Adv.*, 2015, **5**, 64802–64805.
- R. Beaulac, G. Bussière, C. Reber, C. Lescop and D. Luneau, *New J. Chem.*, 2003, **27**, 1200–1206.
- R. Beaulac, D. Luneau and C. Reber, *Chem. Phys. Lett.*, 2005, **405**, 153–158.
- C. Lescop, D. Luneau, G. Bussière, M. Triest and C. Reber, *Inorg. Chem.*, 2000, **39**, 3740–3741.
- H. M. Blatter and H. Lukaszewski, *Tetrahedron Lett.*, 1968, **9**, 2701–2705.
- G. Karecla, P. Papagiorgis, N. Panagi, G. A. Zissimou, C. P. Constantinides, P. A. Koutentis, G. Itskos and S. C. Hayes, *New J. Chem.*, 2017, **41**, 8604–8613.
- Y. Beldjoudi, M. A. Nascimento, Y. J. Cho, H. Yu, H. Aziz, D. Tonouchi, K. Eguchi, M. M. Matsushita, K. Awaga, I. Osorio-Roman, C. P. Constantinides and J. M. Rawson, *J. Am. Chem. Soc.*, 2018, **140**, 6260–6270.
- Y. Beldjoudi, A. Arauzo, J. Campo, E. L. Gavey, M. Pilkington, M. A. Nascimento and J. M. Rawson, *J. Am. Chem. Soc.*, 2019, **141**, 6875–6889.
- R. Gautam, S. J. Petritis, A. V. Astashkin and E. Tomat, *Inorg. Chem.*, 2018, **57**, 15240–15246.
- S. Wang, *Coord. Chem. Rev.*, 2001, **215**, 79–98.
- B. Franck, *Angew. Chem., Int. Ed. Engl.*, 1979, **18**, 429–439.
- H. Falk, *The Chemistry of Linear Oligopyrroles and Bile Pigments*, Springer Verlag, Wien, 1989.
- S. K. Dey, S. Datta and D. A. Lightner, *Monatsh. Chem.*, 2009, **140**, 1171–1181.
- J. Berüter, J.-P. Colombo and U. P. Schlunegger, *Eur. J. Biochem.*, 1975, **56**, 239–244.
- M. Kasha, *Discuss. Faraday Soc.*, 1950, **9**, 14.
- M. Beer and H. C. Longuet-Higgins, *J. Chem. Phys.*, 1955, **23**, 1390–1391.
- M. Sakamoto, X. Cai, M. Hara, S. Tojo, M. Fujitsuka and T. Majima, *J. Am. Chem. Soc.*, 2005, **127**, 3702–3703.
- A. Heil, M. Kleinschmidt and C. M. Marian, *J. Chem. Phys.*, 2018, **149**, 164106.
- S. Grimme and M. Waletzke, *J. Chem. Phys.*, 1999, **111**, 5645–5655.
- M. Kleinschmidt, C. M. Marian, M. Waletzke and S. Grimme, *J. Chem. Phys.*, 2009, **130**, 044708.
- C. M. Marian, A. Heil and M. Kleinschmidt, *Wiley Interdiscip. Rev.: Comput. Mol. Sci.*, 2019, **9**, e1394.
- I. Lyskov, M. Kleinschmidt and C. M. Marian, *J. Chem. Phys.*, 2016, **144**, 034104.
- A. Heil and C. M. Marian, *J. Chem. Phys.*, 2017, **147**, 194104.
- M. Kleinschmidt, C. van Wüllen and C. M. Marian, *J. Chem. Phys.*, 2015, **142**, 094301.
- A. Heil, K. Gollnisch, M. Kleinschmidt and C. M. Marian, *Mol. Phys.*, 2015, 1–16.
- J. Föllner, C. Ganter, A. Steffen and C. M. Marian, *Inorg. Chem.*, 2019, **58**, 5446–5456.
- A. Liske, L. Wallbaum, T. Hölzel, J. Föllner, M. Gernert, B. Hupp, C. Ganter, C. M. Marian and A. Steffen, *Inorg. Chem.*, 2019, **58**, 5433–5445.
- R. W. Wetmore and G. A. Segal, *Chem. Phys. Lett.*, 1975, **36**, 478–483.
- G. A. Segal, R. W. Wetmore and K. Wolf, *Chem. Phys.*, 1978, **30**, 269–297.
- A. Heil and C. M. Marian, *Inorg. Chem.*, 2019, **58**, 6123–6136.
- A. D. Becke, *J. Chem. Phys.*, 1993, **98**, 1372–1377.
- C. Lee, W. Yang and R. G. Parr, *Phys. Rev. B: Condens. Matter Mater. Phys.*, 1988, **37**, 785.
- H. S. Yu, X. He, S. L. Li and D. G. Truhlar, *Chem. Sci.*, 2016, **7**, 5032–5051.

- 49 J. P. Perdew, K. Burke and M. Ernzerhof, *Phys. Rev. Lett.*, 1996, **77**, 3865.
- 50 C. Adamo and V. Barone, *J. Chem. Phys.*, 1999, **110**, 6158–6170.
- 51 A. D. Becke, *J. Chem. Phys.*, 1993, **98**, 5648–5652.
- 52 S. Grimme, S. Ehrlich and L. Goerigk, *J. Comput. Chem.*, 2011, **32**, 1456–1465.
- 53 A. Schäfer, H. Horn and R. Ahlrichs, *J. Chem. Phys.*, 1992, **97**, 2571–2577.
- 54 D. Rappoport and F. Furche, *J. Chem. Phys.*, 2010, **133**, 134105.
- 55 M. Dolg, U. Wedig, H. Stoll and H. Preuss, *J. Chem. Phys.*, 1987, **86**, 866–872.
- 56 D. Figgen, G. Rauhut, M. Dolg and H. Stoll, *Chem. Phys.*, 2005, **311**, 227–244.
- 57 M. J. Frisch, G. W. Trucks, H. B. Schlegel, G. E. Scuseria, M. A. Robb, J. R. Cheeseman, G. Scalmani, V. Barone, G. A. Petersson, H. Nakatsuji, X. Li, M. Caricato, A. V. Marenich, J. Bloino, B. G. Janesko, R. Gomperts, B. Mennucci, H. P. Hratchian, J. V. Ortiz, A. F. Izmaylov, J. L. Sonnenberg, D. Williams-Young, F. Ding, F. Lipparini, F. Egidi, J. Goings, B. Peng, A. Petrone, T. Henderson, D. Ranasinghe, V. G. Zakrzewski, J. Gao, N. Rega, G. Zheng, W. Liang, M. Hada, M. Ehara, K. Toyota, R. Fukuda, J. Hasegawa, M. Ishida, T. Nakajima, Y. Honda, O. Kitao, H. Nakai, T. Vreven, K. Throssell, J. A. Montgomery, Jr., J. E. Peralta, F. Ogliaro, M. J. Bearpark, J. J. Heyd, E. N. Brothers, K. N. Kudin, V. N. Staroverov, T. A. Keith, R. Kobayashi, J. Normand, K. Raghavachari, A. P. Rendell, J. C. Burant, S. S. Iyengar, J. Tomasi, M. Cossi, J. M. Millam, M. Klene, C. Adamo, R. Cammi, J. W. Ochterski, R. L. Martin, K. Morokuma, O. Farkas, J. B. Foresman and D. J. Fox, *Gaussian 16 Revision B.01*, Gaussian Inc., Wallingford CT, 2016.
- 58 K. Aidas, C. Angeli, K. L. Bak, V. Bakken, R. Bast, L. Boman, O. Christiansen, R. Cimiraglia, S. Coriani, P. Dahle, E. K. Dalskov, U. Ekström, T. Enevoldsen, J. J. Eriksen, P. Ettenhuber, B. Fernández, L. Ferrighi, H. Fliegl, L. Frediani, K. Hald, A. Halkier, C. Hättig, H. Heiberg, T. Helgaker, A. C. Hennum, H. Hettema, E. Hjertenæs, S. Høst, I.-M. Høyvik, M. F. Iozzi, B. Jansik, H. J. Aa. Jensen, D. Jonsson, P. Jørgensen, J. Kauczor, S. Kirpekar, T. Kjærgaard, W. Klopper, S. Knecht, R. Kobayashi, H. Koch, J. Kongsted, A. Krapp, K. Kristensen, A. Ligabue, O. B. Lutnæs, J. I. Melo, K. V. Mikkelsen, R. H. Myhre, C. Neiss, C. B. Nielsen, P. Norman, J. Olsen, J. M. H. Olsen, A. Osted, M. J. Packer, F. Pawłowski, T. B. Pedersen, P. F. Provasi, S. Reine, Z. Rinkevicius, T. A. Ruden, K. Ruud, V. V. Rybkin, P. Salek, C. C. M. Samson, A. S. de Merás, T. Saue, S. P. A. Sauer, B. Schimmelpfennig, K. Snegov, A. H. Steindal, K. O. Sylvester-Hvid, P. R. Taylor, A. M. Teale, E. I. Tellgren, D. P. Tew, A. J. Thorvaldsen, L. Thøgersen, O. Vahtras, M. A. Watson, D. J. D. Wilson, M. Ziolkowski and H. Ågren, *Wiley Interdiscip. Rev.: Comput. Mol. Sci.*, 2014, **4**, 269–284.
- 59 Dalton, a molecular electronic structure program, Release v2018.0, 2018, see <http://daltonprogram.org>.
- 60 O. Vahtras, J. Almlöf and M. Feyereisen, *Chem. Phys. Lett.*, 1993, **213**, 514–518.
- 61 F. Weigend and M. Häser, *Theor. Chem. Acc.*, 1997, **97**, 331–340.
- 62 F. Weigend, M. Häser, H. Patzelt and R. Ahlrichs, *Chem. Phys. Lett.*, 1998, **294**, 143–152.
- 63 A. Hellweg and D. Rappoport, *Phys. Chem. Chem. Phys.*, 2015, **17**, 1010–1017.
- 64 M. Etinski, J. Tatchen and C. M. Marian, *J. Chem. Phys.*, 2011, **134**, 154105.
- 65 M. Etinski, J. Tatchen and C. M. Marian, *Phys. Chem. Chem. Phys.*, 2014, **16**, 4740.
- 66 A. Baiardi, J. Bloino and V. Barone, *J. Chem. Theory Comput.*, 2013, **9**, 4097–4115.
- 67 R. Gautam, J. J. Loughrey, A. V. Astashkin, J. Shearer and E. Tomat, *Angew. Chem., Int. Ed.*, 2015, **54**, 14894–14897.
- 68 A. Swain, B. Cho, R. Gautam, C. J. Curtis, E. Tomat and V. Huxter, *J. Phys. Chem. B*, 2019, **123**, 5524–5535.
- 69 S. Miertuš, E. Scrocco and J. Tomasi, *Chem. Phys.*, 1981, **55**, 117–129.
- 70 S. Miertuš and J. Tomasi, *Chem. Phys.*, 1982, **65**, 239–245.
- 71 J. L. Pascual-Ahuir, E. Silla and I. Tuñón, *J. Comput. Chem.*, 1994, **15**, 1127–1138.